Universitat de Girona

PEPTIDE CONJUGATES CONTAINING CHLORAMBUCIL OR TETRADENTATE AMINOPYRIDINE LIGANDS FOR ANTICANCER TREATMENT

Marta Soler Vives

Dipòsit legal: Gi. 324-2015
http://hdl.handle.net/10803/285974

Universitat de Girona

DOCTORAL THESIS

Peptide conjugates containing chlorambucil or tetradentate aminopyridine ligands for anticancer treatment

Marta Soler Vives

2014

Doctoral Programme in Chemistry

Supervised by: Dr. Miquel Costas Salgueiro
Dr. Marta Planas Grabuleda
Dr. Lidia Feliu Soley

Tutor: Dr. Anna Roglans Ribas

This manuscript has been presented to opt for the **Doctoral Degree** from the **Universitat de Girona**

Universitat de Girona

Dr. Miquel Costas Salgueiro, Dr. Marta Planas Grabuleda, Dr. Lidia Feliu Soley and Dr. Anna Roglans Ribas, of Universitat de Girona,

WE DECLARE:

That the thesis entitled “Peptide conjugates containing chlorambucil or tetradentate aminopyridine ligands for anticancer treatment“, presented by Marta Soler Vives to obtain a doctoral degree, has been completed under our supervision and meets the requirements to opt for an International Doctorate.

For all intents and purposes, we hereby sign this document.

Supervisors: Dr. Miquel Costas Salgueiro Dr. Marta Planas Grabuleda Dr. Lidia Feliu Soley

Tutor: Dr. Anna Roglans Ribas

Girona, November 28th 2014

El món, en meravelles i jocs atrafegat,

és petit i vermell i fresc com les maduixes

***Josep Carner**, Els fruits saborosos (1906)*

Als de casa,

que m'ho han ensenyat tot

FULL LIST OF PUBLICATIONS

Publications derived from this thesis:

- **Chapter III.** Soler, M;† González-Bártulos, M;† Soriano-Castell, D; Ribas, X; Costas, M; Tebar, F; Massaguer, A; Feliu, L; and Planas, M. Identification of BP16 as a non-toxic cell-penetrating peptide with highly efficient drug delivery properties. *Org. Biomol. Chem.,* **2014**, 12, 1652–1663 (Impact factor: 3.568, position 12/57 in Chemistry, Organic, 1st quartile, Times cited: 1).

  †Authors contributed equally to this work

- **Chapter IV.** Soler, M; González-Bártulos, M; Figueras, E; Massaguer, A; Ribas, X; Costas, M; Planas, M; and Feliu, L. Enzyme-triggered delivery of chlorambucil from conjugates based on the cell-penetrating peptide BP16. *Organic & Biomolecular Chemistry,* **2014**. DOI: 10.1039/C4OB01875C

Manuscripts in preparation derived from this thesis:

- **Chapter I.** Soler, M; Feliu, L; Planas, M; Ribas, X; and Costas, M. Biomedical application of functional metallopeptides (Review article).

- **Chapter V.** Soler, M; Figueras, E; Serrano, J; Company, A; Martínez, MA; Feliu, L; Planas, M; Ribas, X; and Costas, M. Enhanced and selective DNA cleavage activity of redox-active metallopeptides based on tetradentate aminopyridine ligands.

- **Chapter VI.** Soler, M; González-Bártulos, M; Figueras, E; Massaguer, A; Feliu, L; Planas, M; Ribas, X; and Costas, M. Delivering aminopyridine ligands into cancer cells through conjugation to the cell-penetrating peptide BP16.

- **Chapter VII.** Soler, M; Worm, D; Sosniak, AM; Redeker, B; Hahn, SA; Feliu, L; Planas, M; Metzler-Nolte, N; Ribas, X; and Costas, M. BPBP-PNA conjugate as metal-free artificial nuclease for oncogenic miRNAs targeting.

LIST OF ABBREVIATIONS

Ac	acetyl
Ahx	2-aminohexanoic acid
AMP	antimicrobial peptide
Asc	sodium L-ascorbate
Boc	*tert*-butyloxycarbonyl
(*S,S'*)-BPBP	(2*S*,2*S*')-1,1'-bis(pyrid-2-ylmethyl)-2,2'-bipyrrolidine
CF	5(6)-carboxyfluorescein
CLB	chlorambucil
CPHP	cell-penetrating-homing peptide
CPP	cell-penetrating peptide
d	doublet
Dde	1-(4,4-dimethyl-2,6-dioxocyclohex-1-ylidene)ethyl
DIPCDI	*N,N'*-diisopropylcarbodiimide
DIPEA	*N,N'*-diisopropylethylamine
DMAP	4-(dimethylamino)pyridine
DMF	*N,N*-dimethylformamide
DMSO	dimethyl sulfoxide
DNA	deoxyribonucleic acid
DTT	D,L-dithiothreitol
EDTA	ethylenediaminetetraacetic acid
equiv	equivalents
ESI-MS	electrospray mass spectrometry
Et	ethyl
Fmoc	9-fluorenylmethoxycarbonyl
HOBt	1-hydroxybenzotriazole
HPLC	high performance liquid chromatography
HRMS	high resolution mass spectrometry
J	coupling constant
m	multiplet
m/z	mass-to-charge ratio
MBHA	*p*-methylbenzhydrylamine

MTT	3-(4,5-dimethylthiazol-2-yl)-2,5-diphenyltetrazolium bromide
MWI	microwave irradiation
NMP	*N*-methyl-2-pyrrolidinone
NMR	nuclear magnetic resonance
Oxyma	ethyl 2-cyano-2-(hydroxyimino)acetate
PNA	peptide nucleic acid
PyBOP	(benzotriazol-1-yloxy)tripyrrolidinophosphonium hexafluorophosphate
^{Me2}PyTACN	1,4-dimethyl-7-(2-pyridylmethyl)-1,4,7-triazacyclononane
Rf	retention factor
RNA	ribonucleic acid
ROS	reactive oxygen species
s	singlet
SDDS	smart drug delivery system
SPPS	solid-phase peptide synthesis
t	triplet
TBAF	tetrabutylammonium fluoride
TBS	*tert*-butyldimethylsilyl
TFA	trifluoroacetic acid
THF	tetrahydrofuran
TIS	triisopropylsilane
TLC	thin layer chromatography
t_R	retention time
Ts	*p*-toluenesulfonyl

AMINO ACIDS

Name	Three letter code	One letter code
Aspartic acid	Asp	D
Glutamic acid	Glu	E
Alanine	Ala	A
Arginine	Arg	R
Asparagine	Asn	N
Cysteine	Cys	C
Phenylalanine	Phe	F
Glycine	Gly	G
Glutamine	Gln	Q
Histidine	His	H
Isoleucine	Ile	I
Leucine	Leu	L
Lysine	Lys	K
Methionine	Met	M
Norleucine	Nle	-
Proline	Pro	P
Serine	Ser	S
Tyrosine	Tyr	Y
Threonine	Thr	T
Tryptophan	Trp	W
Valine	Val	V

ACKNOWLEDGEMENTS

This work would not have been possible without the following collaborations:

- Serveis Tècnics de Recerca (STR) from Universitat de Girona for technical support.

- Dr. Anna Massaguer and Marta González from Universitat de Girona for the biological assays during this thesis.

- Dr. Mª Ángeles Martínez from Universitat de Girona for the collaborative research in DNA cleavage studies.

- Prof. Dr. Nils Metzler-Nolte, Prof. Dr. Stephen Hahn, Dr. Anna Sosniak, Dennis Worm and Britta Redeker from Ruhr-Universität Bochum for hosting a scientific visit and the collaborative work within the context of PNA-based artificial nucleases.

- Dr. Francesc Tebar and David Soriano from Hospital Clínic for the cellular uptake characterization of BP16 by confocal studies.

- Dr. Teodor Parella from Universitat Autònoma de Barcelona for helping discussions.

- Eduard Figueras for working with me throughout this new project and providing valuable results for this thesis.

- Consolider Ingenio CSD/CSD2010-00065 financial project from MICINN of Spain. ERC-2009-StG-20081029 from European Research Foundation.

The development of this doctoral thesis has been funded by the following research project from the Spanish government (MICINN):

Chemistry applied to the Design, Synthesis and Evaluation of Bioactive Compounds of Antiinflammatory, Antitumour or Antiparasitic Action (CSD2010-00065).

Marta Soler Vives gratefully acknowledges the financial support from European Research Foundation (ERC-2009-StG-20081029) for her scientific visit at Ruhr-Universität Bochum.

GRAPHICAL ABSTRACT

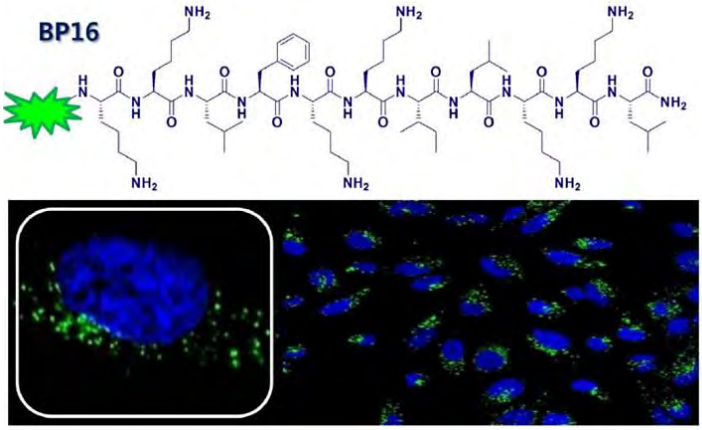

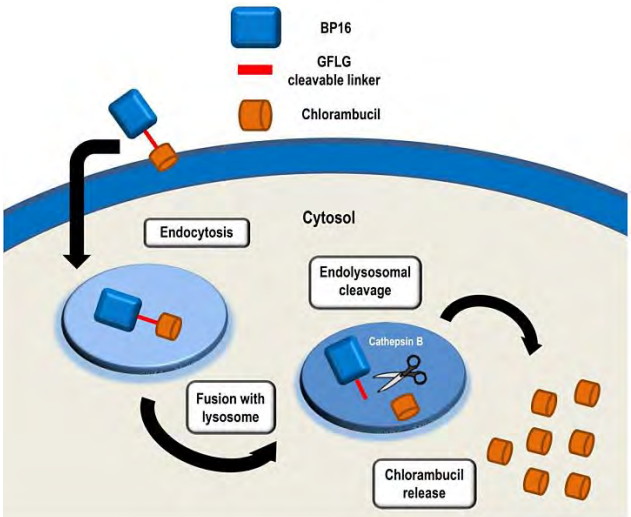

Chapter V. Enhanced and selective DNA cleavage activity of redox-active metallopeptides based on tetradentate aminopyridine ligands (p. 135)

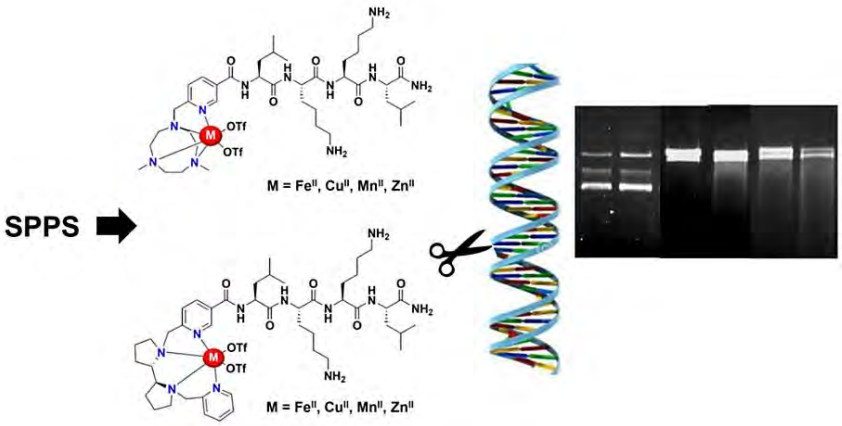

Chapter VI. Delivering aminopyridine ligands into cancer cells through conjugation to the cell-penetrating peptide BP16 (p. 173)

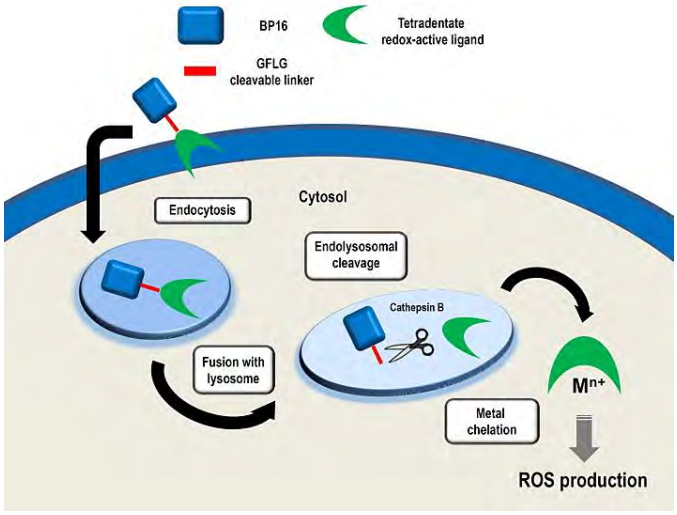

Chapter VII. BPBP-PNA conjugate as metal-free artificial nuclease for oncogenic miRNAs targeting (p. 205)

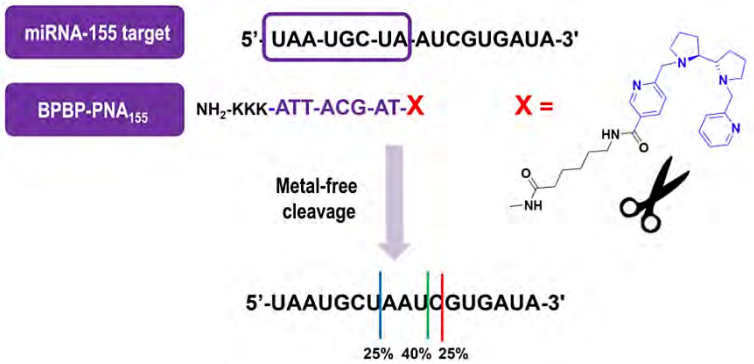

TABLE OF CONTENTS

Supplementary Digital Information

- PhD thesis (pdf file)
- APPENDIX: Electronic supporting information for Chapters III – VII (pdf file)

ABSTRACT

Nowadays one of the major problems in drug delivery is the transport of therapeutic molecules across membrane barriers. Towards the development of efficient delivery methodologies, cell-penetrating peptides (CPPs) have become one of the most effective tools to promote efficient cellular uptake. Although a variety of CPPs have been described for medical applications, most of them exhibit poor stability and potential side-effects in terms of toxicity. Furthermore, the targeting of biochemical alterations in cancer cells is considered as an emerging strategy against drug resistance. Since transition metal complexes based on aminopyridine tetradentate ligands render high redox reactivity, their intracellular vectorization could induce irreversible oxidative stress through reactive oxygen species (ROS)-mediated mechanisms. Towards this end, this thesis is centered on the vectorization of N_4-based ligands into cancer cells through conjugation to non-toxic peptide derivatives.

In the first part (Chapters III and IV), we describe the identification of a non-toxic cell-penetrating peptide from a library of antimicrobial undecapeptides. In this regard, we study the cell internalization capacities and the drug delivery properties of this novel cell-penetrating sequence by using a well-known anticancer drug. Moreover, we explore its applicability in smart drug delivery approaches by evaluating several drug-peptide conjugation strategies as well as by employing enzyme-triggered strategies.

In the second part (Chapters V, VI and VII), we investigate the conjugation of ^{Me2}PyTACN and (*S,S*')-BPBP ligands to different peptide derivatives. In Chapter V, we describe a straightforward solid-phase methodology to prepare redox-active metal binding tetrapeptides, which are further metallated using iron, manganese, zinc and copper ions. The resulting metallopeptides are characterized and further studied as selective DNA nucleases. In Chapter VI, we examine the extension of the synthetic methodology for the conjugation of ^{Me2}PyTACN and (*S,S'*)-BPBP ligands to a novel cell-penetrating peptide. We study the cytotoxic activities and the internalization behaviors of the resulting conjugates in cancer cells as well as the use of an enzyme-cleavable moiety to promote intracellular release. Finally, in Chapter VII we conjugate the (*S,S*')-BPBP ligand to PNA recognition sequences that are meant to target specific oncogenic miRNA sites. The cleavage of RNA by the resulting conjugates under mild conditions is explored.

RESUM

Actualment un dels principals problemes en l'administració de fàrmacs és el transport de molècules terapèutiques a través de la membrana cel·lular. Amb l'objectiu de desenvolupar metodologies d'administració eficients, l'ús de *cell-penetrating peptides* (CPPs) constitueix una de les eines més efectives per promoure una internalització cel·lular eficaç. Tot i la varietat de CPPs que s'han descrit per a aplicacions mèdiques, la gran majoria presenten una estabilitat pobra i efectes secundaris importants. Per altra banda, el *targeting* d'alteracions bioquímiques en cèl·lules cancerígenes es considera una estratègia emergent contra la resistència als medicaments. Tenint en compte l'alta reactivitat redox de complexos metàl·lics basats en lligands nitrogen tetradentats, la seva vectorització intracel·lular pot induir un estrès oxidatiu irreversible a través de mecanismes d'espècies reactives d'oxigen. Amb aquesta finalitat, aquesta tesi se centra en la vectorització de lligands nitrogen tetradentats a les cèl·lules cancerígenes a través de la seva conjugació a derivats peptídics no tòxics.

A la primera part (capítols III i IV), es descriu la identificació d'un *cell-penetrating peptide* no tòxic procedent d'una llibreria d'undecapèptids antimicrobians. En aquest sentit, s'estudien la capacitat d'internalització cel·lular i les propietats d'administració de fàrmacs d'aquesta nova seqüència penetrant mitjançant l'ús d'un medicament anticancerós utilitzat habitualment. A més a més, se n'explora l'aplicabilitat en aproximacions d'administració de fàrmacs intel·ligents a través de l'avaluació diferents estratègies de conjugació entre pèptid i fàrmac, així com mitjançant l'ús d'estratègies enzimàtiques.

A la segona part (capítols V, VI i VII), s'investiga la conjugació dels lligands ^{Me2}PyTACN i (*S,S*')-BPBP a diferents derivats peptídics. Al capítol V, es descriu una metodologia de fase sòlida directa per a la preparació de tetrapèptids redox actius, que són posteriorment metal·lats amb ions de ferro, coure, manganès i zinc. Els metal·lopèptids resultants s'han caracteritzat i s'han estudiat posteriorment com a nucleases de DNA. Al capítol VI, s'examina l'extensió d'aquesta metodologia sintètica per a la conjugació dels lligands ^{Me2}PyTACN i (*S,S*')-BPBP al nou *cell-penetrating peptide*. S'han estudiat les activitats citotòxiques i els comportaments d'internalització dels conjugats resultants, així com l'ús d'una seqüència de clivatge enzimàtic per provocar l'alliberament intracel·lular. Finalment, al capítol VII es conjuga el lligand (*S,S*')-BPBP a seqüències de reconeixement de PNA que tenen com a objectiu llocs de miRNA oncògens específics. L'escissió del RNA provocada pels conjugats resultants s'ha analitzat en condicions suaus.

RESUMEN

Actualmente, uno de los principales problemas en la administración de fármacos es el transporte de moléculas terapéuticas a través de la membrana celular. Con el fin de desarrollar metodologías de administración eficientes, el uso de *cell-penetrating peptides* (CPPs) se presenta como una de las herramientas más válidas para promover una internalización celular eficaz. A pesar de la variedad de CPPs que se han descrito con aplicaciones médicas, la gran mayoría de estos presentan estabilidad pobre y efectos secundarios significativos. Por otra parte, el *targeting* de alteraciones bioquímicas en células cancerosas es considerado como una estrategia emergente contra la resistencia de fármacos. En este contexto y teniendo en cuenta que complejos metálicos basados en ligandos aminopiridinicos tetradentados son capaces de presentar una alta reactividad redox, su vectorización intracelular podría conducir a la formación de especies oxoreactivas (ROS) que llevarían a la célula a un estrés oxidativo irreversible. Con esta finalidad, esta tesis se centra en la vectorización de ligandos de tipo N_4 hacia células cancerígenas a través de su conjugación a derivados peptídicos no tóxicos.

En la primera parte (capítulos III y IV) se describe la identificación de un *cell-penetrating peptide* no tóxico procedente de una librería de undecapéptidos antimicrobianos. Se estudia su capacidad de internalización celular, así como sus propiedades para la administración de fármacos mediante el uso de un antitumoral conocido. Además, se explora su aplicabilidad en aproximaciones de administración de fármacos inteligentes evaluando diferentes estrategias de conjugación entre péptido y fármaco, así como mediante el uso de otras estrategias enzimáticas.

En la segunda parte (capítulos V, VI y VII), se investiga la conjugación de los ligandos ^{Me2}PyTACN y (*S,S*')-BPBP a diferentes derivados peptídicos. En el capítulo V se describe una metodología de fase sólida directa para la preparación de tetrapéptidos redox activos, los cuales son posteriormente metalados con iones hierro, cobre, manganeso y zinc. Los metalopéptidos resultantes se han caracterizado y estudiado como nucleasas de DNA. En el capítulo VI se comprueba la extensión de esta metodología sintética en la conjugación de los ligandos ^{Me2}PyTACN y (*S,S*')-BPBP con el nuevo *cell-penetrating peptide*. Se han estudiado las actividades citotóxicas y los comportamientos de internalización de los conjugados resultantes, así como el uso de una secuencia de escisión enzimática para provocar la liberación intracelular. Finalmente, en el capítulo VII se conjuga el ligando (*S,S*')-BPBP a secuencias de PNA que reconocen lugares específicos de miRNA. Su escisión se ha analizado en condiciones suaves.

CHAPTER I

General Introduction

I. GENERAL INTRODUCTION

I.1. Peptide-based vectors for drug delivery

The poor cell permeability of therapeutics impedes them to gain their intracellular target sites being one of the most important barriers in current medicinal chemistry.[1,2] Consequently, the effective translocation of therapeutic agents commonly requires the administration of high dosages to obtain the expected biological effect. Therefore, their use commonly leads to significant drawbacks related to toxicity and immunogenicity.

Several delivery methodologies have been explored to improve drug efficacy and reduce side-effects on healthy tissues. In this context, numerous pharmaceutical carriers including nanospheres, nanocapsules, micelles or liposomes have been exploited to deliver therapeutic and diagnostic agents. Unfortunately, their clinical application is restrained by their passive accumulation in pathological regions.[3] An alternative is the use of peptide-based strategies which have been considered as powerful tools to enhance cell entry and deliver biologically active cargoes at the subcellular level.[4,5]

I.1.1. Cell-penetrating peptides (CPPs)

Cell-penetrating peptides (CPPs) are a class of short cationic and amphipathic sequences, containing less than 30 amino acids, that are able to cross the cellular membrane.[3,6,7] In the late 1980s the groups of Frankel and Pabo and of Green and Loewenstein discovered the first CPP, the HIV Tat trans-activating factor.[8] Since then, other peptide sequences, like penetratin or transportan, were recognized to efficiently cross the plasma membrane (Table I.1).[3,8] Further investigations reported the use of these CPPs as vectors for the delivery of exogenous molecules into cells.[9,10] From then on, numerous studies were centered on characterizing and optimizing the molecular features of CPPs. Within this regard, CPPs have been successfully used to mediate the intracellular delivery of a variety of biologically active molecules in different cell types (Figure I.1.) Interestingly, different types of structure, such as proteins, nucleic acids, nanoparticles, quantum dots or contrast agents for magnetic resonance imaging, have been conjugated to CPPs in order to improve their cell internalization both *in vitro* and *in vivo*.[8,11–13]

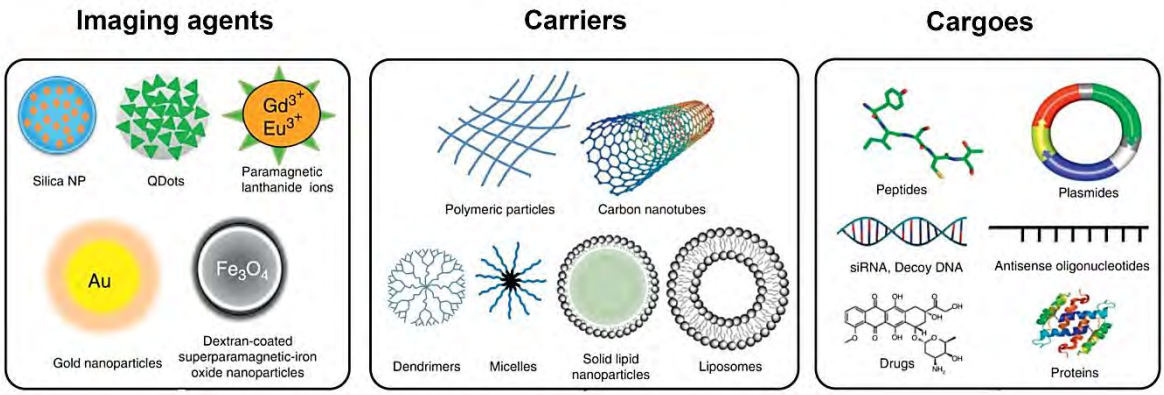

Figure I.1. Applications of CPPs as delivery vectors for a wide range of imaging agents, carriers and drugs (adapted from Koren et al.[3]).

Table I.1. Most common CPPs used for delivery applications.

CPP	Amino acid sequence
Tat (49-57)	RKKRRQRRR-OH
Penetratin	RQIKIWFQNRRMKWKK-NH_2
Polyarginines (R_9)	RRRRRRRRR-NH_2
Transportan	GWTLNSAGYYLLGKINLKALAALAKKIL-NH_2
MAP	KLALKLALKALKAALKLA-NH_2
Pep-1	Ac-KETWWETWWTEWSQPKKKRKV-NH_2
pVEC	IAARIKLRSRQHIKLRHL-NH_2

Regarding their structure, CPPs are commonly divided into different subgroups (Table I.1).[14] The first group includes cationic sequences with a low degree of amphipathicity. These peptides are positively charged at physiological pH, due to the presence of arginine and lysine residues. These residues interact with the negatively charged groups of the cell membrane and are a key structural feature for their uptake efficiency. Examples of this group are the well-known peptides Tat, penetratin or polyarginines. By contrast, the second group of CPPs includes short peptides with a high degree of amphipathicity, being this secondary structure the crucial requirement for their cell internalization. They also contain cationic residues that usually are lysines. Transportan, MAP or Pep-1 are well-established examples of this kind of CPPs. Other cell-penetrating sequences such as the vascular endothelial-cadherin (pVEC), possess charged and hydrophobic residues distributed along the sequence.[15]

As remarkable examples, antisense oligonucleotides or functionalized nanoparticles have been conjugated to Tat peptide leading to an enhanced cellular delivery into the cells.[16,17] In addition, pioneering studies in the development of polymer-based systems examined the intracellular macromolecular delivery mediated by Tat peptide.[18] Interestingly, as observed by live cell microscopy studies (Figure I.2), this peptide enabled the cytoplasmic delivery of a polymer bound doxorubicin, obtaining an efficient accumulation in A2780 human ovarian carcinoma cells.

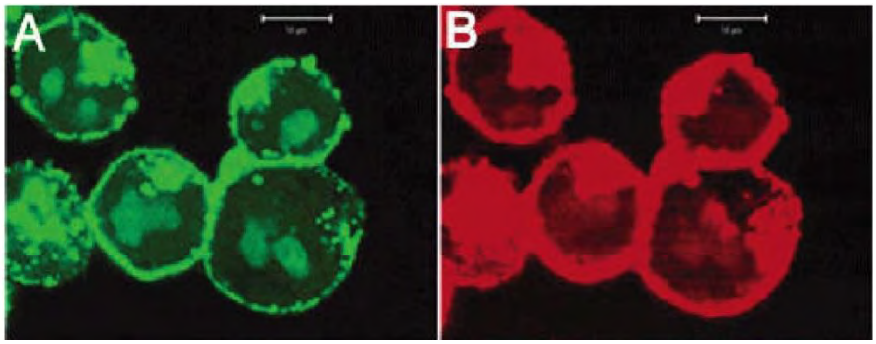

Figure I.2. Confocal fluorescence images of A2780 cells incubated with FITC (A) or Texas Red (B) labeled polymer-Tat conjugate.[18] Both fluorescently labeled conjugates exhibited similar intracellular accumulation, demonstrating their capacity of the former conjugate to efficiently translocate the cell membrane.

I.1.1.1. Cellular uptake mechanisms of CPPs

The mechanism of CPP-mediated cell entry has been the subject of a large number of studies in recent years. However, there is still a controversial debate to define the uptake mechanism.[6,14] The elucidation of the entry mechanism is crucial for the design of new CPPs.[19,20] The difficulty when elucidating this mechanism is attributed to the different structural properties of CPPs, especially those that involve charge and length, and also to the cargo type. Apart from the structural features, the final uptake mechanism of a CPP would be also affected by other factors such as peptide concentration or the physicochemical parameters of the cell type.[19,21] Moreover, it should be taken into account that CPPs can interact with multiple cell surface molecules, therefore different mechanisms may take place concurrently.[22] Despite this complexity, it is generally accepted that two major pathways coexist: direct translocation through the membrane bilayer and endocytosis (Figure I.3).

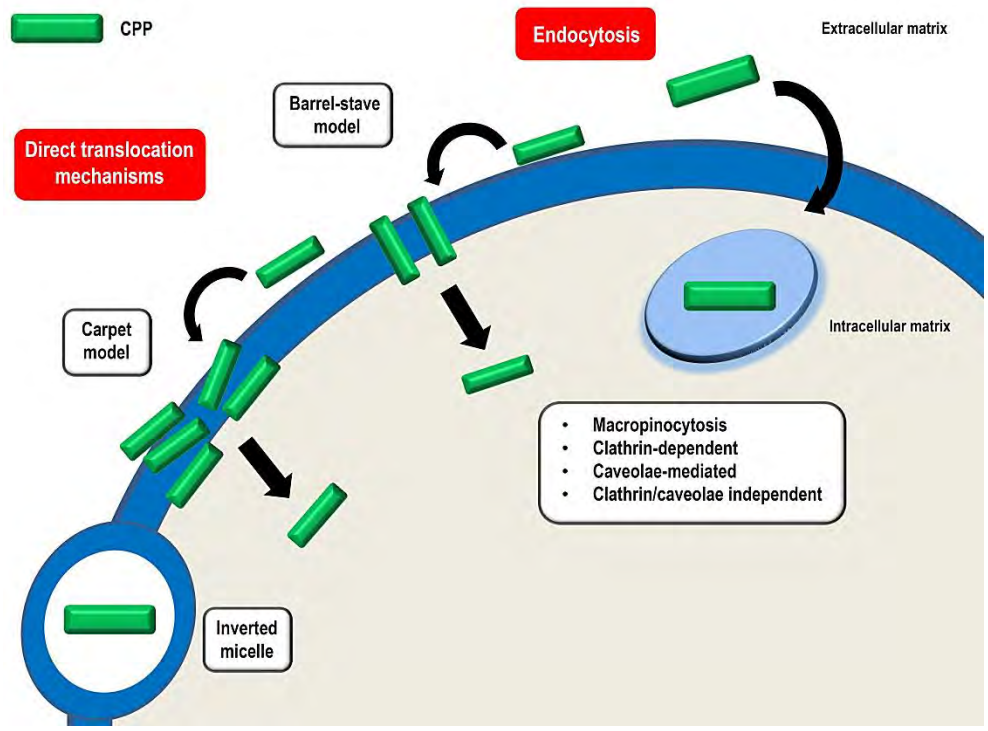

Figure I.3. Mechanisms of CPP-mediated internalization.

Direct translocation mechanisms are energy independent cell entry pathways for CPPs and include different models: inverted micelle, carpet and barrel-stave models (Figure I.3).[3,20,23] All of them involve the interaction of the positively charged CPPs with the negatively charged phospholipids of the cell membrane. This binding evokes a primary membrane destabilization and the subsequent internalization pathway is associated to the structural properties of CPPs. The inverted cell model is based on the aforementioned interaction leading to the insertion of the CPP into the bilayer, being finally entrapped in an inverted micelle. Then, this micelle moves to the opposite site of the bilayer membrane and releases its content in the cytosol. In the carpet model, CPPs bind to phospholipid head groups and align themselves parallel to the membrane surface in a carpet-like fashion leading to a membrane perturbation and subsequent internalization. In contrast, in the barrel stave model peptides self-aggregate in the membrane, resulting in the formation of a transmembrane pore lined by peptide orientation. The formation of these subsequent pores enables the final permeabilization of the CPPs inside the cell. In general, the direct translocation does not involve significant membrane destabilization when using high concentrations of these CPPs.[24] Additionally, peptides using this direct mechanism uptake are totally dependent on susceptible changes related to membrane potentials and independent of temperature. Due to this mechanism of action, these CPPs are suitable to be used as delivery vectors in strategies where an endosomal capture must be avoided. Examples of CPPs that follow this mechanism are polyarginines and Pep-1.[23,25]

On the other hand, endocytosis is an energy-dependent process regulated by the cell to internalize solutes and fluids present in the extracellular matrix (Figure I.3). This mechanism is characterized by the formation of a vesicle, which can undergo different intracellular pathways; macropinocytosis, clathrin-mediated endocytosis, caveloae/lipid raft-mediated or clathrin/caveloae independent endocytosis.[26] Despite these four pathways have been extensively studied, endocytic regulation is highly complex and some mechanistic details are still poorly understood. The pathway followed by a CPP depends on its physicochemical properties as well as on its concentration and type of cargo.[19,27] Consequently, the internalization process could result in vesicles of different sizes that can follow different intracellular trafficking pathways. Notwithstanding, the vesicles can be trafficked back for recycling in the plasma membrane or can follow the degradation pathway, being confined in the lysosomal-endosomal compartment. Hence, a cargo that targets a final organelle located outside of the endocytic vesicles must escape from the confined compartment before trafficking. Tat peptide and penetratin are the most important CPP examples that follow endocytic patterns during their internalization.[28,29] However, their mechanisms are strongly dependent on the attached cargo and, therefore, on the molecular weight of the resulting conjugates.[30]

I.1.1.2. Antimicrobial peptides as CPPs

With the growing problem of pathogenic organisms resistant to conventional antibiotics, antimicrobial peptides (AMPs) are emerging as alternative candidates in pharmaceutical and food industries. AMPs show a broad spectrum of activity and are components of the innate immune system of most organisms.[31,32] Like CPPs, they usually have a short length sequence (between 9 and 30 amino acids), a cationic charge of +4 or +5 and an amphipathic structure.[23,33] The mechanism of action of AMPs also includes their electrostatic interaction with the negatively charged phospholipid membranes causing morphological changes such as pore formation or cell lysis; however, their translocation into the cytoplasm is not uncommon.[34,35] Due to the latter property, the use of AMPs as CPPs is a field of interest to develop non-cytotoxic delivery vectors.

Several AMPs have been studied as templates for designing novel CPPs for therapeutic purposes and some of them have already entered in pre-clinical and clinical trials.[36,37] Moreover, AMPs such as magainin, cecropin, melittin or LL-37 have been used as CPPs.[29] Remarkably, melittin and LL-37 have been reported to transfect extracellular nucleic acids at the subcellular level, being potential delivery vectors for a wide-range of therapeutic cargoes.[38,39] On the other hand, the uptake mechanism of proline-rich peptides has also been extensively studied in

multiple works.[40] Another example of AMP as CPP is the bovine lactoferricin (bLFcin) which shows activity against a wide range of microorganisms, being the antimicrobial center of lactoferrin. Notably, the $bLFcin_6$ fragment of lactoferricin has been recently identified as a new CPP due to its ability to deliver siRNA in HeLa cells, providing potential knockout activity over protein levels.[41]

On the whole, AMPs constitute a powerful template platform to identify novel non-cytotoxic drug delivery vectors. Therefore, they might be potentially used in strategies aimed to obtain efficient drug uptake and delivery.

Table I.2. Most common AMP-derived CPPs.

AMP	Amino acid sequence
Magainin	GIGKFLHSAKKFGKAFVGEIMNS-OH
Cecropin	KWKLFKKIEKVGQNIRDGIIKAGPAVAVVGQATQIAK-NH_2
Melittin	GIGAVLKVLTTGLPALISWIKRKRQQ-NH_2
LL-37	LLGDFFRKSKEKIGKEFKRIVQRIKDFLRNLVPRTES-NH_2
Proline-rich peptide	PPPPPP-NH_2
$bLFcin_6$	RRWQWR-NH_2

In this context, LIPPSO group has described a 125-member library of AMPs based on cecropin-melittin hybrids (CECMEL11).[42] The general structure of this library is R-X^1KLFKKILKX^{10}L-NH_2, where X^1 and X^{10} correspond to amino acids with various degrees of hydrophobicity and hydrophilicity (Leu, Lys, Phe, Trp, Tyr, Val) and R includes different N-terminal derivatizations (H, Ac, Ts, Bz, Bn). Therefore, peptides of this library are highly cationic and their amphipathic character becomes evident when they are represented by means of an Edmunson wheel plot. These structural features are crucial for their antimicrobial activity and also may confer on them cell-penetrating properties. Interestingly, **BP100**, a member of the CECMEL11 library, has been reported as an efficient agent to transport cargoes into plant cells.[43] In light of this, this background renders the opportunity to study the suitability of peptides from this library as new cell-penetrating peptides.

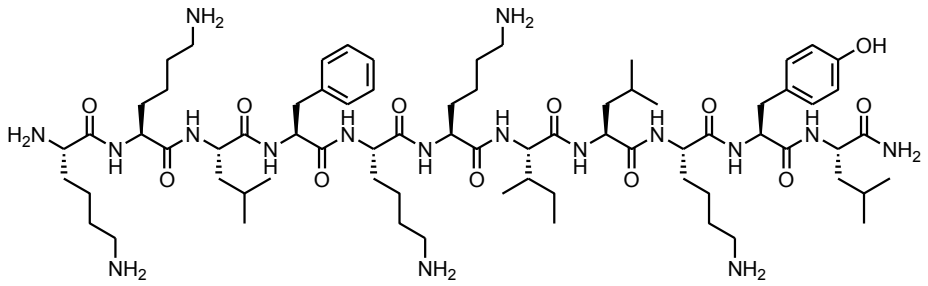

Figure I.4. Structure of BP100.

I.1.2. Targeted drug delivery mediated by homing peptides

Potential drug molecules have been identified, however their lack of cell permeability and selectivity significantly limits their therapeutic employment.[1,44] Hence, novel targeted drug delivery approaches are required to obtain selectivity against diseased tissues.[2] Among targeted vectors for cancer cells, homing peptides can be employed to obtain a selective interaction with cell-surface receptors that are overexpressed in cancer cells (Figure I.5).[4,45] In this fashion, *in vivo* phage display technologies have been widely used to study the tumor heterogeneity as well as to identify tissue-specific markers.[46] This technique allows the recognition of homing peptides that home specifically to different receptor molecules of the cell membrane.[47] Interestingly, most of these molecules are related to the tumor angiogenesis, being potential biomarkers for targeted therapies.[48]

There are generally two different kinds of homing peptides; those which recognize the targeted cell and are also able to internalize inside the cell (Figure I.5, route a) and those with the capacity to recognize specific phenotypes but without cell-penetrating properties (Figure I.5, route b). The former are also called cell-penetrating-homing peptides (CPHPs).

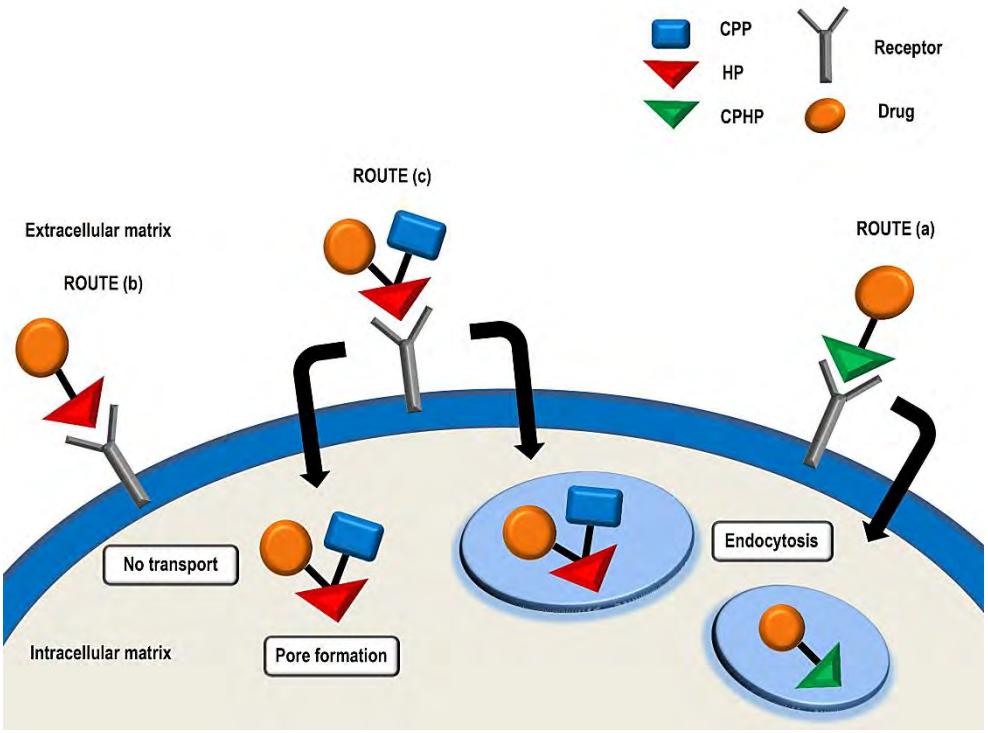

Figure I.5. Cell-targeting and delivery using homing peptides.

CPHPs are usually small peptides that exhibit low cytotoxicity, which facilitates their suitability to be used as selective delivery vectors with reduced side effects. Notably, CPHPs internalize into the cell via a receptor-mediated endocytosis, which involves the endosome formation after crossing the cell membrane. The most used CPHPs so far in targeted strategies are based on the RGD motif, identified in 1988, that recognizes the overexpressed $\alpha_v\beta_3$ integrins on neoendothelial and tumor cells (Figure I.6).[49] These homing peptides internalize *via* receptor-mediated endocytosis and have been conjugated to a wide range of cargoes, such as the tumor necrosis factor-α (TNF-α),[50] doxorubicin[51] or the antimicrobial peptide tachyplesin.[52]

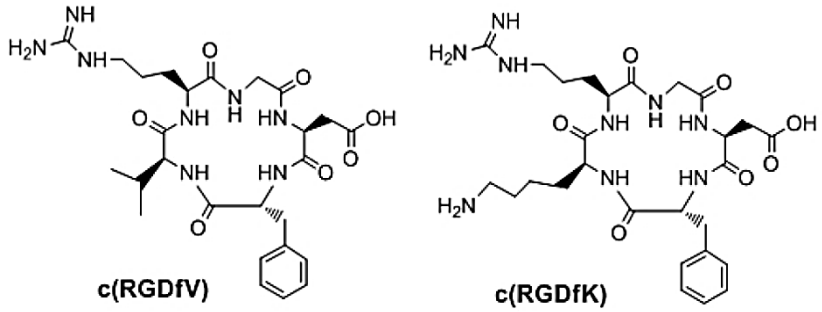

Figure I.6. Structure of two CPHPs based on the RGD motifs.

Another example of CPHP are the NGR homing peptides which recognize the aminopeptidase N (CD13), which is overexpressed in angiogenic endothelial cells and is tightly related to different angiogenic functions as well as protein degradation and cell migration approaches.[53,54] For instance, NGR homing peptides have been conjugated to doxorubicin in order to enhance the efficacy of the drug against human breast xenografts in nude mice.[51] These conjugates exhibited low toxicity and can be applied to develop further targeted chemotherapy strategies based on the selective expression of receptors in tumor vasculature. In addition, CGKRK and CRGRRST are RGR homing peptides that target the cell-nucleus after internalization, being useful tools to deliver anticancer drugs that display their therapeutic effect within the nuclear compartment (Figure I.7).[55,56]

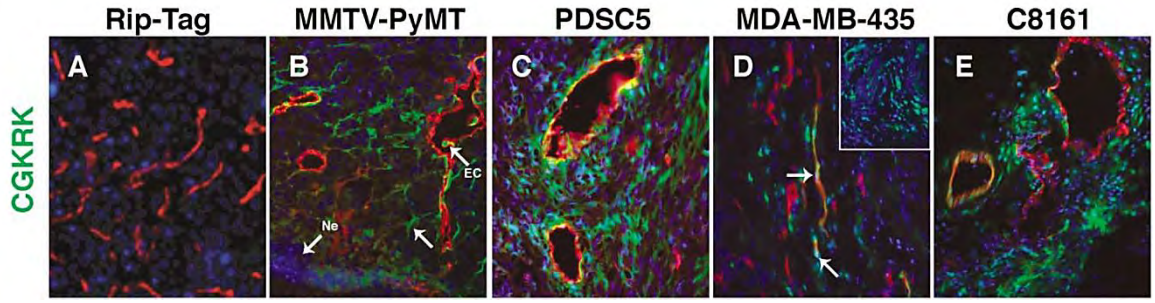

Figure I.7. Fluorescein-CGKRK (images A-E) was detected in 4 of the 5 tumor models examined by Ruoslahti and coworkers.[55] This homing peptide was observed in endothelial cells and tumor cells remaining both in the cytoplasm and nucleus (images B-E, arrow in D). Features indicated with arrows: labels EC (for endothelial cell), TC (for tumor cell), and Ne (for necrotic region). Original magnifications 200-400x (excerpted from Hoffman et al.[55]).

Other examples of CPHPs are somatostatin (SST), bombesin (BN) or luteinizing hormone-releasing hormone (LHRH).[57,58] Remarkably, the LHRH derivative [D-Lys^6]LHRH was conjugated to doxorubicin and camptothecin at the side-chain of a Lys residue.[59,60] The doxorubicin conjugate, known as AEZS-108 (Figure I.8), showed an enhanced affinity for breast, prostate and ovarian cancers overexpressing LHRH-receptor, improving the anticancer activity of the drug.[61] Interestingly, preclinical studies demonstrated that the uptake of AEZS-108 is achieved by receptor-mediated endocytosis. Moreover, in Phase I and II this conjugate displayed potential anticancer activity in patients with gynecological cancers without causing cardiotoxicity. Therefore, targeted chemotherapy using AEZS-108 has been considered for Phase III studies in advanced endometrial cancers positive for LHRH receptor (human colon cancers, melanomas, lymphomas).

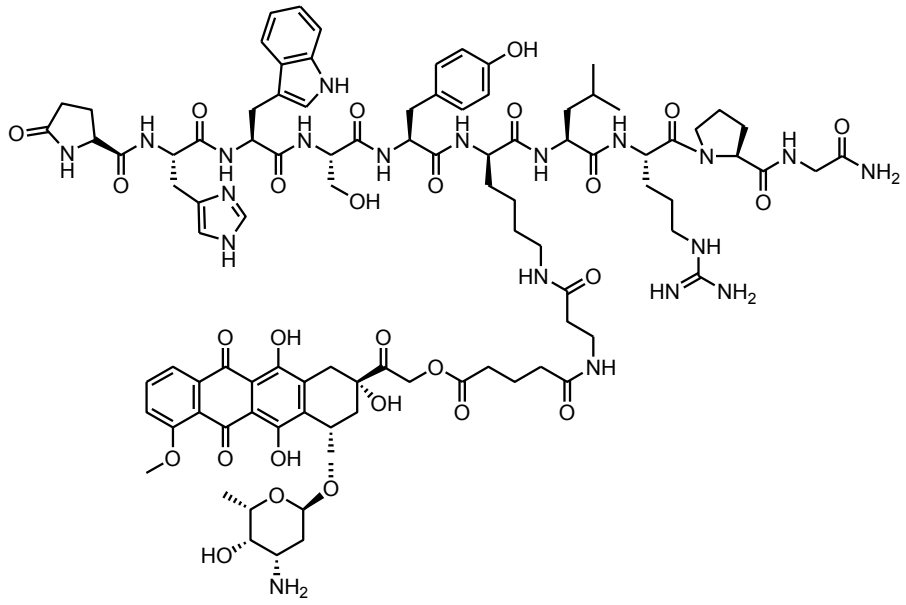

Figure I.8. Structure of AEZS-108.[61]

Nevertheless, homing peptides that recognize specific receptors but lack of cell internalization capacity are the most common.[45,47] Some examples are CGLIIQKNEC (CLT1), CNAGESSKNC (CLT2), PEGA and CREKA, that have been recently identified to bind to tumor blood vessels.[47] To favor their internalization, homing peptides have been conjugated to a CPP (Figure I.5, route c). In such a way, Ming Tan and coworkers reported the design of a CPP-based delivery construction for the specific recognition of the ErbB2 receptor overexpressed in most of the breast cancer cells.[62] The AHNP peptide (FCDGFYACYKDV), that binds to the extracellular domain of the ErbB2 receptor, was conjugated to a Tat-derived CPP (YGRKKRRQR).[63] The resulting conjugate exhibited specificity with an enhanced penetration efficacy both *in vitro* and *in vivo*. In addition, the STAT3-inhibiting peptide was also conjugated to this delivery construct, with the aim of blocking the STAT3 transcription factor of 435.eB tumors (Figure I.9). Since ErbB2 activates multiple signaling pathways, the designed Tat-AHNP conjugate inhibited the ErbB2 growth in cells by blocking this transcription factor.[62] This inhibition effect resulted in a proliferation reduction, a consequent apoptosis and growth suppression of these tumors.

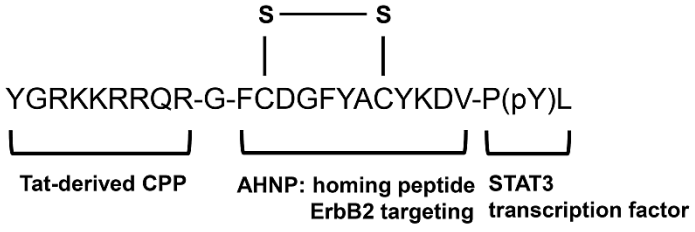

Figure I.9. Structure of Tat-AHNP-STAT3.[62]

Other noteworthy studies include the conjugation of the homing peptides PEGA and CREKA to the cell-penetrating peptide pVEC.[64,65] Langel and coworkers conjugated the PEGA-pVEC and CREKA-pVEC systems to chlorambucil (CLB) to study the selective delivery of this drug in breast cancer cells (Figure I.10). PEGA-pVEC improved by four-fold the *in vitro* activity of CLB alone, whereas CREKA-pVEC enhanced the delivery properties of PEGA-pVEC by achieving homing ability in *in vivo* tumors. Overall, these examples and other studies exemplify the opportunity to optimize the drug delivery properties that render CPPs and homing peptides in the current medical field.

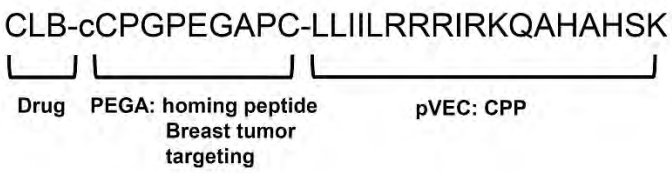

Figure I.10. Structure of CLB-PEGA-pVEC.[64]

I.1.3. Smart drug delivery systems

The controlled release of a drug inside the cell is another important issue to take into account in the design of an efficient therapeutic agent. In this context, smart drug delivery systems (SDDS) have been developed to be applied in cancer treatments.[2,66] In particular, prodrug strategies have emerged as very efficient rational designs to transport the drug across the cell membrane and deliver the active drug *via* a controlled release system.[67–70] In most cases, these smart designs are based on the fact that some stimuli actions take place at the subcellular level and, therefore, they can be employed to release the drug through activation by these physiological changes.

Focusing on CPP-based delivery systems, they can be designed to be responsive to the tumor microenvironment. During endocytosis, the drug-CPP conjugate moves through early to late endosomes, being the fusion with lysosome the last step of the degradation pathway (Figure I.11).[69] At this point, the drug must be cleaved from the drug-CPP conjugate to exhibit its anticancer activity. Hence, endosomal escape and drug release can be mediated by pH gradients, overexpressed enzymes or redox conditions during the endocytic pathway that occur in cancer cells or tissues.[66]

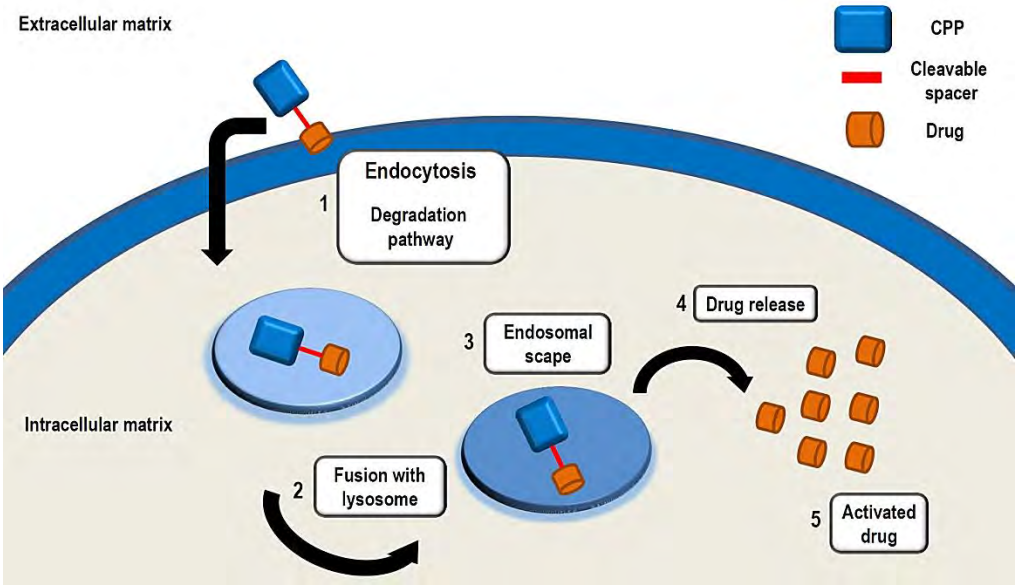

Figure I.11. Schematic representation of a produg-based endocytosis, leading to the drug release by stimuli-cleavable spacer in the endosomal compartment.

Therefore, moieties responsive to intracellular stimuli systems can be introduced into the conjugate systems between the CPP and the drug (Figure I.12). Among these moieties, chemical linkers and enzyme-cleavable peptide sequences have been employed.[57] Generally, these moieties should be stable enough in blood circulation, however should also be self-immolatable or cleavable under certain triggerable conditions, such as change in pH or in redox environment, or the presence of an enzyme. As examples, carboxylic ester, amide, hydrazone, thioether and disulfide bonds have been used in these strategies.[58,67]

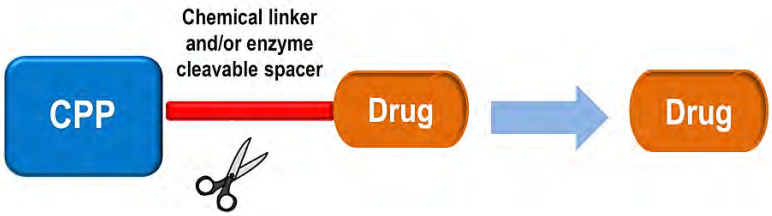

Figure I.12. Prodrug design of a drug-CPP conjugation.

The variety of pH gradients in the body provides the opportunity to obtain site-specific delivery.[2,48] On the other hand, at the extracellular level, the pH of healthy tissues is around 7.4 while in tumor tissues the hypoxic environment renders a pH of 6.5-7.0 due to metabolic disorders. Moreover, the pH differences inside the cells are also noticeable, i.e. cytosol (7.4), Golgi apparatus (6.40), endosomes (5.5-6.0) and lysosomes (4.5-5.0). These differences have

led to the development of pH-responsive systems that can easily be tuned by ionization alterations. Examples of these systems are chemical linkers containing a hydrazone linkage (responsive at pH 5.0). As example, doxorubicin has been conjugated to thermally responsive elastin-like polypeptides through a hydrazone bond in order to improve its transport through the cell membrane and to facilitate its release (Figure I.13).[71]

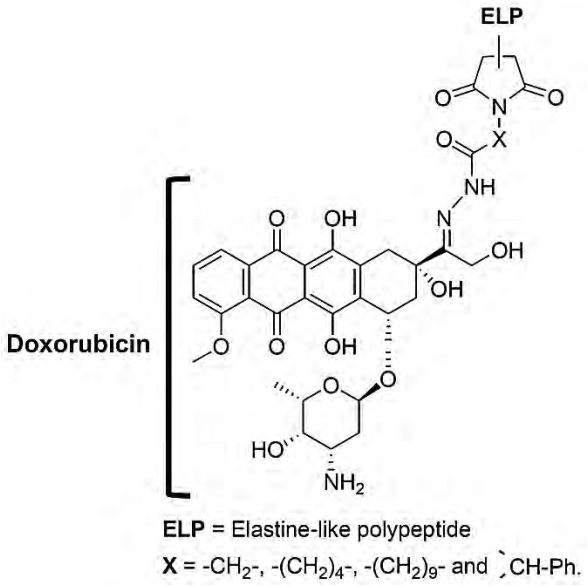

Figure I.13. ELP- Doxorubicin conjugates containing the pH-sensitive hydrazone bond (adapted from Furgeson et al.[71]).

In addition, the redox environment of intracellular compartments could also be a suitable stimulus for triggering drug release at the subcellular level. For example, the levels of glutathione (GSH) are around 2 to 3 orders of magnitude higher in cytosol, mitochondria and nucleus (2-10 mM) than in extracellular fluids (2-20 μM). Thus, chemical linkers bearing a disulfide bond susceptible to reduction in the presence of GSH could lead to an efficient intracellular drug release.[2] Remarkably, polymer nanohydrogels containing disulfide bonds have been involved in drug delivery strategies to release doxorubicin. Authors compared the use of GSH and of synthethic reducing agent such as dithiothreitol (DTT) (Figure I.14).[72] Notably, the doxorubicin-loaded nanohydrogels provided a quicker release of doxorubicin in the presence of GSH. Besides this improved release, these nanohydrogels render an excellent drug loading capacity, biocompatibility and biodegradability.

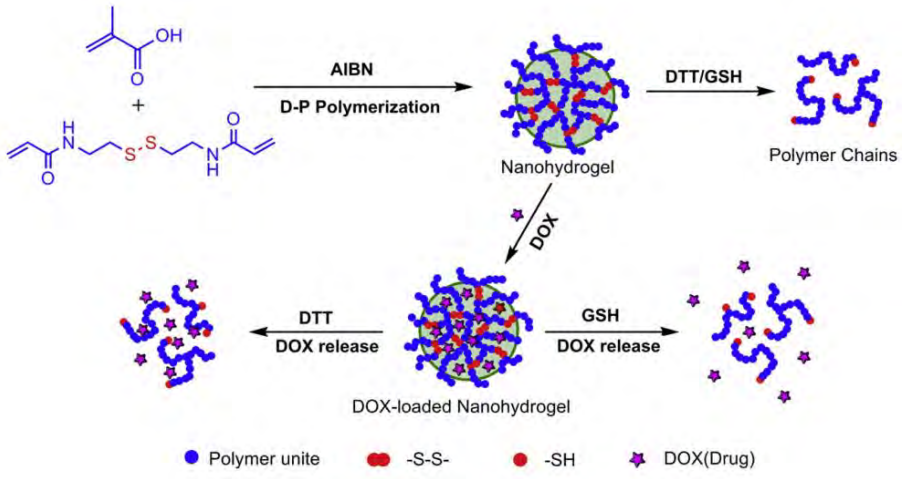

Figure I.14. Doxorubicin (Dox) release from redox stimuli-responsive PMAA nanohydrogels.[72]

Chemical linkers containing amide, ester or carbamate bonds have been commonly used in prodrug approaches.[57,67,73] These bonds can be cleaved by enzymes present in the blood or other organs. Interestingly, the carbamate linker has been used in conjugation strategies involving camptothecin and combretastatin drugs.[74] As depicted in Figure I.15, carbamate linker ensures the release of camptothecin drug in a controlled manner by pH change or enzymatic hydrolysis.

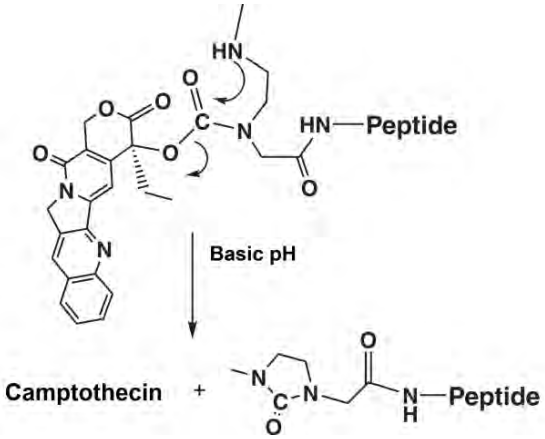

Figure I.15. Controlled release of camptothecin via a carbamate linkage (adapted from Fuselier et al.[74]).

Enzyme-cleavable peptide sequences might also be introduced between the CPP and the drug.[5,75] These sequences should be cleaved by enzymes overexpressed in tumor cells and specifically located inside diseased tissues to ensure the selective release of the drug in cancer cells. The enzymatic peptide spacers SSKYQ, HSSKLQ and GFLG are examples of these type of sequences.[57] Prostate-specific antigen (PSA) is a serine protease located only in prostate tumors and therefore used as prognostic marker for prostate cancer.[76] It is well-known that PSA

recognizes SSKYQ and HSSKLQ peptide sequences.[77] Several drugs such as doxorubicin,[78] paclitaxel (taxol),[77] 5-fluorodeoxyuridine (5FudR)[79] or thapsigargin[80] have been conjugated to these enzymatic cleavable sequences in prodrug constructions. Indeed, the PSA-activated thapsigargin prodrug is currently in clinical trials as treatment for metastatic prostate cancer.[80] This prodrug results from the conjugation of the peptide HSSKLQ to a modified form of thapsigargin (L12ADT), and it is susceptible to be hydrolyzed by PSA in metastatic prostate cancer sites (Figure I.16). Notably, the kinetics of the hydrolysis of this prodrug, as well as its *in vitro* cytotoxicity against several human prostate cancer cells and its *in vivo* pharmacokinetics in mice were examined. The results strongly suggested that the subcutaneous prodrug administration produces complete growth inhibition of prostate tumors.

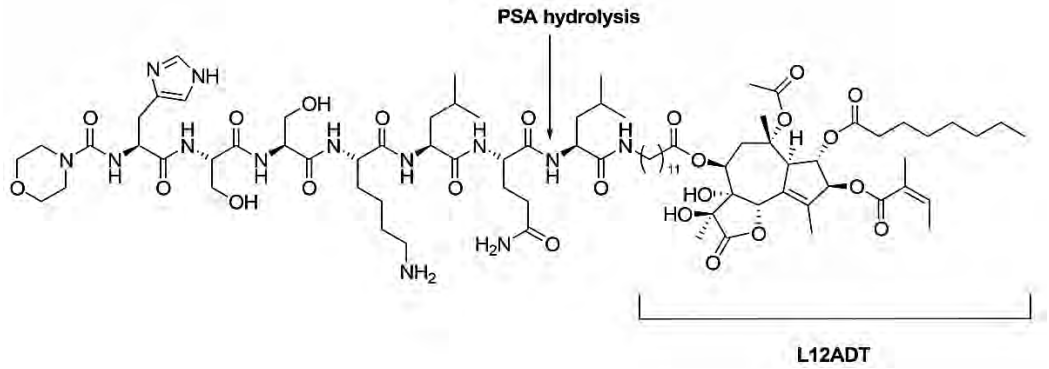

Figure I.16. Structure of the prostate-specific antigen-activated thapsigargin prodrug.[80]

Noteworthy, other studies employing enzyme-cleavable sequences have successfully adopted the tetrapeptide GFLG in prodrug delivery strategies.[81] This strategy takes advantage of the susceptibility of this sequence to cysteine cathepsin, enzymes that are intracellularly located in endolysosomal compartments.[82] Cysteine cathepsins such as cathepsin B or cathepsin L are overexpressed in tumor tissues and have been shown to enhance the malignant progression of tumors, including growth, migration, invasion, angiogenesis or metastasis. Moreover, taking into account that lysosomes are the final stage of the endocytic pathway of CPPs, the encounter between a prodrug conjugate containing this enzyme cleavable sequence and cathepsins might provide an enzyme-mediated cleavage at this stage.[69,73] For instance, Duncan and coworkers conjugated the GFLG sequence to *N*-(2-hydroxypropyl)methacrylamide (HPMA) polymers in order to facilitate the release of different drugs such as cisplatin, doxorubicin, camptothecin and paclitaxel in clinical studies.[83–87] Mezö and coworkers also employed the GFLG linker to improve the release rates of methotrexate *in vitro*.[88] Furthermore, Cui and coworkers conjugated Tat-GFLG to doxorubicin enhancing the drug release and overcoming multidrug resistance.[89] Last but

not least, very recently Giralt and coworkers designed a peptide-polymer strategy in order to release the highly cytotoxic peptide mitoparan (Figure I.17).[90] This strategy also involved the incorporation to the polymer of the GFLG sequence and the homing peptide LTVSPWY. This peptide binds to the HER2 receptor overexpressed in breast tumors,[91,92] thereby they obtained a smart and targeted pro-cytotoxic system.

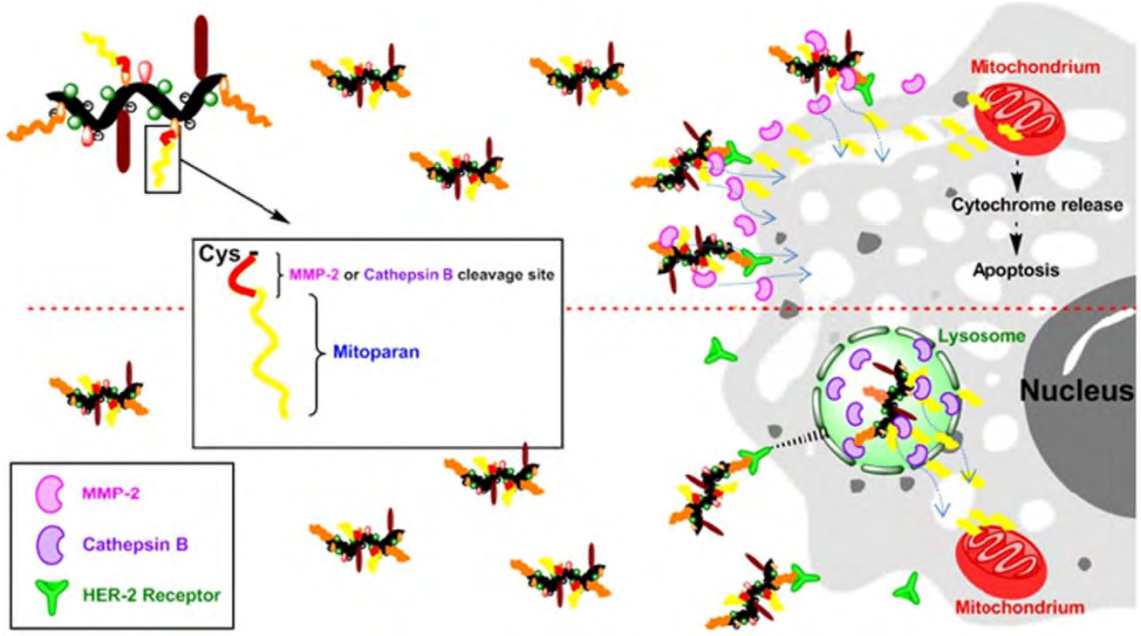

Figure I.17. Schematic illustration of targeted pro-cytotoxic conjugates to HER2 positive tumor cells. MMP-2 (top) or cathepsin B enzymes (bottom) promote the mitoparan release through specific cleavage sequences (excerpted from Moreno et al.[90]).

I.2. Role of organometallic compounds in medicine

Most of the current approved drugs are organic or derived from biological compounds. However, in recent years the development of transition metal-based drugs represents one of the most important challenges in current medicinal chemistry.[93] There is a growing interest in the use of the chemical approaches of these compounds in order to understand biological processes.[94,95] Since some chemical properties of metal ions have been extensively studied in the inorganic field, the design of new features in bioorganometallic chemistry is centered on applying the reactivity of metallic centers in biology.[96,97] Furthermore, the control of the toxic side-effects and the targeting to specific tissues, organs or cells are also key areas in medicinal chemistry. Considering these possibilities, potential applications of metal-based compounds are related to cellular inhibition, trafficking, DNA probing and also as diagnostic and biosensing tools, taking advantage of the unique properties of inorganic coordination complexes.[98]

I.2.1. Therapeutic metallodrugs

Since the discovery in the 1960's of the anticancer drug cisplatin, *cis*-[$(NH_3)_2PtCl_2$], research efforts on platinum-based drugs development were focused on studying the coordination features and the cytotoxic reactivity towards DNA.[99] Some analogues such as *cis*-[$(NH_3)_2$ cyclobutanedicarboxylate)] (carboplatin) and *cis*-[Pt(*1R*,*2R*-diaminocyclohexane)(oxalate)] (oxaliplatin) were also supported by FDA to be used in clinical trials (Figure I.18).

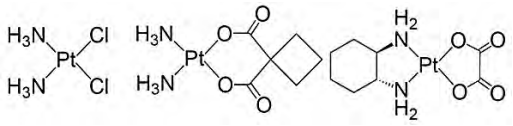

Figure I.18. Structures of anticancer drugs cis-platin, carboplatin and oxaliplatin.

While these platinum derivatives were approved for their application, the harmful side effects derived from their chemotherapeutic practice are their main clinical disadvantages.[100,101] Therefore, other transition metal compounds such as ruthenium or gold complexes were also investigated as alternative anticancer metallodrugs.

The anticancer activity of Ru compounds was extensively evaluated a few decades ago, however only two Ru compounds, NAMI-A and KP1019, are currently undergoing clinical trials (Figure I.19).[102,103]

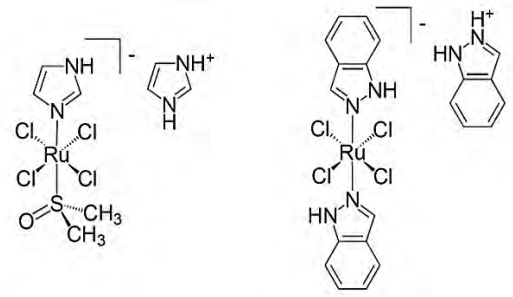

Figure I.19. Ru(III) compounds NAMI-A and KP1019.

Although the mechanism of action and the biological target of these Ru(III) compounds with heterocyclic N-donor ligands is still under debate, it is suspected that their antitumor activities rely on their easy reduction to Ru(II) in vivo, which acts as final prodrug.[104,105] Taking into account the biological activity of these Ru(II) active species, Ru(II)-arene complexes were developed including those containing amine, sulfoxide and phosphine as co-ligands.[106,107] Monofunctional complexes [μ^6-arene)Ru(en)X]$^+$ (X = halide) and bi-functional complexes [μ^6-

arene)Ru(PTA)X_2] (PTA = 1,3,5-triaza-7-phosphaadamantane) (RAPTA) exhibited promising antitumor and antimetastatic activities.[108] For monofunctional complexes, the activity was mainly attributed to subsequent DNA damage where the binding mode differed from the ones observed for the platinum-based drugs, whereas other cellular targets were observed for antimetastatic RAPTA compounds (Figure I.20).[109]

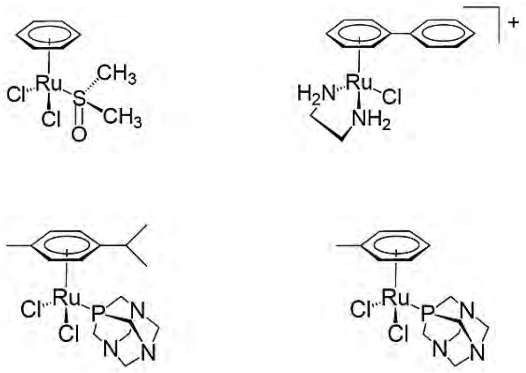

Figure I.20. Organometallic [μ^6-arene] ruthenium anticancer drugs.

Furthermore, additional ruthenium complexes bearing different bioactive ligands have been tested in order to obtain specific biological functions in tumor cells.[96,110–113] In this context, the inhibition of angiogenesis and the involvement of extracellular and intracellular components were determined as the molecular targets by ruthenium-arene complexes.

On the other hand, Au(I) and Au(III) complexes have emerged as novel organometallic compounds for cancer treatment.[114,115] The redox chemistry Au(I)/Au(III) provides the opportunity to use the oxidizing Au(III) agents in reducing intracellular environments. As examples, Au(I) complexes with carbene ligands,[116,117] Au(III) dithiocarbamate[118] and Au(III) porphyrins[119] highlighted as gold-based metallodrugs and have been extensively studied as oxidative agents as well as protein modifiers. Particularly, it is generally assumed that the cytotoxic effects observed by Au(I) and Au(III) complexes are related to the selective targeting of thiol and imidazole groups of proteins.[120,121] The inhibition of the TrxR selenoenzyme by gold complexes is presumed to be the crucial pathway to create an irreversible redox dysfunction.[121–123]

I.2.2. Artificial nucleases

The development of synthetic systems capable of reproducing the activity of natural enzymes is still a biological challenge. Although important progresses have been performed in biological catalysis, mimicking of catalytic centers in order to obtain efficient cleavage rates

remain as a demanding request in chemical biology.[124] Transition metal complexes that act as artificial metallonucleases can be potentially applied in gene regulation as biotechnological tools and in anticancer therapy.[125–127] Within this context, the manipulation of the phosphate ester linkages in deoxyribonucleic acid (DNA) and ribonucleic acid (RNA) holds an opportunity to engineer novel molecules that are able to cleave both substrates with site/structure selectivity. The cleavage of DNA and RNA can occur via two major pathways: oxidative and hydrolytic. Several efforts have been devoted to the implementation of efficient methodologies to determine the cleavage characteristics. Gel electrophoresis, polyacrylamide gel electrophoresis (PAGE), atomic force microscopy (AFM) or the combination of HPLC-MS with other methods are the most common techniques to evaluate the cleavage reaction.[128] Characteristics, mechanistic insights and future perspectives will be discussed for both cleavage scenarios.

I.2.2.1. Oxidative cleavage

Due to the resistance towards hydrolysis, the DNA cleavage promoted by oxidation mechanisms is the most studied in bioinorganic chemistry. DNA-oxidative cleavage relies on the abstraction of hydrogen atoms from the deoxyribose sugar moiety, leading the DNA scission.[129] Taking into account the activation of dioxygen taking place in various natural metalloenzymes based on iron, copper and manganese, these metals are envisioned as potential key elements for the design of oxidative DNA clavage drugs.[129,130] In this way, a large number of redox-active metal complexes of Fe, Cu, Mn, Ni, Pt, Ru or Co have been reported to cleave the DNA in presence of O_2 or H_2O_2. $[Fe(II)\text{-}EDTA]^{2-}$, Fe-BLM (BLM = bleomycin), $[Cu(phen)_2]$ (phen = phenanthroline), metalloporphyrins and metal-salen (salen = *N,N'*-ethylenebis) are some well-studied DNA cleavage examples highlighted by their attractive molecular mechanisms involving oxygen activation and DNA oxidation.[131–135] The cleavage efficiency of these metallonucleases is directly affected by several factors, such as the metal centers, the ligand features, co-factors, the pH or the temperature.[128]

The DNA oxidative mechanism can be divided into different categories based on the active species involved in the reaction, the chemical nature of the oxidant and the target sites. Firstly, the typical Fenton-type chemistry produces different reactive oxygen species (ROS) in the presence of reductant, molecular oxygen and/or H_2O_2.[130] Among them, the generation of the hydroxyl radical $^{\bullet}OH$, which is freely diffusing, mediates the DNA scission in a non-selective way. The most important example among non-specific oxidants is $[Fe^{II}(EDTA)]^{2-}$ and H_2O_2.[129] This negatively charged complex is oxidized by hydrogen peroxide and is known to generate highly

reactive •OH, which is able to perform the cleavage without selective discrimination. On the other hand, metal-centered oxidative species may perform the DNA cleavage *via* a more selective reaction. The coordination and activation of O_2 or H_2O_2 to the metal ion lead to oxidizing intermediates.[130,136] These reactive species include M-OH, M-OOH as well as high-valent metal-oxo species such as M=O, which are extremely efficient when cleaving C-H bond.[137–139]

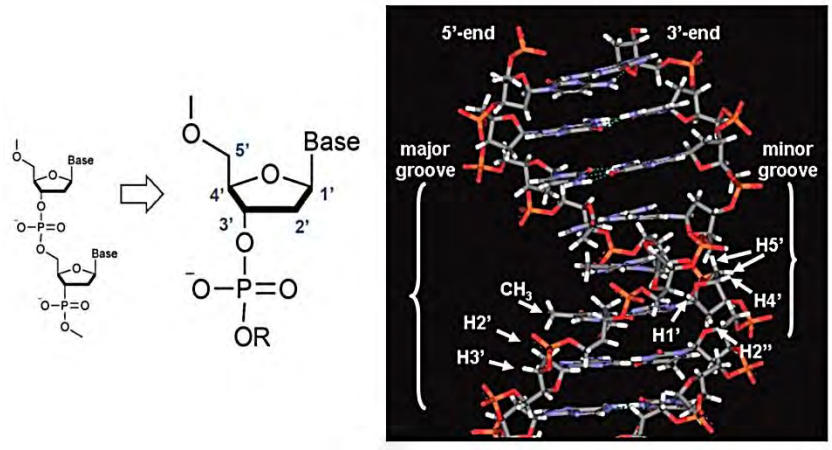

Figure I.21. Five sugar locations that are exposed to C-H abstraction during the DNA oxidative cleavage.[130]

Furthermore, depending on the nature of the oxidant, the sugar-hydrogen abstraction can take place in five different locations.[129] The general preference for hydrogen abstraction is C5' > C4' > C2' = C3 '> C1'. From a structural point of view, the hydrogen atoms at C1', C4' and C5' are accessible from the minor groove on classical B form-DNA whereas those at C2' and C3' are in the major groove (Figure I.21).[128] However, the reactivity towards one C-H bond or another not only depends directly on the accessibility by the oxidant to reach the target site. Hence, modeling the interaction between the oxidant and the DNA might lead to unambiguous characterization of the corresponding oxidative pathway.

Reproducing the specific features of natural reactive centers is an essential study to obtain new efficient synthetic systems for DNA cleavage. One can find a remarkable similarity within the cytotoxicity of BLMs, which have been widely reported as potential natural antitumor glycopeptides.[140–143] In the presence of metal ion cofactor (iron or copper), O_2 and a reducing agent, BLMs are able to mediate the oxidative DNA cleavage. The metal-coordinated center reacts with oxygen forming an oxidizing specie called activated Bleomycin, which is then able to perform the H abstraction from the DNA inducing the oxidative degradation, known to occur at C4' site. This C-H abstraction is established to be the major contribution of the cytotoxic activity displayed by BLMs.[144] Several models have been devised to mimic the metal binding domain of

BLM and to study the mechanism of action towards DNA. However, very recently Roelfes and coworkers have reported the first study where a synthetic BLM mimic shows nuclear DNA cleavage activity in cancer cells (Figure I.22).[145] This Fe(II)-N4Py modeling approach improves the cleavage cytotoxicity of BLM and exemplifies the significance to design synthetic bioinorganic model complexes.

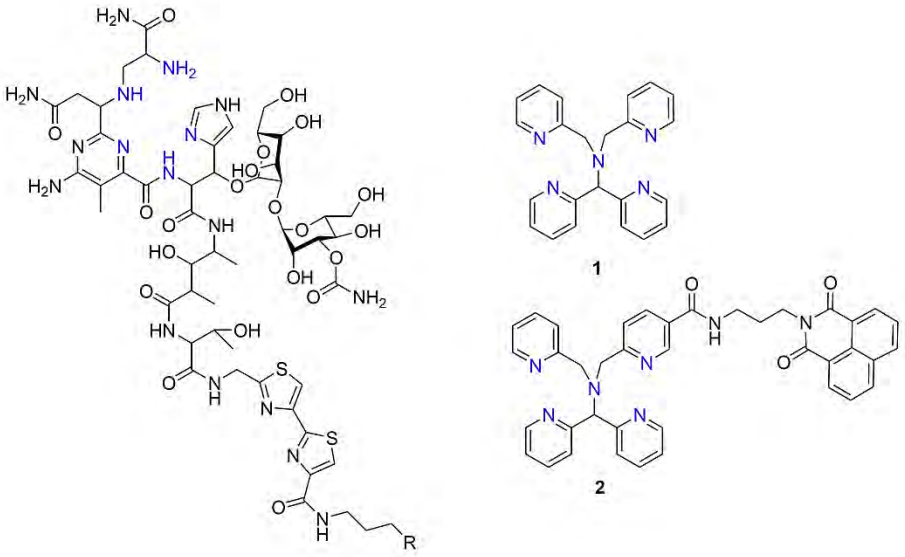

Figure I.22. N4Py ligands (**1** and **2**) studied by Roelfes and coworkers that mimic the metal binding domain of natural BLM (in blue). Fe(II)-**2** (with a 1,8-napthalimide moiety), displays selective cytotoxicity at low micromolar range in front SKOV-3 and MDA-MB-231 cancer cells.[145]

Another particular and relevant objective is to achieve a selective DNA damage. Since DNA can adopt different conformations, in principle it can be envisioned that metal complexes can be designed to interact selectively with DNA. Although the preparation of selective synthetic systems can result in a diminution of the cleavage activity, interesting examples have been described that accomplish selective DNA cleavage. Most of the reported approaches are based on the extension of the aromatic ligand, rendering the opportunity to improve the intercalative binding.[146] Pioneering studies in the field were performed by Barton's group, using different rhodium complexes.[147] On the other hand, DNA cleavage activity by $Cu(phen)_2$, initially reported few decades ago by Sigman and coworkers,[131] has been extensively studied. The DNA oxidation relies on the reactivity of Cu(I)-$(phen)_2$ with dioxygen to form the superoxide anion. Next, electron transfer reactions produce H_2O_2, that reacts with Cu(I)-$(phen)_2$ and consequently mediate the final DNA cleavage.[130] However, the detailed chemistry of these redox events remains confusing. It is strongly believed that phenanthroline ligands play a key role in this reaction due to their DNA binding by intercalation. Thus, different modifications in the phenanthroline aromatic ring have

been reported by Chakravarty and coworkers to enhance the selectivity of the DNA damage, achieving interesting results associated to the intercalation in the minor or the major groove of DNA (Figure I.23).[148–151]

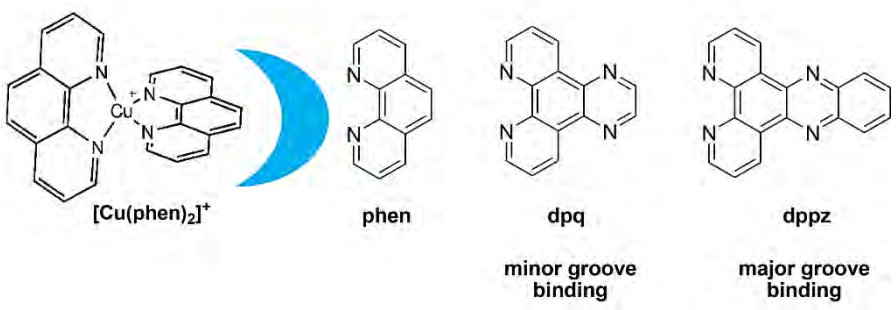

Figure I.23. Some reported examples about the extension of the $[Cu(phen)_2]^+$ macrocycle ligand to increase DNA site selectivity.[130]

Beyond the use of ancillary ligands, the conjugation of the redox-active metal complex to DNA binding moieties such as acridine or anthraquinone also arises as a useful strategy to increase the DNA stacking.[152–154] Besides, the attachment of minor-groove DNA binders (Hoechst 33258 or dystamycin) to the complex also induces DNA oxidation between those bases that are in the minor groove.[155–157] On the other hand, the attachment of cationic charges around the metal core increases electrostatic interactions with the negatively charged DNA. In this fashion, the incorporation of free amines or guanidinium moieties close to the active metal site provides a modification of the final binding to DNA due to their protonation at physiological pH (Figure I.24).[130,158] Additionally, the use of polyamine linkers also contributes to the DNA damage by optimizing the flexibility of the interaction.[159]

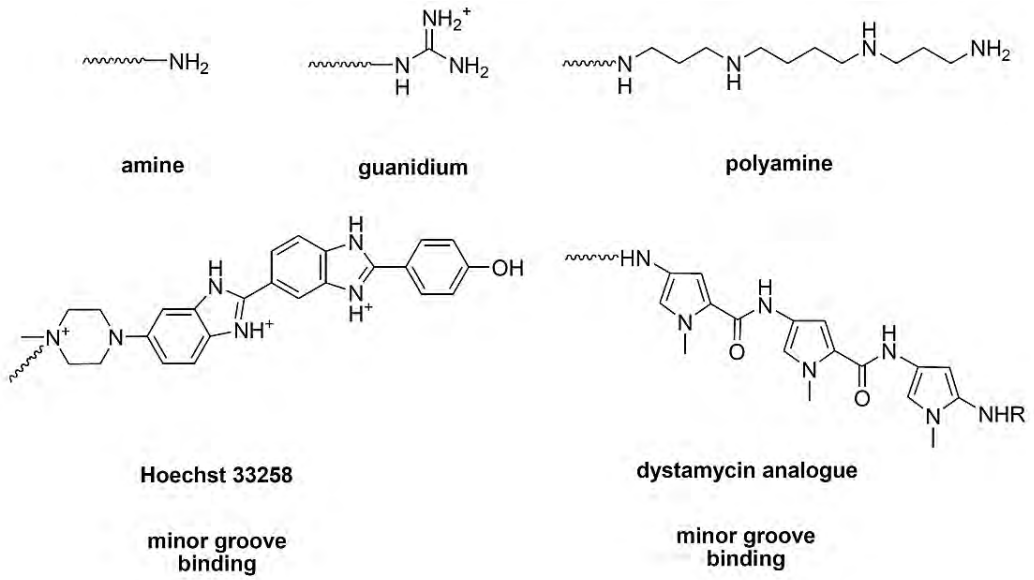

Figure I.24. Modifications of the redox-active center and typical examples DNA minor-groove binders (Hoechst 33258 and dystamycin) to increase DNA binding affinity.

All the above-mentioned strategies focused their targeting to specific regions of DNA. Nevertheless, the conjugation of the redox-active moiety to an oligodeoxynucleotide or oligonucleotide analogue vector (ODN) such as PNA ensures the molecular recognition of longer DNA sequences by specific hydrogen bonding patterns.[160–162] Indeed, the position of the active cleaver can be modulated with the aim of facing the cleavage towards specific bases, depending on the linker length and the accessibility towards DNA groove. Likewise, the conjugation to binding proteins[163–165] or to other simple structures that covalently link to DNA (alkylating agents or cisplatin derivatives)[166,167] are also depicted as attractive platforms to gain sequence specificity of DNA cleavage.

I.2.2.2. Hydrolytic cleavage

In the last decades, many studies have been reported reproducing the catalytic center of natural nucleases and phosphatases capable to hydrolyze the phosphodiester backbone of genetic material.[124,168] However, the inertness of the phosphate esters in front hydrolysis under physiological conditions is challenging to test novel nucleases that mimic DNAzymes and RNAzymes.[124,169–171] These enzymes exhibit high catalytic rates when promoting the P-O hydrolytic cleavage and most of them contain Mg^{2+}, Ca^{2+}, Zn^{2+} or Mn^{2+} ions in their active sites. From then on, the design of synthetic nucleases relied on the previous understanding of the metal ion in the catalytic reaction.

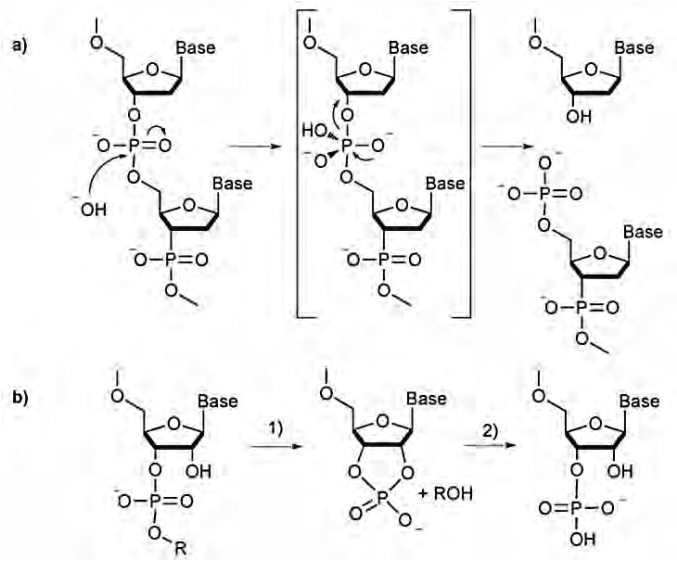

Scheme I.1. a) DNA hydrolytic mechanism promoted by the hydroxide attack to the phosphodiester backbone. b) RNA hydrolysis mediated by the intramolecular transesterification (1) and subsequent breakdown of the cyclic intermediate (2). [124]

From a mechanistic point of view, the hydrolytic cleavage of DNA takes place via a *transesterification* reaction of the phosphate diester mediated by the hydroxide or water-catalyzed hydrolysis. Other alternative pathways involve C-O cleavage or direct attacks by radicals. Regarding the RNA cleavage, the presence of the 2'-hydroxyl ribose in the RNA backbone facilitates the hydrolytic mechanism by an intramolecular transesterification and the final hydrolysis of the phosphate cyclic intermediate (Scheme I.1).[169,171,172] Taking into account the DNA sensitivity for being cleaved via an oxidative pathway, any identification of a plausible hydrolytic cleavage process must be treated with great consideration. Therefore, a number of non-natural substrates mimicking the phosphate ester linkage in DNA and RNA have been used to study hydrolytic cleavage activities. The most common DNA models include bis(4-nitrophenyl)phosphate (BNPP), bis(2,4-dinitrophenyl)phosphate (BDNPP) and ethyl-4-nitrophenylphosphate (ENPP).[173] The cleavage of these substrates resulted in the release of 4-nitrophenoxide (NP) ion, which can be monitored by UV-Visible spectrophotometry.[174] On the other hand, cleavage experiments with RNA substrates must contain the 2'-hydroxyl group in their structures and the most studied involve 2-hydroxypropyl-4-nitrophenylphosphate (HPNPP) and 3'-nitrophenylphosphate uridine (UpNP) (Figure I.25).[169]

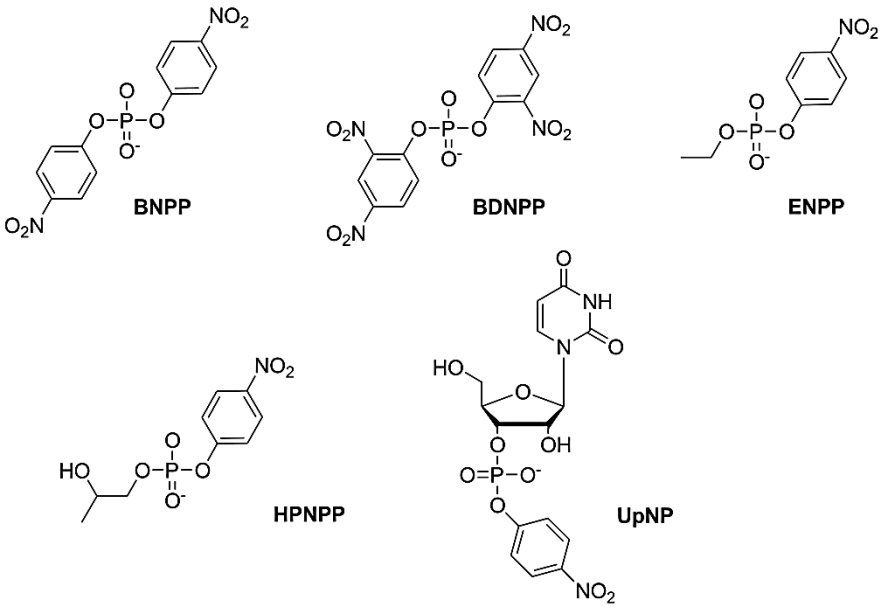

Figure I.25. Structure of non-natural DNA and RNA substrates used in cleavage studies.

Considering the increase of the negative charge on the phosphoryl group, most of the mechanistic pathways proposed are based on the electrostatic activation by the metal ion due to the Lewis acidity of the latter. These modes involve the nucleophilic attack on the phosphate group, the intramolecular nucleophile activation assisted by a water molecule or the leaving group activation. However, these activation modes can occur concurrently and are totally dependent on the nature of the metal ion and the complex structure.

During the last decades, the catalytic hydrolytic cleavages by a large number of mononuclear and bimetallic complexes have been extensively studied. Inspired by natural metalloenzymes, since early beginnings Zn(II), Cu(II), Ni(II) and Co(III) complexes have been employed in DNA and RNA cleavage models.[173] Pioneering studies by Trogler, Burstyn and Morrow reported the development of synthetic nucleases based on these metal complexes that catalytically hydrolyze BNPP and ENPP substrates with high rates.[175–178] Most of these works used simple chelating ligands such as bipyridine (bpy), terpyridine (trpy), triazacyclononane (TACN), 1,4,8,11-tetraazacyclotetradecane (cyclam), 1,4,7,10- tetraazacyclododecane (cyclen) or 1,2-bis-(4-pyridyl)ethane (bpa).[173] Excellent reviews by Spiccia, Lönnberg or Tecilla can be found in this field, where the current literature is extensively discussed as well as the mechanistic insights and the emergent strategies to develop more efficient nuclease systems.[124,171,173]

The main limitation of the aforementioned systems is their relatively low cleavage rates in comparison to those attained by natural enzymes. Therefore, the development of new nuclease

systems by incorporating additional functionalities emerges as a key strategy to improve the DNA/RNA affinity (Figure I.26). Among these functional groups, the introduction of nucleophilic alcohols and charged-pendant groups close to the active center or the direct conjugation to intercalating agents potentially results in selective and enhanced cleavage activities. In this fashion, Barton, Guo, Mancin, Tonellato and others reported interesting approaches, obtaining high cleavage efficiencies.[179–182]

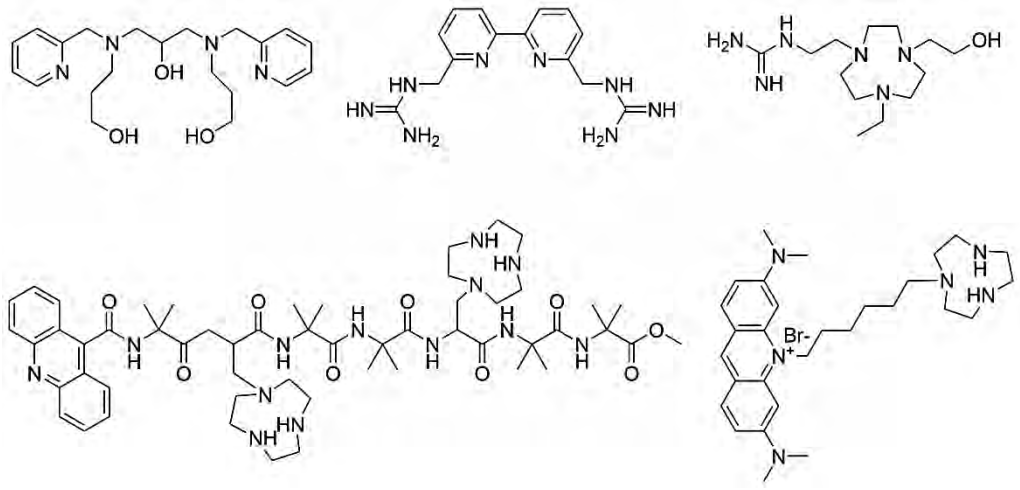

Figure I.26. Structures of ligands containing different functional groups.[173]

Despite the great progress in the development of metallonucleases and enzyme mimics, the most promising approach to manipulate genetics as biotechnological tool arises from the conjugation of active metal complexes to specific recognition motifs. This route potentially enhances the selectivity and allows the cleavage system feasibility to be applied in future drug applications. However, such specificity is difficult to accomplish and few examples are known. Komiyama and coworkers reported a sequence-selective artificial ribonuclease based on the conjugation of a dinuclear Zn(II) complex to a DNA oligonucleotide.[183] This conjugate hydrolyzed RNA at the target site, being the dinuclear Zn(II) complexes the catalytic center. On the other hand, Bashkin and coworkers extensively studied the conjugation of the trpy ligand into different ODN in the presence of Zn(II) and Cu(II) ions (Figure I.27).[184] Interestingly, the cleavage efficiency of this system towards RNA targets was improved when modulating the spacer between the cleaver unit and the oligonucleotide backbone. Different authors also employed phen ligand when designing artificial ribonuclease. In this way, Bashkin and Strömberg studied the sequence-specific RNA cleavage using Cu(II) and Zn(II)-based ODN conjugates.[185–187] These studies put forward the opportunity to study the cleavage efficiencies within different nucleoside bulges while modifying the position of the catalytic complex.

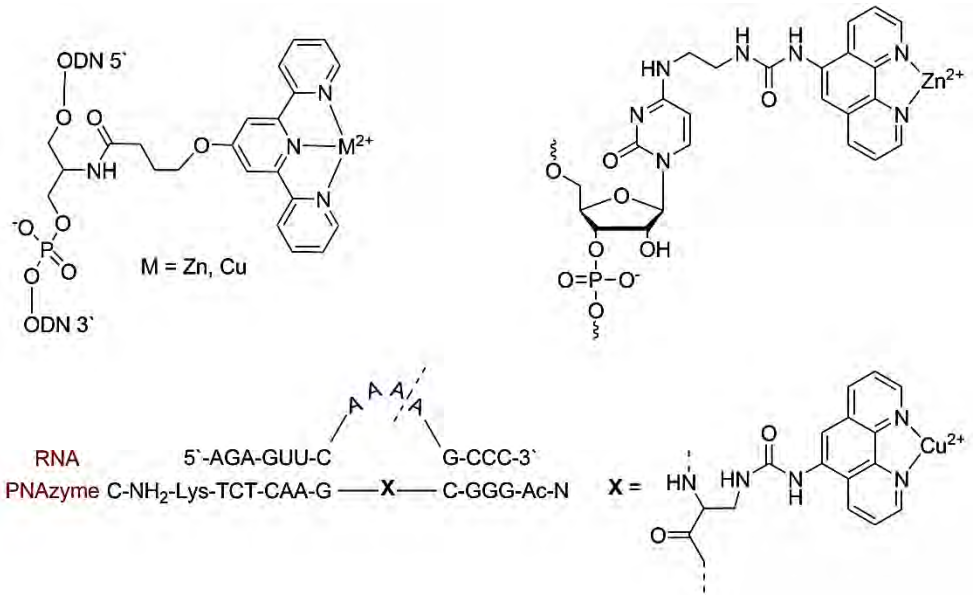

Figure I.27. Structure of sequence-selective conjugates based on Cu(II) and Zn(II) complexes.[184,185,188]

Since their discovery, peptide nucleic acids (PNA) have also been used as recognition sequences to prepare selective nucleases.[189,190] Furthermore, they can be easily obtained by means of solid-phase synthesis, facilitating conjugation strategies to incorporate the active complex. As a remarkable example, Strömberg and coworkers took advantage of their unique properties in order to target RNA substrates upon hybridization.[188] Following these trends, they reported a Cu(II)phen-based PNAzyme able to cleave the target RNA with impressive catalytic turnover (Figure I.27).

I.2.2.3. Metal-free nucleases

Up to now, most of the reported artificial nucleases relied on the catalytic activity of the metal ion as cofactors. However, some metal-free designs have been reported to exhibit DNA cleavage activity. Göbel and coworkers pioneered this design in the last decade since 2-aminopyridines and 2-aminobenzimidazoles were described as powerful metal-free RNA cleavers.[191] Further conjugation of tris(2-aminobenzimidazoles) to DNA oligonucleotide sequences resulted in effective catalytic nucleases with RNA substrate site selectivity (Figure I.28).[192] Moreover, other small organic molecules such as macrocylic polyamines or peptides have been also described to cleave DNA, RNA or their model substrates.[193–196] Although their employment may require higher concentration compared to other artificial metallonuclease systems, metal-free cleaver agents can be considered safer for therapy because of avoiding uncontrolled reactions and additional toxicities derived from metal ions. Interestingly, Yu and

coworkers recently reported a metal-free PNA conjugate that induced site-selective hydrolysis of DNA under physiological conditions (Figure I.28).[197]

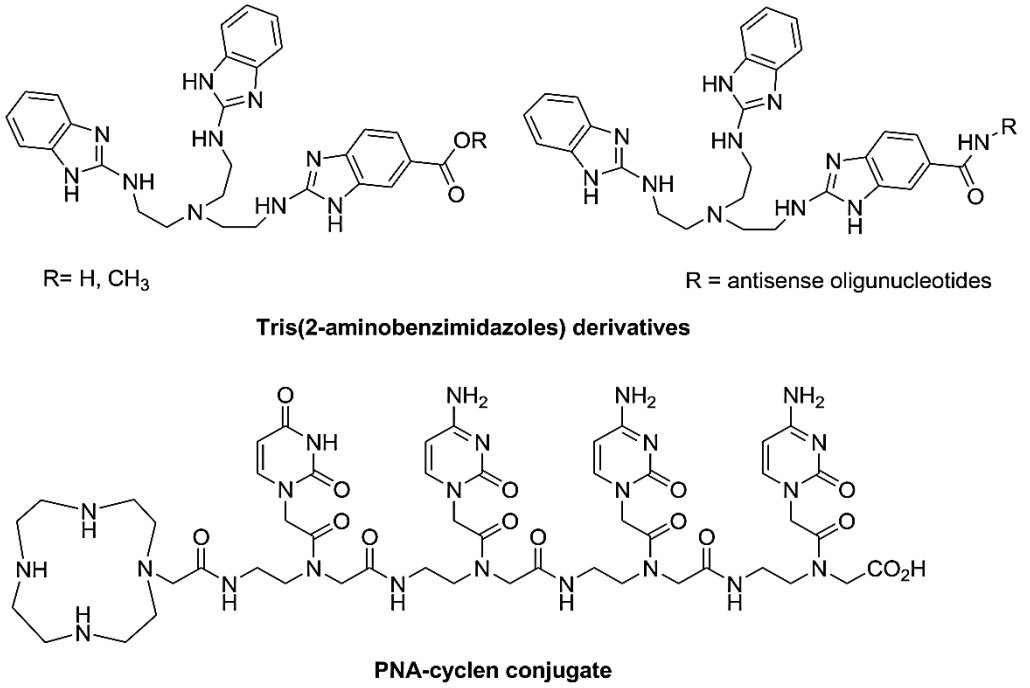

Figure I.28. Structure of highly efficient metal-free cleavage systems reported by Göbel and Yu groups.

Cyclen ligand was conjugated to the N-terminus of a PNA tetramer and its DNA cleaving ability was first assayed against supercoiled pUC19 plasmid as substrate, and analyzed by using agarose gel electrophoresis. In order to corroborate its hydrolytic mechanism, ligation experiments of cleaved pUC19 DNA and PAGE together with MALDI-TOF analyses were performed. The authors also proposed a plausible mechanism displayed by this cyclen-PNA conjugate, which is based on the activation of a H_2O molecule by the protonated ligand motif. Next, 2'-oxygen activates the formation of the phosphorane specie as intermediate and finally, subsequent breakdown resulted in the formation of 2',3'-cyclic phosphate and the 5'-hydroxyl.[197]

Altogether, these remarkable studies pushed forward the opportunity to design new metal-free nucleases in order to obtain high rates of hydrolytic cleavage. Furthermore, the conjugation feasibility of small molecules to DNA/RNA binding peptides, PNA or intercalating proteins describes the opportunity to obtain site-selective cleavage of genetic targets in a straightforward way.

I.2.3. Modulation of the cellular redox balance

I.2.3.1. Metal-based agents with redox chemistry

Improving the selectivity and the therapeutic activity of the drugs is a major goal in the development of novel anticancer compounds. Even when several molecular-targeted drugs discriminate cancer cells from healthy cells, drug resistance and genetic mutations remain as key barriers in current cancer treatments.[66,198] Bearing in mind these real limitations, the targeting of biochemical alterations in cancer cells is one of the most promising strategies against drug resistance. In this fashion, the higher oxidative stress observed in cancer cells results from oncogenic and metabolic alterations and from an increase of the reactive oxygen species (ROS).[199] In biological systems, ROS are generated through different pathways and its homeostasis is essential for the normal cell growth. It is also noteworthy to remark that the redox environment within the cell is variable and differs between the intracellular compartments.[199,200] However, ROS enhancement is generally associated to a disruption in redox homeostasis and thus, such adaptation contributes to a multistage process of cancer development. As a consequence, characteristic failures are perceived in the up-regulation of intracellular signaling pathways.

On the whole, the possibility to target the redox balance in cancer cells has emerged as an effective strategy due to the selectivity over normal cells.[199,201] Nevertheless, the complexity of the role of ROS in cancer and normal cell expose important advantages and disadvantages regarding to oxidant-elevating and oxidant-depleting approaches.[202] In this way, anti-oxidant therapies have been developed with the aim of ceasing the promotion and progression of tumor cells due to the involvement of ROS in multiple signaling cascades of different functions such as survival, proliferation and angiogenesis. However, a moderate increase of ROS derived from a pro-oxidant strategy can break through the antioxidant capacity of the cell and may trigger its death by apoptosis or necrosis. This, in turn means that is extremely important to understand the different redox-modulating strategies in order to develop effective therapeutic strategies. Hence, the insertion of exogenous agents that promote ROS generation requires an extensive underlying study of how to create an irreversible oxidative stress at the subcellular level.

The potential role of ROS-manipulation offers an opportunity to carefully design promising organometallic complexes with specificity on selected biological targets. Since many complexes can readily undergo electron-transfer reactions, this redox activity can be finely tuned

in order to control the oxidation state. Optimized structure can be based on the chelating-ligand and the metal ion choice as specific switches for electronic, chemical, kinetic and photophysical properties.[98] Indeed, a wide variety of transition metal can reach variable oxidation states as observed in enzyme-like activity such as cytochromes and iron-sulfur clusters. These features can be addressed to bring out an appropriate balance in the metallic center while maintaining its redox activity in a biological system. Since redox reactions were associated to the cytotoxic activity of several metallodrugs containing ruthenium(III) or platinum(IV), further studies were developed to explore the direct and indirect involvement of redox chemistry by metal-based anticancer agents.[104,105] In such a way, ferrocifens have been extensively studied as anticancer agents.[96,203–205] The combination of the redox activity of ferrocene and the therapeutic drug tamoxifen confers attractive properties to obtain a targeted cytotoxicity against estrogen receptor positive (ER(+)) human breast cancer cells (Figure I.29).

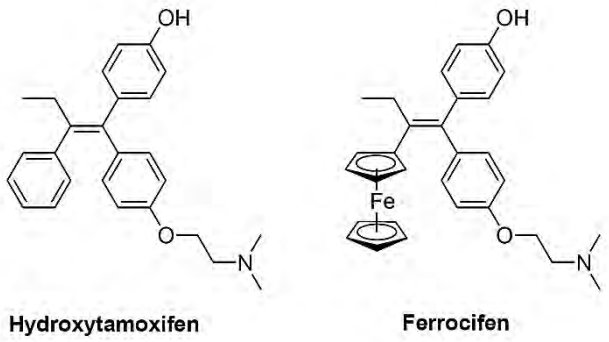

Figure I.29. Structure of hydroxytamoxifen and its analogue ferrocifen.

It was postulated that the oxidation of Fe(II) to Fe(III) in the ferrocene moiety provides the cytotoxic effect owing to the reversible redox behavior of the iron core.[206] Following this approach, although their electrochemistry is substantially different, several Ru analogues of ferrocifen were prepared and showed antiproliferative effects against ER(-) breast cancer cells.[207]

On the other hand, kinetically inert Co(III) complexes have reduction potentials appropriate for being reduced in biological environments. Co(II) complexes generated from Co(III) can be subjected to substitution reactions in order to release cytotoxic ligands such as nitrogen mustards, quinolines, macrocyclics and amines in hypoxic conditions.[104] In a similar manner, Cu(II) complexes can be reduced to form Cu(I) complexes that can act also as releasing agents. Furthermore, Cu(II) complexes with macrocylic ligands like cyclen, cyclam and TACN have been also tested for their cytotoxicity and stability in several cancer cell lines under hypoxic conditions. Although considerable advances have been achieved in the field of medicinal organometallic

chemistry, much effort may be devoted to the development of novel anticancer organometallic-based agents. In this fashion, the versatile redox chemistry of metal complexes provides interesting chances in structural design as well as to tune the redox properties in biological systems. The pharmacological potential of the resulting compounds in medical applications requires extensive work for greater understanding of the mechanism of action.

I.2.3.2. Iron chelating agents

Since iron represents a critical element in the human body, Fe(II) and Fe(III) oxidation states are responsible to perform different reactions involved in energy production and metabolism. For example, syntheses of deoxyribonucleotides, ribonucleotide reductase (RR) as well as iron-sulfur cluster-containing proteins are iron-dependent. Despite the fact that cell holds the iron regulation via particular mechanisms, several diseases like cancer have been associated to the deregulation of iron homeostasis.[208,209] Iron uptake, storage and export are finely controlled and mainly rely on the protein transferrin (Tf) receptors, ceruloplasmin and ferritin functions. Nonetheless, labile iron accumulation in the cell as a result of deregulation can produce a subsequently increase of oxidative stress through Fenton and Haber-Weiss reactions and an important damage for DNA and proteins. Thereafter, free iron tends to generate ROS species excess that outcomes a chronic failure in redox balance and promotes malignant cell proliferation. Special findings have been reported regarding the association of iron deregulation in breast cancer. In kind, a correlation between estrogen and iron has been described. Considering that estrogens are determining for the growth and differentiation of several tissues, iron levels can be directly affected due to the influence of the catecholestrogen metabolites redox cycling. This synergy is more pronounced in postmenopausal women where estrogen levels decrease and iron accumulation takes place attributable to the suspension of the menstrual periods. From then on, high iron levels in breast cancer cells activate oxidative stress pathways and ROS production. However, a relationship among estrogen receptor-associated signaling such as EGFR/ErbB/HER and iron levels has not been established yet.

Keeping all these trends in mind, altering the bioavailability of metal ions by chelating agents is depicted as a promising option for cancer therapy.[98,210] Focusing our attention in iron homeostasis, the insertion of chelating compounds to shift the redox potential represents an encouraging approach to inhibit cellular proliferation.[105,209] In point of fact, multiple signaling pathways have been reported to being affected by the Fe chelators inhibitory effects. For instance, the upregultion of p53, cyclic-dependent kinase inhibitor p21, NDRG1 and the hypoxia-

factor HIF1-α are some genetic pathways that are directly altered by Fe depletion. Although some natural iron chelators like mimosine or diferuloymethane (curcumin) displayed interesting inhibitory effects in breast cancer, several examples of synthetic iron chelators have been described (Figure I.30).[208]

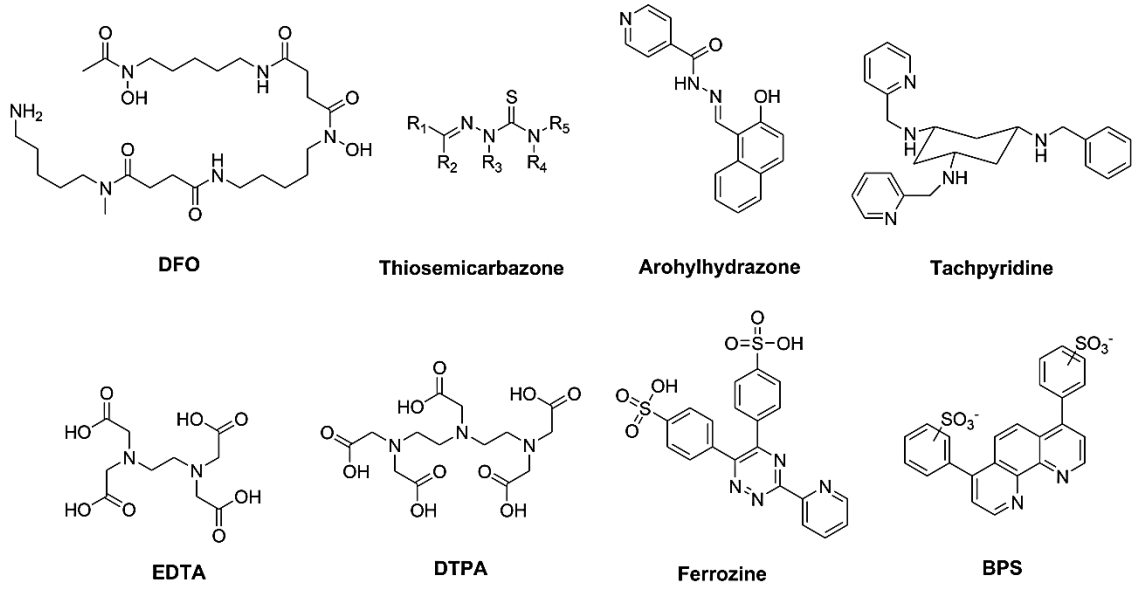

Figure I.30. Most common iron chelating-based structures.

Desferrioxamine (DFO) and tachpyridine are two hexadentate chelating examples that their efficacy to deplete Fe(III) regulatory pools in breast cancer have been described. Moreover, aroylhydrazones and analogues have also shown their potential to induce apoptosis and cell cycle arrest in MCF-7 breast cell line and interesting selectivity towards cancer cells. Likewise, the antiproliferative activity of thiosemicarbazone chelators and derivatives caused by Fe-binding has also been reported *in vitro* and *in vivo* breast cancer cells. Remarkably, it has been demonstrated that this iron depletion by thiosemicarbazones is directly correlated with an enhancement of oxidative stress. Other interesting examples of Fe(III) chelating agents include ethylenediamine tetraacetic (EDTA) and diethylenetriamine pentaacetic acid (DTPA), even their selectivity over Fe(III) is not exclusive. Since the chelation of Fe(II) and Fe(III) is based on the ligand preferences, chelators for Fe(II) are also helpful to module iron bioavailability. In this way, Fe(II) has a preferred octahedral geometry that favors its selectivity over other biometals such as Cu(II) or Zn(II).[98] Considering this factor, ferrozine and disulfonic acid (BPS) are commonly used Fe(II) chelators with large binding constants and are known to promote a nonspecific reduction of iron chelates.

I.2.4. Biomedical application of metallopeptides

Interesting parallels emerge between the use of metal bindings ligands or transition metal complexes with high reactivity and their therapeutic application in cancer cells. However, this medicinal approach is normally hampered by an uptake limitation as well as by the lack of specificity to accumulate the cargo molecule in targeted sites.[210] With the aim of overcoming this particular drawback, the conjugation between the cargo molecule and a functional peptide vector is a versatile and potential strategy to improve the bioavailability and accumulation inside cancer cells. In addition, the stability and the solubility of the cargo can also be enhanced by the influence of the peptide scaffold. While peptide chemistry is really well-established, these advances render the possibility to prepare functional synthetic constructions for being tested in cell culture. Great strides have been made in the last decade to perform conjugation strategies between peptides and stable metal systems.[211] Although these synergies can lead to a decrease in the expected activity of the resulting conjugate compared to the one observed by the cargo alone, some functional metal-peptide conjugates have been described.

In early studies, the attachment of cobaltocenium organometallic specie to the nuclear localization sequence NLS peptide (PKKKRKV) was described by Metzler-Nolte and coworkers (Figure I.31).[212] This heptapeptide is a widely used vector that enables the cell nucleus delivery and its combination with an organometallic moiety provided an enhanced cellular uptake in Hep2G2 living cells as observed by confocal microscopy studies. The study exemplified a novel insight to be further studied in bioorganometallic chemistry involving different functional transition metal complexes for biological purposes.

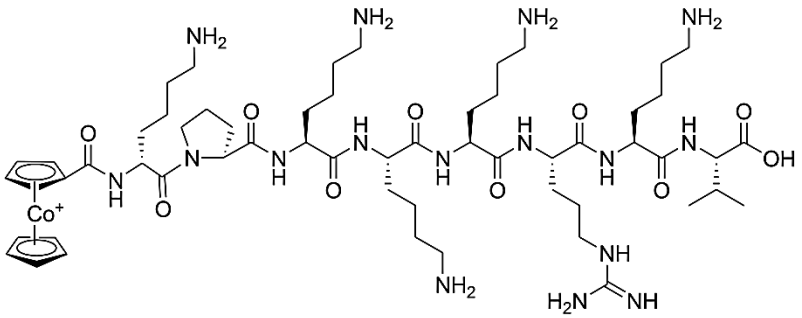

Figure I.31. Cobaltocenium-NLS conjugate prepared by Metzler-Nolte and coworkers.

More recently, Neundorf and coworkers reported the conjugation of bioactive cymantrene $CpMn(CO)_3$ carboxylic acid derivatives to the cell-penetrating peptide sC18, previously identified by the same group (Figure I.32).[213] These conjugations led to the determination of novel

$CpMn(CO)_3$-peptide conjugates with promising antitumor activities due to an enhancement of the uptake level and intracellular release. Notably, preliminary mechanistic insights were studied in an effort to suggest an apoptotic pathway that results in tumor growth inhibition.

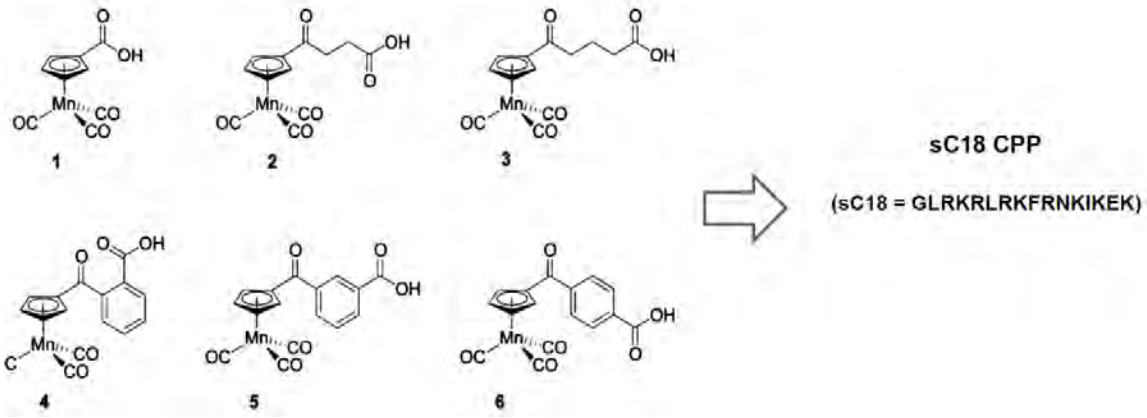

Figure I.32. Cymantrene carboxylic acid derivatives that were coupled to different positions of sC18 cell-penetrating peptide. Their biological activities were tested against MCF-7 and HT29 cell lines.

On the other hand, Marchán and Sadler groups described a potential ruthenium prodrug for anticancer treatment.[214] Two metallopeptides were synthesized based on the conjugation between a ruthenium(II) arene complex and two homing peptides, a dicarba analogue of octreotide and the RGD peptide (Figure I.33). Interestingly, upon irradiation with visible light, both metallopeptides were selectively photodissociated from the ruthenium complex and the resulting aqua species $[(\eta^6\text{-}p\text{-cym})Ru(bpm)(H_2O)]^{2+}$ (cym = η^6-*p*-cymene, bpm = 2,2'-bipyrimidine) reacted preferentially with guanine nucleobases. Their mechanism of action towards DNA was extensively studied by UV-Vis and NMR spectroscopy, suggesting the preference of ruthenium(II) active specie to react with guanine moiety rather than over peptide ligands.

Following studies by the same groups aimed to evaluate the biological activity in cancer cells lines of octreotide conjugates containing $[PtCl_2(dap)]$ (dap = 1-(carboxylic acid)-1,2-diaminoethane), $[(\eta^6\text{-bip})Os(4\text{-}CO_2\text{-pico})Cl]$ (bip = biphenyl, pico = picolinate), $[(\eta^6\text{-}p\text{-cym})RuCl\text{-}(dap)]^+$ and $[(\eta^6\text{-}p\text{-cym})RuCl\text{-(imidazole-}CO_2H)(PPh_3)]^+$.[215] Although the synthesized conjugates displayed lower cytotoxic activities compared with their parent complexes, this study emphasized the opportunity to target tumor cells due to the conjugation to a homing peptide.

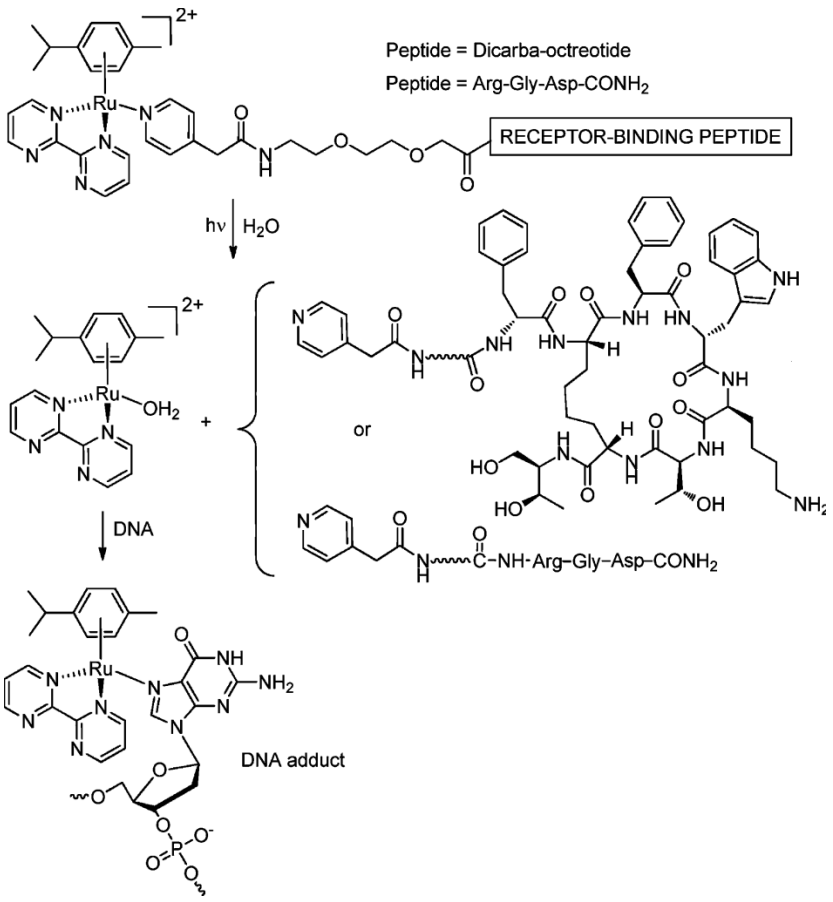

Figure I.33. Structure of the RGD and octreotide conjugates synthesized by Marchán and Sadler groups.[214]

One of the best studied examples has been recently reported by Hartinger and coworkers.[216] Ru(cym) moiety was conjugated to the neuropeptide [Leu^5]-enkephalin using Cu^I-catalyzed alkyne-azide cycloaddition (CuAAC) (Figure I.34). Using this strategy in approach of tagging metal fragments to peptide carriers, the resulting half-sandwich ruthenium(II) exhibited interesting anticancer activity *in vitro* in the low micromolar range.

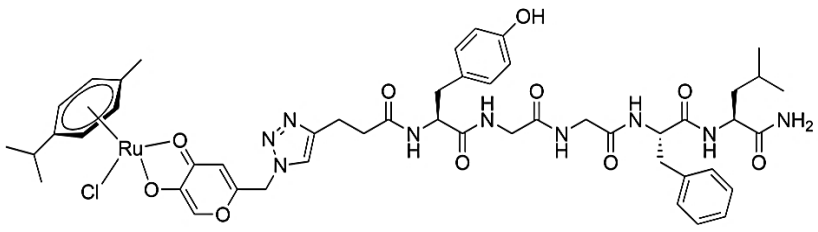

Figure I.34. Structure of Ru(cym)-enkephalin metallopeptide conjugate.

I.2.5. Aminopyridine metal complexes with high redox reactivity

Inspired by the active site of iron and manganese oxidation enzymes, QBIS-CAT group has reported the design of suitable tetradentate ligands based on PyTACN and BPBP families (Figure I.35). Mononuclear metal complexes containing these former tetradentate ligands have been extensively described as excellent catalysts for a wide range of oxidation reactions, on a wide substrate scope with excellent efficiency and remarkable selectivity under mild experimental conditions, environmentally non aggressive.[217–225] On the basis of these precedents, these complexes are emerging as versatile biological catalysts for a number of oxidative processes with biomedical implications. From the therapeutic viewpoint, these metal complexes can interfere in cellular redox chemistry through metal or ligand redox centers. Consequently, the modulation of the intracellular redox balance in cancer cells might promote irreversible damage through reactive oxygen species (ROS)-mediated mechanisms.

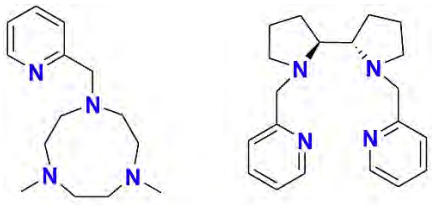

Figure I.35. Schematic representation of PyTACN and BPBP-based ligand structures.

I.3. References

(1) Thanki, K.; Gangwal, R. P.; Sangamwar, A. T.; Jain, S. *J. Control. Release* **2013**, *170*, 15–40.

(2) Alvarez-Lorenzo, C.; Concheiro, A. *Chem. Commun.* **2014**, *50*, 7743–7765.

(3) Koren, E.; Torchilin, V. P. *Trends Mol. Med.* **2012**, *18*, 385–393.

(4) Svensen, N.; Walton, J. G. a; Bradley, M. *Trends Pharmacol. Sci.* **2012**, *33*, 186–192.

(5) Zhang, X.-X.; Eden, H. S.; Chen, X. *J. Control. Release* **2012**, *159*, 2–13.

(6) Bechara, C.; Sagan, S. *FEBS Lett.* **2013**, *587*, 1693–1702.

(7) Copolovici, D. M.; Langel, K.; Eriste, E.; Langel, Ü. *ACS Nano* **2014**, *8*, 1972–1994.

(8) Stewart, K. M.; Horton, K. L.; Kelley, S. O. *Org. Biomol. Chem.* **2008**, *6*, 2242–2255.

(9) Fonseca, S. B.; Pereira, M. P.; Kelley, S. O. *Adv. Drug Deliv. Rev.* **2009**, *61*, 953–964.

(10) Huang, Y.; Jiang, Y.; Wang, H.; Wang, J.; Shin, M. C.; Byun, Y.; He, H.; Liang, Y.; Yang, V. C. *Adv. Drug Deliv. Rev.* **2013**, *65*, 1299–1315.

(11) Foged, C.; Nielsen, H. M. *Expert Opin. Biol. Ther.* **2008**, *5*, 105–118.

(12) Sawant, R.; Torchilin, V. *Mol. Biosyst.* **2010**, *6*, 628–640.

(13) Kersemans, V.; Kersemans, K.; Cornelissen, B. *Curr. Pharm. Des.* **2008**, *14*, 2415–2447.

(14) Milletti, F. *Drug Discov. Today* **2012**, *17*, 850–860.

(15) Elmquist, a; Lindgren, M.; Bartfai, T.; Langel U. *Exp. Cell Res.* **2001**, *269*, 237–244.

(16) Astriab-Fisher, A.; Sergueev, D.; Fisher, M.; Ramsay Shaw, B.; Juliano, R. L. *Pharm. Res.* **2002**, *19*, 744–754.

(17) Zhao, M.; Kircher, M. F.; Josephson, L.; Weissleder, R. *Bioconjug. Chem.* **2002**, *13*, 840–844.

(18) Nori, A.; Jensen, K. D.; Tijerina, M.; Kopecková, P.; Kopeček, J. *Bioconjug. Chem.* **2003**, *14*, 44–50.

(19) Patel, L. N.; Zaro, J. L.; Shen, W.-C. *Pharm. Res.* **2007**, *24*, 1977–1992.

(20) Fischer, R.; Fotin-Mleczek, M.; Hufnagel, H.; Brock, R. *Chembiochem* **2005**, *6*, 2126–2142.

(21) Pujals, S.; Fernández-Carneado, J.; López-Iglesias, C.; Kogan, M. J.; Giralt, E. *Biochim. Biophys. Acta* **2006**, *1758*, 264–279.

(22) Fotin-Mleczek, M.; Fischer, R.; Brock, R. *Curr. Pharm. Des.* **2005**, *11*, 3613–3628.

(23) Henriques, S. T.; Melo, M. N.; Castanho, M. a R. B. *Biochem. J.* **2006**, *399*, 1–7.

(24) Wang, F.; Wang, Y.; Zhang, X.; Zhang, W.; Guo, S.; Jin, F. *J. Control. Release* **2014**, *174*, 126–136.

(25) Terrone, D.; Leung, S.; Sang, W.; Roudaia, L.; Silvius, J. R. *Biochemistry* **2003**, *42*, 13787–13799.

(26) Conner, S. D.; Schmid, S. L. *Nature* **2003**, *422*, 37–44.

(27) Duchardt, F.; Fotin-Mleczek, M.; Schwarz, H.; Fischer, R.; Brock, R. *Traffic* **2007**, *8*, 848–866.

(28) Fischer, R.; Köhler, K.; Fotin-Mleczek, M.; Brock, R. *J. Biol. Chem.* **2004**, *279*, 12625–12635.

(29) Drin, G.; Cottin, S.; Blanc, E.; Rees, A. R.; Temsamani, J. *J. Biol. Chem.* **2003**, *278*, 31192–31201.

(30) Maiolo, J. R.; Ferrer, M.; Ottinger, E. a. *Biochim. Biophys. Acta* **2005**, *1712*, 161–172.

(31) Fjell, C. D.; Hiss, J. a; Hancock, R. E. W.; Schneider, G. *Nat. Rev. Drug Discov.* **2012**, *11*, 37–51.

(32) Li, Y.; Xiang, Q.; Zhang, Q.; Huang, Y.; Su, Z. *Peptides* **2012**, *37*, 207–215.

(33) Bobone, S.; Piazzon, A.; Orioni, B.; Pedersen, J. Z.; Nan, Y. H.; Hahm, K.-S.; Shin, S. Y.; Stella, L. *J. Pept. Sci.* **2011**, *17*, 335–341.

(34) Hancock, R. E. W.; Sahl, H.-G. *Nat. Biotechnol.* **2006**, *24*, 1551–1557.

(35) Marcos, J. F.; Gandía, M. *Expert Opin. Drug Discov.* **2009**, *4*, 659–672.

(36) Eckert, R. *Future Microbiol.* **2011**, *6*, 635–651.

(37) Hoskin, D. W.; Ramamoorthy, A. *Biochim. Biophys. Acta* **2008**, *1778*, 357–375.

(38) Sandgren, S.; Wittrup, A.; Cheng, F.; Jönsson, M.; Eklund, E.; Busch, S.; Belting, M. *J. Biol. Chem.* **2004**, *279*, 17951–17956.

(39) Hou, K. K.; Pan, H.; Lanza, G. M.; Wickline, S. a. *Biomaterials* **2013**, *34*, 3110–3119.

(40) Farrera-Sinfreu, J.; Giralt, E.; Castel, S.; Albericio, F.; Royo, M. *J. Am. Chem. Soc.* **2005**, *127*, 9459–9468.

(41) Fang, B.; Guo, H. Y.; Zhang, M.; Jiang, L.; Ren, F. Z. *FEBS J.* **2013**, *280*, 1007–1017.

(42) Badosa, E.; Ferre, R.; Planas, M.; Feliu, L.; Besalú, E.; Cabrefiga, J.; Bardají, E.; Montesinos, E. *Peptides* **2007**, *28*, 2276–2285.

(43) Eggenberger, K.; Mink, C.; Wadhwani, P.; Ulrich, A. S.; Nick, P. *ChemBioChem* **2011**, *12*, 132–137.

(44) Yamashita, F.; Hashida, M. *Adv. Drug Deliv. Rev.* **2013**, *65*, 139–147.

(45) Martín, I.; Teixidó, M.; Giralt, E. *Pharmaceuticals* **2010**, *3*, 1456–1490.

(46) Bábíčková, J.; Tóthová, Ľ.; Boor, P.; Celec, P. *Biotechnol. Adv.* **2013**, *31*, 1247–1259.

(47) Laakkonen, P.; Vuorinen, K. *Integr. Biol.* **2010**, *2*, 326–337.

(48) Xu, S.; Olenyuk, B. Z.; Okamoto, C. T.; Hamm-Alvarez, S. F. *Adv. Drug Deliv. Rev.* **2013**, *65*, 121–138.

(49) Gehlsen, K.; Argraves, W. .; Pierschbacher, M.; Ruoslahti, E. *J. Cell Biol.* **1988**, *106*, 925–930.

(50) Curnis, F.; Gasparri, A.; Sacchi, A.; Longhi, R.; Corti, A. *Cancer Res.* **2004**, *64*, 565–571.

(51) Arap, W.; Pasqualini, R.; Ruoslahti, E. *Science* **1998**, *279*, 377–380.

(52) Chen, Y.; Xu, X.; Hong, S.; Chen, J.; Liu, N.; Underhill, C. B.; Creswell, K. *Cancer Res.* **2001**, *61*, 2434–2438.

(53) Koivunen, E.; Gay, D. a; Ruoslahti, E. *J. Biol. Chem.* **1993**, *268*, 20205–20210.

(54) Pasqualini, R.; Koivunen, E.; Kain, R.; Lahdenranta, J.; Sakamoto, M.; Stryhn, A.; Ashmun, R. A.; Shapiro, L. H.; Arap, W.; Ruoslahti, E. *Cancer Res.* **2000**, *60*, 722–727.

(55) Hoffman, J. A.; Giraudo, E.; Singh, M.; Zhang, L.; Inoue, M.; Porkka, K.; Hanahan, D.; Ruoslahti, E. *Cancer Cell* **2003**, *4*, 383–391.

(56) Joyce, J. A.; Laakkonen, P.; Bernasconi, M.; Bergers, G.; Ruoslahti, E.; Hanahan, D. *Cancer Cell* **2003**, *4*, 393–403.

(57) Mahato, R.; Tai, W.; Cheng, K. *Adv. Drug Deliv. Rev.* **2011**, *63*, 659–670.

(58) Majumdar, S.; Siahaan, T. J. *Med. Res. Rev.* **2010**, *32*, 637–658.

(59) Schally, A. V; Nagy, A. *Eur. J. Endocrinol.* **1999**, *141*, 1–14.

(60) Schally, A. V; Nagy, A. *Trends Endocrinol. Metab.* **2004**, *15*, 300–310.

(61) Engel, J.; Emons, G.; Pinski, J.; Schally, A. V. *Expert Opin. Investig. Drugs* **2012**, *21*, 891–899.

(62) Tan, M.; Lan, K.-H.; Yao, J.; Lu, C.-H.; Sun, M.; Neal, C. L.; Lu, J.; Yu, D. *Cancer Res.* **2006**, *66*, 3764–3772.

(63) Yarden, Y.; Sliwkowski, M. X. *Nat. Rev. Mol. Cell Biol.* **2001**, *2*, 127–137.

(64) Myrberg, H.; Zhang, L.; Mäe, M.; Langel, U. *Bioconjug. Chem.* **2008**, *19*, 70–75.

(65) Mäe, M.; Myrberg, H.; El-Andaloussi, S.; Langel, Ü. *Int. J. Pept. Res. Ther.* **2008**, *15*, 11–15.

(66) Yin, Q.; Shen, J.; Zhang, Z.; Yu, H.; Li, Y. *Adv. Drug Deliv. Rev.* **2013**, *65*, 1699–1715.

(67) Rautio, J.; Kumpulainen, H.; Heimbach, T.; Oliyai, R.; Oh, D.; Järvinen, T.; Savolainen, J. *Nat. Rev. Drug Discov.* **2008**, *7*, 255–270.

(68) Singh, Y.; Palombo, M.; Sinko, P. J. *Curr. Med. Chem.* **2008**, *15*, 1802–1826.

(69) Bildstein, L.; Dubernet, C.; Couvreur, P. *Adv. Drug Deliv. Rev.* **2011**, *63*, 3–23.

(70) Karaman, R. *Chem. Biol. Drug Des.* **2013**, *82*, 643–668.

(71) Furgeson, D. Y.; Dreher, M. R.; Chilkoti, A. *J. Control. Release* **2006**, *110*, 362–369.

(72) Pan, Y.-J.; Chen, Y.-Y.; Wang, D.-R.; Wei, C.; Guo, J.; Lu, D.-R.; Chu, C.-C.; Wang, C.-C. *Biomaterials* **2012**, *33*, 6570–6579.

(73) Fleige, E.; Quadir, M. A.; Haag, R. *Adv. Drug Deliv. Rev.* **2012**, *64*, 866–884.

(74) Fuselier, J. A.; Sun, L.; Woltering, S. N.; Murphy, W. A.; Vasilevich, N.; Coy, D. H. *Bioorg. Med. Chem. Lett.* **2003**, *13*, 799–803.

(75) Aluri, S.; Janib, S. M.; Mackay, J. A. *Adv. Drug Deliv. Rev.* **2009**, *61*, 940–952.

(76) Kumar, S. K.; Roy, I.; Anchoori, R. K.; Fazli, S.; Maitra, A.; Beachy, P. A.; Khan, S. R. *Bioorg. Med. Chem.* **2008**, *16*, 2764–2768.

(77) Kumar, S. K.; Williams, S. A.; Isaacs, J. T.; Denmeade, S. R.; Khan, S. R. *Bioorg. Med. Chem.* **2007**, *15*, 4973–4984.

(78) Denmeade, S. R.; Nagy, A.; Gao, J.; Lilja, H.; Schally, A. V; Isaacs, J. T. *Cancer Res.* **1998**, *58*, 2537–2540.

(79) Mhaka, A.; Denmeade, S. R.; Yao, W.; Isaacs, J. T.; Khan, S. R. *Bioorg. Med. Chem. Lett.* **2002**, *12*, 2459–2461.

(80) Denmeade, S. R.; Jakobsen, C. M.; Janssen, S.; Khan, S. R.; Garrett, E. S.; Lilja, H.; Christensen, S. B.; Isaacs, J. T. *J. Natl. Cancer Inst.* **2003**, *95*, 990–1000.

(81) Li, C.; Wallace, S. *Adv. Drug Deliv. Rev.* **2008**, *60*, 886–898.

(82) Mohamed, M. M.; Sloane, B. F. *Nat. Rev. Cancer* **2006**, *6*, 764–775.

(83) Gianasi, E.; Wasil, M.; Evagorou, E. G.; Keddle, A.; Wilson, G.; Duncan, R. *Eur. J. Cancer* **1999**, *35*, 994–1002.

(84) Vasey, P. A.; Kaye, S. B.; Morrison, R.; Conjugates, A. D.; Twelves, C.; Wilson, P.; Duncan, R.; Thomson, A. H.; Murray, L. S.; Hilditch, T. E.; Murray, T.; Burtles, S.; Fraier, D.; Frigerio, E. *Clin. Cancer Res.* **1999**, *5*, 89–94.

(85) Loadman, P. M.; Bibby, M. C.; Double, J. A.; Al-shakhaa, W. M.; Duncan, R. *Clin. Cancer Res.* **1999**, *5*, 3682–3688.

(86) Gianasi, E.; Buckley, R. G.; Latigo, J.; Wasil, M.; Duncan, R. *J. Drug Target.* **2002**, *10*, 549–556.

(87) Duncan, R. *Adv. Drug Deliv. Rev.* **2009**, *61*, 1131–1148.

(88) Bai, K. B.; Láng, O.; Orbán, E.; Szabó, R.; Köhidai, L.; Hudecz, F.; Mezö, G. *Bioconjug. Chem.* **2008**, *19*, 2260–2269.

(89) Zhang, P.; Cheetham, A. G.; Lock, L. L.; Cui, H. *Bioconjug. Chem.* **2013**, *24*, 604–613.

(90) Moreno, M.; Zurita, E.; Giralt, E. *J. Control. Release* **2014**, *182*, 13–21.

(91) Shadidi, M.; Sioud, M. *FASEB J.* **2003**, *17*, 256–258.

(92) Wang, X.-F.; Birringer, M.; Dong, L.-F.; Veprek, P.; Low, P.; Swettenham, E.; Stantic, M.; Yuan, L.-H.; Zobalova, R.; Wu, K.; Ledvina, M.; Ralph, S. J.; Neuzil, J. *Cancer Res.* **2007**, *67*, 3337–3344.

(93) Gasser, G.; Metzler-Nolte, N. *Curr. Opin. Chem. Biol.* **2012**, *16*, 84–91.

(94) Schreiber, S. L. *Nat. Chem. Biol.* **2005**, *1*, 64–66.

(95) Sawyer, T. K. *Chem. Biol. Drug Des.* **2006**, *67*, 196–200.

(96) Gasser, G.; Ott, I.; Metzler-Nolte, N. *J. Med. Chem.* **2011**, *54*, 3–25.

(97) Hartinger, C. G.; Metzler-Nolte, N.; Dyson, P. J. *Organometallics* **2012**, *31*, 5677–5685.

(98) Haas, K. L.; Franz, K. J. *Chem. Rev.* **2009**, *109*, 4921–4960.

(99) Komeda, S.; Casini, A. *Curr. Top. Med. Chem.* **2012**, *12*, 219–235.

(100) Hayes, D. M.; Cvitkovic, E.; Golbey, R. B.; Scheiner, E.; Helson, L.; Krakoff, I. H. *Cancer* **1977**, *39*, 1372–1381.

(101) Seeber, S.; Osieka, R.; Schmidt, C. G.; Gottfried, C.; Achterrath, W.; Crooke, T. *Cancer Res.* **1982**, *42*, 4719–4725.

(102) Rademaker-Lakhai, J. M.; van den Bongard, D.; Pluim, D. *Clin. Cancer Res.* **2004**, *10*, 3717–3727.

(103) Hartinger, C. G.; Zorbas-Seifried, S.; Jakupec, M. A.; Kynast, B.; Zorbas, H.; Keppler, B. K. *J. Inorg. Biochem.* **2006**, *100*, 891–904.

(104) Graf, N.; Lippard, S. J. *Adv. Drug Deliv. Rev.* **2012**, *64*, 993–1004.

(105) Romero-Canelón, I.; Sadler, P. J. *Inorg. Chem.* **2013**, *52*, 12276–12291.

(106) Aird, R. E.; Cummings, J.; Ritchie, A. A.; Muir, M.; Morris, R. E.; Chen, H.; Sadler, P. J.; Jodrell, D. I. *Br. J. Cancer* **2002**, *86*, 1652–1657.

(107) Morris, R. E.; Aird, R. E.; Murdoch, P. D. S.; Chen, H.; Cummings, J.; Hughes, N. D.; Parsons, S.; Parkin, a; Boyd, G.; Jodrell, D. I.; Sadler, P. J. *J. Med. Chem.* **2001**, *44*, 3616–3621.

(108) Han Ang, W.; Dyson, P. J. *Eur. J. Inorg. Chem.* **2006**, *2006*, 4003–4018.

(109) Scolaro, C.; Bergamo, A.; Brescacin, L.; Delfino, R.; Cocchietto, M.; Laurenczy, G.; Geldbach, T. J.; Sava, G.; Dyson, P. J. *J. Med. Chem.* **2005**, *48*, 4161–4171.

(110) Kurzwernhart, A.; Kandioller, W.; Bartel, C.; Bächler, S.; Trondl, R.; Mühlgassner, G.; Jakupec, M. A.; Arion, V. B.; Marko, D.; Keppler, B. K.; Hartinger, C. G. *Chem. Commun.* **2012**, *48*, 4839–4841.

(111) Ang, W. H.; Parker, L. J.; De Luca, A.; Juillerat-Jeanneret, L.; Morton, C. J.; Lo Bello, M.; Parker, M. W.; Dyson, P. J. *Angew. Chem. Int. Ed. Engl.* **2009**, *48*, 3854–3857.

(112) Turel, I.; Kljun, J.; Perdih, F.; Morozova, E.; Bakulev, V.; Kasyanenko, N.; Byl, J. A. W.; Osheroff, N. *Inorg. Chem.* **2010**, *49*, 10750–10752.

(113) Kljun, J.; Bytzek, A. K.; Kandioller, W.; Bartel, C.; Jakupec, M. A.; Hartinger, C. G.; Keppler, B. K.; Turel, I. *Organometallics* **2011**, *30*, 2506–2512.

(114) Shaw, F. *Chem. Rev.* **1999**, *99*, 2589–2600.

(115) Nobili, S.; Mini, E.; Landini, I.; Gabbiani, C.; Casini, A.; Messori, L. *Med. Res. Rev.* **2010**, *30*, 550–580.

(116) Barnard, P. J.; Baker, M. V; Berners-Price, S. J.; Day, D. A. *J. Inorg. Biochem.* **2004**, *98*, 1642–1647.

(117) Baker, M. V; Barnard, P. J.; Berners-Price, S. J.; Brayshaw, S. K.; Hickey, J. L.; Skelton, B. W.; White, A. H. *Dalton Trans.* **2006**, *6*, 3708–3715.

(118) Aldinucci, D.; Ronconi, L.; Fregona, D. *Drug Discov. Today* **2009**, *14*, 1075–1076.

(119) Che, C.-M.; Sun, R. W.-Y. *Chem. Commun.* **2011**, *47*, 9554–9560.

(120) Barnard, P. J.; Berners-Price, S. J. *Coord. Chem. Rev.* **2007**, *251*, 1889–1902.

(121) Bindoli, A.; Rigobello, M. P.; Scutari, G.; Gabbiani, C.; Casini, A.; Messori, L. *Coord. Chem. Rev.* **2009**, *253*, 1692–1707.

(122) Urig, S.; Fritz-Wolf, K.; Réau, R.; Herold-Mende, C.; Tóth, K.; Davioud-Charvet, E.; Becker, K. *Angew. Chem. Int. Ed. Engl.* **2006**, *45*, 1881–1886.

(123) Vergara, E.; Casini, A.; Sorrentino, F.; Zava, O.; Cerrada, E.; Rigobello, M. P.; Bindoli, A.; Laguna, M.; Dyson, P. J. *ChemMedChem* **2010**, *5*, 96–102.

(124) Mancin, F.; Scrimin, P.; Tecilla, P. *Chem. Commun.* **2012**, *48*, 5545–5559.

(125) Núñez, M. E.; Barton, J. K. *Curr. Opin. Chem. Biol.* **2000**, *4*, 199–206.

(126) Tullius, T. D.; Greenbaum, J. A. *Curr. Opin. Chem. Biol.* **2005**, *9*, 127–134.

(127) Wolkenberg, S. E.; Boger, D. L. *Chem. Rev.* **2002**, *102*, 2477–2495.

(128) Jiang, Q.; Xiao, N.; Shi, P.; Zhu, Y.; Guo, Z. *Coord. Chem. Rev.* **2007**, *251*, 1951–1972.

(129) Pogozelski, W. K.; Tullius, T. D. *Chem. Rev.* **1998**, *98*, 1089–1108.

(130) Pitié, M.; Pratviel, G. *Chem. Rev.* **2010**, *110*, 1018–1059.

(131) Sigman, S. *Acc. Chem. Res.* **1986**, *19*, 180–186.

(132) Pogozelski, W. K.; McNeese, T. J.; Tullius, T. D. *J. Am. Chem. Soc.* **1995**, *117*, 6428–6433.

(133) Mestre, B.; Jakobs, A.; Pratviel, G.; Meunier, B. *Biochemistry* **1996**, *35*, 9140–9149.

(134) Claussen, C. A.; Long, E. C. *Chem. Rev.* **1999**, *99*, 2797–2816.

(135) Czlapinski, J. L.; Sheppard, T. L. *Chem. Commun.* **2004**, 2468–2469.

(136) Que, L. *Acc. Chem. Res.* **2007**, *40*, 493–500.

(137) Meunier, B.; Visser, P. De; Shaik, S. *Chem. Rev.* **2004**, *104*, 3947–3980.

(138) Denisov, I. G.; Makris, T. M.; Sligar, S. G.; Schlichting, I. *Chem. Rev.* **2005**, *105*, 2253–2277.

(139) Shaik, S.; Kumar, D.; de Visser, S. P.; Altun, A.; Thiel, W. *Chem. Rev.* **2005**, *105*, 2279–2328.

(140) Blum, R. H.; Carter, S. K.; Agre, K. *Cancer* **1973**, *31*, 903–914.

(141) Kross, J.; Henner, D.; Hech, S. M.; A, H. W. *Biochemistry* **1982**, *21*, 4310–4318.

(142) Burger, R. M. *Chem. Rev.* **1998**, *98*, 1153–1169.

(143) Hecht, S. M. *J. Nat. Prod.* **2000**, *63*, 158–168.

(144) Chen, J.; Stubbe, J. *Nat. Rev. Cancer* **2005**, *5*, 102–113.

(145) Li, Q.; van der Wijst, M. G. P.; Kazemier, H. G.; Rots, M. G.; Roelfes, G. *ACS Chem. Biol.* **2014**, *9*, 1044–1051.

(146) Erkkila, K. E.; Odom, D. T.; Barton, J. K. *Chem. Rev.* **1999**, *99*, 2777–2796.

(147) Zeglis, B. M.; Pierre, V. C.; Barton, J. K. *Chem. Commun.* **2007**, 4565–4579.

(148) Thomas, A. M.; Neelakanta, G.; Mahadevan, S.; Nethaji, M.; Chakravarty, A. R. *Eur. J. Inorg. Chem.* **2002**, 2720–2726.

(149) Patra, A. K.; Dhar, S.; Nethaji, M.; Chakravarty, A. R. *Dalt. Trans.* **2005**, 896–902.

(150) Patra, A. K.; Nethaji, M.; Chakravarty, A. R. *Dalt. Trans.* **2005**, 2798–2804.

(151) Dhar, S.; Chakravarty, A. R. *Inorg. Chem.* **2005**, *44*, 2582–2584.

(152) Lown, J. W.; Sondhi, S. M.; Ong, C. W.; Skorobogaty, A.; Kishikawa, H.; Dabrowiak, J. C. *Biochemistry* **1986**, *25*, 5111–5117.

(153) Routier, S.; Cotelle, N.; Catteau, J. P.; Bernier, J. L.; Waring, M. J.; Riou, J. F.; Bailly, C. *Bioorg. Med. Chem.* **1996**, *4*, 1185–1196.

(154) Boldron, C.; Ross, S. A.; Pitié, M.; Meunier, B. *Bioconjug. Chem.* **2002**, *13*, 1013–1020.

(155) Pitié, M.; Van Horn, J. D.; Brion, D.; Burrows, C. J.; Meunier, B. *Bioconjug. Chem.* **2000**, *11*, 892–900.

(156) Chen, C. B.; Mazumder, A.; Constant, J.-F.; Sigman, D. S. *Bioconjug. Chem.* **1993**, *4*, 69–77.

(157) Routier, S.; Bernier, J.-L.; Catteau, J.-P.; Bailly, C. *Bioorg. Med. Chem. Lett.* **1997**, *7*, 1729–1732.

(158) Blondeau, P.; Segura, M.; Pérez-Fernández, R.; de Mendoza, J. *Chem. Soc. Rev.* **2007**, *36*, 198–210.

(159) Pitié, M.; Meunier, B. *Bioconjug. Chem.* **1998**, *9*, 604–611.

(160) Lin, S. B.; Blake, K. R.; Miller, P. S.; Ts'o, P. O. *Biochemistry* **1989**, *28*, 1054–1061.

(161) Bergstrom, D. E.; Gerry, N. P. *J. Am. Chem. Soc.* **1994**, *116*, 12067–12068.

(162) Bigey, P.; Sönnichsen, S. H.; Meunier, B.; Nielsen, P. E. *Bioconjug. Chem.* **1997**, *8*, 267–270.

(163) Mack, D. P.; Sluka, J. P.; Shin, J. A.; Griffin, J. H.; Simon, M. I.; Dervan, P. B. *Biochemistry* **1990**, *29*, 6561–6567.

(164) Ebright, Y. W.; Chen, Y.; Pendergrast, P. S.; Ebright, R. H. *Biochemistry* **1992**, *31*, 10664–10670.

(165) Ermácora, M. R.; Ledman, D. W.; Hellinga, H. W.; Hsu, G. W.; Fox, R. O. *Biochemistry* **1994**, *33*, 13625–13641.

(166) Schatzschneider, U.; Barton, J. K. *J. Am. Chem. Soc.* **2004**, *126*, 8630–8631.

(167) Petitjean, A.; Barton, J. K. *J. Am. Chem. Soc.* **2004**, *126*, 14728–14729.

(168) Mancin, F.; Scrimin, P.; Tecilla, P.; Tonellato, U. *Chem. Commun.* **2005**, 2540–2548.

(169) Morrow, J. R.; Iranzo, O. *Curr. Opin. Chem. Biol.* **2004**, *8*, 192–200.

(170) Morrow, J. R. *Comments Inorg. Chem.* **2008**, *29*, 169–188.

(171) Lönnberg, H. *Org. Biomol. Chem.* **2011**, *9*, 1687–1703.

(172) Perreault, D. M.; Anslyn, E. V. *Angew. Chemie Int. Ed.* **1997**, *36*, 432–450.

(173) Desbouis, D.; Troitsky, I. P.; Belousoff, M. J.; Spiccia, L.; Graham, B. *Coord. Chem. Rev.* **2012**, *256*, 897–937.

(174) Jones, D. R.; Lindoy, L. F.; Sargeson, A. M. *J. Am. Chem. Soc.* **1983**, *105*, 7327–7336.

(175) Morrow, J. R.; Trogler, W. C. *Inorg. Chem.* **1988**, *27*, 3387–3394.

(176) Derosch, M. A. De; Trogler, W. C. *Inorg. Chem.* **1990**, *29*, 2409–2416.

(177) Burstyn, J. N.; Deal, K. A. *Inorg. Chem.* **1993**, *32*, 3585–3586.

(178) Deal, K. A.; Hengge, A. C.; Burstyn, J. N. *J. Am. Chem. Soc.* **1996**, *118*, 1713–1718.

(179) Fitzsimons, M. P.; Barton, J. K. *J. Am. Chem. Soc.* **1997**, *119*, 3379–3380.

(180) Chen, J.; Wang, X.; Zhu, Y.; Lin, J.; Yang, X.; Li, Y.; Lu, Y.; Guo, Z. *Inorg. Chem.* **2005**, *44*, 3422–3430.

(181) Bonomi, R.; Selvestrel, F.; Lombardo, V.; Sissi, C.; Polizzi, S.; Mancin, F.; Tonellato, U.; Scrimin, P. *J. Am. Chem. Soc.* **2008**, *130*, 15744–15745.

(182) Boseggia, E.; Gatos, M.; Lucatello, L.; Mancin, F.; Moro, S.; Palumbo, M.; Sissi, C.; Tecilla, P.; Tonellato, U.; Zagotto, G.; Pado, V.; Marzolo, V.; V, I.-P.; Farmaceutiche, S.; Uni, V.; Cnr, I.; Uniti, S.; Chimiche, S.; Giorgeri, V.; Trieste, I.-. *J. Am. Chem. Soc.* **2004**, *126*, 4543–4549.

(183) Crisma, M.; Broxterman, Q. B.; Kamphuis, J.; Toniolo, C.; Matsuda, S.; Ishikubo, A.; Kuzuya, A.; Yashiro, M.; Komiyama, M. *Angew. Chem. Int. Ed. Engl.* **1998**, *37*, 3284–3286.

(184) Trawick, B. N.; Osiek, T. A.; Bashkin, J. K. *Bioconjug. Chem.* **2001**, *12*, 900–905.

(185) Åström, H.; Williams, H.; Strömberg, R. *Org. Biomol. Chem.* **2003**, *1*, 1461–1465.

(186) Åström, H.; Strömberg, R. *Org. Biomol. Chem.* **2004**, *2*, 1901–1907.

(187) Putnam, W. C.; Daniher, A. T.; Trawick, B. N.; Bashkin, J. K. *Nucleic Acids Res.* **2001**, *29*, 2199–2204.

(188) Murtola, M.; Wenska, M.; Strömberg, R. *J. Am. Chem. Soc.* **2010**, *132*, 8984–8990.

(189) Marin, V. L.; Roy, S.; Armitage, B. A. *Expert Opin. Biol. Ther.* **2004**, *4*, 337–348.

(190) Ray, A.; Nordén, B. *FASEB J.* **2000**, *14*, 1041–1060.

(191) Scheffer, U.; Strick, A.; Ludwig, V.; Peter, S.; Kalden, E.; Göbel, M. W. *J. Am. Chem. Soc.* **2005**, *127*, 2211–2217.

(192) Gnaccarini, C.; Peter, S.; Scheffer, U.; Vonhoff, S.; Klussmann, S.; Göbel, M. W. *J. Am. Chem. Soc.* **2006**, *128*, 8063–8067.

(193) Sheng, X.; Lu, X.; Zhang, J.; Chen, Y.; Lu, G.; Shao, Y.; Liu, F.; Xu, Q.; Cheme, S.; V, J. K. C. R. *J. Org. Chem.* **2007**, *72*, 1799–1802.

(194) Alkhader, S.; Ezra, A.; Kasparkova, J.; Brabec, V.; Yavin, E. *Bioconjug. Chem.* **2010**, *21*, 1425–1431.

(195) Li, C.; Zhao, F.; Huang, Y.; Liu, X.; Liu, Y.; Qiao, R.; Zhao, Y. *Bioconjug. Chem.* **2012**, *23*, 1832–1837.

(196) Li, Z.-F.; Chen, H.-L.; Zhang, L.-J.; Lu, Z.-L. *Bioorg. Med. Chem. Lett.* **2012**, *22*, 2303–2307.

(197) Wang, M.-Q.; Liu, J.-L.; Wang, J.-Y.; Zhang, D.-W.; Zhang, J.; Streckenbach, F.; Tang, Z.; Lin, H.-H.; Liu, Y.; Zhao, Y.-F.; Yu, X.-Q. *Chem. Commun.* **2011**, *47*, 11059–11061.

(198) Markman, J. L.; Rekechenetskiy, A.; Holler, E.; Ljubimova, J. Y. *Adv. Drug Deliv. Rev.* **2013**, *65*, 1866–1879.

(199) Trachootham, D.; Alexandre, J.; Huang, P. *Nat. Rev. Drug Discov.* **2009**, *8*, 579–591.

(200) Pelicano, H.; Carney, D.; Huang, P. *Drug Resist. Updat.* **2004**, *7*, 97–110.

(201) Wang, J.; Yi, Y. *Cancer Biol. Ther.* **2008**, *7*, 1875–1884.

(202) Miguel, M. De; Cordero, M. D. In *Oxidative Therapy Against Cancer, Oxidative Stress and Diseases, Dr. Volodymyr Lushchak (Ed.), ISBN: 978-953-51-0552-7, InTech.*; 2012; pp. 497–520.

(203) Allard, E.; Jarnet, D.; Vessières, A.; Vinchon-Petit, S.; Jaouen, G.; Benoit, J.-P.; Passirani, C. *Pharm. Res.* **2010**, *27*, 56–64.

(204) Huynh, N. T.; Morille, M.; Bejaud, J.; Legras, P.; Vessieres, A.; Jaouen, G.; Benoit, J.-P.; Passirani, C. *Pharm. Res.* **2011**, *28*, 3189–3198.

(205) Schatzschneider, U.; Metzler-Nolte, N. *Angew. Chem. Int. Ed. Engl.* **2006**, *45*, 1504–1507.

(206) Hillard, E.; Vessières, A.; Thouin, L.; Jaouen, G.; Amatore, C. *Angew. Chem. Int. Ed. Engl.* **2005**, *45*, 285–290.

(207) Pigeon, P.; Top, S.; Vessières, A.; Huché, M.; Hillard, E. a; Salomon, E.; Jaouen, G. *J. Med. Chem.* **2005**, *48*, 2814–2821.

(208) Marques, O.; da Silva, B. M.; Porto, G.; Lopes, C. *Cancer Lett.* **2014**, *347*, 1–14.

(209) Heli, H.; Mirtorabi, S.; Karimian, K. *Expert Opin. Ther. Pat.* **2011**, *21*, 819–856.

(210) Scott, L. E.; Orvig, C. *Chem. Rev.* **2009**, *109*, 4885–4910.

(211) Dirscherl, G.; König, B. *European J. Org. Chem.* **2008**, *2008*, 597–634.

(212) Noor, F.; Wüstholz, A.; Kinscherf, R.; Metzler-Nolte, N. *Angew. Chem. Int. Ed. Engl.* **2005**, *44*, 2429–2432.

(213) Splith, K.; Hu, W.; Schatzschneider, U.; Gust, R.; Ott, I.; Onambele, L. A.; Prokop, A.; Neundorf, I. *Bioconjug. Chem.* **2010**, *21*, 1288–1296.

(214) Barragán, F.; López-Senín, P.; Salassa, L.; Betanzos-Lara, S.; Habtemariam, A.; Moreno, V.; Sadler, P. J.; Marchán, V. *J. Am. Chem. Soc.* **2011**, *133*, 14098–14108.

(215) Barragán, F.; Carrion-Salip, D.; Gómez-Pinto, I.; González-Cantó, A.; Sadler, P. J.; de Llorens, R.; Moreno, V.; González, C.; Massaguer, A.; Marchán, V. *Bioconjug. Chem.* **2012**, *23*, 1838–1855.

(216) Meier, S. M.; Novak, M.; Kandioller, W.; Jakupec, M. A.; Arion, V. B.; Metzler-Nolte, N.; Keppler, B. K.; Hartinger, C. G. *Chem. Eur. J.* **2013**, *19*, 9297–9307.

(217) Company, A.; Gómez, L.; Fontrodona, X.; Ribas, X.; Costas, M. *Chem. Eur. J.* **2008**, *14*, 5727–5731.

(218) Company, A.; Feng, Y.; Güell, M.; Ribas, X.; Luis, J. M.; Que, L.; Costas, M. *Chem. Eur. J.* **2009**, *15*, 3359–3362.

(219) Gómez, L.; Garcia-Bosch, I.; Company, A.; Benet-Buchholz, J.; Polo, A.; Sala, X.; Ribas, X.; Costas, M. *Angew. Chemie Int. Ed.* **2009**, *48*, 5720–5723.

(220) Fillol, J. L.; Codolà, Z.; Garcia-Bosch, I.; Gómez, L.; Pla, J. J.; Costas, M. *Nat. Chem.* **2011**, *3*, 807–813.

(221) Garcia-Bosch, I.; Gómez, L.; Polo, A.; Ribas, X. *Adv. Synth. Catal.* **2012**, *354*, 65–70.

(222) Prat, I.; Gómez, L.; Canta, M.; Ribas, X.; Costas, M. *Chem. Eur. J.* **2013**, *19*, 1908–1913.

(223) Codolà, Z.; Garcia-Bosch, I.; Acuña-Parés, F.; Prat, I.; Luis, J. M.; Costas, M.; Lloret-Fillol, J. *Chem. Eur. J.* **2013**, *19*, 8042–8047.

(224) Gómez, L.; Canta, M.; Font, D.; Prat, I.; Ribas, X.; Costas, M. *J. Org. Chem.* **2013**, *78*, 1421–1433.

(225) Cussó, O.; Garcia-Bosch, I.; Ribas, X.; Lloret-Fillol, J.; Costas, M. *J. Am. Chem. Soc.* **2013**, *135*, 14871–14878.

CHAPTER II

Main Objectives

II. MAIN OBJECTIVES

The main objective of this thesis is to explore the biological activity of the nitrogen rich tetradentate aminopyridine ligands ^{Me2}PyTACN and (*S,S'*)-BPBP and of their transition metal complexes when conjugated to peptide derivatives. Since complexes based on ^{Me2}PyTACN and (*S,S'*)-BPBP ligands render high redox reactivity, their peptide vectorization could promote irreversible damage through reactive oxygen species (ROS)-mediated mechanisms.

Towards this end, in the first part of this thesis (Chapters III and IV) we aimed to identify a non-toxic cell-penetrating sequence from a library of antimicrobial undecapeptides, to study its cellular internalization capacities and to test its drug delivery properties using a well-known anticancer drug. Moreover, it was also planned the evaluation of the effect of incorporating an enzyme-cleavable sequence to trigger the drug release.

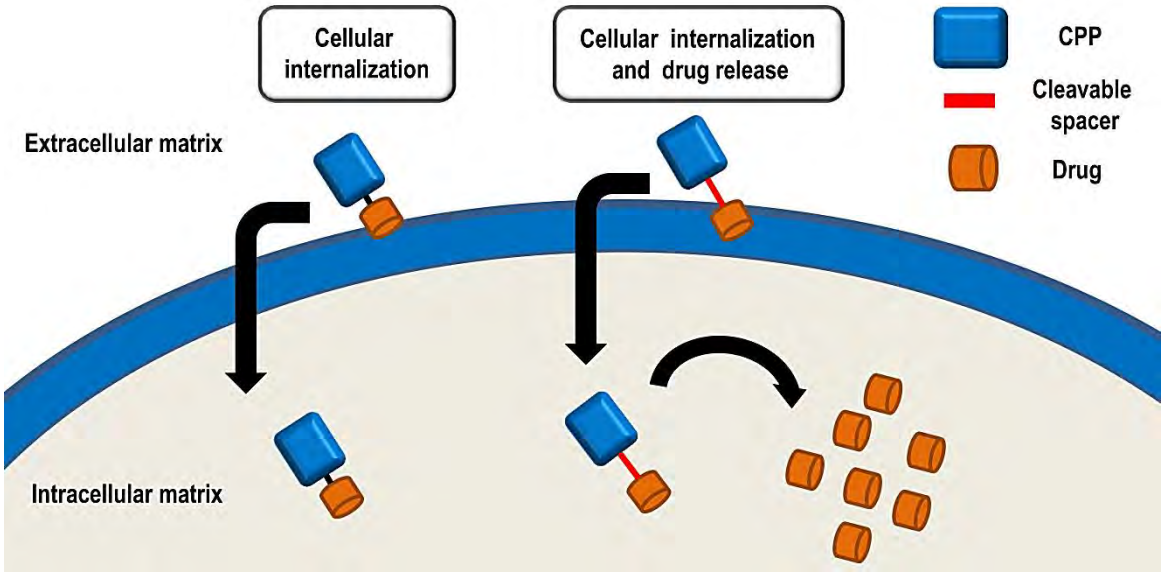

In the second part of this thesis (Chapters V, VI and VII), we aimed to study conjugates bearing the ^{Me2}PyTACN and (*S,S'*)-BPBP ligands and a peptide derivative. First of all, in Chapter V we planned to develop a straightforward solid-phase methodology to synthesize short metal binding peptide conjugates and redox-active metallopeptides containing the above-mentioned ligands as well as to characterize these metallopeptides. It was also envisaged the evaluation of the DNA cleavage ability of these compounds in terms of activity and selectivity. Next, in Chapter VI we sought to examine the extension of the synthetic methodology for the conjugation of ^{Me2}PyTACN and (*S,S'*)-BPBP ligands to a cell-penetrating peptide. We planned to study the cytotoxic activities and the internalization properties in cancer cells of the resulting conjugates as

well as the incorporation of an enzymatic cleavable sequence. Finally, in Chapter VII we aimed to conjugate the (*S,S'*)-BPBP ligand to PNA recognition sequences that are meant to target specific oncogenic miRNA sites. We also sought to explore the cleavage of RNA by the resulting conjugates under mild conditions.

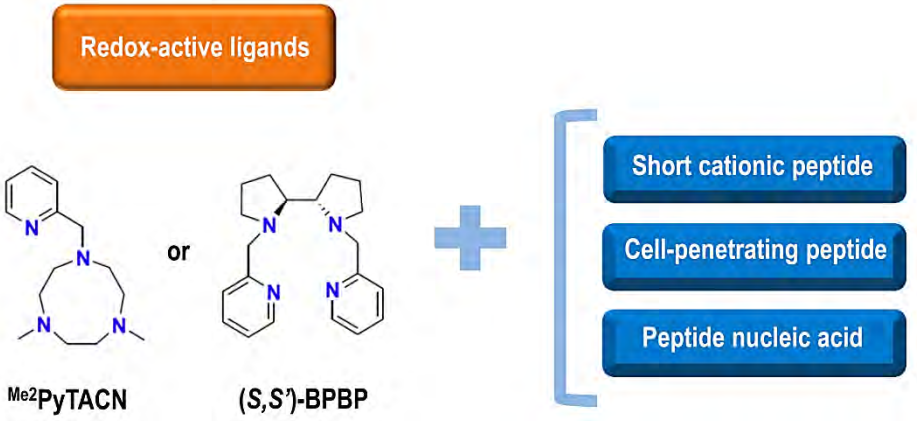

CHAPTER III

Identification of BP16 as a non-toxic cell-penetrating peptide with highly efficient drug delivery properties

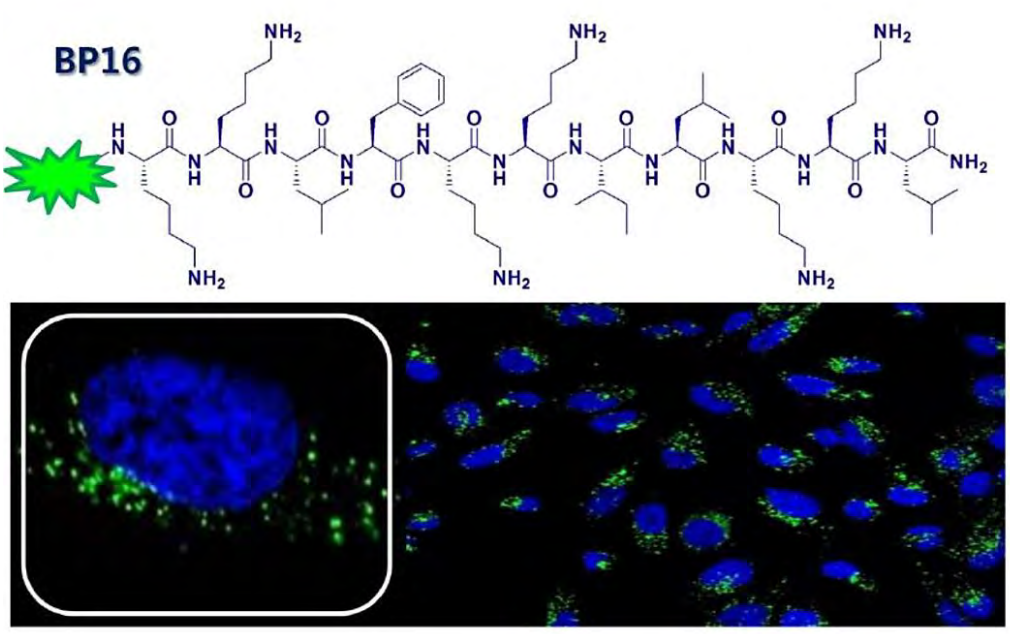

This chapter corresponds to the following publication:

Marta Soler,† Marta González-Bártulos,† David Soriano-Castell, Xavi Ribas, Miquel Costas, Francesc Tebar, Anna Massaguer,* Lidia Feliu,* and Marta Planas*. Identification of BP16 as a non-toxic cell-penetrating peptide with highly efficient drug delivery properties. *Org. Biomol. Chem.,* **2014**, 12, 1652–1663.

†Authors contributed equally to this work

For this publication, M. S. performed the design, the synthesis and the characterization of all the peptide conjugates. Moreover, M. S. was involved in argumentations and discussions, and wrote the manuscript draft.

III.1. Introduction

The efficacy of anticancer treatments remains as a key challenge in medicine. Current therapies are hindered by the appearance of toxic side effects and the development of multi-drug resistance by cancer cells.[1,2] Moreover, the use of therapeutic agents is limited by their low permeability through biological membranes. Therefore, there is an actual interest in developing new approaches to cancer treatment.[3] A promising strategy in this area is the use of cell-penetrating peptides (CPPs) as drug delivery systems.[4-9] CPPs are usually short cationic sequences and may be derived from long peptides or proteins present in nature (i.e., Tat peptide or penetratin) or be de novo designed peptides (i.e., transportan, polyarginine peptides, β-peptides, peptoids, oligocarbamates or polyproline helices).[9-12] The mechanism of action of CPPs initially involves their binding to the negatively charged head groups of lipids or proteins in the plasma membrane which is then followed by their internalization. The exact mode of internalization is still poorly understood but it has been shown to depend on several factors such as the structure and concentration of the CPP as well as the cargo to be transported and the specific cell line.[7,8,12-14] It is believed that endocytosis is the major mode of uptake for CPPs, however direct translocation can also occur. Due to their ability to cross biomembranes in a non-disruptive way, CPPs offer an opportunity to increase bioavailability of drugs, enhancing their activity, and reducing their dosage. In this sense, CPPs have been described as efficient carriers of nucleic acids, proteins, small molecule drugs and imaging agents.[6-8,10,11,15-18]

Focusing on the idea of obtaining new CPPs with very low toxicity, cationic antimicrobial peptides (AMPs) have emerged as good candidates.[12,19-23] Like CPPs, AMPs are short sequences, containing between 9 and 30 amino acids, and most of them are cationic and amphipathic. These peptides show a broad spectrum of activity against bacteria, fungi, enveloped viruses, parasites, and tumor cells, while exhibiting low eukaryotic cytotoxicity.[24-31] Several AMPs are being studied for the treatment of human diseases, and some of them have already entered pre-clinical and clinical trials.[26,27] The mechanism of action of AMPs also includes their electrostatic interaction with the negatively charged phospholipid membranes causing morphological changes such as pore formation or cell lysis, however their translocation into the cytoplasm is not uncommon.[32-35] Due to the latter property, the use of AMPs as CPPs is a field of interest to develop non-cytotoxic delivery vectors. In fact, AMPs, such as LL-37, SynB, melittin and bLFcin$_6$, are able to translocate across human plasma membranes and to act as drug transporters.[36-39]

Binding of a CPP to a low-molecular weight drug results in an improved uptake, which is associated with a decrease of the dose required to achieve a significant therapeutic effect.[7] In particular, several efforts have been made to conjugate the cytotoxic agent chlorambucil (CLB) to CPPs in order to improve its efficacy.[40-43] Chlorambucil (CLB) is a well-known nitrogen mustard typically used to treat leukemia, but also some breast, lung and ovarian cancers. It is believed that CLB is taken up by passive diffusion and alkylates DNA bringing about its cross-linking.[44] Although this nitrogen mustard is highly effective against certain cancers, its use is limited by the lack of selectivity and the low permeability through cell membranes. To overcome these limitations, CLB has been conjugated to CPPs such as pVEC or sC18.[40,41,43]

Despite the high efficiency of CPPs in mediating cellular uptake of pharmacologically active molecules, their use for targeted therapy is limited by their low level of selectivity. Several approaches aimed at improving the specificity of CPPs towards tumor cells have been developed.[45] One of these strategies relies on the conjugation of a CPP with a homing peptide. These peptides bind selectively to overexpressed receptors in human tumor cells providing a means of targeting CPPs towards desired cells or tissues.[46-49] However, most homing peptides have no internalization properties and only can deliver cargos to the cell surface. Thus, homing peptide-CPP conjugates may act as efficient vectors for drug delivery into a specific cell target, improving drug bioavailability, and decreasing side effects and toxicity in healthy cells. An example of homing peptide is CREKA (Cys-Arg-Glu-Lys-Ala) which was identified by in vivo screening of phage-displayed peptide libraries in breast tumors of MMTV-PyMT transgenic mice. CREKA specifically homes to tumors by binding to fibrin and fibrin-associated clotted plasma proteins present in the vessels and the interstitial stroma of tumors.[47,50-52] Since CREKA is not able to internalize cancer cells, it is a good candidate to design peptide-mediated systems for targeted cell delivery of drugs.[41,42]

This study is focused on the search for new CPP candidates and was based on a library of linear undecapeptides (CECMEL11) previously described by Badosa and co-workers to be used for plant protection.[53] This library included sequences highly active against phytopathogenic bacteria and fungi, and low haemolytic activity. Similarly to CPPs, these peptides are cationic and are able to adopt an amphipathic structure. In fact, one member of this library, **BP100**, has been described as an efficient CPP in plant tobacco cells.[54] This background prompted us to study the suitability of peptides from the CECMEL11 library as drug delivery vectors in cancer cells. We first selected several members of this library displaying different antimicrobial and hemolytic activity profiles. Some analogues containing arginine residues were also synthesized and included in the

study. The cytotoxicity of these peptides was evaluated in cancer and healthy cell lines. The cellular uptake properties of the peptide with the optimal cytotoxic profile as CPP were then evaluated. We also examined the potential of this CPP candidate as drug carrier by conjugating it to CLB. In addition, this candidate was conjugated to the homing peptide CREKA to obtain a selective delivery vector for CLB in cancer cells and to confirm that the cell penetrating properties were retained after the incorporation of CREKA and CLB. Thus, we evaluated the cytotoxicity of the CLB-CREKA-CPP conjugate against cancer and healthy cells and its cellular uptake properties.

III.2. Results and Discussion

III.2.1. Peptide design and synthesis

AMPs represent a source of CPPs because both families share similar structural characteristics. With the aim of identifying new CPPs, we focused our attention on a 125-member library of AMPs (CECMEL11) previously described by Badosa and co-workers.[53] The general structure of this library is R X^1KLFKKILKX^{10}L-NH_2, where X^1 and X^{10} correspond to amino acids with various degrees of hydrophobicity and hydrophilicity (Leu, Lys, Phe, Trp, Tyr, Val) and R includes different N-terminal derivatizations (H, Ac, Ts, Bz, Bn). Thus, peptides of this library are highly cationic and their amphipathic character becomes evident when are represented by means of an Edmunson wheel plot. These structural features have been described as crucial for their antimicrobial activity and also may confer on them cell-penetrating properties.[32-35] In fact, **BP100**, a member of the CECMEL11 library, has been reported as an efficient agent to transport cargoes into plant cells.[54]

In the present study, we examined the ability of sequences of this CECMEL11 library to internalize cancer cells and to transport a drug. Two sets of peptides were considered: (i) undecapeptides **BP16**, **BP76**, **BP81**, **BP100** and **BP105**, and the Arg-containing peptides **BP307** and **BP308**; and (ii) peptide conjugates containing in their structure: the undecapeptide **BP16** and the DNA alkylating agent CLB (**BP325**), **BP16** and the homing peptide CREKA (**BP327**), and **BP16**, CLB and CREKA (**BP329**). To analyze the cellular internalization, **BP16**, **BP325**, **BP327**, and **BP329** were labeled with 5(6)-carboxyfluorescein (CF).

The five peptides of the first set (**BP16**, **BP76**, **BP81**, **BP100** and **BP105**) (Table III.1) were selected based on their distinct antibacterial activity against the plant pathogens *Erwinia amylovora*, *Pseudomonas syringae* and *Xanthomonas vesicatoria*, and their different hemolysis

percentage at 150 μM.[53] **BP100** and **BP76** are highly active against these phytopathogens (MIC of 2.5 to 7.5 μM) and low hemolytic (22-34%), **BP81** is highly active (MIC of < 2.5 to 5 μM) and moderately hemolytic (65%), **BP105** is highly active (MIC of 2.5 to 7.5 μM) and highly hemolytic (91%), and **BP16** is poorly active (MIC > 7.5 μM) and non-hemolytic (0%).

The Arg-containing peptides **BP307** and **BP308** were derived from **BP100** and **BP16**, respectively (Table III.1). They were included in this study because most common CPPs, such as Tat or penetratin, are Arg-rich peptides.[55] This residue has been shown to play a key role in peptide internalization due to the hydrogen-bond formation of the guanidino moiety with phosphates, sulfates and carboxylates on cellular components. **BP307** and **BP308** were tested for their antibacterial activity against the above pathogens and for their hemolysis. The replacement of Lys for Arg in **BP16** and **BP100** significantly influenced the antibacterial activity. While **BP307** resulted to be less active (MIC of 6.2 to 12.5 μM) than **BP100**, **BP308** displayed higher antibacterial activity (MIC of 3.1 to 12.5 μM) than **BP16**. In contrast, the hemolysis was not affected and **BP307** and **BP308** exhibited similar hemolytic activity (28% and 1%, respectively) than the corresponding parent peptide.

Peptide conjugates included in the second set were designed based on **BP16** (Table III.1), which showed the best profile as drug delivery vector among all the above tested undecapeptides (see below). Peptide **BP325** was prepared by coupling CLB to the N-terminus of **BP16** via an amide bond. The use of CLB is hampered by its low stability in aqueous environments and its low permeability through biomembranes, limitations that have been overcome by its conjugation to a CPP.[41-44] Moreover, since the use of homing peptides has been described to increase the cell-type specificity of CPPs, **BP327** was designed by conjugating the homing peptide CREKA to the N-terminus of **BP16**. CREKA was selected for its excellent targeting ability to breast tumors and because its linear structure avoids the additional cyclization step required for most other homing peptides. In addition, with the aim of improving the specificity of the cytotoxic agent CLB, **BP329** was synthesized by attaching CLB to CREKA-BP16. Control peptides CREKA and CLB-CREKA were also prepared (Table III.1).

These peptides were manually synthesized on a Fmoc-Rink-MBHA resin or on an aminomethyl ChemMatrix resin following a standard Fmoc/*t*Bu strategy and were obtained as C-terminal amides. Couplings of the conveniently protected Fmoc-amino acids and of CLB were mediated by ethyl 2-cyano-2-(hydroxyimino)acetate (Oxyma) and *N,N'*-diisopropylcarbodiimide (DIPCDI) in *N,N*-dimethylformamide (DMF) or *N*-methyl-2-pyrrolidinone (NMP), depending on the

length of the sequence. Peptides were cleaved from the resin by acidolytic treatment and were obtained in excellent purities (87-100%, Table III.1), as determined by analytical HPLC. Their identity was confirmed by ESI-MS and HRMS.

Table III.1. Peptide sequences, retention times and purities on HPLC, and HRMS data.

Peptide	Sequence[a]	t_R (min)[b]	Purity (%)[c]	HRMS
BP16	KKLFKKILKKL	5.98	87	347.2575 $[M+4H]^{4+}$, 462.6733 $[M+3H]^{3+}$
BP76	KKLFKKILKFL	6.40	93	352.0004 $[M+4H]^{4+}$, 468.9983 $[M+3H]^{3+}$
BP81	LKLFKKILKFL	6.80	92	348.2477 $[M+4H]^{4+}$, 463.9946 $[M+3H]^{3+}$
BP100	KKLFKKILKYL	7.40	100	355.9977 $[M+4H]^{4+}$, 474.3282 $[M+3H]^{3+}$
BP105	LKLFKKILKYL	6.65	90	352.2490 $[M+4H]^{4+}$, 469.3289 $[M+3H]^{3+}$
BP307	RRLFRRILRYL	7.83	100	391.0091 $[M+4H]^{4+}$, 521.0091 $[M+3H]^{3+}$
BP308	RRLFRRILRRL	6.08	99	311.6168 $[M+5H]^{5+}$, 389.2674 $[M+4H]^{4+}$
	CREKA	6.63	98	303.1636 $[M+2H]^{2+}$, 605.3194 $[M+H]^{+}$
BP327	CREKA-KKLFKKILKKL	6.99	95	395.4636 $[M+5H]^{5+}$, 494.0771 $[M+4H]^{4+}$
BP325	CLB-KKLFKKILKKL	7.71	91	418.5260 $[M+4H]^{4+}$, 558.3644 $[M+3H]^{3+}$
	CLB-CREKA	6.90	90	445.6966 $[M+2H]^{2+}$, 890.3832 $[M+H]^{+}$
BP329	CLB-CREKA-KKLFKKILKKL	6.92	92	452.4770 $[M+5H]^{5+}$, 565.3442 $[M+4H]^{4+}$
CF-BP16	CF-KKLFKKILKKL	6.76, 6.80[d]	93	437.0217 $[M+4H]^{4+}$, 582.3589 $[M+3H]^{3+}$
	CF-CREKA	6.25	95	482.1862 $[M+2H]^{2+}$, 963.3620 $[M+H]^{+}$
BP328	CF-CREKA-KKLFKKILKKL	7.89	97	583.5907 $[M+4H]^{4+}$, 777.7843 $[M+3H]^{3+}$
BP326	CLB-KKLFKKILK(CF)KL	7.56	81	677.0473 $[M+3H]^{3+}$, 1015.0638 $[M+2H]^{2+}$
BP330	CLB-CREKA-KKLFKKILK(CF)KL	7.53	91	654.8565 $[M+4H]^{4+}$, 872.8045 $[M+3H]^{3+}$

[a]All peptides are C-terminal amides. [b]HPLC retention time. [c]Percentage determined by HPLC at 220 nm from the crude reaction mixture. [d]Retention time corresponding to the two isomers of the 5(6)-carboxyfluorescein (CF) labeled peptide.

On the other hand, **BP16** and **BP327** (CREKA-BP16) were labeled with 5(6)-carboxyfluorescein by coupling this fluorescent label to their N-terminus leading to **CF-BP16** and **BP328**, respectively (Table III.1). 5(6)-Carboxyfluorescein labeled CREKA was also prepared (CF-CREKA). Moreover, **BP325** (CLB-BP16) and **BP329** (CLB-CREKA-BP16), incorporating CLB at the N-terminus, were labeled at the side-chain of Lys^9 of the **BP16** fragment, affording **BP326** and **BP330**, respectively. 5(6) Carboxyfluorescein was introduced using DIPCDI and Oxyma,

followed by piperidine washes before cleavage of the peptide from the resin. These washes served to remove overincorporated carboxyfluorescein moieties.[56] For the synthesis of peptides **BP326** (CLB-BP16(CF)) and **BP330** (CLB-CREKA-BP16(CF)), the lysine residue to be labeled was incorporated as Fmoc-Lys(Dde)-OH. The *N*-[1-(4,4-dimethyl-2,6-dioxocyclohex-1-ylidene)ethyl] (Dde) group was selectively removed by treatment with hydrazine prior to the coupling of the fluorescent label. Acidolytic cleavage afforded the labeled peptides in excellent purities (81-97%), and they were characterized by ESI-MS and HRMS.

III.2.2. Cell cytotoxicity of the CPP candidates

A good CPP to be used as a delivery vector of an anticancer drug must display no toxicity against cancer as well as healthy cells. Hence, the cytotoxicity of undecapeptides **BP16**, **BP76**, **BP81**, **BP100**, **BP105**, **BP307** and **BP308** was screened in breast adenocarcinoma MCF-7 and pancreas adenocarcinoma CAPAN-1 cell lines. The IC_{50} was determined by the 3-(4,5-dimethylthiazol-2-yl)-2,5-diphenyltetrazolium bromide (MTT) assay after 48 h of peptide exposure. As shown in Table III.2, except for **BP100**, the undecapeptides were more active against CAPAN-1 than against MCF-7 cells. The cytotoxic activity of **BP76** and **BP105** was significant against these two cell lines, displaying IC_{50} values of 23.5 and 22.7 μM against CAPAN-1, respectively, and of 26.3 and 29.2 μM against MCF-7 cells, respectively. **BP81**, **BP100** and its Arg-containing analogue **BP307** were considerably active against one cell line with IC_{50} values ranging from 24.2 to 35.7 μM. **BP16** and **BP308** were the least cytotoxic undecapeptides. **BP308** showed an IC_{50} of 148.2 and 97.0 μM against MCF-7 and CAPAN-1 cells, respectively, and **BP16** displayed no cytotoxic effects against any of the cancer cell lines tested (IC_{50} > 200 μM).

Table III.2. Cytotoxicity of the set of undecapeptides in 3T3, MCF-7 and CAPAN-1 cells and their hemolytic activity.

	Cell line	BP16	BP76	BP81	BP100	BP105	BP307	BP308
IC_{50}[a] (μM)	3T3	>200	13.5 ± 0.7	15.5 ± 0.7	62.5 ± 6.4	39.0 ± 8.5	40.0 ± 7.1	68.0 ± 7.6
	MCF-7	>200	26.3 ± 7.5	40.0 ± 3.4	34.3 ± 4.0	29.2 ± 4.2	64.7 ± 12.5	148.2 ± 8.8
	CAPAN-1	>200	23.5 ± 7.0	24.2 ± 7.2	57.7 ± 13.3	22.7 ± 1.5	35.7 ± 1.5	97.0 ± 15.4
Hemolysis[b] (%)		0	34 ± 2.1	65 ± 1.5	22 ± 2.8	91 ± 6.2	28 ± 3.2	1 ± 0.1

[a]The IC_{50} values were determined by the MTT assay after 48 h of peptide exposure. Data represents the mean ± SD of at least three independent experiments made in triplicates. [b]Percent hemolysis at 150 μM. The confidence interval for the mean is included.

These results indicate that these undecapeptides exhibit lower cytotoxicity against cancer cells in comparison with their antibacterial activity. However, the structural features that govern the anticancer activity of the CECMEL11 library sequences, **BP16**, **BP76**, **BP81**, **BP100** and **BP105**, correlate with the general trend for the antibacterial activity of this library.[53] Thus, peptides with a net charge of +5 or +6 displayed high cytotoxic activity, whereas **BP16** that has a net charge of +7 was inactive. Moreover, **BP16**, **BP76**, and **BP100** that only differ in the amino acid at position 10 displayed a very distinct cytotoxic activity. The same effect was observed for **BP307** and **BP308**. This result confirms previous data on how subtle changes in a peptide sequence influence the biological activity.[57-59] On the other hand, the replacement of Lys with Arg in **BP16** and **BP100** caused a different effect in the cytotoxicity. While this replacement slightly influenced the cytotoxicity of **BP100**, the Arg-containing sequence **BP308** showed an increased antiproliferative activity compared to **BP16**.

One of the major drawbacks for drug delivery applications of CPPs is their toxicity to normal cells. In this sense, AMPs are interesting CPP candidates because it has been reported that some AMPs with anticancer activity do not show significant cytotoxicity against normal cells at peptide concentrations that are able to kill cancer cells.[19,24,26,28] Parameters that would account for the selective binding of AMPs to cancer cells involves the higher net negative charge and membrane fluidity of cancer cells as compared to normal cells. Therefore, due to their cationic nature, the undecapeptides of this study may preferentially bind to cancer cell membranes by electrostatic interaction and subsequently enter cells.

The analysis of the activity of undecapeptides on non-malignant mouse embryonic fibroblasts 3T3 revealed that the antiproliferative activity of **BP76** and **BP81** was high, with IC_{50} values of 13.5 and 15.5 μM, respectively (Table III.2). **BP100**, **BP105**, **BP307** and **BP308** were moderately active (IC_{50} of 39.0 to 68.0 μM). Notably, **BP16** was non-toxic against this cell line exhibiting an IC_{50} > 200 μM. Furthermore, we also used the hemolysis assay to assess the toxicity of these peptides.[53] As mentioned above, except for **BP105** and **BP81**, undecapeptides displayed low hemolysis at 150 μM (0-34%). Interestingly, **BP16** and its Arg analogue **BP308** were non hemolytic even at 375 μM (data not shown). Even though these undecapeptides did not show selectivity between the malignant and non-malignant cell lines tested, some sequences (**BP76**, **BP100**, and **BP307**) did not show significant hemolytic activity at concentrations much higher than the IC_{50} values against the cancer cell lines tested.Moreover, the stability in fetal bovine serum of **BP16** was also evaluated and compared to that of Tat_{49}. After exposure to 10%

serum at different time intervals, the presence of peptide was analyzed by HPLC. Results showed that both peptides exhibited similar stability, with 70% degradation after 45 min of incubation.

Taken together, these results allowed the identification of **BP16**, a short and highly cationic peptide with a suitable activity profile to be considered as an excellent CPP candidate. In particular, in contrast to most common CPPs that exhibited cytotoxicity even at low concentrations,[60-63] **BP16** was non-toxic to both malignant and non-malignant cell lines at concentrations up to 200 μM and, therefore, was selected for further studies.

III.2.3. Cellular uptake of BP16

To characterize the capacity of internalization of **BP16** into cancer and non-malignant cells, MCF-7 and 3T3 cells were incubated at 37 ºC with 5(6)-carboxyfluorescein labeled **BP16** (**CF-BP16**) at different concentrations (0, 5, 25 and 50 μM) for different times (1, 3 and 6 h) (Figure III.1). The mean fluorescence of the cells, corresponding to the peptide uptake, was quantified by flow cytometry. Cells were harvested by trypsinization, which also prevented non-specific plasma membrane binding of the peptide.

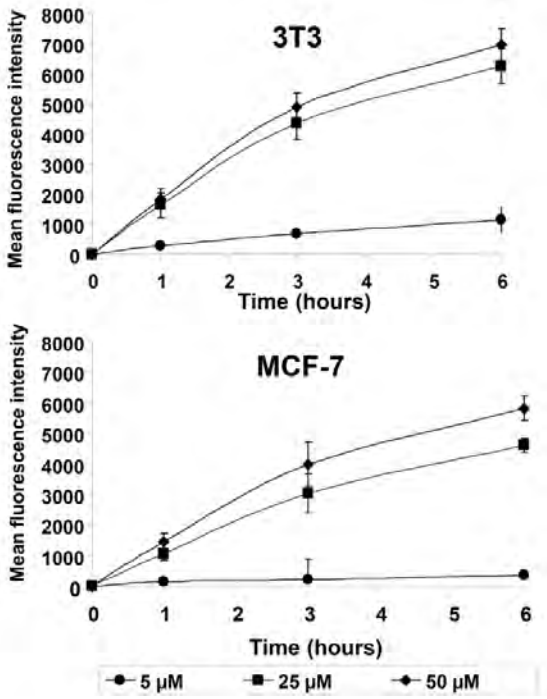

Figure III.1. Kinetics of the cellular uptake of **BP16**. 3T3 and MCF-7 cells were exposed to different concentrations of 5(6)-carboxyfluorescein-labeled **BP16** (**CF-BP16**) (0, 5, 25 and 50 μM) at 37 ºC for 1, 3 and 6 h. The fluorescence intensity of the cells, corresponding to the intracellular uptake of the peptide, was determined by flow cytometry. Each point in the graphs represents the mean intracellular fluorescence intensity of three independent experiments + SE.

As represented in Figure III.1, **CF-BP16** was efficiently internalized by the cells in a time and concentration-dependent manner. The mean fluorescence of the cells increased over time with parallel internalization kinetics in both cell lines. The cellular uptake of **CF-BP16** was intense during the first 3 h of incubation, particularly when the cells were treated with the peptide at 25 and 50 μM. After treatment with 50 μM **CF-BP16**, the mean fluorescence of 3T3 cells increased from 5 ± 2 (0 h) to 1829 ± 335 (1 h), 4895 ± 464 (3 h) and 6953 ± 536 (6 h), while the mean fluorescence of MCF-7 cells rose from 4 ± 1 (0 h) to 1431 ± 307 (1 h), 3997 ± 720 (3 h) and 5830 ± 410 (6 h). These results point out that the internalization of **CF-BP16** is more elevated in the non-malignant 3T3 cells than in MCF-7 cells, indicating the lack of selectivity of **BP16** for cancer cells.

A good correlation between peptide concentration and its uptake by cells was observed, especially when they were treated with 5 and 25 μM **CF-BP16**. At the different incubation times, when **CF-BP16** concentration was increased from 5 to 25 μM, the mean cellular fluorescence increased by 5 to 6-fold in 3T3 cells and by 8 to 13-fold in MCF-7 cells. In contrast, slight differences in the mean cellular fluorescence (less than 1.7-fold increase) were determined when both cell lines were incubated with **CF-BP16** at 25 or 50 μM, revealing a saturation of the peptide uptake by the cells at concentrations higher than 25 μM.

We compared the capacity of internalization of **BP16** with that of the well-known CPP Tat_{49}.[10] With this aim, MCF-7 cells were incubated at 37ºC with **CF-BP16** and CF-Tat_{49} at 25 μM for 1, 3 and 6 h (Figure III.2). Interestingly, **CF-BP16** and CF-Tat_{49} showed the same mean fluorescence intensity values indicating that **BP16** exhibits an excellent cellular uptake.

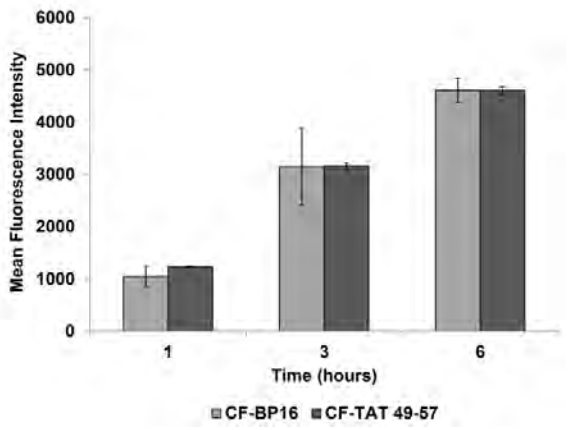

Figure III.2. Uptake of 5(6)-carboxyfluorescein labeled peptides **CF-BP16** and CF-Tat_{49} into MCF-7 cells. Cells were exposed to the peptide at 25 μM at 37 ºC for 1, 3 and 6 h. Each column in graph represents the mean fluorescence intensity of the cells determined in three independent experiments ± SD.

To gain more insight into the internalization and intracellular distribution of **BP16**, the cellular uptake of CF-BP16 was further analyzed by confocal microscopy. For this purpose, MCF-7 cells were incubated with 25 µM **CF-BP16** at 4 ºC for 30 min and at 37 ºC for 10, 30, 60, 120 and 180 min (Figure III.3A).

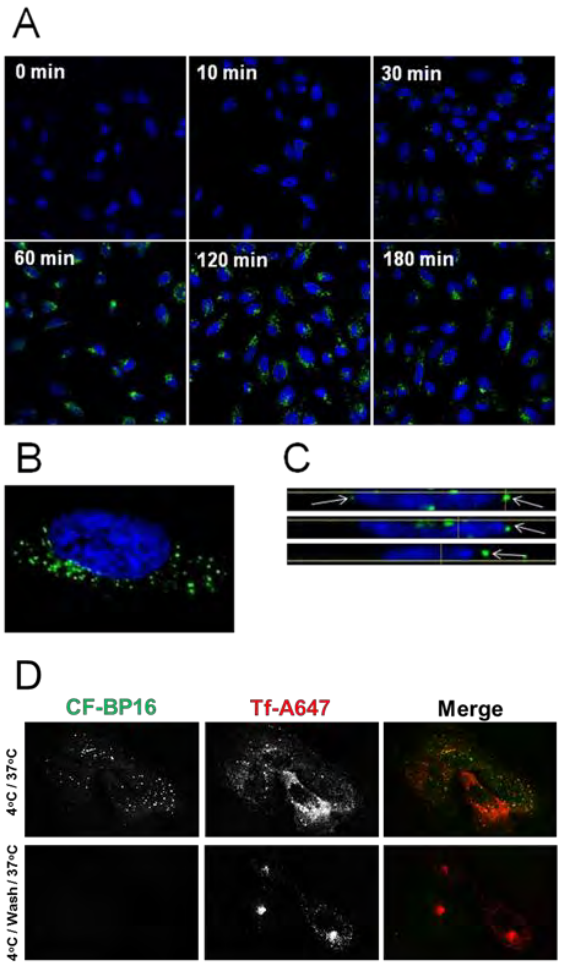

Figure III.3. Confocal microscopic imaging of the internalization of 5(6)-carboxyfluorescein-labeled BP16 (**CF-BP16**) into MCF-7 cells. (A) MCF-7 cells were exposed for 30 min at 4 ºC to 25 µM **CF-BP16** then incubated for the indicated times at 37 ºC. The localization of **CF-BP16** is indicated by the green fluorescence. The cell nuclei were stained with Hoeschst (blue). (B) Higher-magnification (1000X) image of a MCF-7 cell after 180 minutes of treatment. (C) Three slices of a merged xz reconstruction of the image stack (slices at 0.3 microns on z axis) are represented. Arrows indicate the perinuclear localization of **CF-BP16**. (D) MCF-7 cells were pre-incubated for 30 min at 4 ºC with 25 µM **CF-BP16** and transferrin-A647 (Tf-A467, 60 µg ml^{-1}) and then incubated for 25 min at 37 ºC with or without previous saline phosphate buffer wash as indicated. Confocal images were acquired through the Alexa647 (red) and CF (green) channels.

No fluorescence was observed after 30 min of incubation at 4 ºC. However, when the cells were treated at 37 ºC, a very faint punctuate fluorescent staining was observed inside the

cells after 10 min, revealing an incipient cellular uptake of the peptide. The number of fluorescent particles gradually increased over time and, after 180 min of incubation, there was a prominent fluorescent staining inside the cells, demonstrating an intense internalization of the peptide during this period of time. Higher magnification (1000x) images from cells exposed to **CF-BP16** for 180 min (Figure III.3B) revealed that the fluorescent particle were located throughout the whole cytoplasm, with a significant clustering at the periphery of the cell nucleus. An optical sectioning indicated that no fluorescence particles were placed inside the cell nucleus (Figure III.3C). In addition, to find out whether **CF-BP16** cellular entry was dependent on specific interaction with the plasma membrane, MCF-7 cells were pre-incubated with 25 μM **CF-BP16** at 4ºC for 30 min and, after extensive washing with saline phosphate buffer, were incubated at 37ºC for 25 min. **CF-BP16** internalization was also compared with the Alexa647-conjugated transferrin (Tf-A647) which is a well-known model of receptor dependent internalized ligands. Confocal images revealed that while transferrin-A647 labelled endocytic structures inside the cell as expected, no intracellular **CF-BP16** was observed (Figure III.3D). This result may indicate the possibility that **CF-BP16** is weakly membrane associated and removed after washes or that **CF-BP16** could be receptor independent and preferentially fluid phase internalized.

These findings highlight a plausible mechanism for the internalization of **BP16**. The mechanism of CPP uptake is controversial and still under debate. Two main pathways have been suggested: endocytosis and direct translocation across the membrane bilayer.[7,8,12-14] These cell uptake phenomena can be related to the hydrophobicity of the CPP. Translocation has been associated with hydrophobic peptides while hydrophilic and amphipathic sequences can be internalized by both mechanisms.[64] In addition, the endocytosis process is energy-dependent and is assumed to be inhibited by peptide incubation at low temperature. Altogether, the results observed for the incubation of **CF-BP16** in MCF-7 cells at 4 and 37 ºC suggest that the endocytic pathway may play a major role in **BP16** internalization.

To further characterize the **BP16** endocytosis, the role of dynamin, which is involved in vesicle scission from plasma membrane, was analysed by means of dynamin inhibition using the specific inhibitor dynasore (Figure III.4).[65] The **BP16** endocytosis was also compared with the transferrin protein as a specific marker of a dynamin dependent endocytosis. MCF-7 cells were pre-incubated with 100 μM of dynasore for 15 min at 37 ºC and then **CF-BP16** and Tf-A647 were added and further incubated for 60 min. Confocal microscopy images showed an accumulation of Tf-A647 and **CF-BP16** in the same structures at the plasma membrane after dynasore treatment, likely unscissored clathrin coated pits (CCPs) (Figure III.4A). On the other hand, in control cells,

CF-BP16 and Tf-A647 were found mostly in different endocytic structures inside the cell (Figure III.4A). Indeed, high degree of co-localization between **CF-BP16** and the ectopically expressed RFP-Lamp1,[66] a marker of late endosomes and lysosomes, was clearly detected (Figure III.4B). These results suggest that CCPs, are an important port of entry for **BP16**. However, **BP16** and transferrin follow different endocytic pathways inside the cell, a known recycling pathway for transferrin and a degradation route for **BP16**.

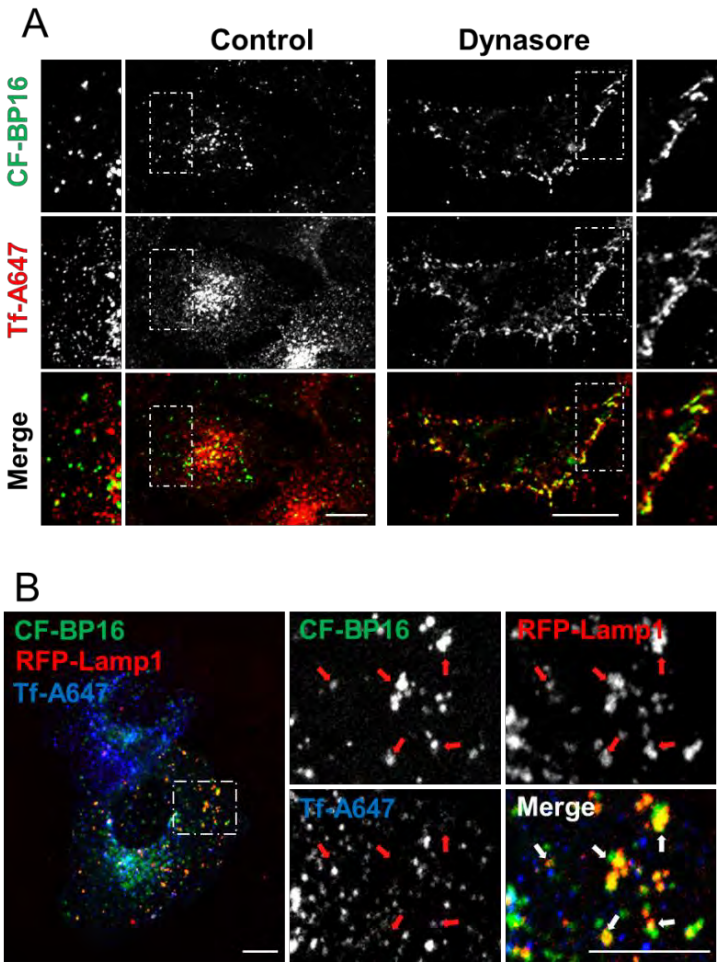

Figure III.4. CF-BP16 is dynamin dependent internalized and follows the endocytic degradation pathway. (A) MCF-7 cells were pre-incubated for 15 min at 37 ºC with or without 100 µM dynasore and then **CF-BP16** (25 µM) and Alexa647-labelled transferrin (Tf-A647, 60 µg ml^{-1}) were added and further incubated for 60 min. Confocal images were acquired through the Alexa647 (red) and CF (green) channels. (B) MCF-7 cells expressing RFP-Lamp1 (red) were incubated with **CF-BP16** (green) and Tf-A647 (blue) for 60 min at 37 ºC. Insets show magnified images and arrows indicate **CF-BP16**/RFP-Lamp1 positive vesicles (bars are 10 µm).

Next, in order to ascertain the importance of clathrin dependent endocytosis (CDE), the role of this dynamin dependent pathway in **CF-BP16** uptake was examined in cells overexpressing the Cherry-DPF fragment of Eps15 protein, which by sequestering AP-2 inhibits

CDE (Figure III.5).[67] The **CF-BP16** endocytosis was also compared with the related CF-Tat$_{49}$ peptide and the Tf-A647, which is specifically internalized *via* CDE. Confocal images in Figure III.5 (panels A and B) showed that Tf-A647, **CF-BP16** and CF-Tat$_{49}$ entry was strongly inhibited in those Cherry-DPF overexpressing cells compared to non-expressing cells. In order to quantify such inhibition, internalization of Tf-A647 and **CF-BP16** or CF-Tat$_{49}$ were measured by flow cytometry and compared to dextran-FITC, which enters into cells by fluid phase and therefore via clathrin dependent and independent pathways. Flow cytometry analysis revealed that transferrin uptake was ~55% inhibited in highly cherry-DPF expressing cells compared to non-transfected cells, while **BP16** and dextran were inhibited by ~47% and ~33% respectively (Figure III.5C).

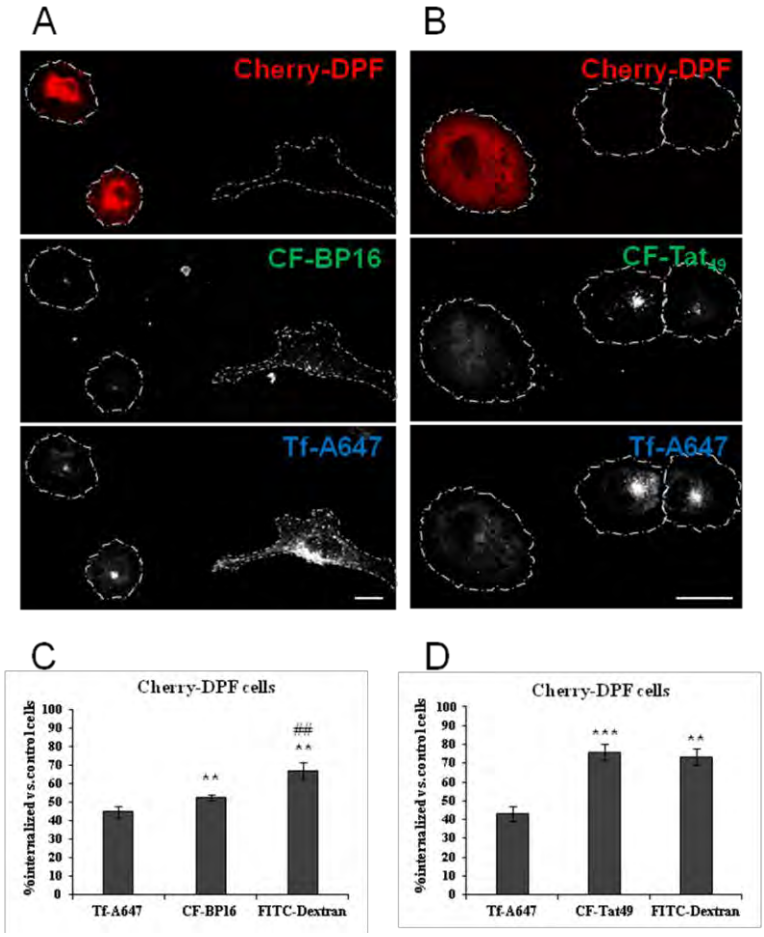

Figure III.5. Clathrin dependent endocytosis is playing a key role in **CF-BP16** uptake. (A, B) Confocal images of MCF-7 cells expressing Cherry-DPF and incubated with Tf-A647 (60 µg ml^{-1}) and **CF-BP16** (25 µM) (A) or CF-Tat$_{49}$ (25 µM) (B) for 60 min at 37 ºC (bars are 20 µm). (C, D) Internalization of FITC-Dextran (2mg ml^{-1}), Tf-A647 and **CF-BP16** (C) or CF-Tat$_{49}$ (D) after 60 min at 37 ºC were quantified by flow cytometry in Cherry-DPF expressing cells as described in Experimental section. Histograms show the percentage of the indicated molecules internalized in highly Cherry-DPF expressing cells versus non-expressing cells. Each column represents the mean fluorescence intensity of the cells determined in four independent experiments ± SD. Statistical significances between different molecules were determined using the Student's t-test, ***p*<0.01 and ****p*<0.001 vs Tf-A647; ##*p*<0.01 vs **CF-BP16**.

Given that transferrin endocytosis, which is totally dependent on CDE, was ~55% inhibited and that inhibition of **BP16** was close to transferrin and higher than dextran (~47% vs ~33%), it can be reasoned that CDE is playing a major role in **BP16** internalization. Moreover, flow cytometry inhibition data obtained from Tat_{49} uptake (~19%) compared to dextran (Figure III.5D) suggests that CDE is less important for Tat_{49} internalization than for **BP16**. These results indicate that both peptides, **BP16** and Tat_{49}, are differentially internalized.

In summary, **BP16** internalization is dynamin dependent and it is mainly internalised via clathrin dependent endocytosis possibly through a weak plasma membrane interaction or by fluid phase, which is also in agreement with the **BP16** localization in late endosomes after 60 min of endocytosis in MCF-7 cells.

III.2.4. Cell cytotoxicity of peptide conjugates

The potential use of **BP16** as vector for the delivery of the DNA alkylating agent CLB was assessed by exposing MCF-7, CAPAN-1 and 3T3 cells to CLB and the CLB-BP16 conjugate (**BP325**). The IC_{50} was determined by the MTT assay after 48 h of peptide exposure. As shown in Table III.3, CLB alone exhibited low cytotoxicity against the three cell lines (IC_{50} of 73.7 to 152.5 μM). In contrast, **BP325** displayed high activity, with IC_{50} values of 12.0, 13.7 and 20.6 μM against MCF-7, CAPAN-1 and 3T3 cells, respectively. Thus, the conjugation of CLB to **BP16** increased the cell cytotoxicity of this nitrogen mustard by 6-fold in MCF-7 cells, by 7-fold in 3T3 cells and by 9-fold in CAPAN-1 cells. Since **BP16** is non-toxic at these concentrations (IC_{50} > 200 μM), this toxicity must be attributed to the CLB moiety. This increase of activity clearly demonstrates that **BP16** contributes to the internalization of CLB through the cell membrane, enhancing its efficacy. Therefore, in agreement with earlier reports, the mechanism of action of the CLB-BP16 conjugate seems to be much more efficient than the passive diffusion mechanism suggested for CLB alone.[41 44]

Homing peptides are employed to enhance the selectivity of CPPs towards malignant cells.[46-49] Thus, we next investigated whether the cell-penetrating properties of **BP16** were retained after conjugation with the breast tumor homing peptide CREKA and also if this homing peptide-CPP conjugate could provide selective internalization of CLB into cancer cells. With this aim, the cytotoxicity of the conjugate CLB-CREKA-BP16 (**BP329**) was evaluated in MCF-7, CAPAN-1 and 3T3 cells. CREKA, CLB-CREKA and the conjugate CREKA-BP16 (**BP327**) were also assayed for comparison purposes. CREKA and CLB-CREKA were non-toxic (IC_{50} > 200 μM)

and **BP327** displayed low cytotoxicity (IC_{50} of 74.5 to 76.2 μM). In contrast, the conjugate CLB-CREKA-BP16 (**BP329**) was significantly active, with IC_{50} values ranging from 33.0 to 35.2 μM. These results showed that the incorporation of CREKA decreased the activity of the CLB-BP16 conjugate **BP325**, however they confirmed that **BP16** was able to internalize both CREKA and CLB since the cytotoxicity of **BP329** (CLB-CREKA-BP16) increased 2- to 4.5-fold the one of CLB alone. Furthermore, the lack of selectivity observed for **BP329** could be attributed to the fact that CREKA was originally identified by in vivo phage display and recognized fibrin-associated clotted plasma proteins in the tumor stroma.[47,50 52] On this basis, the behavior of CREKA in vitro could differ to the one previously described in vivo. However, these results show that **BP329** displayed a higher activity than CLB alone proving the validity of **BP16** as CPP for cell delivery of therapeutically useful molecules.

Table III.3. Cytotoxicity of **BP16**, CREKA, chlorambucil (CLB), CLB-CREKA, and peptide conjugates in 3T3, MCF-7 and CAPAN-1 cells.

	Cell line	**BP16**	CREKA	**BP327**	CLB	CLB-CREKA	**BP325**	**BP329**
IC_{50}[a] (μM)	3T3	>200	>200	74.5 ± 4.1	152.5 ± 5.6	>200	20.6 ± 3.3	33.7 ± 1.9
	MCF-7	>200	>200	74.7 ± 8.8	73.7 ± 4.5	>200	12.0 ± 2.7	35.2 ± 1.8
	CAPAN-1	>200	>200	76.2 ± 0.8	129.0 ± 35.5	>200	13.7 ± 2.4	33.0 ± 1.0

[a]The IC_{50} values were determined by the MTT assay after 48 h of peptide exposure. Data represents the mean ± SD of at least three independent experiments made in triplicates.

III.2.5. Cellular uptake of CLB peptide conjugates

In order to determine if the differences in the cytotoxic activity of the CLB peptide conjugates **BP325** (CLB-BP16) and **BP329** (CLB-CREKA-BP16) were related to their internalization properties, these conjugates were labeled with 5(6)-carboxyfluorescein (CF) affording **BP326** and **BP330**, respectively, and analyzed by flow cytometry. In addition, the homing peptide CREKA and the CREKA-BP16 conjugate (**BP327**) were also labeled (CF-CREKA and **BP328**, respectively) and included in the study.

The cellular uptake of CF-CREKA and **BP328** at 25 μM was determined by flow cytometry after 3 h of incubation in 3T3 and MCF-7 cells at 37 ºC. As represented in Figure III.6, very low intracellular fluorescence levels were detected in both cell lines when treated with CF-CREKA, indicating that CREKA alone was unable to internalize into the cells. These results are in accordance with previous studies describing that CREKA displays no cell-penetrating capacity in

cultured breast cancer cells.[42] When comparing the fluorescence of **CF-BP16** and **BP328** (CF-CREKA-BP16), it was observed that the cell-penetrating properties of **BP16** were significantly reduced when conjugated to the homing peptide, probably because the coupling of CREKA restricts the interaction of **BP16** with the cell membrane. Notably, as shown by the intracellular fluorescence levels, **BP328** retains significant internalization ability which is required to deliver cytotoxic agents inside the cells.

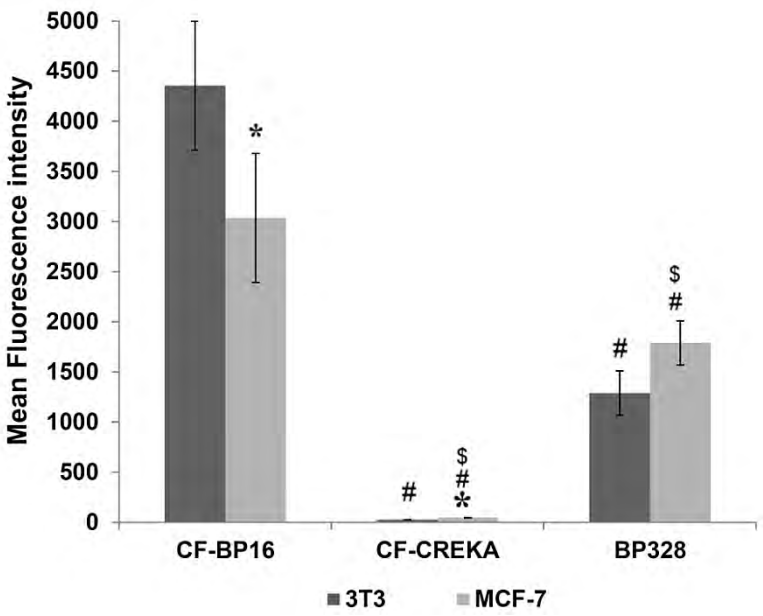

Figure III.6. Uptake of 5(6)-carboxyfluorescein labeled peptides **CF-BP16**, CF-CREKA and **BP328** (CF-CREKA-BP16) into 3T3 and MCF-7 cells. Cells were exposed to the peptides at 25 μM for 3 h at 37 ºC. Each column in graph represents the mean fluorescence intensity of the cells determined in three independent experiments ± SD. *p<0.05 vs 3T3 cells; #p<0.05 vs **CF-BP16** treated cells; $$p$<0.05 vs CF-CREKA.

The internalization ability of the CLB peptide conjugates **BP326** (CLB-BP16(CF)) and **BP330** (CLB-CREKA-BP16(CF)) at 25 μM was evaluated by flow cytometry in MCF-7 cells after 3 h of incubation at 37 ºC. To our surprise, while the fluorescence of **BP326** (4272 ± 453) was not significantly different to that of **CF-BP16** (3035 ± 643), **BP330** showed a considerably higher intracellular fluorescence (3966 ± 217) than **BP328** (CF-CREKA-BP16) (1789 ± 221). These results are noteworthy since they prove that **BP16** is able to efficiently internalize both CLB and CREKA.

These findings also reveal that the incorporation of either CREKA and/or CLB has a strong influence on the cellular uptake of **BP16**, reflecting that any modification in the molecular structure of this peptide can lead to relevant changes in its cell penetrating properties. In fact, it has been reported that the cargo play an important role in the internalization mechanism of

CPPs.[8,11] Interestingly, despite these modifications, **BP16** remains as an efficient drug delivery vector.

III.3. Conclusions

In the present study, we have identified **BP16** as a new CPP with high cellular uptake *in vitro*. In contrast to other CPPs previously reported, **BP16** displays no cytotoxicity against malignant and non-malignant cells and, moreover, shows no hemolytic activity. We have demonstrated that **BP16** exhibits high efficient penetration through endocytic mechanisms, accumulating in the cell cytoplasm at short time periods. In addition, the conjugation of the DNA alkylating agent CLB to **BP16** dramatically increases the cytotoxicity of this drug between 6- to 9-fold. We have also shown that, in conjugation with the homing peptide CREKA, **BP16** is able to improve the cytotoxic activity of CLB from 2- to 4.5-fold. Taken together, these results confirm that **BP16** is an excellent non-toxic delivery vector suitable for the effectively transport of drugs. Further studies on applications of this CPP are underway in our laboratory.

III.4. Experimental Section

III.4.1. Materials and methods

Unless otherwise stated, common chemicals and solvents (HPLC-grade or reagent-grade quality) were purchased from commercial sources and used without further purification. The 9-fluorenylmethoxycarbonyl (Fmoc) derivatives and Fmoc-Rink-4-methylbenzhydrylamine (MBHA) resin (0.56 mmol/g^{-1}) were obtained from Senn Chemicals International (Gentilly, France), NovaBiochem (Schwalbach, Germany) or from IRIS Biotech GmbH (Marktredwitz, Germany). Aminomethyl ChemMatrix resin (0.66 mmol/g^{-1}) was obtained from Matrix Innovation Inc (St-Hubert, Canada). Ethyl 2-cyano-2-(hydroxyimino)acetate (Oxyma) was purchased from Novabiochem (Nottingham, UK). Trifluoroacetic acid (TFA), triisopropylsilane (TIS), dimethyl sulfoxide (DMSO), D,L-dithiothreitol (DTT), *N*,*N'*-diisopropylcarbodiimide (DIPCDI), chlorambucil (CLB), 5(6)-carboxyfluorescein (CF), fluorescein isothiocyanate dextran mol. wt 10000 (FITC-Dextran) and dynasore hydrate were from Sigma–Aldrich (St. Louis, MO, USA). Transferrin Alexa Fluor® 647 Conjugate was from Molecular Probes (Invitrogen, Life Technologies, Carlsbad, CA). Piperidine was purchased from Fluka (Buchs, Switzerland). *N*-Methyl-2-pyrrolidinone (NMP), *N*,*N* dimethylformamide (DMF), CH_3OH, CH_2Cl_2, diethyl ether and solvents for high performance liquid chromatography (HPLC) were obtained from Scharlau (Sentmenat, Spain).

3-(4,5-Dimethylthiazol-2-yl)-2,5-diphenyltetrazolium bromide (MTT), paraformaldehyde, and bisbenzimide trihydrochloroacetic acid (Hoechst 33258) were purchased from Sigma-Aldrich (St. Louis, MO, USA). Dulbecco's modified Eagle's medium (DMEM), phosphate buffered saline (PBS), fetal bovine serum (FBS), penicillin-streptomycin and trypsin were obtained from GIBCO BRL (Grand Island, NY, USA). The RFP-Lamp1plasmid was kindly provided by Walther Mothes (Addgene plasmid 1817).[66]

Electrospray ionization mass spectrometry (ESI-MS) analyses were performed with an Esquire 6000 ESI ion Trap LC/MS (Bruker Daltonics) instrument equipped with an electrospray ion source. The instrument was operated in the positive ESI(+) ion mode. Samples (5 µL) were introduced into the mass spectrometer ion source directly through an HPLC autosampler. The mobile phase (80:20 CH_3CN/H_2O at a flow rate of 100 $\mu L/min^{-1}$) was delivered by a 1100 Series HPLC pump (Agilent). Nitrogen was employed as both the drying and nebulizing gas.

High-resolution mass spectra (HRMS) were recorded under conditions of ESI with a Bruker MicrOTOF-Q IITM instrument using a hybrid quadrupole time-of-flight mass spectrometer (University of Girona). Samples were introduced into the mass spectrometer ion source by direct infusion through a syringe pump and were externally calibrated using sodium formate. The instrument was operated in the positive ESI(+) ion mode.

III.4.2. Cell lines

The human breast cancer cell line MCF-7, the human pancreas cancer cell line CAPAN-1 and the mouse fibroblast cell line 3T3 were obtained from the American Tissue Culture Collection (ATCC, Rockville, MD, USA). Cells were maintained in DMEM supplemented with 10% FBS and 100 UmL^{-1} penicillin-streptomycin at 37 ºC in a humidified atmosphere containing 5% CO_2. Cells were passaged two times per week.

III.4.3. Peptide synthesis

General method for solid-phase peptide synthesis. Peptides from Table 1, Tat_{49} and CF-Tat_{49} were synthesized manually by the solid-phase method using Fmoc-type chemistry and the following side-chain protecting groups: tert-butyloxycarbonyl (Boc) for Lys, *t*Bu for Tyr and Glu, trityl (Tr) for Cys, and 2,2,5,7,8-pentamethylchroman-6-sulphonyl (Pmc) for Arg. A Fmoc-Rink-MBHA resin (0.56 $mmol/g^{-1}$) or an aminomethyl ChemMatrix resin (0.66 $mmol/g^{-1}$) were used as solid support to obtain peptide amides. Coupling of Fmoc-Rink (4 equiv) onto the aminomethyl

ChemMatrix resin was mediated by DIPCDI (4 equiv) and Oxyma (4 equiv) in DMF at room temperature overnight. Couplings of the Fmoc-aminoacids (4 equiv) were performed using DIPCDI (4 equiv) and Oxyma (4 equiv) in DMF under stirring at room temperature for 2 h, and monitored by the Kaiser test.[68] For sequences containing up to eleven residues, the Fmoc group was removed by treating the resin with a mixture of piperidine/DMF (3:7, 1 × 2 min + 1 × 10 min). For longer sequences, Fmoc group removal was carried out with piperidine/DMF (3:7, 1 × 3 min + 3 × 10 min). After each coupling and deprotection step, the resin was washed with DMF (6 × 1 min), and CH_2Cl_2 (6 × 1 min), and air-dried. After the coupling of the eleventh residue, NMP was used instead of DMF. Peptide elongation was performed by repeated cycles of Fmoc group removal, coupling and washings.

Once the synthesis was completed, peptidyl resins were subjected to N-terminal Fmoc group removal. Then, peptides were cleaved or the peptidyl resins were derivatized with CLB and/or with 5(6)-carboxyfluorescein. Cleavage of peptides from the resin was performed by treatment with TFA/TIS/H_2O (95:2.5:2.5) for 3 h at room temperature. Peptides containing a cysteine residue were cleaved with TFA/TIS/H_2O/DTT (92.5:2.5:2.5:2.5) for 3 h at room temperature. Both procedures were followed by TFA evaporation by bubbling N_2 into the solution. Crude peptides were precipitated by adding cold diethyl ether (-20 ºC) and collected by centrifugation. This procedure was repeated twice. Finally, peptides were dissolved in H_2O/CH_3CN (50:50 v/v containing 0.1% TFA), lyophilized and tested for purity by HPLC. Analysis was carried out with a Kromasil C18 reverse-phase column (4.6 × 40 mm; 3.5 μm particle size) with a 2-100% B linear gradient over 7 min at a flow rate of 1.0 mL min^{-1}. Solvent A was 0.1% aqueous TFA and solvent B was 0.1 % TFA in CH_3CN. Detection was performed at 220 nm. ESI-MS and HRMS (ESI) were used to confirm peptide identity. Peptides from Table 1, Tat_{49} and CF-Tat_{49} were obtained in purities ranging from 81 to 100% (Table 1).

Synthesis of CLB-peptide conjugates. Derivatization with CLB was performed by treating the corresponding peptidyl resin with CLB (5 equiv), DIPCDI (5 equiv) and Oxyma (5 equiv) in DMF or NMP under stirring at room temperature for 5 h. The completion of the reaction was checked by the Kaiser test.[68] The resin was then washed with NMP (6 × 1 min), CH_3OH (6 × 1 min), and CH_2Cl_2 (6 × 1 min), and air dried.

Synthesis of N-terminal 5(6)-carboxyfluorescein-labeled peptides. For the N-terminal derivatization with 5(6)-carboxyfluorescein, this fluorophore (2.5 equiv) was first pre-activated with Oxyma (2.5 equiv) and DIPCDI (2.5 equiv) in CH_2Cl_2/NMP (1:9) for 10 min. The mixture was

added to the corresponding N-terminal deprotected peptidyl resin and reacted overnight at room temperature protected from light by covering it with aluminum foil due to the light sensitivity of the 5(6)-carboxyfluorescein. Completeness of the coupling was confirmed using the Kaiser test.[68] The resin was then washed with NMP (1 × 5 min), piperidine/NMP (1:5, 1 × 15 min), NMP (6 × 1 min), CH_2Cl_2 (6 × 1 min), CH_3OH (6 × 1 min), and CH_2Cl_2 (6 × 1 min) and air dried.[56]

Synthesis of 5(6)-carboxyfluorescein-labeled CLB-peptide conjugates. These conjugates were prepared from a peptidyl resin incorporating the lysine residue to be labeled protected with *N*-[1-(4,4-dimethyl-2,6-dioxocyclohex-1-ylidene)ethyl] (Dde) at the N^{ε}-amino group. After CLB coupling, the Dde group was removed by treatment with hydrazine/NMP (2:98, 5 × 20 min) under stirring at room temperature and the deprotection progress was monitored by the Kaiser test.[68] Then, the resin was washed with NMP (6 × 1 min) and CH_2Cl_2 (6 × 1 min) and air dried. Next, fluorophore labeling with 5(6)-carboxyfluorescein was carried out as described for the N-terminal carboxyfluorescein labeled peptides.

III.4.4. Cytotoxicity assays

Cytotoxicity of peptides **BP16**, **BP76**, **BP81**, **BP100**, **BP105**, **BP307**, **BP308**, CREKA and **BP327**, CLB-peptide conjugates CLB-CREKA, **BP325** and **BP329**, and CLB in 3T3, MCF-7 and CAPAN-1 cells was determined by the MTT assay. Peptides and CLB-peptide conjugates were diluted in Milli-Q water to obtain 2 mM stock solutions. CLB was dissolved in DMSO to provide a 75 mM stock solution.[69] Appropriate aliquots of these solutions were diluted in the cell culture medium to obtain the final working concentrations. Aliquots of 4000 3T3 cells, 6000 MCF-7 cells or 10 000 CAPAN-1 cells were seeded on 96-well plates 24 h prior to the treatments. Then, cells were treated for 48 h with the corresponding compound at concentrations ranging from 0 to 200 μM. After removal of the treatment, cells were washed with PBS and incubated for additional 2 h in the darkness with fresh culture medium (100 μL) with MTT (10 μL). The medium was discarded and DMSO (100 μL) was added to each well to dissolve the purple formazan crystals. Plates were agitated at room temperature for 10 min and the absorbance of each well was determined with an absorbance microplate reader (ELx800, BioTek, Winooski, USA) at a wavelength of 570 nm. Three replicates for each compound were used, and all treatments were tested at least in three independent experiments. For each treatment, the cell viability was determined as a percentage of the control untreated cells, by dividing the mean absorbance of each treatment by the mean absorbance of the untreated cells. The concentration that reduces by 50% the cell viability (IC_{50}) was established for each compound.

III.4.5. Hemolysis

The data corresponding to the hemolytic activity of peptides was previously reported by Badosa et al.[53] It was evaluated at 150 μM by determining the hemoglobin release from erythrocyte suspensions of fresh human blood (5% v/v) using absorbance at 540 nm.

III.4.6. Stability of BP16 and Tat_{49} in serum

The stability of **BP16** and Tat_{49} was evaluated in fetal bovine serum. Each peptide (1 mg) was exposed to 10% aqueous filtered fetal bovine serum (2 mL) at 37 ºC. After 5, 10, 15, 30 and 45 min exposure, aliquots (200 μL) were removed and proteins were precipitated with acetonitrile (200 μL). Samples were cooled to 0 ºC for 15 min and centrifuged (11 000 rpm, 5 min). The supernatant was analyzed by HPLC. The digestion was estimated as the percentage of degraded peptide calculated from the decrease of the HPLC peak area of the native peptide.

III.4.7. Flow cytometry

The uptake efficiency of **CF-BP16**, CF-CREKA, and **BP328** by 3T3 and MCF-7 cells, and of CF-Tat_{49}, **BP326**, and **BP330** by MCF-7 cells was quantified by flow cytometry. Aliquots of 50 000 cells were seeded in 24 well-plates and allowed to attach for 24 h. Next, cells were incubated with **CF-BP16** at 5, 25 and 50 μM for 1, 3 and 6 h, with CF-CREKA, **BP328**, **BP326** and **BP330** at 25 μM for 3 h or with **CF-BP16** and CF-Tat_{49} at 25 μM for 1, 3 and 6 h at 37 ºC. The cells were harvested by trypsinization and gently washed with 2% FBS in cold PBS. The fluorescence of the cells, corresponding to the cellular uptake of the carboxyfluorescein labeled peptides, was analyzed using a FACSCalibur (Becton Dickinson Immunocytometry Systems, San Jose, CA) equipped with the CellQuestTM software (Becton Dickinson). The mean fluorescence intensity was represented on a four orders of magnitude log scale (1–10 000). The effect of Cherry-DPF expression on **CF-BP16**, CF-Tat_{49}, transferrin-A647 and FITC-Dextran uptake in MCF-7 cells was also analysed by flow cytometry. MCF-7 cells seeded in 6 well-plates were transfected with Cherry-DPF plasmid using Effectene (Qiagen, Hiden, Germany) according to the manufacturer's specifications. To generate the Cherry-DPF plasmid, the DPF fragment (aas: 501-874) from human Eps15 was obtained by polymerase chain reaction, cloned into pEGFP-C1 vector (Clontech) using XhoI and Pst1 restriction sites and after that GFP was replaced with the mCherry fluorescent protein. After 24 h of protein expression, cells were incubated with transferrin-A647 (60 μg ml^{-1}) combined with **CF-BP16** (25 μM), CF-Tat_{49} (25 μM) or FITC-Dextran (2 mg ml^{-1}) for 60 min at 37ºC and washed two times with cold PBS. The remaining

fluorescence at the cell surface was removed by a 3 min cold acid wash (sodium acetate 0.2 M, sodium chloride 0.5 M, pH 4.5) and the intracellular fluorescence was quantified using a LSRFortessa (Becton Dickinson) equipped with the CellQuestTM software (Becton Dickinson). Ten thousand cells were analyzed in each experiment.

III.4.8. Confocal microscopy

MCF-7 cells grown on coverslips and incubated with the different fluorescent-labeled molecules were washed with cold PBS and fixed with freshly prepared 4% paraformaldehyde in PBS for 15 min at 4ºC. After washing twice with PBS, the coverslips were mounted in Mowiol (Calbiochem, Merck, KGaA, Darmstadt, Germany) or using a fluorescence mounting medium (Dako, Carpinteria, CA, USA). The images were acquired using a Leica TCS SP5 laser scanning confocal microscope (Leica Microsystems Heidelberg GmbH) equipped with DMI6000 inverted microscope, blue diode (405 nm), argon (458/476/488/514), diode pumped solid state (561 nm) and HeNe (633) lasers. Final imaging was performed using ImageJ software.

III.4.9. Statistical analysis

The statistical analysis was performed with the SPSS statistical software for Windows (version 15.0; SPSS Inc., Chicago, IL, USA). Quantitative variables were expressed as mean and standard deviation (SD). The normality of the data was tested using the Shapiro-Wilk test. The differences between data with normal distribution and homogeneous variances were analyzed using the parametric Student's t test. A value of $p<0.05$ was considered significant.

III.5. References

(1) D. Hanahan and R. A. Weinberg, *Cell*, **2011**, *144*, 646–674.

(2) C. H. Takimoto and E. Calvo in Cancer Management: A Multidisciplinary Approach (Eds.: R. Pazdur, L. D. Wagman, K. A. Camphausen, W. J. Hoskins), UBM Medica, London, **2008**, pp. 42–58.

(3) E. Raschi, V. Vasina, M. G. Ursino, G. Boriani, A. Martoni and F. De Ponti, *Pharmacol. Ther.*, **2010**, *125*, 196–218.

(4) E. L. Snyder and S. F. Dowdy, *Pharm. Res.*, **2004**, *21*, 389–393.

(5) E. Vivès, J. Schmidt and A. Pèlegrin, *Biochim. Biophys. Acta*, **2008**, *1786*, 126–138.

(6) K. M. Stewart, K. L. Horton and S. O. Kelly, *Org. Biomol. Chem.*, **2008**, *6*, 2242-2255.

(7) S. B. Fonseca, M. P. Pereira and S. O. Kelley, *Adv. Drug. Deliv. Rev.*, **2009**, *61*, 953–964.

(8) E. Koren and V. P. Torchilin, *Trends Mol. Med.*, **2012**, *18*, 385–393.

(9) F. Milleti, *Drug Discov. Today*, **2012**, *17*, 850–860.

(10) J. S. Wadia and S. F. Dowdy, *Adv. Drug Delivery Rev.*, **2005**, *57*, 579–596.

(11) V. Kersemans, K. Kersemans and B. Cornelissen, *Curr. Pharm. Design*, **2008**, *14*, 2415–2427.

(12) R. Fischer, M. Fotin-Mleczek, H. Hufnagel and R. Brock, *ChemBioChem*, **2005**, *6*, 2126–2142.

(13) S. Pujals, J. Fernández-Carneado, C. López-Iglesias, M. J. Kogan and E. Giralt, *Biochim. Biophys. Acta*, **2006**, *1758*, 264–279.

(14) P. Lundberg and U. Langel, *J. Mol. Recognit.*, **2003**, *16*, 227–233.

(15) M. Gooding, L. P. Browne, F. M. Quinteiro and D. L. Selwood, *Chem. Biol. Drug Des.*, **2012**, *80*, 787–809.

(16) S. A. Nasrollahi, C. Taghibiglou, E. Azizi and E. S. Farboud, *Chem. Biol. Drug Des.*, **2012**, *80*, 639–646.

(17) T. Lehto, K. Kurrikoff and U. Langel, *Expert Opin. Drug Deliv.*, **2012**, *9*, 823–836.

(18) I. Nakase, H. Akita, K. Kogure, A. Gräslund, U. Langel, H. Harashima and S. Futaki, *Acc. Chem. Res.*, **2012**, *45*, 1132–1139.

(19) F. Schweizer, *Eur. J. Pharm.*, **2009**, *625*, 190–194.

(20) Y. Li, Q. Xiang, Q. Zhang, Y. Huang and Z. Su, *Peptides*, **2012**, *37*, 207–215.

(21) K. Takeshima, A. Chikushi, K-K. Lee, S. Yonehara and K. Matsuzako, *J. Biol. Chem.*, **2003**, *278*, 1310–1315.

(22) S. T. Henriques, M. N. Melo and M. A. R. B. Castanho, *Biochem. J.*, **2006**, *399*, 1–7.

(23) J. Fernández-Carneado, M. J. Kogan, S. Pujals and E. Giralt, *Biopolymers*, **2004**, *76*, 196–203.

(24) C. Leuschner and W. Hansel, *Curr. Pharm. Des.*, **2004**, *10*, 2299–2310.

(25) C. D. Fjell, J. A. Hiss, R. E. W. Hancock and G. Schneider, *Nat. Rev. Drug Discov.*, **2012**, *11*, 37–51.

(26) D. W. Hoskin and A. Ramanoorthy, *Biochim. Biophys. Acta*, **2008**, *1778*, 357–375.

(27) E. Randal, *Future Microbiol.*, **2011**, *6*, 635–666.

(28) J. S. Mader and D. W. Hoskin, *Expert Opin. Inv. Drugs*, **2006**, *15*, 933–946.

(29) P. Bulet, R. Stöcklin and L. Menin, *Immunol. Rev.*, **2004**, *198*, 169–184.

(30) H. Jenssen, P. Hamill and R. E. W. Hancock, *Clin. Microbiol. Rev.*, **2006**, *19*, 491–511.

(31) M. Zasloff, *Nature*, **2002**, *415*, 389–395.

(32) B. Bechinger and K. Lohner, *Biochim. Biophys. Acta*, **2006**, *1758*, 1529–1539.

(33) R. E. W. Hancock and H. G. Sahl, *Nature Biotechnol.*, **2006**, *24*, 1551–1557.

(34) J. F. Marcos and M. Gandía, *Expert Opin. Drug Discov.*, **2009**, *4*, 659–671.

(35) H. W. Huang, Biochim. *Biophys. Acta*, **2006**, *1758*, 1292–1302.

(36) B. Fang, H. Y. Guo, M. Zhang, L. Jiang and F. Z. Ren, *FEBS J.*, **2013**, *280*, 1007–1017.

(37) G. Drin, S. Cottin, E. Blanc, A. R. Rees and J. Temsamani, *J. Biol. Chem.*, **2003**, *278*, 31192–31201.

(38) K. K. Hou, H. Pan, G. M. Lanza and S. A. Wickline, *Biomaterials*, **2013**, *34*, 3110–3119.

(39) S. Sandgren, A. Wittrup, F. Cheng, M. Jönsson, E. Eklund, S. Busch and M. Belting, *J. Biol. Chem.*, **2004**, *279*, 17951–17956.

(40) H. Myrberg, L. Zhang, M. Mäe and U. Langel, *Bioconjugate Chem.*, **2008**, *19*, 70–75.

(41) M. Mäe, H. Myrberg, S. El-Andaloussi and U. Langel, *Int. J. Pept. Res. Ther.*, **2009**, *15*, 11–15.

(42) S. B. Fonseca and S. O. Kelley, *ACS Med. Chem. Lett.*, **2011**, *2*, 419–423.

(43) J. Hoyer, U. Schatzschneider, M. Schulz-Siegmund and I. Neundorf, Beilstein *J. Org. Chem.*, **2012**, *8*, 1788–1797.

(44) S. R. Rajski and R. M. Williams, *Chem. Rev.*, **1998**, *98*, 2723–2795.

(45) I. Martín, M. Teixidó and E. Giralt, *Pharmaceuticals*, **2010**, *3*, 1456–1490.

(46) S. Majumdar and T. J. Siahaan, *Med. Res. Rev.*, **2012**, *32*, 637–658.

(47) N. Svensen, J. G. A. Walton and M. Bradley, *Trends Pharmacol. Sci.*, **2012**, *33*, 186–192.

(48) P. Laakkonen and K. Vuorinen, *Integr. Biol.*, **2010**, *2*, 326–337.

(49) O. H. Aina, R. Liu, J. L. Sutcliffe, J. Marik, C-X. Pan and K. S. Lam, *Mol. Pharm.*, **2007**, *4*, 631–651.

(50) D. Simberg, T. Duza, J. H. Park, M. Essler, J. Pilch, L. Zhang, A. M. Derfus, M. Yang, R. M. Hoffman, S. Bhatia, M. J. Sailor and E. Ruoslahti, *Proc. Natl. Acad. Sci. USA*, **2007**, *104*, 932–936.

(51) E. H. M. Lempens, M. Merkx, M. Tirrel and E. W. Meijer, *Bioconjugate Chem.*, **2011**, *22*, 397–405.

(52) W. Qu, W. H. Chen, Y. Kuang, X. Zeng, S. X. Cheng, X. Zhou, R. X. Zhuo and X. Z. Zhang, *Mol. Pharm.*, **2013**, *10*, 261–269.

(53) E. Badosa, R. Ferre, M. Planas, L. Feliu, E. Besalú, J. Cabrefiga, E. Bardají and E. Montesinos, *Peptides*, **2007**, *28*, 2276–2285.

(54) K. Eggenberger, C. Mink, P. Wadhwani, A. S. Ulrich and P. Nick, *ChemBioChem*, **2011**, *12*, 132–137.

(55) K. Melikov and L. V. Chernomordik, *Cell. Mol. Life Sci.*, **2005**, *62*, 2739–2749.

(56) R. Fischer, O. Mader, G. Jung and R. Brock, *Bioconjugate Chem.*, **2003**, *14*, 653–660.

(57) I. Güell, J. Cabrefiga, E. Badosa, R. Ferre, M. Talleda, E. Bardají, M. Planas, L. Feliu and E. Montesinos, *Appl. Environ. Microbiol.*, **2011**, *77*, 2667–2675.

(58) S. Monroc, E. Badosa, E. Besalú, M. Planas, E. Bardají, E. Montesinos and L. Feliu, *Peptides*, **2006**, *27*, 2575–2584.

(59) E. Badosa, R. Ferre, J. Francés, E. Bardají, L. Feliu, M. Planas and E. Montesinos, *Appl. Environ. Microbiol.*, **2009**, *75*, 5563–5569.

(60) S. Aroui, S. Brahim, M. De Waard and A. Kenani, *Biochem. Biophys. Res. Commun.*, **2010**, *391*, 419–425.

(61) H. Yang, S. Liu, H. Cai, L. Wan, S. Li, Y. Li, J. Cheng and X. Lu, *J. Biol. Chem.*, **2010**, *285*, 25666–25676.

(62) J. Song, M. Kai, W. Zhang, J. Zhang, L. Liu, B. Zhang, X. Liu and R. Wang, *Peptides*, **2011**, *32*, 1934–1941.

(63) S. Jones and J. Howl, *Bioconjugate Chem.*, **2012**, *23*, 47–56.

(64) J. Farrera-Sinfreu, E. Giralt, S. Castel, A. Albericio and M. Royo, *J. Am. Chem. Soc.*, **2005**, *127*, 9459–9468.

(65) E. Macia, M. Ehrlich, R. Massol, E. Boucrot, C. Brunner and T. Kirchhausen, *Dev. Cell.*, **2006**, *10*, 839–850.

(66) N. M. Sherer, M. J. Lehmann, L. F. Jimenez-Soto, A. Ingmundson, S. M. Horner, G. Cicchetti, P. G. Allen, M. Pypaert, J. M. Cunningham, and W. Mothes, *Traffic*, **2003**, *4*, 785–801.

(67) A. Benmerah, C. Lamaze, B. Bègue, S. L. Schmid, A. Dautry-Varsat and N. Cerf-Bensussan, *J. Cell Biol*. **1998**, *140*, 1055–1062.

(68) E. Kaiser, R. L. Colescott, C. D. Bossinger and P. Cook, *Anal. Biochem.*, **1970**, *34*, 595–598.

(69) A. Guaragna, A. Chiaviello, C. Paolella, D. D'Alonzo, G. Palumbo and G. Palumbo, *Bioconjugate Chem.*, **2012**, *23*, 84–96.

CHAPTER IV

Enzyme-triggered release of chlorambucil from BP16 conjugates

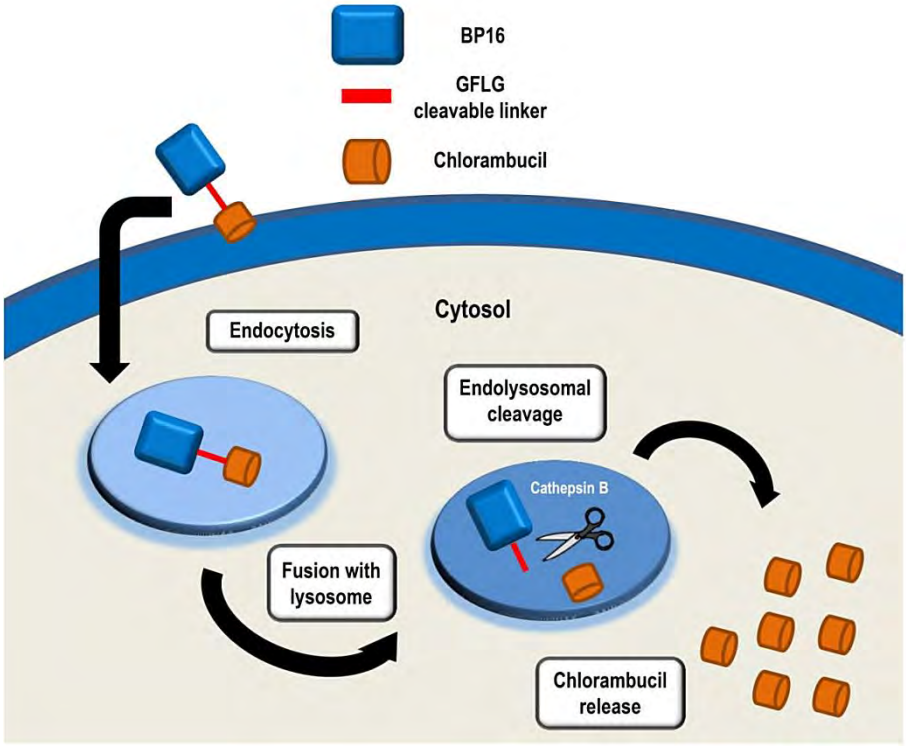

This chapter corresponds to the following accepted manuscript:

Marta Soler, Marta González-Bártulos, Eduard Figueras, Xavi Ribas, Miquel Costas, Anna Massaguer, Marta Planas,* and Lidia Feliu*. Enzyme-triggered delivery of chlorambucil from conjugates based on the cell-penetrating peptide BP16. *Organic & Biomolecular Chemistry,* **2014**. DOI: 10.1039/C4OB01875C

For this publication, M. S. performed the design, the synthesis and the characterization of all the peptide conjugates. Moreover, M. S. carried out the cathepsin B enzymatic assays. Finally, M. S. was involved in argumentations and discussions, and wrote the manuscript draft.

IV.1. Introduction

In recent years, drug delivery systems have been extensively studied in an effort to improve cancer treatments.[1,2] The use of well-known anticancer drugs is usually hindered by their poor bioavailability and their low capacity to cross cell membranes.[3] One strategy to overcome these limitations is their conjugation to a convenient carrier able to promote an efficient cell uptake of the drug. Cell-penetrating peptides (CPPs) have been established as peptide-based delivery systems to transport a wide range of cell-membrane impermeable cargoes into the cells.[4-9] CPPs have been shown to increase the bioavailability of anticancer drugs, improving their cytotoxic activity while dramatically reducing their dosage and side-effects.[10-14]

The exact internalization pathway of CPPs is still under debate. However, it is widely assumed that their high positive charge facilitates their interaction with the negatively charged plasma membrane and that they are mainly internalized by endocytosis.[15,16] Since following this endocytic pathway CPPs generally end up in the lysosomal compartment of cells, enzyme-triggered strategies are recently being used in smart drug delivery systems to improve intracellular drug release.[17,18] Lysosomal proteases are expected to selectively cleave and release active drug moieties within the cell.[19] This proteolytic activity depends on the pH gradients occurring at the subcellular level and allows an intracellular-specific delivery.[20-25] The tetrapeptide Gly-Phe-Leu-Gly is a well-known cleavable sequence, which is selectively hydrolyzed by cathepsin B cysteine protease, overexpressed in lysosomes.[19,26-28] Indeed, this sequence has been employed in several drug-peptide conjugation strategies, leading to a selective intracellular drug release and enhancement of its cytotoxic activity.[29-32]

Recently, we identified the undecapeptide KKLFKKILKKL-NH_2 (**BP16**) as a non-cytotoxic CPP with high cellular uptake *in vitro*.[33] We demonstrated that **BP16** is mainly internalized in MCF-7 cells through clathrin dependent endocytosis and that it efficiently accumulates in the cell endosomes. **BP16** displayed high efficient drug delivery properties since it was able to enhance the uptake of the DNA alkylating drug chlorambucil (CLB), improving its cytotoxicity against cancer cells between 6 to 9-fold. In conjugation with the homing peptide CREKA, **BP16** was also able to internalize CLB increasing its cytotoxic effect from 2- to 4.5-fold.

These findings prompted us to further explore the CPP properties of **BP16**. With this aim, we investigated the influence of conjugating CLB at the N- or at the C-terminus of **BP16** on the cellular uptake and on the cytotoxic activity against cancer cells. Moreover, taking into account the

clathrin dependent endocytic mechanism of **BP16**, we envisaged that the introduction of the cleavable sequence Gly-Phe-Leu-Gly in CLB-BP16 conjugates could result in an efficient release of the drug. Thus, we evaluated the effect on the cytotoxicity of incorporating this tetrapeptide at the N- or at the C-terminal end of **BP16**. A similar study was planned with the BP16-arginine analogue **BP308** (RRLFRRILRRL-NH_2).[33] This undecapeptide was previously identified and it also displayed no cytotoxicity against both malignant and non-malignant cells and, therefore, **BP308** showed a suitable activity profile to be considered as a CPP candidate.[34] Moreover, it has been recently reported that the replacement of Lys by Arg in the *KLA* antimicrobial peptide led to an enhancement of the peptide accumulation in mitochondria.[35] Thus, **BP308** could favor the selective delivery of CLB into the mitochondria. The internalization of **BP16** and **BP308** was examined by flow cytometry and confocal microscopy studies were performed in order to determine their final localization at the subcellular level. The cytotoxicity of the **BP16** and **BP308** CLB-conjugates was evaluated against cancer and healthy cell lines and the correlation with their cellular uptake was analyzed. In addition, the CLB release from **BP16** conjugates incorporating the tetrapeptide Gly-Phe-Leu-Gly was evaluated by cathepsin B enzymatic digestion.

IV.2. Experimental Section

IV.2.1. Materials and methods

Unless otherwise stated, common chemicals and solvents (HPLC-grade or reagent-grade quality) were purchased from commercial sources and used without further purification. The 9-fluorenylmethoxycarbonyl (Fmoc) derivatives and Fmoc-Rink-4-methylbenzhydrylamine (MBHA) resin (0.56 mmol g^{-1}) were obtained from Senn Chemicals International (Gentilly, France), NovaBiochem (Schwalbach, Germany) or IRIS Biotech GmbH (Marktredwitz, Germany). Ethyl 2-cyano-2-(hydroxyimino)acetate (Oxyma) was purchased from Novabiochem (Nottingham, UK). Trifluoroacetic acid (TFA), triisopropylsilane (TIS), dimethyl sulfoxide (DMSO), *N,N'*-diisopropylcarbodiimide (DIPCDI), chlorambucil (CLB), 5(6)-carboxyfluorescein (CF), hydrazine monohydrate and ethylenediaminetetraacetic acid (EDTA) were from Sigma–Aldrich (St. Louis, MO, USA). Cathepsin B (bovine spleen) was purchased from EMD chemicals (San Diego, CA, USA). L-(+)-Cysteine was obtained from Fischer Scientific (Waltham, MA USA). Piperidine and pyridine were purchased from Fluka (Buchs, Switzerland). Acetic anhydride (Ac_2O) was purchased from Panreac (Barcelona, Spain). *N*-Methyl-2-pyrrolidinone (NMP), *N,N*-dimethylformamide (DMF), CH_3OH, CH_2Cl_2, diethyl ether and solvents for high performance liquid chromatography (HPLC) were obtained from Scharlau (Sentmenat, Spain). 3-(4,5-Dimethylthiazol-2-yl)-2,5-

diphenyltetrazolium bromide (MTT), paraformaldehyde and bisbenzimide trihydrochloroacetic acid (Hoechst 33258) were purchased from Sigma-Aldrich (St. Louis, MO, USA). MitoTracker(R)Red CMXRos was from Molecular Probes, Life Technologies (Eugene, Oregon, USA). Dulbecco's modified Eagle's medium (DMEM), phosphate buffered saline (PBS), fetal bovine serum (FBS), penicillin-streptomycin and trypsin were obtained from GIBCO BRL (Grand Island, NY, USA).

Compounds were analyzed under standard analytical HPLC conditions with a Dionex liquid chromatography instrument composed of an UV/Vis Dionex UVD170U detector, a P680 Dionex bomb, an ASI-100 Dionex automatic injector, and CHROMELEON 6.60 software. Detection was performed at 220 nm. Solvent A was 0.1% aq. TFA and solvent B was 0.1% TFA in CH_3CN. Analysis was carried out with a Kromasil 100 C_{18} (4.6 mm × 40 mm, 3.5 μm) column with a 2-100% B linear gradient over 7 min at a flow rate of 1.0 mL min^{-1}.

Electrospray ionization mass spectrometry (ESI-MS) analyses were performed with an Esquire 6000 ESI ion Trap LC/MS (Bruker Daltonics) instrument equipped with an electrospray ion source (University of Girona). The instrument was operated in the positive ESI(+) ion mode. Samples (5 μL) were introduced into the mass spectrometer ion source directly through an HPLC autosampler. The mobile phase (80:20 CH_3CN/H_2O at a flow rate of 100 μL min^{-1}) was delivered by a 1200 Series HPLC pump (Agilent). Nitrogen was employed as both the drying and nebulizing gas.

High-resolution mass spectra (HRMS) were recorded under conditions of ESI with a Bruker MicrOTOF-Q IITM instrument using a hybrid quadrupole time-of-flight mass spectrometer (University of Girona). Samples were introduced into the mass spectrometer ion source by direct infusion through a syringe pump and were externally calibrated using sodium formate. The instrument was operated in the positive ESI(+) ion mode.

HPLC-MS analyses were performed under standard analytical HPLC conditions described above with an Agilent Technologies **1200 HPLC** system equipped with a VWD detector and coupled with an Esquire 6000 ESI ion Trap LC/MS (Bruker Daltonics) instrument with an electrospray ion source (University of Girona). The instrument was operated in the positive ESI(+) ion mode.

IV.2.2. Cell Lines

The human breast cancer MCF-7, melanoma SKMEL-28, prostate cancer PC-3 and pancreas cancer CAPAN-1 cell lines were obtained from the American Tissue Culture Collection

(ATCC, Rockville, MD, USA). The human skin fibroblasts 1BR3G were obtained from EucellBank (University of Barcelona, Barcelona, Spain). Cells were maintained in DMEM supplemented with 10% FBS and 100 UmL^{-1} penicillin-streptomycin at 37 ºC under a humidified atmosphere containing 5% CO_2. Cells were passaged two times per week.

IV.2.3. Peptide synthesis

General method for solid-phase peptide synthesis

All peptides (Table 1) were synthesized manually by the solid-phase method using Fmoc-type chemistry and the following side-chain protecting groups: *tert*-butyloxycarbonyl (Boc) for Lys and 2,2,5,7,8-pentamethylchroman-6-sulphonyl (Pmc) for Arg. A Fmoc-Rink-MBHA resin (0.56 mmol g^{-1}) was used as solid support to obtain peptide amides. Couplings of the Fmoc-amino acids (4 equiv) were performed using DIPCDI (4 equiv) and Oxyma (4 equiv) in DMF under stirring at room temperature for 2 h, and monitored by the Kaiser test.[36] For sequences containing up to eleven residues, the Fmoc group was removed by treating the resin with a mixture of piperidine/DMF (3:7, 2 + 10 min). For longer sequences, Fmoc group removal was carried out with piperidine/NMP (3:7, 1 × 3 min + 3 × 10 min). After each coupling and deprotection step, the resin was washed with DMF (6 × 1 min) and CH_2Cl_2 (6 × 1 min), and air-dried. After the coupling of the eleventh residue, NMP was used instead of DMF. Peptide elongation was performed by repeated cycles of Fmoc group removal, coupling and washings. Once the synthesis was completed, peptidyl resins were subjected to N-terminal Fmoc group removal. Then, peptides were cleaved or the peptidyl resins were derivatized with CLB, with 5(6)-carboxyfluorescein or with an acetyl group. Cleavage of peptides from the resin was performed by treatment with TFA/TIS/H_2O (95:2.5:2.5) for 3 h at room temperature, followed by TFA evaporation by bubbling N_2 into the solution. Crude peptides were precipitated by adding cold diethyl ether (-20 ºC) and collected by centrifugation. This procedure was repeated twice. Finally, peptides were dissolved in H_2O/CH_3CN (50:50 v/v containing 0.1% TFA), lyophilized and tested for purity by HPLC. ESI-MS and HRMS (ESI) were used to confirm the peptide identity. Peptides were obtained in purities ranging from 81 to >99%.

Synthesis of the N-terminal CLB-peptide conjugates BP325, BP332, BP334, and BP336

Peptide conjugates were prepared from the peptidyl resin Fmoc-Lys(Boc)-Lys(Boc)-Leu-Phe-Lys(Boc)-Lys(Boc)-Ile-Leu-Lys(Boc)-Lys(Boc)-Leu-Rink-MBHA (**1**) and Fmoc-Arg(Pmc)-Arg(Pmc)-Leu-Phe-Arg(Pmc)-Arg(Pmc)-Ile-Leu-Arg(Pmc)-Arg(Pmc)-Leu-Rink-MBHA (**2**). For the synthesis of **BP325** and **BP334**, after Fmoc removal and washings, the corresponding peptidyl resin was

treated with CLB (5 equiv), DIPCDI (5 equiv) and Oxyma (5 equiv) in DMF or NMP under stirring at room temperature for 5 h. The completion of the reaction was checked by the Kaiser test.[36] The resin was then washed with NMP (6 × 1 min), CH_3OH (6 × 1 min), and CH_2Cl_2 (6 × 1 min), and air dried. To obtain **BP332** and **BP336**, after Fmoc removal and washes, the amino acids of the Gly-Leu-Phe-Gly moiety and CLB were sequentially incorporated.

CLB-Lys-Lys-Leu-Phe-Lys-Lys-Ile-Leu-Lys-Lys-Leu-NH_2 (BP325). t_R = 7.71 min (91% purity). HRMS (ESI): *m/z* calcd. for $C_{83}H_{150}Cl_2N_{19}O_{12}$ $[M + 5H]^{5+}$ 335.4208; found 335.4228; calcd. for $C_{83}H_{149}Cl_2N_{19}O_{12}$ $[M + 4H]^{4+}$ 418.5247; found 418.5260; calcd. for $C_{83}H_{148}Cl_2N_{19}O_{12}$ $[M + 3H]^{3+}$ 558.3631; found 558.3644; calcd. for $C_{83}H_{147}Cl_2N_{19}O_{12}$ $[M + 2H]^{2+}$ 836.0421; found 836.0404.

CLB-Gly-Phe-Leu-Gly-Lys-Lys-Leu-Phe-Lys-Lys-Ile-Leu-Lys-Lys-Leu-NH_2 (BP332). t_R = 7.50 min (92% purity). HRMS (ESI): *m/z* calcd. for $C_{102}H_{176}Cl_2N_{23}O_{16}$ $[M + 5H]^{5+}$ 409.8603; found 409.8592; calcd. for $C_{102}H_{175}Cl_2N_{23}O_{16}$ $[M + 4H]^{4+}$ 512.0736; found 512.0709; calcd. for $C_{102}H_{174}Cl_2N_{23}O_{16}$ $[M + 3H]^{3+}$ 682.4290; found 682.4259.

CLB-Arg-Arg-Leu-Phe-Arg-Arg-Ile-Leu-Arg-Arg-Leu-NH_2 (BP334). t_R = 7.59 min (>99% purity). HRMS (ESI): *m/z* calcd. for $C_{83}H_{151}Cl_2N_{31}O_{12}$ $[M + 6H]^{6+}$ 307.5256; found 307.5239; calcd. for $C_{83}H_{150}Cl_2N_{31}O_{12}$ $[M + 5H]^{5+}$ 368.6286; found 368.6283; calcd. for $C_{83}H_{149}Cl_2N_{31}O_{12}$ $[M + 4H]^{4+}$ 460.5339; found 460.5337; calcd. for $C_{83}H_{148}Cl_2N_{31}O_{12}$ $[M + 3H]^{3+}$ 613.7095; found 6131.7079.

CLB-Gly-Phe-Leu-Gly-Arg-Arg-Leu-Phe-Arg-Arg-Ile-Leu-Arg-Arg-Leu-NH_2 (BP336). t_R = 7.82 min (>99% purity). HRMS (ESI): *m/z* calcd. for $C_{102}H_{177}Cl_2N_{35}O_{16}$ $[M + 6H]^{6+}$ 369.7243; found 369.7224; calcd. for $C_{102}H_{176}Cl_2N_{35}O_{16}$ $[M + 5H]^{5+}$ 443.4677; found 443.4666; calcd. for $C_{102}H_{175}Cl_2N_{35}O_{16}$ $[M + 4H]^{4+}$ 554.0828; found 554.0806; calcd. for $C_{102}H_{174}Cl_2N_{35}O_{16}$ $[M + 3H]^{3+}$ 738.4413; found 738.4394.

Synthesis of the C-terminal CLB-peptide conjugates BP331, BP333, BP335 and BP337

For the synthesis of these peptide conjugates, the Lys residue to be derivatized at the side-chain was incorporated as Fmoc-Lys(Dde)-OH (Dde = *N*-[1-(4,4-dimethyl-2,6-dioxocyclohex-1-ylidene)ethyl]). **BP331** and **BP333** were prepared from the peptidyl resin Fmoc-Lys(Boc)-Lys(Boc)-Leu-Phe-Lys(Boc)-Lys(Boc)-Ile-Leu-Lys(Boc)-Lys(Boc)-Leu-Lys(Dde)-Rink-MBHA (**3**), and **BP335** and **BP337** were prepared from Fmoc-Arg(Pmc)-Arg(Pmc)-Leu-Phe-Arg(Pmc)-Arg(Pmc)-Ile-Leu-Arg(Pmc)-Arg(Pmc)-Leu-Lys(Dde)-Rink-MBHA (**4**). After Fmoc removal and washes, the resins were treated with acetic anhydride/pyridine/CH_2Cl_2 (1:1:1, 2 × 30 min) under stirring, and washed

with NMP (6 × 1 min) and CH_2Cl_2 (6 × 1 min). The completion of the reaction was checked by the Kaiser test.[36] The resulting peptidyl resins were subjected to Dde group removal by treatment with a mixture of hydrazine/NMP (2:98, 5 × 20 min). The resins were then washed with NMP (6 × 1 min) and CH_2Cl_2 (1 × 1 min). For the synthesis of **BP331** and **BP335**, the free amino group of the resulting resin was acylated with CLB as described above for the N-terminal CLB conjugates. To obtain **BP333** and **BP337**, the amino acids of the Gly-Leu-Phe-Gly moiety and CLB were sequentially incorporated at the free amino group of the corresponding resin following the protocol previously described.

Ac-Lys-Lys-Leu-Phe-Lys-Lys-Ile-Leu-Lys-Lys-Leu-Lys(CLB)-NH_2 (BP331). t_R = 7.24 min (>99% purity). HRMS (ESI): *m/z* calcd. for $C_{91}H_{165}Cl_2N_{21}O_{14}$ $[M + 6H]^{6+}$ 307.7032; found 307.7014; calcd. for $C_{91}H_{164}Cl_2N_{21}O_{14}$ $[M + 5H]^{5+}$ 369.0423; found 369.0408; calcd. for $C_{91}H_{163}Cl_2N_{21}O_{14}$ $[M + 4H]^{4+}$ 461.0511; found 461.0494; calcd. for $C_{91}H_{162}Cl_2N_{21}O_{14}$ $[M + 3H]^{3+}$ 614.3990; found 614.3963.

Ac-Lys-Lys-Leu-Phe-Lys-Lys-Ile-Leu-Lys-Lys-Leu-Lys(Gly-Leu-Phe-Gly-CLB)-NH_2 (BP333). t_R = 7.38 min (91% purity). HRMS (ESI): *m/z* calcd. for $C_{110}H_{190}Cl_2N_{25}O_{18}$ $[M + 5H]^{5+}$ 443.8814; found 443.8797; calcd. for $C_{110}H_{189}Cl_2N_{25}O_{18}$ $[M + 4H]^{4+}$ 554.5999; found 554.5986; calcd. for $C_{110}H_{188}Cl_2N_{25}O_{18}$ $[M + 3H]^{3+}$ 739.1308; found 739.1295.

Ac-Arg-Arg-Leu-Phe-Arg-Arg-Ile-Leu-Arg-Arg-Leu-Lys(CLB)-NH_2 (BP335). t_R = 7.51 min (>99% purity). HRMS (ESI): *m/z* calcd. for $C_{91}H_{165}Cl_2N_{33}O_{14}$ $[M + 6H]^{6+}$ 335.7093; found 335.7093; calcd. for $C_{91}H_{164}Cl_2N_{33}O_{14}$ $[M + 5H]^{5+}$ 402.6497; found 402.6502; calcd. for $C_{91}H_{163}Cl_2N_{33}O_{14}$ $[M + 4H]^{4+}$ 503.0603; found 503.0609; calcd. for $C_{91}H_{162}Cl_2N_{33}O_{14}$ $[M + 3H]^{3+}$ 670.4113; found 670.4114; calcd. for $C_{91}H_{161}Cl_2N_{33}O_{14}$ $[M + 2H]^{2+}$ 1006.1123; found 1006.1246.

Ac-Arg-Arg-Leu-Phe-Arg-Arg-Ile-Leu-Arg-Arg-Leu-Lys(Gly-Leu-Phe-Gly-CLB)-NH_2 (BP337). t_R = 7.67 min (>99% purity). HRMS (ESI): *m/z* calcd. for $C_{110}H_{191}Cl_2N_{37}O_{18}$ $[M + 6H]^{6+}$ 398.0752; found 398.0749; calcd. for $C_{110}H_{190}Cl_2N_{37}O_{18}$ $[M + 5H]^{5+}$ 477.4888; found 477.4890; calcd. for $C_{110}H_{189}Cl_2N_{37}O_{18}$ $[M + 4H]^{4+}$ 596.6092; found 596.6090; calcd. for $C_{110}H_{188}Cl_2N_{37}O_{18}$ $[M + 3H]^{3+}$ 795.1431; found 795.1443.

Synthesis of the N-terminal 5(6)-carboxyfluorescein labeled peptides CF-BP16 and CF-BP308

The N-terminal labeled peptides **CF-BP16** and **CF-BP308** were prepared from peptidyl resins **1** and **2**, respectively. 5(6)-Carboxyfluorescein (2.5 equiv) was first pre-activated with Oxyma (2.5 equiv)

and DIPCDI (2.5 equiv) in CH_2Cl_2/NMP (1:9) for 10 min. The mixture was added to the corresponding N-terminus deprotected peptidyl resin and reacted overnight at room temperature protected from light by covering it with aluminium foil due to the light sensitivity of the 5(6)-carboxyfluorescein. Completeness of the coupling was confirmed using the Kaiser test.[36] The resin was then washed with NMP (1 × 5 min), piperidine/NMP (1:5, 1 × 15 min), NMP (6 × 1 min), CH_2Cl_2 (6 × 1 min), CH_3OH (6 × 1 min), and CH_2Cl_2 (6 × 1 min), and air dried.[37]

CF-Lys-Lys-Leu-Phe-Lys-Lys-Ile-Leu-Lys-Lys-Leu-NH_2 (CF-BP16). t_R = 6.76 and 6.80 min, corresponding to the two isomers of the 5(6)-carboxyfluorescein (94% purity). HRMS (ESI): *m/z* calcd. for $C_{90}H_{143}N_{18}O_{17}$ $[M + 5H]^{5+}$ 349.6170; found 349.6186; calcd. for $C_{90}H_{142}N_{18}O_{17}$ $[M + 4H]^{4+}$ 437.0203; found 437.0217; calcd. for $C_{90}H_{141}N_{18}O_{17}$ $[M + 3H]^{3+}$ 582.3579; found 582.3589.

CF-Arg-Arg-Leu-Phe-Arg-Arg-Ile-Leu-Arg-Arg-Leu-NH_2 (CF-BP308). t_R = 6.92 and 6.99 min, corresponding to the two isomers of the 5(6)-carboxyfluorescein (>99% purity). HRMS (ESI): *m/z* calcd. for $C_{90}H_{144}N_{30}O_{17}$ $[M + 6H]^{6+}$ 319.5215; found 319.5195; calcd. for $C_{90}H_{143}N_{30}O_{17}$ $[M + 5H]^{5+}$ 383.2244; found 383.2234; calcd. for $C_{90}H_{142}N_{30}O_{17}$ $[M + 4H]^{4+}$ 478.7787; found 478.7778; calcd. for $C_{90}H_{141}N_{30}O_{17}$ $[M + 3H]^{3+}$ 638.0358; found 638.0341.

Synthesis of the 5(6)-carboxyfluorescein labeled CLB-peptide conjugates BP326, BP338, BP339, and BP340

BP338 and **BP340**, bearing the 5(6)-carboxyfluorescein at the N-terminus and the CLB at the C-terminus, were prepared from peptidyl resins **3** and **4**, respectively. After Fmoc removal, the resulting resins were acylated with 5(6)-carboxyfluorescein as described above for **CF-BP16** and **CF-BP308**, and treated with hydrazine/NMP (2:98, 5 × 20 min) under stirring at room temperature. Then, resins were washed with NMP (6 × 1 min) and CH_2Cl_2 (6 × 1 min), and air dried. Next, CLB coupling was carried out as described for N-terminal CLB derivatized peptides.

BP326 and **BP339**, incorporating a CLB moiety at the N-terminus and a 5(6)-carboxyfluorescein group at the C-terminus, were prepared from peptidyl resins Fmoc-Lys(Boc)-Lys(Boc)-Leu-Phe-Lys(Boc)-Lys(Boc)-Ile-Leu-Lys(Dde)-Lys(Boc)-Leu-Rink-MBHA and **4**, respectively. After Fmoc removal, the resulting resins were acylated with CLB as described above for the N-terminal CLB conjugates, and treated with hydrazine/NMP (2:98, 5 × 20 min) under stirring at room temperature. Then, resins were washed with NMP (6 × 1 min) and CH_2Cl_2 (6 × 1 min), and air dried. Next, labeling with 5(6)-carboxyfluorescein was carried out as described for the N-terminal carboxyfluorescein labeled peptides **CF-BP16** and **CF-BP308**.

CLB-Lys-Lys-Leu-Phe-Lys-Lys-Ile-Leu-Lys(CF)-Lys-Leu-NH_2 (BP326). t_R = 7.56 min (81% purity). HRMS (ESI): *m/z* calcd. for $C_{104}H_{159}Cl_2N_{19}O_{18}$ $[M + 4H]^{4+}$ 508.0366; found 508.0384; calcd. for $C_{104}H_{158}Cl_2N_{19}O_{18}$ $[M + 3H]^{3+}$ 677.0464; found 677.0473; calcd. for $C_{104}H_{157}Cl_2N_{19}O_{18}$ $[M + 2H]^{2+}$ 1015.0660; found 1015.0638.

CF-Lys-Lys-Leu-Phe-Lys-Lys-Ile-Leu-Lys-Lys-Leu-Lys(CLB)-NH_2 (BP338). t_R = 7.68 and 7.83 min, corresponding to the two isomers of the 5(6)-carboxyfluorescein (97% purity). HRMS (ESI): *m/z* calcd. for $C_{110}H_{173}Cl_2N_{21}O_{19}$ $[M + 6H]^{6+}$ 360.3760; 360.3766; calcd. for $C_{110}H_{172}Cl_2N_{21}O_{19}$ $[M + 5H]^{5+}$ 432.2498; 432.2496; calcd. for $C_{110}H_{171}Cl_2N_{21}O_{19}$ $[M + 4H]^{4+}$ 540.0604; found 540.0575; calcd. for $C_{110}H_{170}Cl_2N_{21}O_{19}$ $[M + 3H]^{3+}$ 719.7447; found 719.7458.

CLB-Arg-Arg-Leu-Phe-Arg-Arg-Ile-Leu-Arg-Arg-Leu-Lys(CF)-NH_2 (BP339). t_R = 7.86 min (>99% purity). HRMS (ESI): *m/z* calcd. for $C_{110}H_{173}Cl_2N_{33}O_{19}$ $[M + 6H]^{6+}$ 388.3822; found 388.3821; calcd. for $C_{110}H_{172}Cl_2N_{33}O_{19}$ $[M + 5H]^{5+}$ 465.8571; found 465.8573; calcd. for $C_{110}H_{171}Cl_2N_{33}O_{19}$ $[M + 4H]^{4+}$ 582.0696; found 582.0687; calcd. for $C_{110}H_{170}Cl_2N_{33}O_{19}$ $[M + 3H]^{3+}$ 775.7570; found 775.7576.

CF-Arg-Arg-Leu-Phe-Arg-Arg-Ile-Leu-Arg-Arg-Leu-Lys(CLB)-NH_2 (BP340). t_R = 7.47, 7.61, 7.70 and 7.79 min, corresponding to the isomers of the 5(6)-carboxyfluorescein (>99% purity). HRMS (ESI): *m/z* calcd. for $C_{110}H_{173}Cl_2N_{33}O_{19}$ $[M + 6H]^{6+}$ 388.3822; found 388.3820; $C_{110}H_{172}Cl_2N_{33}O_{19}$ $[M + 5H]^{5+}$ 465.8571; found 465.8572; $C_{110}H_{171}Cl_2N_{33}O_{19}$ $[M + 4H]^{4+}$ 582.0696; found 582.0681; $C_{110}H_{170}Cl_2N_{33}O_{19}$ $[M + 3H]^{3+}$ 775.7570; found 775.7565.

IV.2.4. Cytotoxicity assays

Cytotoxicity of CLB and of the CLB-peptide conjugates **BP325**, **BP331**, **BP332**, **BP333**, **BP334**, **BP335**, **BP336**, **BP337** and CLB in CAPAN-1, MCF-7, PC-3 and SKMEL-28 tumor cells and in 1BR3G non-malignant cells was determined by the MTT assay. CLB-peptide conjugates were diluted in Milli-Q water to obtain 2 mM stock solutions. CLB was dissolved in DMSO to provide a 75 mM stock solution.[38] Appropriate aliquots of these solutions were diluted in the cell culture medium to obtain the final working concentrations. Aliquots of 10 000 CAPAN-1, 6000 MCF-7 or PC-3, 4000 SKMEL-28 and 5000 1BR3G cells were seeded on 96-well plates 24 h prior to the treatments. Then, cells were treated for 48 h with the corresponding compound at concentrations ranging from 0 to 100 µM. After removal of the treatment, cells were washed with PBS and incubated for additional 2 h in the dark with fresh culture medium (100 µL) with MTT (10 µL). The medium was discarded and DMSO (100 µL) was added to each well to dissolve the purple formazan crystals. Plates were agitated at room temperature for 2 min and the absorbance of each

well was determined with an absorbance microplate reader (ELx800, BioTek, Winooski, USA) at a wavelength of 570 nm. Three replicates for each compound were used, and all treatments were tested at least in three independent experiments. For each treatment, the cell viability was determined as a percentage of the control untreated cells by dividing the mean absorbance of each treatment by the mean absorbance of the untreated cells. The concentration that reduces by 50% the cell viability (IC_{50}) was established for each compound using a four-parameter curve fit (Gen5 BioTeck Instruments).

IV.2.5. Flow cytometry

The uptake efficiency of **CF-BP16**, **CF-BP308**, **BP326** (CLB-BP16-CF), **BP338** (CF-BP16-CLB), **BP339** (CLB-BP308-CF) and **BP340** (CF-BP308-CLB) by MCF-7 cells was quantified by flow cytometry. Aliquots of 50 000 cells were seeded in 24 well-plates and allowed to attach for 24 h. Next, cells were incubated with **CF-BP16** and **CF-BP308** at 25 μM for 1, 3 and 6 h, or with **BP326**, **BP338, BP339** and **BP340** at 25 μM for 6 h at 37 ºC. The cells were harvested by trypsinization and washed with 2% FBS in cold PBS. The fluorescence of the cells, corresponding to the cellular uptake of the carboxyfluorescein labelled peptides, was analysed using a FACSCalibur (Becton Dickinson Immunocytometry Systems, San Jose, CA) equipped with the CellQuestTM software (Becton Dickinson). The mean fluorescence intensity was represented on a four orders of magnitude log scale (1-10 000). Ten thousand cells were analysed in each experiment.

IV.2.6. Confocal microscopy

MCF-7 cells were seeded on coverslips and allowed to attach overnight. Mitochondria were stained with 500 nM Mitotracker red for 30 min at 37 ºC. The cells were incubated with **CF-BP16** and **CF-BP308** at 50 μM for 30 min at 4 ºC and for 3 h at 37 ºC, washed with cold PBS and fixed with 4% paraformaldehyde in PBS for 15 min at 4 ºC. The cell nucleus were stained with 2 Ug/mL Hoescht 33258 (excitation/emission: 352 nm/461 nm) during 15 min at room temperature. After washing twice with cold PBS, the coverslips were mounted using a fluorescence mounting medium (Dako, Carpinteria, CA, USA) and examined using a Leica TCS-SP5 multiphoton and high-velocity spectral confocal microscope (Leica Microsystems, Nussloch, Germany).

IV.2.7. Cathepsin B enzymatic assays

The enzymatic digestion of the CLB-peptide conjugates **BP332** (CLB-GFLG-BP16) and **BP333** (BP16-GLFG-CLB) was evaluated using a previously reported method with minor

modifications.[30] A cathepsin B stock solution (1 × 10^4 U/L, 60 µL) was added to phosphate buffer (pH 5.0, 25 mM L-Cys, 1 mM EDTA; 890 µL) and preactivated for 10 min at 37 ºC. Next, **BP332** and **BP333** (1.8 mM, 50 µL) were added to the mixture. Aliquots of this mixture (110 µL) were sampled at 0, 10, 30, 60, 90, 120 and 180 min, flash frozen in liquid nitrogen and analyzed by HPLC-MS. The analytical HPLC conditions used for these analyses were the same as described above in the Materials and Methods section to test the purity of the peptides.

IV.3. Results and Discussion

IV.3.1. Peptide design and synthesis

During previous studies, **BP16** and **BP308** were identified from a library of antimicrobial undecapeptides as potential CPP candidates.[33] Both peptides were neither cytotoxic nor hemolytic. **BP16** was highly internalized in cancer cells and was able to transport CLB into these cells enhancing its efficacy.

Based on this, we decided to gain a further insight into the cell-penetrating properties of **BP16** and **BP308**. In particular, in this study we investigated: (i) the influence of the position of CLB in the peptide sequence on the cytotoxicity and on the cellular uptake, and (ii) whether the incorporation of the cathepsin B-cleavable sequence Gly-Phe-Leu-Gly in CLB-peptide conjugates could provide the intracellular release of the drug. Towards these aims, we designed two sets of peptide conjugates. For a list of the full set of peptides prepared in this work see Table IV.1. The first set incorporated CLB at the N- or at the C-terminus of **BP16** and **BP308**. The conjugates derived from **BP16** were CLB-BP16 (**BP325**) and BP16-CLB (**BP331**), and those derived from **BP308** were CLB-BP308 (**BP334**) and BP308-CLB (**BP335**). To analyze the cellular internalization of these peptides, they were labeled with 5(6)-carboxyfluorescein leading to **CF-BP16**, CLB-BP16-CF (**BP326**), CF-BP16-CLB (**BP338**), **CF-BP308**, CLB-BP308-CF (**BP339**), and CF-BP308-CLB (**BP340**). The second set of peptides was designed by incorporating CLB-Gly-Phe-Leu-Gly at the N- or at the C-terminus of **BP16** and **BP308**. Thus, this set included CLB-GFLG-BP16 (**BP332**), BP16-GLFG-CLB (**BP333**), CLB-GFLG-BP308 (**BP336**) and BP308-GLFG-CLB (**BP337**). For the conjugates that contain CLB or GLFG-CLB at the C-terminus, these moieties were incorporated at the side-chain of an additional Lys residue. This amino acid was included to allow the introduction of these moieties without affecting the cationic charges of the corresponding parent sequence.

Table IV.1. Peptide sequences, retention times and purities on HPLC, and HRMS data.

Peptide	Sequence[a]	Notation
BP16	KKLFKKILKKL	
BP308	RRLFRRILRRL	
BP325	CLB-KKLFKKILKKL	CLB-BP16
BP331	Ac-KKLFKKILKKLK(CLB)	BP16-CLB
BP332	CLB-GFLG-KKLFKKILKKL	CLB-GFLG-BP16
BP333	Ac-KKLFKKILKKLK(GLFG-CLB)	BP16-GLFG-CLB
BP334	CLB-RRLFRRILRRL	CLB-BP308
BP335	Ac-RRLFRRILRRLK(CLB)	BP308-CLB
BP336	CLB-GFLG-RRLFRRILRRL	CLB-GFLG-BP308
BP337	Ac-RRLFRRILRRLK(GLFG-CLB)	BP308-GLFG-CLB
CF-BP16	CF-KKLFKKILKKL	CF-BP16
CF-BP308	CF-RRLFRRILRRL	CF-BP308
BP326	CLB-KKLFKKILK(CF)KL	CLB-BP16-CF
BP338	CF-KKLFKKILKKLK(CLB)	CF-BP16-CLB
BP339	CLB-RRLFRRILRRLK(CF)	CLB-BP308-CF
BP340	CF-RRLFRRILRRLK(CLB)	CF-BP308-CLB

[a]All peptides are C-terminal amides.

Peptide conjugates were manually prepared on solid-phase following a standard Fmoc/*t*Bu strategy and were obtained as C-terminal amides. The synthesis of the N-terminal CLB-peptide conjugates **BP325** (CLB-BP16) and **BP334** (CLB-BP308) involved the preparation of the peptidyl resins Fmoc-Lys(Boc)-Lys(Boc)-Leu-Phe-Lys(Boc)-Lys(Boc)-Ile-Leu-Lys(Boc)-Lys(Boc)-Leu-Rink-MBHA (**1**) and Fmoc-Arg(Pmc)-Arg(Pmc)-Leu-Phe-Arg(Pmc)-Arg(Pmc)-Ile-Leu-Arg(Pmc)-Arg(Pmc)-Leu-Rink-MBHA (**2**), respectively (Scheme IV.1).

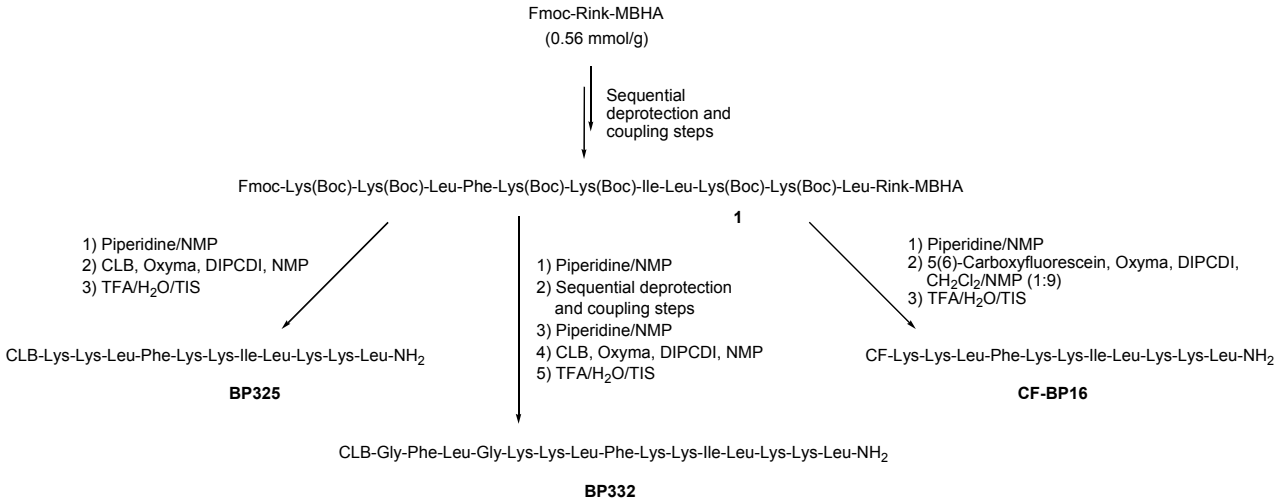

Scheme IV.1. Synthesis of the conjugates **BP325** and **BP332** and of the fluorescently labeled peptide **CF-BP16**.

They were obtained from an Fmoc-Rink-MBHA resin through sequential Fmoc removal and amino acid coupling steps. The Fmoc group was removed by treatment with a piperidine/DMF (3:7) solution. Couplings of the conveniently protected Fmoc amino acids were mediated by *N,N'*-diisopropylcarbodiimide (DIPCDI) and ethyl 2-cyano-2-(hydroxyimino)acetate (Oxyma) in *N,N*-dimethylformamide (DMF). Once the synthesis was completed, peptidyl resins **1** and **2** were treated with piperidine/NMP (3:7) and CLB was coupled using DIPCDI and Oxyma in NMP. Acidolytic cleavage with trifluoroacetic acid (TFA)/triisopropylsilane (TIS)/H_2O (95:2.5:2.5) afforded peptide conjugates **BP325** and **BP334** in 91 and >99% purity, respectively. Peptide conjugates **BP332** (CLB-GFLG-BP16) and **BP336** (CLB-GFLG-BP308), incorporating CLB-GFLG at the N-terminus of **BP16** or **BP308**, were prepared from peptidyl resins **1** and **2**, respectively. After removal of the N-terminal Fmoc group, the corresponding Fmoc-protected amino acids of the GFLG moiety and CLB were sequentially incorporated. Acidolytic treatment of the resulting resins yielded **BP332** and **BP336** in 92 and >99% purity, respectively. All these peptides were characterized by HRMS.

The synthesis of peptide conjugates **BP331** (BP16-CLB), **BP333** (BP16-GLFG-CLB), **BP335** (BP308-CLB) and **BP337** (BP308-GLFG-CLB), bearing CLB or GLFG-CLB at the C-terminus of **BP16** or **BP308** is depicted in Scheme IV.2 for the **BP16** derivatives. These moieties were incorporated at the side-chain of a Lys residue present at the C-terminal end of the peptide. To allow its selective derivatization, this Lys residue was incorporated as Fmoc-Lys(Dde)-OH (Dde = *N*-[1-(4,4-dimethyl-2,6-dioxocyclohex-1-ylidene)ethyl]). Thus, peptidyl resins Fmoc-Lys(Boc)-Lys(Boc)-Leu-Phe-Lys(Boc)-Lys(Boc)-Ile-Leu-Lys(Boc)-Lys(Boc)-Leu-Lys(Dde)-Rink-MBHA (**3**) and Fmoc-Arg(Pmc)-Arg(Pmc)-Leu-Phe-Arg(Pmc)-Arg(Pmc)-Ile-Leu-Arg(Pmc)-Arg(Pmc)-Leu-Lys(Dde)-Rink-MBHA (**4**) were prepared.

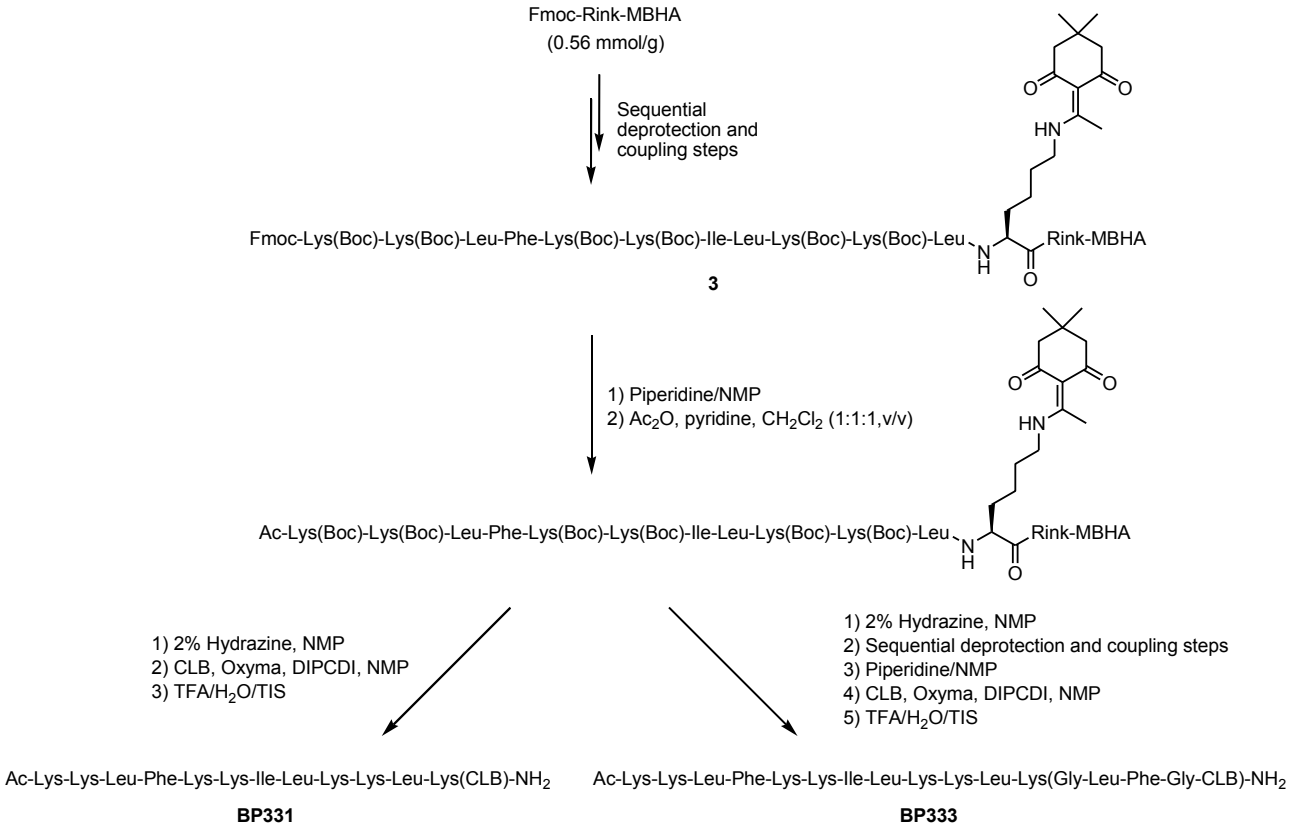

Scheme IV.2. Synthesis of peptide conjugates **BP331** and **BP333**.

After deprotection and acetylation of the N-terminus, the Dde group was selectively removed by treatment with hydrazine. In the case of **BP331** and **BP335**, the resulting free amino group was acylated with CLB. For **BP333** and **BP337**, the corresponding amino acids of the GLFG moiety and CLB were sequentially incorporated at this free amino group. Peptide conjugates were cleaved from the resin by acidolytic treatment and were obtained in excellent purities (91->99%, Table IV.1), as determined by analytical HPLC. Their identities were further confirmed by HRMS.

The fluorescently labeled peptides **CF-BP16** and **CF-BP308** were obtained from peptidyl resins **1** and **2**, respectively, by Fmoc removal and coupling of 5(6)-carboxyfluorescein (CF) using DIPCDI and Oxyma (Scheme IV.1). Piperidine washes were performed before cleavage of the peptide from the resin which served to remove overincorporated carboxyfluorescein moieties.[37] The CF-labeled peptides **BP338** (CF-BP16-CLB) and **BP340** (CF-B308-CLB), bearing the carboxyfluorescein at the N-terminus and the CLB at the C-terminus, were prepared from peptidyl resins **3** and **4**, respectively (Scheme IV.3).

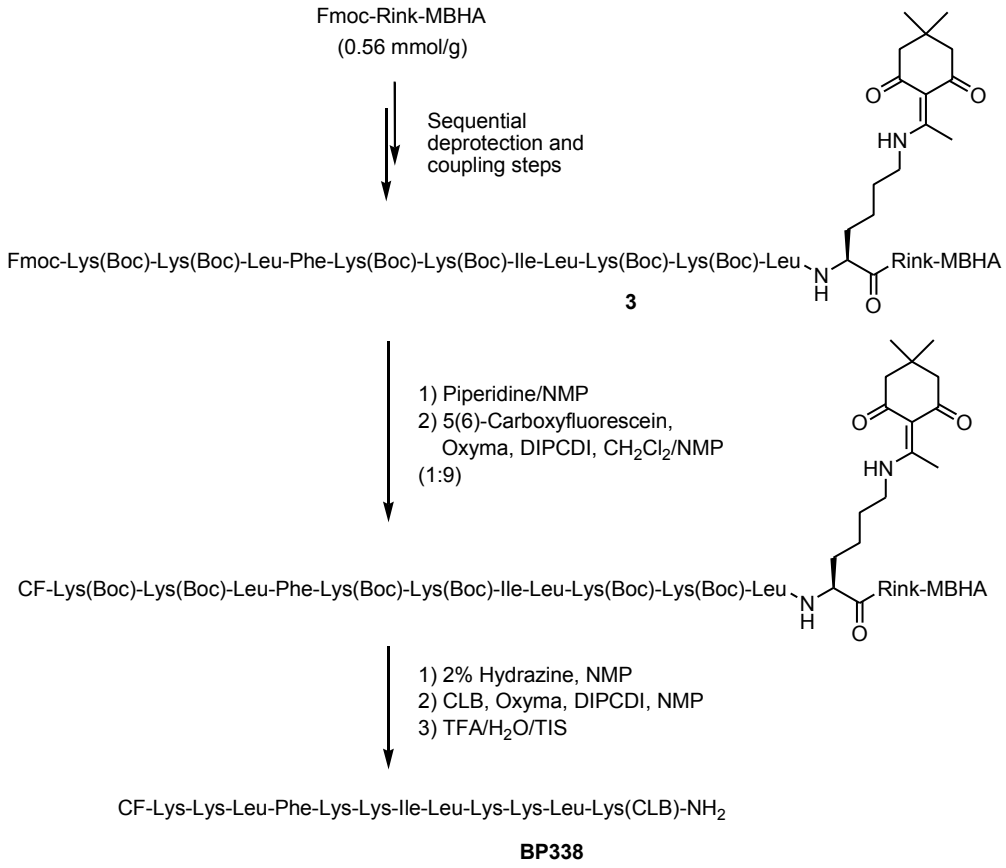

Scheme IV.3. Synthesis of fluorescently labeled conjugate **BP338**.

The synthesis consisted of deprotection of the N-terminus, carboxyfluorescein coupling, Dde group removal and acylation with CLB. The preparation of the CF-labeled peptides **BP326** (CLB-BP16-CF) and **BP339** (CLB-BP308-CF), incorporating a CLB moiety at the N-terminus and a carboxyfluorescein group at the C-terminus involved the synthesis of peptidyl resins Fmoc-Lys(Boc)-Lys(Boc)-Leu-Phe-Lys(Boc)-Lys(Boc)-Ile-Leu-Lys(Dde)-Lys(Boc)-Leu-Rink-MBHA and **4**, respectively. Fmoc removal and *N*$^{\alpha}$-amino group acylation with CLB was followed by Dde group removal and derivatization with 5(6)-carboxyfluorescein. Acidolytic cleavage afforded the CF-labeled peptides in excellent purities (81->99%), and they were characterized by HRMS.

IV.3.2. Cellular uptake of CF-BP16 and CF-BP308

In order to evaluate the influence of replacing Lys residues with Arg on the cellular uptake of **CF-BP16**, we first examined the capacity of internalization of **CF-BP308** into MCF-7 cells by flow cytometry and compared it with that of **CF-BP16**. MCF-7 cells were incubated with **CF-BP308** or with **CF-BP16** at 25 μM for different times (1, 3 and 6 h) at 37 ºC. Cells were harvested by trypsinization, which also prevented non-specific plasma membrane binding of the peptide. As

depicted in Figure IV.1, the mean intracellular fluorescence of the cells incubated with either **CF-BP308** or **CF-BP16** increased over time. No significant differences were observed in the mean fluorescence intensity values for both peptides (1065 ± 44 and 981 ± 159 after 6 h, respectively).

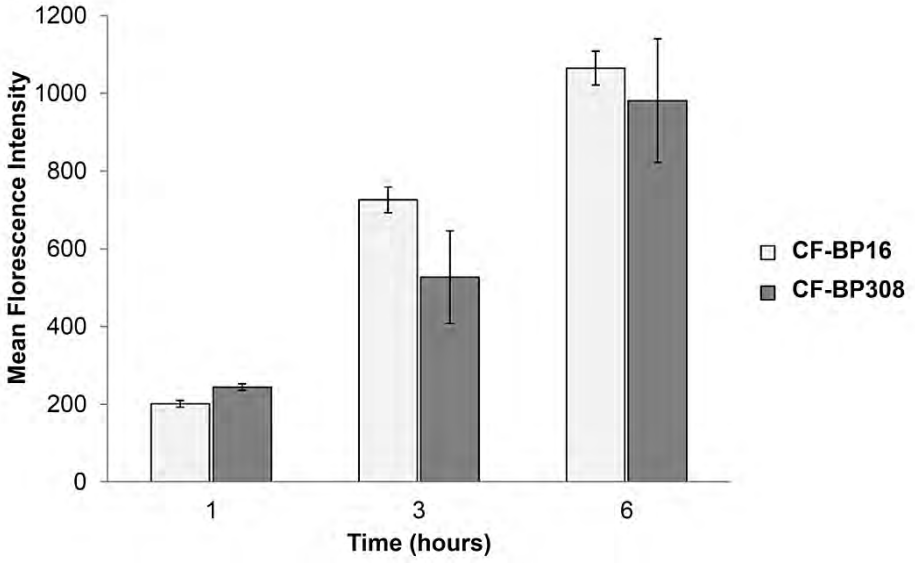

Figure IV.1. Comparison of the cellular uptake between CF-BP16 and CF-BP308 in MCF-7 cells. Cells were exposed to the peptide at 25 μM for 1, 3 and 6 h at 37 ºC. Each column in the graph represents the mean fluorescence intensity of the cells determined in three independent experiments ± SD.

Confocal studies were carried out to examine if the internalization in MCF-7 cells of the arginine analogue **CF-BP308** correlated with that of **CF-BP16**. In a previous study we observed that **CF-BP16** accumulates in vesicles throughout the cytoplasm of these cells, with significant clustering at the periphery of the nucleus.[33] An optical sectioning indicated that no fluorescence particles were placed inside the nucleus. Moreover, it has been described that the replacement of D-Lys by D-Arg in the *KLA* antimicrobial peptide led to an enhancement of the mitochondrial accumulation in HeLa cells.[35] Thus, further confocal microscopy studies were performed in order to find out whether these peptides colocalize with mitochondrial markers.

To achieve these aims, MCF-7 cells were incubated with the corresponding CF-labeled peptide at 50 μM for 30 min at 4 ºC and for 3 h at 37 ºC. The cell nuclei and mitochondria were stained with Hoechst and Mitotracker Red, respectively (Figure IV.2).

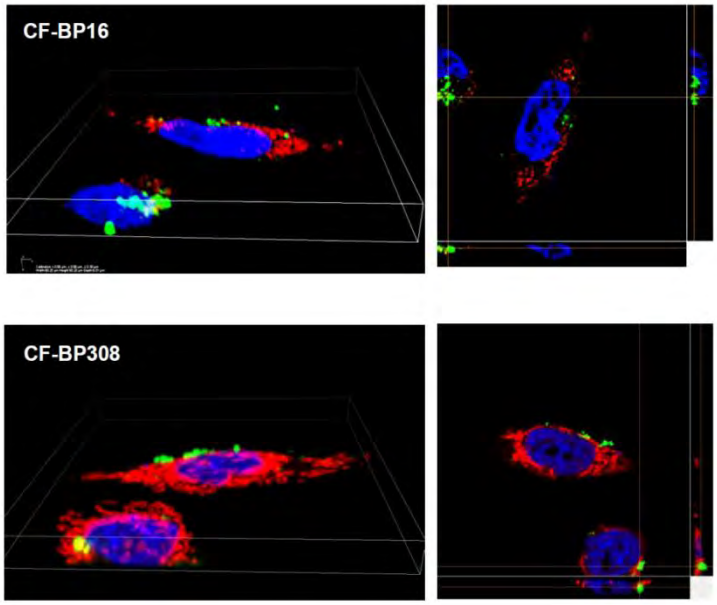

Figure IV.2. Confocal microscopic imaging of the internalization of CF-BP16 and CF-BP308 into MCF-7 cells. Cells were incubated with **CF-BP16** and **CF-BP308** at 50 μM for 30 min at 4 ºC and for 3 h at 37 ºC. Cell nuclei were stained with Hoechst (blue) and the mitochondria were stained with Mitotracker Red (red). The localization of peptides is indicated by the green fluorescence. The images show the 3D reconstruction of the confocal Z stack images.

As expected, **CF-BP308** showed the same cellular uptake behavior as **CF-BP16** and no fluorescence was observed after 30 min of incubation at 4 ºC, demonstrating that both CF-labeled peptides internalize through energy-dependent mechanisms.[33] The number of fluorescent particles gradually increased over time and a dot-like distribution pattern was observed for both peptides after 3 h of incubation. Similarly to **CF-BP16**, higher-magnification (1000×) images of MCF-7 cells incubated with **CF-BP308** revealed that the fluorescent particles were located throughout the cytoplasm and that no colocalization was observed in the nucleus (Figure IV.2). Moreover, as shown by optical sectioning, neither **CF-BP16** nor **CF-BP308** accumulated inside the mitochondria, indicating that these peptides do not show mitochondria targeting properties.

Although **CF-BP16** and **CF-BP308** did not colocalize with the nucleus or mitochondria, these results indicate that both peptides display potential internalization properties for use in drug delivery systems. In particular, since previous mechanistic studies on the cellular uptake of **BP16** suggested its localization in late endosomes,[33] these peptides could be useful in site-specific release strategies occurring at the lysosomal compartment.[19]

IV.3.3. Cell cytotoxicity of the CLB-peptide conjugates

The cytotoxic activity profile of the CLB-peptide conjugates was explored to determine the influence of incorporating CLB at the N- or at the C-terminus of the peptide as well as of the presence of the Gly-Phe-Leu-Gly enzymatic cleavable sequence. Thus, MCF-7, CAPAN-1, PC-3, SKMEL-28 and 1BR3G cells were exposed to the CLB-peptide conjugates, and the IC_{50} was determined by the 3-(4,5-dimethylthiazol-2-yl)-2,5-diphenyltetrazolium bromide (MTT) assay after 48 h of peptide exposure. CLB was included in the study for comparison purposes.

Table IV.2. Cytotoxicity (IC_{50}) of CLB and CLB-peptide conjugates in CAPAN-1, MCF-7, PC-3, SKMEL-28 and 1BR3G cells.[a]

Peptide	Notation	CAPAN-1	MCF-7	PC-3	SKMEL-28	1BR3G
CLB		> 100	73.7 ± 4.5	> 100	> 100	> 100
BP325	CLB-BP16	13.7 ± 2.4	12.0 ± 2.7	11.3 ± 3.2	15.0 ± 3.0	18.2 ± 3.5
BP331	BP16-CLB	11.2 ± 2.5	25.5 ± 0.7	12.9 ± 2.0	8.7 ±3.4	24.0 ± 1.3
BP332	CLB-GFLG-BP16	7.2 ± 0.3	14.0 ± 1.4	3.6 ± 0.4	3.9 ± 1.5	14.3 ± 0.6
BP333	BP16-GLFG-CLB	6.2 ± 0.3	16.2 ± 1.8	8.2 ± 0.5	6.4 ± 2.3	15.7 ± 0.6
BP334	CLB-BP308	11.2 ± 1.9	15.0 ± 5.0	16.4 ± 3.4	12.8 ± 2.9	13.8 ± 3.4
BP335	BP308-CLB	> 100	> 100	> 100	> 100	> 100
BP336	CLB-GFLG-BP308	> 100	> 100	> 100	> 100	> 100
BP337	BP308-GLFG-CLB	> 100	> 100	> 100	> 100	> 100

[a]The IC_{50} values were determined by the MTT assay after 48 h of CLB-peptide conjugate exposure. Data represent the mean ± SD of at least three independent experiments performed in triplicate.

As shown in Table IV.2, except for **BP335**, **BP336** and **BP337**, peptide conjugates were active against the cancer and healthy cell lines tested. In contrast, CLB was not cytotoxic against the five cell lines (IC_{50} of 73.7 to >100 μM). Notably, conjugation of CLB at the N- or at the C-terminus of **BP16** resulted in peptides **BP325** (CLB-BP16) and **BP331** (BP16-CLB), respectively, with important activity (IC_{50} of 8.7 to 25.5 μM). No significant differences were observed between the cytotoxicity of these two peptide conjugates against CAPAN-1 and PC-3 cells. **BP325** was more active than **BP331** against MCF-7 and 1BR3G cells, but less active against SKMEL-28 cells. A further improvement of the activity of CLB was achieved when the tetrapeptide Gly-Phe-Leu-Gly was incorporated between CLB and the N- or the C-terminus of **BP16**. Thus, **BP332** (CLB-GFLG-BP16) exhibited higher cytotoxicity than **BP325** (CLB-BP16), being 2- to 4-fold more active against

CAPAN-1, PC-3 and SKMEL-28 cells (IC_{50} of 7.2, 3.6 and 3.9 μM, respectively). **BP333** (BP16-GLFG-CLB) was around 1.5-fold more active against all cell lines than **BP331** (BP16-CLB) (IC_{50} of 6.2 to 16.2 μM vs 8.7 to 25.5 μM). These results revealed that the efficacy of CLB is enhanced when conjugated to either the N- or the C-terminal end of **BP16**. Remarkably, the introduction of the Gly-Phe-Leu-Gly enzymatic cleavable sequence further increased this efficacy irrespective of the peptide end into which it is incorporated. The presence of this tetrapeptide might provide a specific recognition site for cathepsin B which could induce the release of CLB, enhancing its cytotoxicity. As previously reported, **BP16** is mainly internalized into cancer cells by clathrin dependent endocytosis and might follow a degradation pathway, where the fusion between late endosomes and lysosomes occurs. Therefore, the release of CLB from the sequences containing Gly-Phe-Leu-Gly could take place in the lysosomal compartments, which are the final stage of this endocytic pathway.

A different cytotoxic activity profile was observed for CLB-peptide conjugates derived from **BP308**. The activity of CLB was only increased when it was introduced at the N-terminus of this peptide. **BP334** (CLB-BP308) displayed IC_{50} values ranging from 11.2 to 16.4 μM against the cell lines tested, whereas **BP335** (BP308-CLB) was not active (IC_{50} >100 μM). Unlike in the case of **BP16**, the attachment of the tetrapeptide Gly-Phe-Leu-Gly to the N- or the C-terminal end of **BP308** did not improve the activity of CLB, being **BP336** (CLB-GFLG-BP308) and **BP337** (BP308-GLFG-CLB) surprisingly inactive against all cell lines (IC_{50} >100 μM).

The different behaviour of CLB-conjugates derived from **BP16** and **BP308** revealed the importance of evaluating the influence of the position of the drug in the peptide sequence on the cytotoxicity. Moreover, even though **BP308** displays similar cellular uptake than **BP16**, the fact that the incorporation of Gly-Phe-Leu-Gly in **BP308** does not enhance the cytotoxic activity of CLB suggests that the replacement of Lys by Arg in **BP16** might be associated to a different cellular uptake pattern.

IV.3.4. Cellular uptake of CLB peptide conjugates

In order to determine whether the cytotoxic activity profile exhibited by **BP325** (CLB-BP16), **BP331** (BP16-CLB), **BP334** (CLB-BP308) and **BP335** (BP308-CLB) correlated with their internalization properties, these CLB conjugates were labeled with 5(6)-carboxyfluorescein (CF) and analyzed by flow cytometry. The cellular uptake of the CF-labeled peptide conjugates **BP326** (CLB-BP16-CF), **BP338** (CF-BP16-CLB), **BP339** (CLB-BP308-CF) and **BP340** (CF-BP308-CLB) at

25 μM was determined after 6 h of incubation in MCF-7 cells at 37 ºC (Figure IV.3). Results showed that the position of CLB in **BP16** did not influence the internalization properties of this peptide, since **BP326** (CLB-BP16-CF) and **BP338** (CF-BP16-CLB) displayed similar mean intracellular intensity values (1151 ± 50 vs 1100 ± 20). Notably, the internalization ability of these peptides correlated with the cytotoxic activity exhibited by the corresponding non-labeled sequences **BP325** (CLB-BP16) and **BP331** (BP16-CLB) (Table IV.2).

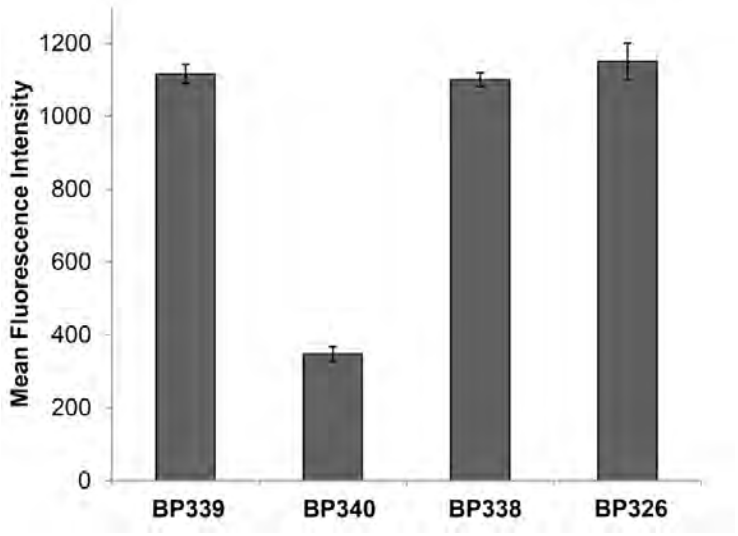

Figure IV.3. Comparison of the cellular uptake of 5(6)-carboxyfluorescein labeled peptides BP326 (CLB-BP16-CF), BP338 (CF-BP16-CLB), BP339 (CLB-BP308-CF) and BP340 (CF-BP308-CLB) in MCF-7 cells. Cells were exposed to the peptide at 25 μM for 6 h at 37 ºC. Each column in the graph represents the mean fluorescence intensity of the cells determined in three independent experiments ± SD.

Unlike the **BP16** derivatives, the **BP308** conjugates were differentially internalized. While **BP339** (CLB-BP308-CF) exhibited high internalization capacity (1116 ± 25), comparable to that of CLB-BP16-CF (**BP326**), **BP340** bearing the CLB moiety at the C-terminus showed a low intracellular fluorescence (348 ± 20). These results were consistent with the cytotoxic activity profile observed for the corresponding non-labeled peptides **BP334** (CLB-BP308) and **BP335** (BP308-CLB). The former was active against all cell lines whereas the latter exhibited IC_{50} values >100 μM. Thus, the low cytotoxicity of **BP335** could be attributed to its low ability to cross the cell membrane.

These studies showed that for CPPs with similar cellular uptake properties, it is important to analyse the effect of the position of the cargo in the sequence.[30,39,40] In this case, **BP16** and **BP308** have the same net charge of +6 and display comparable cell-penetrating properties in MCF-7 cells as observed by flow cytometry and confocal microscopy. However, when a cargo is attached to one of the peptide ends, the resulting **BP16** and **BP308** conjugates have a different behaviour.

Whereas the uptake properties of N- and C-terminal **BP16** conjugates are similar, **BP308** derivatives display significantly different internalization capacities.

IV.3.5. Cathepsin B enzymatic assays

To prove that the release of CLB from **BP332** (CLB-GFLG-BP16) and **BP333** (BP16-GLFG-CLB) might occur in the lysosomes, the hydrolysis of these sequences by cathepsin B was evaluated. Conditions were chosen to mimic the lysosomal medium and were based on a previously reported method.[30] The peptide conjugate **BP332** was exposed to a solution of cathepsin B in phosphate buffer (pH 5) containing 25 mM L-Cys and 1 mM EDTA. The digestion after 10, 30, 60, 90, 120 and 180 min was monitored by HPLC-MS (Figure IV.4A). Just after adding **BP332** to the enzyme solution (digestion time = 0 min), a mixture of this peptide (t_R = 6.3 min) together with low intensity peaks was observed. After 10 min, the peak corresponding to **BP332** significantly decreased and a peak at a retention time of 5.2 min appeared. This peak increased over time becoming the major one after 90 min of digestion. HPLC-MS analysis revealed that this peak corresponded to CLB-Gly-OH (*m/z* = 361.1, 363.1 $[M+H]^+$; 383.0, 385.0 $[M+Na]^+$) (Figure IV.4C). This result indicated that the hydrolytic cleavage occurred between the Gly and Phe residues of the enzymatic cleavable sequence Gly-Phe-Leu-Gly. The cleavage of the C-terminal analogue **BP333** (BP16-GLFG-CLB) by cathepsin B was tested and monitored (Figure IV.4B) using the conditions described above for **BP332**. CLB was also released from **BP333** in a time-dependent manner and following a pattern similar to that of **BP332**. The peak corresponding to CLB-Gly-OH (t_R = 5.2 min) also increased over time during the digestion. All these data are in agreement with previous studies based on cathepsin B delivery strategies.[31,32] Moreover, they support the hypothesis that CLB might be released from **BP332** and **BP333** in the lysosomes leading to the high activity observed for these peptide conjugates in cancer cells.

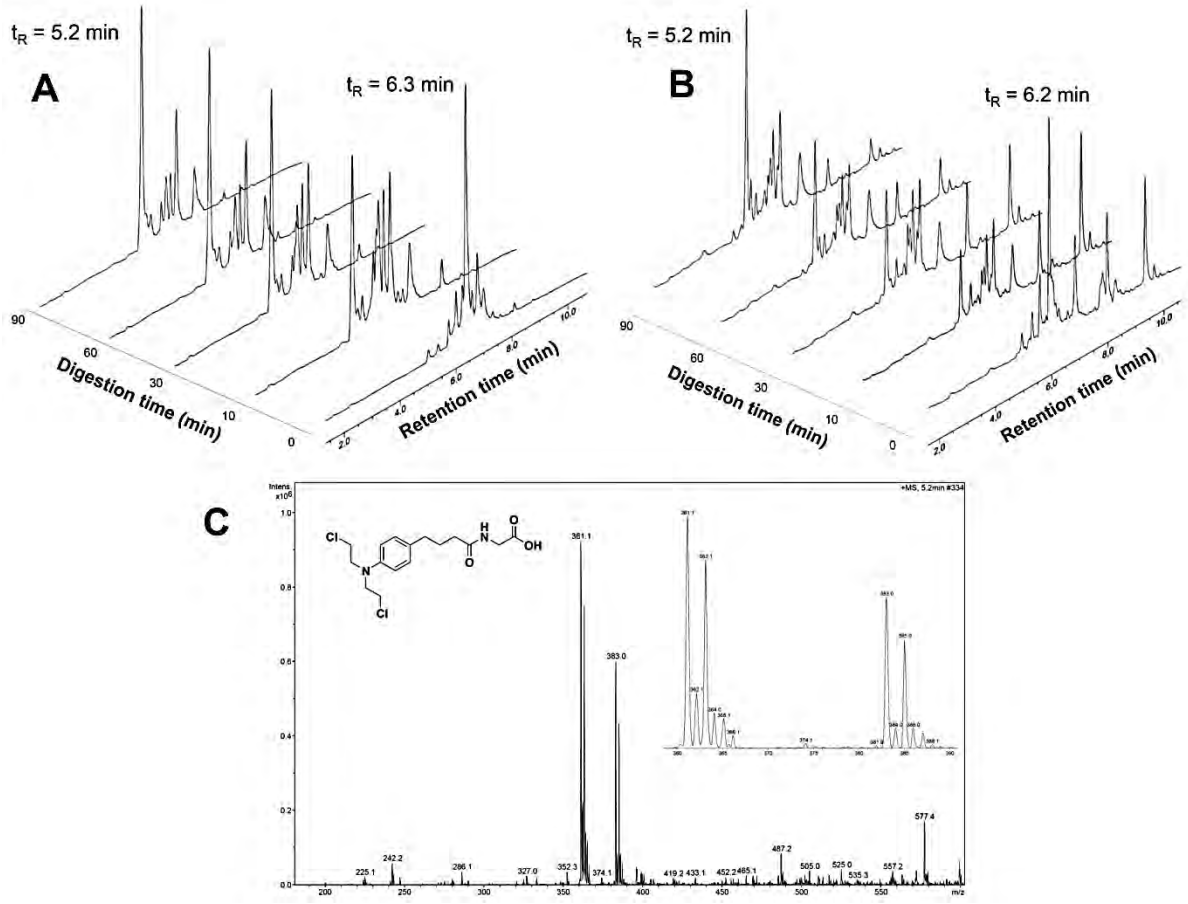

Figure IV.4. Enzymatic digestion of BP332 and BP333 by cathepsin B monitored by HPLC-MS. **A)** HPLC traces of the enzymatic digestion of **BP332** after 0, 10, 30, 60 and 90 min of enzyme exposure; **B)** HPLC traces of the enzymatic digestion of **BP333** at 0, 10, 30, 60 and 90 min of enzyme exposure; **C)** ESI-MS spectrum of the peak at t_R = 5.2 min after 1 h of enzymatic digestion.

IV.4. Conclusions

In this work we developed an efficient CLB delivery system based on **BP16**. The design of this system combined CLB and the enzymatic cleavable tetrapeptide Gly-Phe-Leu-Gly at either the N- or the C-terminus of **BP16**. The resulting sequences **BP332** and **BP333** exhibited high cytotoxic activity against cancer cells which could be attributed to the enzymatic release of CLB in the lysosomes. These results reveal that this delivery system could be applied to transport and efficiently release therapeutic agents in cancer treatments.

IV.5. References

(1) Alvarez-Lorenzo, C., and Concheiro, A. (2014) Smart drug delivery systems: from fundamentals to the clinic. *Chem. Commun. 50,* 7743–7765.

(2) Kleiner, L. W., Wright, J. C., and Wang, Y. (2014) Evolution of implantable and insertable drug delivery systems. *J. Controlled Release 181,* 1–10.

(3) Thanki, K., Gangwal, R. P., Sangamwar, A. T., and Jain, S. (2013) Oral delivery of anticancer drugs: challenges and opportunities. *J. Controlled Release 170,* 15–40.

(4) Foged, C., and Nielsen, H. M. (2008) Cell-penetrating peptides for drug delivery across membrane barriers. *Expert Opin. Biol. Ther. 5,* 105–118.

(5) Fonseca, S. B., Pereira, M. P., and Kelley, S. O. (2009) Recent advances in the use of cell-penetrating peptides for medical and biological applications. *Adv. Drug Deliv. Rev. 61,* 953–964.

(6) Heitz, F., Morris, M. C., and Divita, G. (2009) Twenty years of cell-penetrating peptides: from molecular mechanisms to therapeutics. *Br. J. Pharmacol. 157,* 195–206.

(7) Vivès, E., Schmidt, J., and Pèlegrin, A. (2008) Cell-penetrating and cell-targeting peptides in drug delivery. *Biochim. Biophys. Acta 1786,* 126–138.

(8) Khafagy, E.-S., and Morishita, M. (2012) Oral biodrug delivery using cell-penetrating peptide. *Adv. Drug Deliv. Rev. 64,* 531–539.

(9) Huang, Y., Jiang, Y., Wang, H., Wang, J., Shin, M. C., Byun, Y., He, H., Liang, Y., and Yang, V. C. (2013) Curb challenges of the “Trojan Horse” approach: smart strategies in achieving effective yet safe cell-penetrating peptide-based drug delivery. *Adv. Drug Deliv. Rev. 65,* 1299–1315.

(10) Bechara, C., and Sagan, S. (2013) Cell-penetrating peptides: 20 years later, where do we stand? *FEBS Lett. 587,* 1693–1702.

(11) Copolovici, D. M., Langel, K., Eriste, E., and Langel, Ü. (2014) Cell-penetrating peptides: design, synthesis, and applications. *ACS Nano 8,* 1972–1994.

(12) Koren, E., and Torchilin, V. P. (2012) Cell-penetrating peptides: breaking through to the other side. *Trends Mol. Med. 18,* 385–393.

(13) Majumdar, S., and Siahaan, T. J. (2010) Peptide-mediated targeted drug delivery. *Med. Res. Rev. 32,* 637–658.

(14) Zhang, X.-X., Eden, H. S., and Chen, X. (2012) Peptides in cancer nanomedicine: drug carriers, targeting ligands and protease substrates. *J. Controlled Release 159,* 2–13.

(15) Fotin-Mleczek, M., Fischer, R., and Brock, R. (2005) Endocytosis and cationic cell-penetrating peptides - A merger of concepts and methods. *Curr. Pharm. Des. 11,* 3613–3628.

(16) Pujals, S., Fernández-Carneado, J., López-Iglesias, C., Kogan, M. J., and Giralt, E. (2006) Mechanistic aspects of CPP-mediated intracellular drug delivery: relevance of CPP self-assembly. *Biochim. Biophys. Acta 1758,* 264–279.

(17) Andresen, T. L., Thompson, D. H., and Kaasgaard, T. (2010) Enzyme-triggered nanomedicine: drug release strategies in cancer therapy. *Mol. Membr. Biol. 27,* 353–363.

(18) Fleige, E., Quadir, M. A., and Haag, R. (2012) Stimuli-responsive polymeric nanocarriers for the controlled transport of active compounds: concepts and applications. *Adv. Drug Deliv. Rev. 64,* 866–884.

(19) Bildstein, L., Dubernet, C., and Couvreur, P. (2011) Prodrug-based intracellular delivery of anticancer agents. *Adv. Drug Deliv. Rev. 63,* 3–23.

(20) Bae, Y., Nishiyama, N., Fukushima, S., Koyama, H., Yasuhiro, M., and Kataoka, K. (2005) Preparation and biological characterization of polymeric micelle drug carriers with intracellular pH-triggered drug release property: tumor permeability, controlled subcellular drug distribution, and enhanced in vivo antitumor efficacy. *Bioconjugate Chem. 16,* 122–130.

(21) Guo, M., Que, C., Wang, C., Liu, X., Yan, H., and Liu, K. (2011) Multifunctional superparamagnetic nanocarriers with folate-mediated and pH-responsive targeting properties for anticancer drug delivery. *Biomaterials 32,* 185–194.

(22) Qiu, F., Wang, D., Zhu, Q., Zhu, L., Tong, G., Lu, Y., Yan, D., and Zhu, X. (2014) Real-time monitoring of anticancer drug release with highly fluorescent star-conjugated copolymer as a drug carrier. *Biomacromolecules 15,* 1355–1364.

(23) Singh, N., Karambelkar, A., Gu, L., Lin, K., Miller, J. S., Chen, C. S., Sailor, M. J., and Bhatia, S. N. (2011) Bioresponsive mesoporous silica nanoparticles for triggered drug release. *J. Am. Chem. Soc. 133,* 19582–19585.

(24) Sun, C., Shen, W.-C., Tu, J., and Zaro, J. L. (2014) Interaction between cell-penetrating peptides and acid-sensitive anionic oligopeptides as a model for the design of targeted drug carriers. *Mol. Pharm. 11,* 1583–1590.

(25) Tian, J., Ding, L., Xu, H.-J., Shen, Z., Ju, H., Jia, L., Bao, L., and Yu, J.-S. (2013) Cell-specific and pH-activatable rubyrin-loaded nanoparticles for highly selective near-infrared photodynamic therapy against cancer. *J. Am. Chem. Soc. 135,* 18850–18858.

(26) Mahato, R., Tai, W., and Cheng, K. (2011) Prodrugs for improving tumor targetability and efficiency. *Adv. Drug Deliv. Rev. 63,* 659–670.

(27) Aluri, S., Janib, S. M., and Mackay, J. A. (2009) Environmentally responsive peptides as anticancer drug carriers. *Adv. Drug Deliv. Rev. 61,* 940–952.

(28) Mohamed, M. M., and Sloane, B. F. (2006) Cysteine cathepsins: multifunctional enzymes in cancer. *Nat. Rev. Cancer 6,* 764–775.

(29) Shankar, R., Samykutty, A., Riggin, C., Kannan, S., Wenzel, U., and Kolhatkar, R. (2013) Cathepsin B degradable star-shaped peptidic macromolecules for delivery of 2-methoxyestradiol. *Mol. Pharm. 10,* 3776–3788.

(30) Zhang, P., Cheetham, A. G., Lock, L. L., and Cui, H. (2013) Cellular uptake and cytotoxicity of drug-peptide conjugates regulated by conjugation site. *Bioconjugate Chem. 24,* 604–613.

(31) Moreno, M., Zurita, E., and Giralt, E. (2014) Delivering wasp venom for cancer therapy. *J. Controlled Release 182,* 13–21.

(32) Bai, K. B., Láng, O., Orbán, E., Szabó, R., Köhidai, L., Hudecz, F., and Mezö, G. (2008) Design, synthesis, and in vitro activity of novel drug delivery systems containing tuftsin derivatives and methotrexate. *Bioconjugate Chem. 19,* 2260–2269.

(33) Soler, M., González-Bártulos, M., Soriano-Castell, D., Ribas, X., Costas, M., Tebar, F., Massaguer, A., Feliu, L., and Planas, M. (2014) Identification of BP16 as a non-toxic cell-penetrating peptide with highly efficient drug delivery properties. *Org. Biomol. Chem. 12,* 1652–1663.

(34) Brock, R. (2014) The uptake of arginine-rich cell-penetrating peptides: putting the puzzle together. *Bioconjugate Chem. 25,* 863–868.

(35) Nakase, I., Okumura, S., Katayama, S., Hirose, H., Pujals, S., Yamaguchi, H., Arakawa, S., Shimizu, S., and Futaki, S. (2012) Transformation of an antimicrobial peptide into a plasma membrane-permeable, mitochondria-targeted peptide via the substitution of lysine with arginine. *Chem. Commun. 48,* 11097–11099.

(36) Kaiser, E., Colescott, R. L., Bossinger, C. D., and Cook, P. (1970) Color test for detection of free terminal amino groups in the solid-phase synthesis of peptides. *Anal. Biochem. 34,* 595-598.

(37) Fischer, R., Mader, O., Jung, G., and Brock, R. (2003) Extending the applicability of carboxyfluorescein in solid-phase synthesis. *Bioconjugate Chem. 14,* 653–660.

(38) Guaragna, A., Chiaviello, A., Paolella, C., D'Alonzo, D., Palumbo, G., and Palumbo, G. (2012) Synthesis and evaluation of folate-based chlorambucil delivery systems for tumor-targeted chemotherapy. *Bioconjugate Chem. 23,* 84–96.

(39) Brieger, A., Plotz, G., Hinrichsen, I., Passmann, S., Adam, R., and Zeuzem, S. (2012) C-terminal fluorescent labeling impairs functionality of DNA mismatch repair proteins. *PLoS One 7,* e31863.

(40) Zhang, W., Song, J., Mu, L., Zhang, B., Liu, L., Xing, Y., Wang, K., Li, Z., and Wang, R. (2011) Improving anticancer activity and selectivity of camptothecin through conjugation with releasable substance P. *Bioorg. Med. Chem. Lett. 21,* 1452–1455.

CHAPTER V

Enhanced and selective DNA cleavage activity of redox-active metallopeptides based on tetradentate aminopyridine ligands

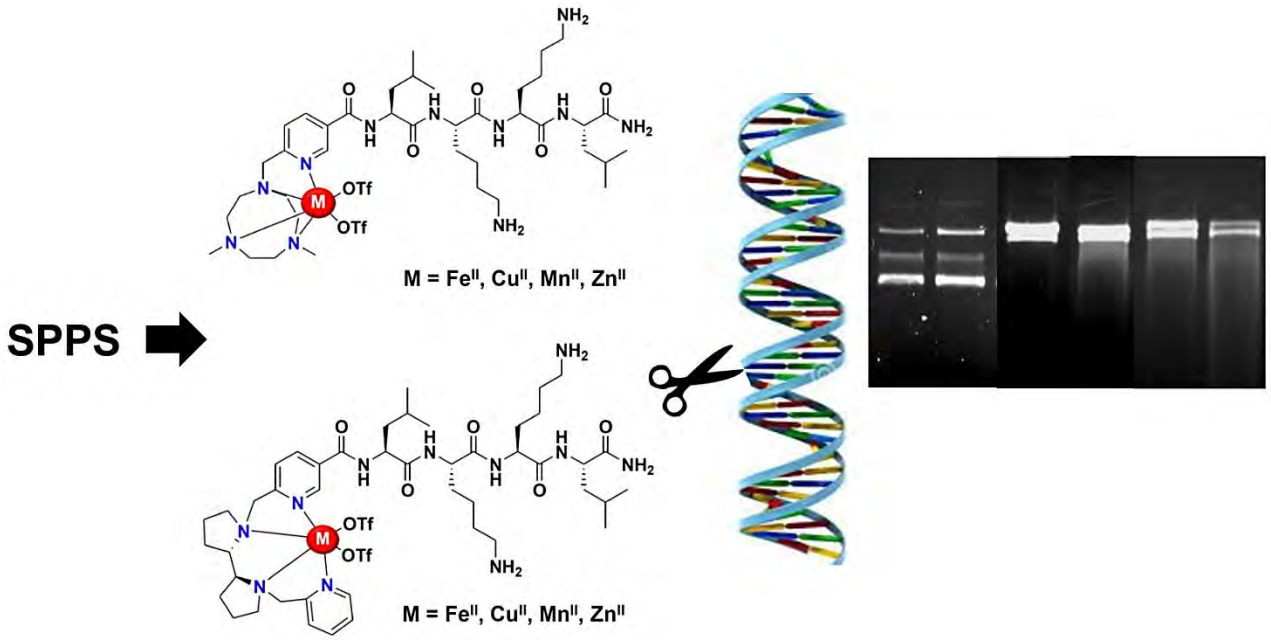

This chapter corresponds to a manuscript in preparation:

Marta Soler, Eduard Figueras, Joan Serrano, Anna Company, Mª Ángeles Martínez, Lidia Feliu, Marta Planas, Xavi Ribas, Miquel Costas. Enhanced and selective DNA cleavage activity of redox-active metallopeptides based on tetradentate aminopyridine ligands. *In preparation*

For this work, M. S. performed the synthesis and the characterization of all the compounds. Moreover, M. S. carried out the DNA cleavage experiments. Finally, M. S. was involved in argumentations and discussions, and wrote the manuscript draft.

V.1. Introduction

In recent years, the design of metallopeptides as hybrid structures has emerged as versatile tools to explore new features in the bioinorganic discipline.[1-6] Particularly, redox-active metallopeptides are of potential use for different biological purposes, especially those involving DNA targeting.[7-12] However, the contributions of peptide-based transition metal complexes in this area are relatively limited, usually hampered by their synthetic preparation and characterization.[13-15] In this context, effective designs and straightforward synthetic methodologies must be addressed in order to obtain redox-active metallopeptides that selectively interact with DNA.[16-21] To this end, peptides could be especially attractive templates to be considered as promising recognition sites in DNA-binding.[19,22-27] Interestingly, the recognition specificity of positively charged short peptides towards DNA has been demonstrated. Facing the precedent literature, SPKK or KWKK cationic motifs have been particularly reported to preferentially bind to the minor groove of the DNA with a degree of sequence specificity for A/T-rich sites.[28-30] This selective binding opens new perspectives for controlling the DNA interaction by molecules with useful properties. On the basis of these precedents, we have targeted the conjugation of redox-active complexes that can function as chemical nucleases to cationic tetrapeptides in order to explore the expected synergistic effect. Within this regard, we focused our attention on the conjugation of complexes of biologically relevant first row redox active transition metals, such as Fe, Cu or Mn, containing the tetradentate 1,4-dimethyl-7-(2-pyridylmethyl)-1,4,7-triazacyclononane (^{Me2}PyTACN) and (2*S*,2*S*')-1,1'-bis(pyrid-2-ylmethyl)-2,2'-bipyrrolidine ((*S,S*)-BPBP) to a cationic LKKL tetrapeptide sequence. The enhanced reactivity of these aminopyridine complexes differs from most common approaches in this topic to render metallopeptides. Their high reactivity can be traced in first place to the presence of labile sites in the metal ion coordination sphere that enable fast reaction with external molecules. For example, it has been shown that these sites enable fast reactivity of the complexes with O_2 and peroxides, forming metal based reactive species.[31-35] Furthermore, metal complexes containing the former tetradentate ligands have been described as powerful and selective catalysts that operate under mild experimental conditions, and at the basis of this activity is the ability of these ligands to enable the metal ion to reach highly electrophilic high oxidation states.[31-39]

Aiming at taking advantage of the high reactivity of this class of complexes in a biological frame, herein, we report the solid-phase synthesis and the characterization of novel redox-active metallotetrapeptides based on ^{Me2}PyTACN and (*S,S'*)-BPBP ligands. Moreover, the DNA cleavage activity of different metallopeptides was evaluated using gel electrophoresis technique and compared to their metal-binding conjugates as well as to the parent complexes.

CHAPTER VI

Delivering aminopyridine ligands into cancer cells through conjugation to the cell-penetrating peptide BP16

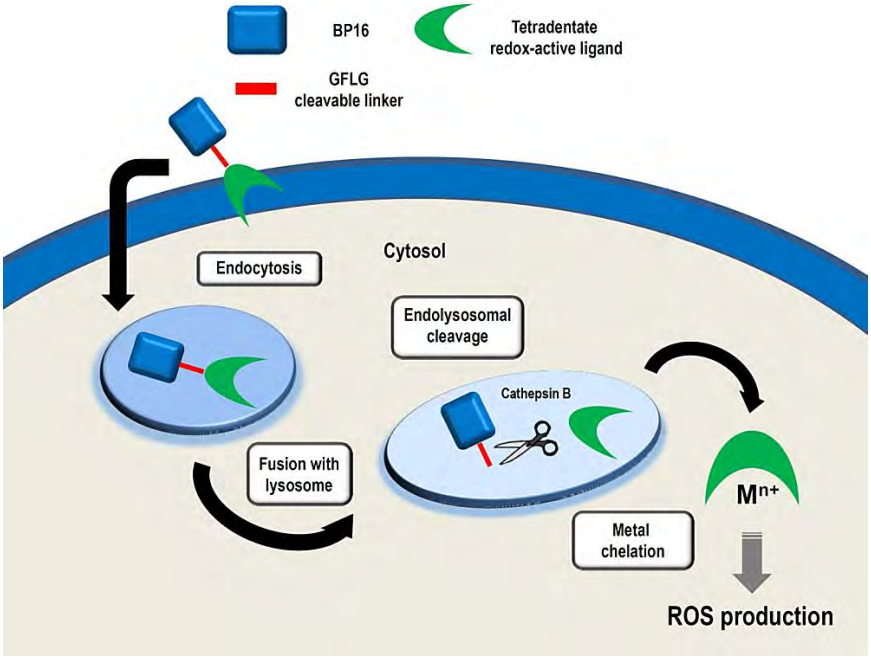

This chapter corresponds to a manuscript in preparation:

Marta Soler, Marta González-Bártulos, Eduard Figueras, Anna Massaguer, Lidia Feliu, Marta Planas, Xavi Ribas, Miquel Costas. Delivering aminopyridine ligands into cancer cells through conjugation to the cell-penetrating peptide BP16. *In preparation*

For this work, M. S. performed the design, the synthesis and the characterization of all the compounds. Moreover, M. S. carried out the cathepsin B enzymatic assays. Finally, M. S. was involved in argumentations and discussions, and wrote the manuscript draft.

VI.1. Introduction

Great strides have been made in recent years in finding effective cancer treatments. Despite the significant efforts invested in this field, current anticancer therapies are hindered by the poor solubility of drugs as well as their low cellular uptake and lack of selectivity. In this sense, targeted drug delivery has emerged as a convenient strategy to overcome these limitations.[1-7]

Peptide-mediated drug delivery constitutes a powerful and versatile tool to enhance the uptake and trigger the release of therapeutic agents into cancer cells.[8-10] In particular, one of the most common approaches to facilitate the cellular uptake of anticancer drugs is based on their conjugation to a cell-penetrating peptide (CPP).[11-15] On the other hand, the efficacy of the drug can be further increased by its conjugation to a CPP bearing an enzyme-cleavable moiety which could allow its intracellular release.[9] Despite the exact mode of action of CPPs is not well understood, it is generally accepted that CPPs are mainly internalized by endocytosis.[16] Following this pathway, they will end up inside lysosomes where lysosomal proteases are expected to hydrolytically cleave drugs from CPPs incorporating specific cleavage sites recognized by these enzymes.[8,9,15,17] For example, cathepsin B is able to promote the pH-sensitive release of therapeutic agents from CPPs holding the tetrapeptide Gly-Phe-Leu-Gly.[18] The resulting peptide conjugates have been successfully used in drug delivery strategies.[19-24]

Recently, we identified KKLFKKILKKL-NH_2 (**BP16**) from a library of antimicrobial undecapeptides as a novel CPP. **BP16** efficiently internalizes into cancer cells mainly through a clathrin-dependent endocytic mechanism and is an excellent vector for the intracellular delivery of the DNA-alkylating drug chlorambucil (CLB), improving its cytotoxic effect against cancer cells (IC_{50} of 8.7 to 25.5 μM).[25] Besides, the incorporation of the cleavable spacer Gly-Phe-Leu-Gly in CLB-BP16 conjugates allows the selective release of CLB leading to a further increase of the efficacy of this drug (IC_{50} of 3.6 to 16.2 μM).[24] Moreover, the efficacy of CLB was improved irrespective of the peptide end into which it was incorporated. Thus, this study showed the usefulness of **BP16** as a delivery system of CLB in cancer cells and paved the way for its potential application to transport other therapeutic agents.

One of our recent research lines is devoted to investigate the use of transition metal complexes in anticancer treatments. Metal complexes can interfere in cellular redox chemistry through metal or ligand redox centers. Furthermore, targeting the redox balance in cancer cells might promote irreversible damage through reactive oxygen species (ROS)-mediated

mechanisms.[26-29] In this context, nitrogen rich tetradentate aminoyridine ligands 1,4-dimethyl-7-(2-pyridylmethyl)- 1,4,7-triazacyclononane (^{Me2}PyTACN) and (2*S*,2*S'*)-1,1'-bis(pyrid-2-ylmethyl)-2,2'-bipyrrolidine ((*S*,*S'*)-BPBP) and their transition metal complexes have been recently described as excellent catalysts for several oxidation reactions on a wide substrate scope.[30-38] Interestingly, these redox-active transition metal complexes have been successfully conjugated to a cationic tetrapeptide using solid-phase peptide synthesis (SPPS) and the resulting conjugates have been characterized by NMR, HRMS (ESI) and UV-VIS.[39] This stepwise solid-phase synthetic strategy was optimized, constituting a versatile approach to obtain a wide variety of metal binding peptide conjugates. In addition, recently, it has been demonstrated that ^{Me2}PyTACN and (*S*,*S'*)-BPBP ligands are able to chelate the labile iron pool in cancer cells and that the resulting redox-active moieties promote apoptosis *via* iron-dependent prooxidant mechanisms.[40] Therefore, the intracellular delivery of ^{Me2}PyTACN and (*S*,*S'*)-BPBP ligands into cancer cells could constitute an effective approach to obtain a promising anticancer agent.

Based on the above considerations, we envisaged that the conjugation of a ^{Me2}PyTACN or a (*S*,*S'*)-BPBP ligand to a CPP, such as **BP16**, could enhance their cellular uptake improving their biological activity. In this study, we report the solid-phase synthesis of **BP16** conjugates incorporating a ^{Me2}PyTACN or a (*S*,*S'*)-BPBP ligand at either the N- or the C-terminus. Considering the clathrin-dependent endocytic mechanism of **BP16**, metal binding peptide conjugates bearing the ligand and the enzymatic cleavable tetrapeptide Gly-Phe-Leu-Gly at both ends of **BP16** were also prepared. The cytotoxicity of all these sequences was evaluated in cancer and healthy cell lines. In addition, the internalization of the corresponding 5(6)-carboxyfluorescein-labeled metal binding peptides was examined by flow cytometry. Finally, the ligand release from the metal binding peptides incorporating the tetrapeptide Gly-Phe-Leu-Gly was evaluated by cathepsin B enzymatic digestion.

VI.2. Experimental Section

VI.2.1. Materials and Methods

Unless otherwise stated, common chemicals and solvents (HPLC-grade or reagent-grade quality) were purchased from commercial sources and used without further purification. The 9-fluorenylmethoxycarbonyl (Fmoc) derivatives and Fmoc-Rink-4-methylbenzhydrylamine (MBHA) resin (0.56 mmol/g) were obtained from Senn Chemicals International (Gentilly, France), NovaBiochem (Schwalbach, Germany) or IRIS Biotech GmbH (Marktredwitz, Germany). Ethyl 2-cyano-2-(hydroxyimino)acetate (Oxyma) and 1-[(1-(Cyano-2-ethoxy-2-oxoethylideneaminooxy)

CHAPTER VII

BPBP-PNA conjugate as metal-free artificial nuclease for oncogenic miRNAs targeting

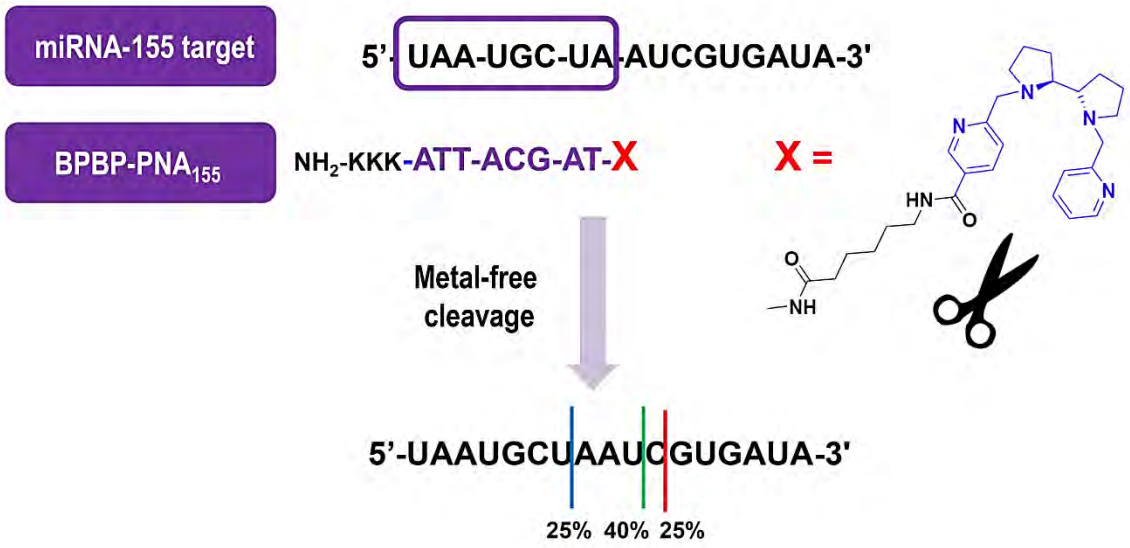

This chapter corresponds to a manuscript in preparation:

Marta Soler, Dennis Worm, Anna M. Sosniak, Britta Redeker, Stephen A. Hahn, Lidia Feliu, Marta Planas, Nils Metzler-Nolte, Xavi Ribas, Miquel Costas. BPBP-PNA conjugate as metal-free artificial nuclease for oncogenic miRNAs targeting. *In preparation*

For this work, M. S. performed the design, the synthesis and the characterization of all the conjugates. Moreover, M. S. performed some of the RNA cleavage experiments. Finally, M. S. was involved in argumentations and discussions, and wrote the manuscript draft.

VII.1. Introduction

The development of synthetic small molecules that interact with target gene sequences has attracted interest in medicinal, drug development and molecular biology fields.[1] The application of gene-targeted therapeutics as molecular tools holds a great approach for the modulation of gene expression. Within this context, DNA:RNA hybridization represents one of the most challenging goals to interfere with the transcription (antigene) or translational (antisense) cellular processes. Particularly, peptide nucleic acids (PNA) originally developed by Nielsen and coworkers, have been extensively described in molecular design to be used as nucleic acid-targeting therapeutics.[2-6] PNA are DNA analogues, in which a 2-aminoethyl-glycine units substitutes the common sugar-phosphate backbone and a methyl carbonyl linker connects the nucleobases to this backbone at the amino nitrogens. Despite of these modifications from natural nucleic acids, PNA oligomers have the ability to recognize DNA as well as RNA in a sequence-specific way obeying the Watson-Crick hydrogen bonding rules.[7-9] Due to their excellent properties in terms of hybridization, protease resistance and chemical stability, PNA oligomers have been involved in the design of new gene modulators with high-specific sequence recognition for several biotechnological applications.[10-12]

In the antisense approach for RNA targeting,[13-16] PNAs have been recently described as oligonucleotides able to selective recognize miRNAs.[1,17-20] MiRNAs are short single-stranded noncoding RNAs that regulate the gene expression of specific mRNA during the translational process by binding to the 3' untranslated regions (3'-UTR).[21-25] The activity of miRNAs plays a key role in cellular homeostasis and is involved in a large range of human diseases that include cardiovascular pathologies, diabetes, Alzheimer and specially cancer.[26] The clinical potential of targeting miRNAs is focused on the fact that a single miRNA regulate multiple oncogenic pathways that are usually deregulated in cancer. Their interaction with mRNAs leads to the regulation of very important biological process such as proliferation, differentiation, cell fate determination, cell cycle and apoptosis.[27] On the basis of these precedents, modulation of miRNA expression levels has emerged as key research interest for novel therapeutic strategies against cancer.[28-32]

Although the targeting of miRNA function is already under consideration in current clinical trials, new antisense oligonucleotides are required to be studied *in vitro* and *in vivo* as therapeutic approaches in miRNA-based therapy.[30,33-35] In particular, the functional activity of only a handful miRNAs such as miRNA-122, miRNA-155, miRNA-210 or miRNA-372 has been experimentally modeled in pancreatic cancer.[17,36-38] Considering the therapeutic potential towards miRNAs, current challenges in pancreatic cancer aim to study novel PNA-like oligonucleotides that comprehend

different properties to accomplish a specific inhibition of gene expression.[39] Within this context, the design of efficient sequence-selective artificial nucleases renders an opportunity to combine cleavage agents with site-specific RNA recognition systems.[40,41] A number of strategies focused on the development of efficient synthetic nucleases that act as RNA cleavage agents have been reported.[42-44] Intensive studies performed in this field provide better understanding in the RNA cleavage chemistry as well as a correlation with the activity exhibited by natural RNAzymes.[45-47] In this fashion, to date almost of the artificial nucleases described are based on synthetic metallonucleases where metal complexes are able to act as catalytic entities with rate accelerations similar to those of enzymes.[48-51] Nevertheless, metal-free artificial nucleases have recently attracted attention due to their effective capacity to cleave DNA or RNA in a hydrolytic way.[52-54] Although their cleavage activities usually require higher concentration in comparison with metallonucleases, the absence of redox-active metal ions such as Cu(II) offers an attractive alternative that avoid uncontrolled redox reactions and additional toxicities resulted from metal excesses.[55-57]

Herein, we report a metal-free artificial nuclease based on aminopyridine molecule-modified PNA. This is a highly basic structure that forms stable coordination compounds when associated with transition metal ions. It was envisioned that its basicity will serve to engage in nucleophilic reactions. Also, its ability to bind metal ions makes it attractive for delivering reactive metal-based species with site-selectivity. We have focused our attention on the targeting of miRNA-155 and miRNA-135b, which are overexpressed in many pancreatic cancers cell lines and proposed to be oncogenic miRNAs (onco-miRNA).[39,58-60] Our synthetic approach required the preparation by means of solid-phase synthesis of two short PNA recognition sequences that are meant to target the above-mentioned miRNAs. The conjugation of (2*S*,2*S*')-1,1'-bis(pyrid-2-ylmethyl)-2,2'-bipyrrolidine ((*S*,*S*')-BPBP) ligand on the solid support was optimized by using different coupling conditions and the resulting conjugates were purified by RP-HPLC. Moreover, 5(6)-carboxyfluorescein dye was also attached at this position in order to study the uptake of the BPBP-PNA oligomer in cell culture. Their identities were further confirmed by high resolution mass spectra (HRMS). The **BPBP-PNA$_{155}$** was tested for its ability to hydrolyze the miRNA-155 2-18 (5'-UAAUGCUAAUCGUGAUA-3'). IE-HPLC and MALDI-TOF analyses allowed the identification of the main cleavage sites and the resulting RNA cleavage fragments. To obtain a preliminary uptake profile of the BPBP-based nuclease design, **CF-PNA$_{155}$** was transfected into targeted pancreatic cancer cell lines (IMIM-PC2, PancTul and PT45), in which miRNA-155 is overexpressed. FACS

CHAPTER VIII

General Discussion

VIII. GENERAL DISCUSSION

Since drug administration is hampered by different physiological barriers, the development of novel delivery systems has attracted interest in the last decades.[1,2] Among different drug delivery approaches, the use of CPP-based delivery systems has been reported to enhance drug permeability, stability and solubility in anticancer therapies.[3,4] Moreover, taking advantage of the intracellular stimuli systems, several efforts have been devoted to the identification of prodrug strategies as efficient rational designs. Indeed, interesting examples of controlled drug-release systems incorporating CPPs have been described.[5–8] Therefore, the identification of novel non-toxic CPP sequences renders the opportunity to explore new drug conjugation strategies based on smart drug delivery systems.

On the other hand, medicinal inorganic chemistry is a discipline of growing significance in both therapeutic and diagnostic medicine.[9–11] Particularly, redox-active metal complexes and metal binding compounds are emerging as potential anticancer agents due to rich reactivity.[12–14] Within this context, metal-based drugs have been suggested to target biochemical alterations in cancer cells. In particular, since the alteration of redox environment through ROS species is directly correlated with oncogenic and metabolic dysregulations,[15,16] pro-oxidant strategies are considered as emerging anticancer therapies due to their involvement in apoptosis and necrosis.[17]

This PhD thesis deals with the development of an efficient CPP-based delivery system for the vectorization of N_4-based ligands into cancer cells. Bearing in mind this objective, in the first part of the thesis (Chapters III and IV) we have studied the identification of a new non-toxic cell-penetrating sequence and its applicability in smart drug delivery approaches. Next, in Chapters V, VI and VII a straightforward methodology to conjugate tetradentate aminopyridine ligands to peptide derivatives has been developed. The cytotoxicity, the cellular uptake and the intracellular drug release have been explored.

VIII.1. Identification of a non-toxic cell-penetrating peptide (CPP)

CPPs have emerged as efficient vectors to deliver different types of cargoes into the cell. Therefore, the search for new non-toxic peptide sequences has attracted attention in medicinal chemistry.[18] In recent years, several antimicrobial peptides (AMPs) have been reported to display cell-penetrating properties. AMPs share structural features with CPPs in terms of charge, amphipathicity and length.[19] Moreover, it has been reported that they can translocate into the cells. Thus, AMPs can be considered as an interesting source of non-cytotoxic drug delivery vectors.

With the aim of identifying new CPPs, we have evaluated the cell-penetrating ability of sequences from a 125-member library of AMPs (CECMEL11), previously designed to be used in plant protection.[20] Five peptides (**BP16**, **BP76**, **BP81**, **BP100** and **BP105**) have been selected based on their distinct antibacterial activity against several plant pathogens and their distinct hemolysis profile (Table VIII.1). Moreover, the arginine-rich peptides **BP307** and **BP308**, derived from **BP100** and **BP16**, respectively, have also been included in this study. These two last sequences have been considered because most common CPPs such as Tat or penetratin are arginine-rich peptides, and it is well-known that this residue is crucial for the peptide internalization levels as well as for their uptake mechanism through the lipid bilayer membrane.[21] Furthermore, **BP16** and **BP308** have been labeled with 5(6)-carboxyfluorescein by coupling this fluorophore to the N-terminus, leading to **CF-BP16** and **CF-BP308**.

These peptides have been manually synthesized on a Fmoc-Rink-MBHA resin or on an aminomethyl ChemMatrix resin following a standard Fmoc/*t*Bu strategy and have been obtained as C-terminal amides in excellent purities (87-100%), as determined by analytical HPLC. Their identities have been confirmed by ESI-MS and HRMS (Table III.1)

Table VIII.1. Peptide sequences and notation.

Peptide	Sequence[a]
BP16	KKLFKKILKKL
BP76	KKLFKKILKFL
BP81	LKLFKKILKFL
BP100	KKLFKKILKYL
BP105	LKLFKKILKYL
BP307	RRLFRRILRYL
BP308	RRLFRRILRRL
CF-BP16	CF- KKLFKKILKKL
CF-BP308	CF- RRLFRRILRRL

[a]All peptides are C-terminal amides.

Cytotoxicity assays have demonstrated that **BP16** and **BP308** display no cytotoxic effects against MCF-7, CAPAN-1 and 3T3 cell lines, and are non-hemolytic, even at high concentrations (see Table III.2). Moreover, as shown in Figure IV.1, **CF-BP16** and **CF-BP308** display the same cellular uptake properties in a time-dependent manner. Although it would be expected that **BP308**

could have mitochondria-targeting properties, by confocal studies we have observed that both labeled-peptides remain throughout the cytoplasm without any organelle localization (see Figure IV.2). Despite both CPPs do not have specific organelle-targeting properties, these potential uptake characteristics allow the involvement of **BP16** and **BP308** in drug delivery approaches. Interestingly, **CF-BP16** has shown the same mean fluorescence intensity values than **CF-Tat$_{49}$** as observed by flow cytometry studies (see Figure III.2). In addition, using confocal microscopy studies we have demonstrated that **BP16** is mainly internalized into the cells through a clathrin dependent endocytosis and that it efficiently accumulates in the cell cytoplasm (see Figure III.3, III.4, III.5 and VIII.1).

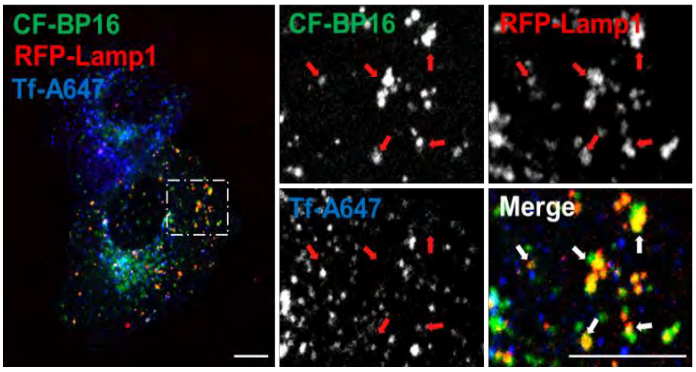

Figure VIII.1. Confocal studies that confirm the endocytic degradation pathway of **BP16**.

Based on these results, the capacity of **BP16** and **BP308** to transport the anticancer drug chlorambucil (CLB) into the cells has been explored. Towards this aim, we have investigated the influence on the cytotoxicity and on the cellular uptake of conjugating CLB at the N- or the C-terminal end of these undecapeptides (see Table VIII.2). Thus, conjugates **BP325** (CLB-BP16), **BP331** (BP16-CLB), **BP334** (CLB-BP308), and **BP335** (BP308-CLB) have been prepared. Moreover, the tetrapeptide Gly-Phe-Leu-Gly, which is cathepsin-B sensitive sequence, has been incorporated at both N- and C-terminal ends of these CLB-conjugates, leading to **BP332** (CLB-GFLG-BP16), **BP333** (BP16-GLFG-CLB), **BP336** (CLB-GFLG-BP308) and **BP337** (BP308-GLFG-CLB). In order to evaluate the cellular uptake of these conjugates, 5(6)-carboxyfluorescein has been attached to these sequences resulting in conjugates **BP326** (CLB-BP16-CF), **BP338** (CF-BP16-CLB), **BP339** (CLB-BP308-CF) and **BP340** (CF-BP308-CLB). For the sequences bearing CLB, CF or GLFG-CLB at the C-terminus, these moieties have been incorporated at the side-chain of an additional Lys residue present at this position. To allow the selective derivatization of this residue, Fmoc-Lys(Dde)-OH has been employed. This Lys residue provides an anchoring point for these moieties without affecting the cationic charge of the parent peptide. On the other hand, in

order to confer cancer cell selectivity to CLB-BP16, the homing peptide CREKA has been incorporated to this conjugate leading to conjugate **BP329** (CLB-CREKA-BP16). CLB-CREKA and **BP327** (CREKA-BP16) have been included in the study for comparison purposes.

These peptides have been manually synthesized on a Fmoc-Rink-MBHA resin or on an aminomethyl ChemMatrix resin following a standard Fmoc/*t*Bu strategy. Peptides have been obtained as C-terminal amides in excellent purities (81-100%), as determined by analytical HPLC. Their identities have been confirmed by ESI-MS and/or HRMS.

Table VIII.2. Sequences and notation of **BP16** and **BP308** conjugates.

Peptide	Sequence[a]	Notation
	CREKA	CREKA
	CLB-CREKA	CLB-CREKA
	CF-CREKA	CF-CREKA
BP327	CREKA-KKLFKKILKKL	CREKA-BP16
BP328	CF- CREKA-KKLFKKILKKL	CF-CREKA-BP16
BP325	CLB-KKLFKKILKKL	CLB-BP16
BP329	CLB-CREKA- KKLFKKILKKL	CLB-CREKA-BP16
BP330	CLB-CREKA-KKLFKKILK(CF)KL	CLB-CREKA-BP16(CF)
BP331	Ac-KKLFKKILKKLK(CLB)	BP16-CLB
BP332	CLB-GFLG-KKLFKKILKKL	CLB-GFLG-BP16
BP333	Ac-KKLFKKILKKLK(GLFG-CLB)	BP16-GLFG-CLB
BP334	CLB-RRLFRRILRRL	CLB-BP308
BP335	Ac-RRLFRRILRRLK(CLB)	BP308-CLB
BP336	CLB-GFLG-RRLFRRILRRL	CLB-GFLG-BP308
BP337	Ac-RRLFRRILRRLK(GLFG-CLB)	BP308-GLFG-CLB
BP326	CLB-KKLFKKILK(CF)KL	CLB-BP16-CF
BP338	CF-KKLFKKILKKLK(CLB)	CF-BP16-CLB
BP339	CLB-RRLFRRILRRLK(CF)	CLB-BP308-CF
BP340	CF-RRLFRRILRRLK(CLB)	CF-BP308-CLB

[a]All peptides are C-terminal amides.

While CLB alone is not active (IC_{50} of 73.7 to >100 μM), cytotoxicity assays have shown that the efficacy of the drug increases when conjugated to either the N- or C-terminus of **BP16** (**BP325** and **BP331**, respectively), being dramatically more effective (see Table IV.2). In the case of **BP308**, this increase of efficacy has been only observed for the N-terminal conjugate **BP334**, showing excellent results similar to that of its analogue **BP325**. The resulting conjugates have shown cytotoxic activity against CAPAN-1, MCF-7, PC-3, 1BR3G and SKMEL-28 cell lines with IC_{50} values ranging from 8.7 to 25.5 μM. Notably, the efficacy of the drug also increases between 2 and 4.5 times when attached to the CREKA-BP16 derivative against MCF-7, CAPAN-1 and 3T3 cells (IC_{50} values ranging from 33 to 35.2 μM cells). Unfortunately, conjugate **BP329** (CLB-CREKA-BP16) has not shown selectivity against cancer cells.

The internalization properties of 5(6)-carboxyfluorescein-labeled CLB-BP16 and CLB-BP308 conjugates are in agreement with the cytotoxic results described above as shown by flow cytometry (see Figure IV.3). Hence, the high cytotoxicity displayed by **BP325** (CLB-BP16), **BP331** (BP16-CLB) and **BP334** (CLB-BP308) is attributed to their high internalization properties whereas **BP335** is not cytotoxic and shows a poor cellular uptake. Thus, these results emphasize that the position of the cargo in a CPP sequence could have significant influence in terms of cytotoxicity and/or cellular uptake. Moreover, we have confirmed that the cell-penetrating properties of **BP16** in MCF-7 cancer cells are retained after conjugating it to the breast tumor homing peptide CREKA (**BP328**, CF-CREKA-BP16) and to CLB and CREKA (**BP330**, CLB-CREKA-BP16-CF) (see Figure III.6). Therefore, **BP16** is able to internalize both CLB and CREKA.

The presence of the cleavable GFLG peptide further increased the efficacy of CLB in CLB-BP16 conjugates (IC_{50} of 3.6 to 16.2 μM against CAPAN-1, MCF-7, PC-3, 1BR3G and SKMEL-28 cell lines), while this improvement has not been observed for CLB-GFLG-BP308 conjugates. Taking into account that **BP16** follows the degradation pathway and might be trapped in late endosomes, the enhanced cytotoxic activity of the CLB-BP16 conjugates can be associated to the selective release of CLB in the lysosomal compartment. To prove this intracellular drug release, enzymatic assays with cathepsin B have demonstrated the release of CLB-Gly-OH as main fragment from the sequence within a short time (see Figures IV.4 and VIII.2).

In sum, these data confirm the identification of **BP16** as a novel non-cytotoxic CPP, which internalizes into the cell cytoplasm by clathrin-mediated endocytosis. Very interestingly, **BP16** is able to enhance the cellular uptake of CLB while improving its cytotoxic activity against cancer

cells. Furthermore, the combination of **BP16** with an enzymatic cleavable sequence can be used as a smart drug delivery system for the effective uptake and release of drugs in cancer cells.

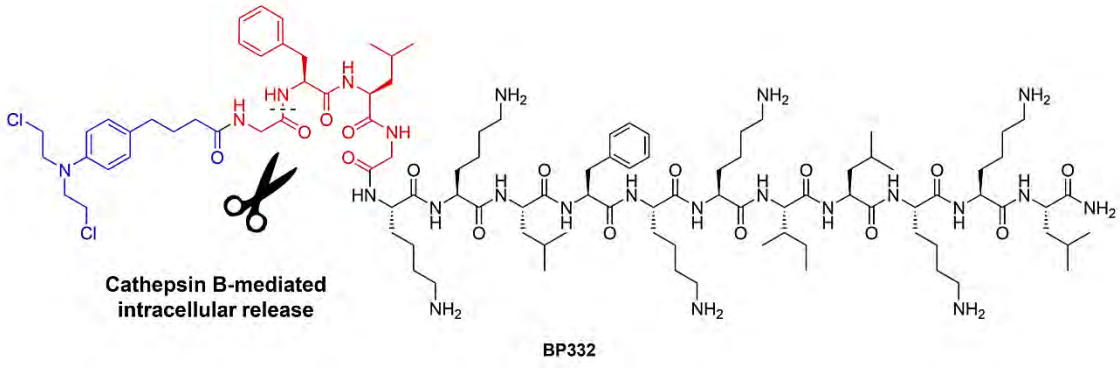

Figure VIII.2. Schematic representation of the enzymatic release of chlorambucil from **BP332** conjugate.

VIII.2. Enhanced and selective DNA cleavage activity of redox-active metallopeptides based on tetradentate aminopyridine ligands

The design of functional redox-active metallopeptides has gained enormous interest in recent years. Among different bioinorganic applications, challenges remain in achieving specific-DNA targeting by peptide-based nucleases.[22,23] Moreover, design strategy and synthetic preparation usually limit the contributions in this area. To overcome these restrictions, effective methodologies need to be addressed in order to prepare redox-active metallopeptides in a straightforward way.

In Chapter V we have investigated the conjugation of ^{Me2}PyTACN and (*S,S'*)-BPBP ligands to a cationic tetrapeptide. These metal complexes have been described as excellent catalysts for a wide range of oxidation reactions, operating under mild experimental conditions.[24–27] On the other hand, the recognition specificity towards DNA of positively charged tetrapeptides has been reported.[28,29] Therefore, we have developed a straightforward methodology to obtain redox-active metallotetrapeptides in order to explore their chemical nuclease activity.

The synthesis of the redox-active metallotetrapeptides of general structure $\mathbf{1_M}$ and $\mathbf{2_M}$, has been extensively optimized by means of solid-phase synthesis (Scheme VIII.1). The synthetic strategy has involved the preparation of the metal binding peptides **3** and **4**. Their synthesis was planned by attachment of the nicotinyl derivative **5** to the N-terminus of the tetrapeptidyl resin **6a**,

TBS group removal, chlorination, alkylation with the corresponding secondary amine **7** or **8** and final acidolytic cleavage.

Following this protocol, the use of an MBHA resin has provided better results for the synthesis of both metal binding peptides than the use of ChemMatrix resin. The conjugation of **5** to the peptidyl resin **6a** and the N-alkylation of resin **12a** with secondary amine **7** have been optimized under conventional heating and under microwave irradiation (Scheme VIII.1). The synthesis of metal binding peptide **4** has been achieved using the optimized conditions. In contrast, following this strategy, the metal binding peptide **3** was obtained together with a non-identified by-product. An alternative route which involves the direct coupling of the nicotinic acid derivative **14** to the tetrapeptidyl resin **6a** has been established (Scheme VIII.1).

Next, metallation of **3** and **4** has been studied. First, the metallation of **3** as TFA salt has been attempted by treatment with $Zn(OTf)_2$ in DPBS (pH = 7.0-7.3) or in $Na_2CO_3/NaHCO_3$ (pH = 9.8) buffers at different reaction temperatures. Unfortunately, both attempts have failed to give the expected metallopeptide. Next, basification assays to remove TFA counterions have been carried out using 100 mM NaOH solution (pH 11-12) followed by extraction with $CHCl_3$ or by column chromatography eluting with $CH_2Cl_2/CH_3OH/NH_3$. The success of both procedures has been analyzed by ^{19}F-NMR. The basification by column chromatography has been the best procedure for the isolation of the pure amine ligand. Henceforth, it has also been used to yield free amine metal binding peptide **4**. Both conjugates have been obtained in good purities as determined by analytical HPLC, ESI-MS, HRMS and ^{1}H-NMR spectroscopy.

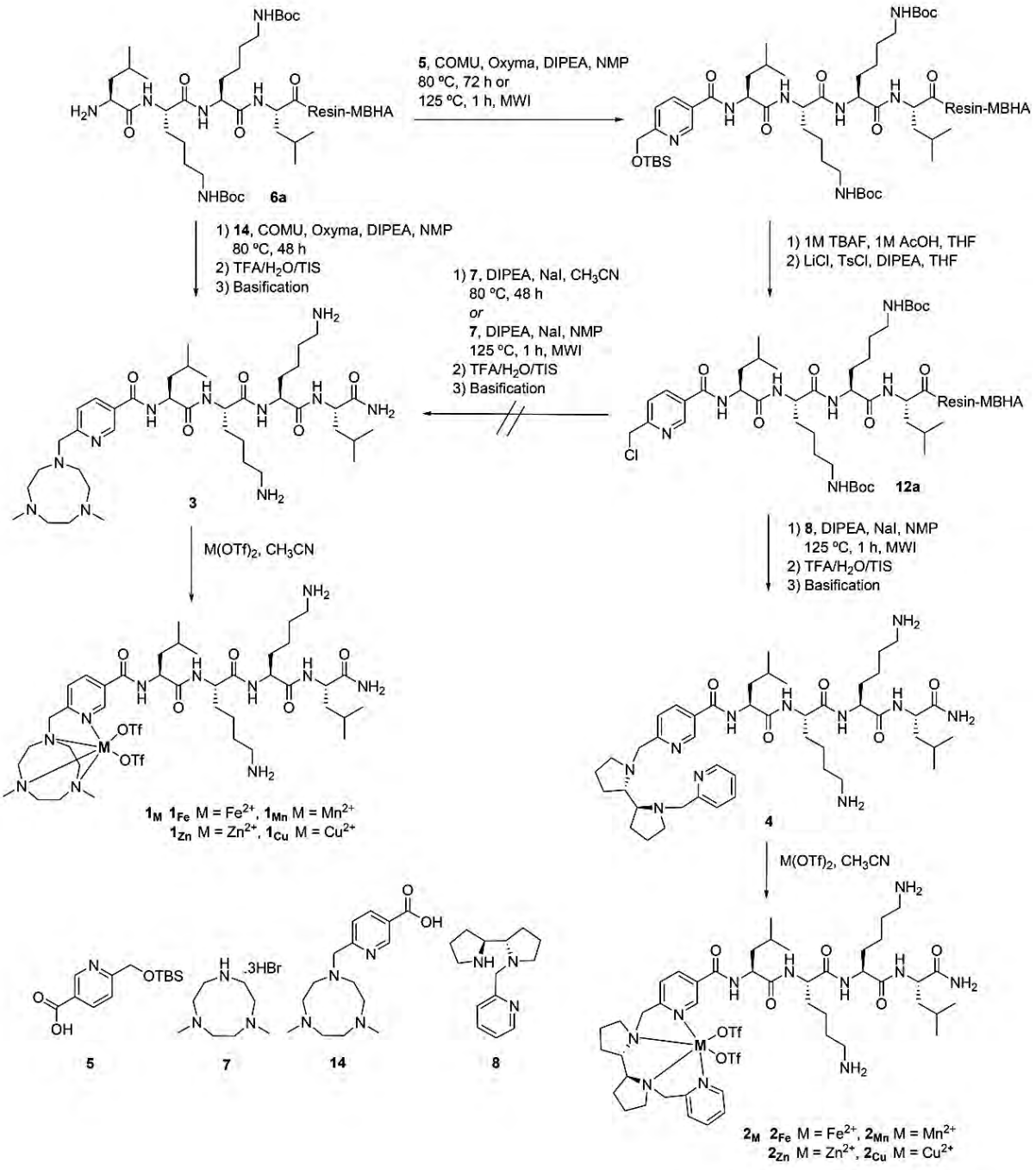

Scheme VIII.1. Synthetic strategy for the preparation of the redox-active metallotetrapeptides $\mathbf{1_M}$ and $\mathbf{2_M}$.

Metallation of ^{Me2}PyTACN and (*S,S'*)-BPBP peptide conjugates **3** and **4** with metal triflates salts (iron, manganese, zinc and copper ions) has been performed in solution. Subsequent filtration and precipitation with diethyl ether yielded metallotetrapeptides $\mathbf{1_M}$ and $\mathbf{2_M}$ as powders which were characterized by HRMS. The stoichiometry of the reaction between metal binding peptides **3** and **4** and Cu(II) has been studied by performing UV-visible spectrophotometric titrations. Since their maximum of absorbance have been accomplished after the addition of one equivalent of $Cu(OTf)_2$,

Job plots of absorbance at λ_{max} of each titration vs the mole fraction of conjugates **3** and **4** have confirmed the 1:1 complexation stoichiometries. Moreover, additional titrations of the Fmoc deprotected tetrapeptide with $Cu(OTf)_2$ have evidenced that Lys side chains are excluded from metal coordination and the chelations. Binding of Zn(II) to the metal binding peptides **3** and **4** to form $\mathbf{1_{Zn}}$ and $\mathbf{2_{Zn}}$ have been also settled by ^{1}H-NMR spectrum, indicating that the signals corresponding to the pyridine moieties downshift after the addition of one equivalent of one $Zn(OTf)_2$. Moreover, metallopeptides $\mathbf{1_{Fe}}$ and $\mathbf{2_{Fe}}$ have also been studied by ^{1}H-NMR spectroscopy. Interestingly, the iron(II) center in $\mathbf{1_{Fe}}$ is in a low spin state in acetonitrile, with a minor contribution from the high spin state. In contrast, the iron(II) center in $\mathbf{2_{Fe}}$ is in high spin configuration as ascertained by the very broad signals in its ^{1}H-NMR spectrum that expanded up to 190 ppm as a result of a paramagnetic shift. These behaviours have been directly compared with the ones observed by the parent iron complexes of both tetradentate ligands.

Next, the DNA cleavage activity of different metallopeptides has been evaluated and compared to metal binding conjugates as well as to the parent ligands and complexes using gel electrophoresis technique. Both tetradentate ligands and conjugates **3** and **4** are able to moderately interact with the supercoiled DNA (Form I) at moderate concentrations and short reaction times (50 μM, 1 h) (see Figure V.10). The same results are obtained when Zn^{2+} and Cu^{2+} metal ions are added in the assays. Remarkably, the addition of sodium L-ascorbate (Asc) as reducing agent in Cu^{2+} complexes of both series promotes the total conversion of supercoiled DNA (Form I) to the nicked form (Form II) followed by smeared bands due to the DNA fragmentation (Figure V.10A lane 9 and 10, Figure VI.10B lane 9 and 10). In Figure VIII.3, the results clearly prove that the efficiency of the oxidative mechanism by Cu(PyTACN) and Cu(BPBP) is improved once attached to the LKKL peptide sequence ($\mathbf{1_{Cu}}$ and $\mathbf{2_{Cu}}$) at low micromolar range (25 and 15 μM, Figure VIII.3 lane 3, 5, 9 and11). Moreover, the oxidative cleavage mechanism by Cu(BPBP) and $\mathbf{2_{Cu}}$ have been employed to determine the main ROS species. As depicted in Figure V.14, both oxidative systems generate ROS species, suggesting that superoxide radical (O_2^{-}) and singlet oxygen ($^1O_2$) could be predominantly implicated in both mechanisms.

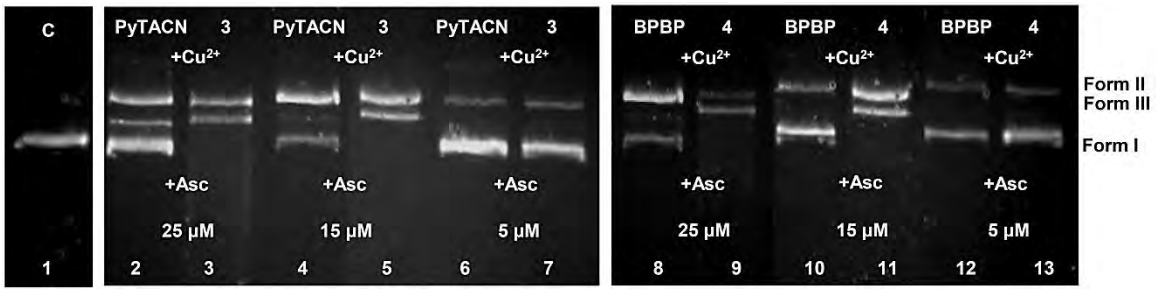

Figure VIII.3. Representative comparative assays of pUC18 DNA (18.9 µM (bp)) incubated with **PyTACN**, **BPBP**, **3** and **4** at different concentrations in Cacodylate buffer (0.1 M, pH 6) at 37 ºC for 1 h. Cu^{2+} was added in a 1:1 (M:L) ratio. C = DNA control. Asc = Sodium L-Ascorbate.

Further cleavage experiments have been performed in the presence of major groove and minor groove DNA inhibitors for Cu(BPBP) and $\mathbf{2_{Cu}}$ (Figure VIII.4). While nuclease activity of Cu(BPBP) complex is partially inhibited in both cases, the presence of Hoechst induces a complete inhibition of the nuclease activity provided by $\mathbf{2_{Cu}}$, suggesting that this conjugate could preferentially interact into the DNA minor groove (Figure VIII.4 lane 3 and 4). Hence, this apparent selective interaction in this region could be associated to the minor-groove orientation induced by cationic LKKL sequence.

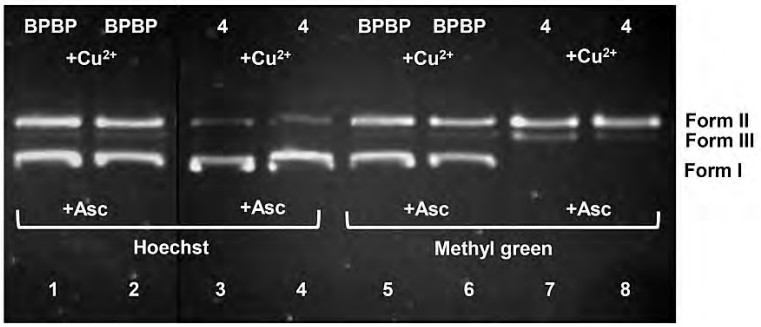

Figure VIII.4. Agarose gel images of pUC18 DNA (18.9 µM (bp)) incubating **BPBP** (50 µM) and **4** (15 µM) in the presence of DNA minor groove inhibitor Hoechst (20 µM) and major groove inhibitor Methyl green (20 µM) in Cacodylate buffer (0.1 M, pH 6) at 37 ºC for 1 h. Cu^{2+} was added in a 1:1 (M:L) ratio. C = DNA control. Asc = Sodium L-Ascorbate.

On the whole, the developed synthetic methodology renders the preparation of redox-active metallotetrapeptides with potential nuclease activities at very low concentrations. In addition, the presence of positively charged lysines within the peptide scaffold could induce a minor-groove orientation of the resulting conjugate. Consequently, the improved DNA cleavage observed for $\mathbf{1_{Cu}}$ and $\mathbf{2_{Cu}}$ under reducing conditions might be attributed to an enhanced DNA binding.

VIII.3. Delivering aminopyridine ligands into cancer cells through conjugation to the cell-penetrating peptide BP16

In Chapters III and IV we have shown that **BP16** is an efficient CPP to internalize the anticancer drug CLB. On the other hand, a straightforward solid-phase methodology to prepare metal binding peptide conjugates based on tetradentate aminopyridine ligands has been developed in Chapter V. Based on the above findings, in Chapter VI we have explored the feasibility to conjugate ^{Me2}PyTACN and (*S*,*S'*)-BPBP ligands to the **BP16**. Considering that the iron complexes containing these ligands produce apoptosis by metal-induced oxidative stress,[30] the intracellular delivery of these aminopyridine ligands have been studied in view of their potential application in anticancer treatment.

The peptide conjugates have been designed by incorporating the ^{Me2}PyTACN or the (*S*,*S'*)-BPBP ligand at either the N- or the C-terminal end of **BP16** leading to PyTACN-BP16 (**BP341**), BP16-PyTACN (**BP342**), BPBP-BP16 (**BP343**) and BP16-BPBP (**BP344**) (see Figure VI.1 and Table VIII.3). Furthermore, we have also synthesized metal binding peptides bearing at the N-terminus an additional Lys, a β-Ala and the corresponding ligand (PyTACN-βAK-BP16 (**BP345**) and BPBP-βAK-BP16 (**BP346**)). Moreover, the cathepsin B cleavable sequence Gly-Phe-Leu-Gly has been incorporated on the sequences BPBP-BP16 (**BP343**) and BP16-BPBP (**BP344**), rendering peptide conjugates BPBP-GFLG-BP16 (**BP347**) and BP16-GLFG-BPBP (**BP348**), respectively. To study the internalization properties of the N-terminal metal binding peptides **BP346** and **BP347**, 5(6)-carboxyfluorescein (CF) moiety has been incorporated on these sequences leading to compounds BPBP-βAK(CF)-BP16 (**BP349**) and BPBP-GFLG-BP16-CF (**BP350**), respectively. In derivatives **BP342**, **BP344**, **BP348** and **BP350** the ligands ^{Me2}PyTACN or (*S*,*S'*)-BPBP, the GLFG-BPBP or the CF moieties, respectively, have been conjugated to the N^{ε}-amino group of an additional C-terminal Lys residue.

These peptides have been manually synthesized on a Fmoc-Rink-MBHA resin following a standard Fmoc/*t*Bu strategy. The conjugation of the ^{Me2}PyTACN or the (*S*,*S'*)-BPBP ligand in conjugates **BP341**-**BP346** has been accomplished following the stepwise solid-phase synthetic protocol previously described for the preparation of metal binding tetrapeptides (see Schemes VI.1 and VI.4). This protocol is based on the attachment of the 2-pyridylmethylene moiety and the subsequent derivatization on the solid support to incorporate the corresponding secondary amine to the peptide backbone. For the incorporation of (*S*,*S'*)-BPBP ligand in conjugates **BP347**-**BP350,** the

(*S,S'*)-BPBP carboxylic acid derivative, properly prepared in solution (Scheme VI.2), has been directly conjugated to the corresponding peptidyl resin (see Schemes VI.3, VI.5 and VI.6). All the metal binding peptides have been obtained as C-terminal amides in excellent purities, as determined by analytical HPLC and HRMS.

Table VIII.3. Peptide sequences and notation of the ^{Me2}PyTACN and (*S,S'*)-BPBP-BP16 conjugates.

Peptide	Sequence[a]	Notation
BP341	^{Me2}PyTACN-KKLFKKILKKL	PyTACN-BP16
BP342	Ac-KKLFKKILKKLK(^{Me2}PyTACN)	BP16-PyTACN
BP343	(*S,S'*)-BPBP-KKLFKKILKKL	BPBP-BP16
BP344	Ac-KKLFKKILKKLK((*S,S'*)-BPBP)	BP16-BPBP
BP345	^{Me2}PyTACN-βAK-KKLFKKILKKL	PyTACN-βAK-BP16
BP346	(*S,S'*)-BPBP-βAK-KKLFKKILKKL	BPBP-βAK-BP16
BP347	(*S,S'*)-BPBP-GFLG-KKLFKKILKKL	BPBP-GFLG-BP16
BP348	Ac-KKLFKKILKKLK(GLFG-(*S,S'*)-BPBP)	BP16-GLFG-BPBP
BP349	(*S,S'*)-BPBP-βAK(CF)-KKLFKKILKKL	BPBP-βAK(CF)-BP16
BP350	(*S,S'*)-BPBP-GFLG-KKLFKKILKKLK(CF)	BPBP-GFLG-BP16-CF

[a]All peptides are C-terminal amides.

(*S,S'*)-BPBP-based metal binding peptides have displayed higher cytotoxic activity than their ^{Me2}PyTACN analogues against MCF-7, CAPAN-1 and 1BR3G cell lines (see Table VI.1). Moreover, N- and C-terminal derivatives have shown different cytotoxic profiles. While conjugates bearing the ligands at the N-terminus do not display significant activities, the C-terminal ^{Me2}PyTACN and (*S,S'*)-BPBP derivatives show interesting antiproliferative activities. In addition, the introduction of the dipeptide β-Ala-Lys between the cargo and the N-terminus of the **BP16** carrier has significantly reduced the biological activity. As observed in Chapter IV, the incorporation of the cathepsin B cleavable sequence Gly-Phe-Leu-Gly has significantly increased the release of the cargo. Notably, **BP347** (BPBP-GFLG-BP16) and **BP348** (BP16-GLFG-BPBP) conjugates have shown excellent cytotoxic activities with IC_{50} values ranging from 5.0 to 11.7 μM. The best conjugate has been **BP347**, bearing the BPBP-GFLG fragment at the N-terminus of **BP16**, which exhibits high cytotoxic activity against the three cell lines tested (IC_{50} values 4.3-5 μM). The enzymatic degradations of **BP347** and **BP348** with cathepsin B have confirmed that the main cleavage fragments are (*S,S'*)-BPBP-Gly-OH and (*S,S'*)-BPBP-Gly-Phe-OH (see Figure VI.3).

Furthermore, the uptake studies of the CF-labeled conjugate **BP347** (**BP350**, BPBP-GFLG-BP16-CF) has shown high internalization behavior in MCF-7 cells by flow cytometry (see Figure VI.2). These results confirm that the high cytotoxic activity of **BP347** correlates with its high internalization capacity as well as with the subsequent intracellular release of the (*S*,*S'*)-BPBP ligand.

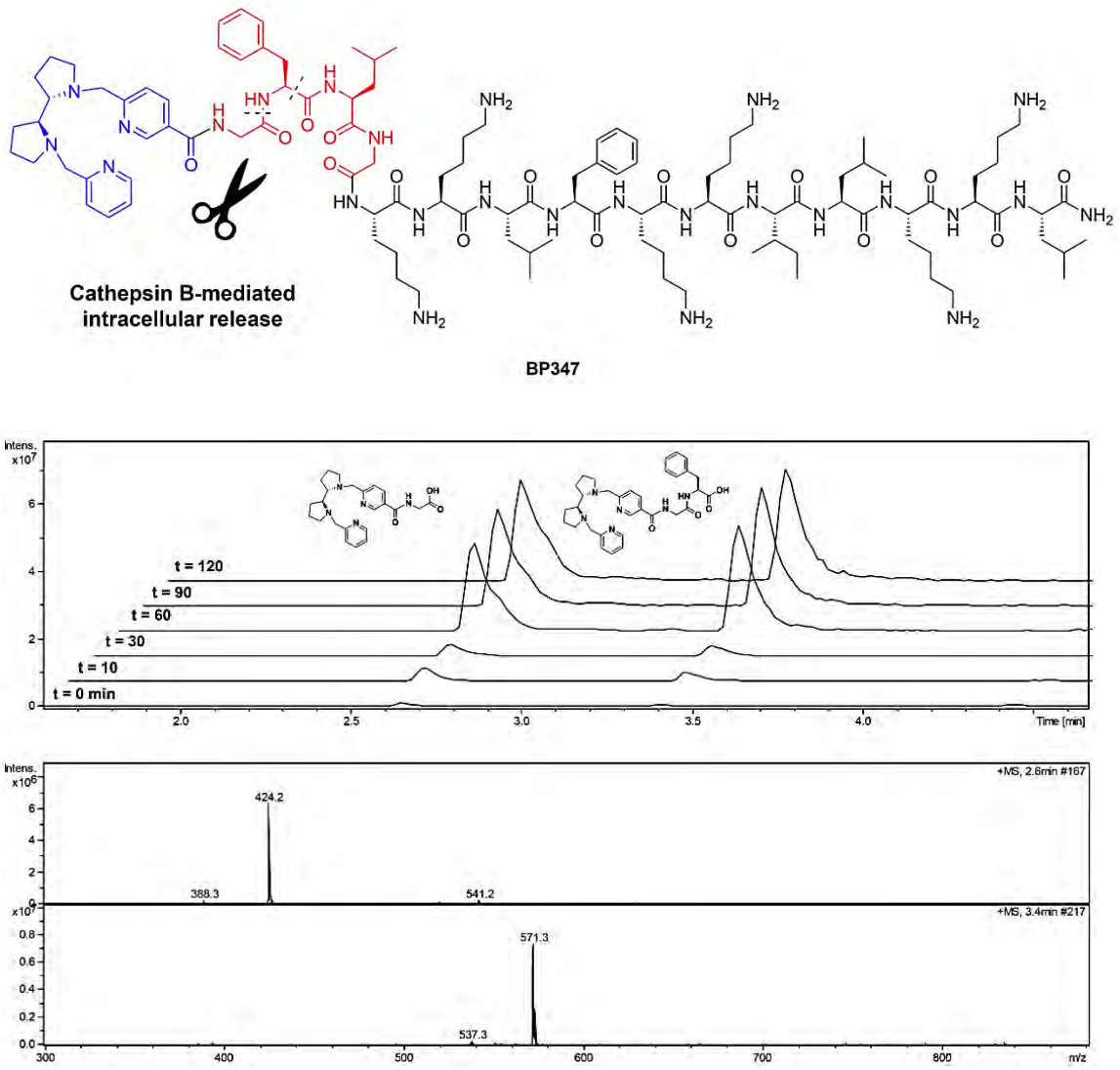

Figure VIII.5. Structure of **BP347** and the extracted ion chromatogram of its cathepsin B enzymatic digestion.

Taking into account these excellent biological results, these findings point out that (*S*,*S'*)-BPBP ligand is a promising candidate to interfere in cancer redox balance with the aim of promoting irreversible damage to cancer cells. Additionally, this study also validates the versatility to use **BP16** in smart drug delivery designs.

VIII.4. BPBP-PNA conjugate as metal-free artificial nuclease for oncogenic miRNA targeting

Given our expertise in the use of solid-phase methodology, emerging opportunities arise to conjugate our bioactive motifs to other biological vectors. In light of this, the targeting of gene-expression in cancer cells offers the opportunity to design novel oligonucleotide-based conjugates. In this regard, modulation of oncogenic miRNA expression directly disrupts the regulation of biological processes involved in cancer disease.[31] Therefore, in Chapter VII we have conjugated the (*S,S'*)-BPBP ligand to two short PNA recognition sequences that are meant to target the miRNA-155 and miRNA-135b, which are overexpressed in many pancreatic cancers cell lines.[32,33]

We aimed to obtain PNA-based artificial nucleases promoting the site-selective cleavage of the above-mentioned miRNA. Hence, after assembling the PNA complementary sequences on the resin, the resulting conjugates have been readily available by optimizing the conjugation of (*S,S'*)-BPBP carboxylic acid derivative to the N-terminal position. Moreover, three lysine residues at the C-terminus as well as an aminohexanoic acid (Ahx) spacer between the BPBP motif and the oligonucleotide sequence have also been included in the design (see Scheme VII.1 for synthetic route). The resulting conjugates **BPBP-PNA$_{155}$** and **BPBP-PNA$_{135}$** have been obtained in excellent purities and their identity have been further confirmed by HRMS analysis. On the other hand, in order to obtain an uptake profile in several pancreatic cancer cell lines, 5(6)-carboxyfluorescein has also been attached to both PNA complementary sequences, rendering **CF-PNA$_{155}$** and **CF-PNA$_{135}$** (see Table VII.1 for the synthesized PNA conjugates). The fluorescein-labeled **CF-PNA$_{155}$** and **CF-PNA$_{135}$** oligomers have been afforded in excellent purities and further characterization by ESI-MS and HRMS analyses confirmed their identities. These PNA conjugates have been prepared by manual standard Fmoc solid-phase synthesis on a TentaGel R RAM using Fmoc/Bhoc-protected PNA monomers.

Cleavage experiments have evaluated the efficacy of **BPBP-PNA$_{155}$** to promote the *in vitro* scission of miRNA-155 2-18 (5'-UAAUGCUAAUCGUGAUA-3'), complementary to the PNA$_{155}$ sequence in antiparallel orientation. **BPBP-PNA$_{155}$** contains the externally placed BPBP unit facing the nucleotides that are in the middle or closed to the 3'-end of the targeted RNA chain with the presence of one spacer between the PNA complementary sequences and the cleaver unit.

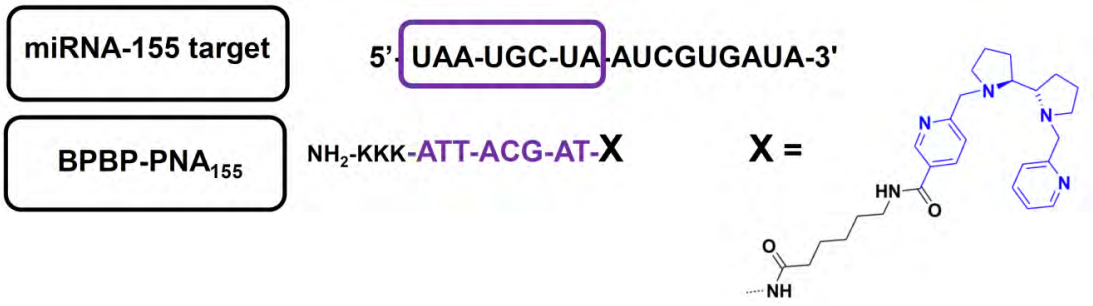

Scheme VIII.2. Schematic representation of the RNA cleavage promoted by **BPBP-PNA$_{155}$**.

While control assays by IE-HPLC analysis with **PNA$_{155}$** and free BPBP ligand in front the targeted miRNA have not shown any cleavage activity (see Figure VIII.1), the cleavage activity of the **BPBP-PNA$_{155}$** conjugate has been examined. The targeted RNA substrate has been incubated with **BPBP-PNA$_{155}$** (1:1 molar ratio, 24 h, 37 ºC) and with BPBP-PNA$_{155}$ in the presence of Zn under the same reaction conditions. IE-HPLC chromatograms suggest that metal-free **BPBP-PNA$_{155}$** displays higher cleavage activity than the former Zn(BPBP), and thus was further studied (see Figure VII.3 and 4). Next, the RNA substrate has been incubated with **BPBP-PNA$_{155}$** for 48 h (1:1 molar ratio, 37 ºC). Remarkably, IE-HPLC combined with MALDI-TOF analyses have shown the presence of four peaks, revealing that two plausible cleavage sites take place during the scission. Cleavage fragments eluting at 22.5 min and 24.9 min correspond to 5'-UAAUGCU and AAUCGUGAUA-3' with a 23% of cleavage yield within the complementary region. Additionally, CGUGAUA-3' (20.1 min) and 5'-UAAUGCUAAU (26.5 min) fragments have also been identified with a 11% of cleavage efficiency (see Figure VII.5).

Further hydrolysis experiments have been carried out by increasing the concentration of **BPBP-PNA$_{155}$** conjugate in front the miRNA-155 substrate. Thus, the RNA substrate has been incubated with **BPBP-PNA$_{155}$** with a 1:10 ratio (RNA: PNA conjugate) for 48 h at 37 ºC. Under these conditions the cleavage efficiency is dramatically improved up to 93%, showing three main cleavage sites (Figure VIII.6). The scission between U-C nucleotides has been the most significant contributing up to 40% cleavage yield. Cleavage fragments derived from this scission elute at 20.3 min and 26.6 min and correspond to CGUGAUA-3' and 5'-UAAUGCUAAU, respectively. Moreover, two other cleavage sites have been observed. RNA fragments 5'-UAAUGCU (22.7 min) and AAUCGUGAUA-3' (24.9 min) contribute with a 25% cleavage efficiency, which confirms that the scission between U-A nucleotides is retained in all cleavage assays. Finally, the last cleavage site takes place between C-G nucleotides, since two more fragments are found to be GUGAUA-3' (18.2 min) and 5'-UAAUGCUAAUC (27.5 min), contributing also with a 25% in the overall cleavage yield.

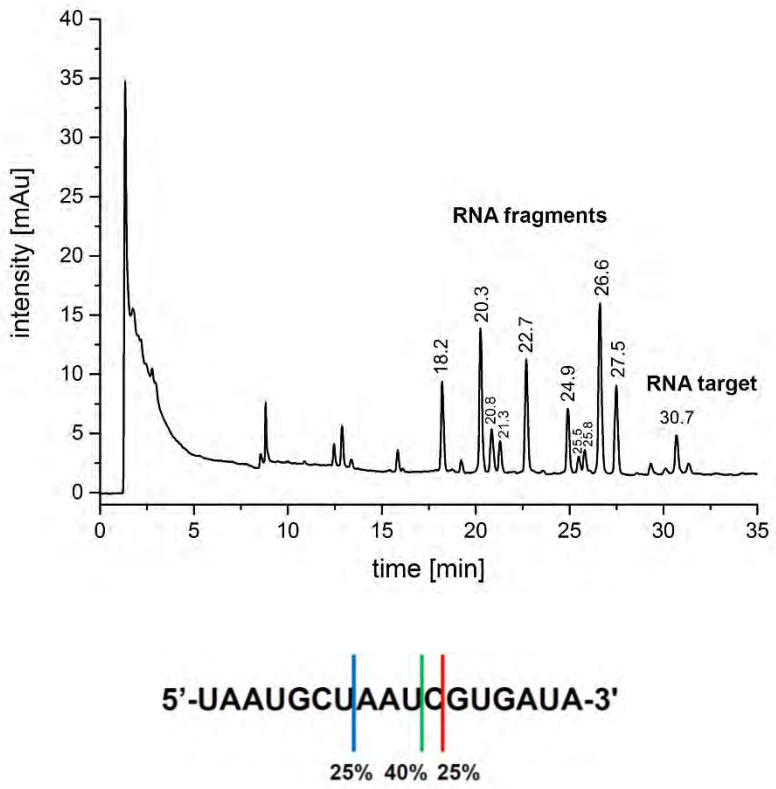

Figure VIII.6. IE-HPLC analysis and RNA cleavage sites derived from the incubation of RNA substrate (miRNA-155 2-18) and **BPBP-PNA$_{155}$** for 50 h at 37 ºC (1:10 molar ratio).

In sum, the miRNA-155 2-18 is cleaved more efficiently using 1:10 molar ratio (RNA:PNA conjugate than using 1:1 molar ratio. Remarkably, at 1:10 molar ratio the main scission occurs outside of the complementary region (U-C nucleotides) whereas at 1:1 molar ratio the main cleavage site takes place within the complementary region (U-A nucleotides). Interestingly, the scission between U-A and U-C nucleotides occurs at both concentrations. However, at higher concentrations **BPBP-PNA$_{155}$** hydrolyzes the RNA substrate between the bases neighboring the main cleavage site on the 3'-side (C-G nucleotides), suggesting that the cleavage efficiency is improved from 5' to 3' direction. Despite the site-selective cleavage is not completely maintained, these results suggest that the RNA cleavage activity of **BPBP-PNA$_{155}$** conjugate results from the BPBP unit once attached to the recognition sequence and is dependent on its concentration.

The presence of 2',3'-cyclic phosphate in the resulting fragments demonstrate that the cleavage is in agreement with hydrolytic cleavage patterns. This simple RNA cleavage chemistry by **BPBP-PNA$_{155}$** might operate by activating H_2O molecules with the BPBP moiety, in analogous manner as the one reported for DNA (see Scheme VII.3 for the proposed mechanism).[34] In fact,

facing the precedent literature in this field, other polyamine-based compounds have shown DNA and RNA cleavage activities avoiding the use of transition metal centers.[34–36].

On the other hand, the fluorescein-labeled conjugate **CF-PNA$_{155}$** has been transfected to IMIM-PC2, PancTul and PT45 cell lines. Flow cytometry analyses allow the quantification of cellular uptake by **CF-PNA$_{155}$** (see Figure VIII.9 for flow cytometry histograms). Notably, excellent cellular uptakes of 80% have been observed for IMIM-PC2 and PancTul.

Altogether, the *in vitro* cleavage results by **BPBP-PNA$_{155}$** and the successful uptake obtained by **CF-PNA$_{155}$**, strongly suggest the feasibility to apply the **BPBP-PNA$_{155}$** cleavage system in miRNA-based therapy. Furthermore, this unique miRNA metal-free cleavage opens challenging therapeutic purposes to control the expression of miRNA under non-aggressive conditions.

Based on the sum of results obtained in these studies, future work should be directed to confer selectivity to the metal binding conjugates designed in this thesis. In this regard, one approach could be the introduction of a homing peptide with the aim of targeting specific biomarkers in cancer cells. This will open new insights in the design of effective anticancer agents.

VIII.5. References

(1) Thanki, K.; Gangwal, R. P.; Sangamwar, A. T.; Jain, S. *J. Control. Release* **2013**, *170*, 15–40.

(2) Alvarez-Lorenzo, C.; Concheiro, A. *Chem. Commun.* **2014**, *50*, 7743–7765.

(3) Khafagy, E.-S.; Morishita, M. *Adv. Drug Deliv. Rev.* **2012**, *64*, 531–539.

(4) Huang, Y.; Jiang, Y.; Wang, H.; Wang, J.; Shin, M. C.; Byun, Y.; He, H.; Liang, Y.; Yang, V. C. *Adv. Drug Deliv. Rev.* **2013**, *65*, 1299–1315.

(5) Rautio, J.; Kumpulainen, H.; Heimbach, T.; Oliyai, R.; Oh, D.; Järvinen, T.; Savolainen, J. *Nat. Rev. Drug Discov.* **2008**, *7*, 255–270.

(6) Bildstein, L.; Dubernet, C.; Couvreur, P. *Adv. Drug Deliv. Rev.* **2011**, *63*, 3–23.

(7) Mahato, R.; Tai, W.; Cheng, K. *Adv. Drug Deliv. Rev.* **2011**, *63*, 659–670.

(8) Yin, Q.; Shen, J.; Zhang, Z.; Yu, H.; Li, Y. *Adv. Drug Deliv. Rev.* **2013**, *65*, 1699–1715.

(9) Hartinger, C. G.; Metzler-Nolte, N.; Dyson, P. J. *Organometallics* **2012**, *31*, 5677–5685.

(10) Gasser, G.; Metzler-Nolte, N. *Curr. Opin. Chem. Biol.* **2012**, *16*, 84–91.

(11) Haas, K. L.; Franz, K. J. *Chem. Rev.* **2009**, *109*, 4921–4960.

(12) Storr, T.; Thompson, K. H.; Orvig, C. *Chem. Soc. Rev.* **2006**, *35*, 534–544.

(13) Graf, N.; Lippard, S. J. *Adv. Drug Deliv. Rev.* **2012**, *64*, 993–1004.

(14) Romero-Canelón, I.; Sadler, P. J. *Inorg. Chem.* **2013**, *52*, 12276–12291.

(15) Pelicano, H.; Carney, D.; Huang, P. *Drug Resist. Updat.* **2004**, *7*, 97–110.

(16) Trachootham, D.; Alexandre, J.; Huang, P. *Nat. Rev. Drug Discov.* **2009**, *8*, 579–591.

(17) Wang, J.; Yi, Y. *Cancer Biol. Ther.* **2008**, *7*, 1875–1884.

(18) Stewart, K. M.; Horton, K. L.; Kelley, S. O. *Org. Biomol. Chem.* **2008**, *6*, 2242–2255.

(19) Henriques, S. T.; Melo, M. N.; Castanho, M. a R. B. *Biochem. J.* **2006**, *399*, 1–7.

(20) Badosa, E.; Ferre, R.; Planas, M.; Feliu, L.; Besalú, E.; Cabrefiga, J.; Bardají, E.; Montesinos, E. *Peptides* **2007**, *28*, 2276–2285.

(21) Horton, K. L.; Stewart, K. M.; Fonseca, S. B.; Guo, Q.; Kelley, S. O. *Chem. Biol.* **2008**, *15*, 375–382.

(22) Zeglis, B. M.; Pierre, V. C.; Barton, J. K. *Chem. Commun.* **2007**, 4565–4579.

(23) Komor, A. C.; Barton, J. K. *Chem. Commun.* **2013**, *49*, 3617–3630.

(24) Gómez, L.; Garcia-Bosch, I.; Company, A.; Benet-Buchholz, J.; Polo, A.; Sala, X.; Ribas, X.; Costas, M. *Angew. Chemie Int. Ed.* **2009**, *48*, 5720–5723.

(25) Fillol, J. L.; Codolà, Z.; Garcia-Bosch, I.; Gómez, L.; Pla, J. J.; Costas, M. *Nat. Chem.* **2011**, *3*, 807–813.

(26) Prat, I.; Gómez, L.; Canta, M.; Ribas, X.; Costas, M. *Chem. Eur. J.* **2013**, *19*, 1908–1913.

(27) Cussó, O.; Garcia-Bosch, I.; Ribas, X.; Lloret-Fillol, J.; Costas, M. *J. Am. Chem. Soc.* **2013**, *135*, 14871–14878.

(28) Suzuki, M. *EMBO J.* **1989**, *8*, 797–804.

(29) Suzuki, M. *EMBO J.* **1989**, *8*, 4189–4195.

(30) González-Bártulos, M et al. *Submitted*.

(31) Khan, S.; Ansarullah; Kumar, D.; Jaggi, M.; Chauhan, S. C. *Cancer Res.* **2013**, *73*, 6541–6547.

(32) Thai, T.-H.; Calado, D. P.; Casola, S.; Ansel, K. M.; Xiao, C.; Xue, Y.; Murphy, A.; Frendewey, D.; Valenzuela, D.; Kutok, J. L.; Schmidt-Supprian, M.; Rajewsky, N.; Yancopoulos, G.; Rao, A.; Rajewsky, K. *Science* **2007**, *316*, 604–608.

(33) Szafranska, a E.; Davison, T. S.; John, J.; Cannon, T.; Sipos, B.; Maghnouj, a; Labourier, E.; Hahn, S. a. *Oncogene* **2007**, *26*, 4442–4452.

(34) Wang, M.-Q.; Liu, J.-L.; Wang, J.-Y.; Zhang, D.-W.; Zhang, J.; Streckenbach, F.; Tang, Z.; Lin, H.-H.; Liu, Y.; Zhao, Y.-F.; Yu, X.-Q. *Chem. Commun.* **2011**, *47*, 11059–11061.

(35) Scheffer, U.; Strick, A.; Ludwig, V.; Peter, S.; Kalden, E.; Göbel, M. W. *J. Am. Chem. Soc.* **2005**, *127*, 2211–2217.

(36) Li, Z.-F.; Chen, H.-L.; Zhang, L.-J.; Lu, Z.-L. *Bioorg. Med. Chem. Lett.* **2012**, *22*, 2303–2307.

CHAPTER IX

General Conclusions

IX. GENERAL CONCLUSIONS

- **BP16** has been identified as a new cell-penetrating peptide (CPP): it is non-hemolytic, displays no cytotoxicity against malignant and non-malignant cells, is mainly internalized into the cells through clathrin-mediated endocytosis and shows the same cellular uptake levels as the well-known CPP Tat_{49}.

- **BP308**, an arginine analogue of **BP16**, also displays interesting properties as CPP: it is non-hemolytic, shows low cytotoxicity against malignant and non-malignant cells and exhibits the same cellular uptake behavior than **BP16**. Unlike other arginine-containing peptides, **BP308** does not show mitochondria targeting properties.

- **BP16** and **BP308** are suitable vectors for the delivery of therapeutic agents into cancer cells. It has been shown that the position of the cargo has a strong influence on the biological profile of the resulting conjugates. The conjugation of the anticancer drug chlorambucil (CLB) at both ends of **BP16** (**BP325** and **BP331**), dramatically improved the efficacy of CLB against cancer cells (IC_{50} values ranging from of 8.7 to 25.5 μM). In contrast, the cytotoxic activity of CLB only increased when conjugated at the N-terminus of **BP308** (**BP334**) (IC_{50} values ranging from 11.2 to 16.4 μM). The different cytotoxic profile of these CLB-conjugates correlates with their different cellular internalization properties.

- A smart drug delivery system based on **BP16** has been developed, which could be applied to transport and efficiently release therapeutic agents in cancer treatments. This system has been designed by incorporating the cathepsin B-cleavable sequence Gly-Phe-Leu-Gly between CLB and **BP16** in CLB-BP16 and BP16-CLB conjugates. The resulting derivatives **BP332** (CLB-GFLG-BP16) and **BP333** (BP16-GLFG-CLB) further improved the activity of CLB (IC_{50} values ranging from 3.6 to 16.2 μM) compared to the conjugates without this cleavable sequence. Cathepsin B enzymatic assays have proved that CLB might be released from conjugates **BP332** and **BP333** in the lysosomes, being CLB-Gly-OH the main fragment observed.

- A straightforward solid-phase synthetic methodology to prepare redox-active metallopeptides based on the tetradentate (N_4) ^{Me2}PyTACN and (*S,S'*)-BPBP ligands has been developed. The conjugation of these N_4-based ligands to the tetrapeptide LKKL has

been optimized. Subsequent metallation of the resulting ^{Me2}PyTACN and (*S,S'*)-BPBP metal binding peptide conjugates with iron, manganese, zinc and copper afforded metallotetrapeptides, that have been fully characterized by HRMS, NMR and UV-VIS. The stoichiometry of the complexation has been found to be 1:1.

- DNA cleavage studies using gel electrophoresis have shown that the attachment of the ^{Me2}PyTACN and BPBP-based complexes to the LKKL peptide sequence resulted in an enhancement of the nuclease activity. The presence of the cationic tetrapeptide might induce an improved binding affinity to the DNA-minor groove through protonated lysine ε-NH_3^+ groups. The sum of these observations strongly suggests that these redox-active hybrid structures might operate as minor-groove nucleases.

- Peptide conjugates incorporating the ^{Me2}PyTACN or (*S,S'*)-BPBP ligands at the either N- or the C-terminus of **BP16** have been synthesized on solid-phase. Peptide conjugates derived from the (*S,S'*)-BPBP ligand are more active than those bearing ^{Me2}PyTACN. The introduction of the dipeptide β-Ala-Lys between the ligand and the N-terminus of **BP16** has significantly reduced the biological activity of the resulting conjugates (**BP345** and **BP346**). In contrast, the conjugation of the (*S,S'*)-BPBP ligand to the enzymatic cleavable tetrapeptide Gly-Phe-Leu-Gly placed at the N- or the C-terminus of **BP16** renders conjugates **BP347** and **BP348**, respectively, which display excellent cytotoxic activities against cancer cells (IC_{50} values ranging from 4.3 to 11.7 μM). Cathepsin B enzymatic assays have demonstrated that the (*S,S'*)-BPBP ligand might be released from conjugates **BP347** and **BP348** in the lysosomes, being (*S,S'*)-BPBP-Gly-OH and (*S,S'*)-BPBP-Gly-Phe-OH the main fragments observed. These observations, together with the high internalization ability of fluorescein-labeled conjugate **BP350** (BPBP-GFLG-BP16-CF), correlate with the high cytotoxic activities observed for conjugates **BP347** and **BP348**.

- A PNA-based artificial nuclease containing the N_4-tetradentate (*S,S'*)-BPBP ligand has been designed and synthesized. This BPBP-PNA oligomer exhibits excellent nuclease activity *in vitro* against the oncogenic miRNA-155 2-18, rendering a cleavage efficiency of 93% under optimized conditions. It has been shown that its RNA cleavage ability comes from the BPBP unit once attached to the PNA recognition sequence.

- The nature of the RNA fragments clearly indicates the involvement of a metal-free hydrolytic cleavage mechanism by BPBP-PNA oligomer. These findings, combined with the high cellular uptake exhibited by the PNA recognition sequence in pancreatic cancer cells, put forward the potential of this BPBP-PNA oligomer to be used in miRNA-based therapy.

Available in Spotify's user: msolervives - Thesis soundtrack playlist

THESIS SOUNDTRACK

Shout Out Louds
Hermila

The Pains Of Being Pure At Heart
Come Saturday

Massive Attack
Unfinished sympathy

New Order
Hellbent

Franz Ferdinand
The dark of the matinée

The Vaccines
Melody callin

Femme
Sur la planche

The Smiths
Bigmout strikes again

Saint Etienne
Finisterre

Broncho
Class historian

The Wave Pictures
Little surprise

We Are Scientists
Rules don't stop

Quimi Portet
Flors i violes

Fanfarlo
Cell song

Vampire Weekend
A-Punk

Aur Revoir Simone
Somebody who

Dum Dum Girls
It only takes one night

Metronomy
The look

Baden Baden
You'll see

Kakkmaddafakka
Restless

Joana Serrat
Summer on the beach

Foster The People
Ask yourself

Portishead
Strangers

Veronica Falls
If you still want me

Texas
Prayer for you

Roger Mas
La lluna

M83
Midnight city

The Drums
Let's go surfing

Beast Coast
Lonely morning

Pj Harvey
Good fortune

Very Pomelo
He quedat a les set

Nouvelle Vague
Dance with me

The Kooks
The junk of the heart

She & Him
In the sun

Kings of Leon
Supersoaker

Tennis
Origins

Coconut Records
West coast

Kings of Convenience
Failure

St. Germain
Rose rouge

Cro
Einmal um die welt

Love of Lesbian
La niña imantada

Bruce Springsteen
Born to run

Mazes
Bodies

Editors
Münich

Temples
Mesmerise

Crystal Fighters
LA callin

The Radio Dept.
Where damage isn't already done

Arcade Fire
Neighbourhood # 3

I am Kloot
Fingerprints

Primal Scream
Some velvet morning

Wilco
I Might

Joan Colomo
Hort mort

Tame Impala
Feels like we only go backwards

The Flaming Lips
Race for the prize

Phoenix
Lisztomania

The Antlers
Parentheses

Death Cab for Cutie
I will possess your heart

Ladytron
Blue jeans

The D.O.T
Most of my time

La iaia
On ets Matilda?

Koop
Come to me

Mood Rings
Come lay down in lined arrangements

The Brand New Heavies
Shelter

Beirut
Santa Fe

Anímic
Blue eyed tree

Los Campesinos!
Hello sadness

Katie Melua
On the road again

The Raveonettes
Killer in the streets

Bishop Allen
Rain

Band of Horses
Knock knock

Sigur Rós
Við spilum endalaust

Belle & Sebastian
White collar boy

Noah and The Wahle
5 Years Time

The Do
Too insistent

Capital Cities
Save and sound

Maika Makovski
Your reflection

La Banda Munic. del Polo Norte
La noticia del siglo

Deerhunter
Agarophobia

Coldplay
Shiver

The Sounds
Painted by numbers

Bon Iver
Perth

Ski Lodge
Just to be like you

The Postal Service
Such great heights

Two Door Cinema Club
I can talk

Elephant
Elusive youth

Antònia Font
A Rússia

Beach House
New Year

LCD Soundsystem
Dance yrself clean

Miles Kane
Better than that

Belle Ghoul
Saturday knife fight

Cut your hair
Mad Love

Mishima
La tarda esclata

Destroyer
China Town

Jack Johnson
Staple it together

Oasis
She's electric

St Vincent
Birth in reverse

Villeneuve
The falling

The Whitest Boy Alive
1517

Cut Copy
Free your mind

Bat For Lahses
Horses of the sun

Micah P.Hinson
A dream of her

No Joy
Last boss

The Charlatans
The only one I know

Aretha Franklin
I never loved a man

Sanjosex
Quatre pensaments

The Black Keys
Fever

Cat Power
Ruin

Yeah Yeah Yeahs
Sacrilege

The XX
Islands

Manel
Desapareixíem lentament

The Strokes
Reptilia

Atlas Sound
Angel is broken

Aaron Thomas
Out of your hands

Stereolab
Three women

Elbow
Grounds for divorci

Foals
My number

Röyksopp
Eple

Emiliana Torrini
Jungle Drum

Ducktails
Ivy covered house

El Petit de Cal Eril
Ei, sents com refila l'òliba?

Los Tiki Phantoms
Fuego

Inspira
Amunt

Angus & Julia Stone
Silver coin

Mazoni
Totsants

The Pastels
Check my heart

Peptide conjugates containing chlorambucil or tetradentate aminopyridine ligands for anticancer treatment

Marta Soler Vives

2014

APPENDIX

Supporting Information

Chapter III: Identification of BP16 as a non-toxic cell-penetrating peptide with highly efficient drug delivery properties

Marta Soler, Marta González, David Soriano-Castell, Xavi Ribas, Miquel Costas,

Francesc Tebar, Anna Massaguer,* Lidia Feliu,* Marta Planas*

Table of contents

1. HPLC, ESI-MS and HRMS of peptides

BP16 (KKLFKKILKKL-NH_2)

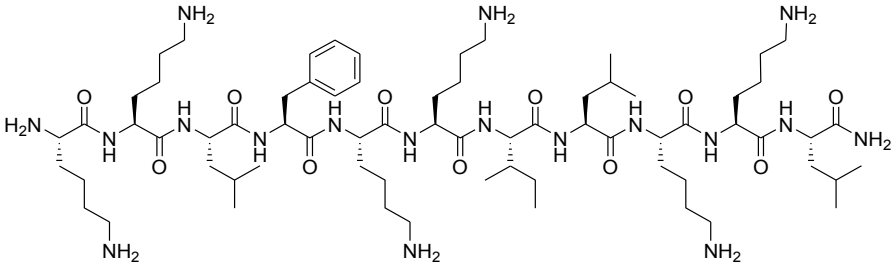

HPLC (λ= 220 nm)

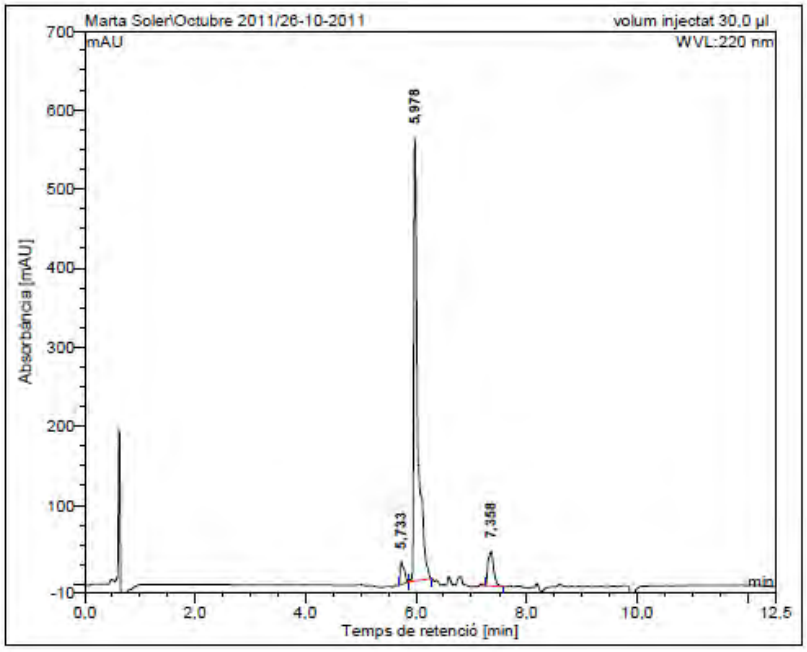

No.	mps retenc min	alçada mAU	Area mAU*min	Area relativa %
1	5,73	29,200	2,392	4,34
2	5,98	560,424	47,628	86,44
3	7,36	43,883	5,076	9,21
Total:		633,507	55,097	100,00

ESI/MS (m/z)

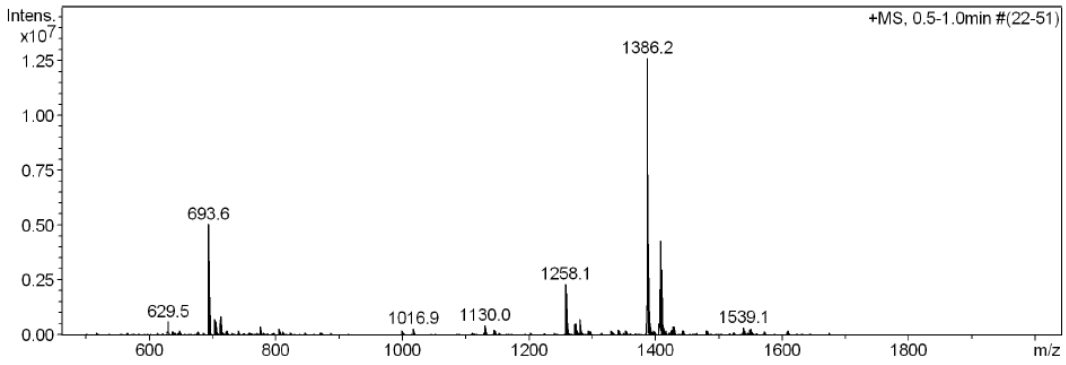
Intens.
x10^7
+MS, 0.5-1.0min #(22-51)
1.25
1.00
0.75
0.50
0.25
0.00
1386.2
693.6
1258.1
629.5
1016.9
1130.0
1539.1
600
800
1000
1200
1400
1600
1800
m/z

HRMS (m/z)

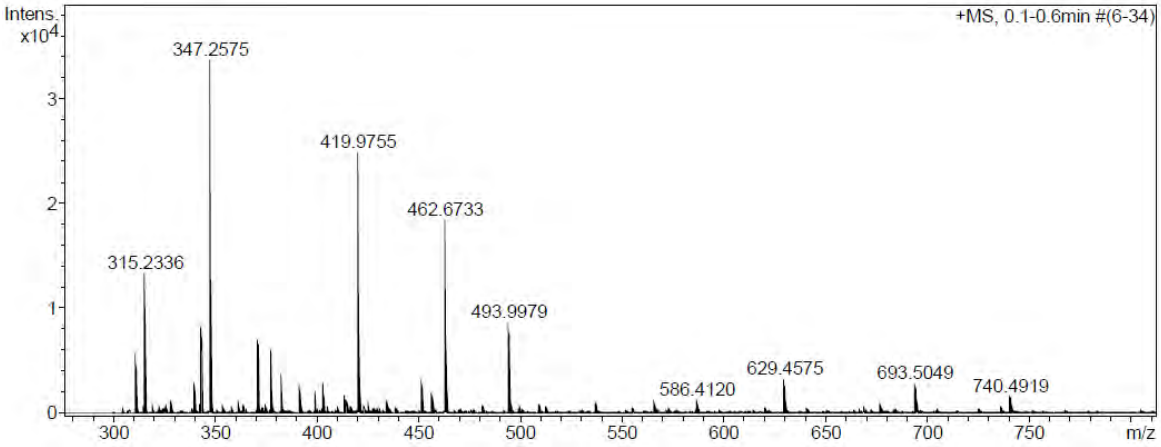
Intens.
x10^4
+MS, 0.1-0.6min #(6-34)
347.2575
419.9755
462.6733
315.2336
493.9979
586.4120
629.4575
693.5049
740.4919
m/z

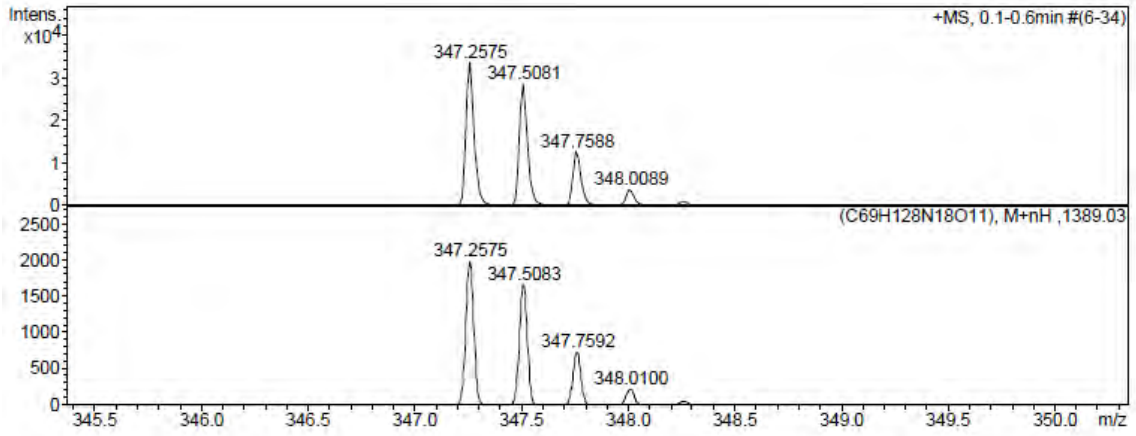
Intens.
x10^4
+MS, 0.1-0.6min #(6-34)
347.2575
347.5081
347.7588
348.0089
(C69H128N18O11), M+nH ,1389.03
347.2575
347.5083
347.7592
348.0100
m/z

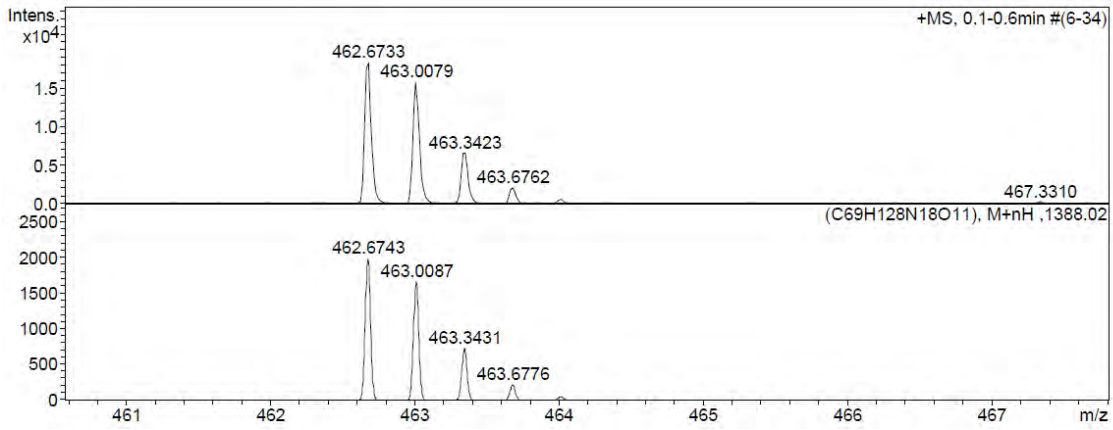
Intens.
x10^4
+MS, 0.1-0.6min #(6-34)
462.6733
463.0079
463.3423
463.6762
467.3310
(C69H128N18O11), M+nH ,1388.02
462.6743
463.0087
463.3431
463.6776
m/z

BP76 (KKLFKKILKFL-NH_2)

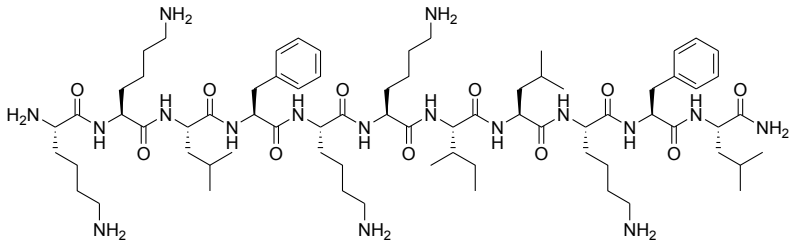

HPLC (λ= 220 nm)

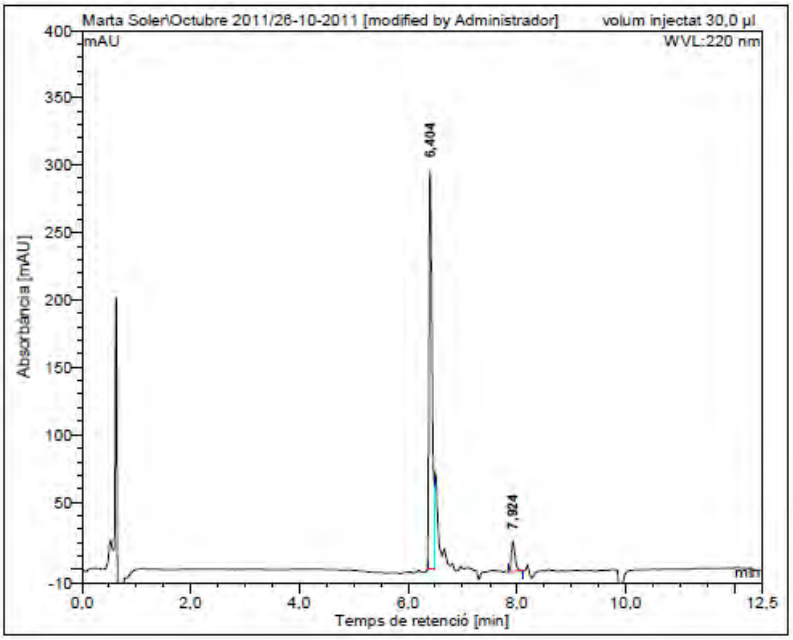

No.	mps retenc min	alçada mAU	Area mAU*min	Area relativa %
1	6,40	295,207	19,989	92,39
2	7,92	21,793	1,647	7,61
Total:		317,000	21,636	100,00

ESI/MS (m/z)

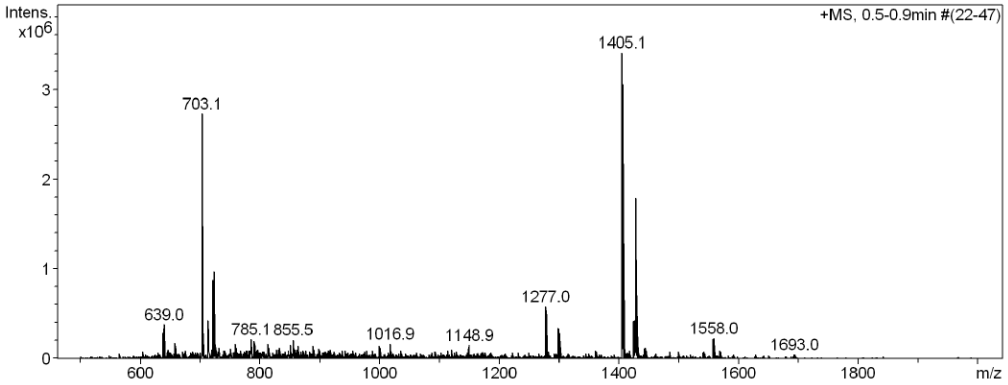
Intens.
x10^6
+MS, 0.5-0.9min #(22-47)
1405.1
703.1
1277.0
639.0
785.1
855.5
1016.9
1148.9
1558.0
1693.0
m/z

HRMS (m/z)

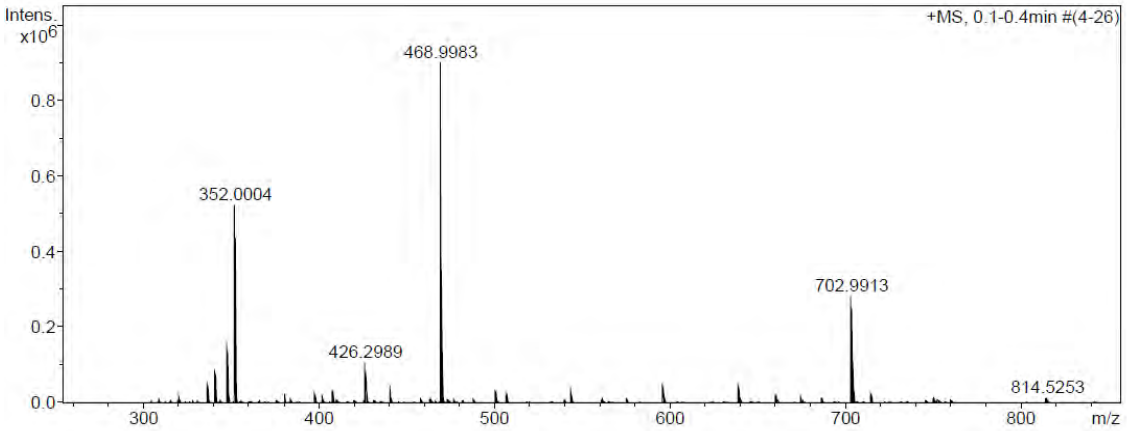
Intens.
x10^6
+MS, 0.1-0.4min #(4-26)
468.9983
352.0004
702.9913
426.2989
814.5253
m/z

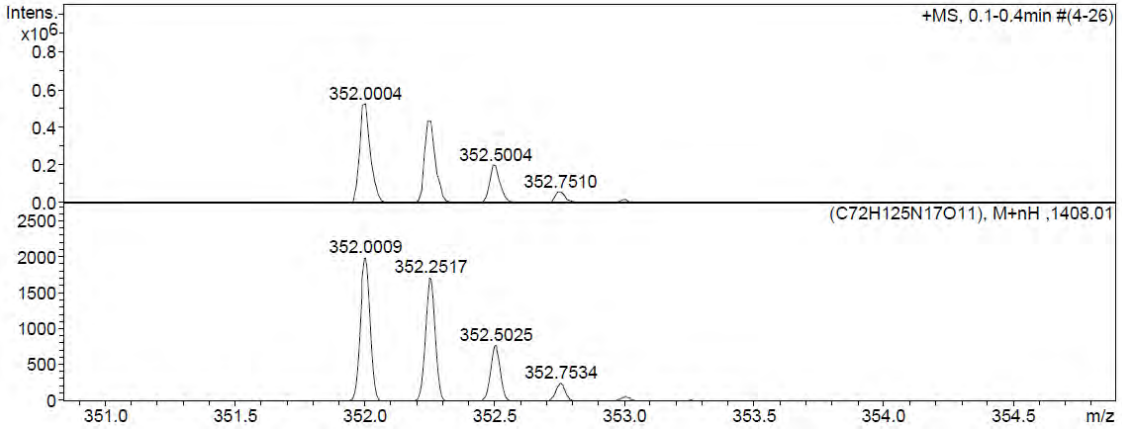
Intens.
x10^6
+MS, 0.1-0.4min #(4-26)
352.0004
352.5004
352.7510
(C72H125N17O11), M+nH ,1408.01
352.0009
352.2517
352.5025
352.7534
m/z

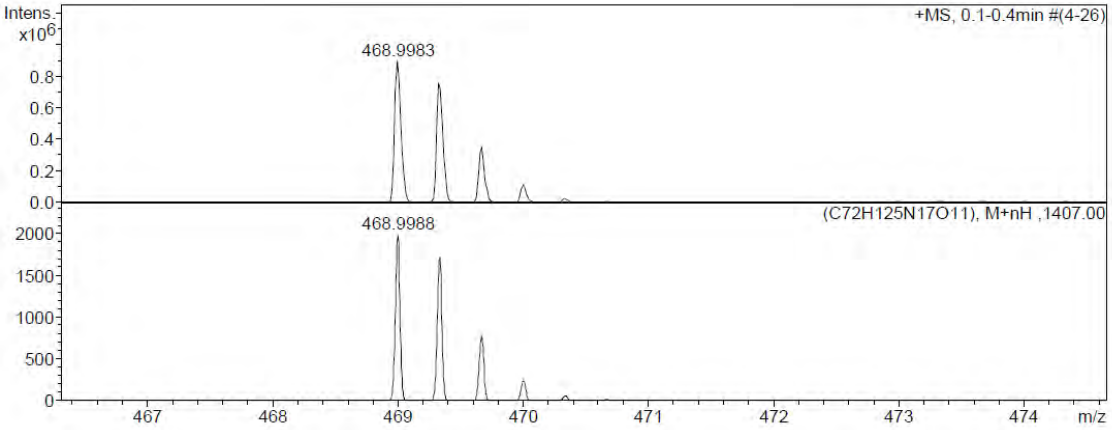
Intens.
x10^6
+MS, 0.1-0.4min #(4-26)
468.9983
(C72H125N17O11), M+nH ,1407.00
468.9988
m/z

BP81 (LKLFKKILKFL-NH_2)

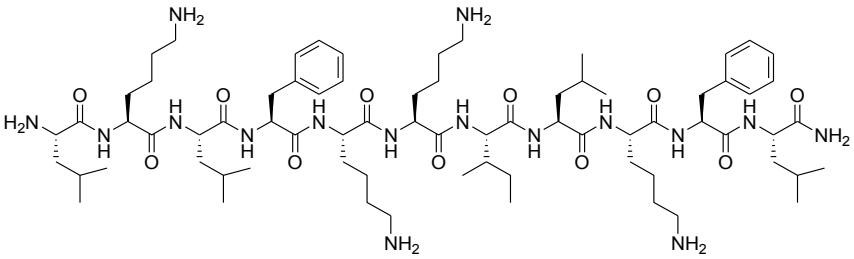

HPLC (λ= 220 nm)

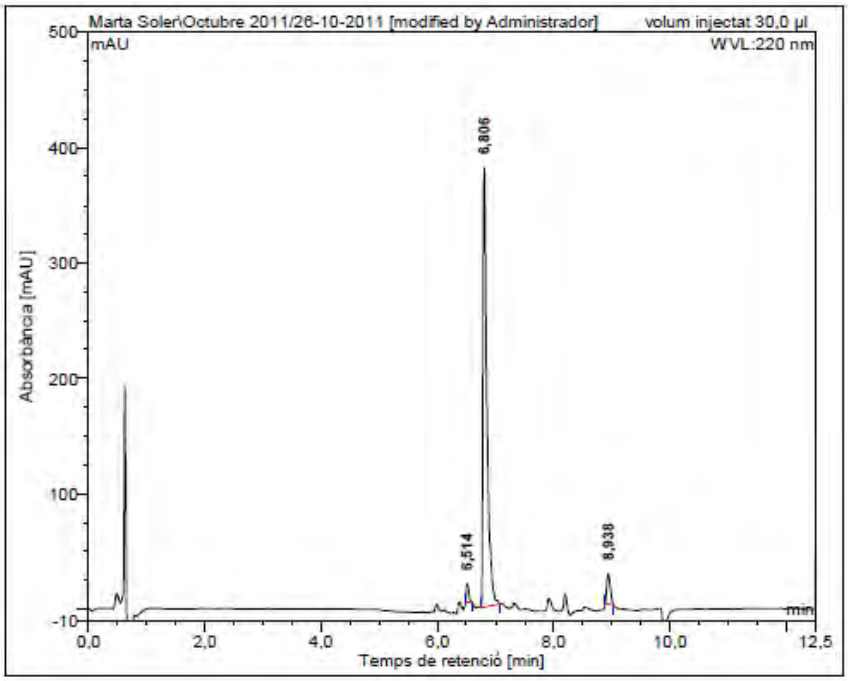

No.	mps retenc min	alçada mAU	Area mAU*min	Area relativa %
1	6,51	16,053	0,810	2,50
2	6,81	380,292	29,747	91,85
3	8,94	26,120	1,831	5,65
Total:		422,465	32,388	100,00

ESI/MS (m/z)

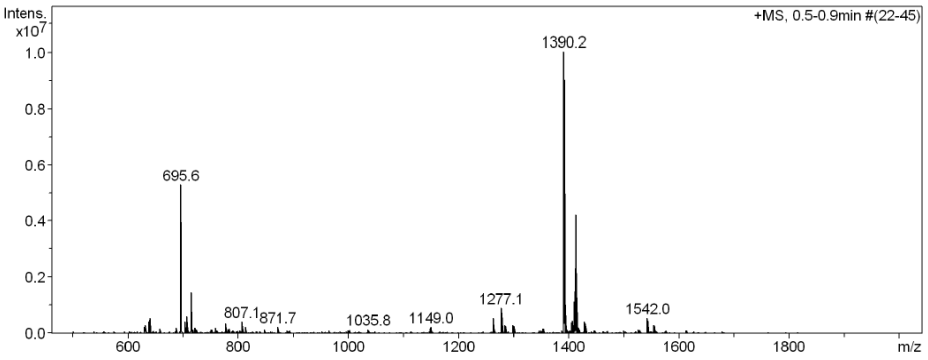
Intens.
x10^7
+MS, 0.5-0.9min #(22-45)
1.0
0.8
0.6
0.4
0.2
0.0
695.6
807.1
871.7
1035.8
1149.0
1277.1
1390.2
1542.0
600
800
1000
1200
1400
1600
1800
m/z

HRMS (m/z)

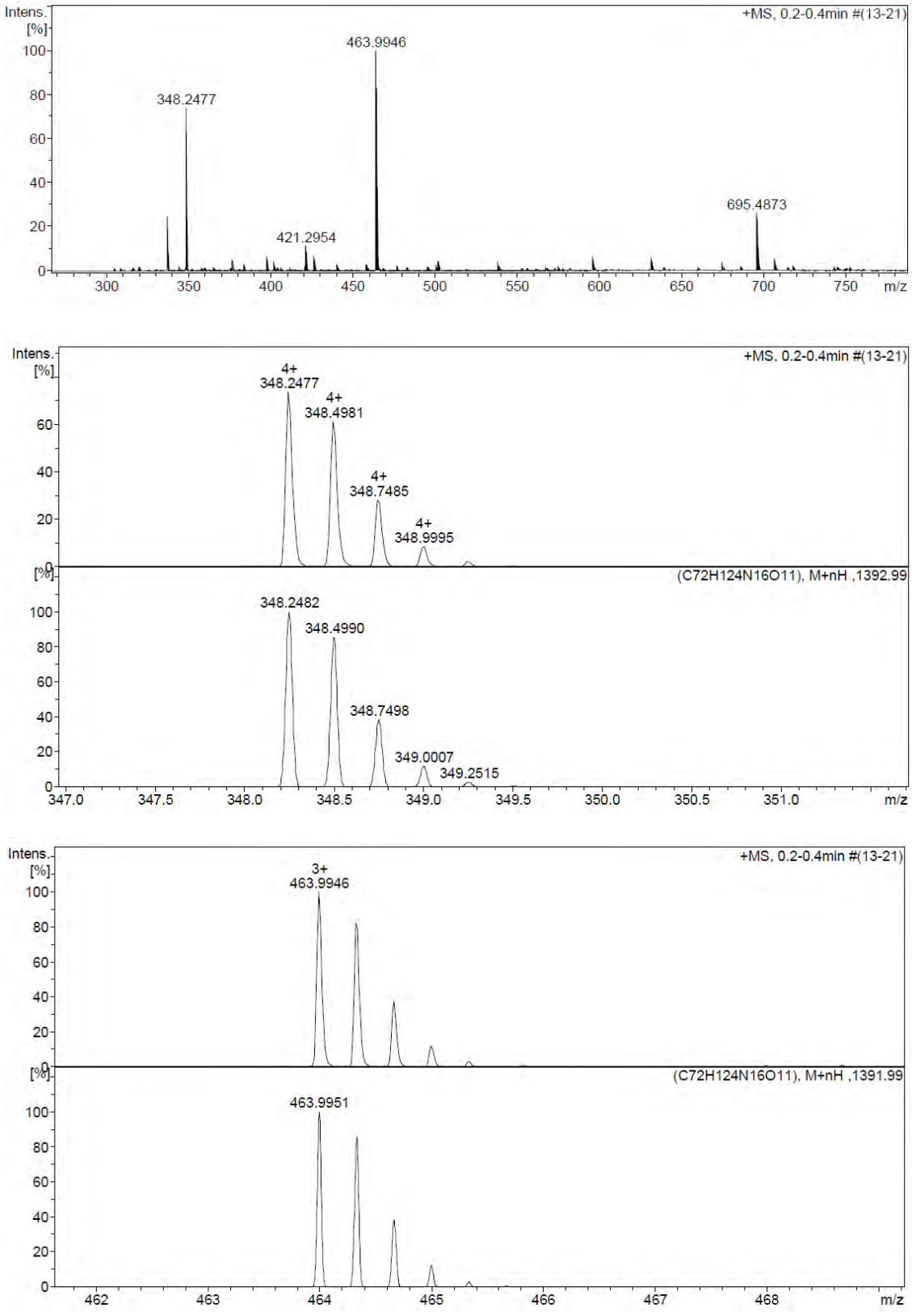
Intens.
[%]
+MS, 0.2-0.4min #(13-21)
463.9946
348.2477
695.4873
421.2954
m/z
4+
348.2477
4+
348.4981
4+
348.7485
4+
348.9995
(C72H124N16O11), M+nH ,1392.99
348.2482
348.4990
348.7498
349.0007
349.2515
3+
463.9946
(C72H124N16O11), M+nH ,1391.99
463.9951

BP100 (KKLFKKILKYL-NH_2)

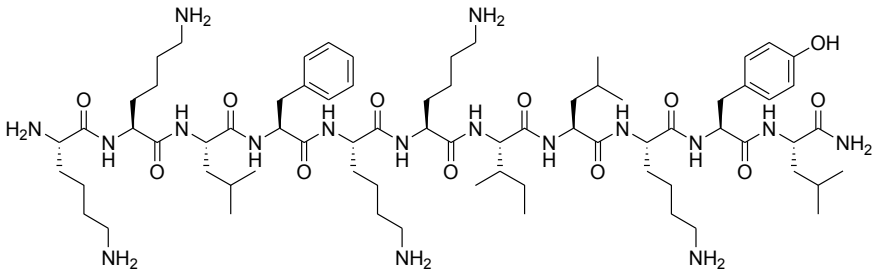

HPLC (λ= 220 nm)

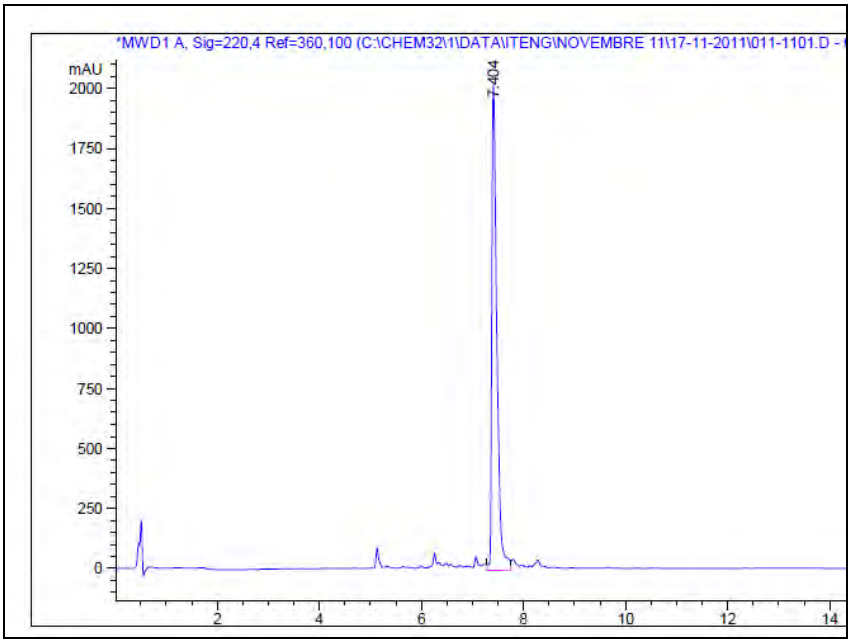

Peak #	RetTime [min]	Type	Width [min]	Area [mAU*s]	Height [mAU]	Area %
1	7.404	VV	0.1018	1.38823e4	2028.39783	100.0000

ESI/MS (m/z)

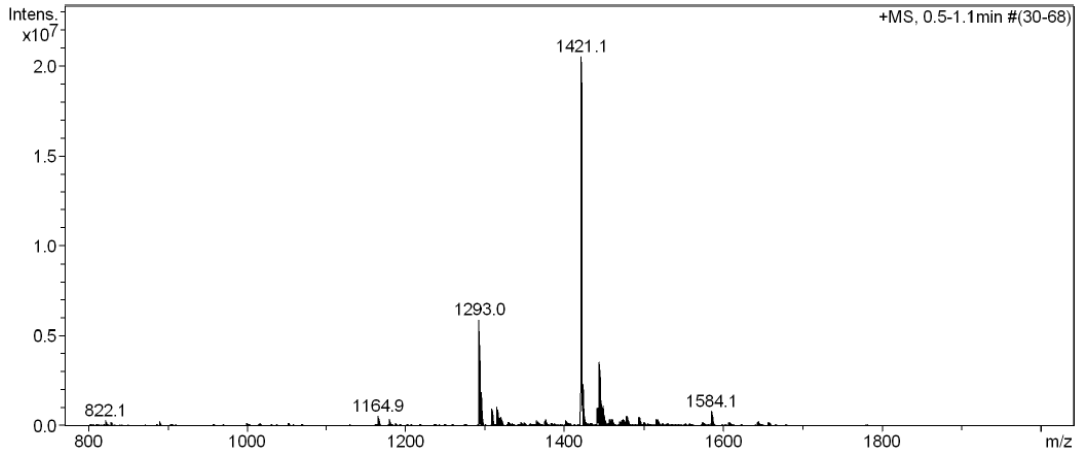
Intens.
x10^7
2.0
1.5
1.0
0.5
0.0
+MS, 0.5-1.1min #(30-68)
1421.1
1293.0
822.1
1164.9
1584.1
800
1000
1200
1400
1600
1800
m/z

HRMS (m/z)

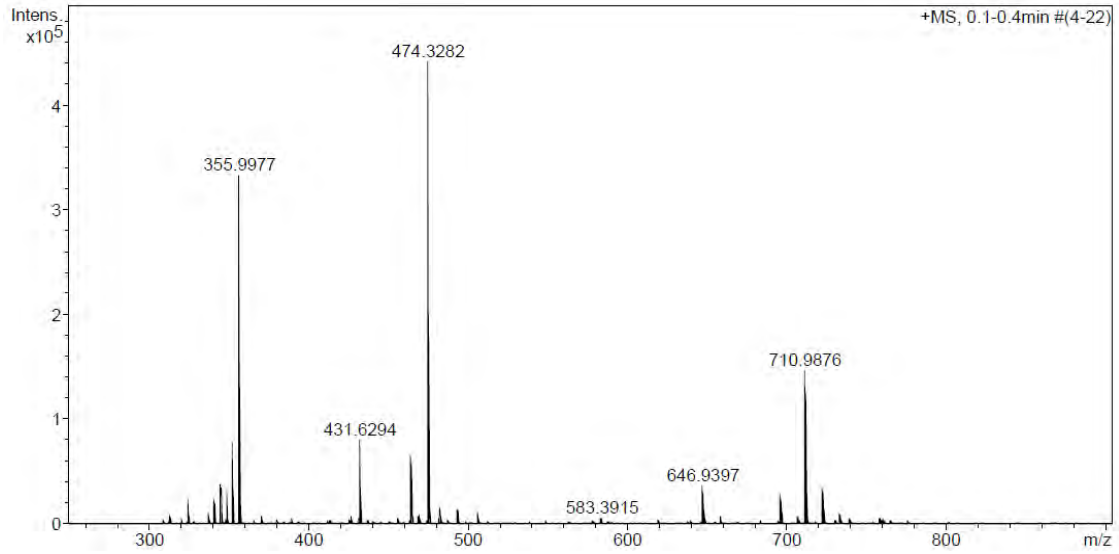
Intens.
x10^5
+MS, 0.1-0.4min #(4-22)
474.3282
355.9977
710.9876
431.6294
646.9397
583.3915
m/z

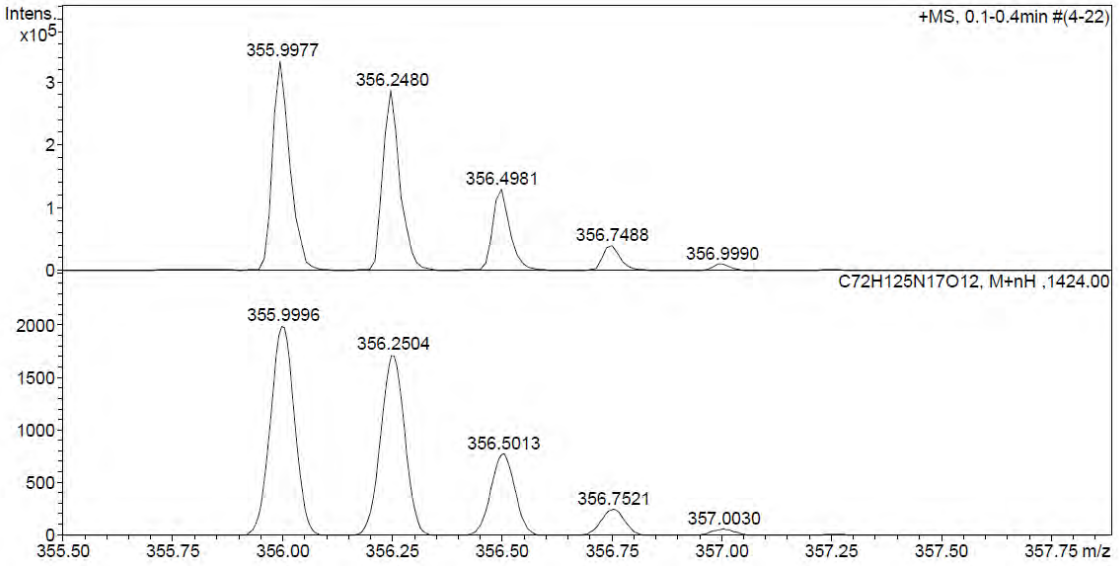
Intens.
x10^5
+MS, 0.1-0.4min #(4-22)
355.9977
356.2480
356.4981
356.7488
356.9990
C72H125N17O12, M+nH ,1424.00
355.9996
356.2504
356.5013
356.7521
357.0030
m/z

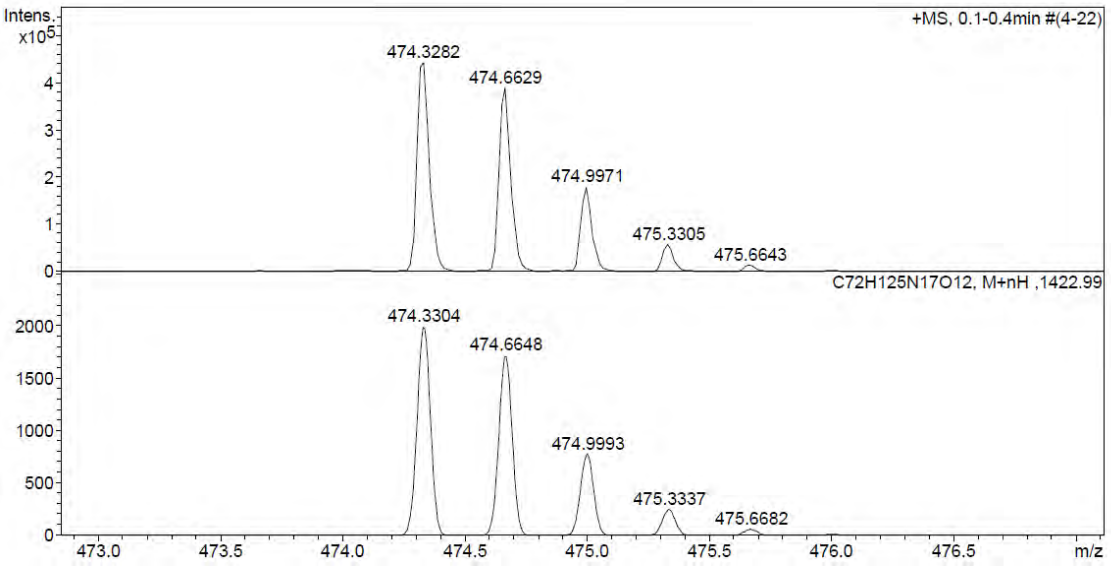
Intens.
x10^5
+MS, 0.1-0.4min #(4-22)
474.3282
474.6629
474.9971
475.3305
475.6643
C72H125N17O12, M+nH ,1422.99
474.3304
474.6648
474.9993
475.3337
475.6682
m/z

BP105 (LKLFKKILKYL-NH_2)

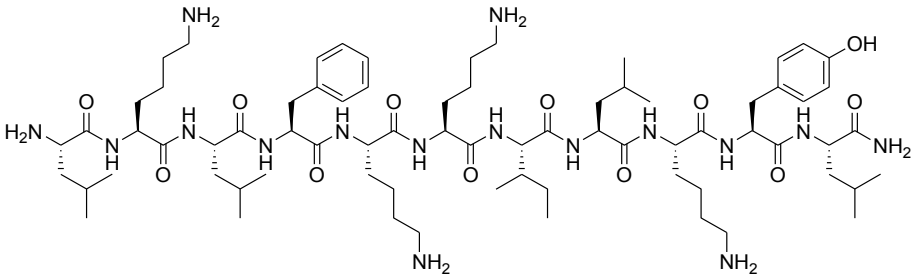

HPLC (λ= 220 nm)

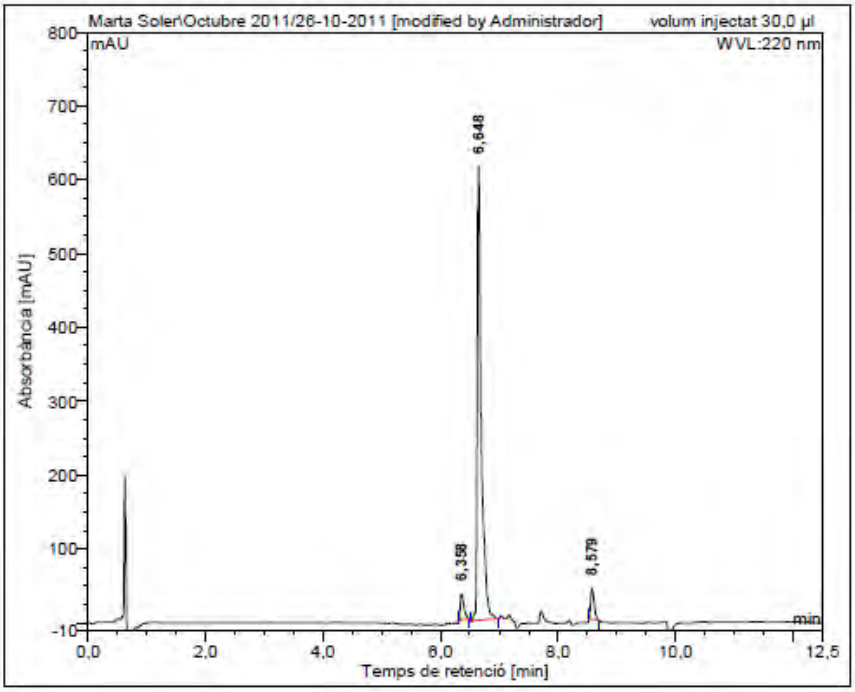

No.	mps retenc min	alçada mAU	Area mAU*min	Area relativa %
1	6,36	34,663	2,418	4,45
2	6,65	613,828	48,957	90,14
3	8,58	41,362	2,936	5,41
Total:		689,853	54,311	100,00

ESI/MS (m/z)

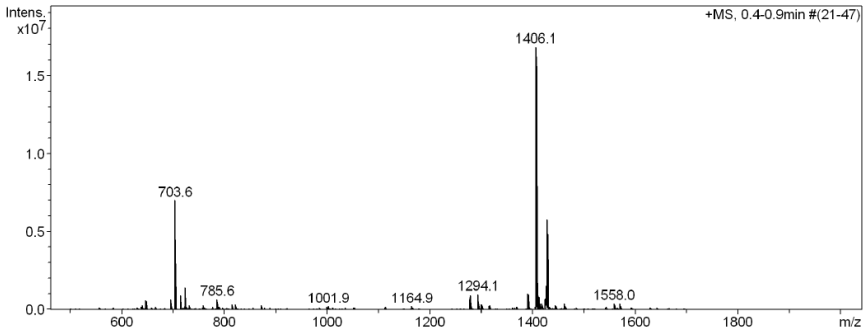
Intens.
x10^7
+MS, 0.4-0.9min #(21-47)
1406.1
1.5
1.0
703.6
0.5
785.6
1001.9
1164.9
1294.1
1558.0
0.0
600
800
1000
1200
1400
1600
1800
m/z

HRMS (m/z)

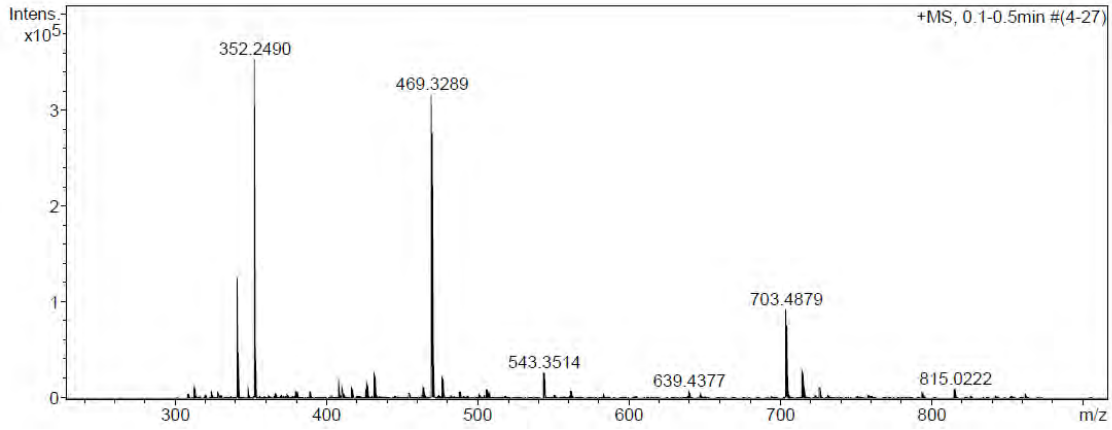
Intens.
x10^5
+MS, 0.1-0.5min #(4-27)
352.2490
469.3289
703.4879
543.3514
639.4377
815.0222
m/z

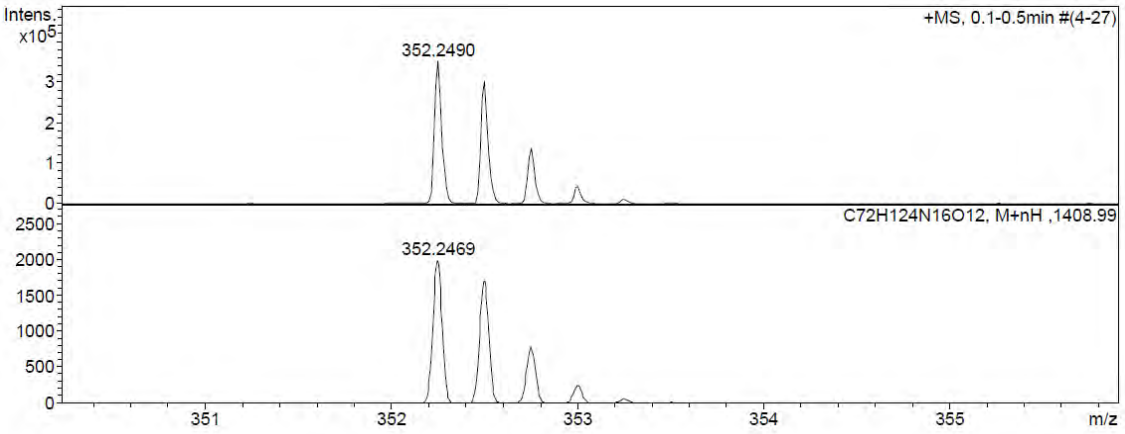
Intens.
x10^5
+MS, 0.1-0.5min #(4-27)
352.2490
C72H124N16O12, M+nH ,1408.99
352.2469
m/z

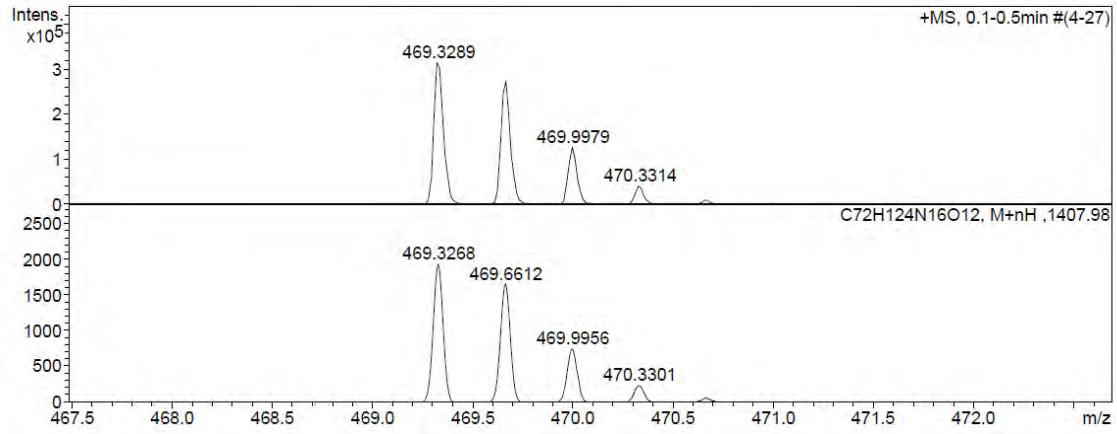
Intens.
x10^5
+MS, 0.1-0.5min #(4-27)
469.3289
469.9979
470.3314
C72H124N16O12, M+nH ,1407.98
469.3268
469.6612
469.9956
470.3301
m/z

BP307 (RRLFRRILRYL-NH_2)

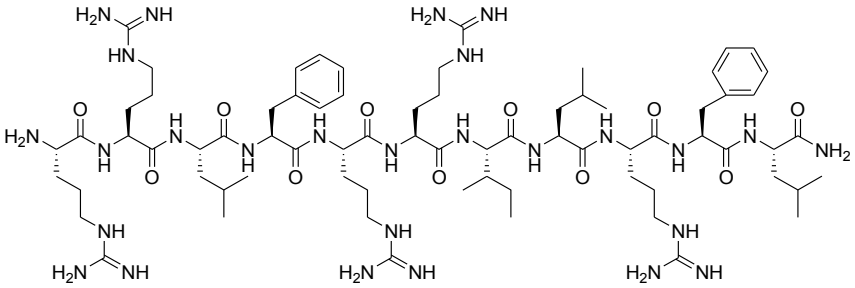

HPLC (λ= 220 nm)

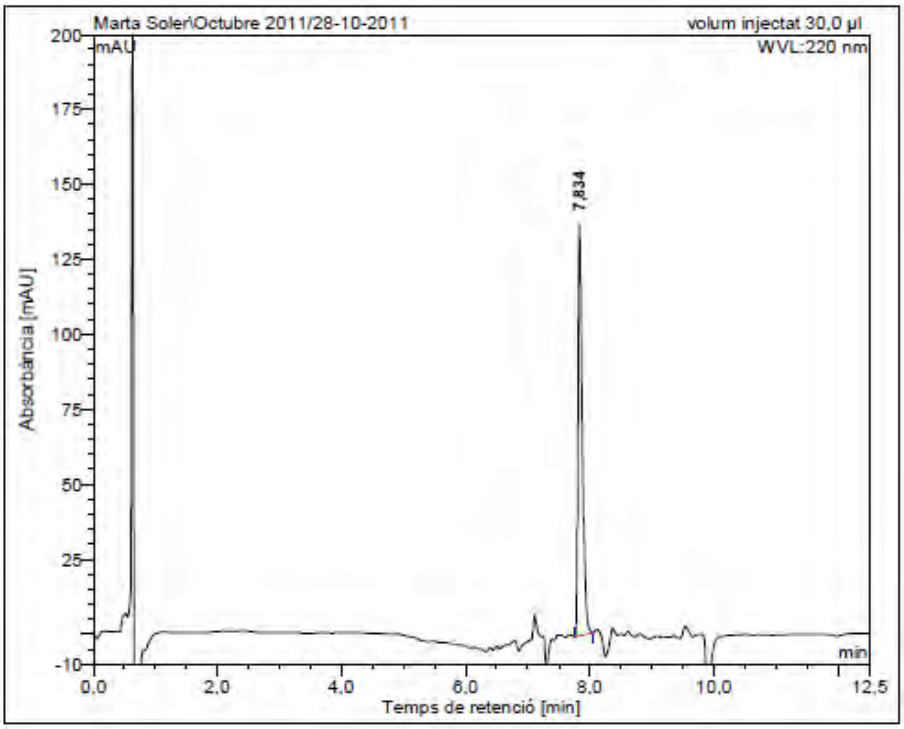

No.	mps retenc min	alçada mAU	Area mAU*min	Area relativa %
1	7,83	137,092	10,854	100,00
Total:		137,092	10,854	100,00

ESI/MS (m/z)

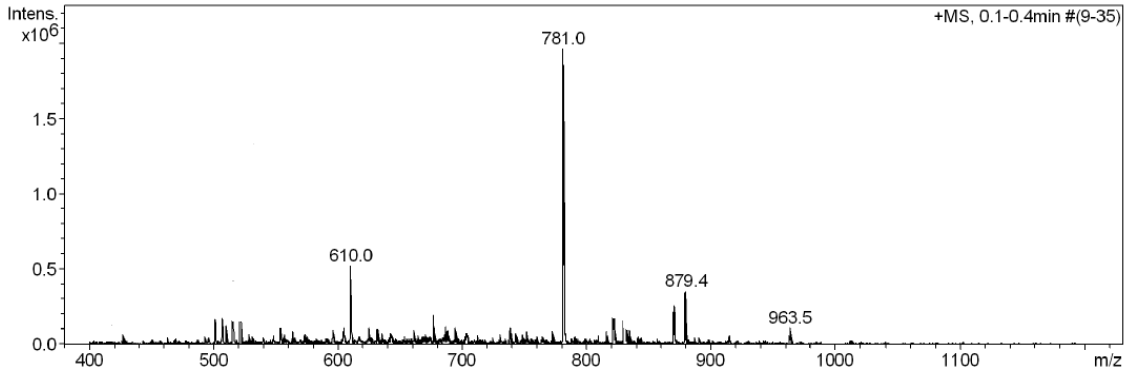
Intens.
x10^6
+MS, 0.1-0.4min #(9-35)
781.0
610.0
879.4
963.5
1.5
1.0
0.5
0.0
400
500
600
700
800
900
1000
1100
m/z

HRMS (m/z)

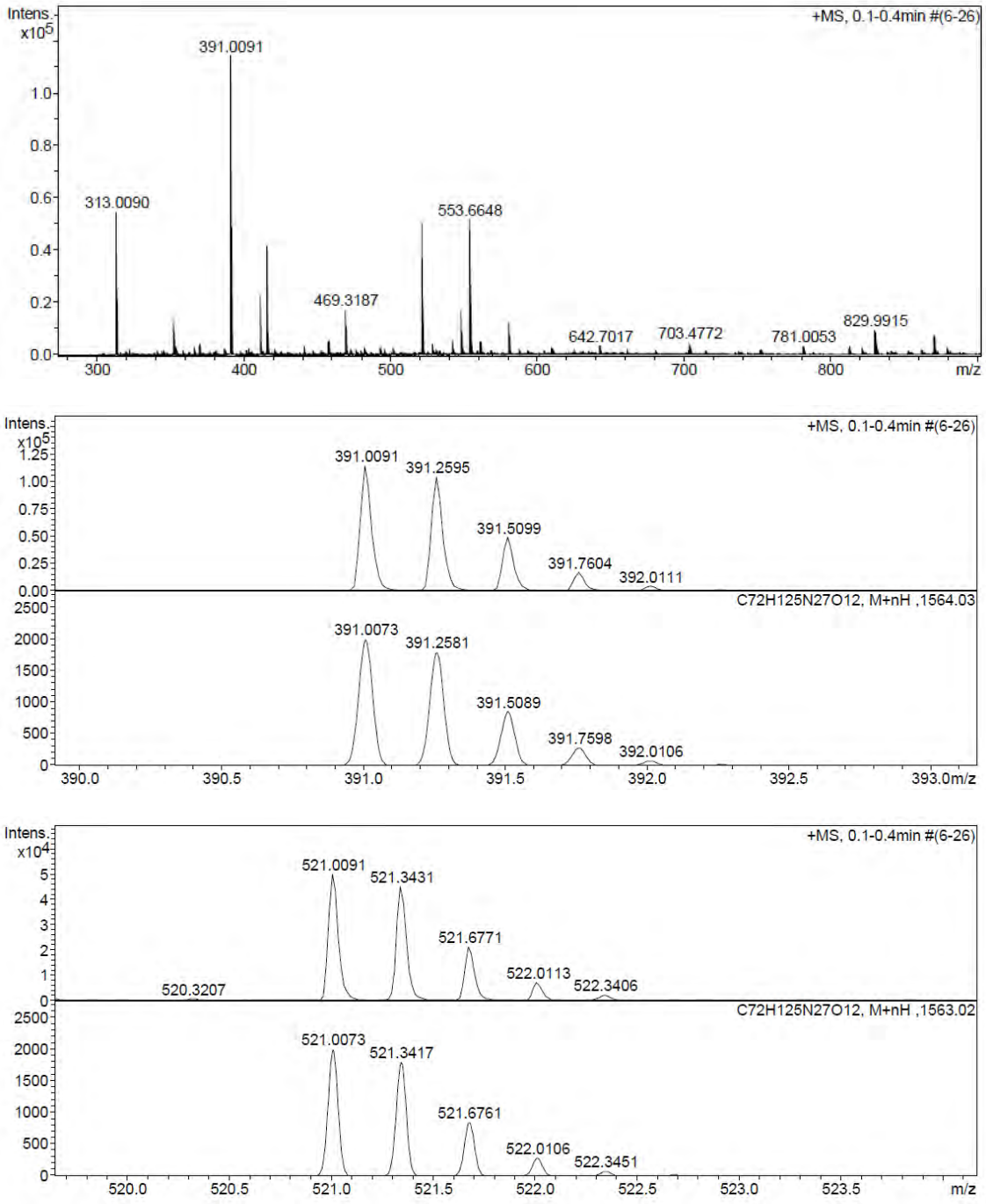
Intens.
x10^5
+MS, 0.1-0.4min #(6-26)
391.0091
313.0090
553.6648
469.3187
642.7017
703.4772
781.0053
829.9915
m/z
Intens.
x10^5
+MS, 0.1-0.4min #(6-26)
391.0091
391.2595
391.5099
391.7604
392.0111
C72H125N27O12, M+nH ,1564.03
391.0073
391.2581
391.5089
391.7598
392.0106
m/z
Intens.
x10^4
+MS, 0.1-0.4min #(6-26)
521.0091
521.3431
521.6771
522.0113
522.3406
520.3207
C72H125N27O12, M+nH ,1563.02
521.0073
521.3417
521.6761
522.0106
522.3451
m/z

BP308 (RRLFRRILRRL-NH_2)

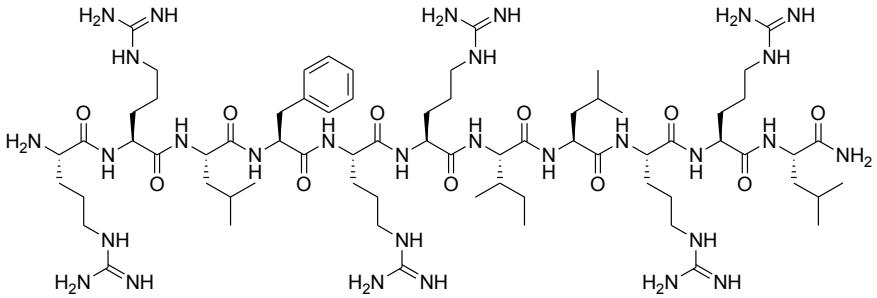

HPLC (λ= 220 nm)

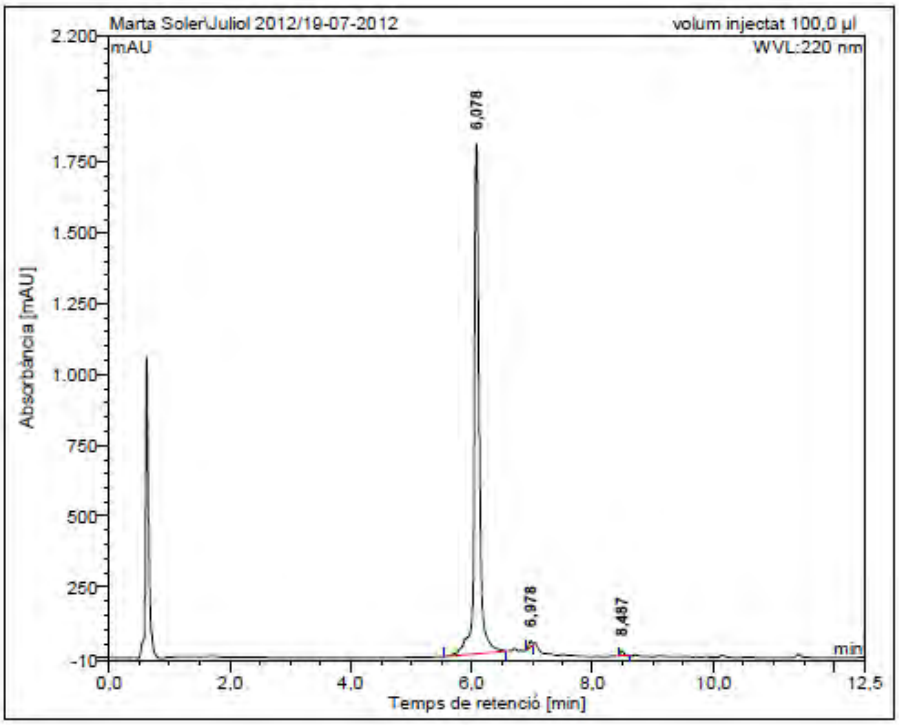

No.	mps retenc min	alçada mAU	Area mAU*min	Area relativa %
1	6,08	1801,317	177,418	98,51
2	6,98	19,947	1,208	0,67
3	8,49	20,643	1,470	0,82
Total:		1841,907	180,096	100,00

ESI/MS (m/z)

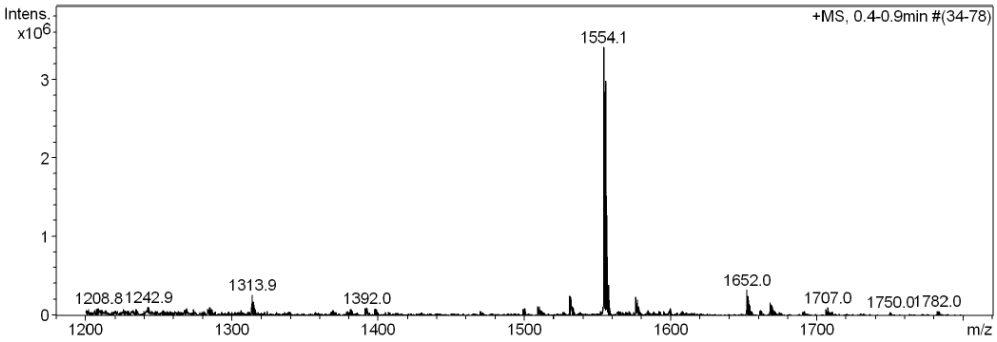
Intens.
x10^6
+MS, 0.4-0.9min #(34-78)
1554.1
1652.0
1313.9
1392.0
1707.0
1208.8
1242.9
1750.0
1782.0
m/z

HRMS (m/z)

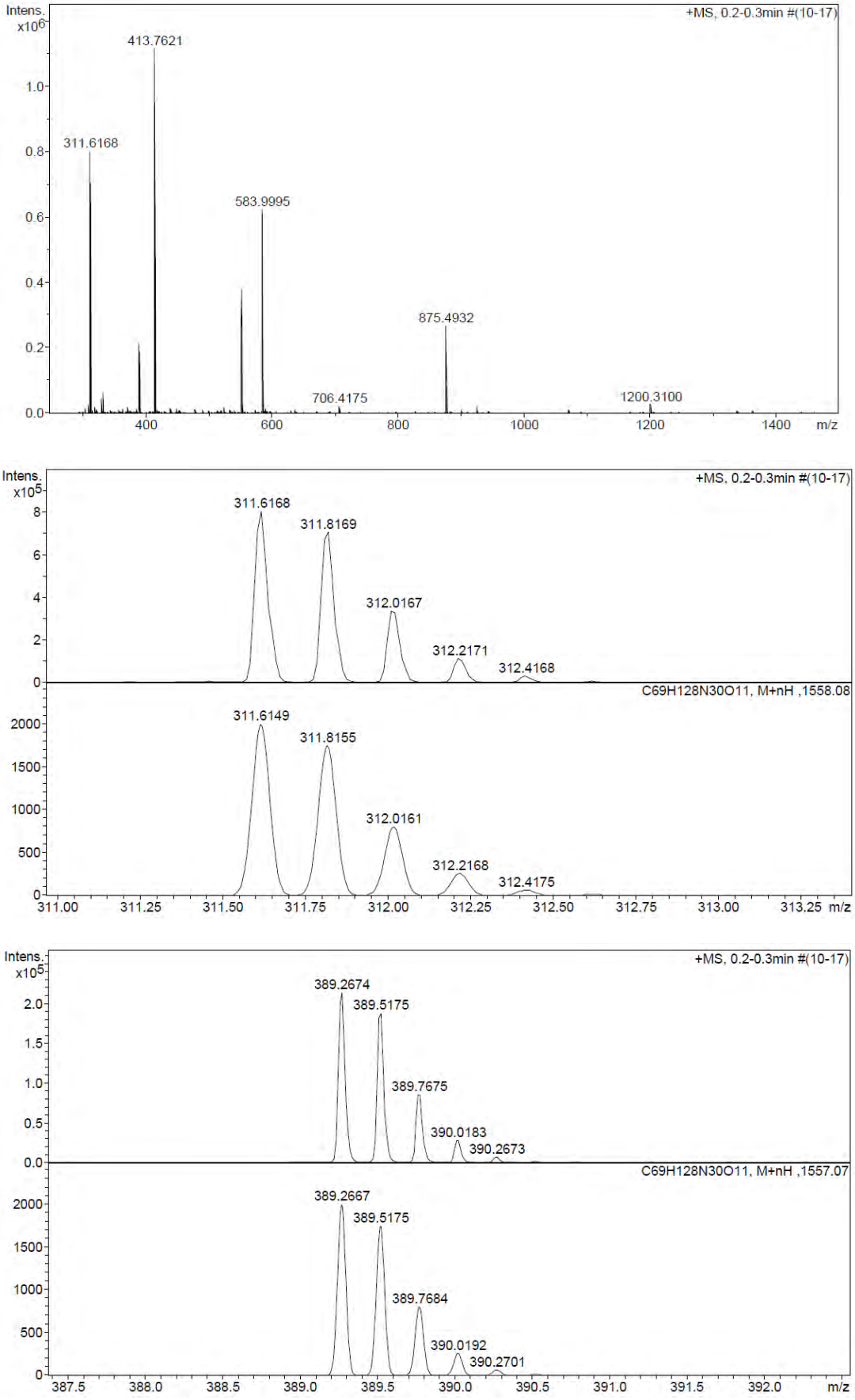
Intens.
x10^6
+MS, 0.2-0.3min #(10-17)
413.7621
311.6168
583.9995
875.4932
706.4175
1200.3100
m/z
Intens.
x10^5
+MS, 0.2-0.3min #(10-17)
311.6168
311.8169
312.0167
312.2171
312.4168
C69H128N30O11, M+nH ,1558.08
311.6149
311.8155
312.0161
312.2168
312.4175
m/z
Intens.
x10^5
+MS, 0.2-0.3min #(10-17)
389.2674
389.5175
389.7675
390.0183
390.2673
C69H128N30O11, M+nH ,1557.07
389.2667
389.5175
389.7684
390.0192
390.2701
m/z

CREKA (CREKA-NH_2)

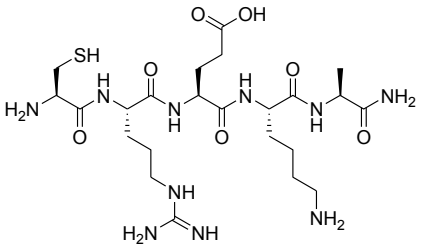

HPLC (λ= 220 nm)

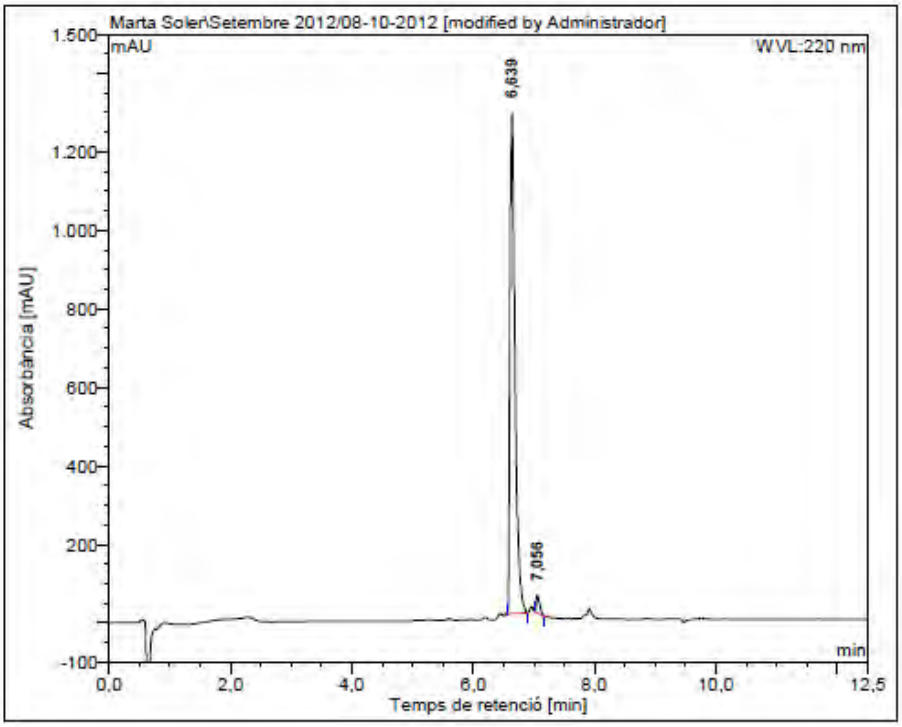

No.	mps retenc min	alçada mAU	Area mAU*min	Area relativa %
1	6,64	1276,937	124,743	97,73
2	7,06	43,895	2,896	2,27
Total:		1320,832	127,639	100,00

ESI/MS (m/z)

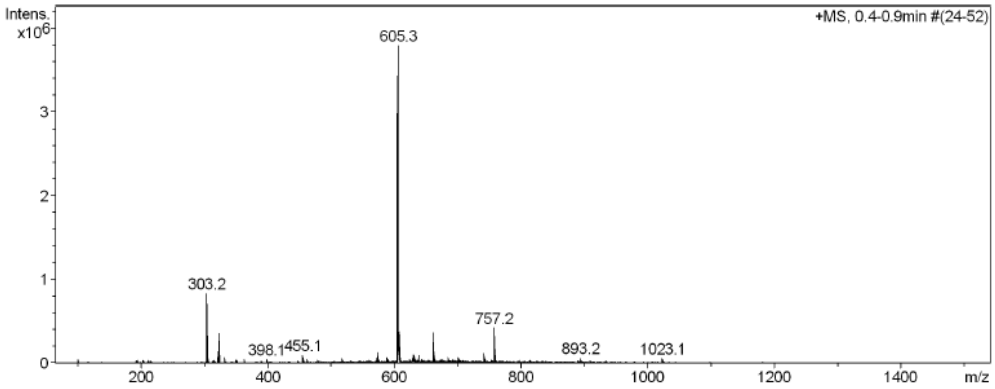
Intens.
x10^6
+MS, 0.4-0.9min #(24-52)
605.3
303.2
757.2
398.1
455.1
893.2
1023.1
m/z

HRMS (m/z)

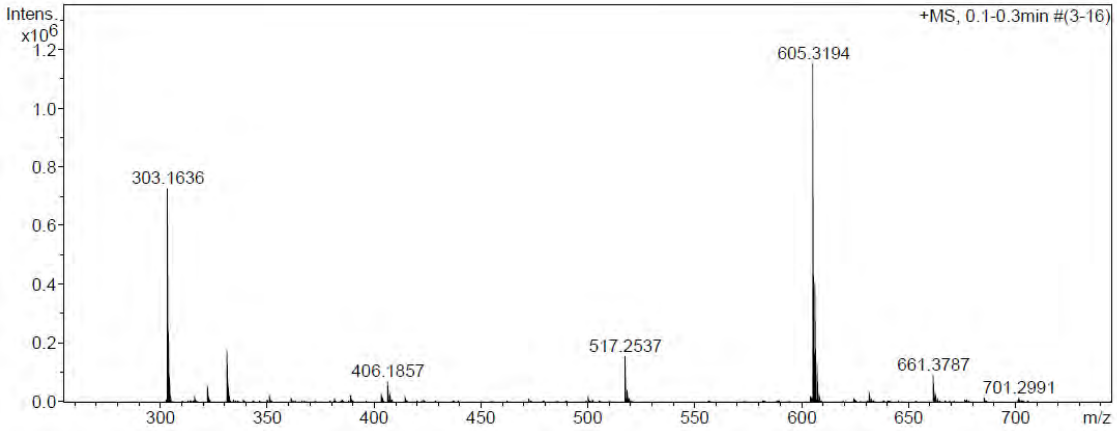
Intens.
x10^6
+MS, 0.1-0.3min #(3-16)
605.3194
303.1636
517.2537
406.1857
661.3787
701.2991
m/z

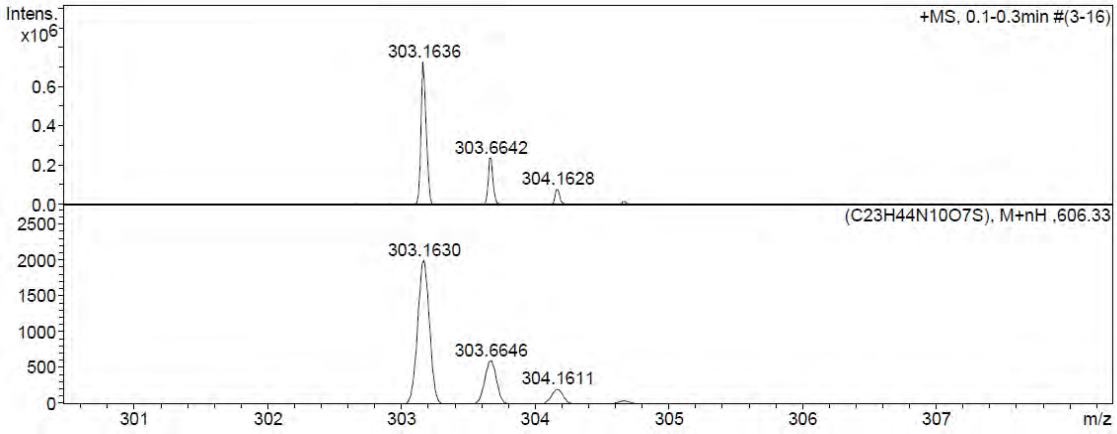
Intens.
x10^6
+MS, 0.1-0.3min #(3-16)
303.1636
303.6642
304.1628
(C23H44N10O7S), M+nH ,606.33
303.1630
303.6646
304.1611
m/z

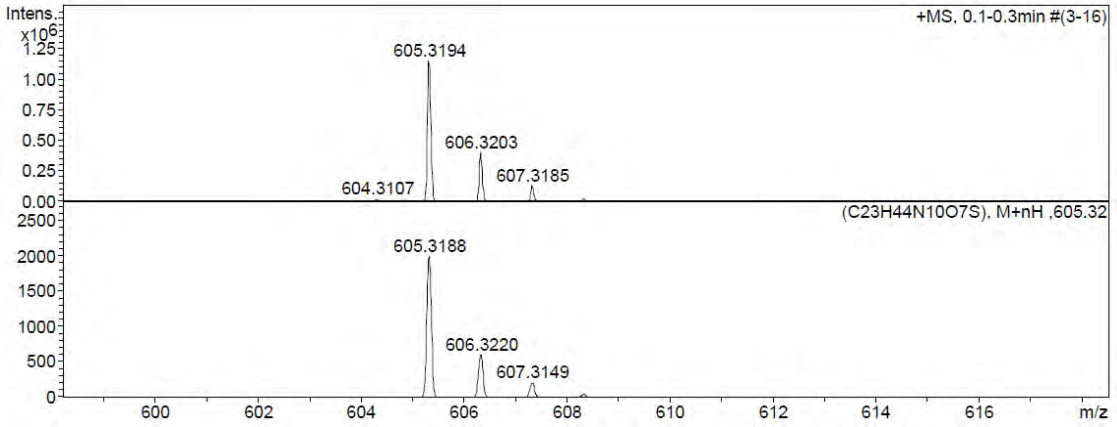
Intens.
x10^6
+MS, 0.1-0.3min #(3-16)
605.3194
606.3203
604.3107
607.3185
(C23H44N10O7S), M+nH ,605.32
605.3188
606.3220
607.3149
m/z

Tat_{49} (RKKRRQRRR-NH_2)

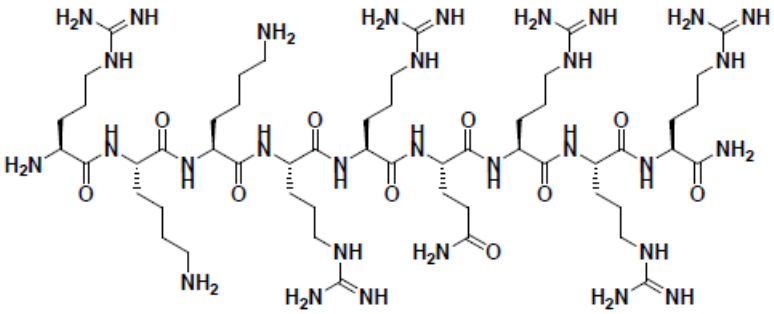

HPLC (λ= 220 nm)

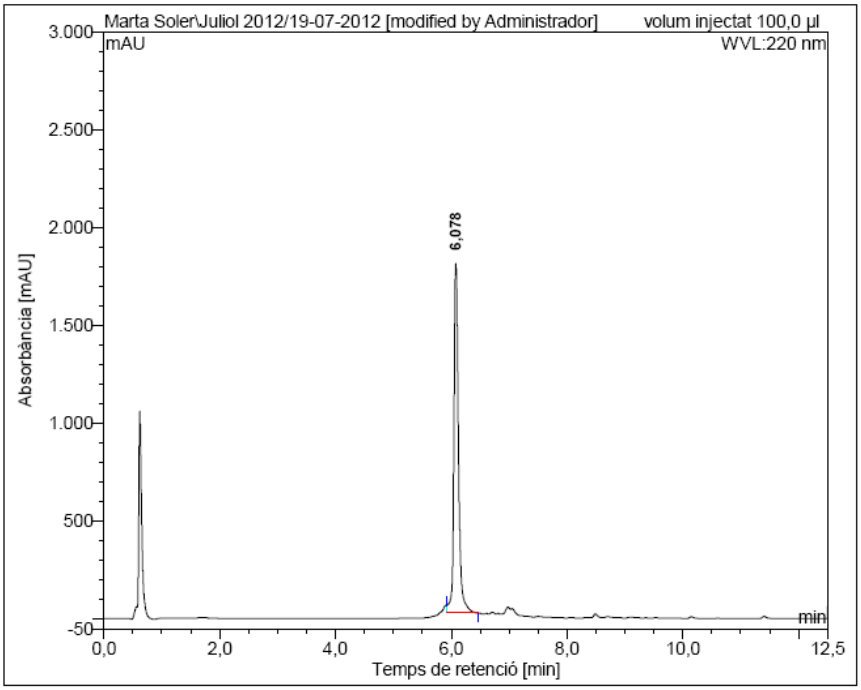

No.	mps retenc min	alçada mAU	Area mAU*min	Area relativa %
1	6,08	1786,528	164,197	100,00
Total:		1786,528	164,197	100,00

ESI/MS (m/z)

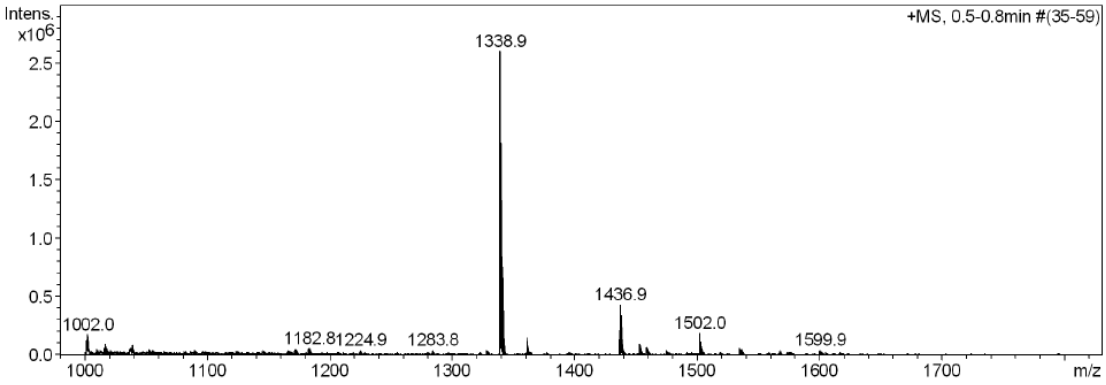

HRMS (m/z)

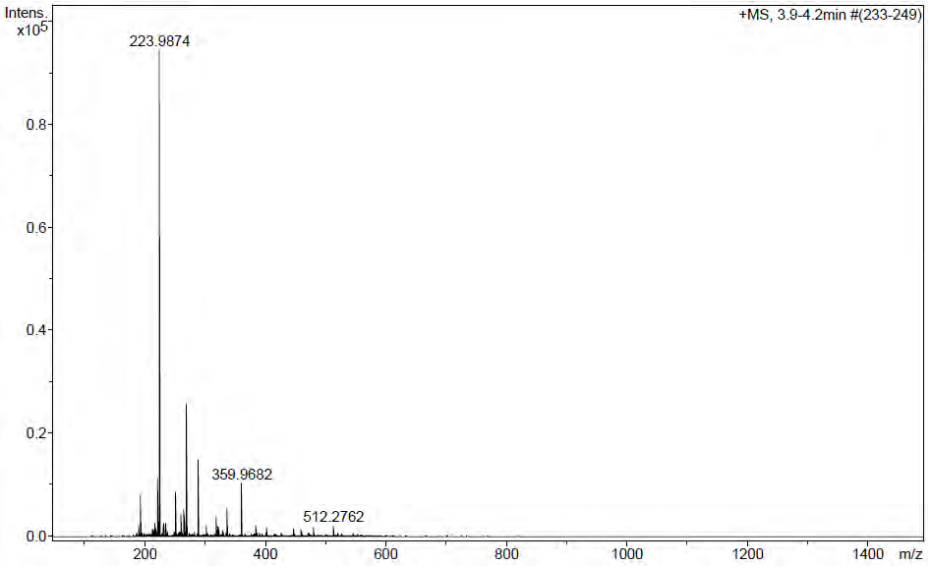

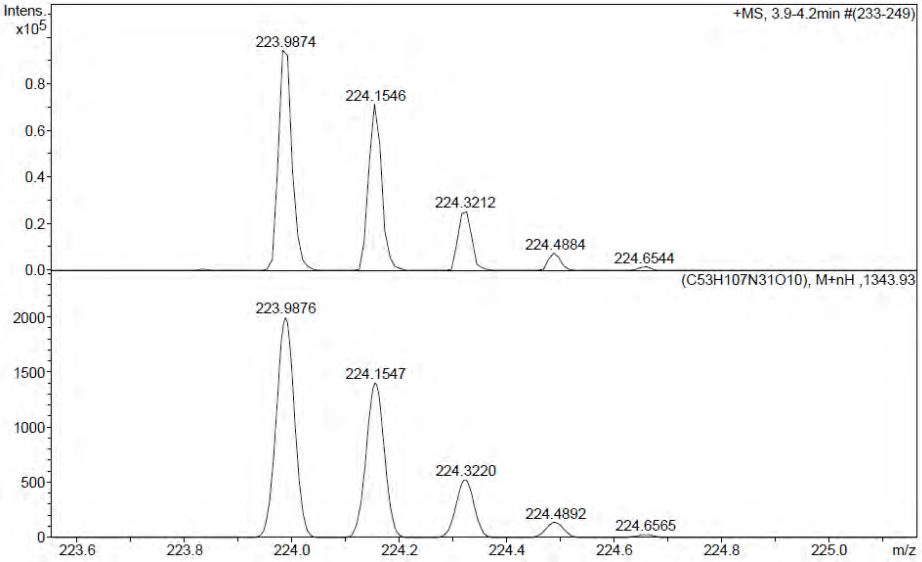

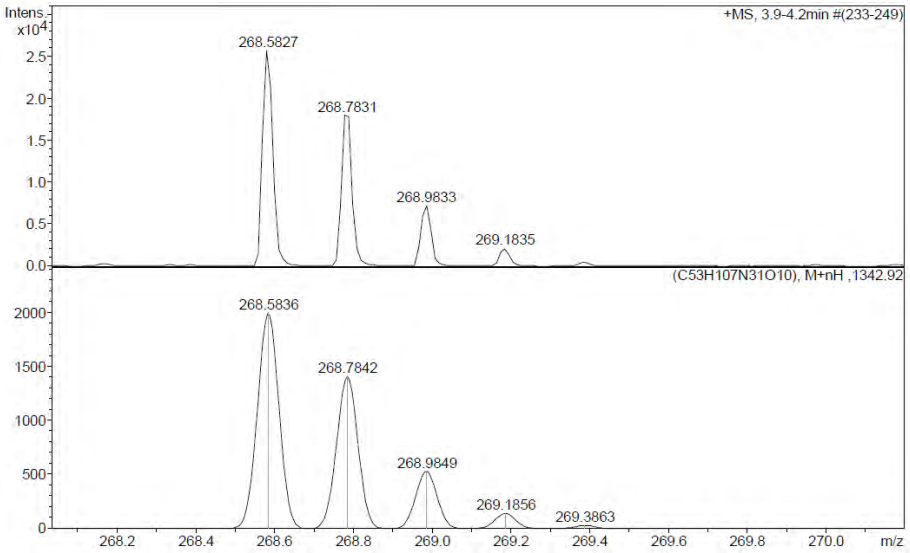
Intens.
x10^4
+MS, 3.9-4.2min #(233-249)
268.5827
268.7831
268.9833
269.1835
(C53H107N31O10), M+nH ,1342.92
268.5836
268.7842
268.9849
269.1856
269.3863
m/z

2. HPLC, ESI-MS and HRMS of CLB-peptide conjugates

BP327 (CREKA**-**KKLFKKILKKL-NH_2)

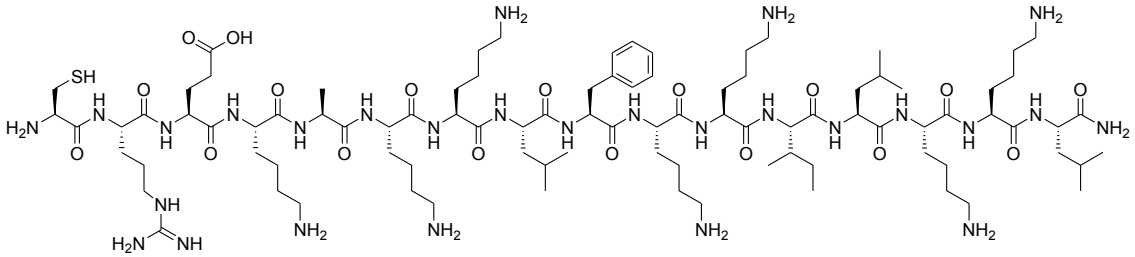

HPLC (λ= 220 nm)

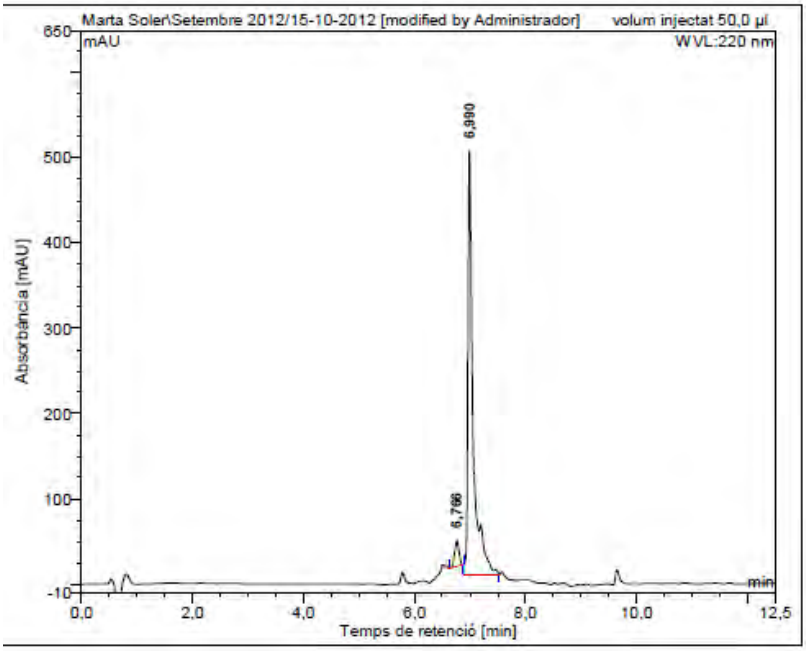

No.	mps retenc min	alçada mAU	Area mAU*min	Area relativa %
1	6,77	30,250	2,690	4,81
2	6,99	496,563	53,191	95,19
Total:		526,814	55,881	100,00

ESI/MS (m/z)

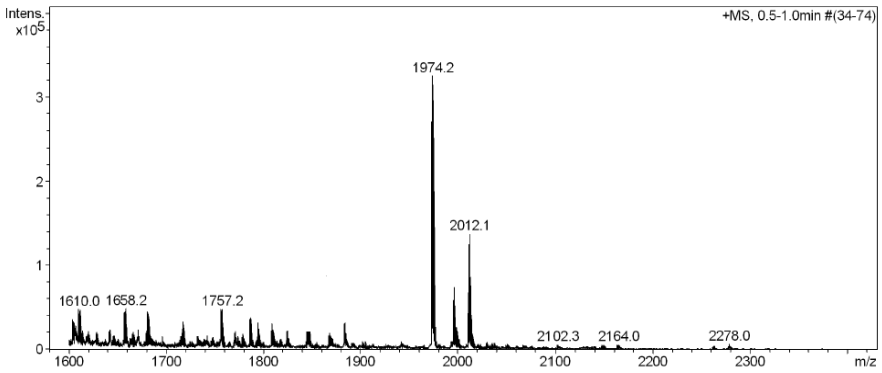
Intens.
x10^5
+MS, 0.5-1.0min #(34-74)
1974.2
2012.1
1610.0
1658.2
1757.2
2102.3
2164.0
2278.0
m/z

HRMS (m/z)

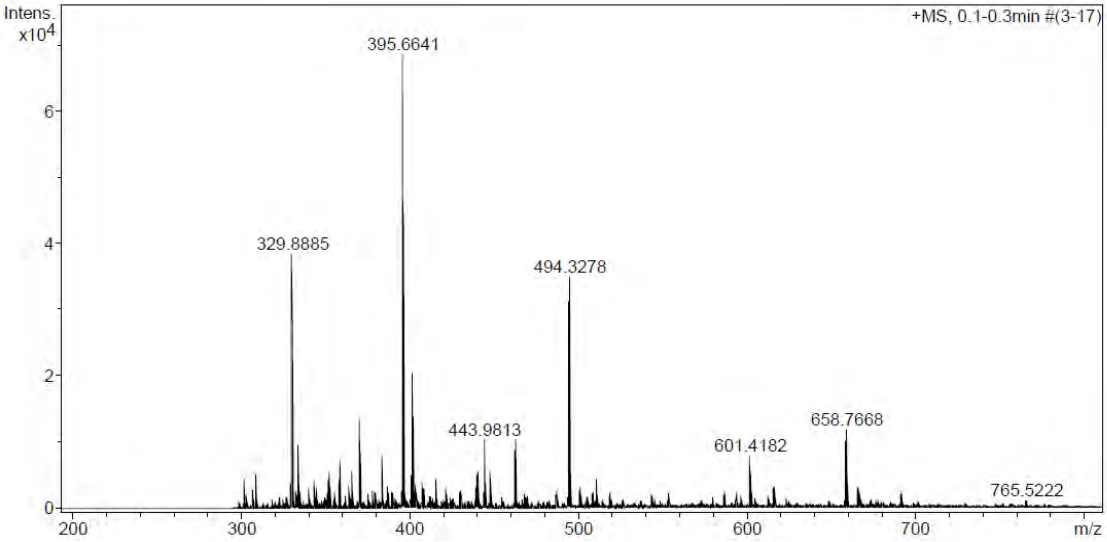
Intens.
x10^4
+MS, 0.1-0.3min #(3-17)
395.6641
329.8885
494.3278
443.9813
658.7668
601.4182
765.5222
m/z

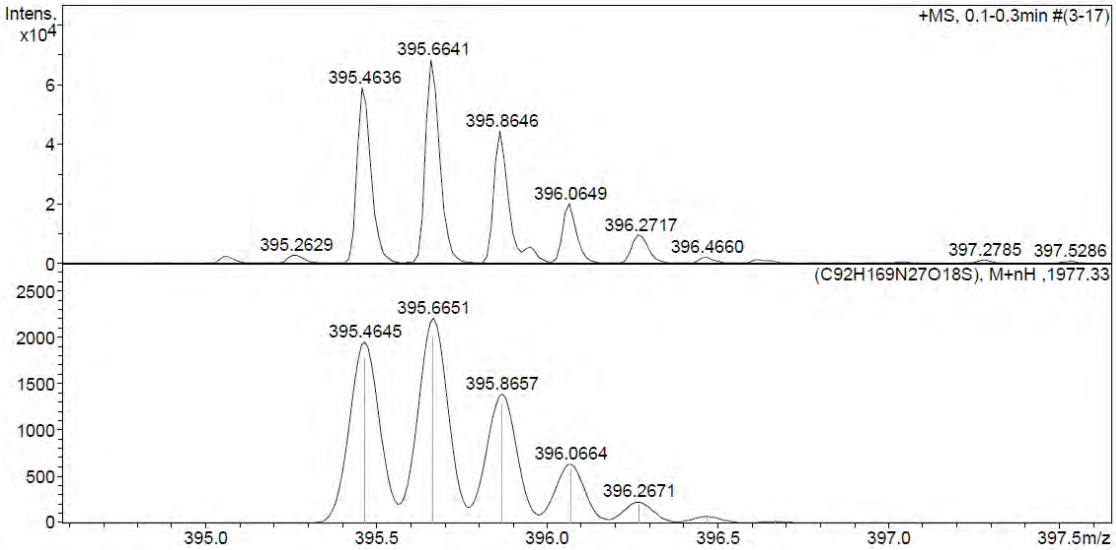
Intens.
x10^4
+MS, 0.1-0.3min #(3-17)
395.6641
395.4636
395.8646
396.0649
396.2717
395.2629
396.4660
397.2785
397.5286
(C92H169N27O18S), M+nH ,1977.33
395.6651
395.4645
395.8657
396.0664
396.2671
m/z

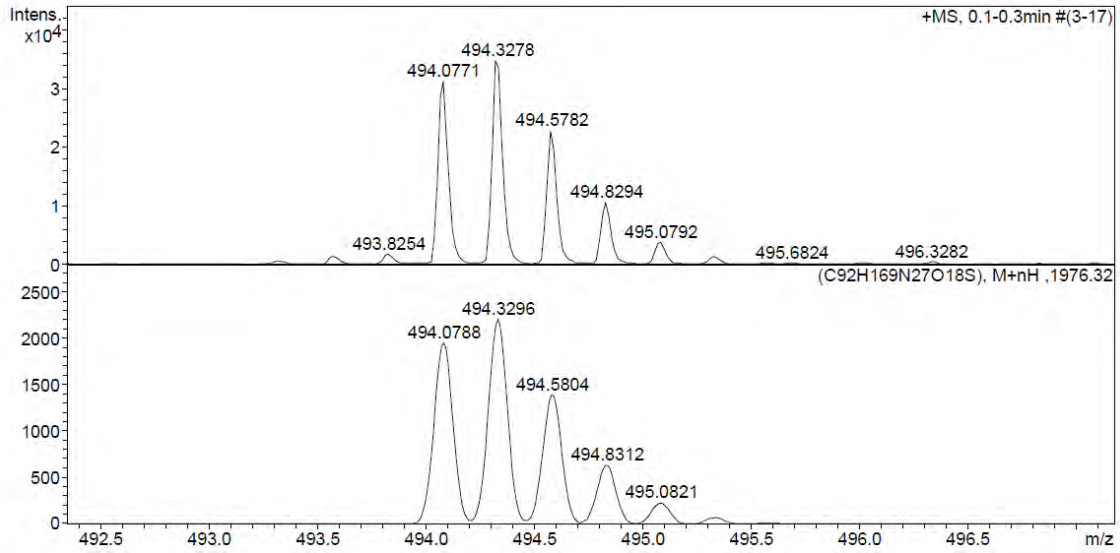
Intens.
x10^4
+MS, 0.1-0.3min #(3-17)
494.3278
494.0771
494.5782
494.8294
495.0792
493.8254
495.6824
496.3282
(C92H169N27O18S), M+nH ,1976.32
494.3296
494.0788
494.5804
494.8312
495.0821
m/z

BP325 (CLB-KKLFKKILKKL-NH_2)

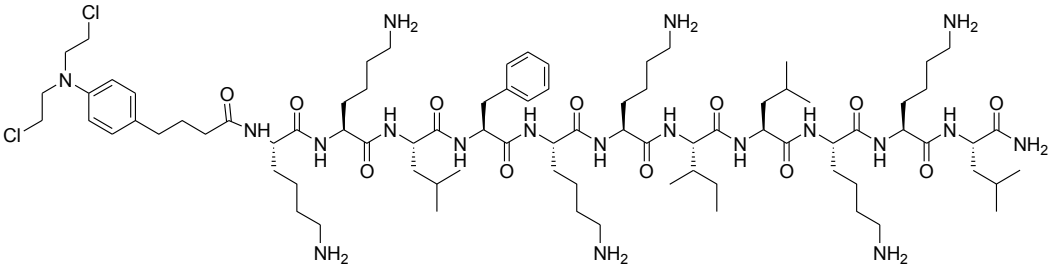

HPLC (λ= 220 nm)

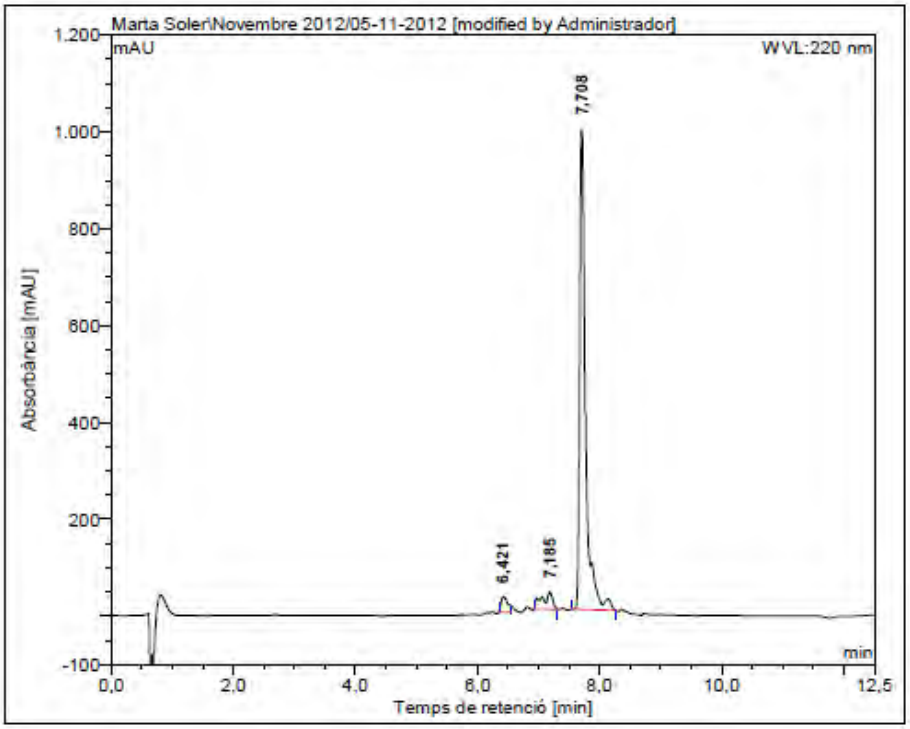

No.	mps retenc min	alçada mAU	Area mAU*min	Area relativa %
1	6,42	31,278	3,951	3,28
2	7,19	35,817	7,126	5,91
3	7,71	991,334	109,512	90,81
Total:		1058,429	120,589	100,00

ESI/MS (m/z)

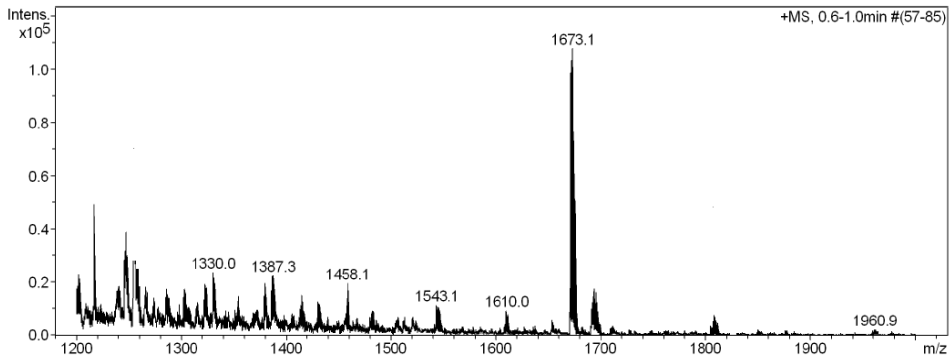
Intens.
x10^5
+MS, 0.6-1.0min #(57-85)
1673.1
1330.0
1387.3
1458.1
1543.1
1610.0
1960.9
m/z

HRMS (m/z)

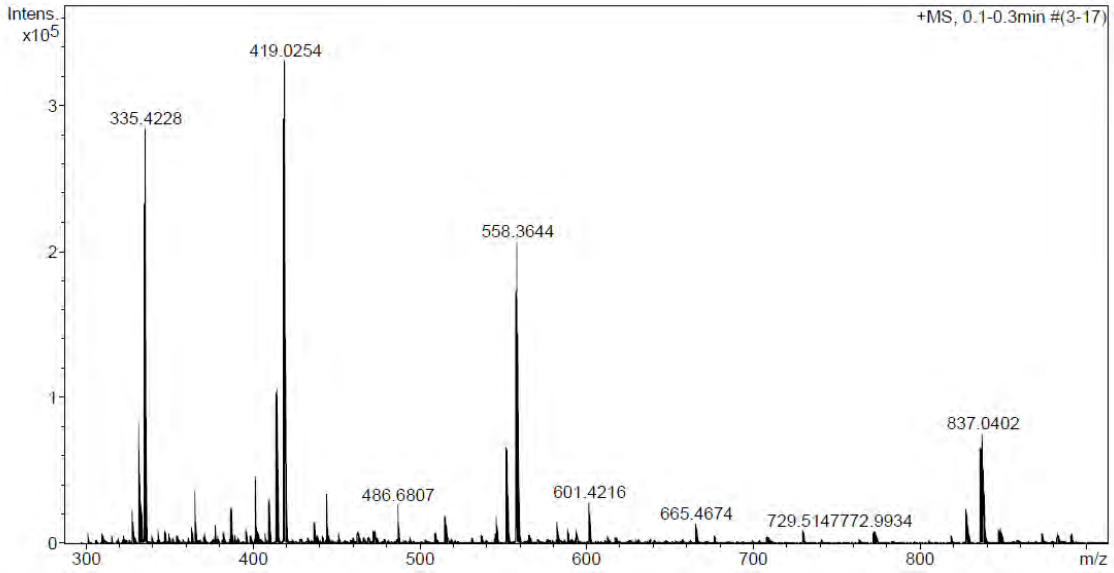
Intens.
x10^5
+MS, 0.1-0.3min #(3-17)
419.0254
335.4228
558.3644
837.0402
486.6807
601.4216
665.4674
729.5147772.9934
m/z

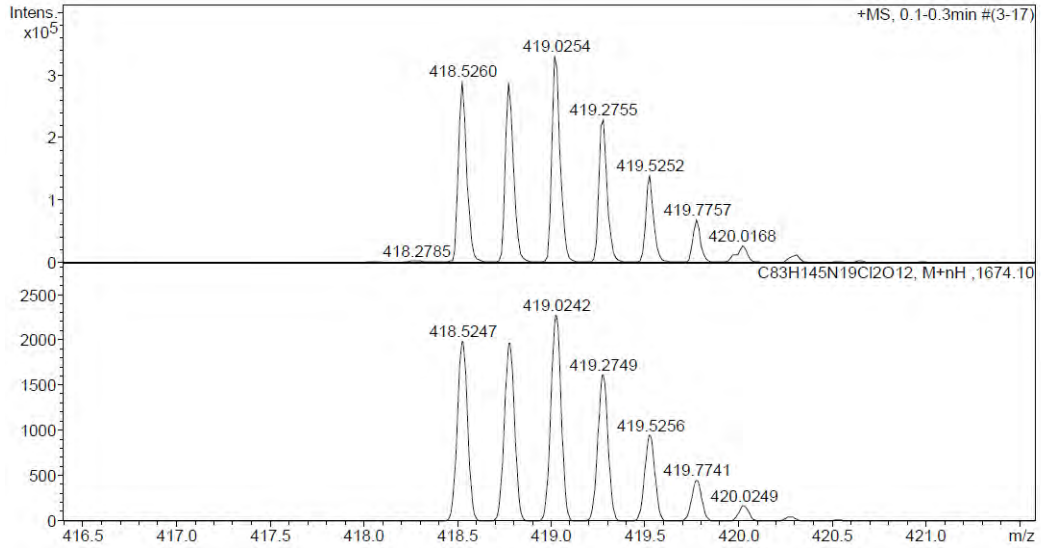
Intens.
x10^5
+MS, 0.1-0.3min #(3-17)
419.0254
418.5260
419.2755
419.5252
419.7757
420.0168
418.2785
C83H145N19Cl2O12, M+nH ,1674.10
419.0242
418.5247
419.2749
419.5256
419.7741
420.0249
m/z

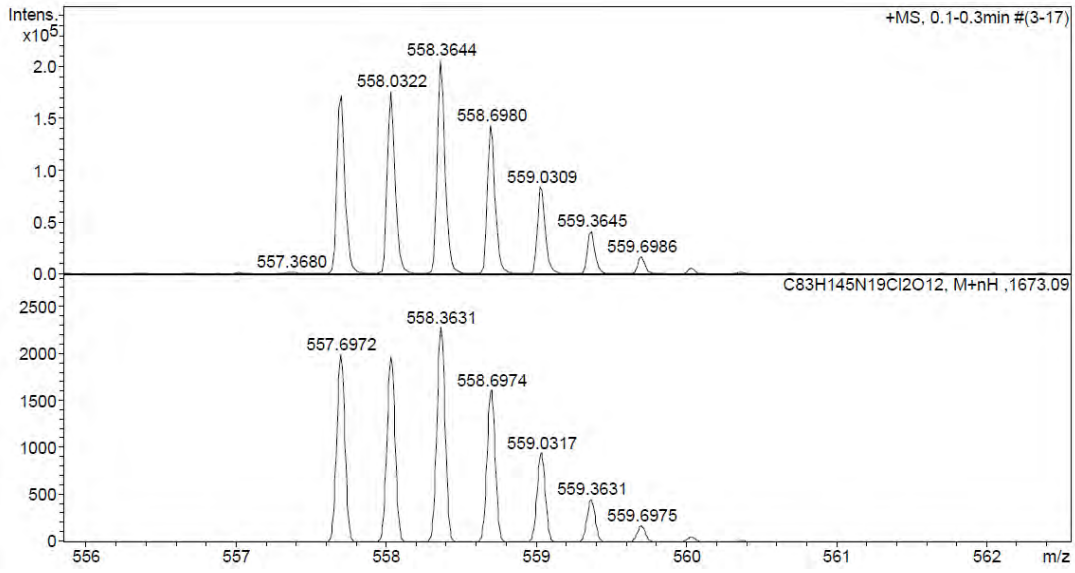
Intens.
x10^5
+MS, 0.1-0.3min #(3-17)
558.3644
558.0322
558.6980
559.0309
559.3645
559.6986
557.3680
C83H145N19Cl2O12, M+nH ,1673.09
558.3631
557.6972
558.6974
559.0317
559.3631
559.6975
m/z

CLB-CREKA (CLB-CREKA-NH_2)

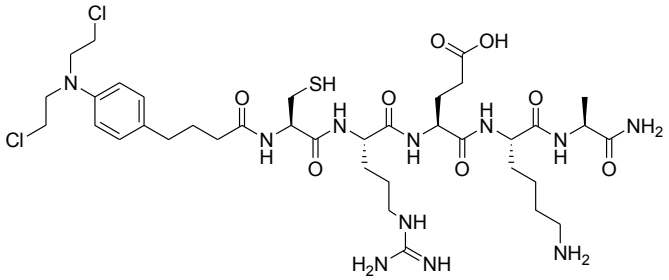

HPLC (λ= 220 nm)

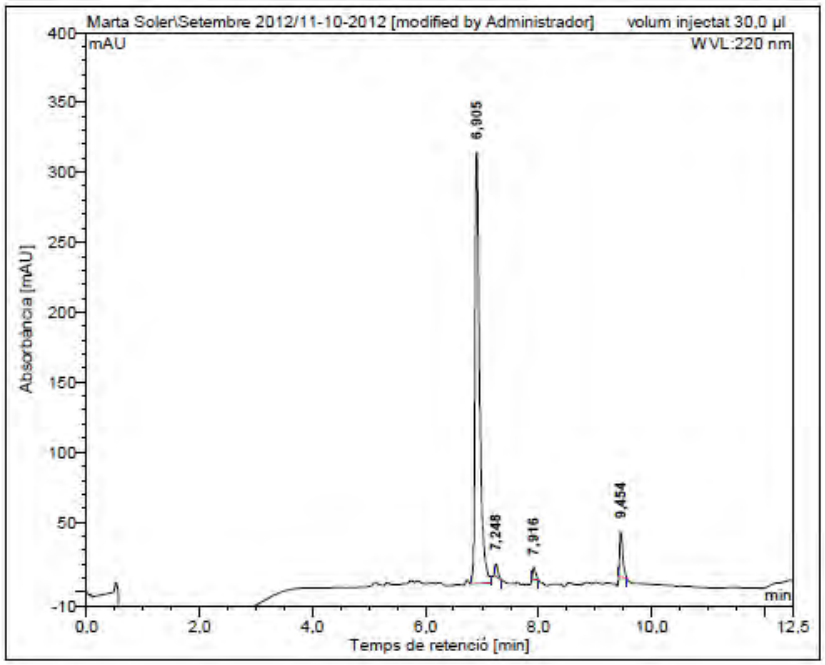

No.	mps retenc min	alçada mAU	Area mAU*min	Area relativa %
1	6,90	308,101	29,232	90,40
2	7,25	8,884	0,513	1,59
3	7,92	8,897	0,566	1,75
4	9,45	32,366	2,026	6,26
Total:		358,248	32,336	100,00

ESI/MS (m/z)

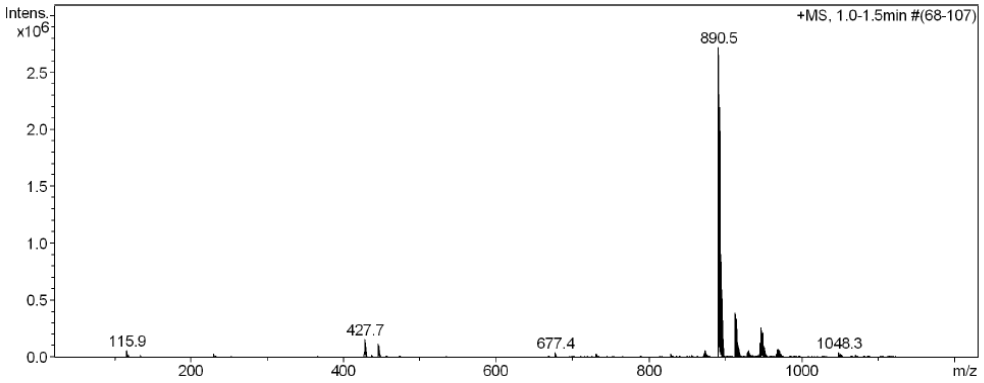
Intens.
x10^6
+MS, 1.0-1.5min #(68-107)
890.5
2.5
2.0
1.5
1.0
0.5
0.0
115.9
427.7
677.4
1048.3
200
400
600
800
1000
m/z

HRMS (m/z)

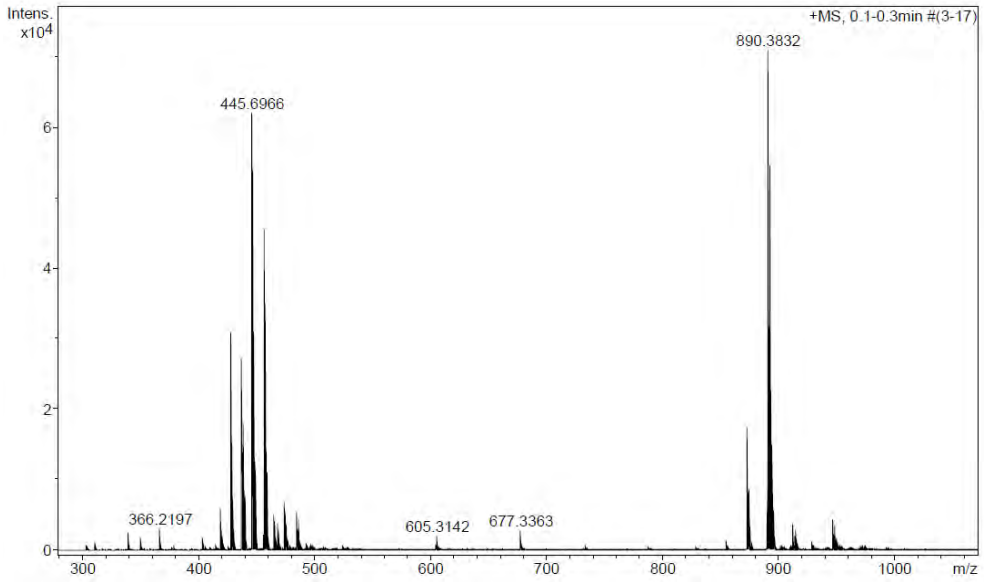
Intens.
x10^4
+MS, 0.1-0.3min #(3-17)
890.3832
445.6966
366.2197
605.3142
677.3363
m/z

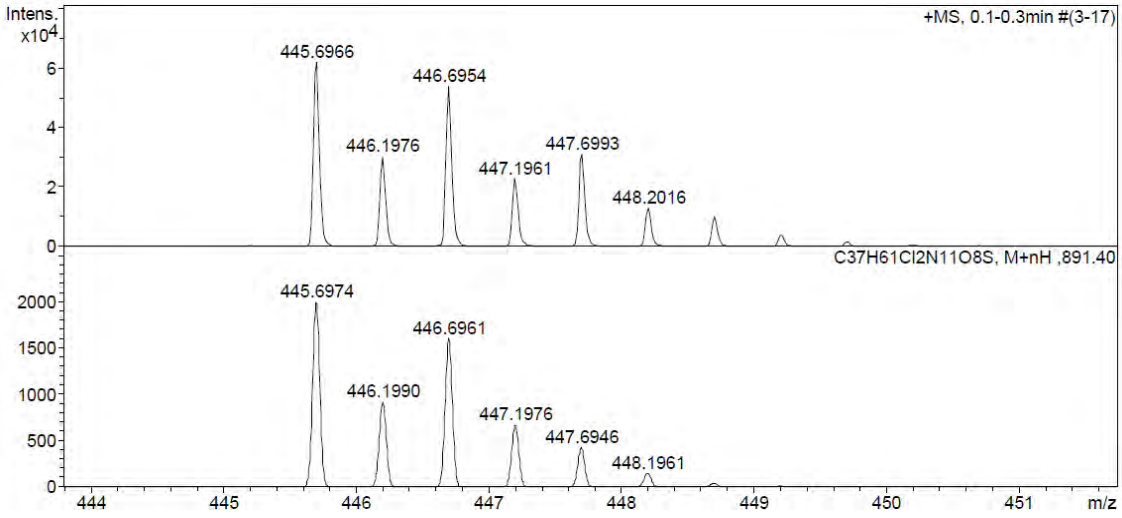
Intens.
x10^4
+MS, 0.1-0.3min #(3-17)
445.6966
446.6954
446.1976
447.6993
447.1961
448.2016
C37H61Cl2N11O8S, M+nH ,891.40
445.6974
446.6961
446.1990
447.1976
447.6946
448.1961
m/z

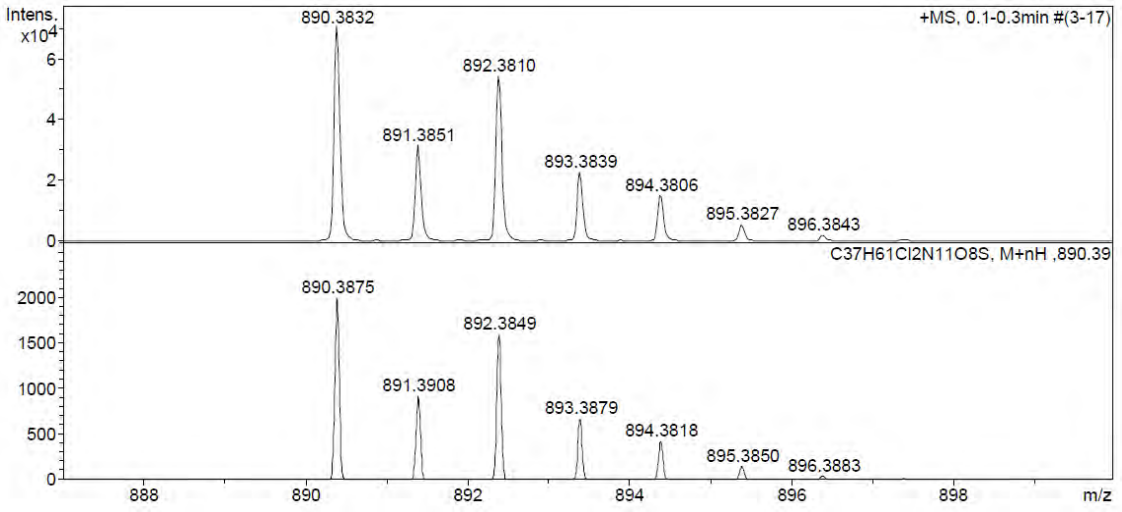
Intens.
x10^4
+MS, 0.1-0.3min #(3-17)
890.3832
892.3810
891.3851
893.3839
894.3806
895.3827
896.3843
C37H61Cl2N11O8S, M+nH ,890.39
890.3875
892.3849
891.3908
893.3879
894.3818
895.3850
896.3883
m/z

BP329 (CLB-CREKA-KKLFKKILKKL-NH_2)

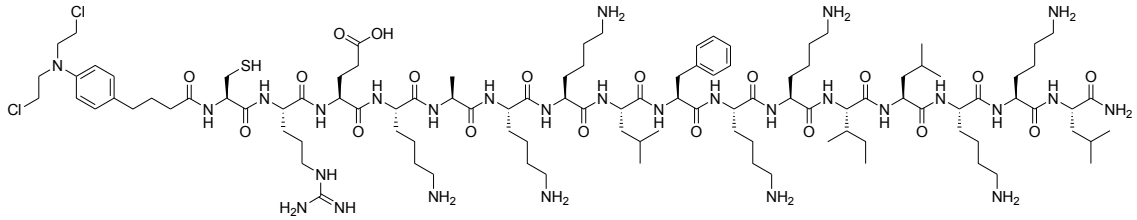

HPLC (λ= 220 nm)

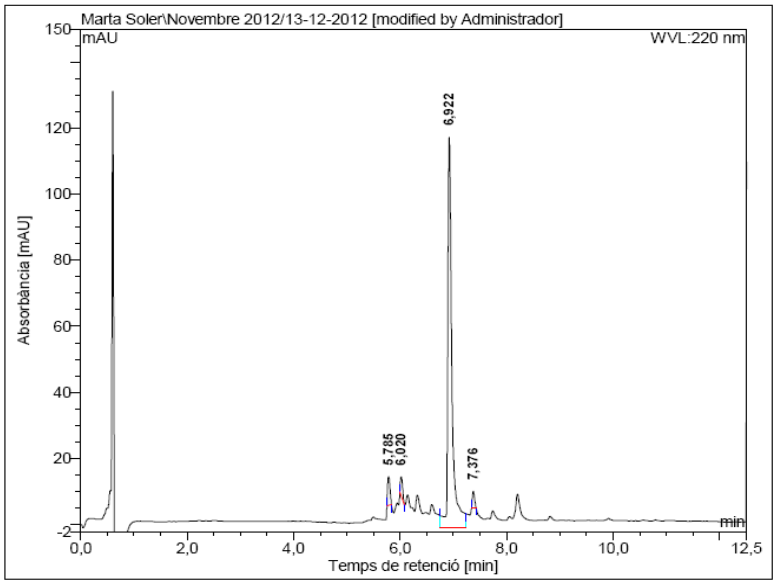

No.	mps retenc min	alçada mAU	Area mAU*min	Area relativa %
1	5,78	8,646	0,445	3,85
2	6,02	5,670	0,271	2,34
3	6,92	118,158	10,618	91,76
4	7,38	4,902	0,237	2,05
Total:		137,376	11,572	100,00

ESI/MS (m/z)

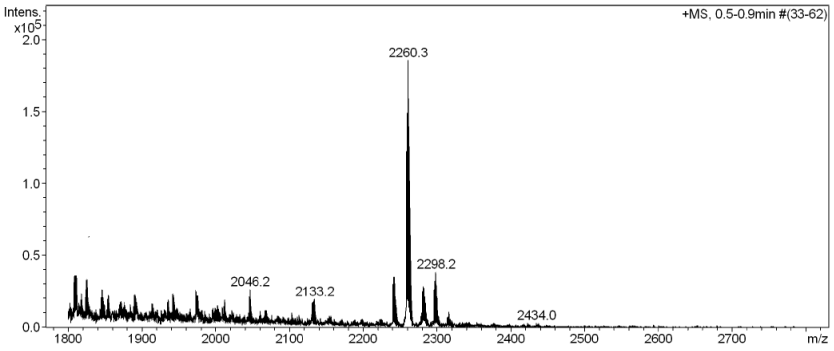
Intens.
x10^5
2.0
1.5
1.0
0.5
0.0
+MS, 0.5-0.9min #(33-62)
2260.3
2298.2
2046.2
2133.2
2434.0
1800
1900
2000
2100
2200
2300
2400
2500
2600
2700
m/z

HRMS (m/z)

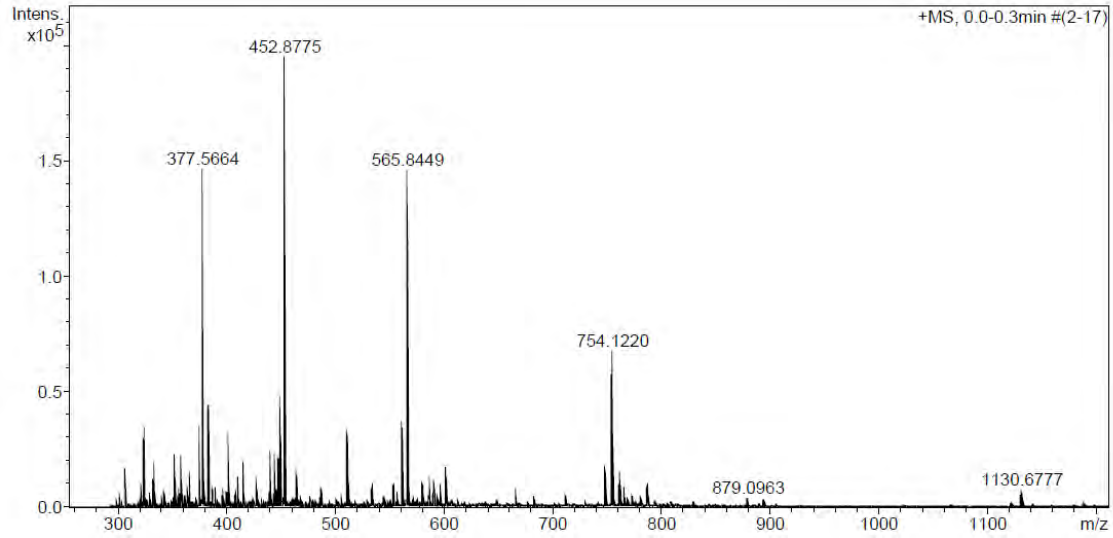
Intens.
x10^5
+MS, 0.0-0.3min #(2-17)
452.8775
377.5664
565.8449
754.1220
879.0963
1130.6777
m/z

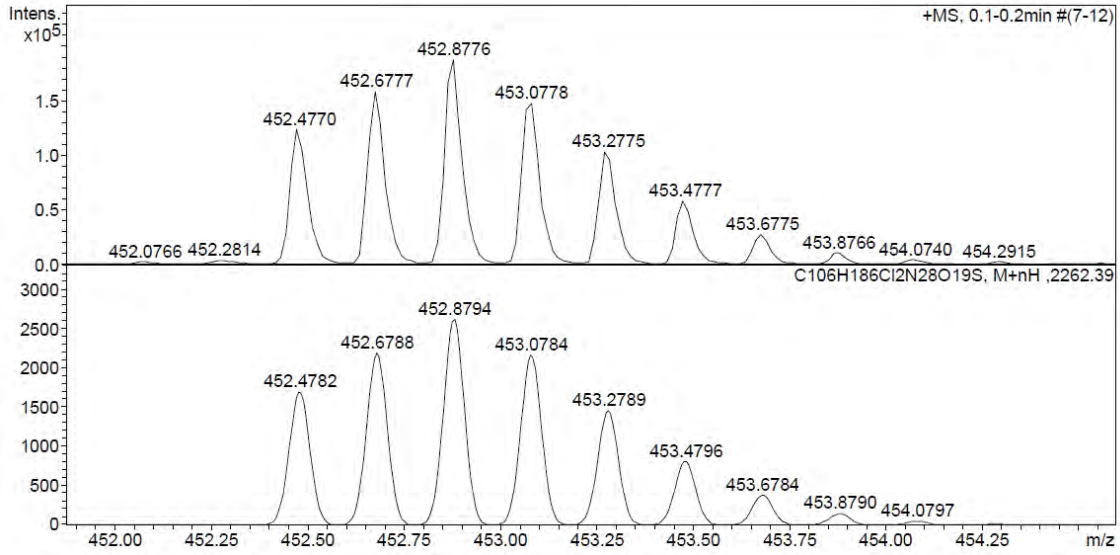
Intens.
x10^5
+MS, 0.1-0.2min #(7-12)
452.8776
452.6777
453.0778
452.4770
453.2775
453.4777
453.6775
453.8766
454.0740
454.2915
452.0766
452.2814
C106H186Cl2N28O19S, M+nH ,2262.39
452.8794
452.6788
453.0784
452.4782
453.2789
453.4796
453.6784
453.8790
454.0797
m/z

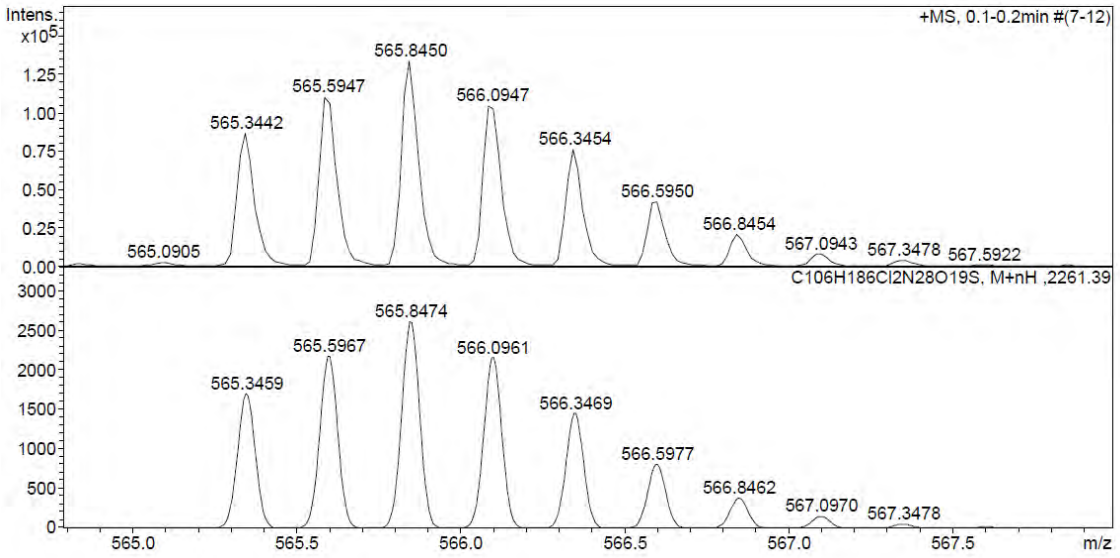
Intens.
x10^5
+MS, 0.1-0.2min #(7-12)
565.8450
565.5947
566.0947
565.3442
566.3454
566.5950
566.8454
567.0943
567.3478
567.5922
565.0905
C106H186Cl2N28O19S, M+nH ,2261.39
565.8474
565.5967
566.0961
565.3459
566.3469
566.5977
566.8462
567.0970
567.3478
m/z

3. HPLC, ESI-MS and HRMS of 5(6)-carboxyfluorescein labeled peptides

CF-BP16 (CF-KKLFKKILKFL-NH_2)

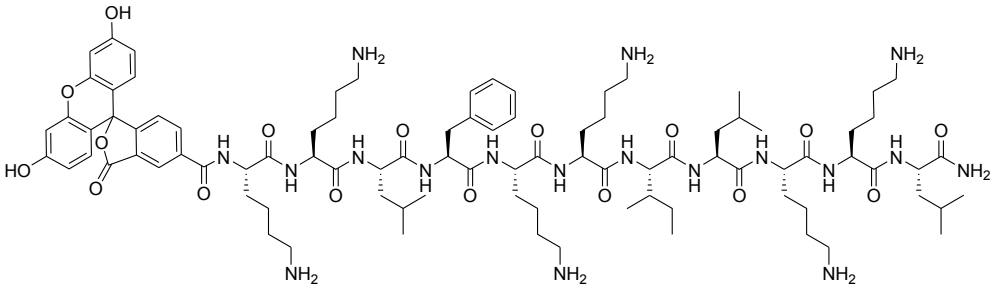

HPLC (λ= 220 nm)

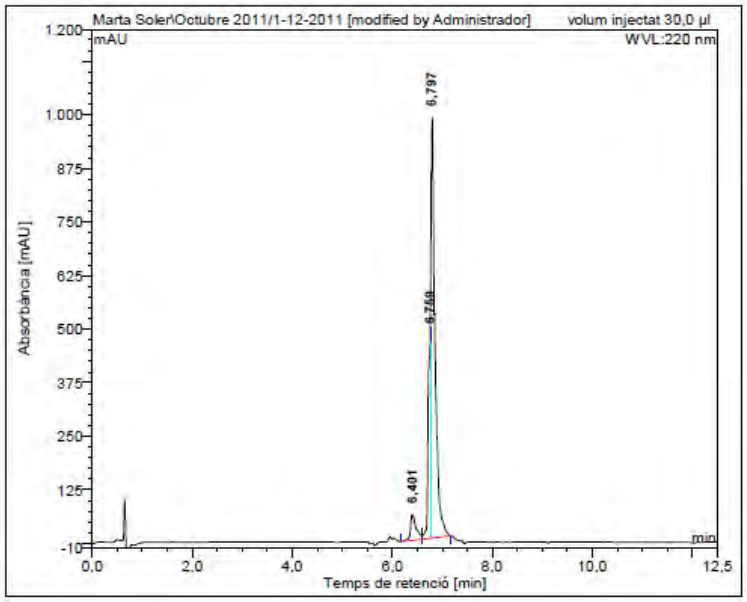

No.	mps retenc min	alçada mAU	Area mAU*min	Area relativa %
1	6,40	60,473	8,138	6,40
2	6,76	473,768	22,057	17,34
3	6,80	981,748	97,024	76,26
Total:		1515,990	127,220	100,00

ESI/MS (m/z)

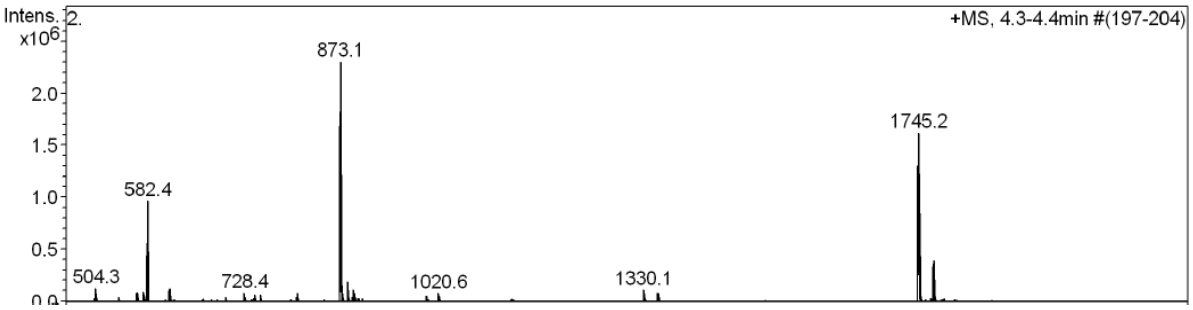
Intens.
x10^6
2.
+MS, 4.3-4.4min #(197-204)
2.0
1.5
1.0
0.5
873.1
1745.2
582.4
504.3
728.4
1020.6
1330.1

HRMS (m/z)

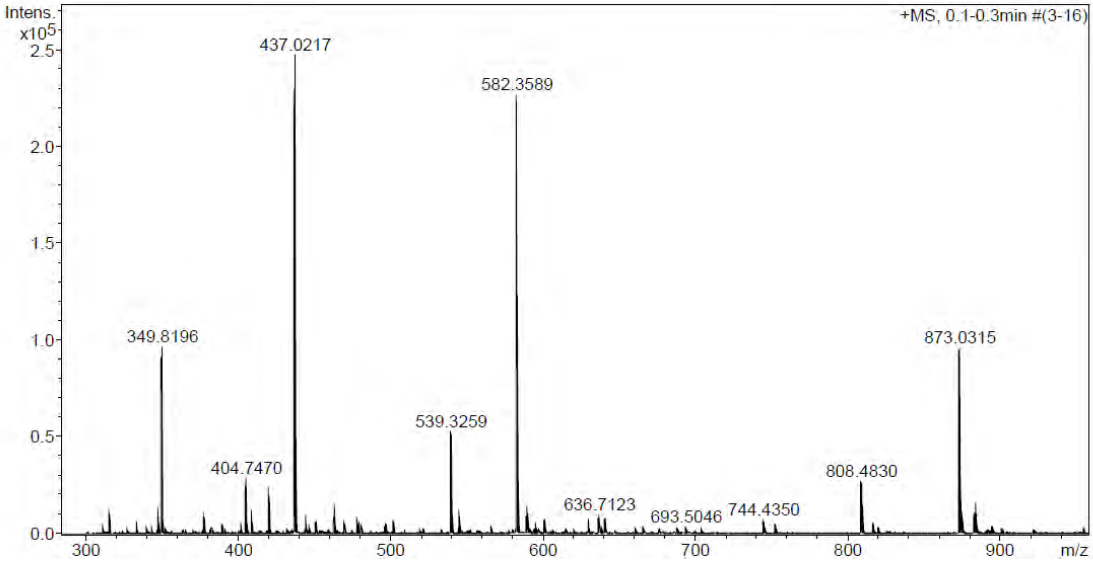
Intens.
x10^5
+MS, 0.1-0.3min #(3-16)
437.0217
582.3589
349.8196
873.0315
539.3259
404.7470
808.4830
636.7123
693.5046
744.4350
m/z

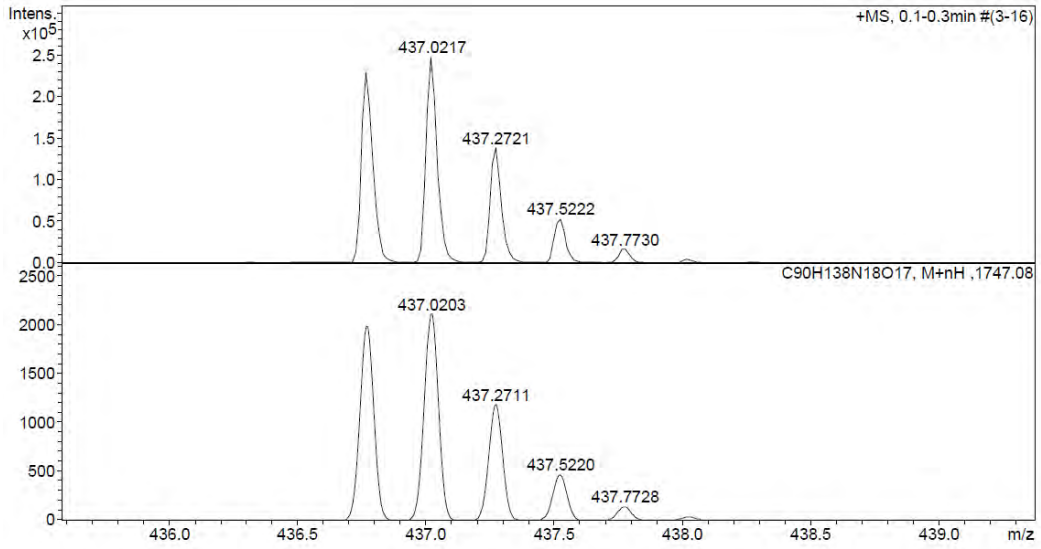
Intens.
x10^5
+MS, 0.1-0.3min #(3-16)
437.0217
437.2721
437.5222
437.7730
C90H138N18O17, M+nH ,1747.08
437.0203
437.2711
437.5220
437.7728
m/z

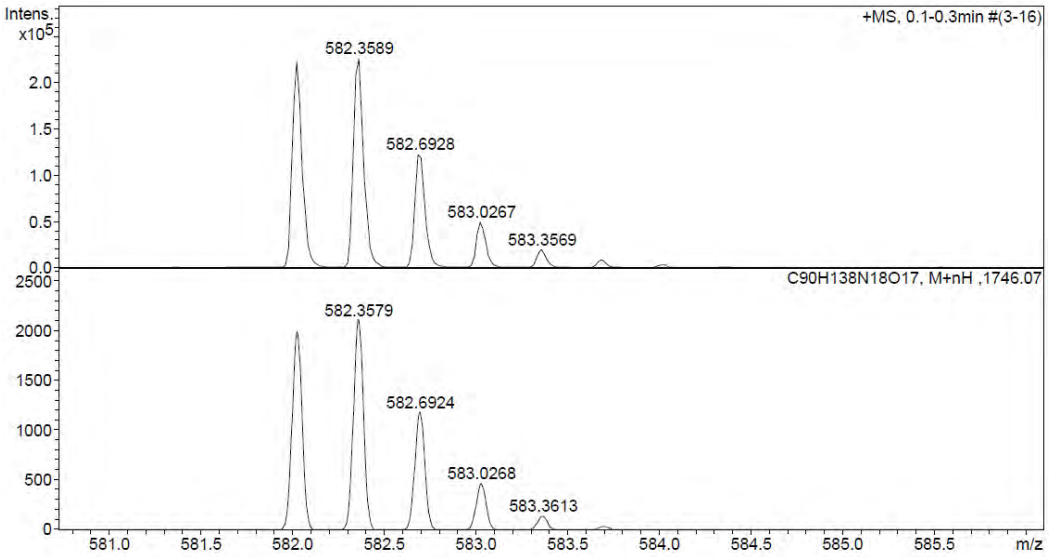
Intens.
x10^5
+MS, 0.1-0.3min #(3-16)
582.3589
582.6928
583.0267
583.3569
C90H138N18O17, M+nH ,1746.07
582.3579
582.6924
583.0268
583.3613
m/z

CF-CREKA (CF-CREKA-NH_2)

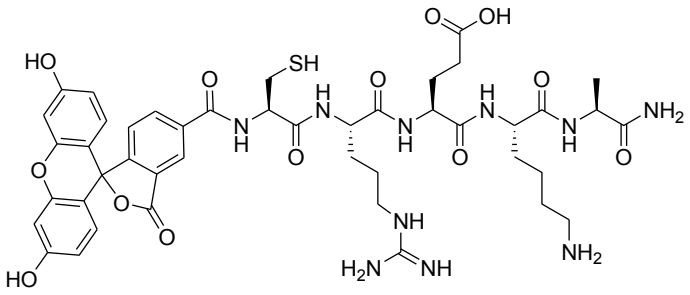

HPLC (λ= 220 nm)

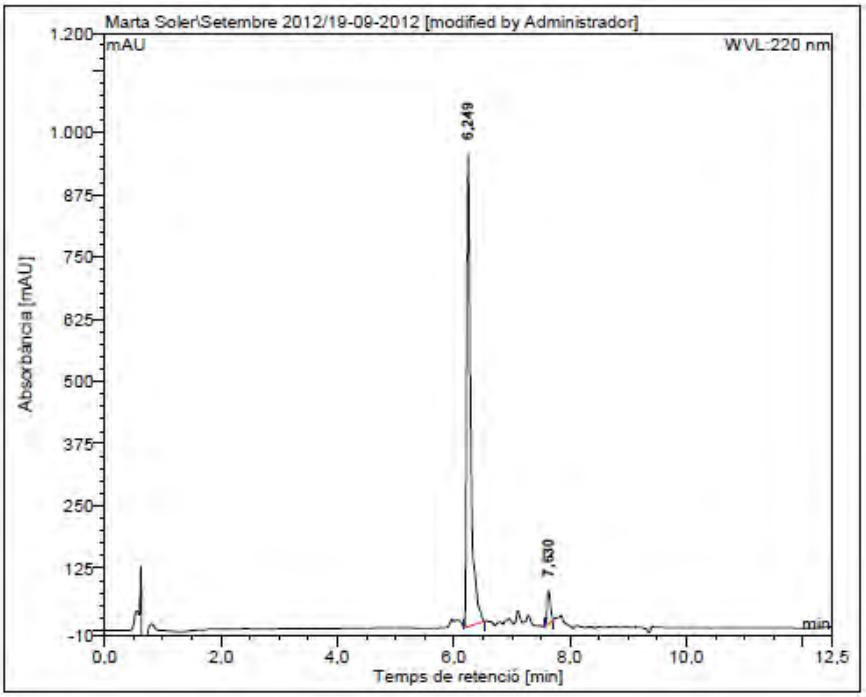

No.	mps retenc min	alçada mAU	Area mAU*min	Area relativa %
1	6,25	948,097	76,186	94,71
2	7,63	67,005	4,253	5,29
Total:		1015,101	80,439	100,00

ESI/MS (m/z)

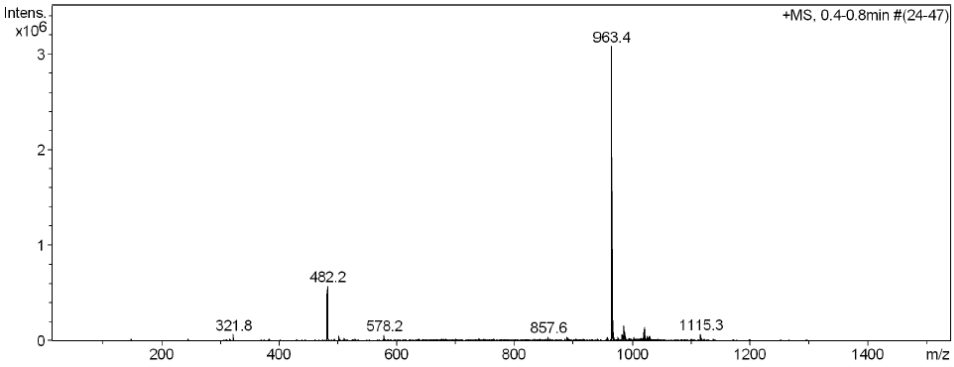
Intens.
x10^6
+MS, 0.4-0.8min #(24-47)
963.4
482.2
321.8
578.2
857.6
1115.3
m/z

HRMS (m/z)

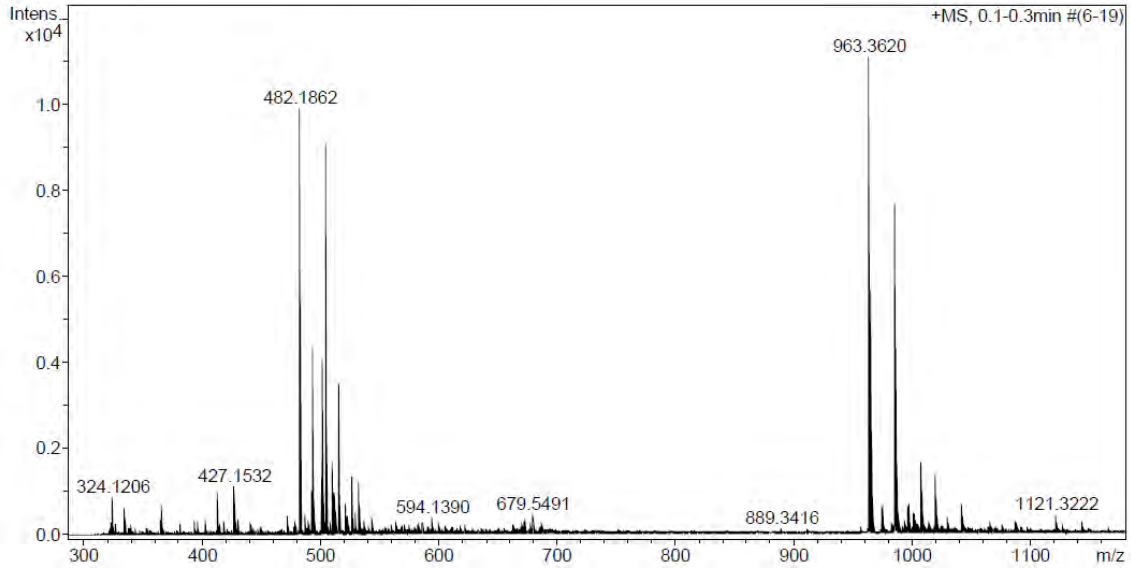
Intens.
x10^4
+MS, 0.1-0.3min #(6-19)
963.3620
482.1862
324.1206
427.1532
594.1390
679.5491
889.3416
1121.3222
m/z

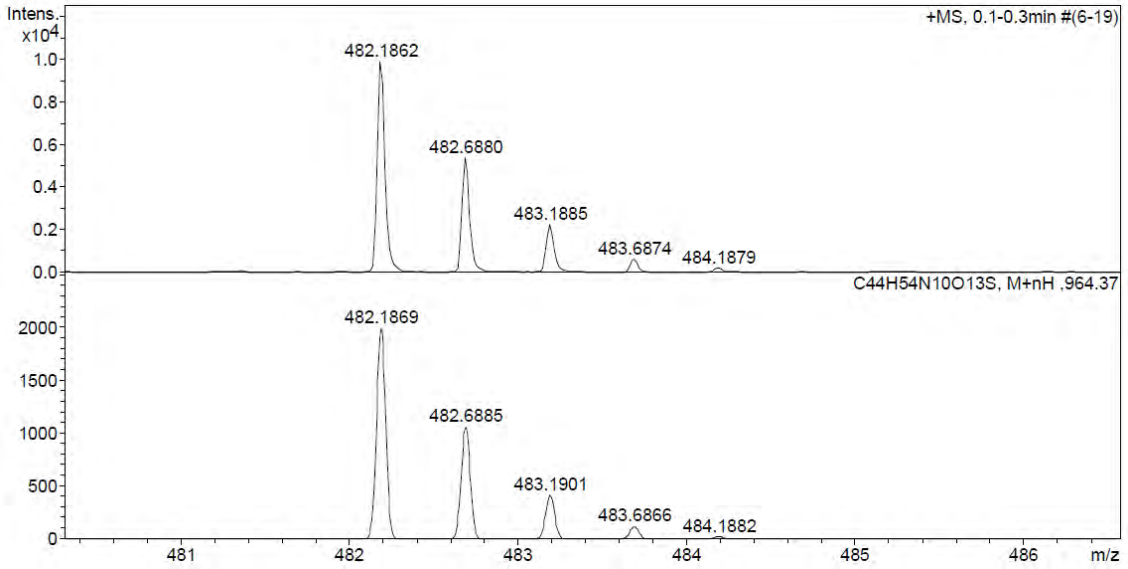
Intens.
x10^4
+MS, 0.1-0.3min #(6-19)
482.1862
482.6880
483.1885
483.6874
484.1879
C44H54N10O13S, M+nH ,964.37
482.1869
482.6885
483.1901
483.6866
484.1882
m/z

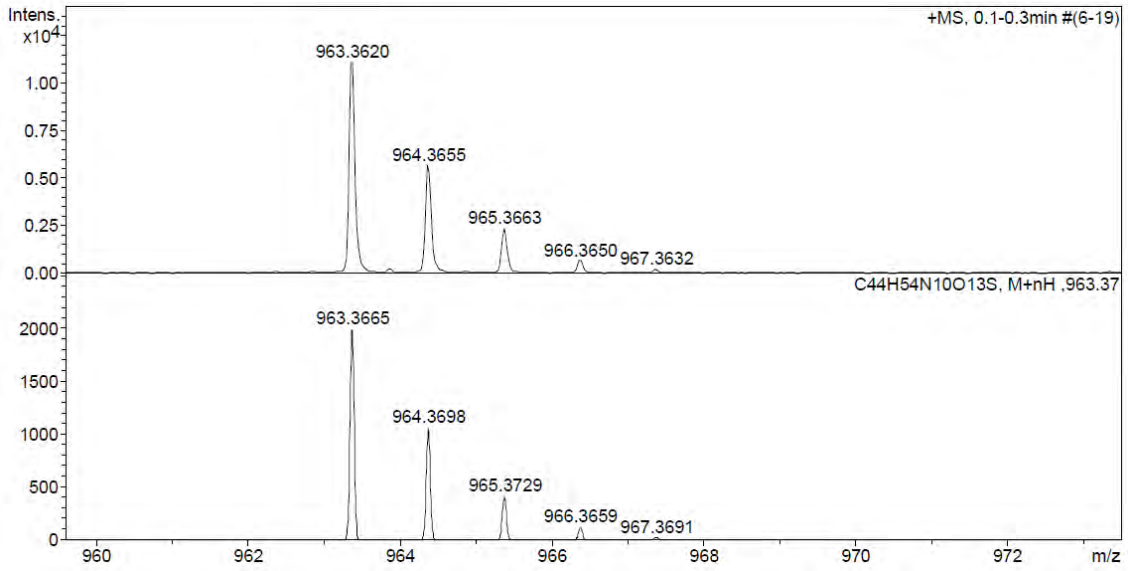
Intens.
x10^4
+MS, 0.1-0.3min #(6-19)
963.3620
964.3655
965.3663
966.3650
967.3632
C44H54N10O13S, M+nH ,963.37
963.3665
964.3698
965.3729
966.3659
967.3691
m/z

BP328 (CF-CREKA-KKLFKKILKKL-NH_2)

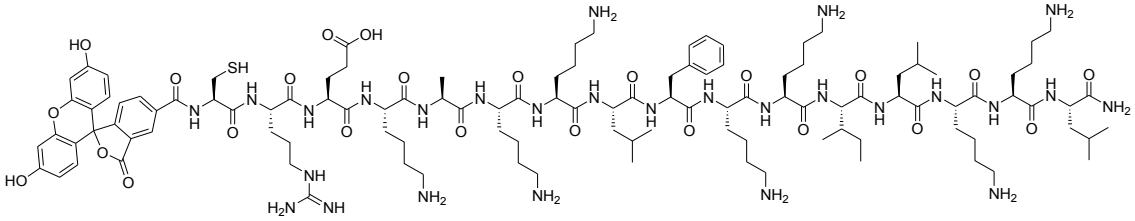

HPLC (λ= 220 nm)

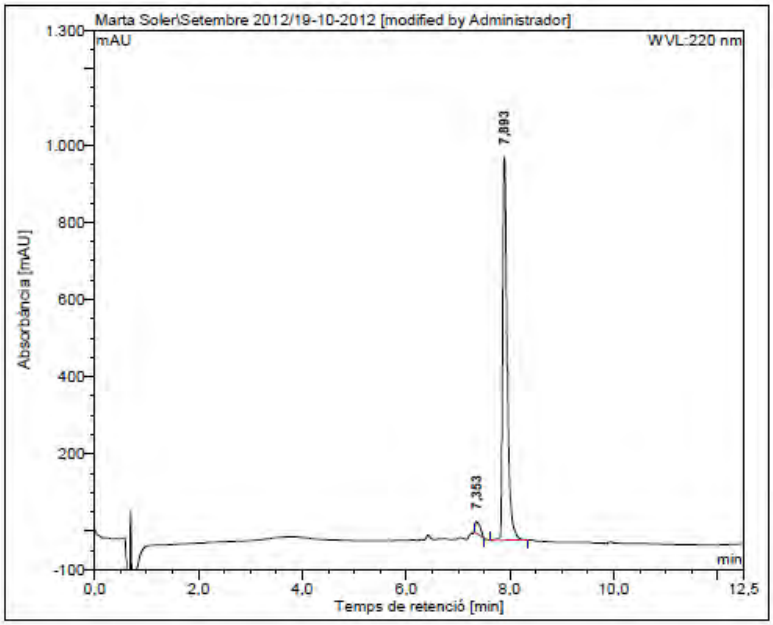

No.	mps retenc min	alçada mAU	Area mAU*min	Area relativa %
1	7,35	30,131	3,543	3,40
2	7,89	993,729	100,753	96,60
Total:		1023,860	104,296	100,00

ESI/MS (m/z)

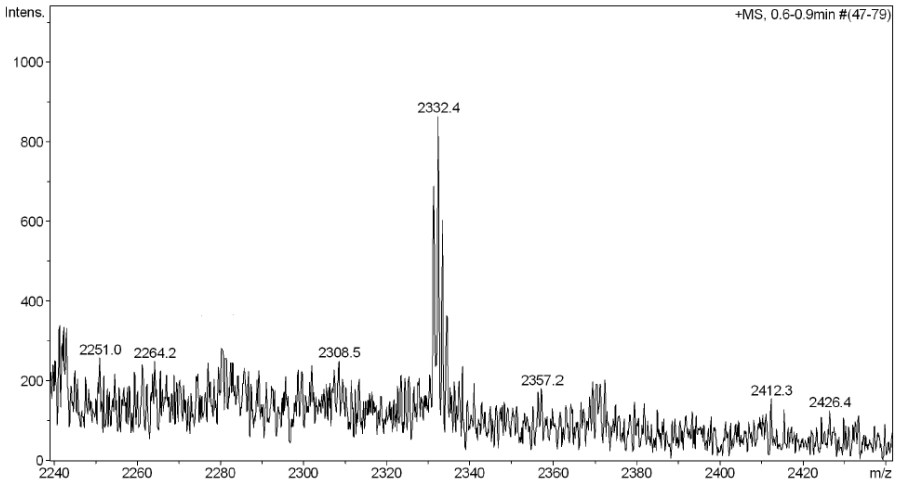
Intens.
+MS, 0.6-0.9min #(47-79)
1000
800
600
400
200
0
2332.4
2251.0
2264.2
2308.5
2357.2
2412.3
2426.4
2240
2260
2280
2300
2320
2340
2360
2380
2400
2420
m/z

HRMS (m/z)

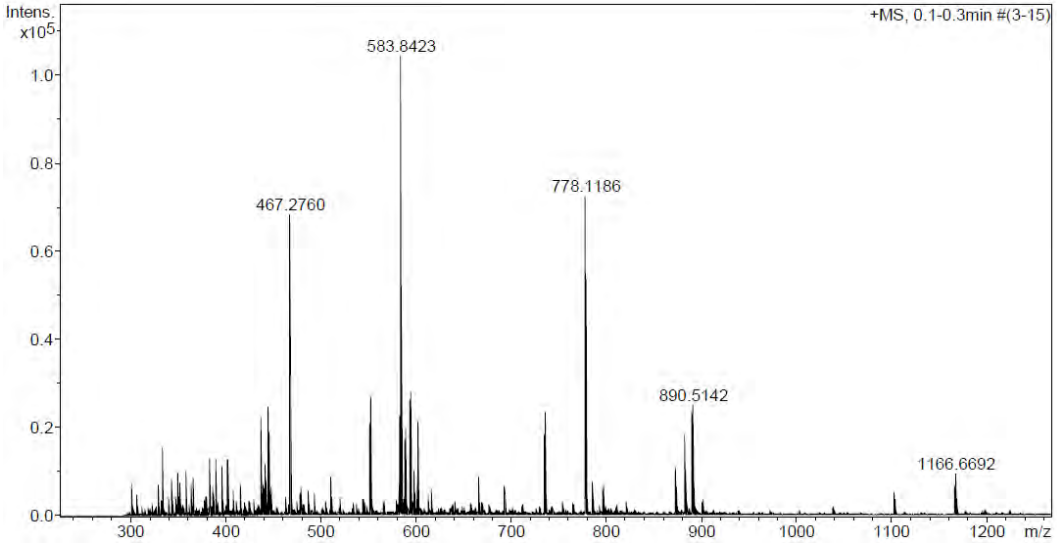
Intens.
x10^5
+MS, 0.1-0.3min #(3-15)
583.8423
778.1186
467.2760
890.5142
1166.6692
m/z

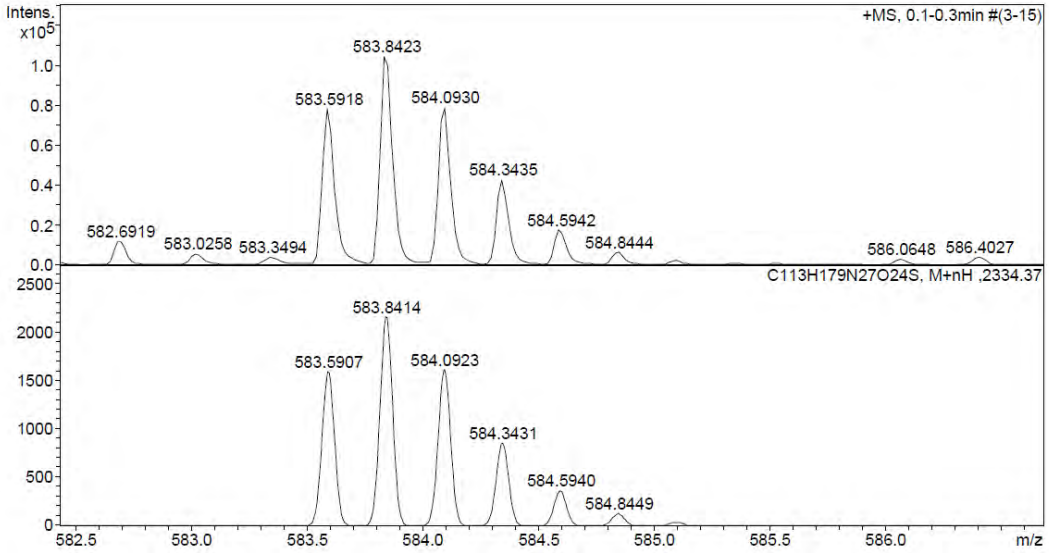
Intens.
x10^5
+MS, 0.1-0.3min #(3-15)
583.8423
583.5918
584.0930
584.3435
584.5942
582.6919
583.0258
583.3494
584.8444
586.0648
586.4027
C113H179N27O24S, M+nH ,2334.37
583.8414
583.5907
584.0923
584.3431
584.5940
584.8449
m/z

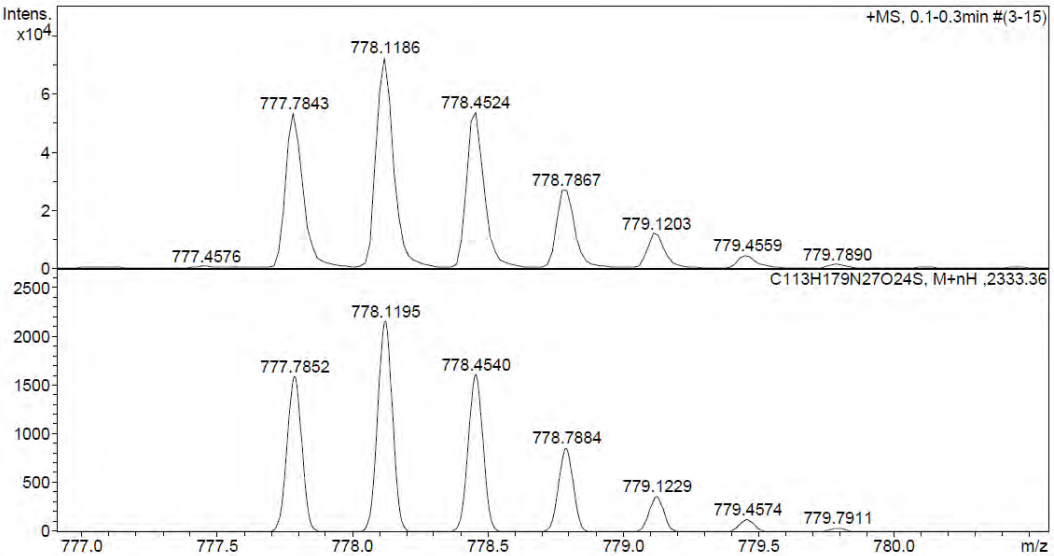
Intens.
x10^4
+MS, 0.1-0.3min #(3-15)
778.1186
777.7843
778.4524
778.7867
779.1203
777.4576
779.4559
779.7890
C113H179N27O24S, M+nH ,2333.36
778.1195
777.7852
778.4540
778.7884
779.1229
779.4574
779.7911
m/z

BP326 (CLB-KKLFKKILK(CF)KL-NH_2)

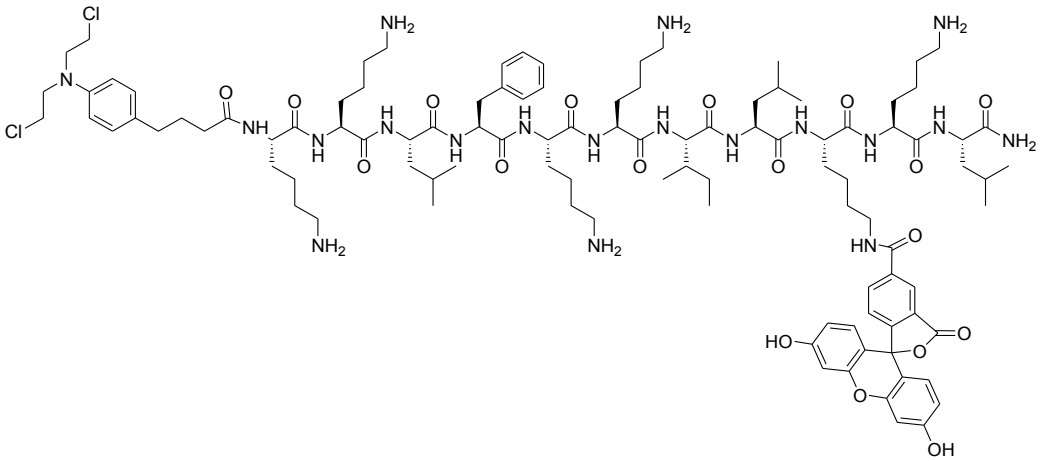

HPLC (λ= 220 nm)

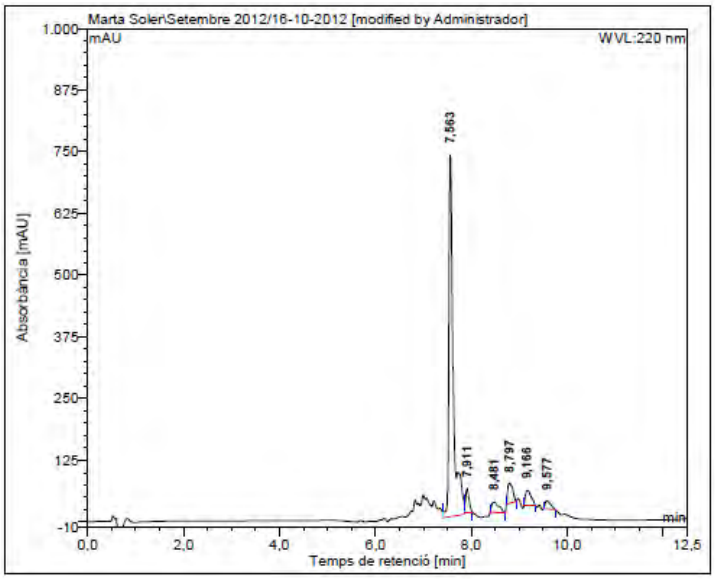

No.	mps retenc min	alçada mAU	Area mAU*min	Area relativa %
1	7,56	732,423	77,055	80,59
2	7,91	48,005	3,811	3,99
3	8,48	20,782	3,596	3,76
4	8,80	40,837	4,961	5,19
5	9,17	29,235	3,969	4,15
6	9,58	17,041	2,219	2,32
Total:		888,322	95,611	100,00

ESI/MS (m/z)

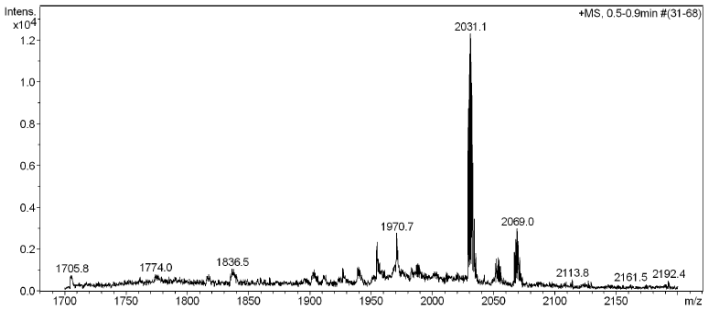
Intens.
x10^4
+MS, 0.5-0.9min #(31-68)
2031.1
1970.7
2069.0
1705.8
1774.0
1836.5
2113.8
2161.5
2192.4
m/z

HRMS (m/z)

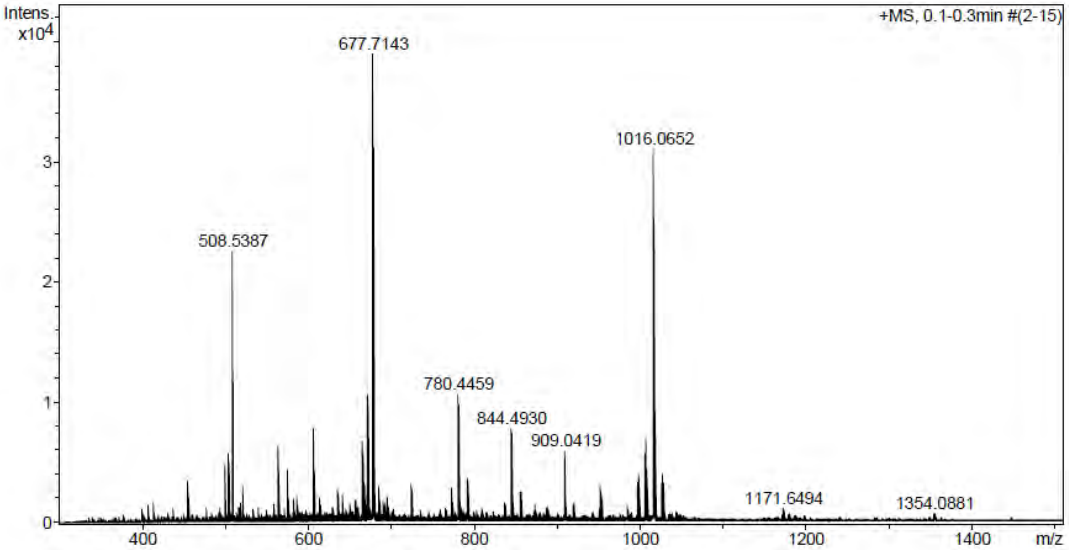
Intens.
x10^4
+MS, 0.1-0.3min #(2-15)
677.7143
1016.0652
508.5387
780.4459
844.4930
909.0419
1171.6494
1354.0881
m/z

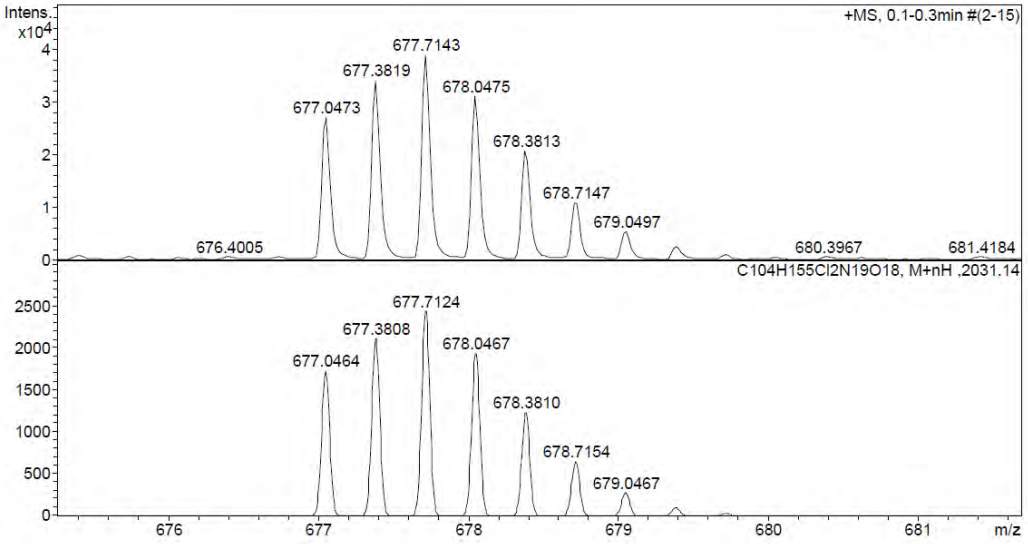
Intens.
x10^4
+MS, 0.1-0.3min #(2-15)
677.7143
677.3819
678.0475
677.0473
678.3813
678.7147
679.0497
676.4005
680.3967
681.4184
C104H155Cl2N19O18, M+nH ,2031.14
677.7124
677.3808
678.0467
677.0464
678.3810
678.7154
679.0467
m/z

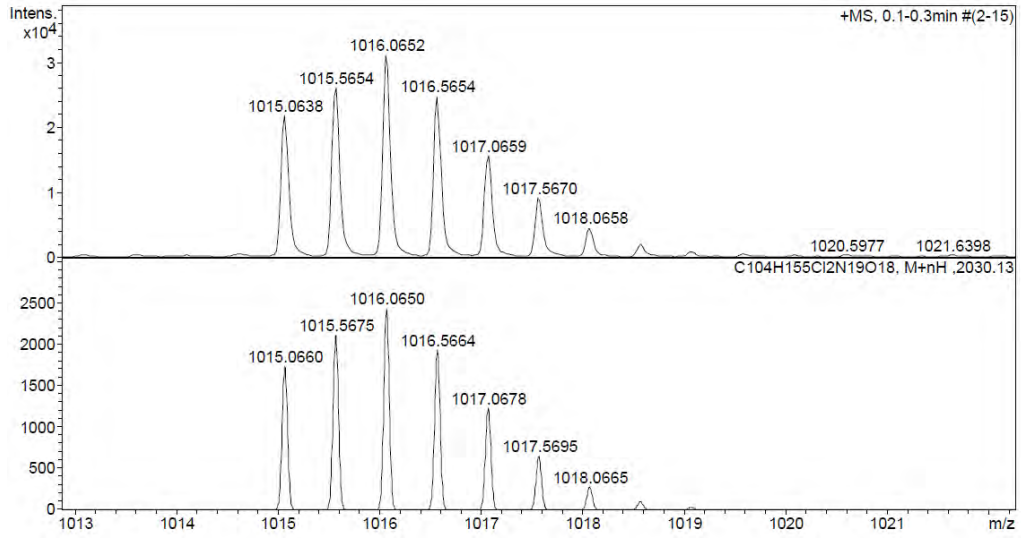
Intens.
x10^4
+MS, 0.1-0.3min #(2-15)
1016.0652
1015.5654
1016.5654
1015.0638
1017.0659
1017.5670
1018.0658
1020.5977
1021.6398
C104H155Cl2N19O18, M+nH ,2030.13
1016.0650
1015.5675
1016.5664
1015.0660
1017.0678
1017.5695
1018.0665
m/z

BP330 (CLB-CREKA-KKLFKKILK(CF)KL-NH_2)

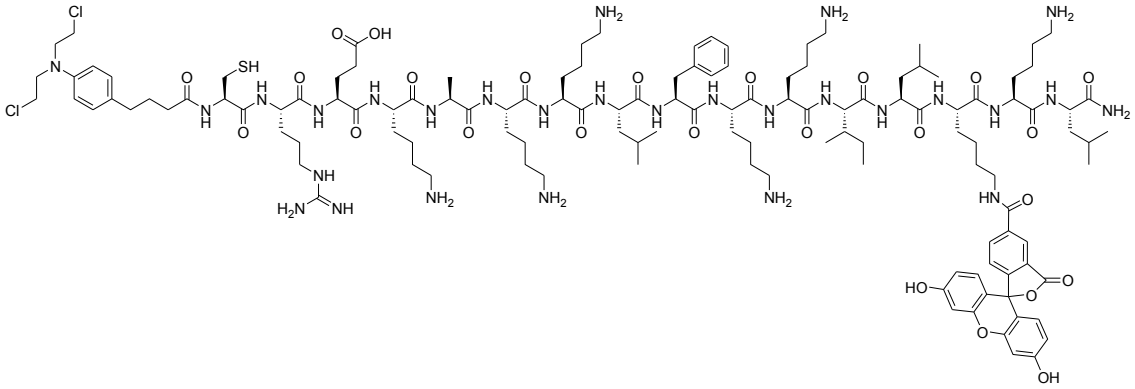

HPLC (λ= 220 nm)

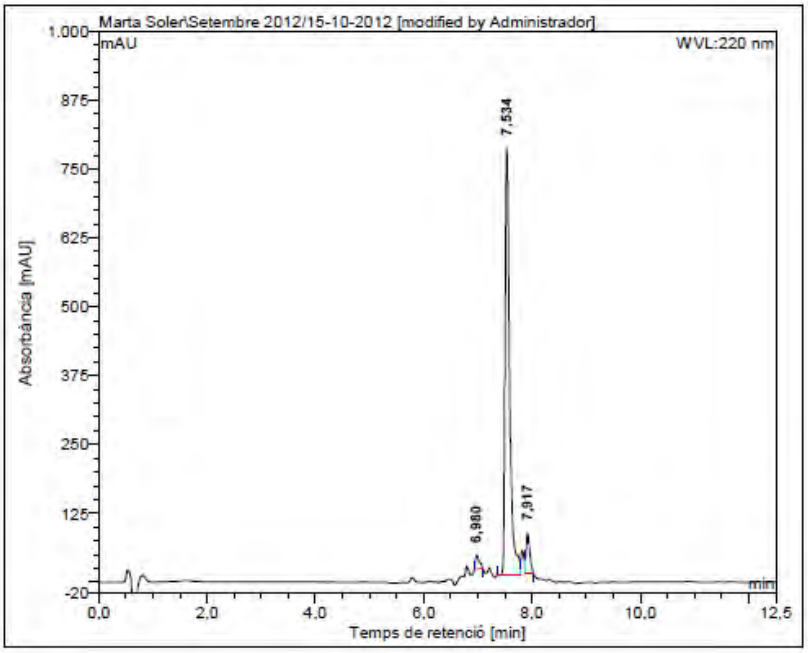

No.	mps retenc min	alçada mAU	Area mAU*min	Area relativa %
1	6,98	26,172	2,204	2,64
2	7,53	775,511	75,679	90,75
3	7,92	72,800	5,508	6,60
Total:		874,483	83,390	100,00

ESI/MS (m/z)

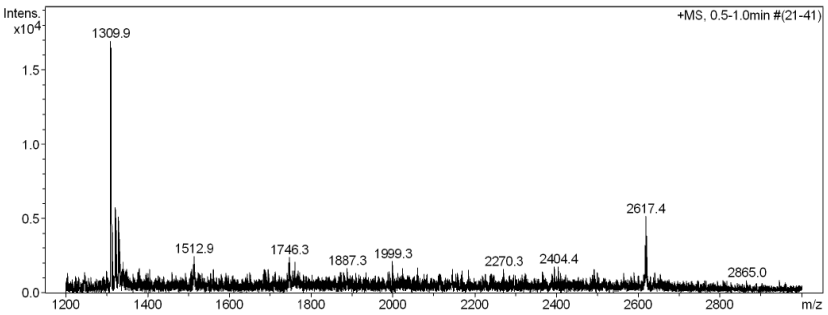
Intens.
x10^4
+MS, 0.5-1.0min #(21-41)
1309.9
1512.9
1746.3
1887.3
1999.3
2270.3
2404.4
2617.4
2865.0
1.5
1.0
0.5
0.0
1200
1400
1600
1800
2000
2200
2400
2600
2800
m/z

HRMS (m/z)

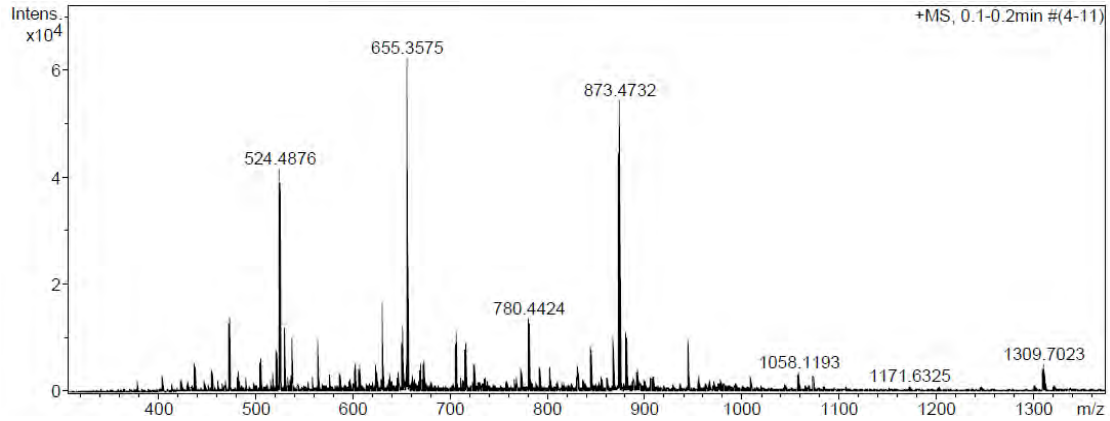
Intens.
x10^4
+MS, 0.1-0.2min #(4-11)
655.3575
873.4732
524.4876
780.4424
1058.1193
1171.6325
1309.7023
m/z

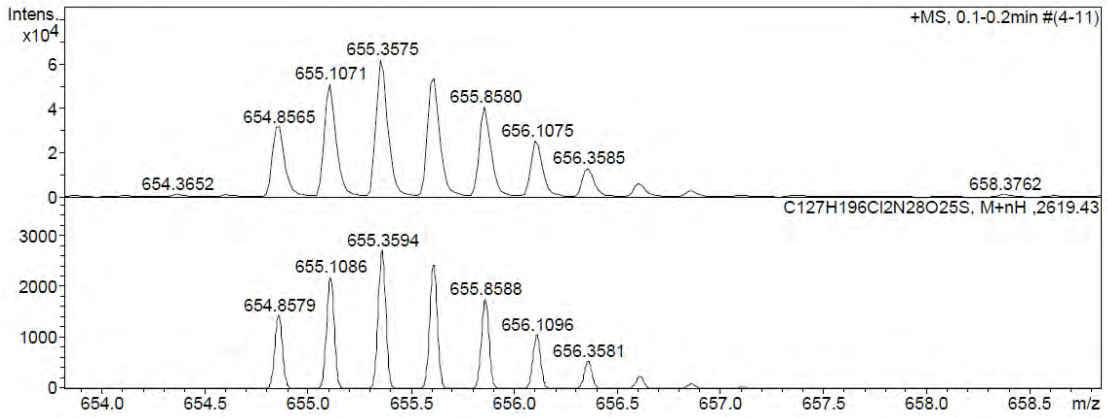
Intens.
x10^4
+MS, 0.1-0.2min #(4-11)
655.3575
655.1071
654.8565
655.8580
656.1075
656.3585
654.3652
658.3762
C127H196Cl2N28O25S, M+nH ,2619.43
655.3594
655.1086
654.8579
655.8588
656.1096
656.3581
m/z

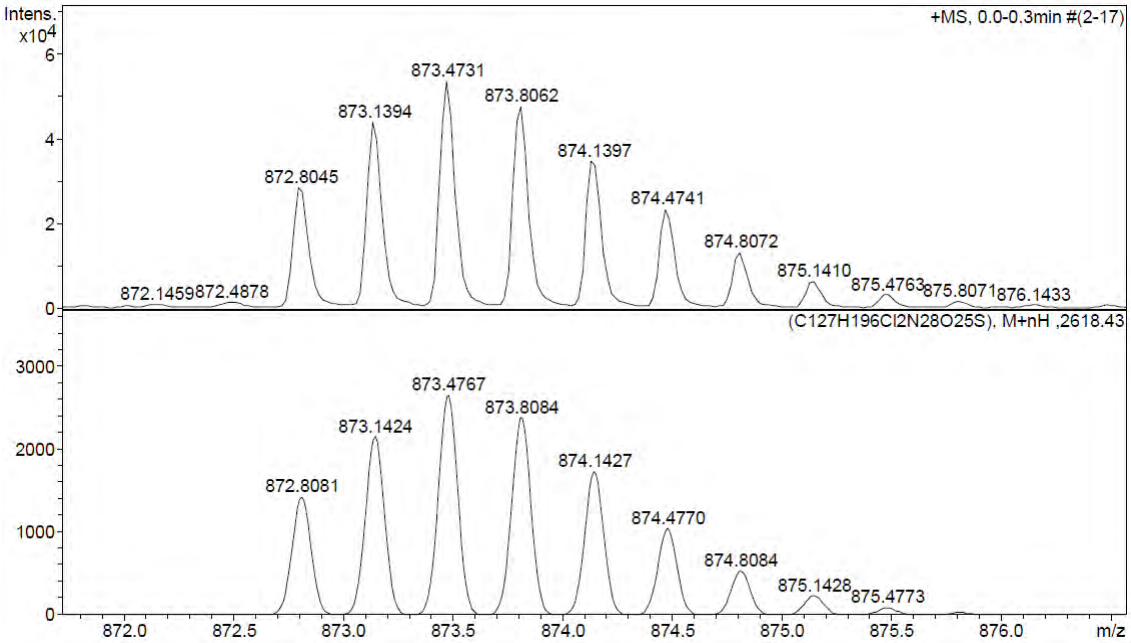
Intens.
x10^4
+MS, 0.0-0.3min #(2-17)
873.4731
873.8062
873.1394
874.1397
872.8045
874.4741
874.8072
875.1410
875.4763
875.8071
876.1433
872.1459
872.4878
(C127H196Cl2N28O25S), M+nH ,2618.43
873.4767
873.8084
873.1424
874.1427
872.8081
874.4770
874.8084
875.1428
875.4773
m/z

CF-Tat$_{49}$ (CF-RKKRRQRRR-NH$_2$)

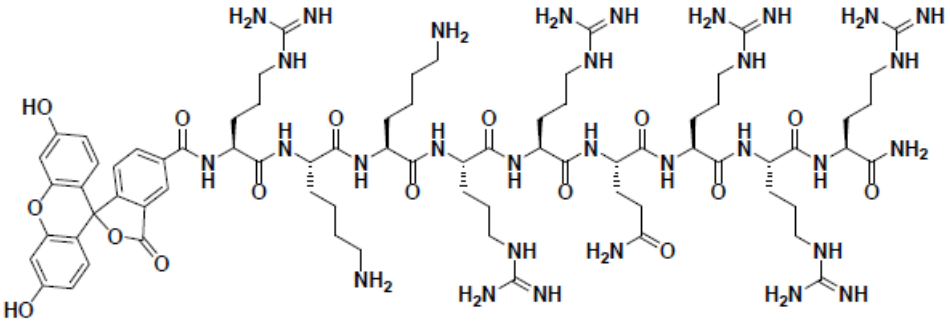

HPLC (λ= 220 nm)

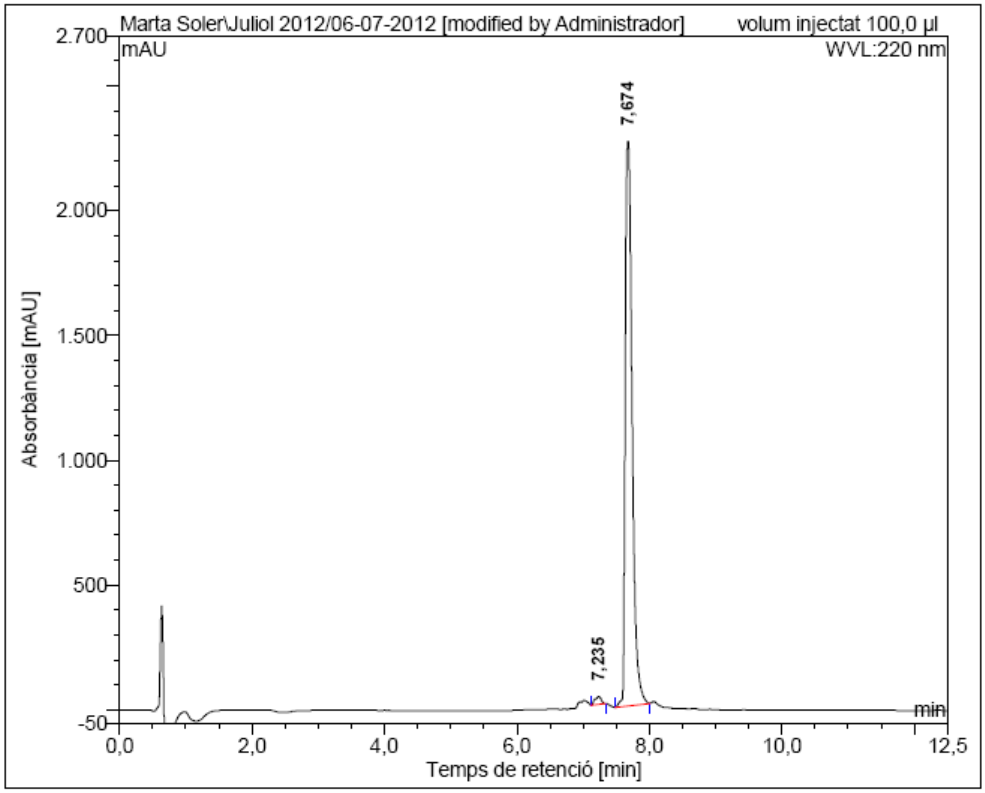

No.	mps retenc min	alçada mAU	Area mAU*min	Area relativa %
1	7,24	32,190	3,591	1,29
2	7,67	2260,922	274,786	98,71
Total:		2293,113	278,377	100,00

Supporting Information

Chapter IV: Enzyme-triggered release of chlorambucil from BP16 conjugates

Marta Soler, Marta González-Bártulos, Eduard Figueras, Xavi Ribas, Miquel Costas, Anna Massaguer, Marta Planas,* and Lidia Feliu*

Table of contents

Figure SIV.1: a) HPLC chromatogram (λ= 220 nm), b) HRMS spectrum (*m/z*).

BP16

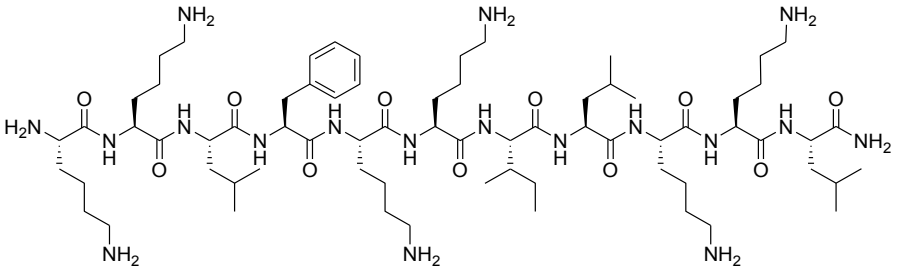

a)

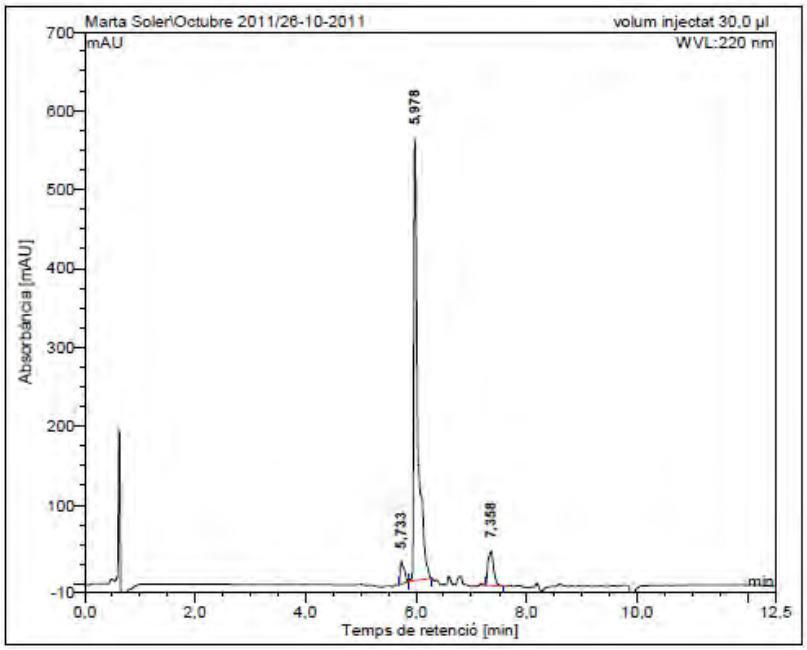

No.	mps retenc min	alçada mAU	Area mAU*min	Area relativa %
1	5,73	29,200	2,392	4,34
2	5,98	560,424	47,628	86,44
3	7,36	43,883	5,076	9,21
Total:		633,507	55,097	100,00

b)

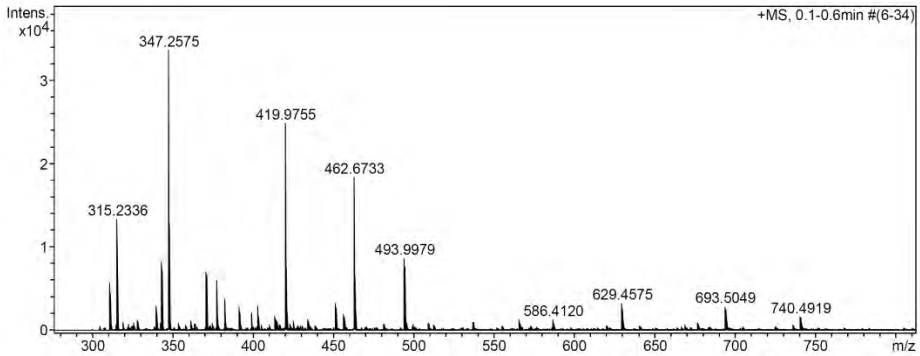

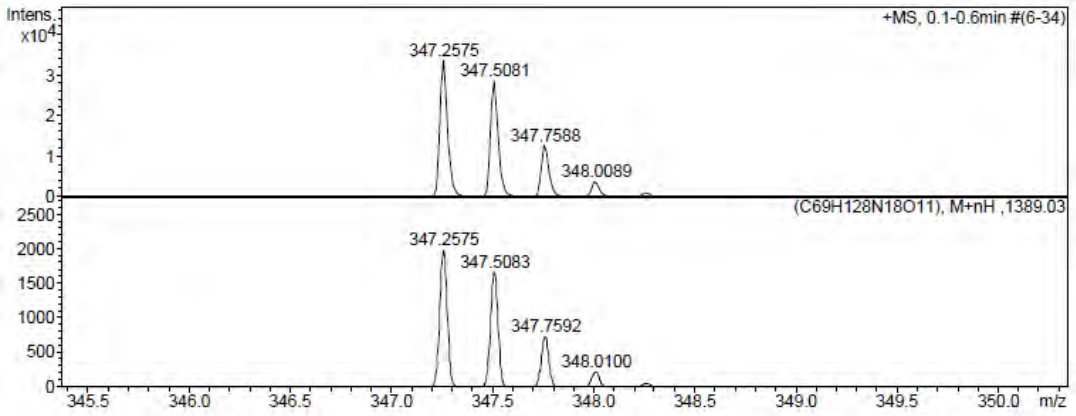

Observed HRMS (top) with the theoretical isotope prediction (bottom).

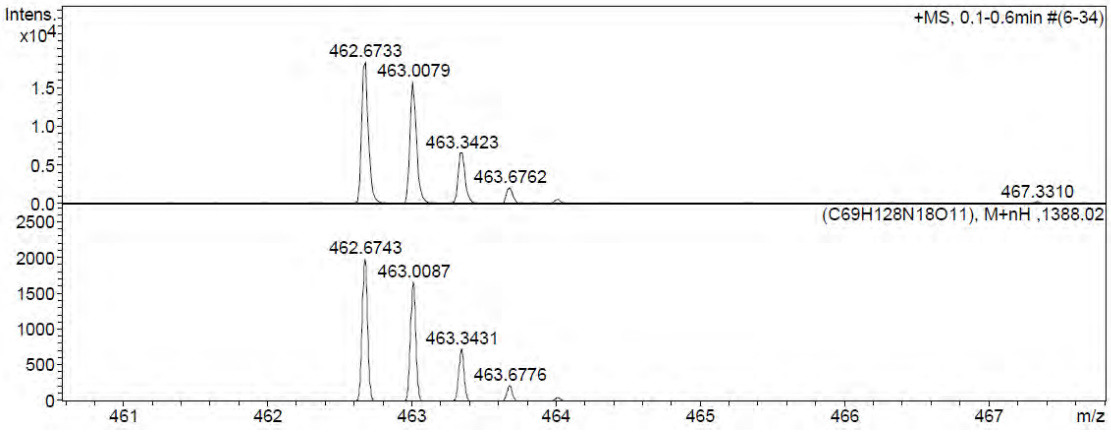

Observed HRMS (top) with the theoretical isotope prediction (bottom).

Figure SIV.2: a) HPLC chromatogram (λ= 220 nm), b) HRMS spectrum (*m/z*).

BP308

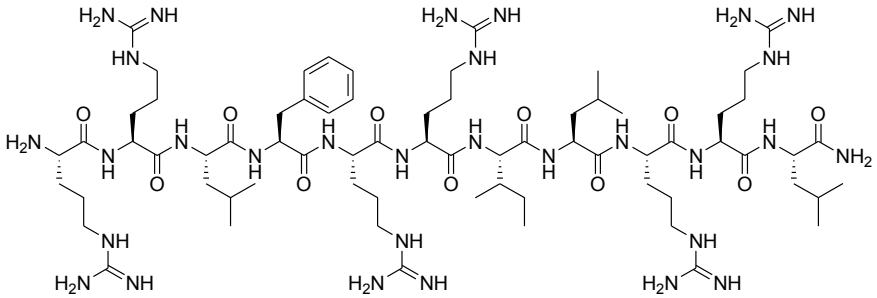

a)

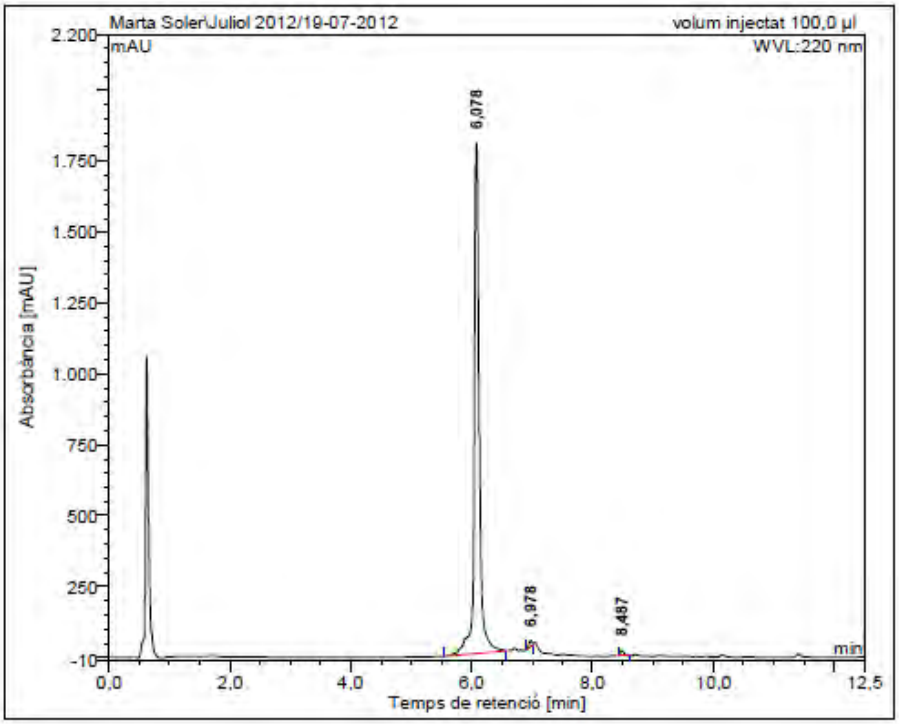

No.	mps retenc min	alçada mAU	Area mAU*min	Area relativa %
1	6,08	1801,317	177,418	98,51
2	6,98	19,947	1,208	0,67
3	8,49	20,643	1,470	0,82
Total:		1841,907	180,096	100,00

b)

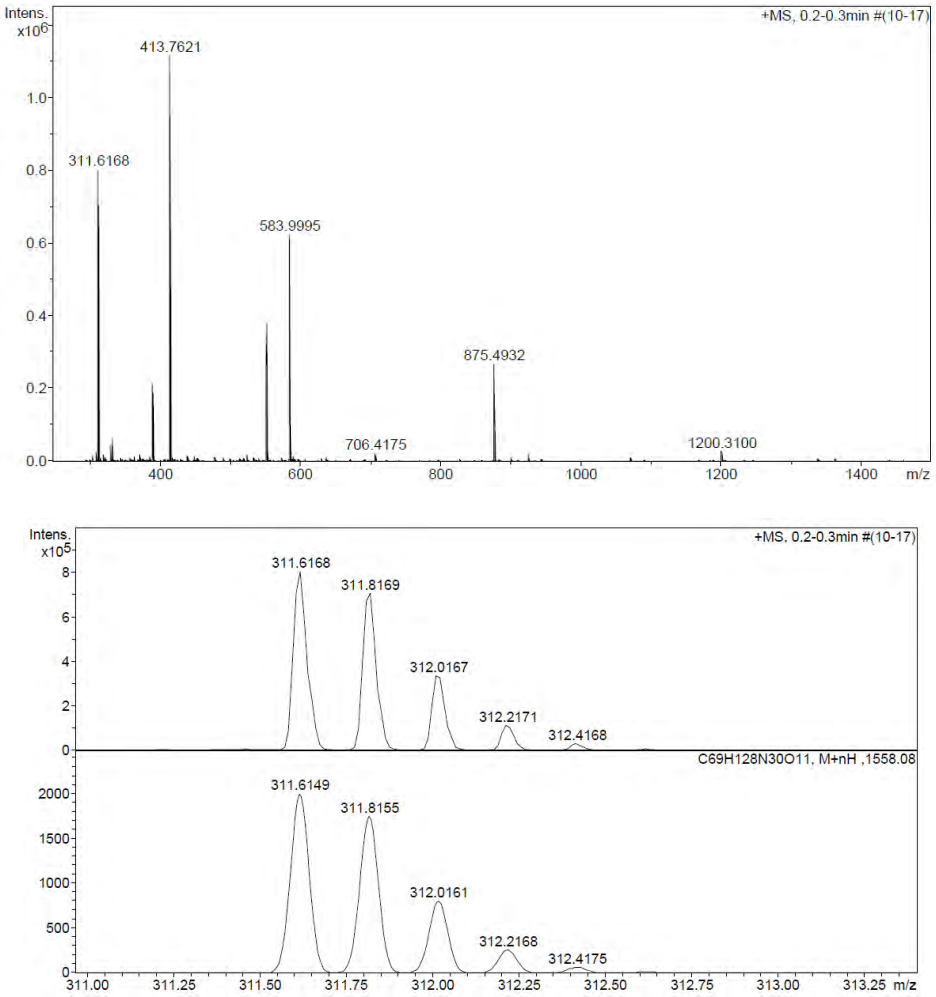

Observed HRMS (top) with the theoretical isotope prediction (bottom).

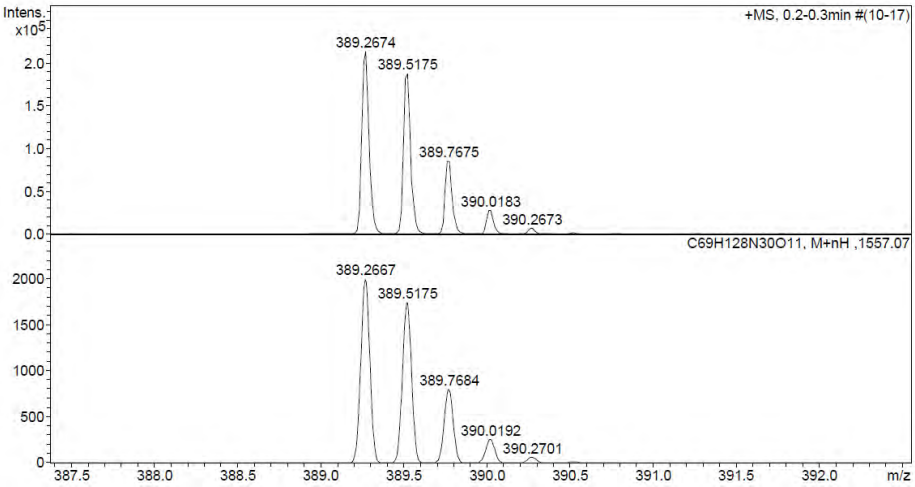

Observed HRMS (top) with the theoretical isotope prediction (bottom).

Figure SIV.3: a) HPLC chromatogram (λ= 220 nm), b) HRMS spectrum (*m/z*).

BP325

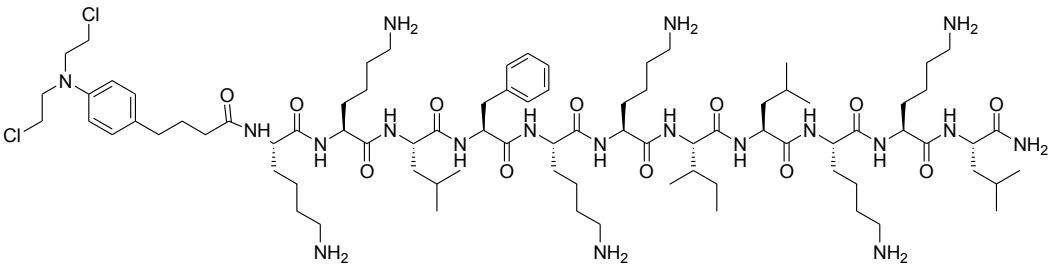

a)

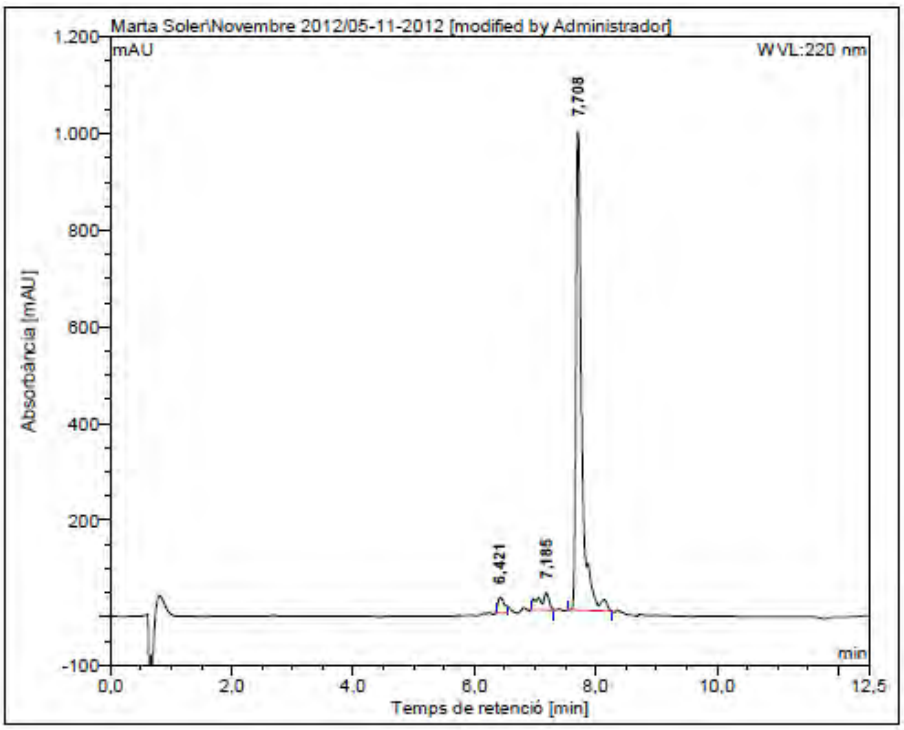

No.	mps retenc min	alçada mAU	Area mAU*min	Area relativa %
1	6,42	31,278	3,951	3,28
2	7,19	35,817	7,126	5,91
3	7,71	991,334	109,512	90,81
Total:		1058,429	120,589	100,00

b)

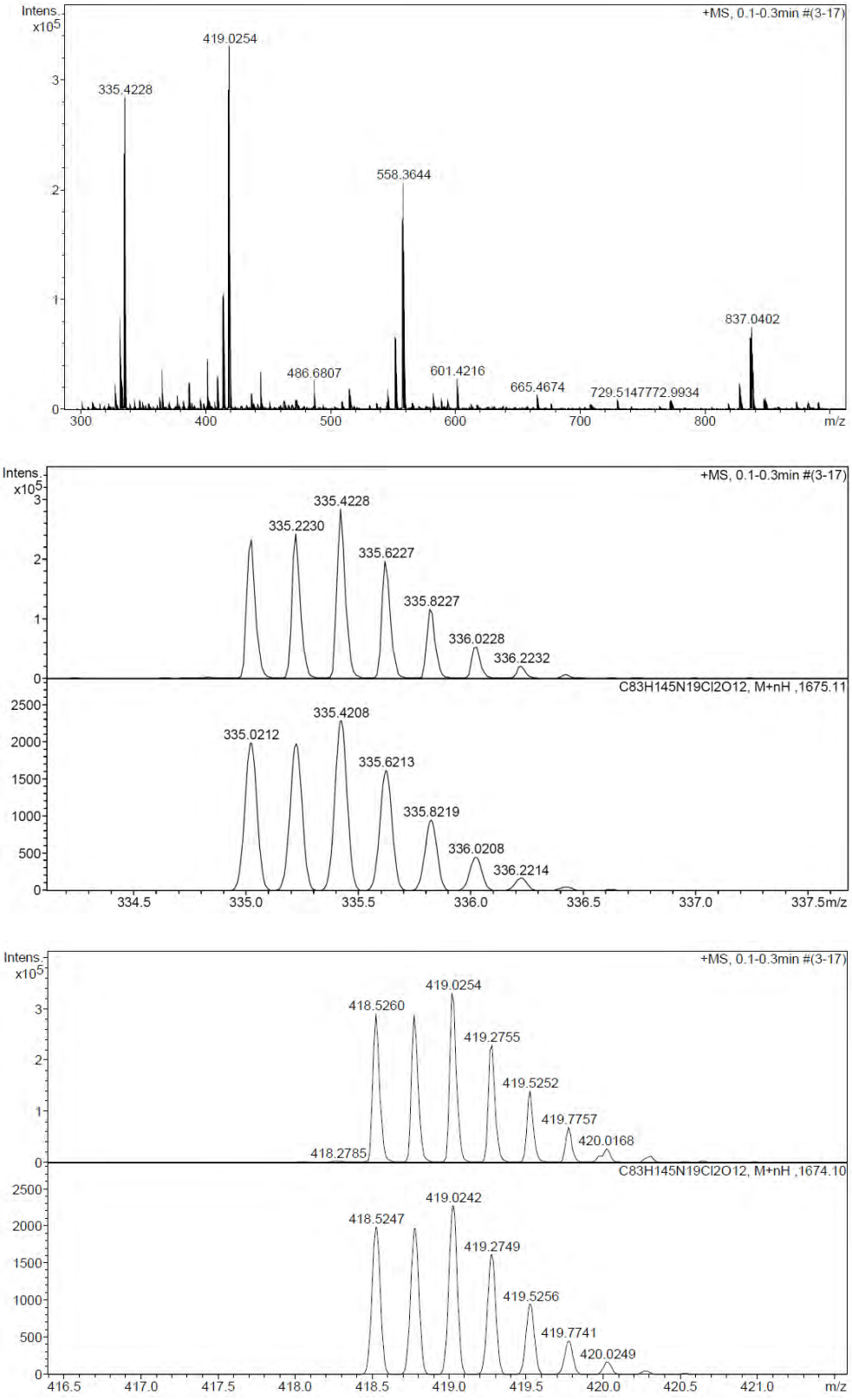

Observed HRMS (top) with the theoretical isotope prediction (bottom).

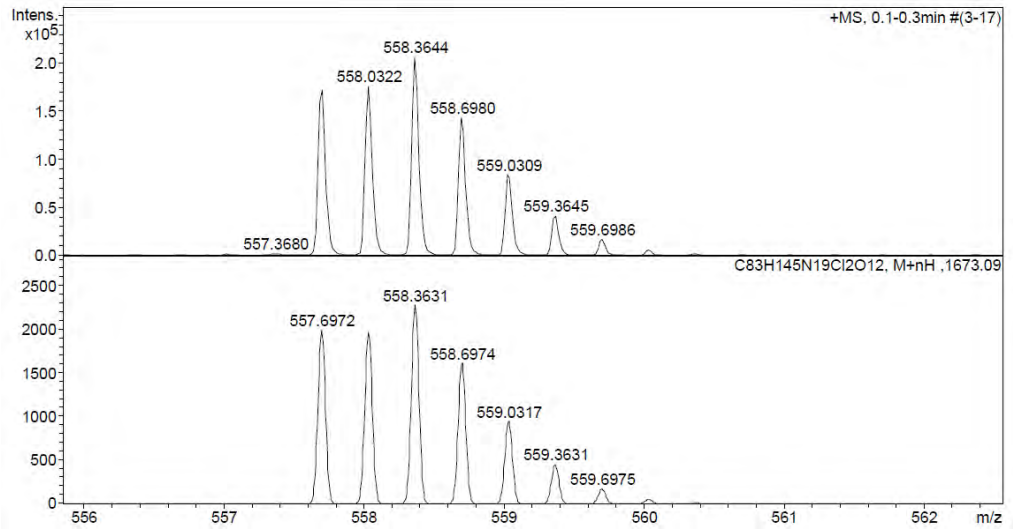

Observed HRMS (top) with the theoretical isotope prediction (bottom).

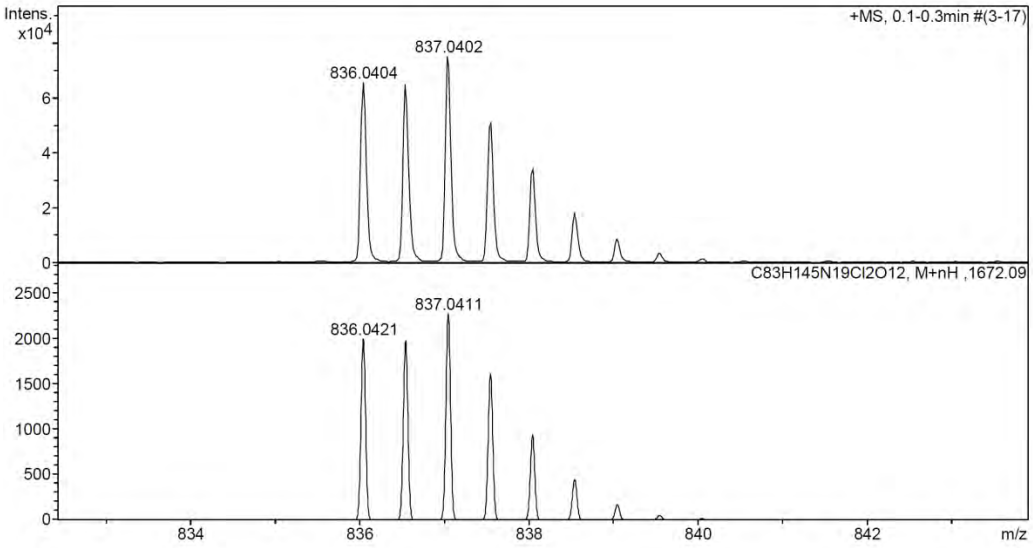

Observed HRMS (top) with the theoretical isotope prediction (bottom).

Figure SIV.4: a) HPLC chromatogram (λ= 220 nm), b) HRMS spectrum (*m/z*).

BP331

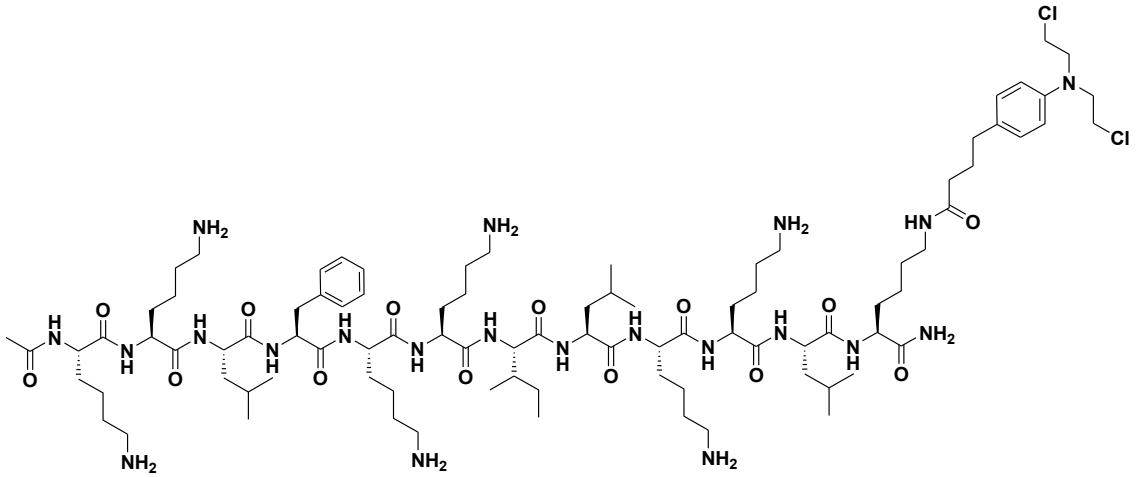

a)

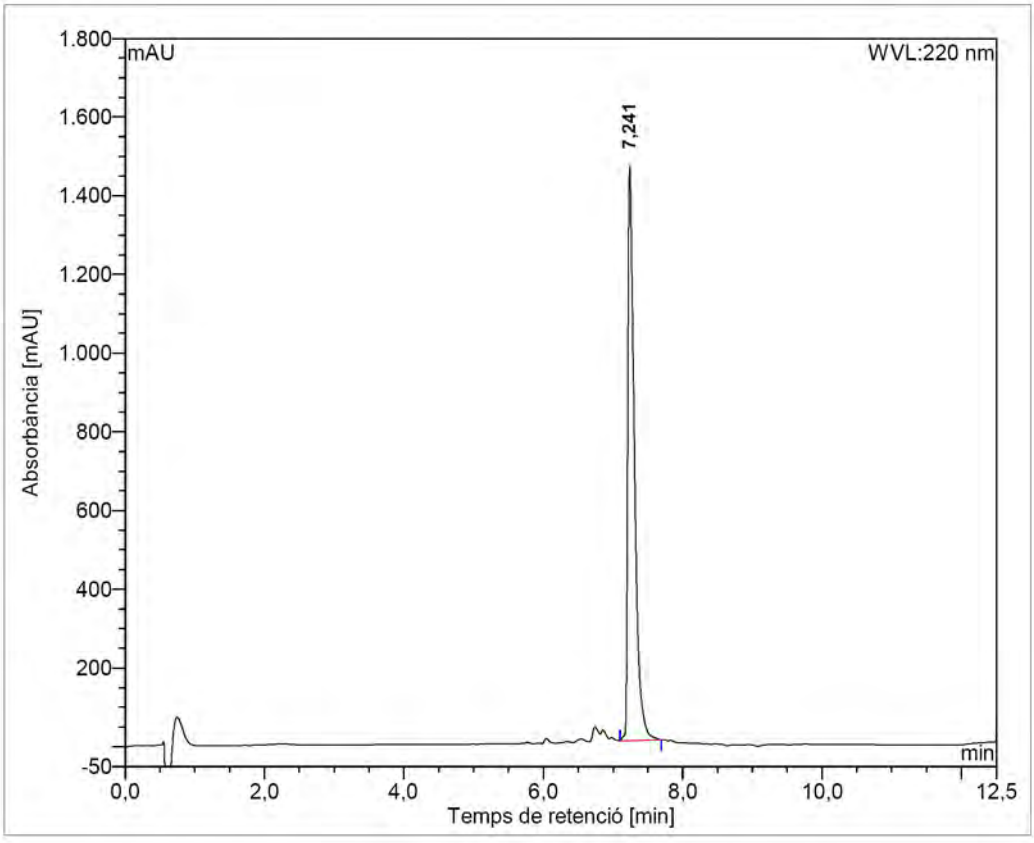

No.	mps retenc min	alçada mAU	Area mAU*min	Area relativa %
1	7,24	1460,388	161,177	100,00
Total:		1460,388	161,177	100,00

b)

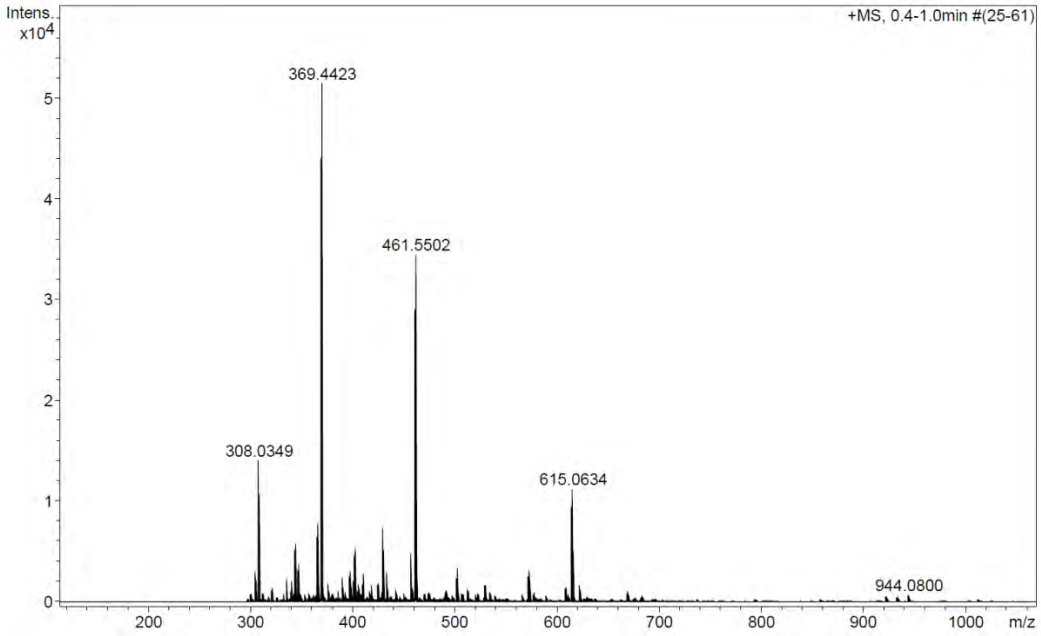

Observed HRMS (top) with the theoretical isotope prediction (bottom).

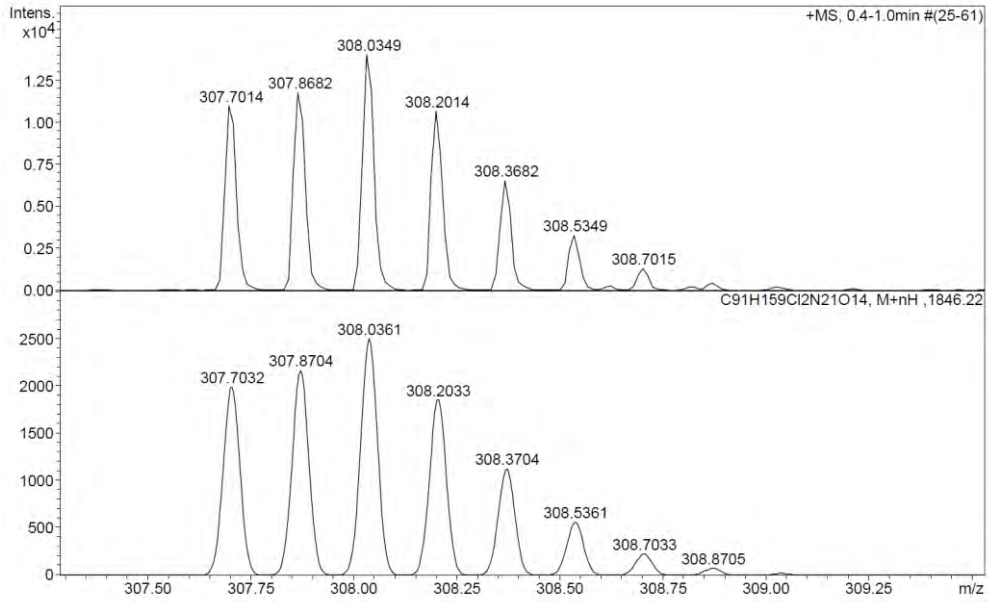

Observed HRMS (top) with the theoretical isotope prediction (bottom).

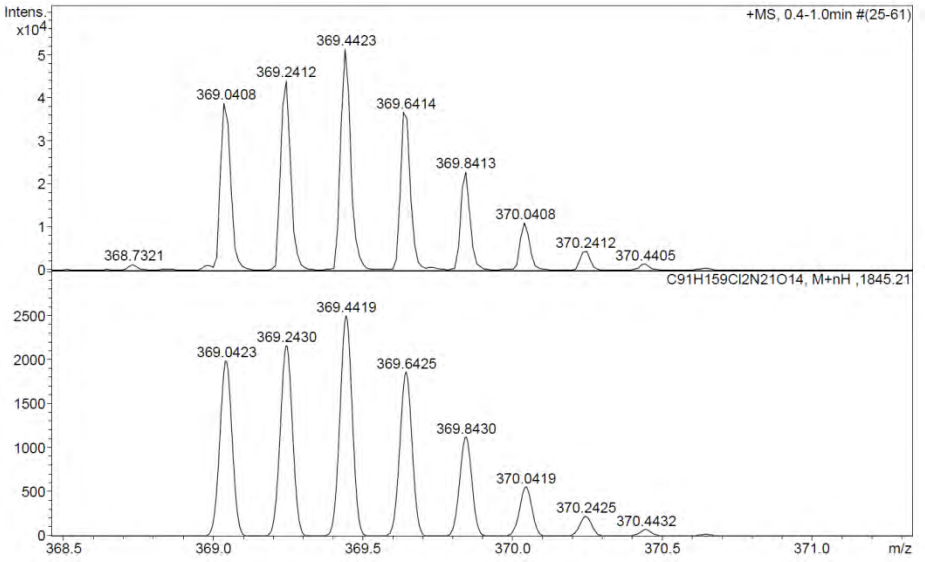

Observed HRMS (top) with the theoretical isotope prediction (bottom).

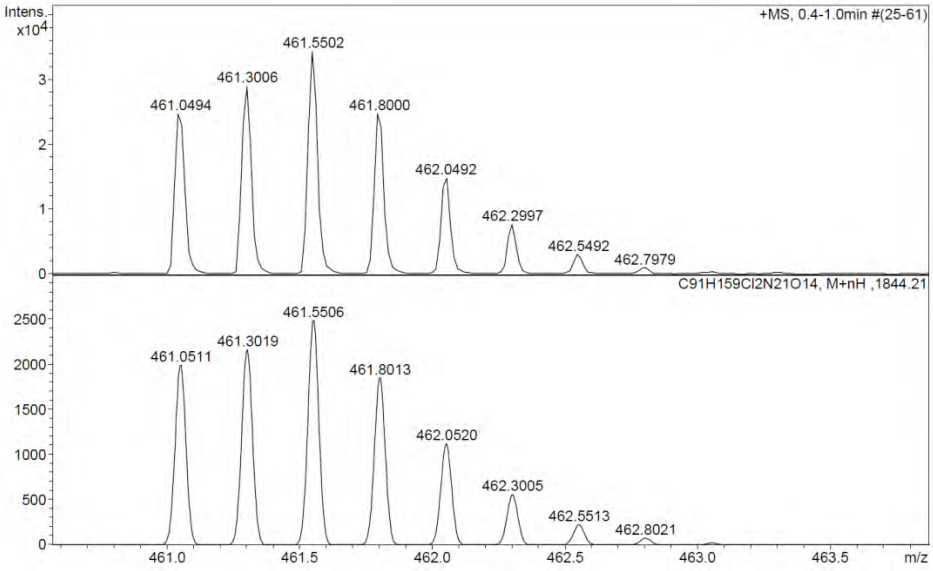

Observed HRMS (top) with the theoretical isotope prediction (bottom).

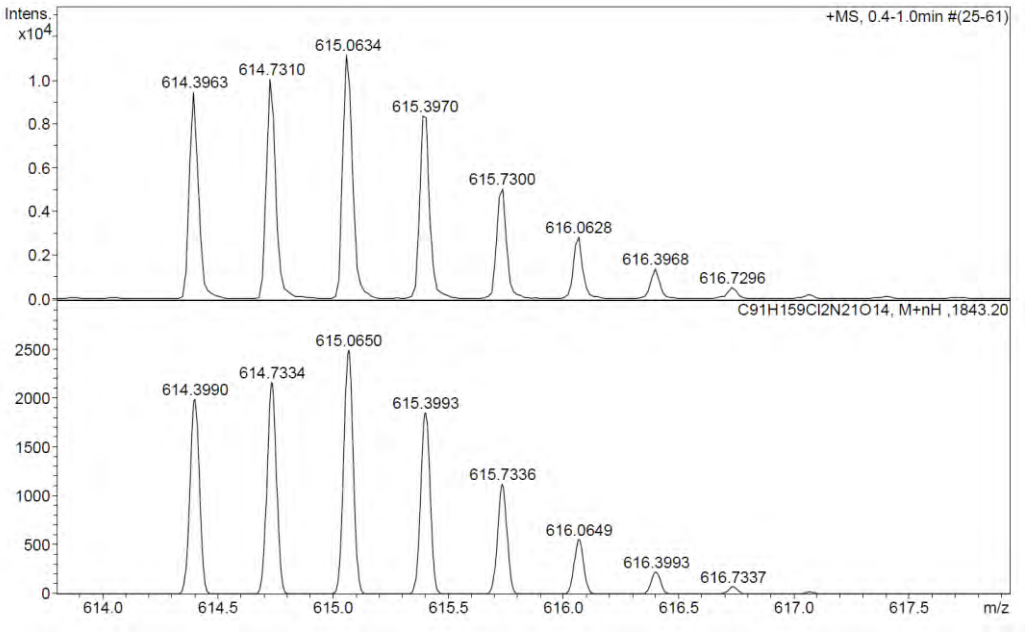

Observed HRMS (top) with the theoretical isotope prediction (bottom).

Figure SIV.5: a) HPLC chromatogram (λ= 220 nm), b) HRMS spectrum (*m/z*).

BP332

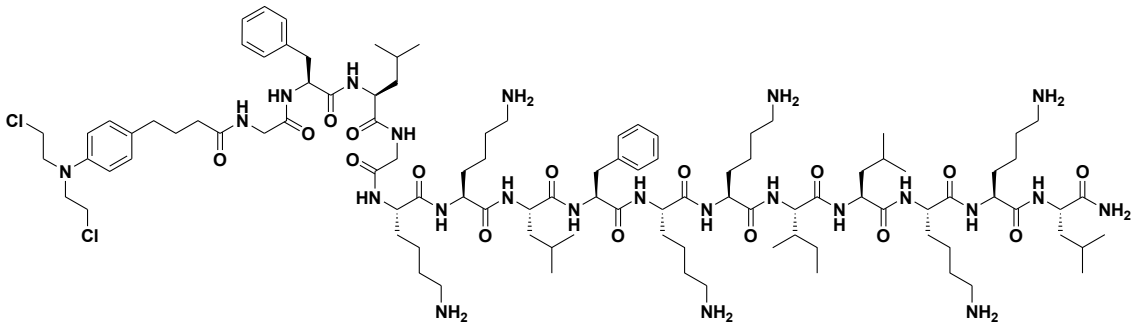

a)

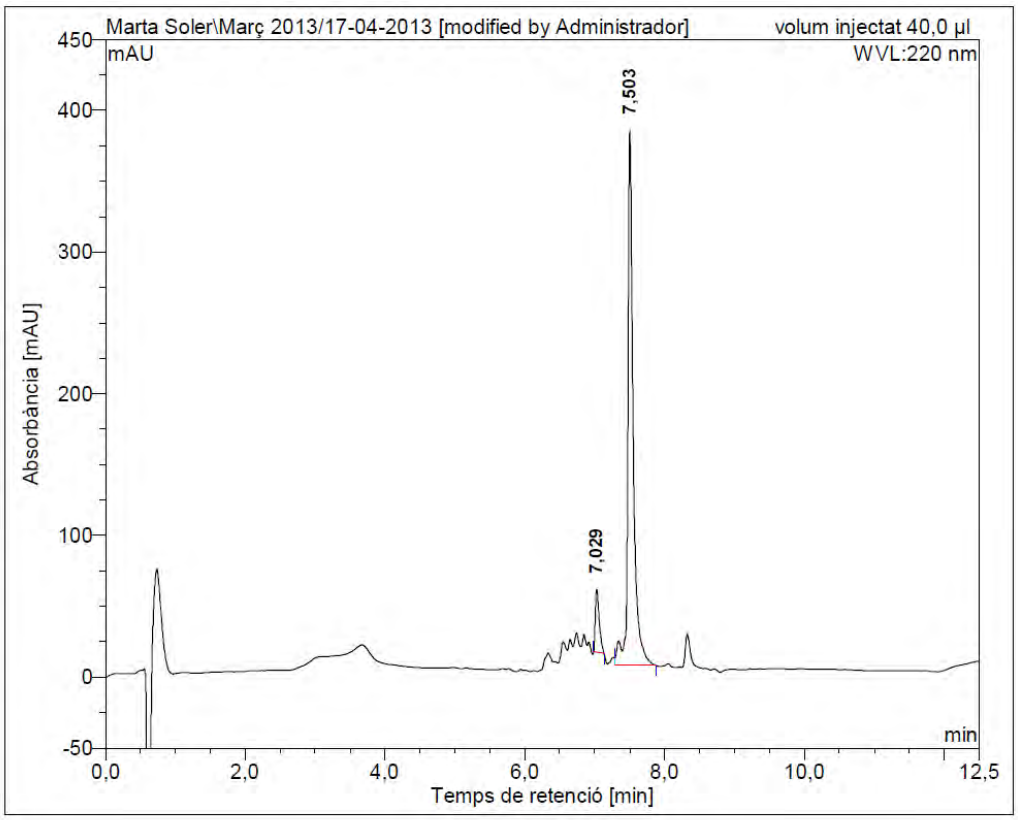

No.	mps retenc min	alçada mAU	Area mAU*min	Area relativa %
1	7,03	44,244	2,866	7,83
2	7,50	377,981	33,741	92,17
Total:		422,225	36,607	100,00

b)

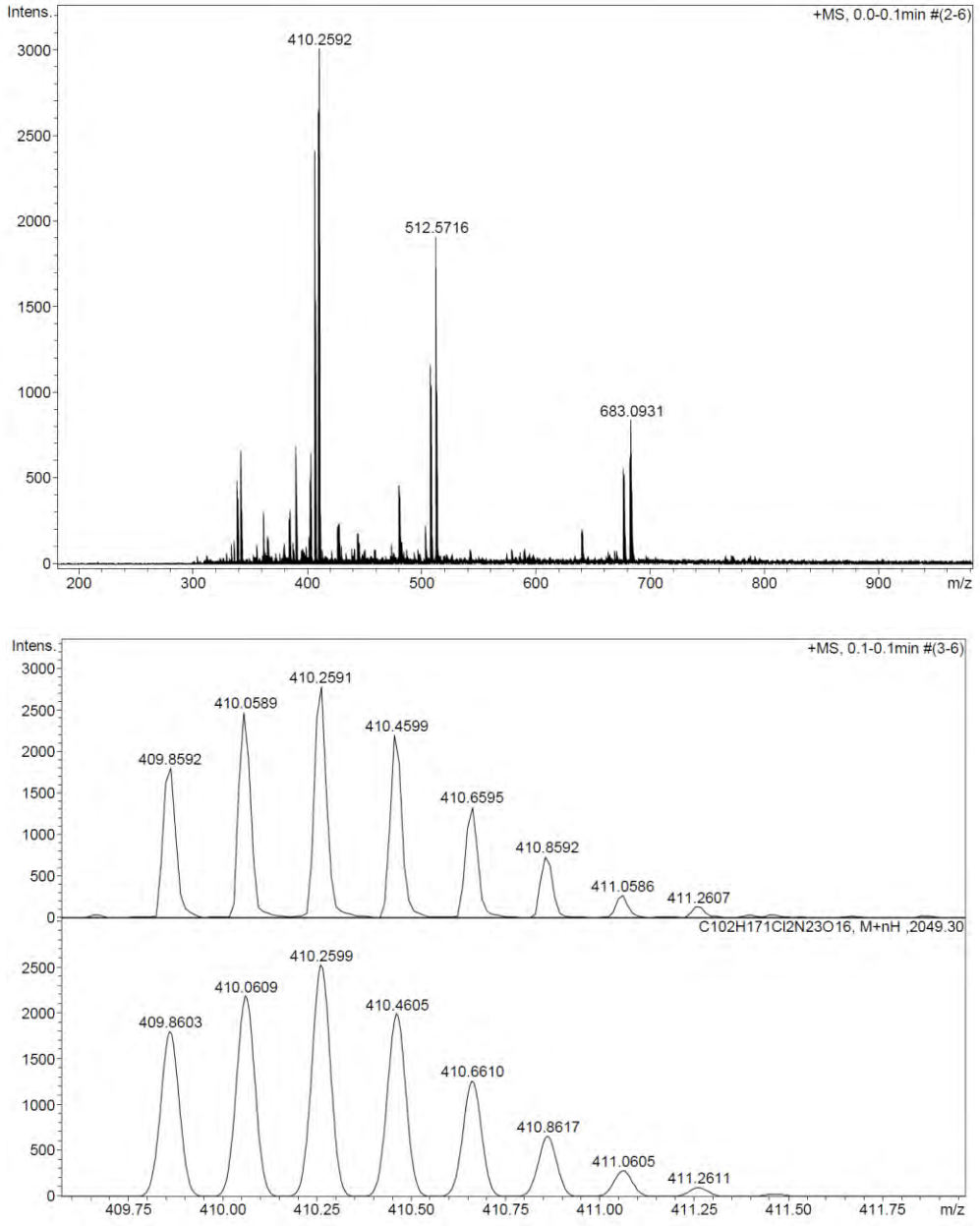

Observed HRMS (top) with the theoretical isotope prediction (bottom).

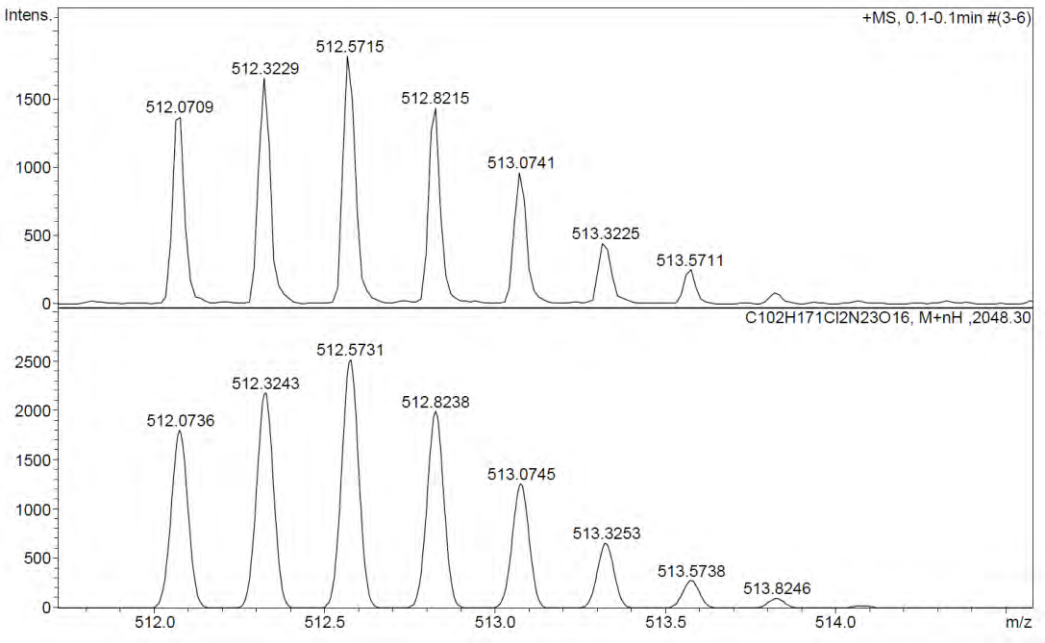

Observed HRMS (top) with the theoretical isotope prediction (bottom).

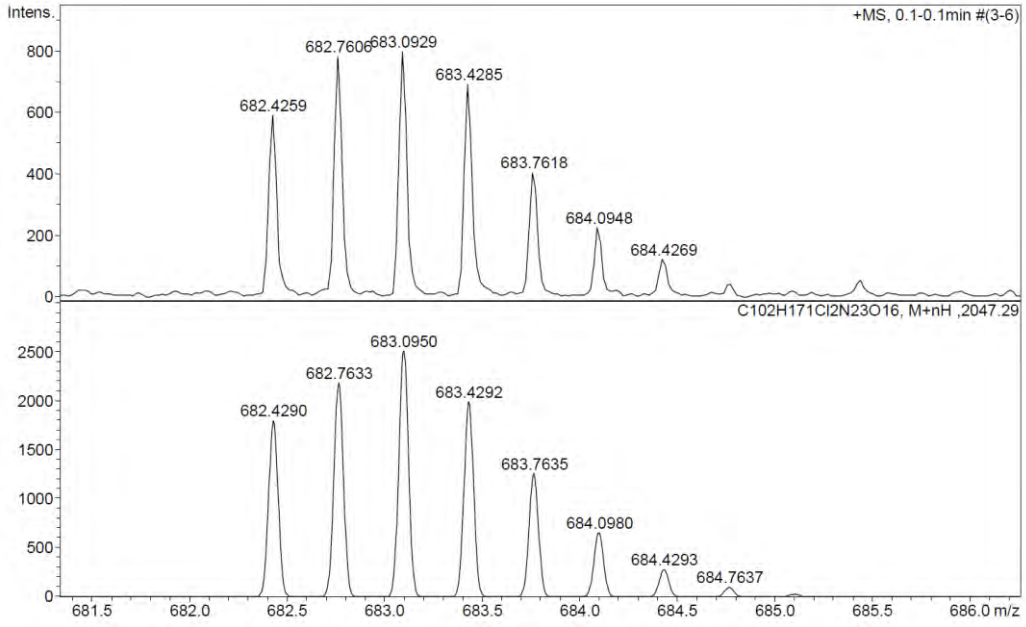

Observed HRMS (top) with the theoretical isotope prediction (bottom).

Figure SIV.6: a) HPLC chromatogram (λ= 220 nm), b) HRMS spectrum (*m/z*).

BP333

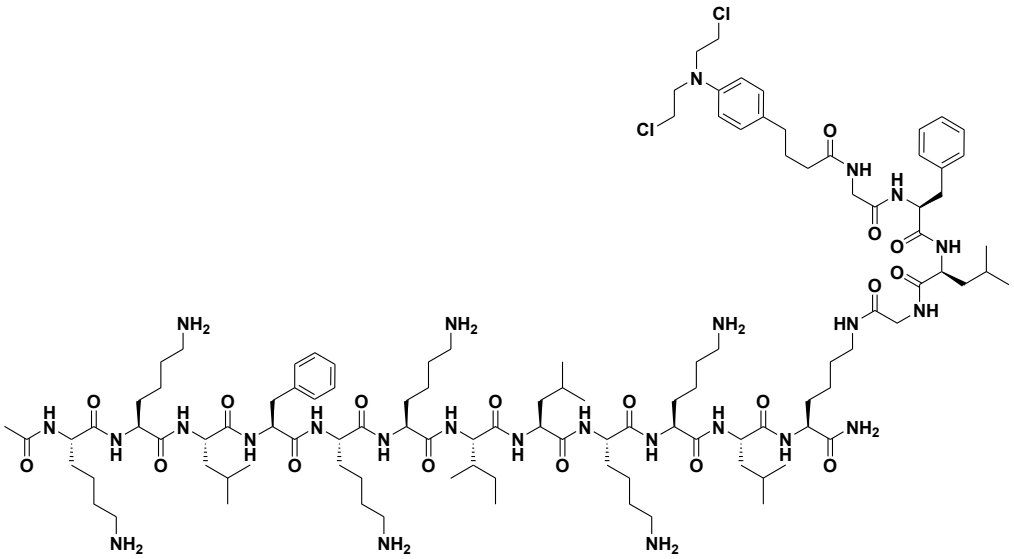

a)

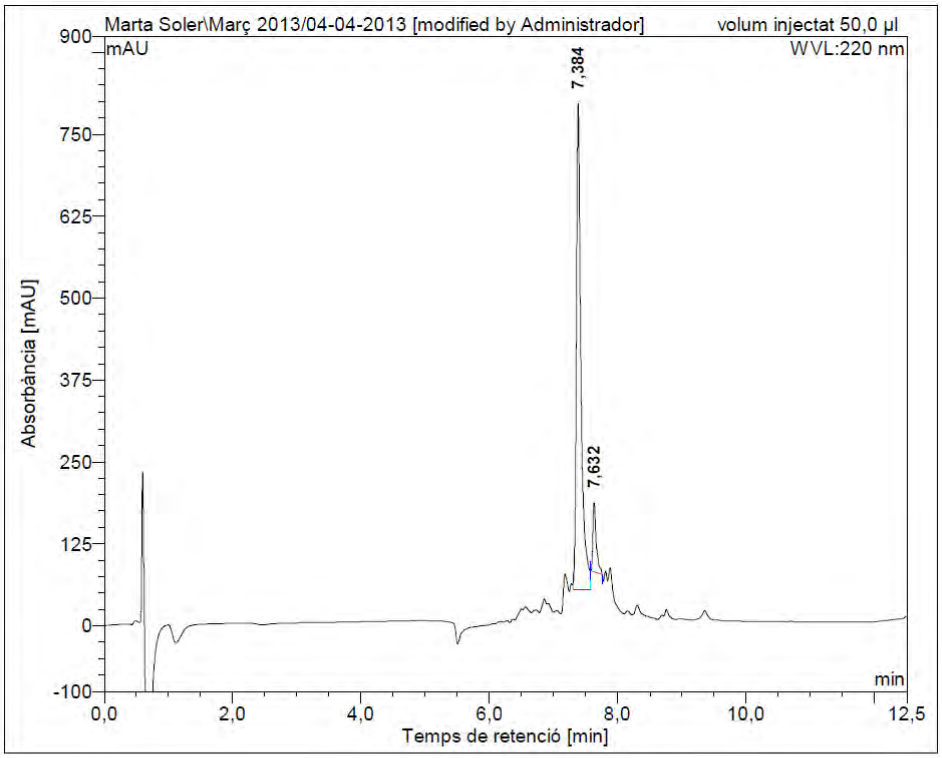

No.	mps retenc min	alçada mAU	Area mAU*min	Area relativa %
1	7,38	742,124	61,018	90,51
2	7,63	104,960	6,398	9,49
Total:		847,085	67,416	100,00

b)

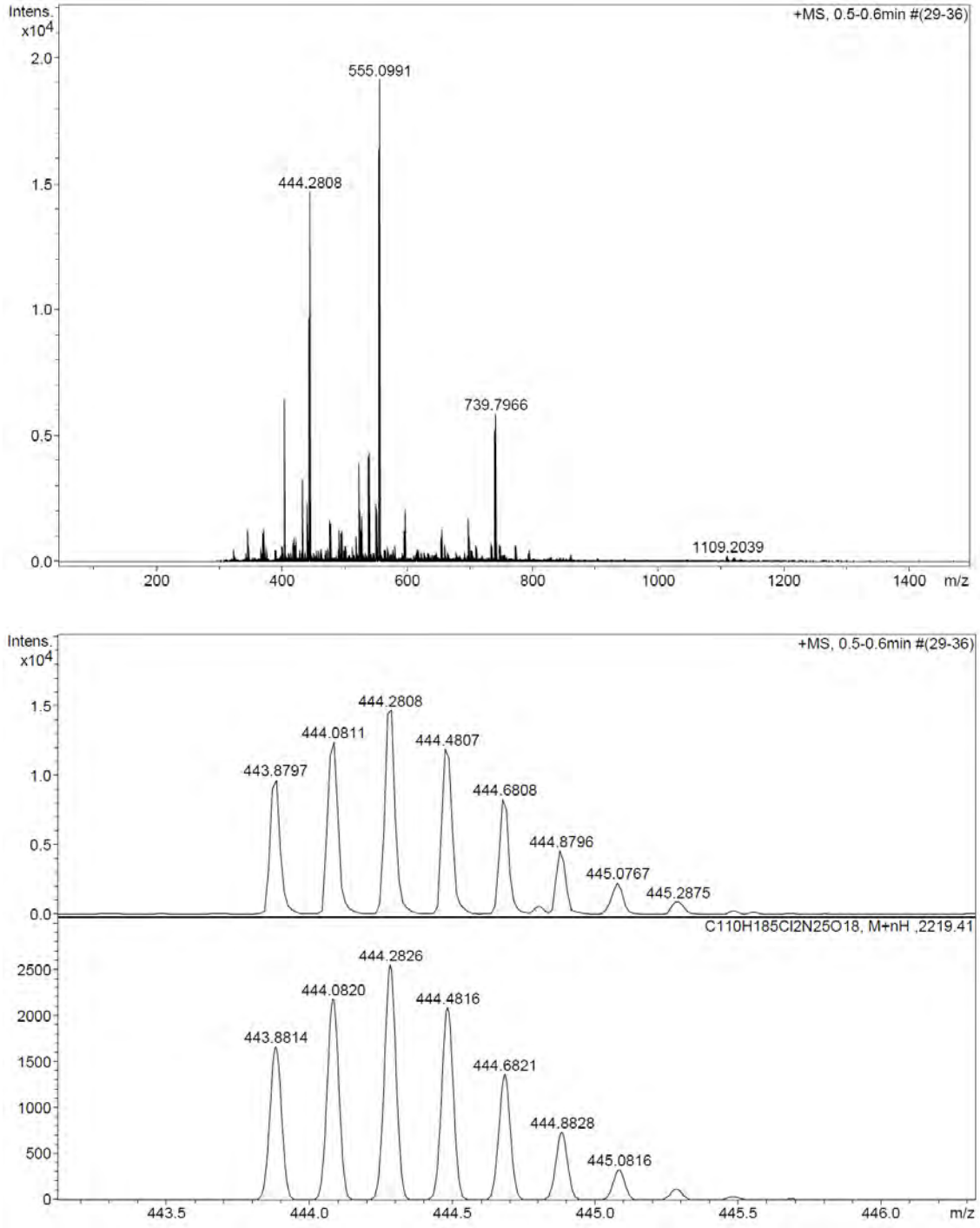

Observed HRMS (top) with the theoretical isotope prediction (bottom).

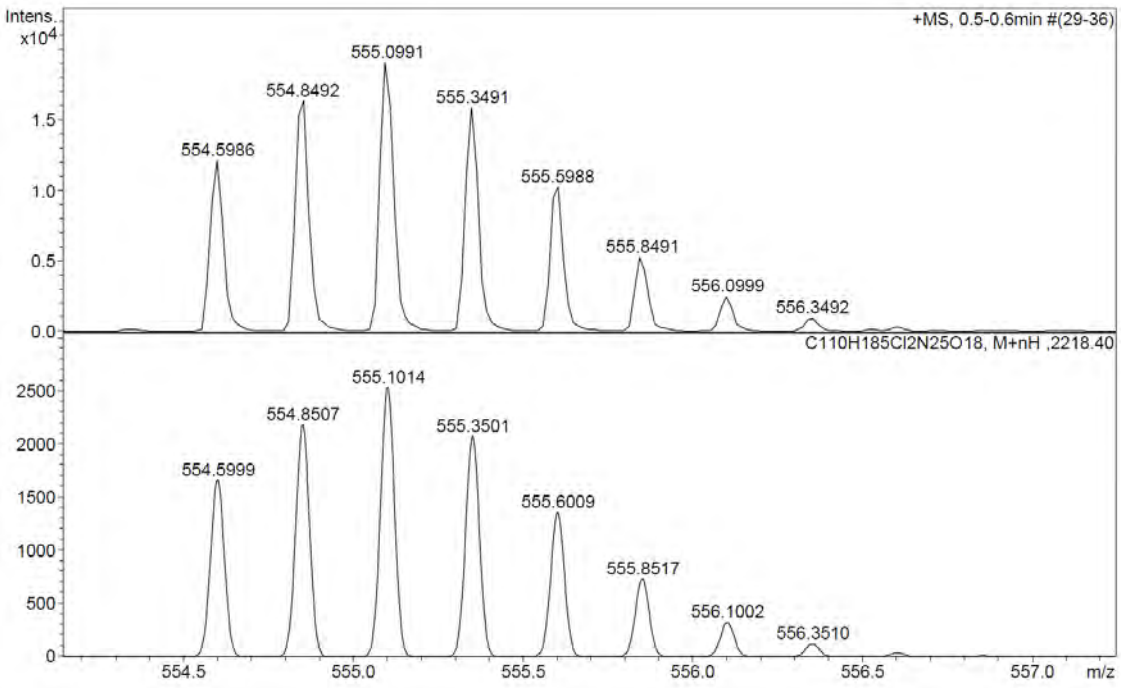

Observed HRMS (top) with the theoretical isotope prediction (bottom).

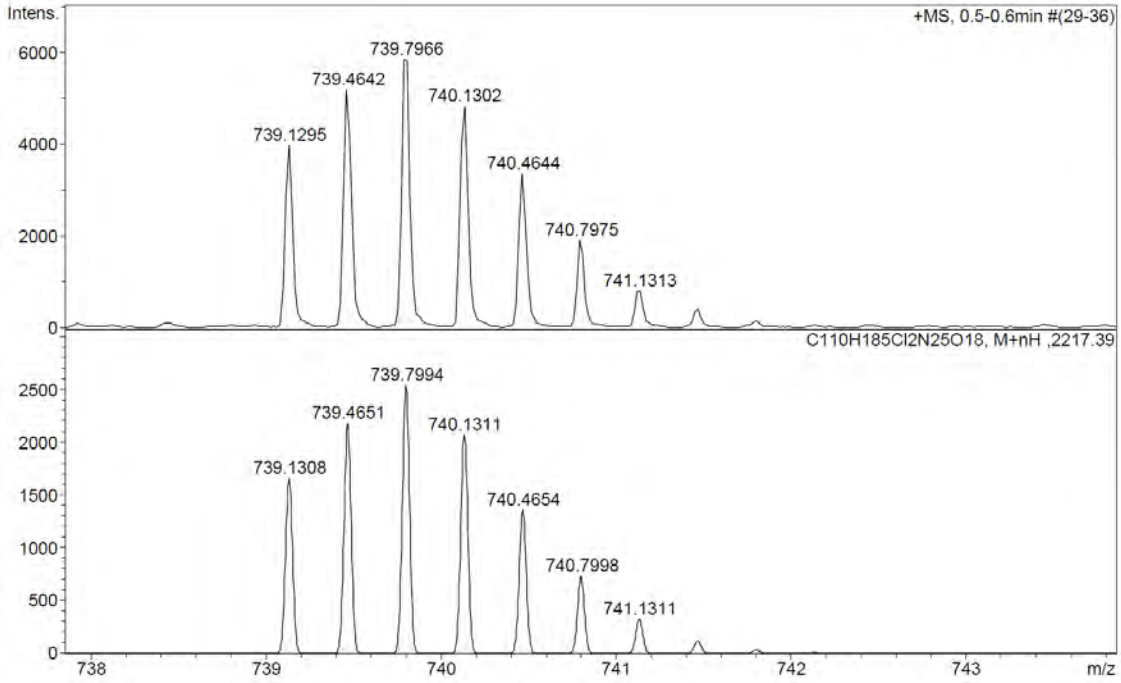

Observed HRMS (top) with the theoretical isotope prediction (bottom).

Figure SIV.7: a) HPLC chromatogram (λ= 220 nm), b) HRMS spectrum (*m/z*).

BP334

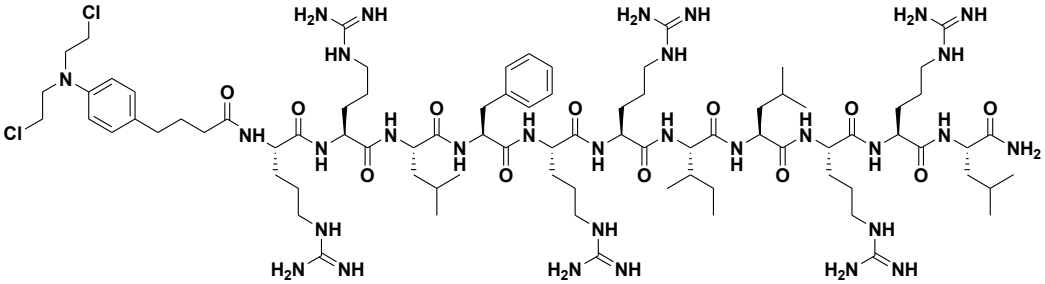

a)

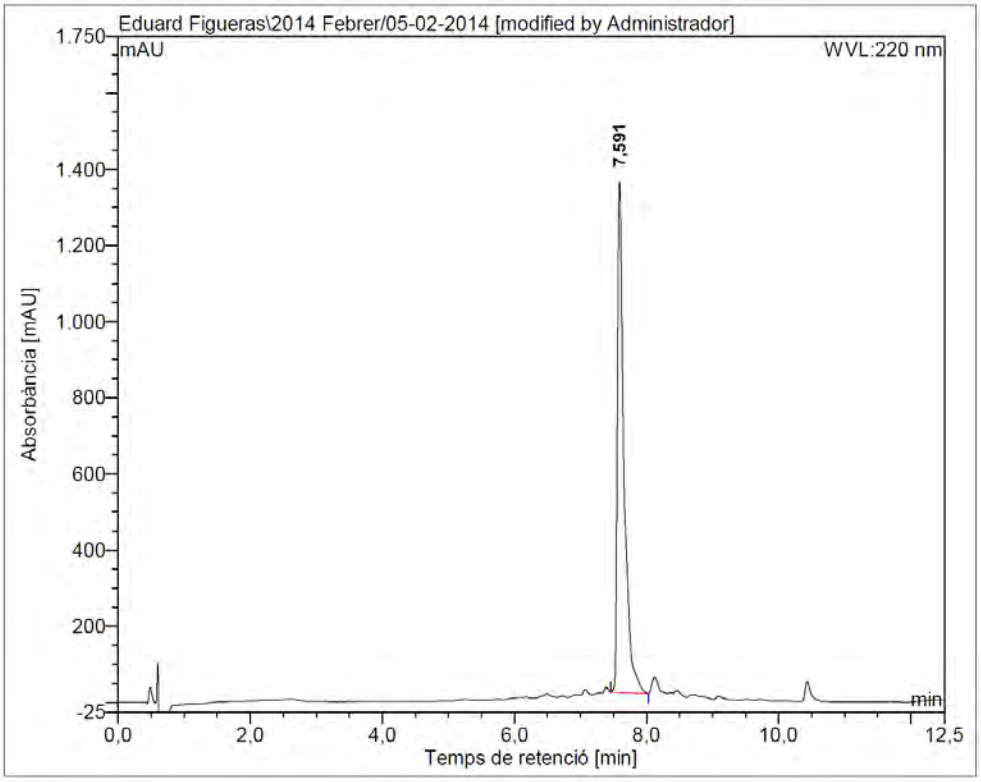

No.	Temps retenció min	alçada mAU	Area mAU*min	Area relativa %
1	7,59	1340,298	155,670	100,00
Total:		1340,298	155,670	100,00

b)

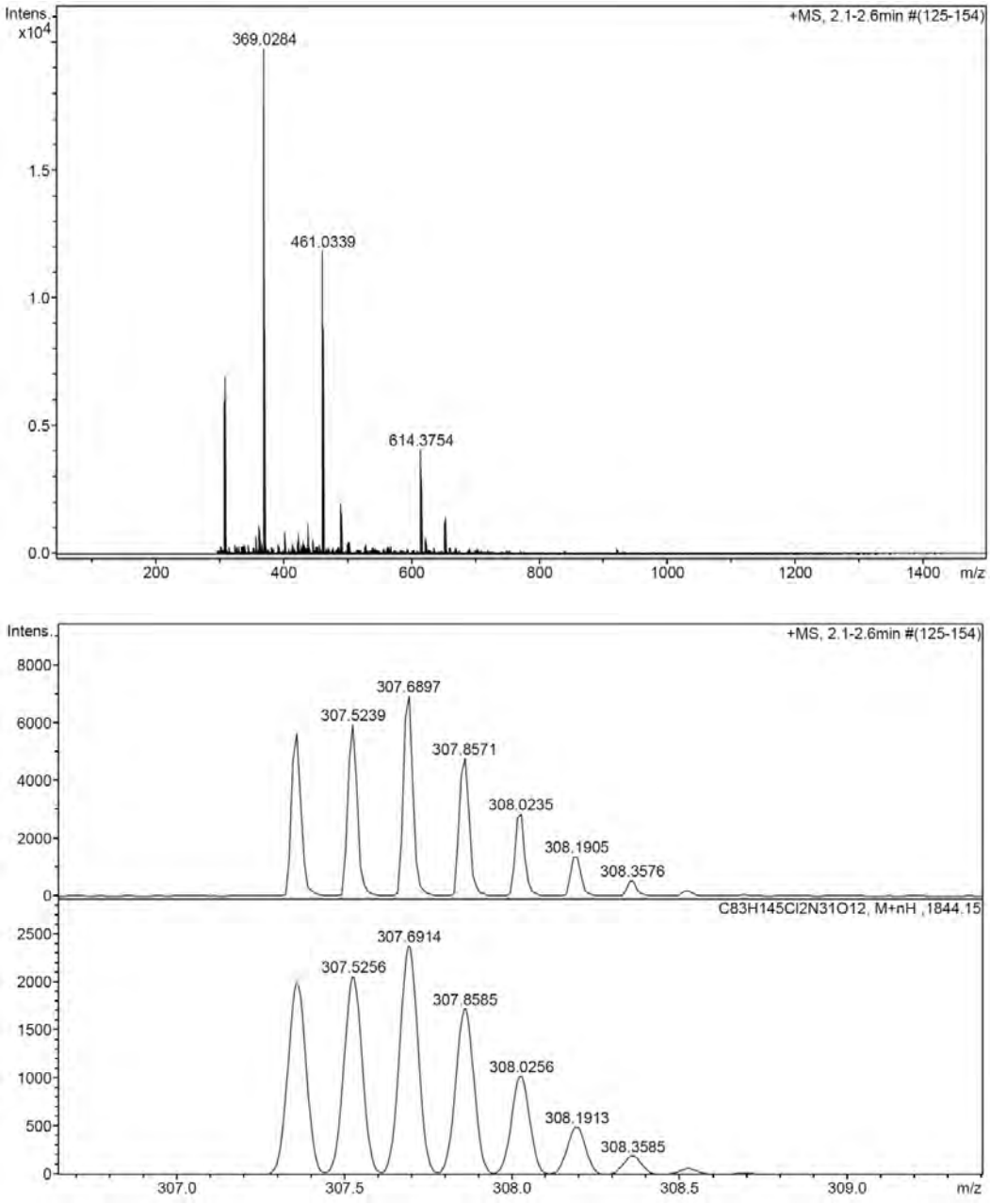

Observed HRMS (top) with the theoretical isotope prediction (bottom).

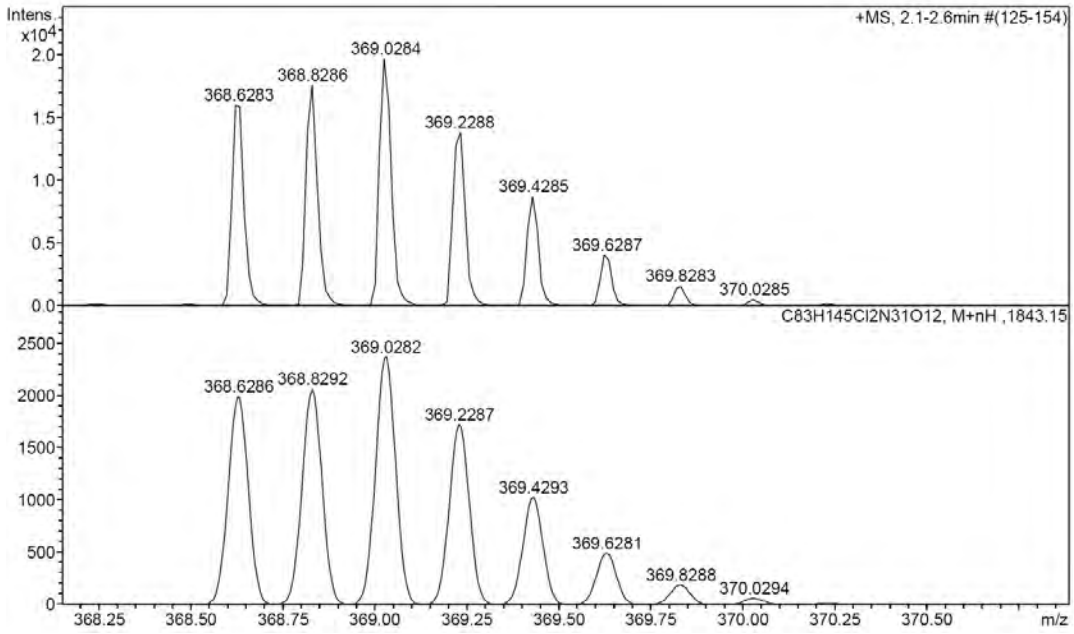

Observed HRMS (top) with the theoretical isotope prediction (bottom).

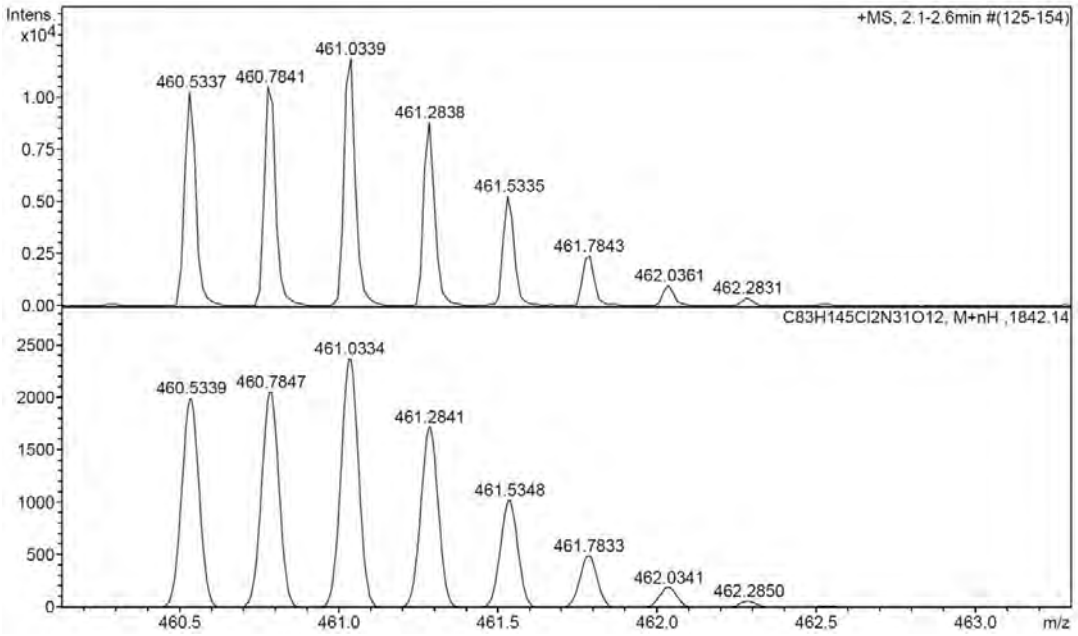

Observed HRMS (top) with the theoretical isotope prediction (bottom).

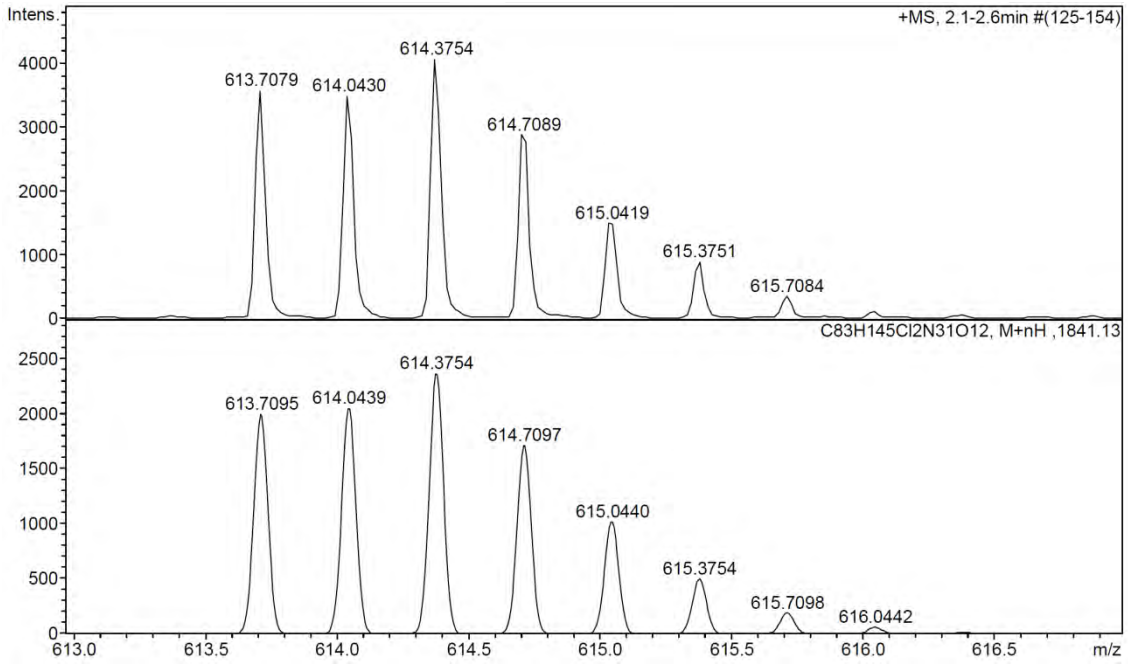

Observed HRMS (top) with the theoretical isotope prediction (bottom).

Figure SIV.8: a) HPLC chromatogram (λ= 220 nm), b) HRMS spectrum (*m/z*).

BP335

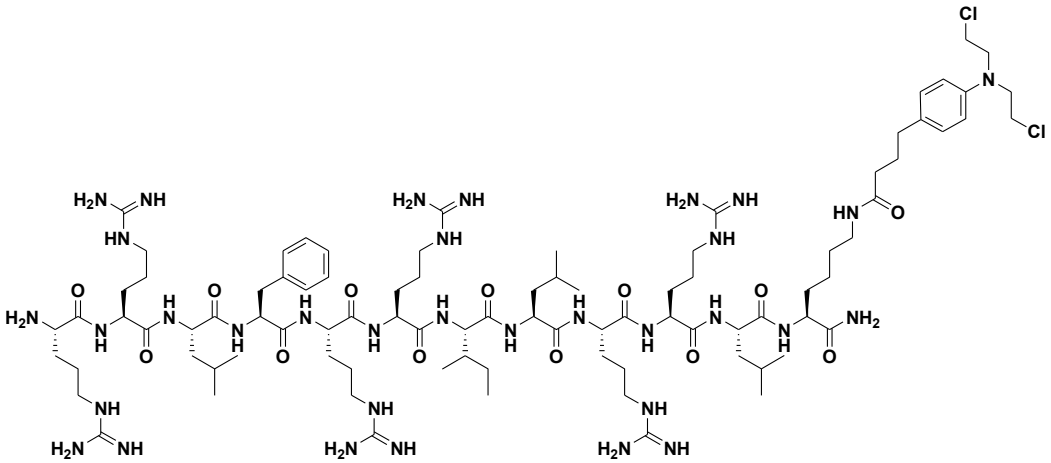

a)

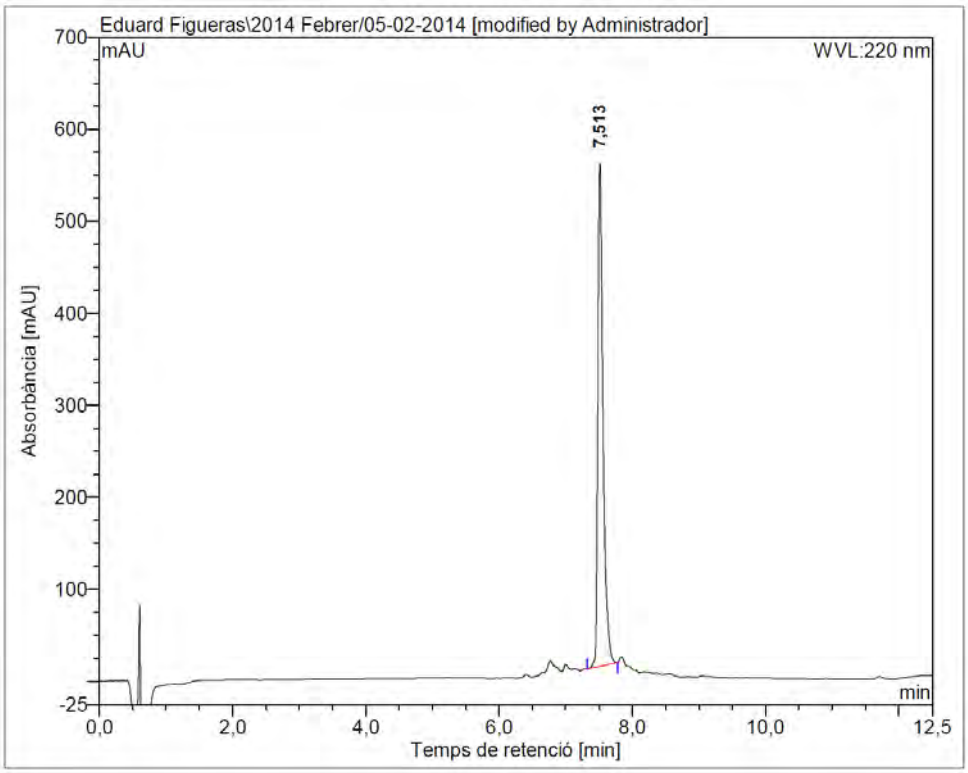

No.	Temps retenció min	alçada mAU	Area mAU*min	Area relativa %
1	7,51	546,652	49,784	100,00
Total:		546,652	49,784	100,00

b)

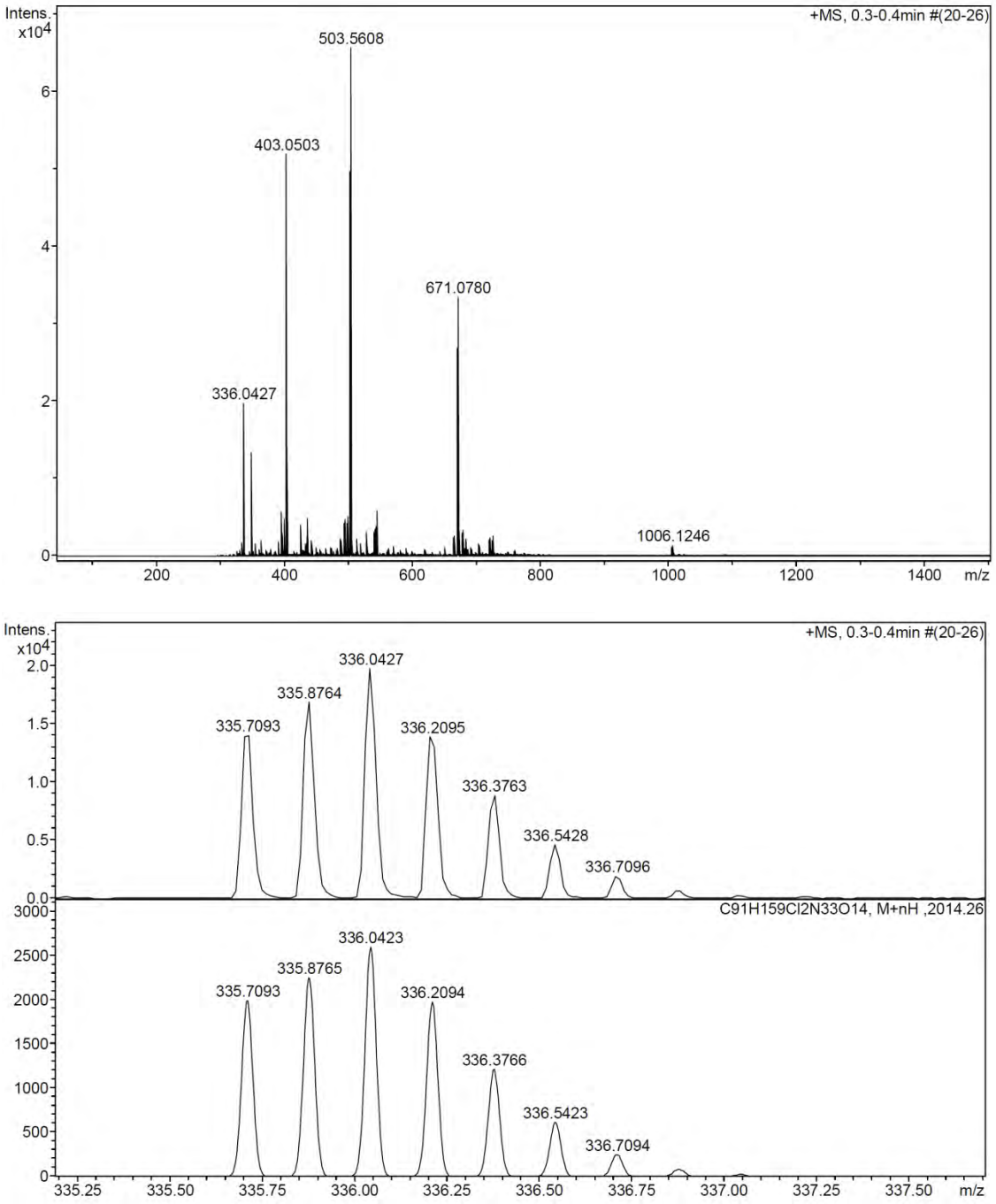

Observed HRMS (top) with the theoretical isotope prediction (bottom).

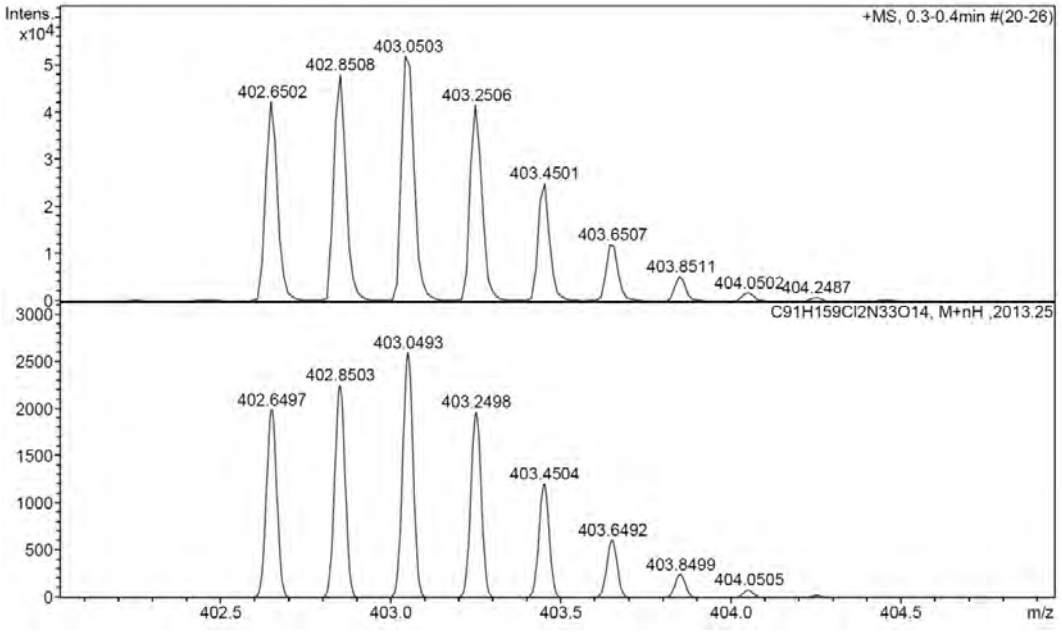

Observed HRMS (top) with the theoretical isotope prediction (bottom).

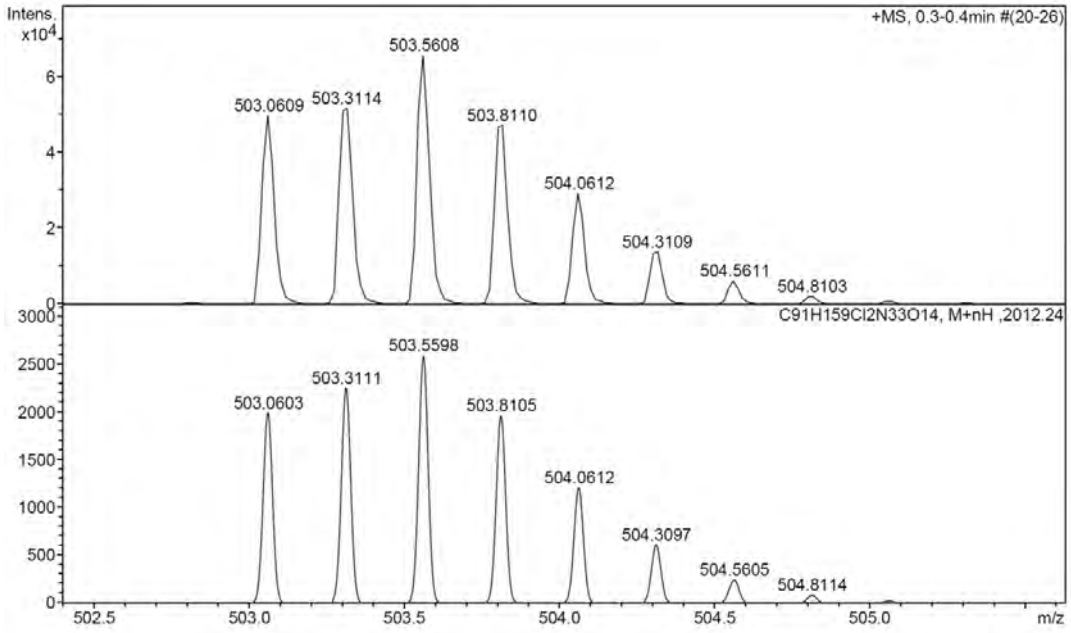

Observed HRMS (top) with the theoretical isotope prediction (bottom).

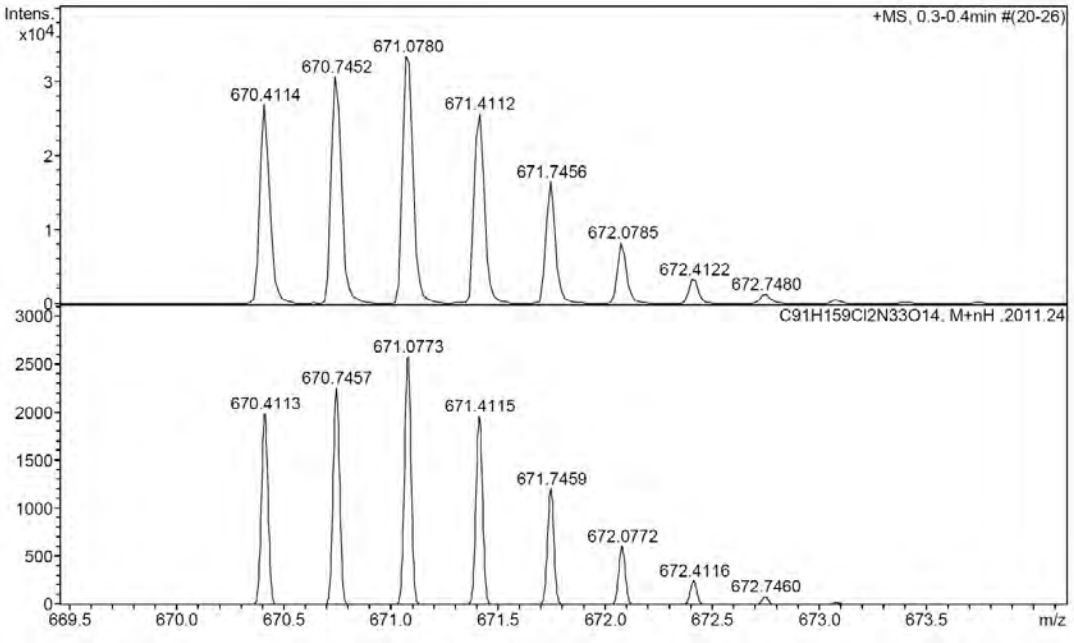

Observed HRMS (top) with the theoretical isotope prediction (bottom).

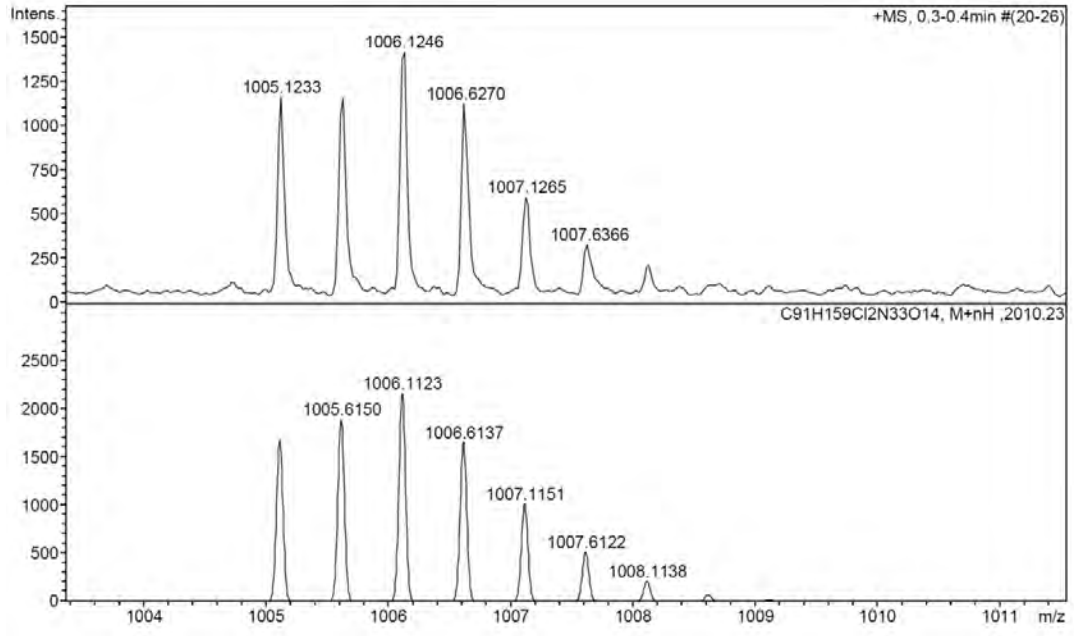

Observed HRMS (top) with the theoretical isotope prediction (bottom).

Figure SIV.9: a) HPLC chromatogram (λ= 220 nm), b) HRMS spectrum (*m/z*).

BP336

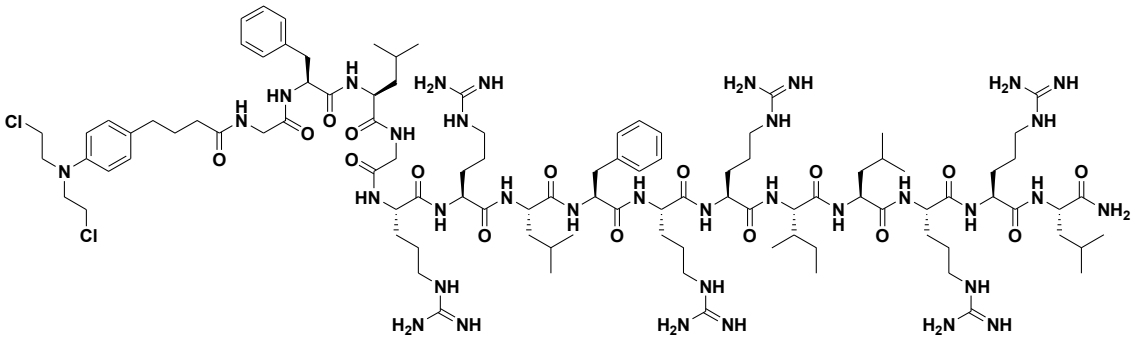

a)

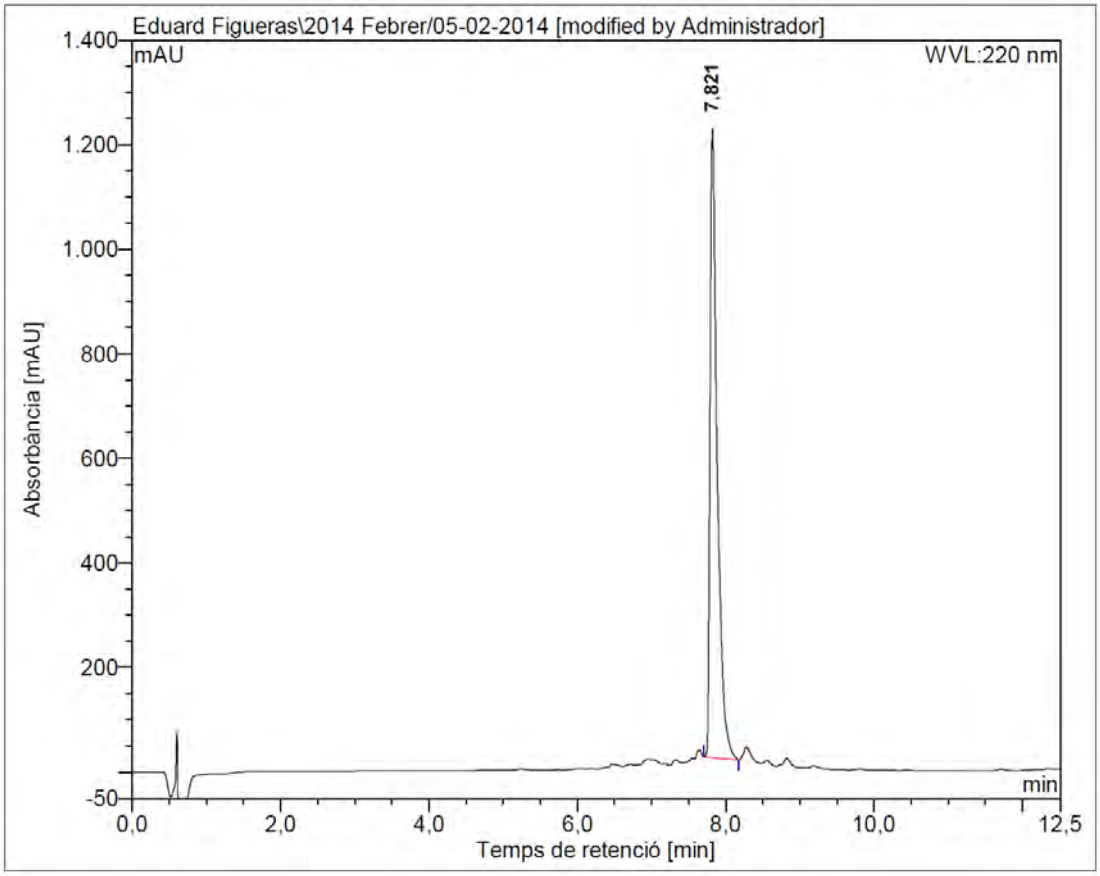

No.	Temps retenció min	alçada mAU	Area mAU*min	Area relativa %
1	7,82	1201,956	133,830	100,00
Total:		1201,956	133,830	100,00

b)

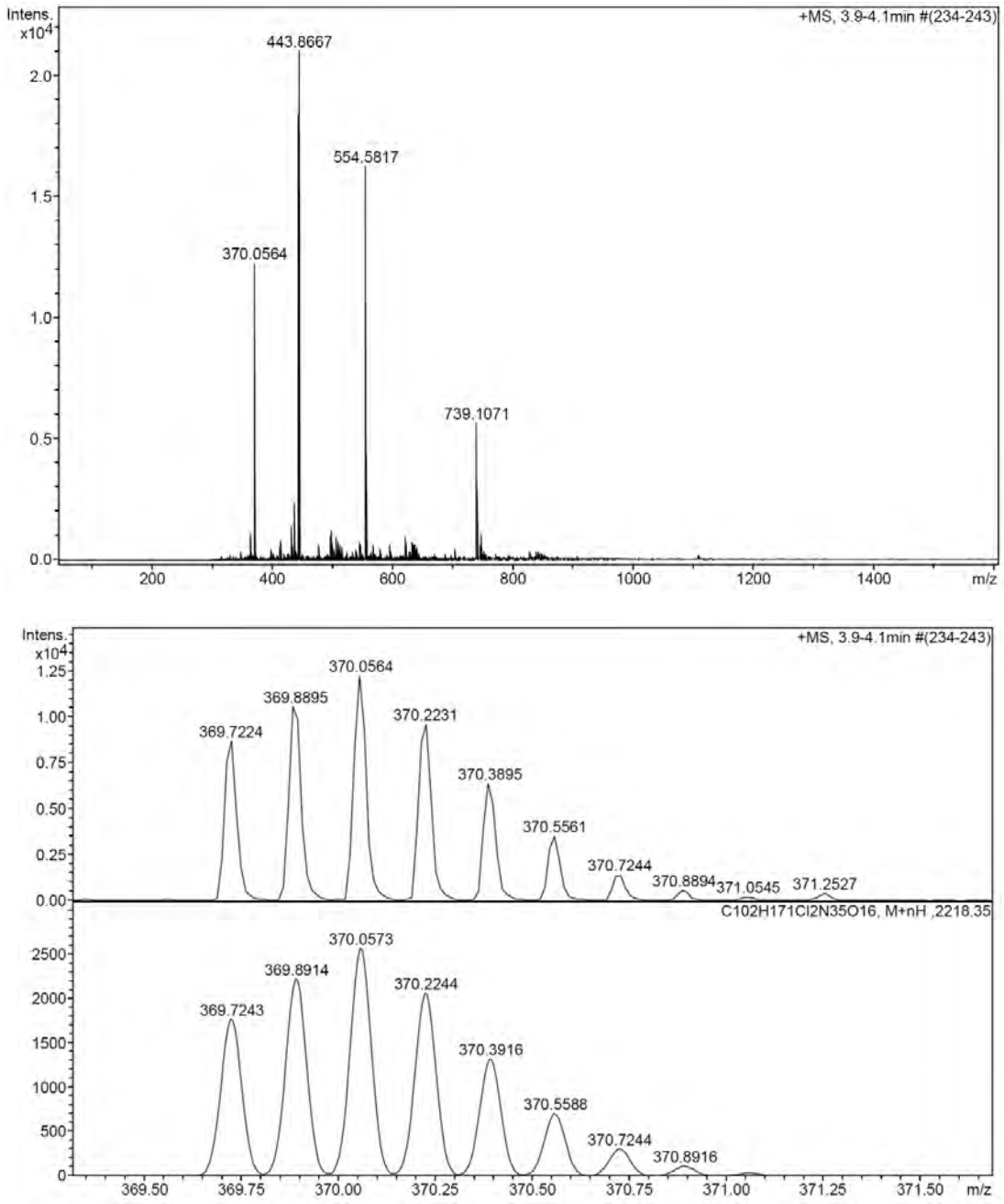

Observed HRMS (top) with the theoretical isotope prediction (bottom).

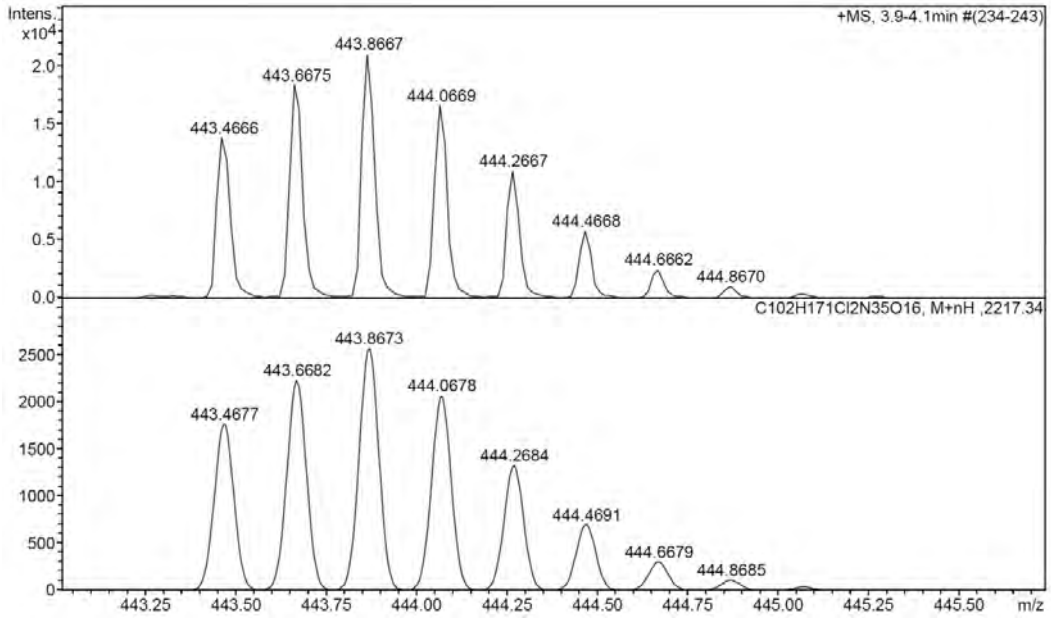

Observed HRMS (top) with the theoretical isotope prediction (bottom).

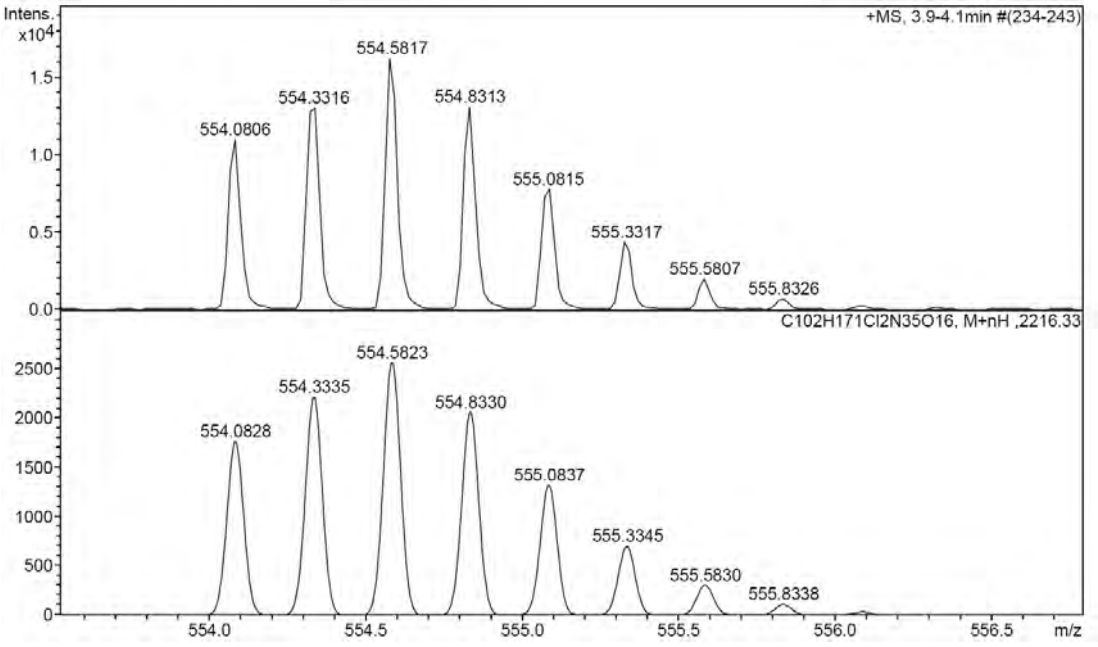

Observed HRMS (top) with the theoretical isotope prediction (bottom).

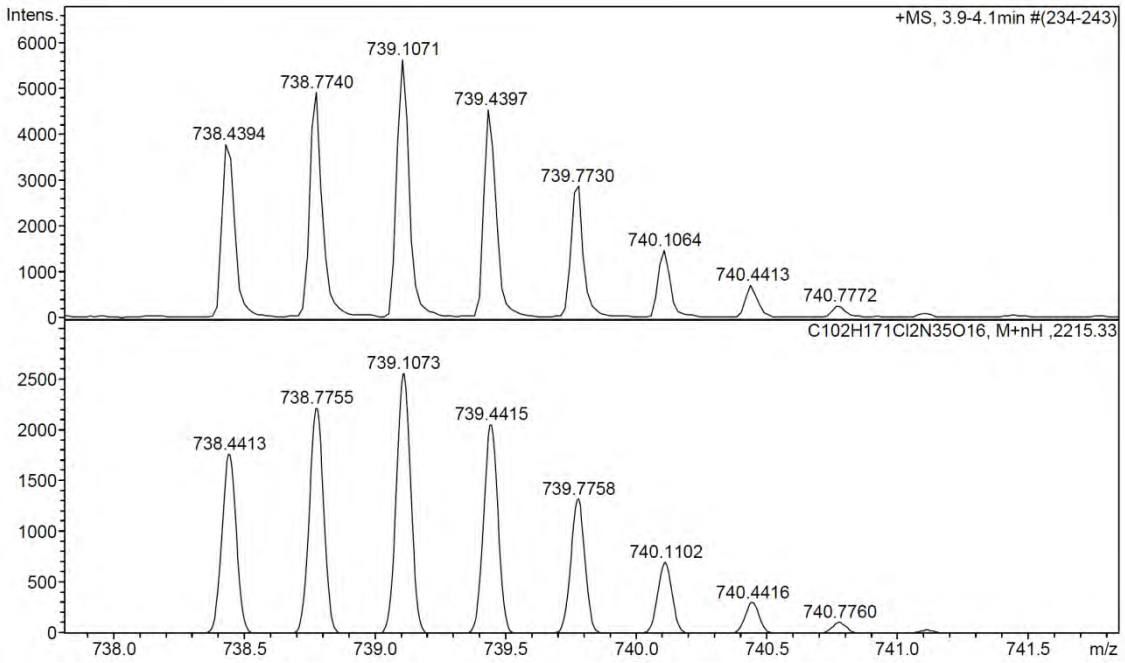

Observed HRMS (top) with the theoretical isotope prediction (bottom).

Figure SIV.10: a) HPLC chromatogram (λ= 220 nm), b) HRMS spectrum (*m/z*).

BP337

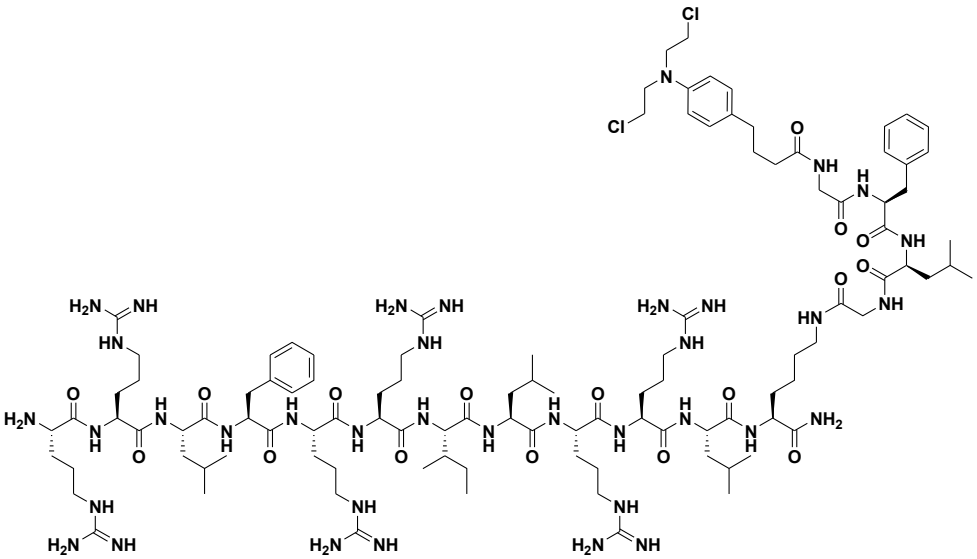

a)

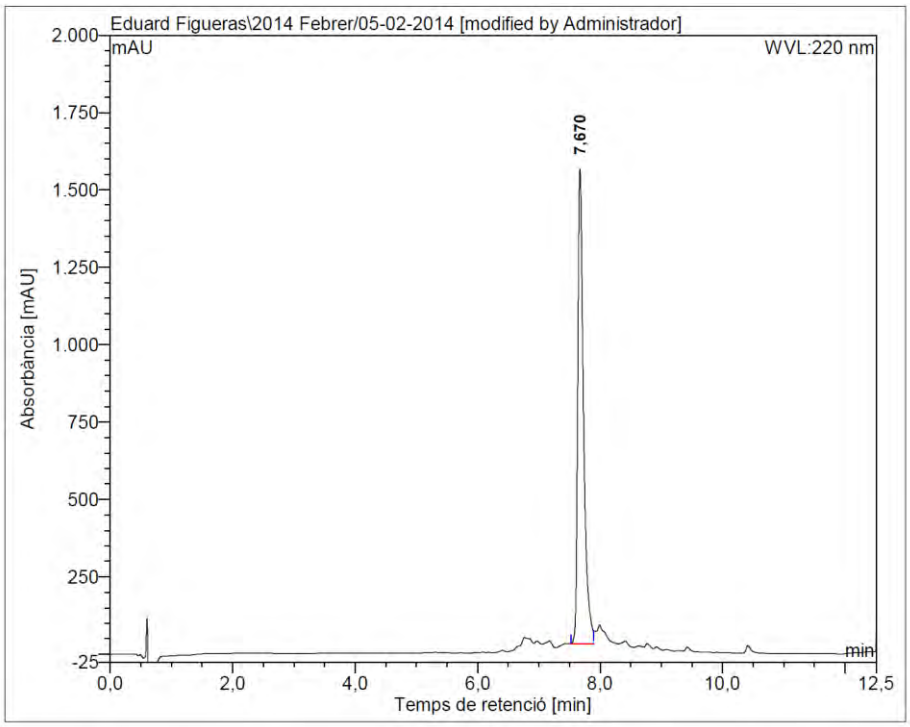

No.	Temps retenció min	alçada mAU	Area mAU*min	Area relativa %
1	7,67	1534,141	168,935	100,00
Total:		1534,141	168,935	100,00

b)

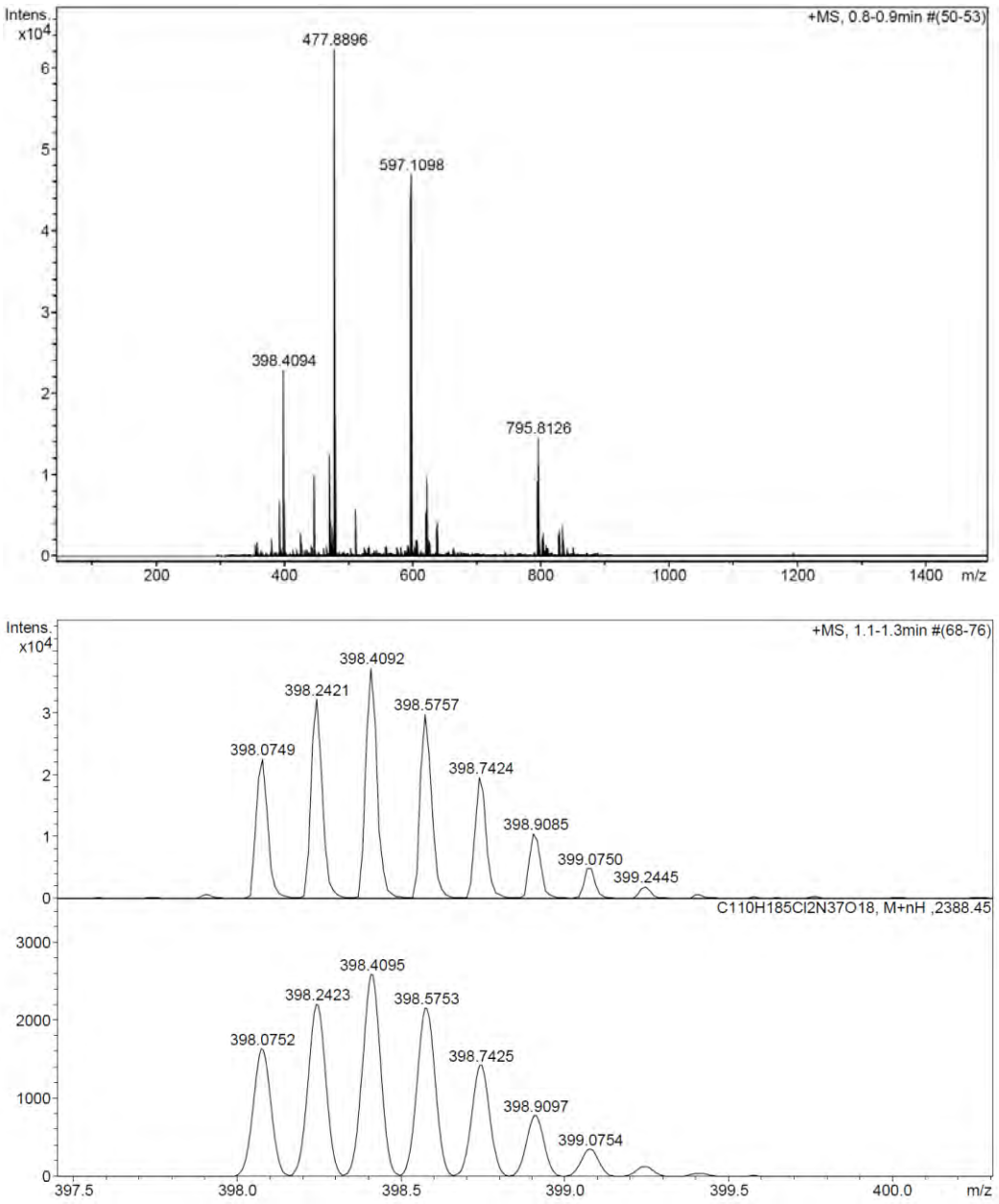

Observed HRMS (top) with the theoretical isotope prediction (bottom).

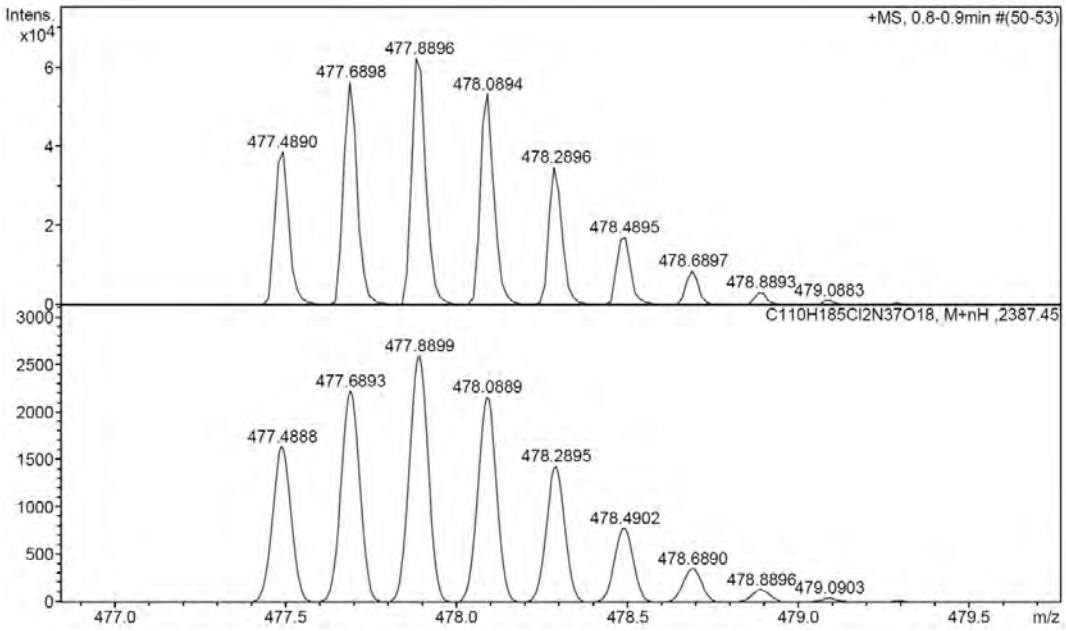

Observed HRMS (top) with the theoretical isotope prediction (bottom).

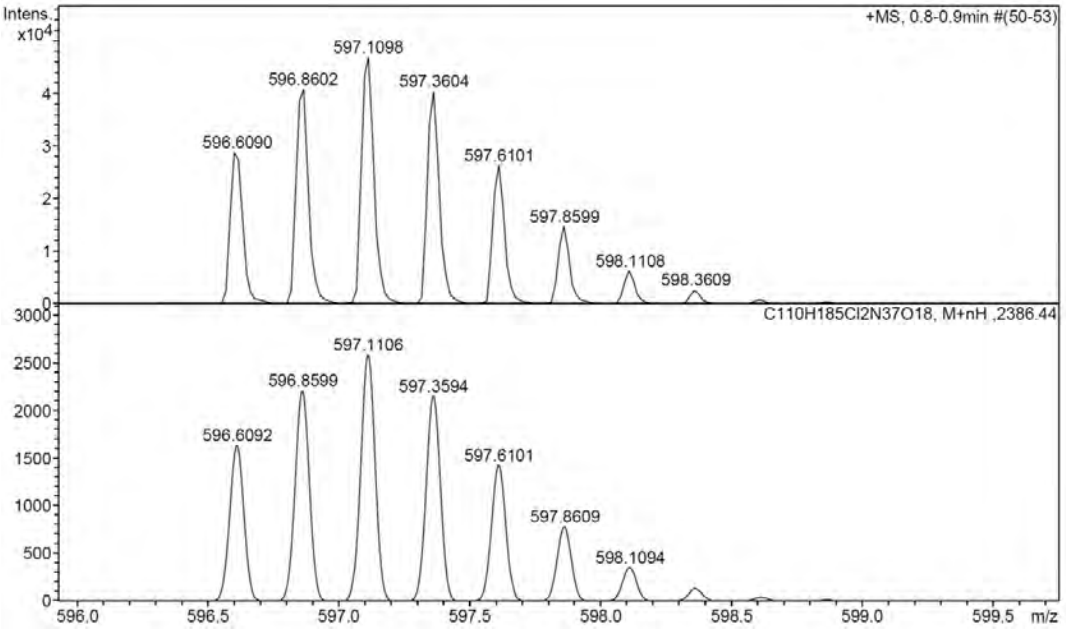

Observed HRMS (top) with the theoretical isotope prediction (bottom).

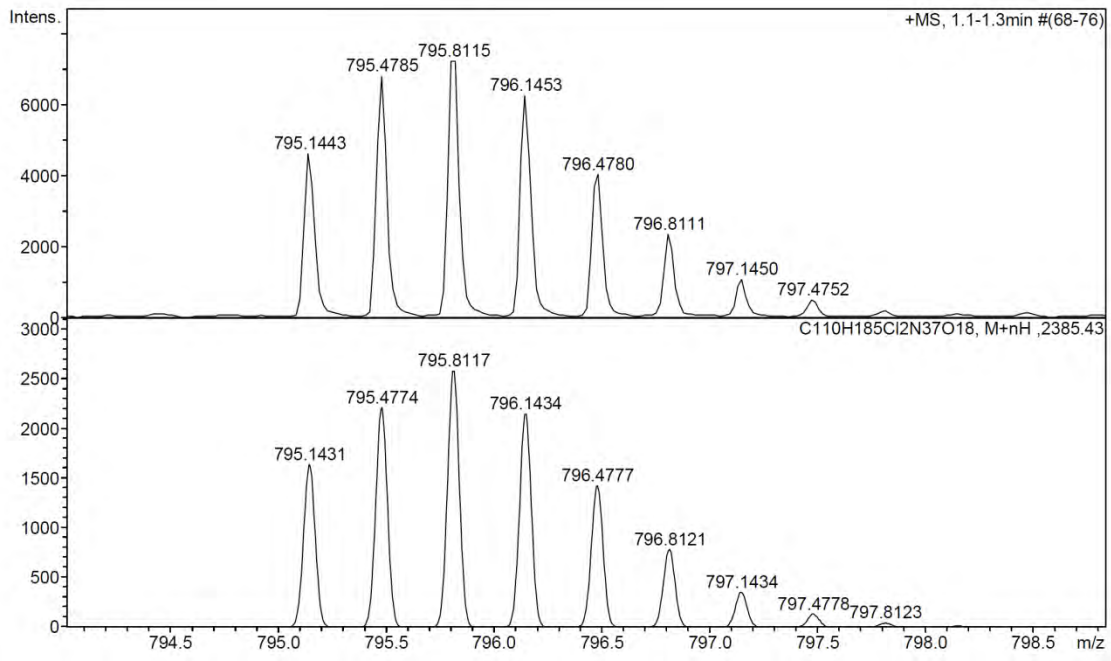

Observed HRMS (top) with the theoretical isotope prediction (bottom).

Figure SIV.11: a) HPLC chromatogram (λ= 220 nm), b) HRMS spectrum (*m/z*).

CF-BP16

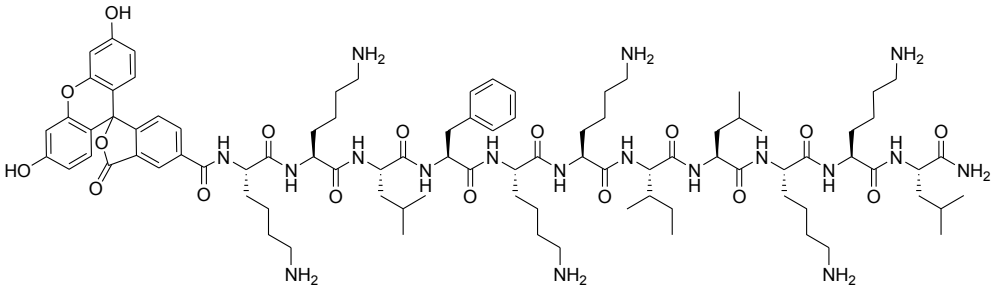

a)

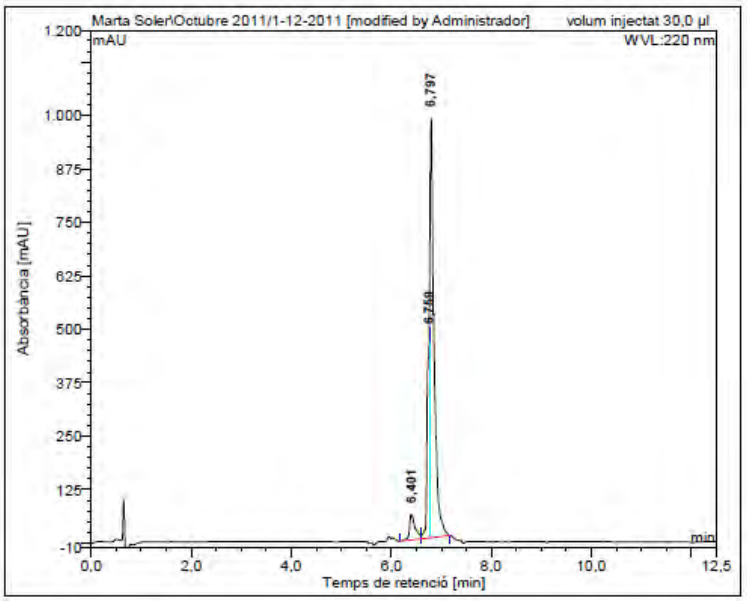

No.	mps retenc min	alçada mAU	Area mAU*min	Area relativa %
1	6,40	60,473	8,138	6,40
2	6,76	473,768	22,057	17,34
3	6,80	981,748	97,024	76,26
Total:		1515,990	127,220	100,00

b)

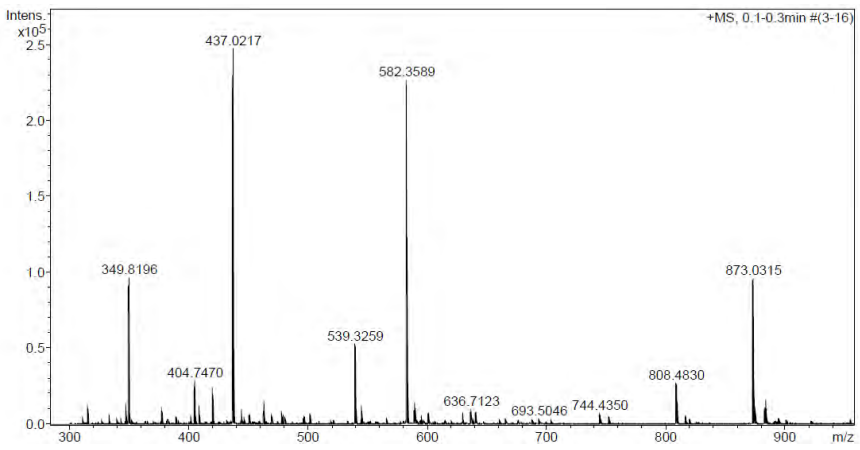

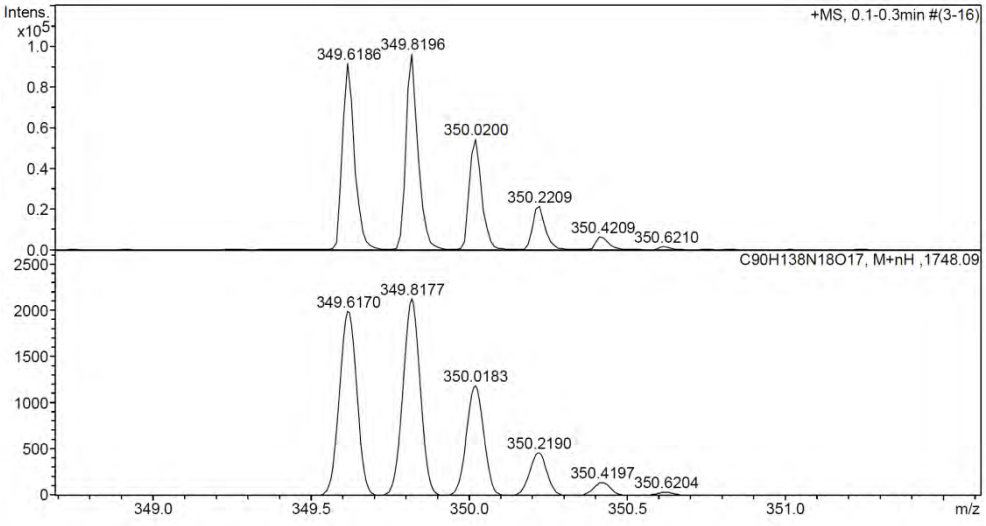

Observed HRMS (top) with the theoretical isotope prediction (bottom).

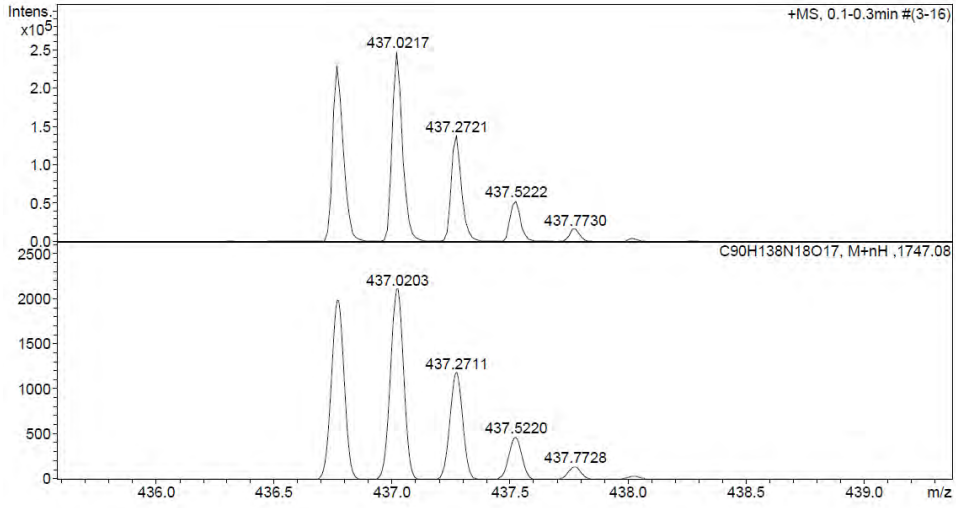

Observed HRMS (top) with the theoretical isotope prediction (bottom).

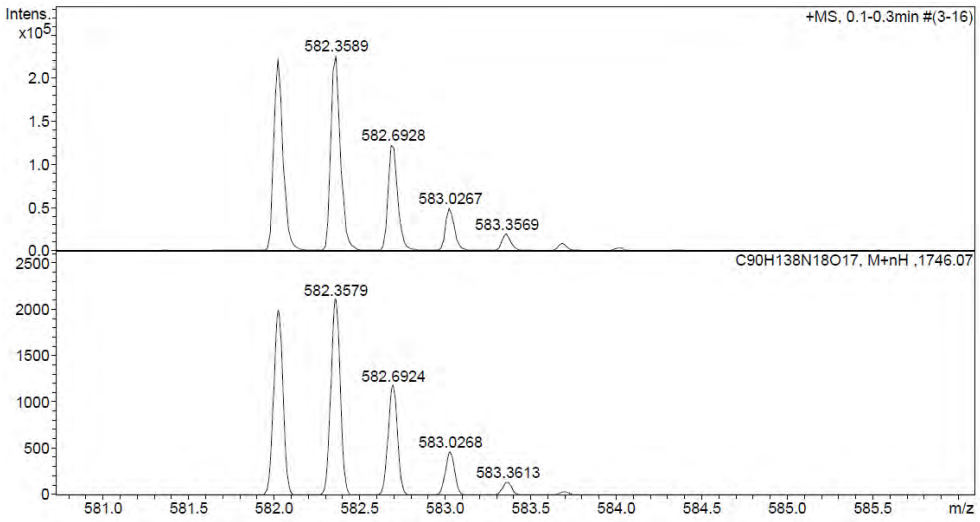

Observed HRMS (top) with the theoretical isotope prediction (bottom).

Figure SIV.12: a) HPLC chromatogram (λ= 220 nm), b) HRMS spectrum (*m/z*).

CF-BP308

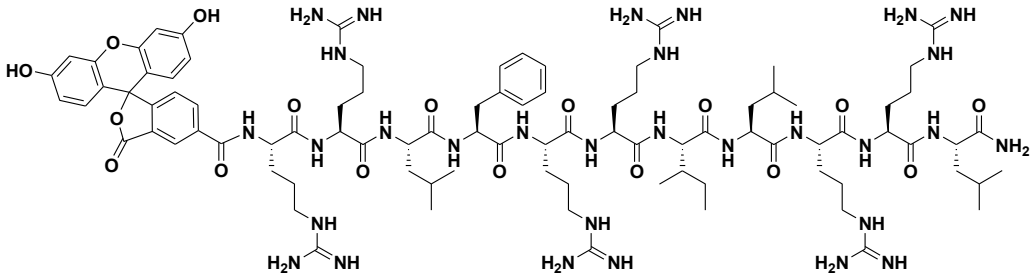

a)

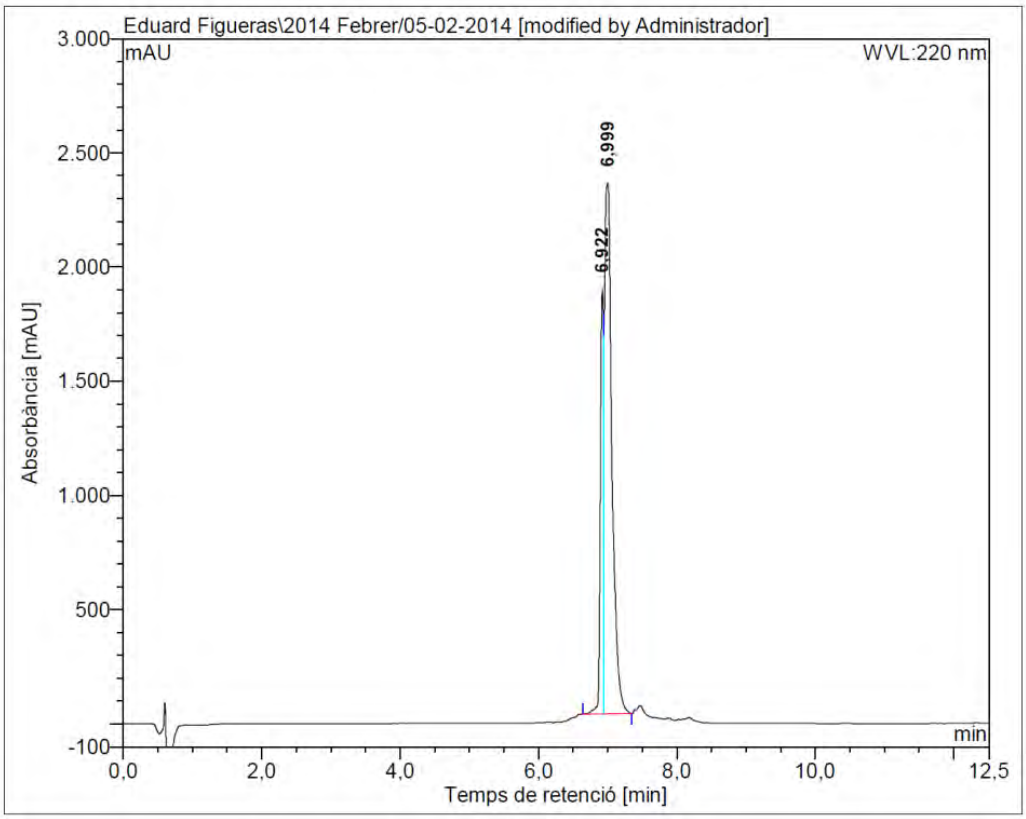

No.	Temps retenció min	alçada mAU	Area mAU*min	Area relativa %
1	6,92	1859,025	98,247	25,25
2	7,00	2323,905	290,924	74,75
Total:		4182,930	389,171	100,00

b)

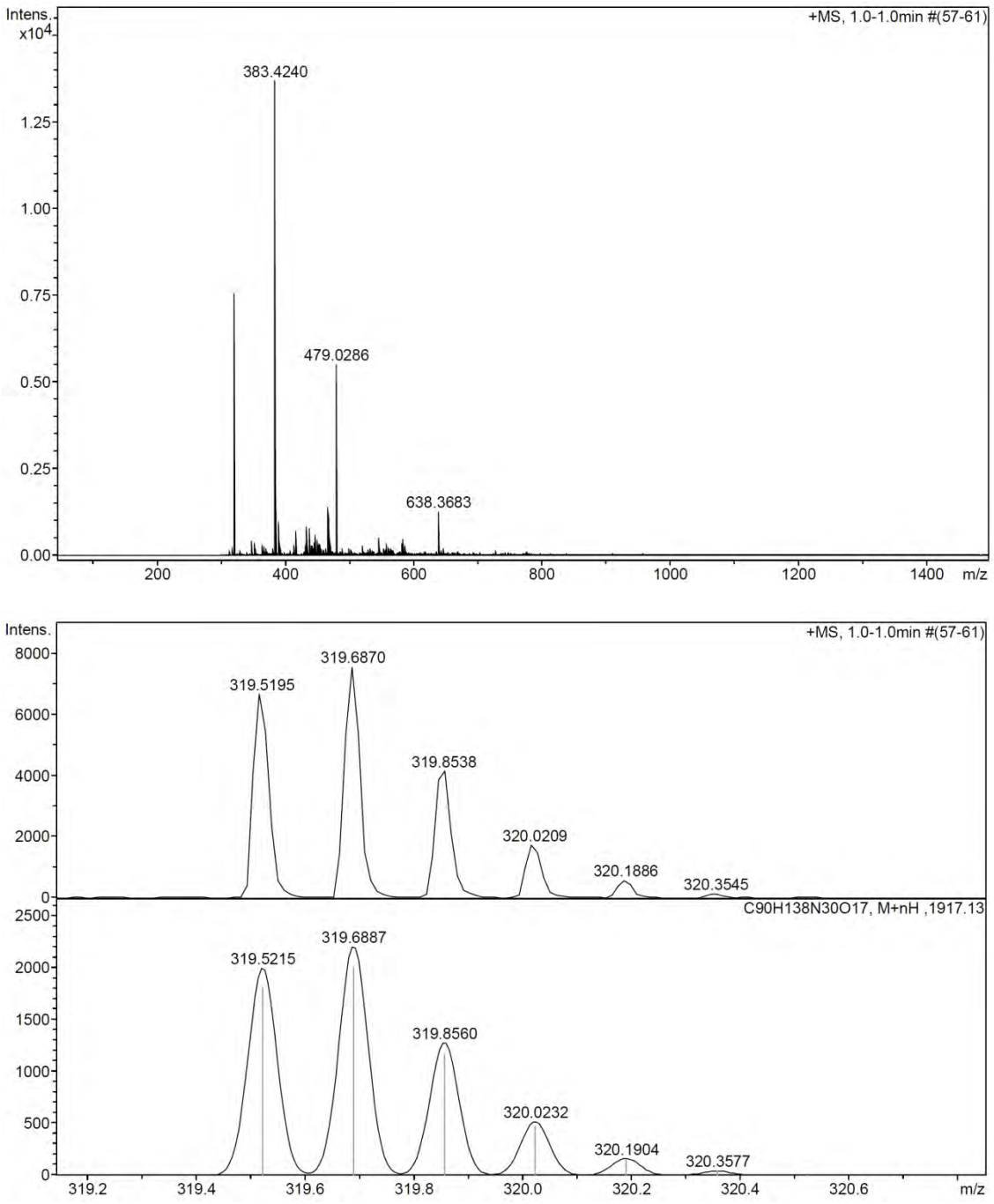

Observed HRMS (top) with the theoretical isotope prediction (bottom).

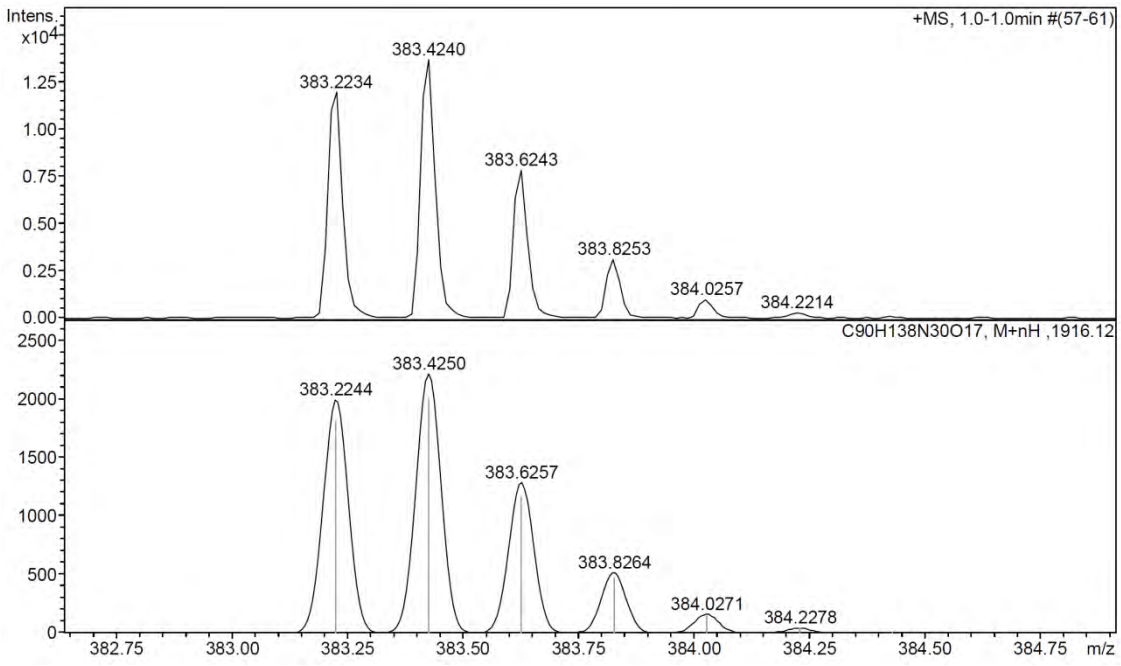

Observed HRMS (top) with the theoretical isotope prediction (bottom).

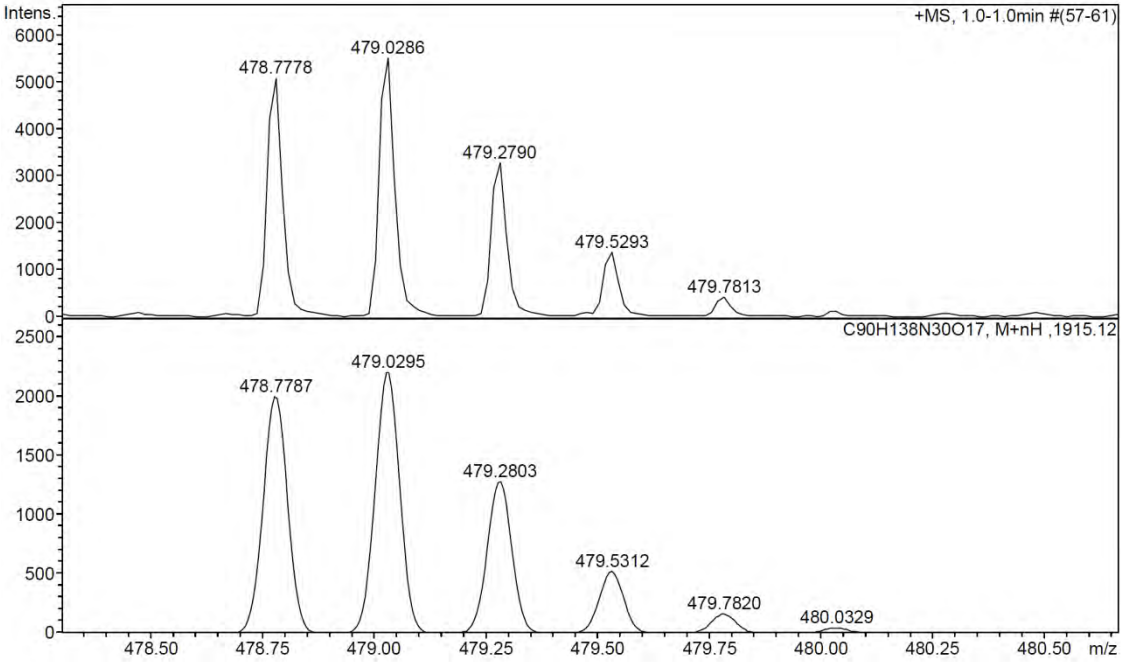

Observed HRMS (top) with the theoretical isotope prediction (bottom).

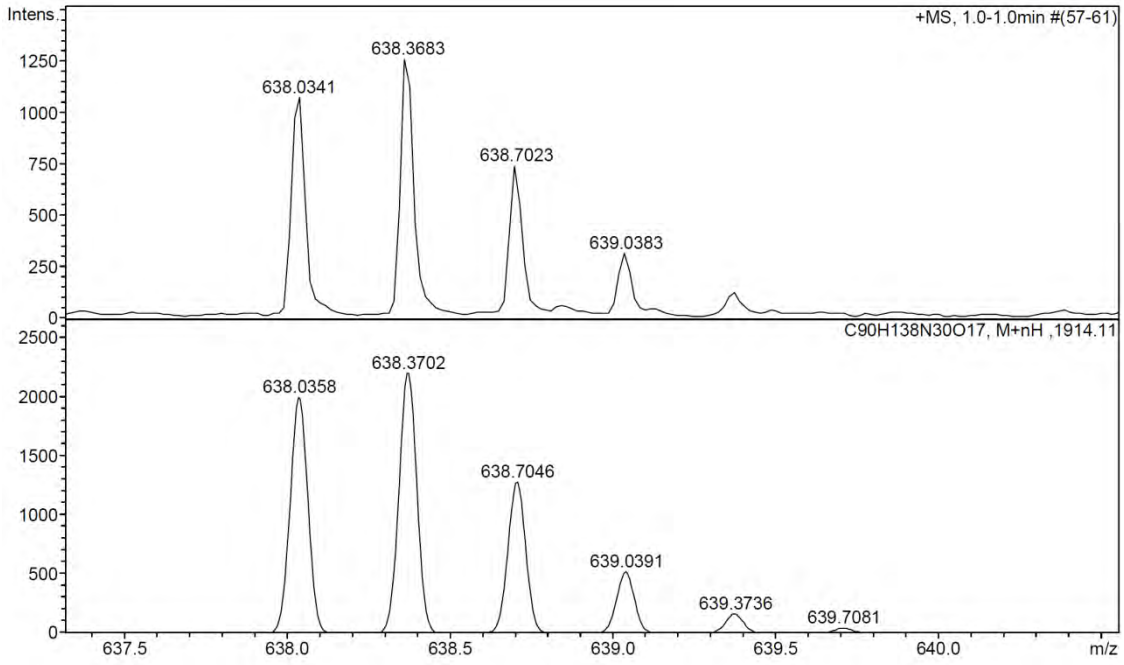

Observed HRMS (top) with the theoretical isotope prediction (bottom).

Figure SIV.13: a) HPLC chromatogram (λ= 220 nm), b) HRMS spectrum (*m/z*).

BP326

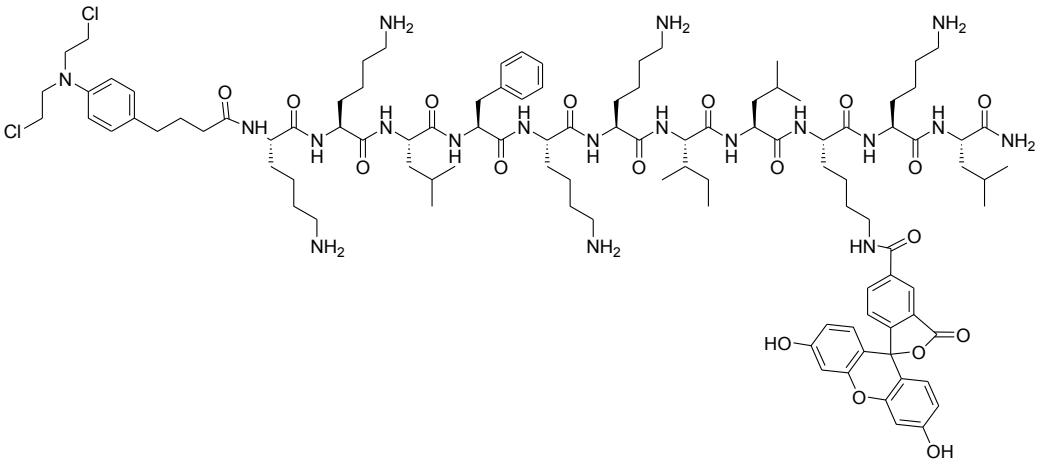

a)

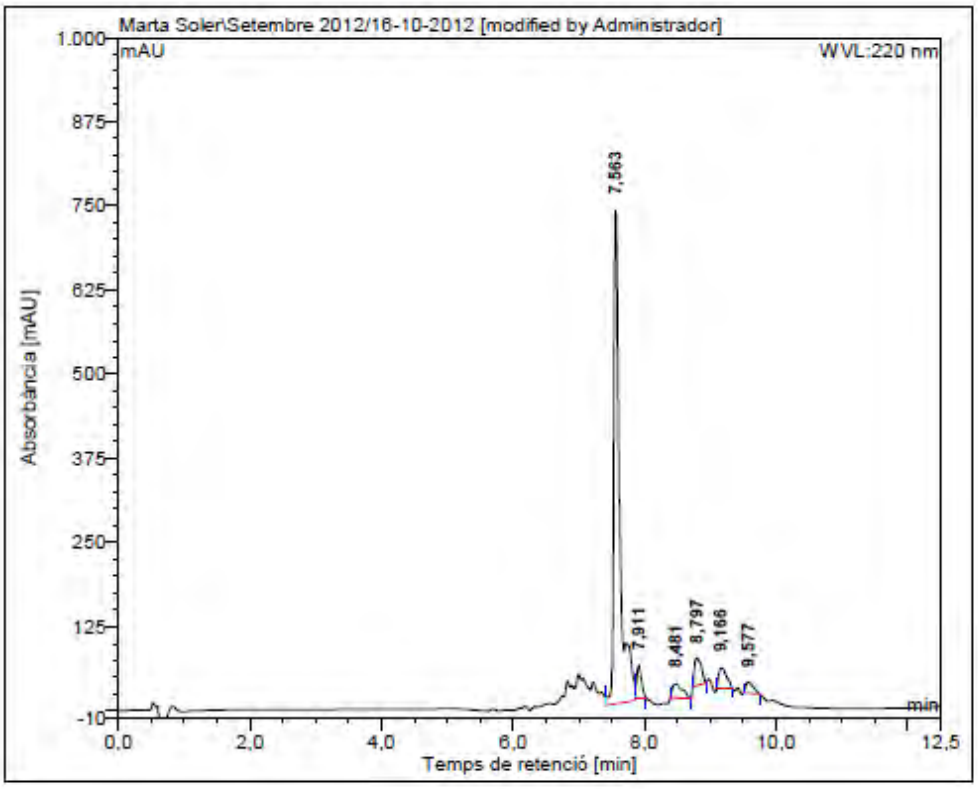

No.	mps retenc min	alçada mAU	Area mAU*min	Area relativa %
1	7,56	732,423	77,055	80,59
2	7,91	48,005	3,811	3,99
3	8,48	20,782	3,596	3,76
4	8,80	40,837	4,961	5,19
5	9,17	29,235	3,969	4,15
6	9,58	17,041	2,219	2,32
Total:		888,322	95,611	100,00

b)

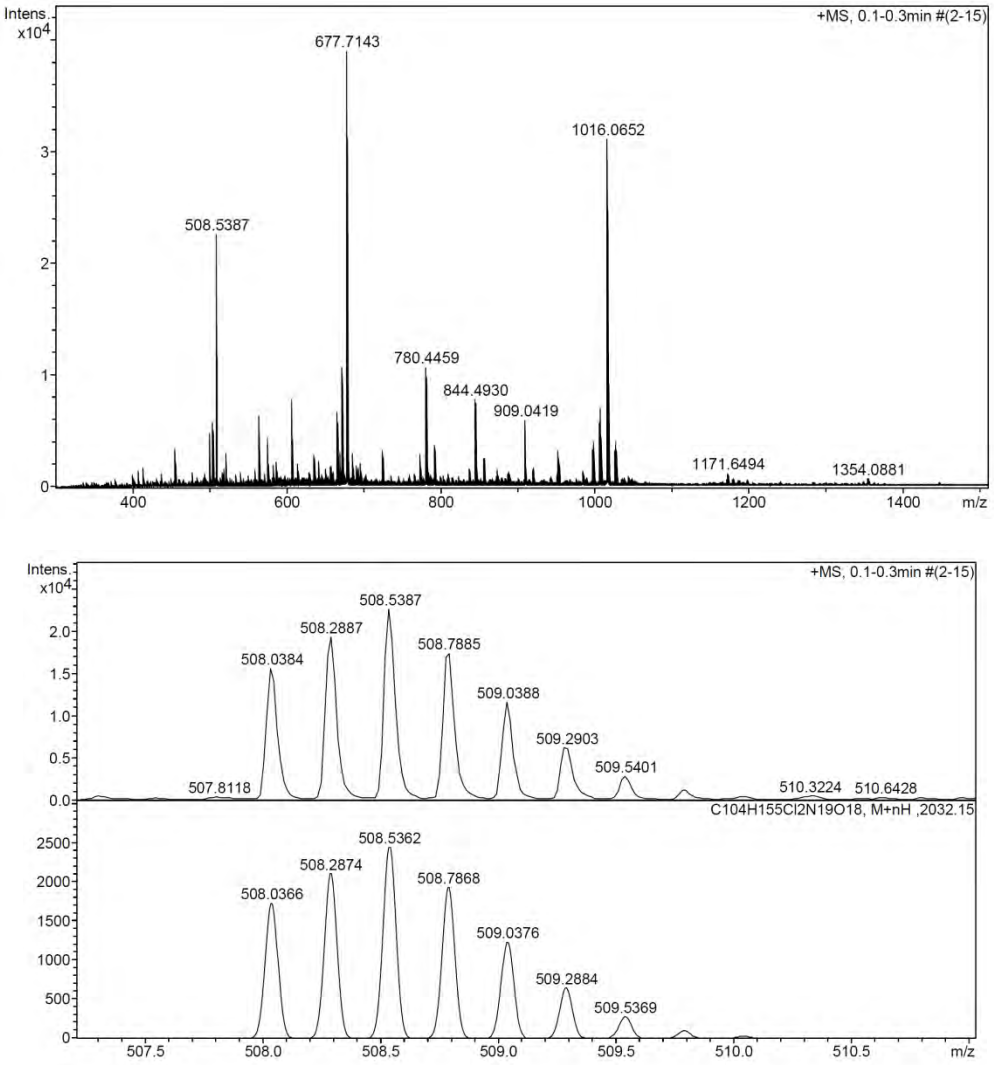

Observed HRMS (top) with the theoretical isotope prediction (bottom).

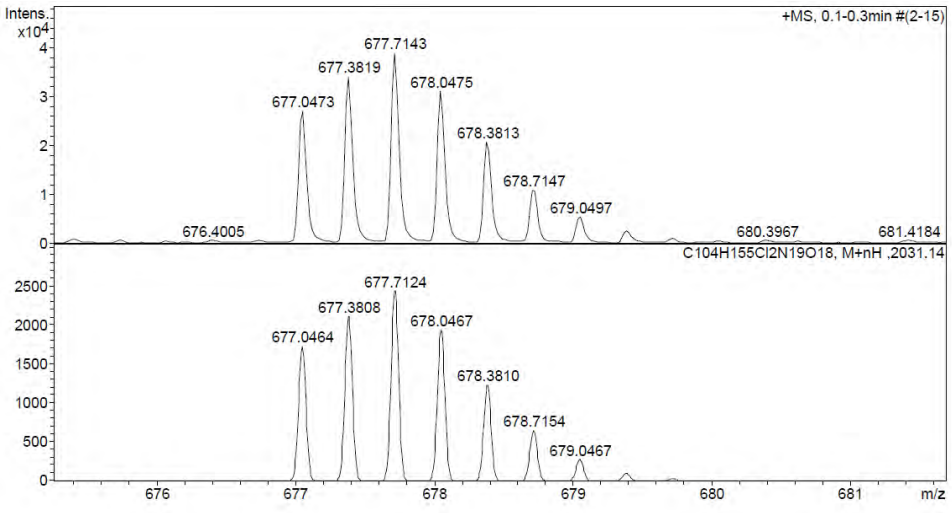

Observed HRMS (top) with the theoretical isotope prediction (bottom).

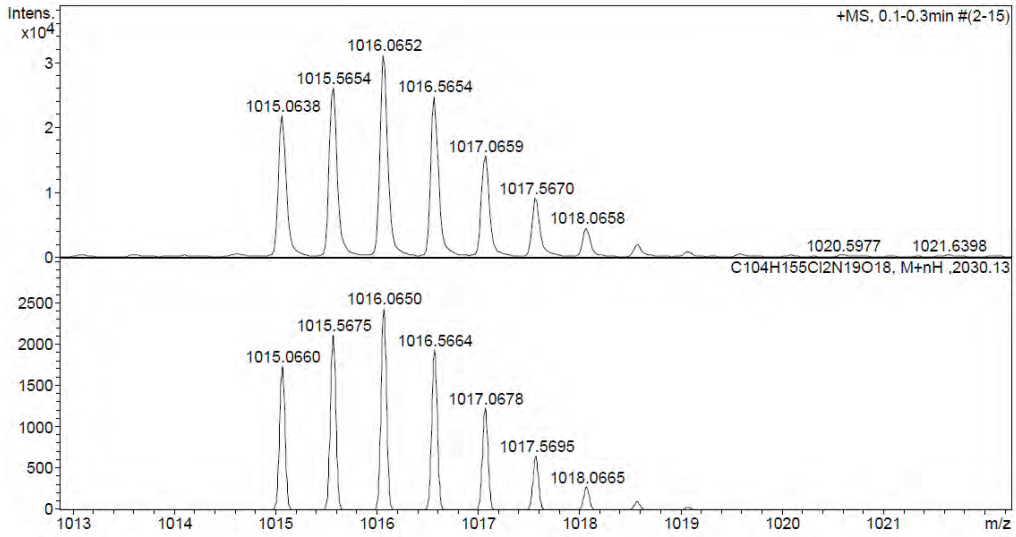

Observed HRMS (top) with the theoretical isotope prediction (bottom).

Figure SIV.14: a) HPLC chromatogram (λ= 220 nm), b) HRMS spectrum (*m/z*).

BP338

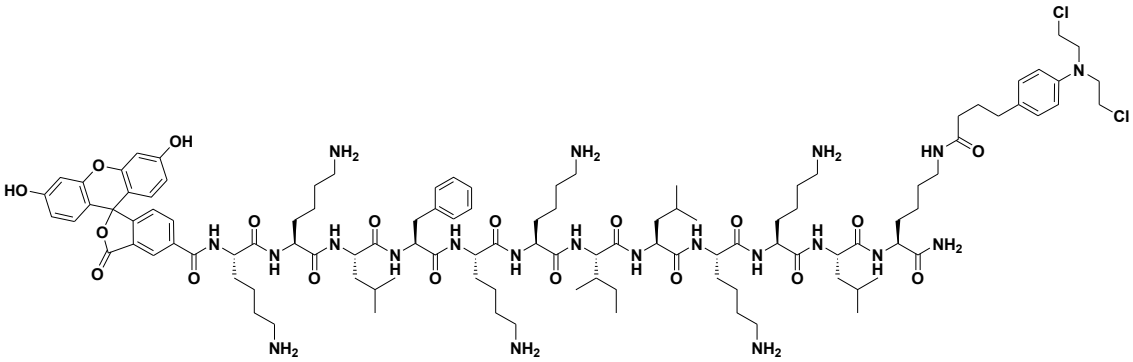

a)

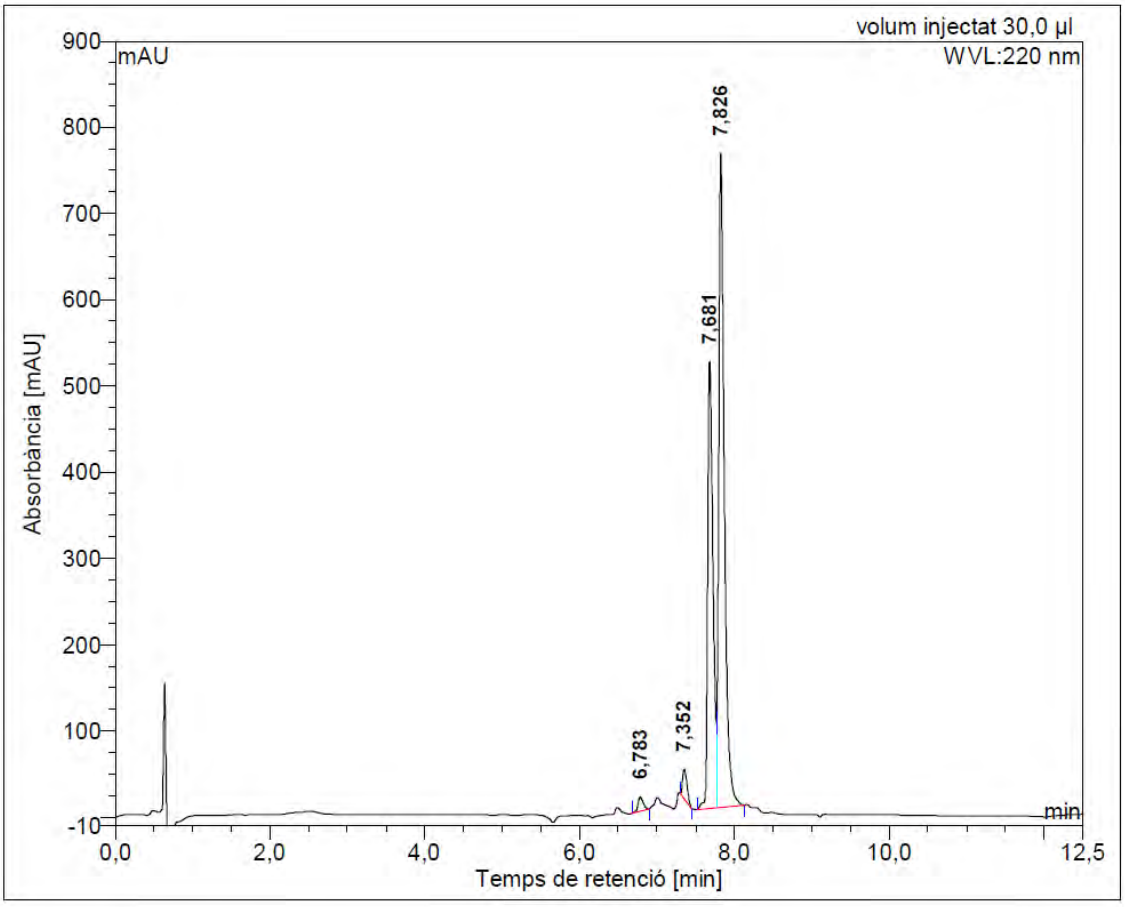

No.	mps retenc min	alçada mAU	Area mAU*min	Area relativa %
1	6,78	16,216	1,282	1,19
2	7,35	34,135	2,255	2,09
3	7,68	518,041	40,429	37,41
4	7,83	758,095	64,094	59,31
Total:		1326,487	108,061	100,00

b)

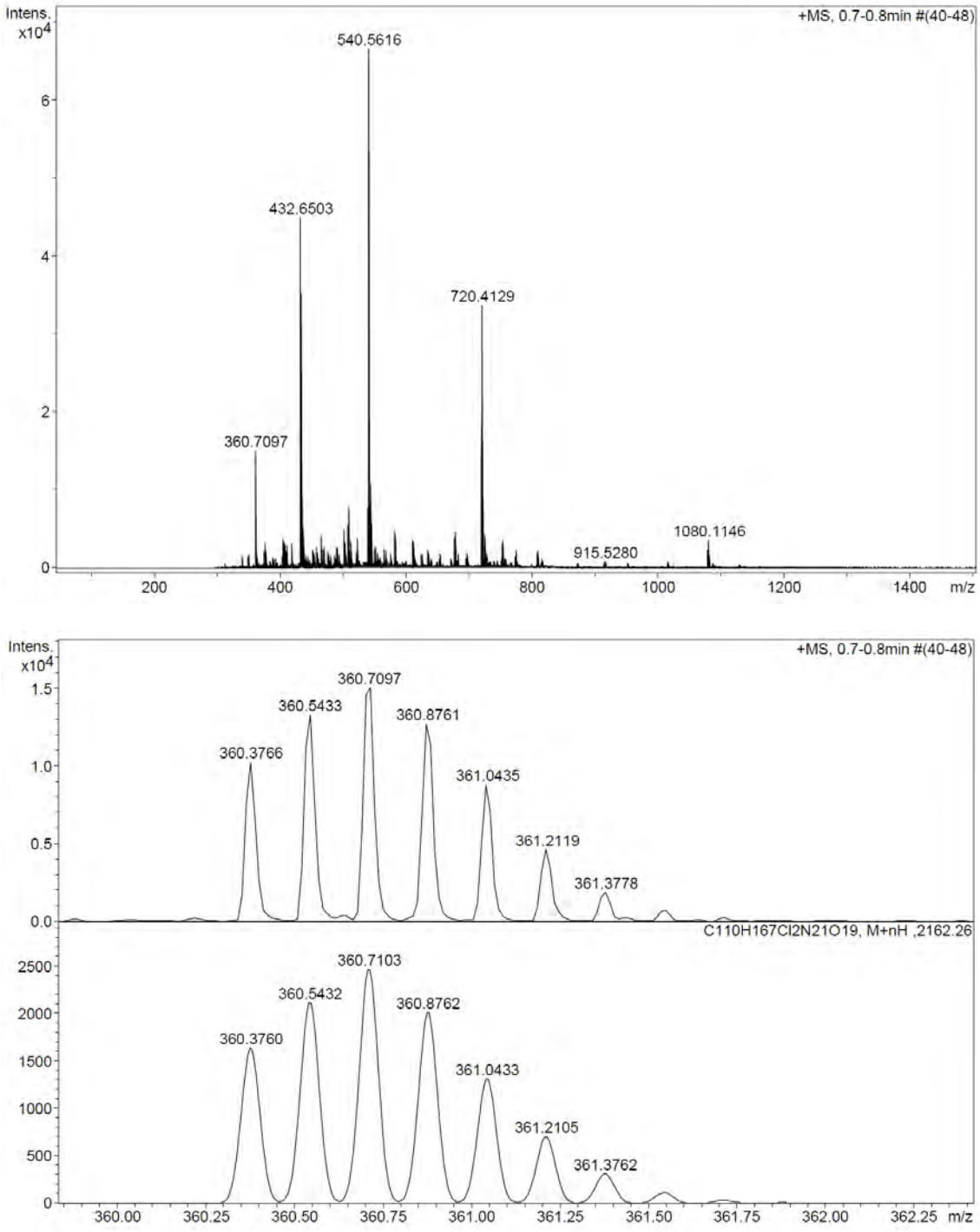

Observed HRMS (top) with the theoretical isotope prediction (bottom).

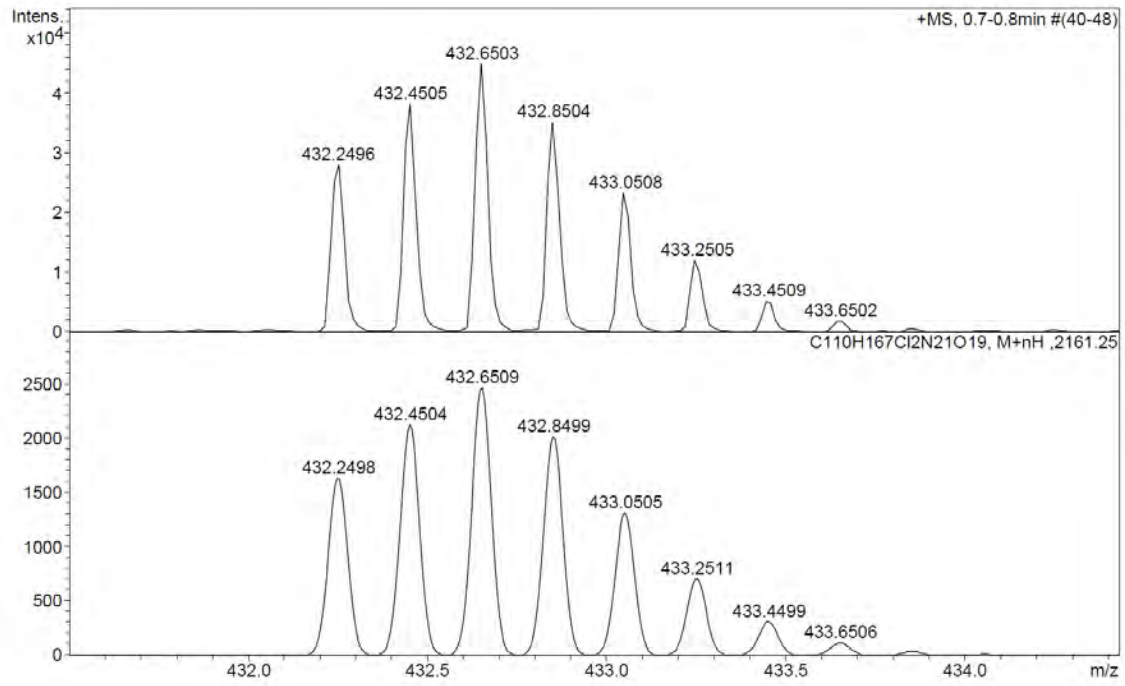

Observed HRMS (top) with the theoretical isotope prediction (bottom).

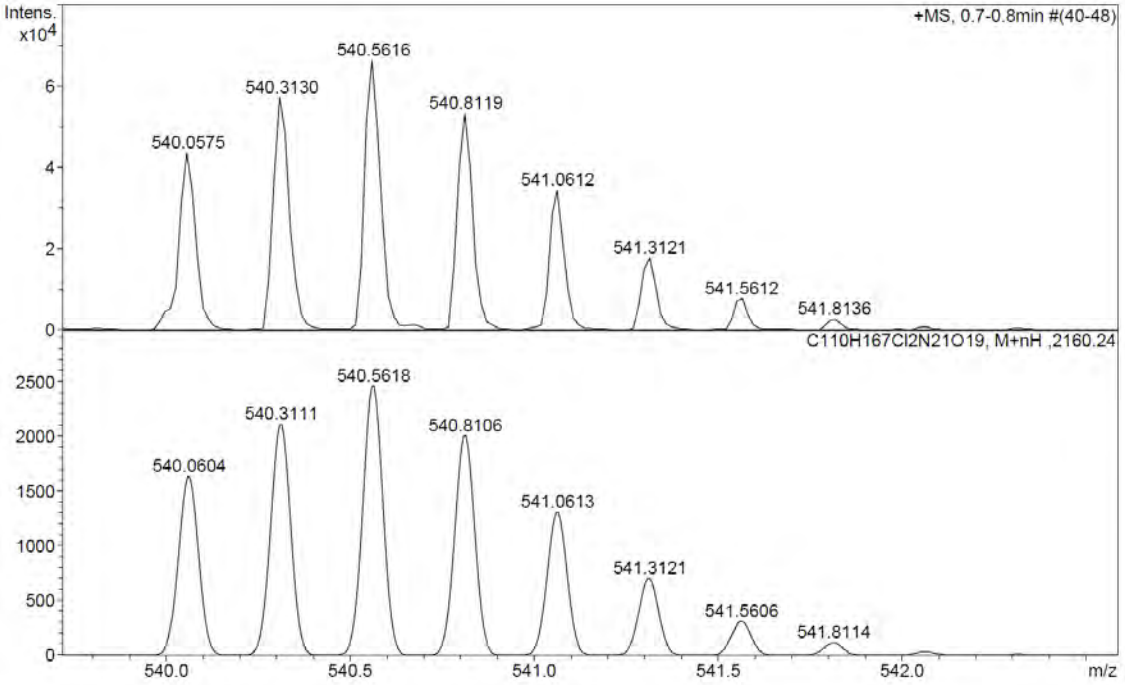

Observed HRMS (top) with the theoretical isotope prediction (bottom).

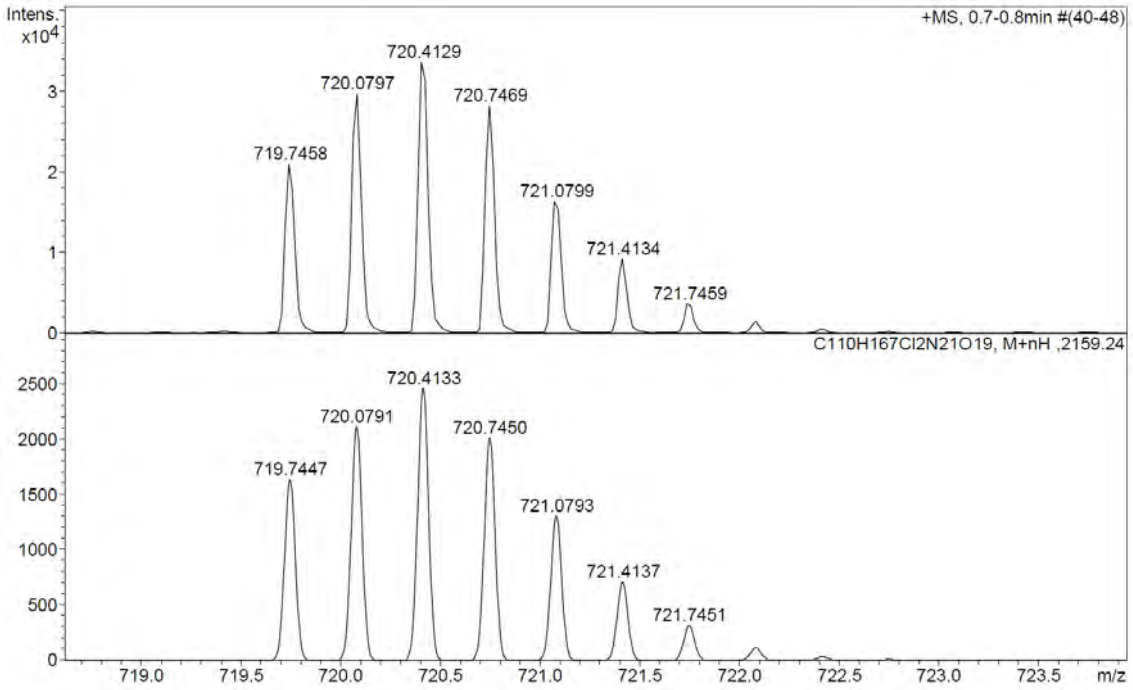

Observed HRMS (top) with the theoretical isotope prediction (bottom).

Figure SIV.15: a) HPLC chromatogram (λ= 220 nm), b) HRMS spectrum (*m/z*).

BP339

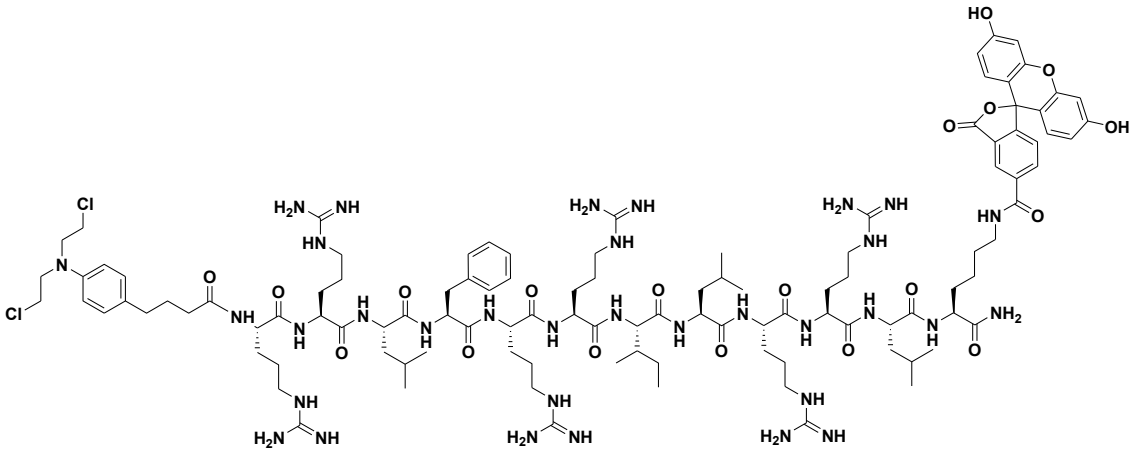

a)

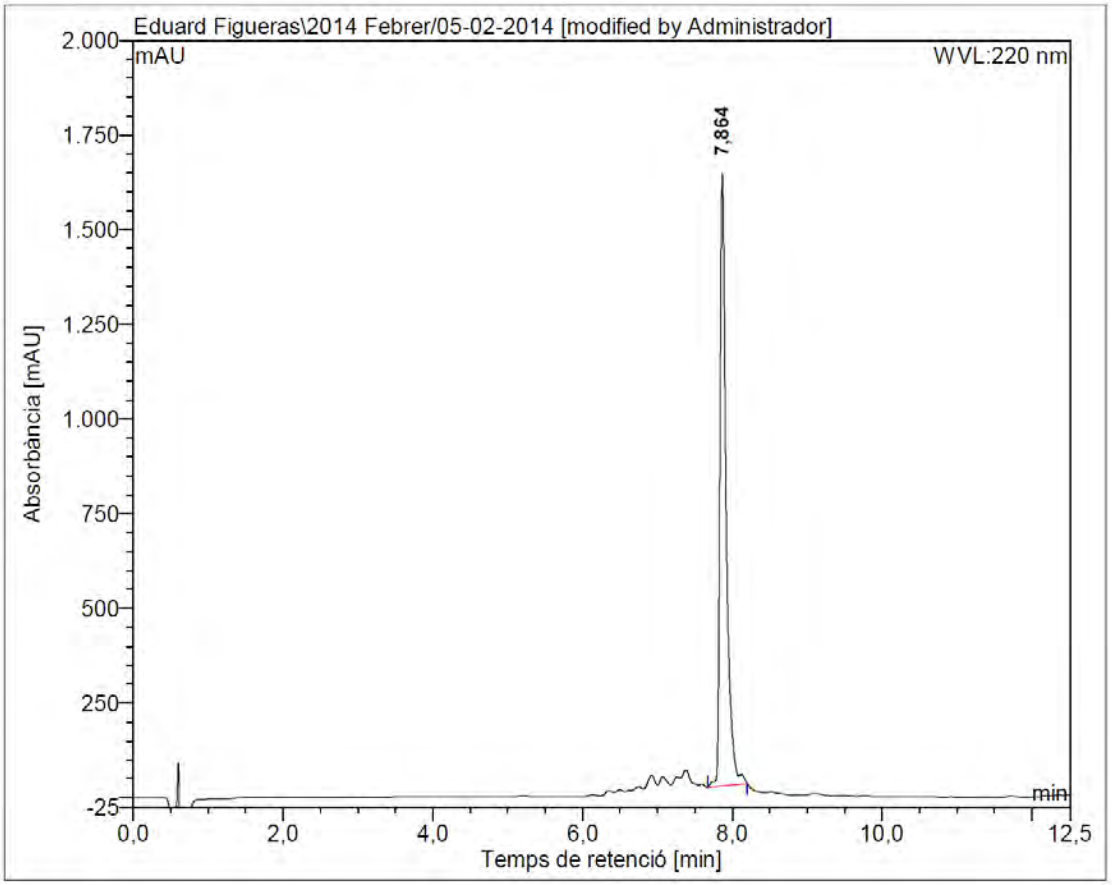

No.	Temps retenció min	alçada mAU	Area mAU*min	Area relativa %
1	7,86	1616,497	156,827	100,00
Total:		1616,497	156,827	100,00

b)

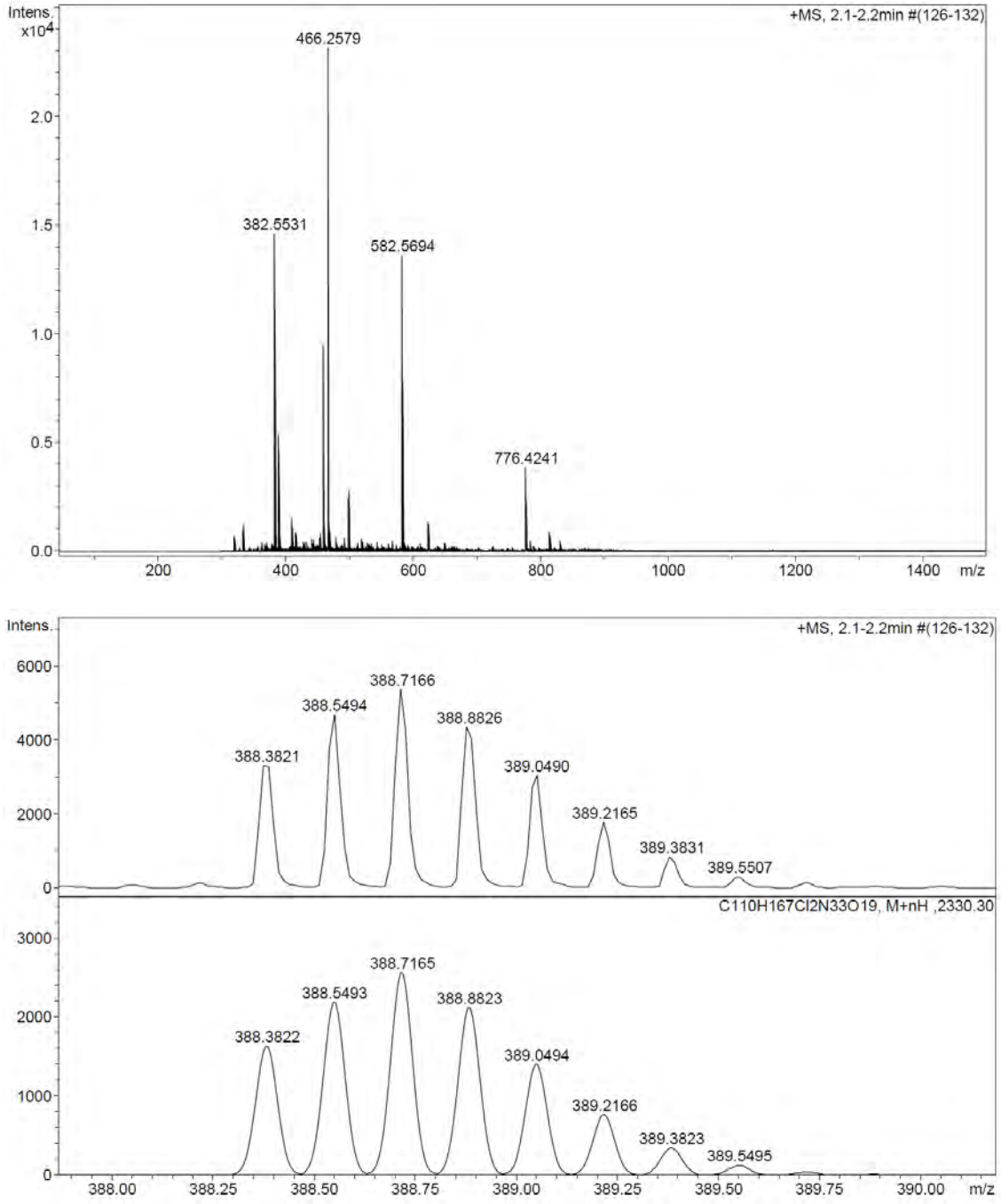

Observed HRMS (top) with the theoretical isotope prediction (bottom).

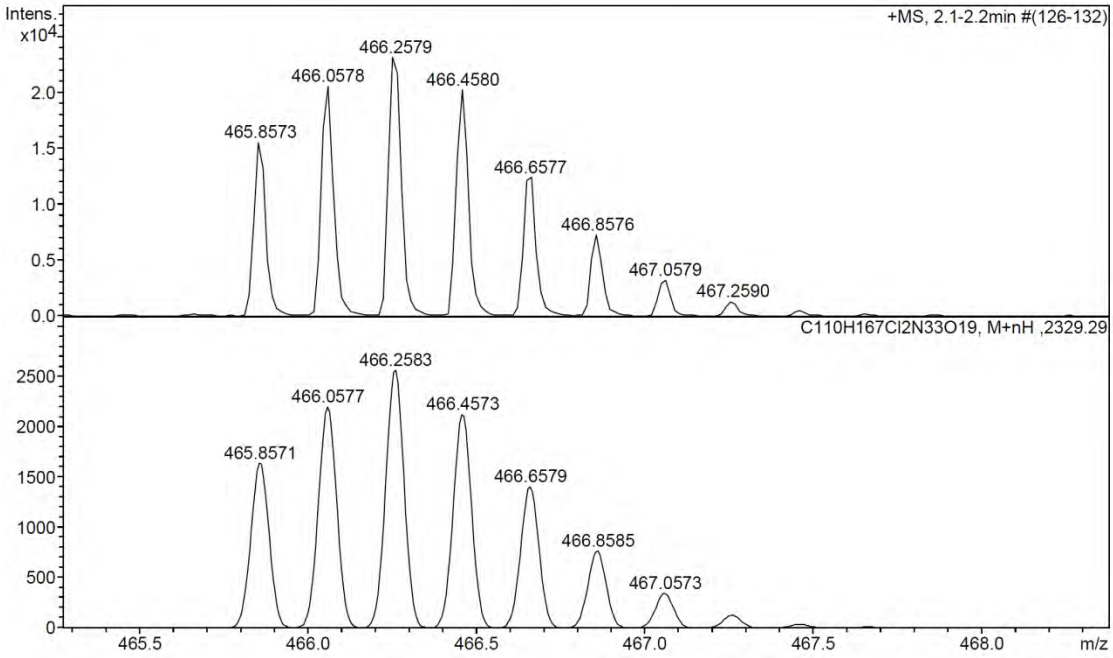

Observed HRMS (top) with the theoretical isotope prediction (bottom).

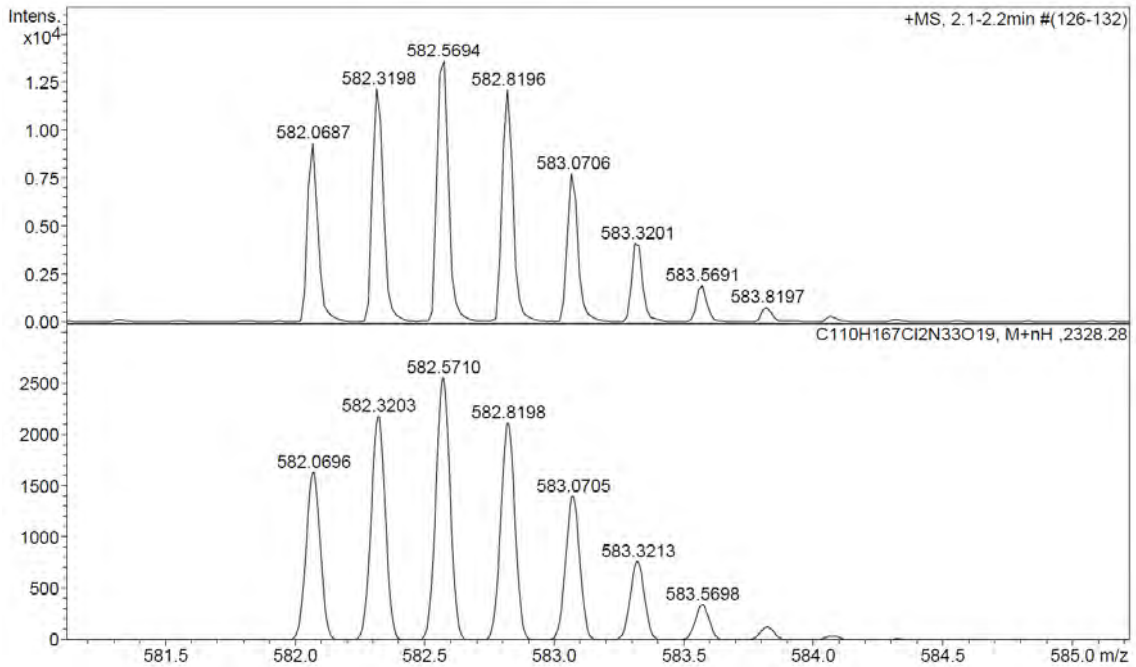

Observed HRMS (top) with the theoretical isotope prediction (bottom).

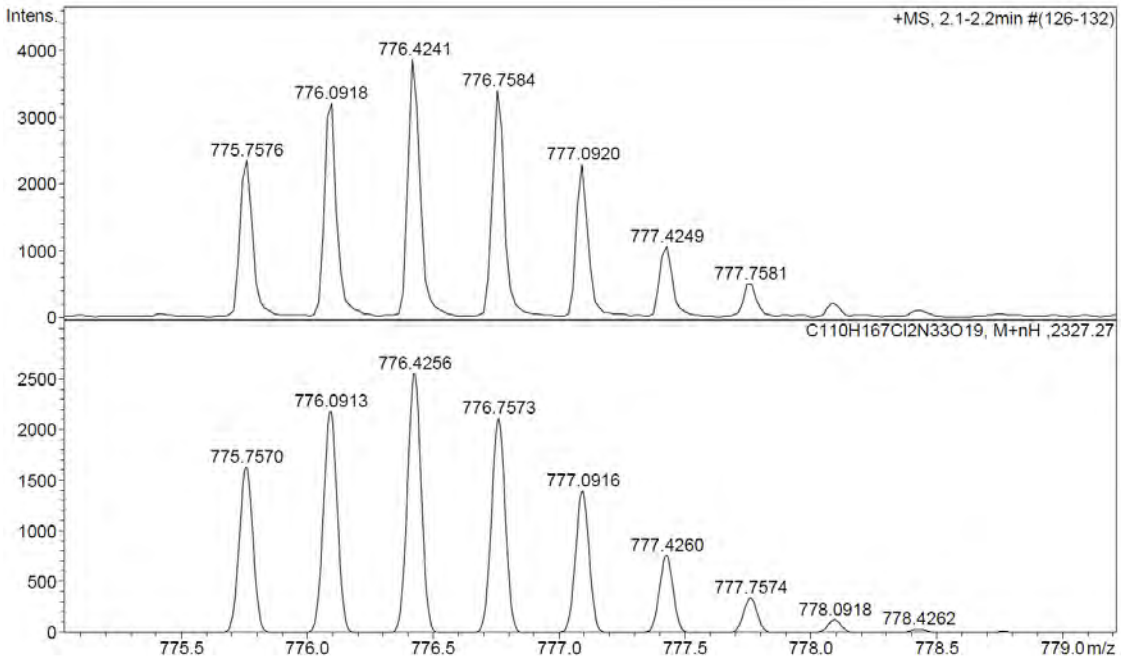

Observed HRMS (top) with the theoretical isotope prediction (bottom).

Figure SIV.16: a) HPLC chromatogram (λ= 220 nm), b) HRMS spectrum (*m/z*).

BP340

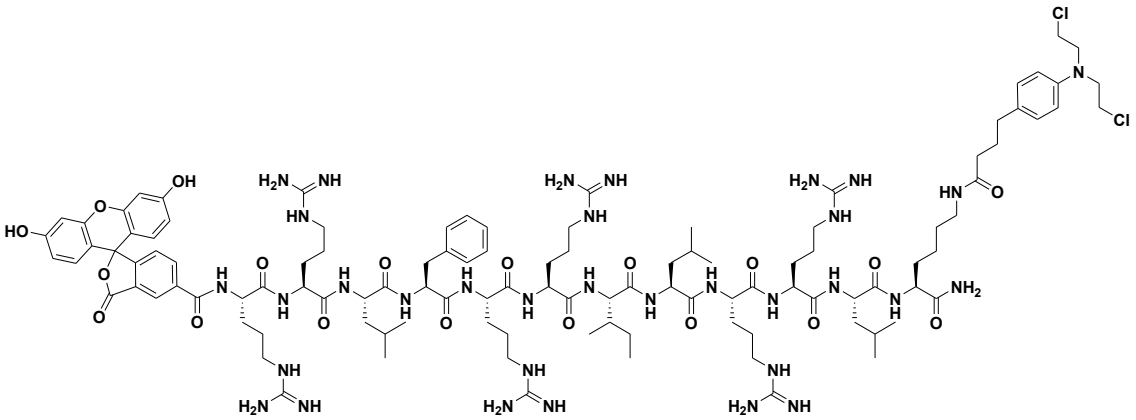

a)

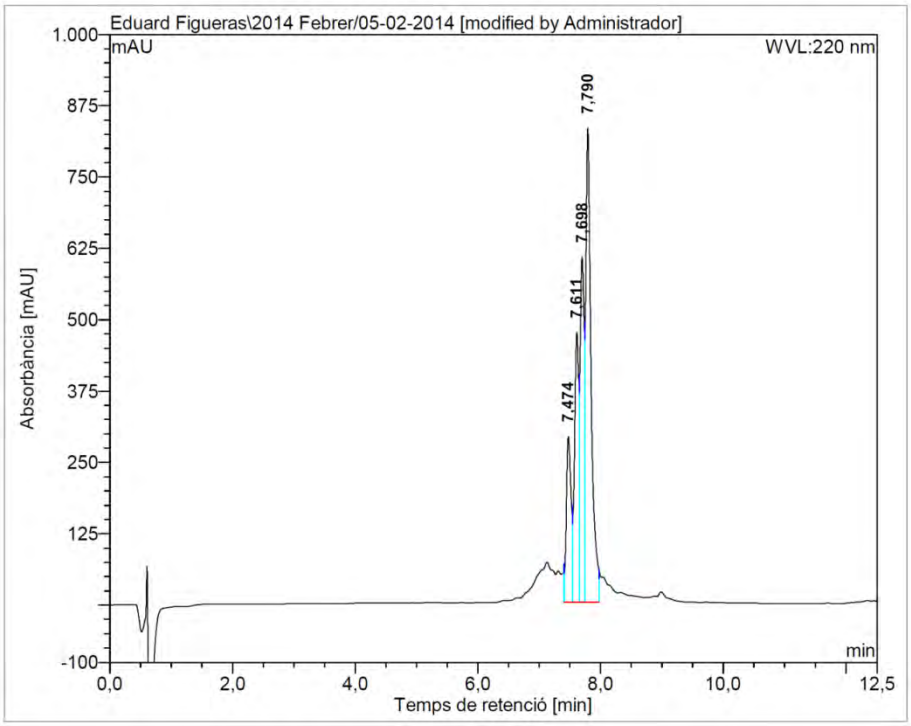

No.	Temps retenció min	alçada mAU	Area mAU*min	Area relativa %
1	7,47	290,082	25,776	13,11
2	7,61	472,827	37,592	19,13
3	7,70	604,560	47,196	24,01
4	7,79	830,108	85,978	43,75
Total:		2197,577	196,541	100,00

b)

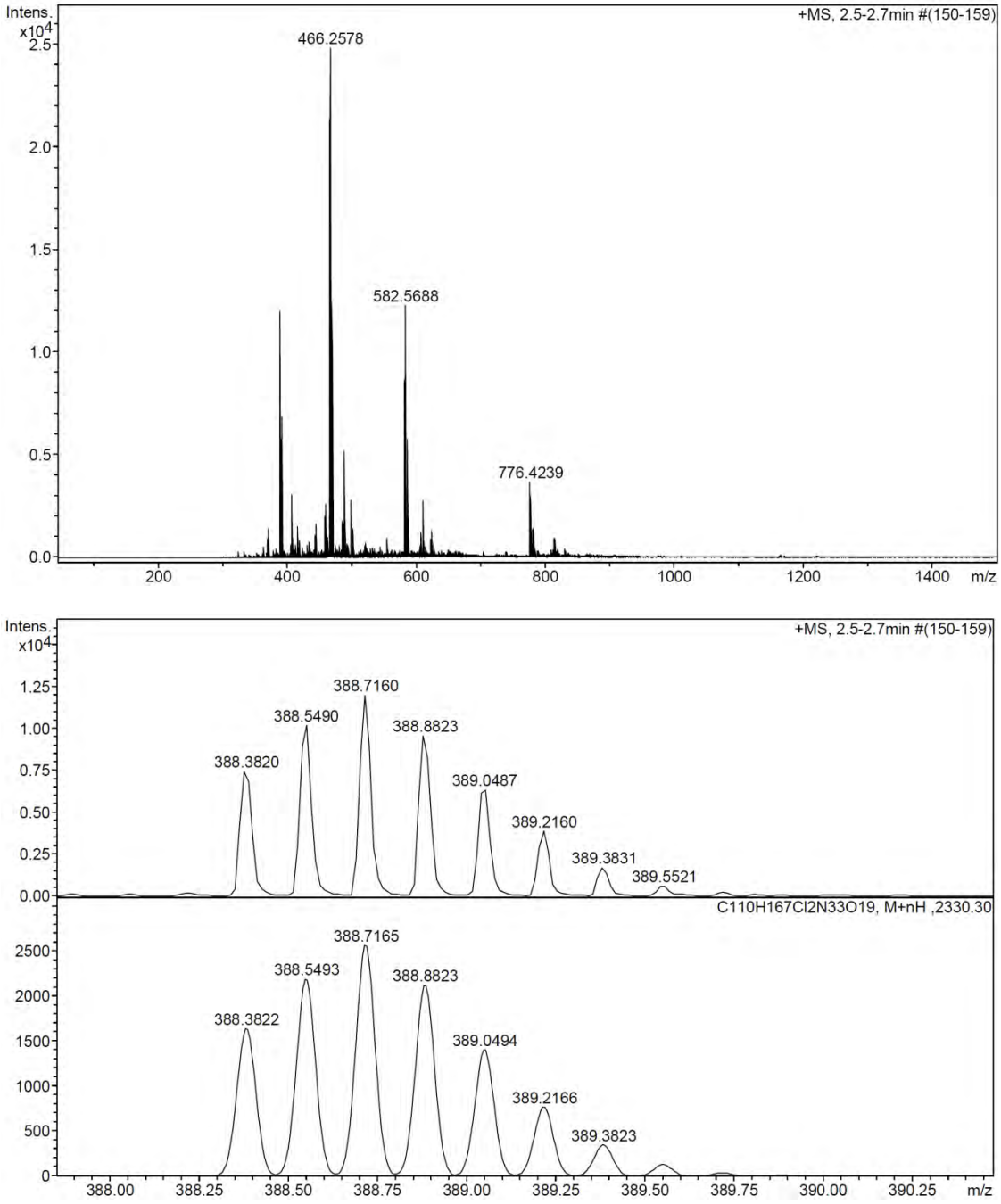

Observed HRMS (top) with the theoretical isotope prediction (bottom).

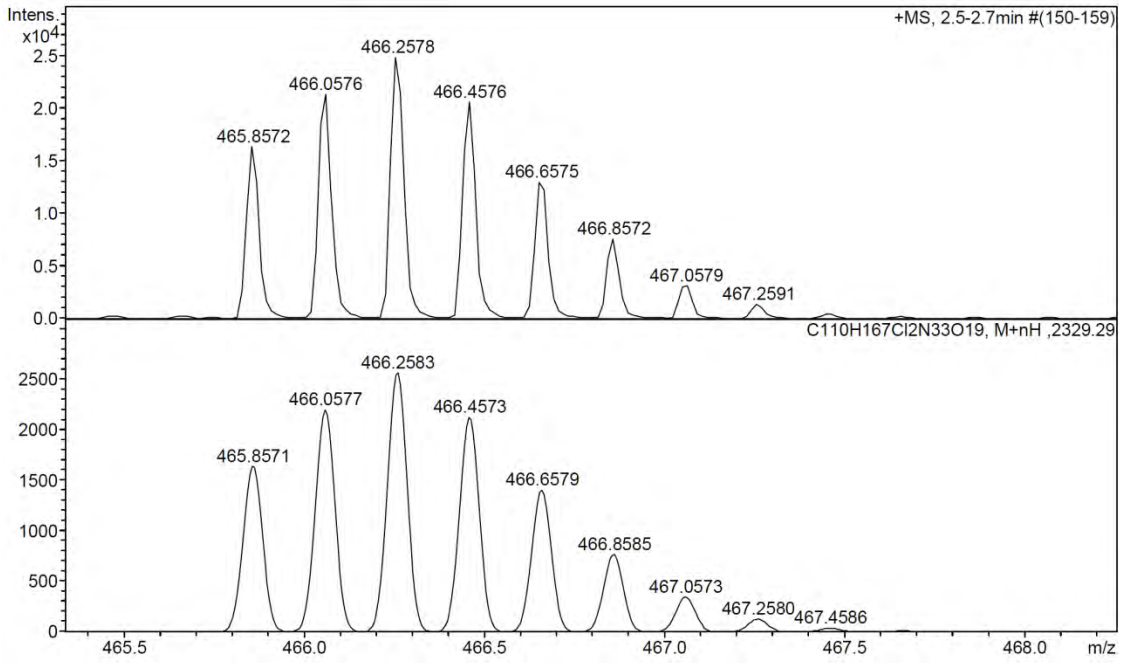

Observed HRMS (top) with the theoretical isotope prediction (bottom).

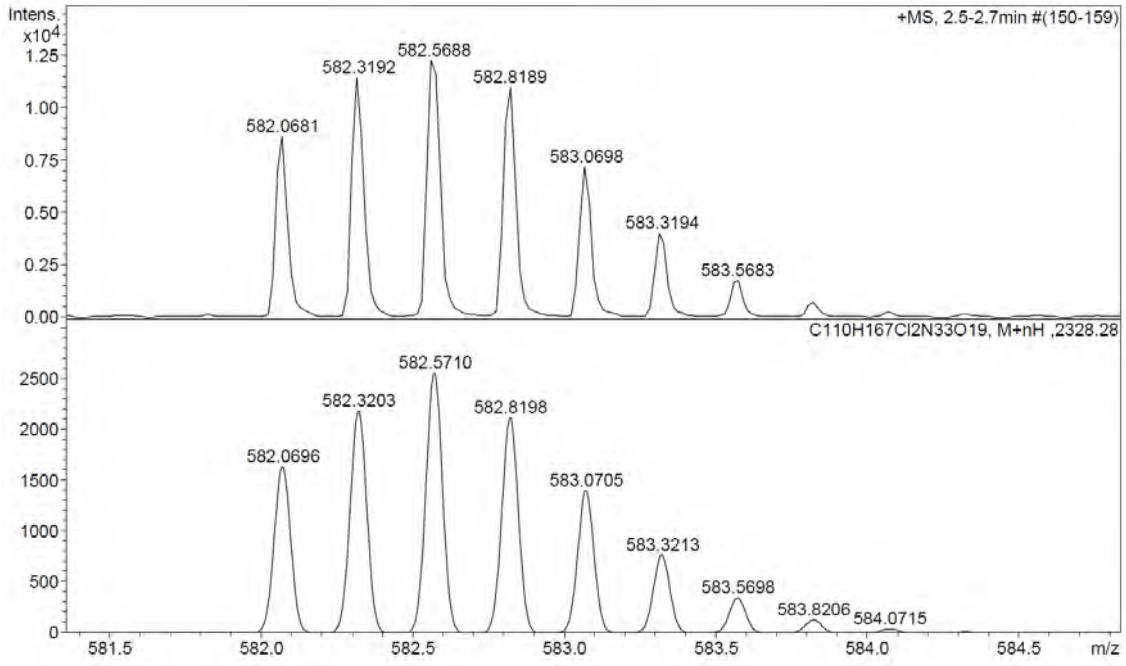

Observed HRMS (top) with the theoretical isotope prediction (bottom).

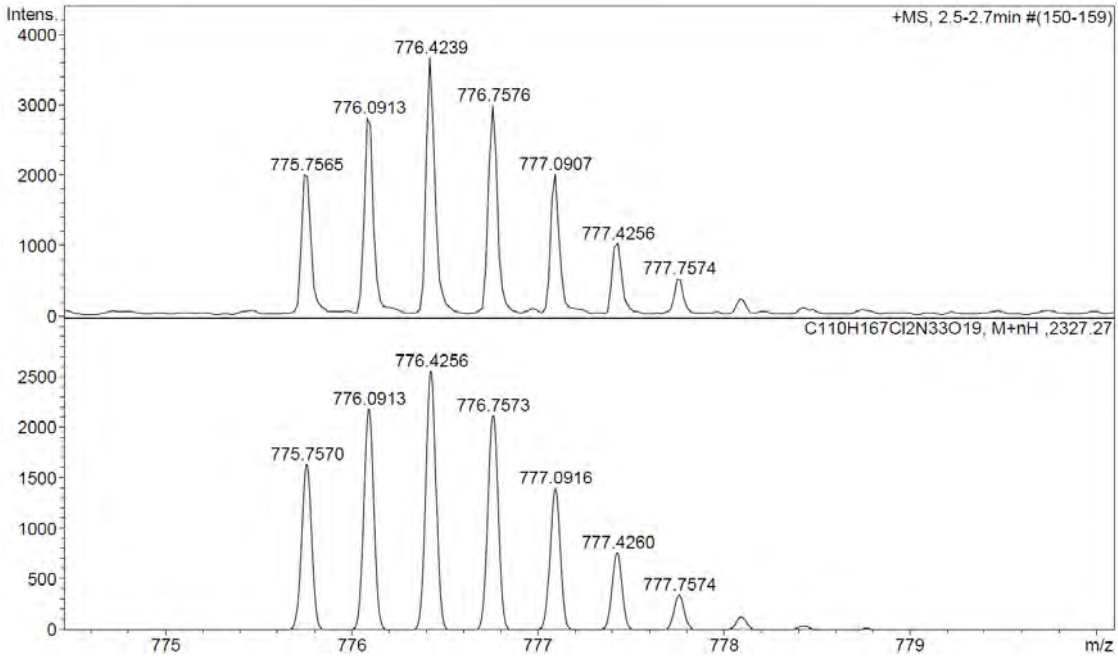

Observed HRMS (top) with the theoretical isotope prediction (bottom).

Supporting Information

Chapter V: Enhanced and selective DNA cleavage activity of redox-active metallopeptides based on tetradentate aminopyridine ligands

Table of contents

Figure SV.1: a) ^{1}H NMR spectrum (400 MHz, $CDCl_3$), b) ^{13}C NMR spectrum (100 MHz, $CDCl_3$), c) ESI/MS spectrum (*m/z*)

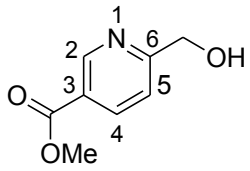

9

a)

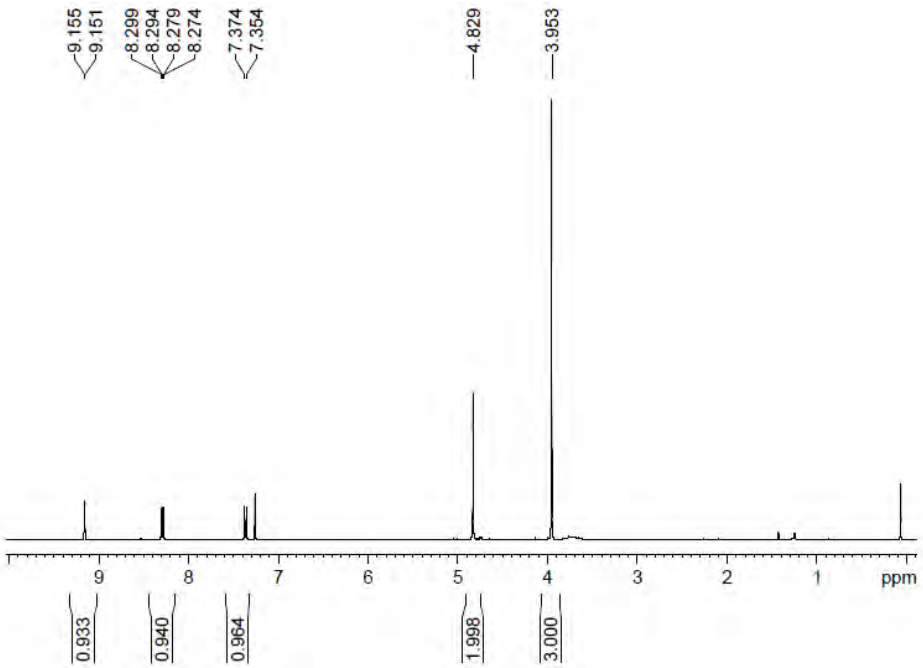

b)

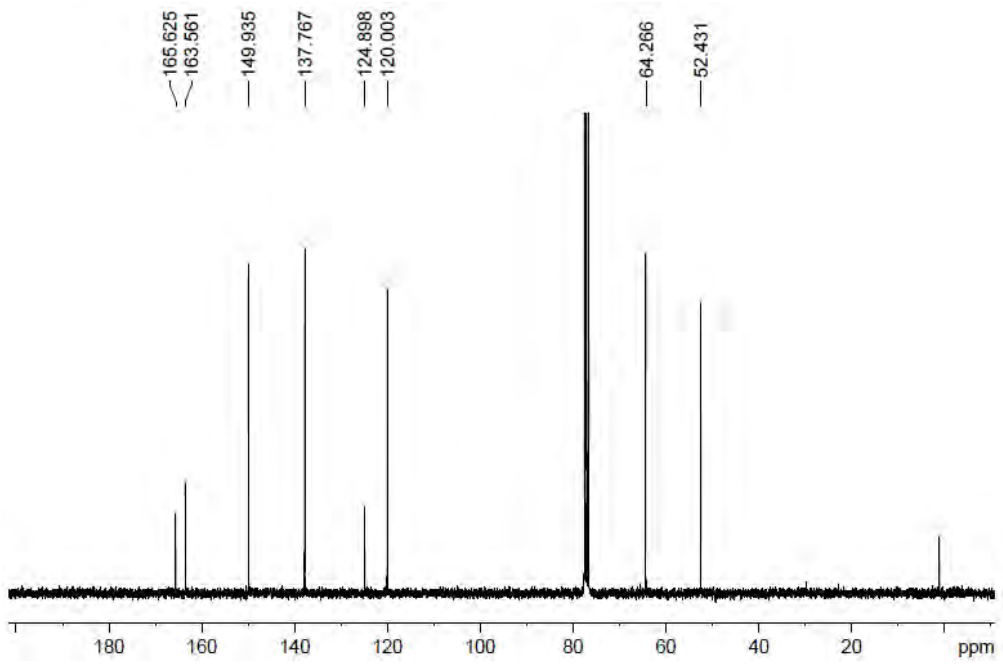
165.625
163.561
149.935
137.767
124.898
120.003
64.266
52.431
180
160
140
120
100
80
60
40
20
ppm

c)

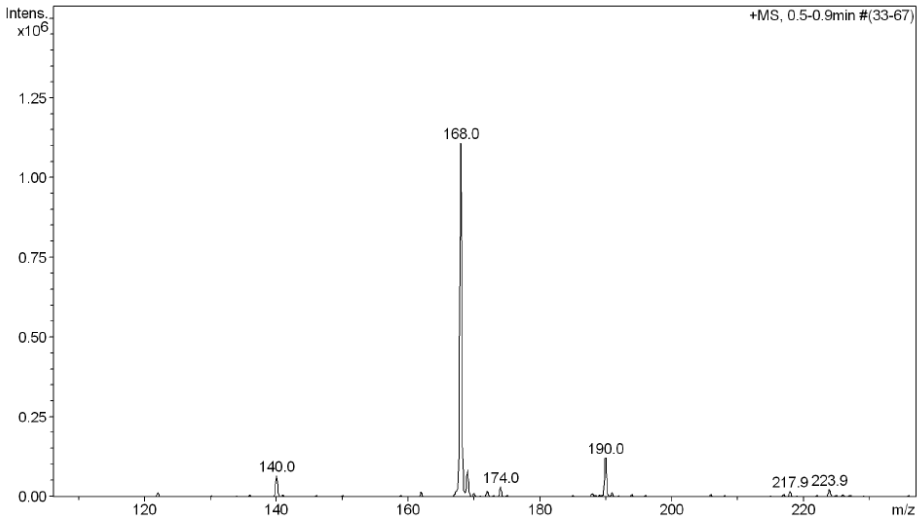
Intens.
x10^6
+MS, 0.5-0.9min #(33-67)
1.25
1.00
0.75
0.50
0.25
0.00
168.0
140.0
174.0
190.0
217.9
223.9
120
140
160
180
200
220
m/z

Figure SV.2: a) ^{1}H NMR spectrum (400 MHz, $CDCl_3$), b) ^{13}C NMR spectrum (100 MHz, $CDCl_3$), c) ESI/MS spectrum (*m/z*)

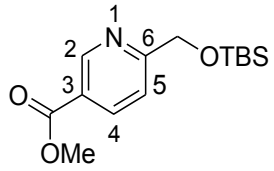

a)

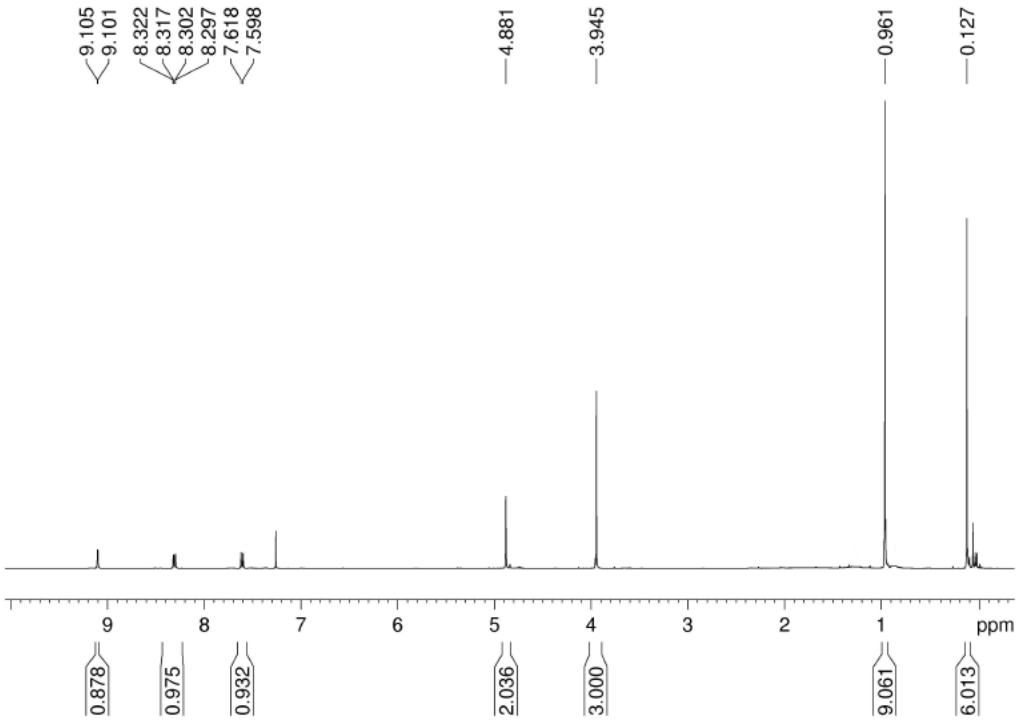

b)

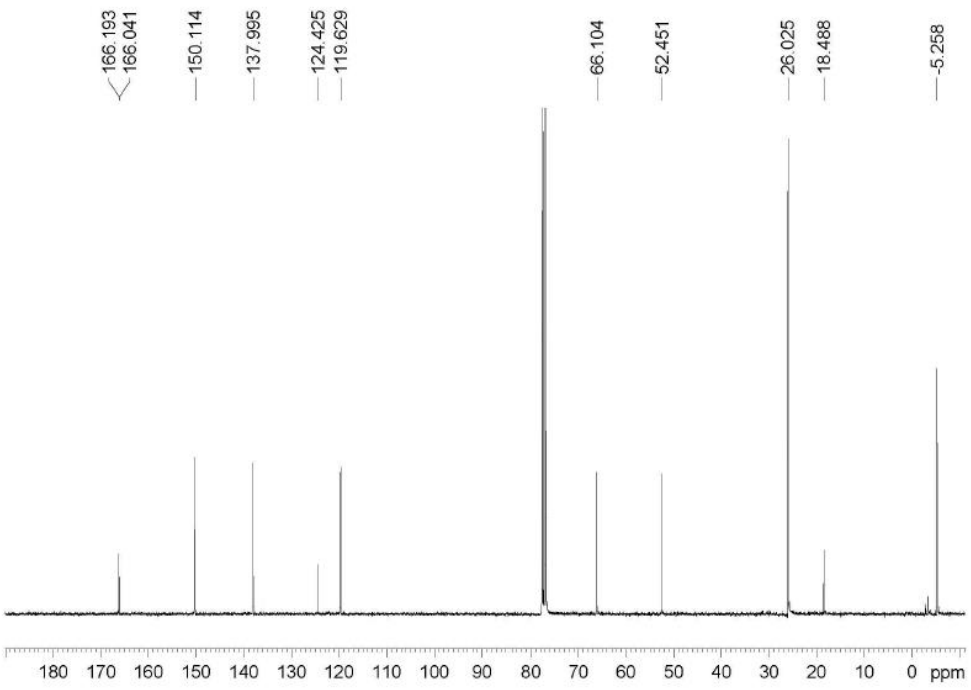
166.193
166.041
150.114
137.995
124.425
119.629
66.104
52.451
26.025
18.488
-5.258
180 170 160 150 140 130 120 110 100 90 80 70 60 50 40 30 20 10 0 ppm

c)

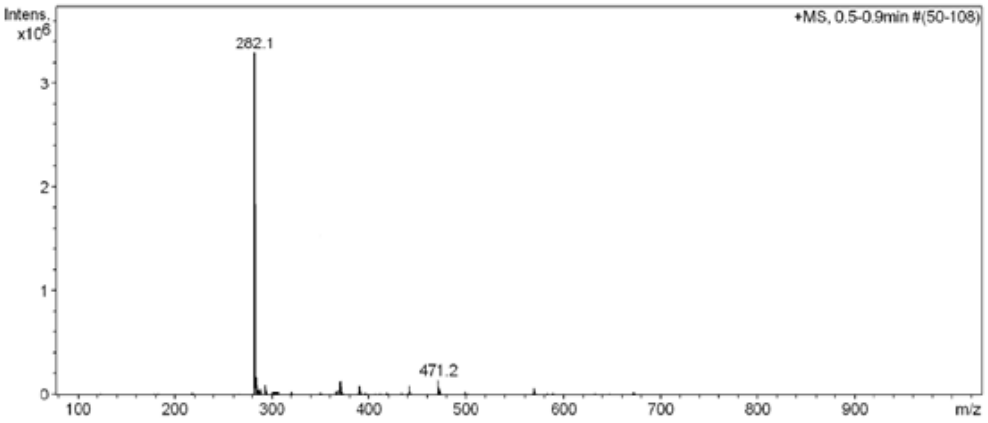
Intens.
x10^6
+MS, 0.5-0.9min #(50-108)
282.1
471.2
0
1
2
3
100 200 300 400 500 600 700 800 900 m/z

Figure SV.3: a) ^{1}H NMR spectrum (400 MHz, $[D_6]$DMSO), b) ESI/MS spectrum (*m/z*)

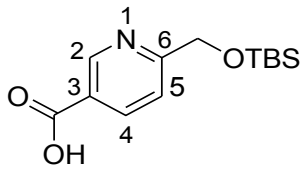

5

a)

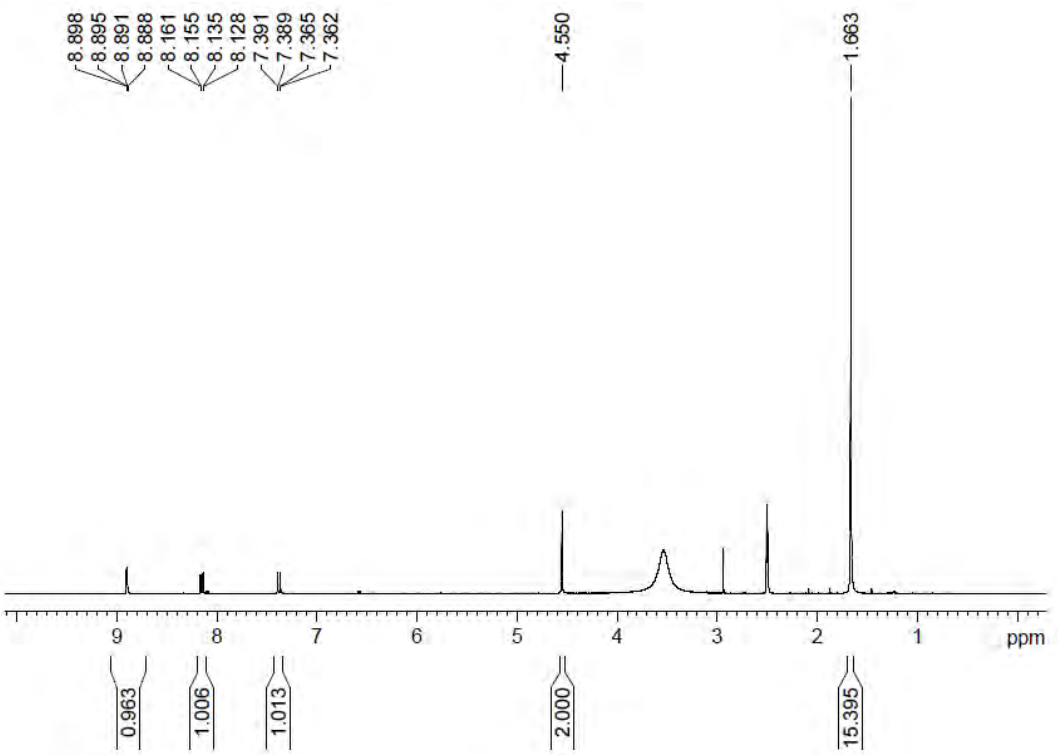

b)

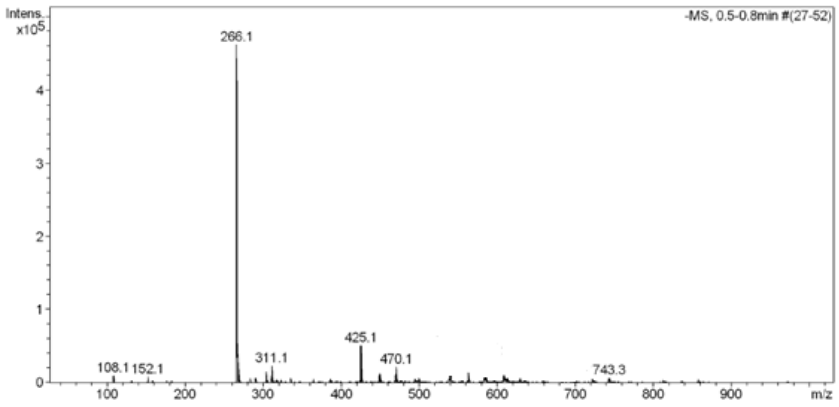

Figure SV.4: a) ^{1}H NMR spectrum (400 MHz, $CDCl_3$), b) ^{13}C NMR spectrum (100 MHz, $CDCl_3$), c) ESI/MS spectrum (*m/z*), d) HRMS spectrum (*m/z*)

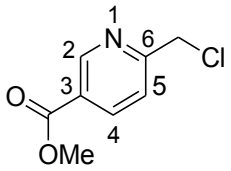

a)

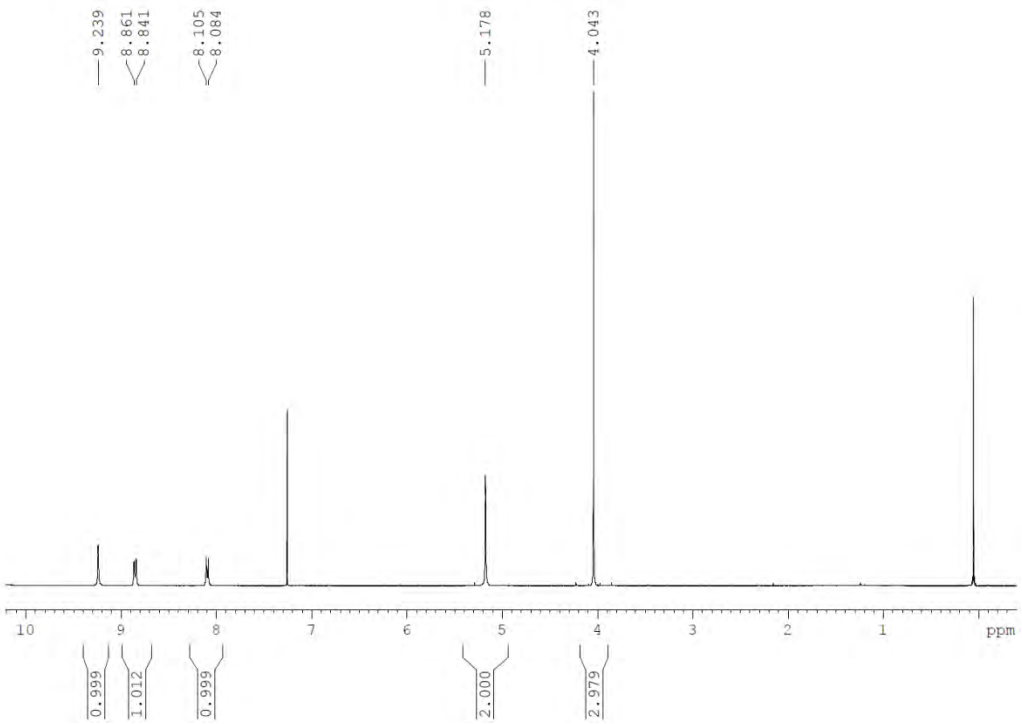

b)

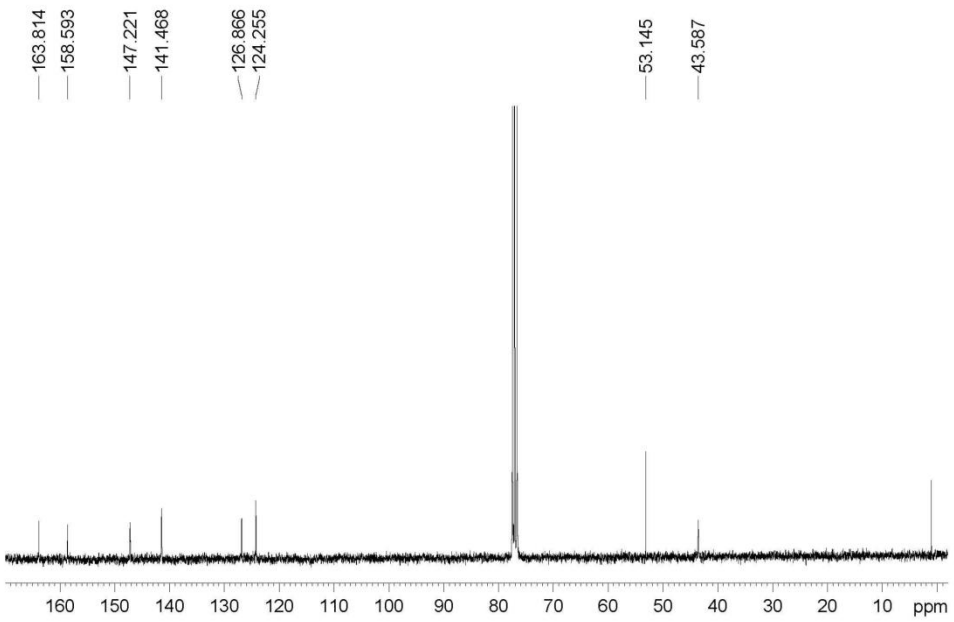

c)

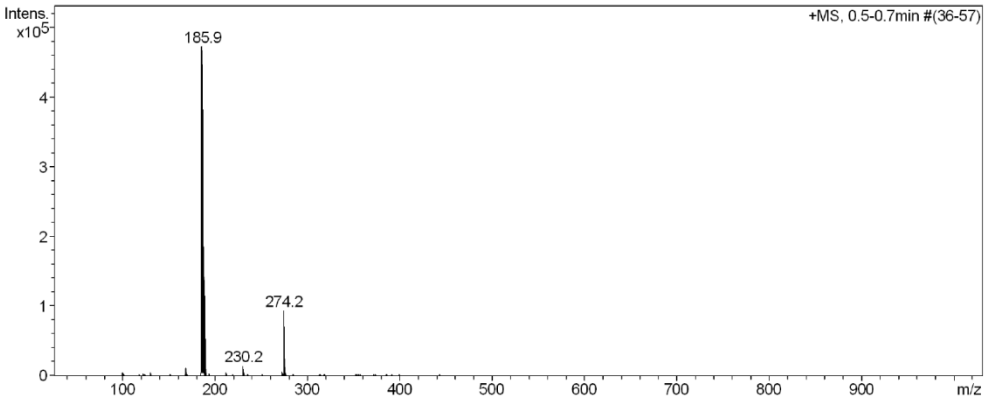

d)

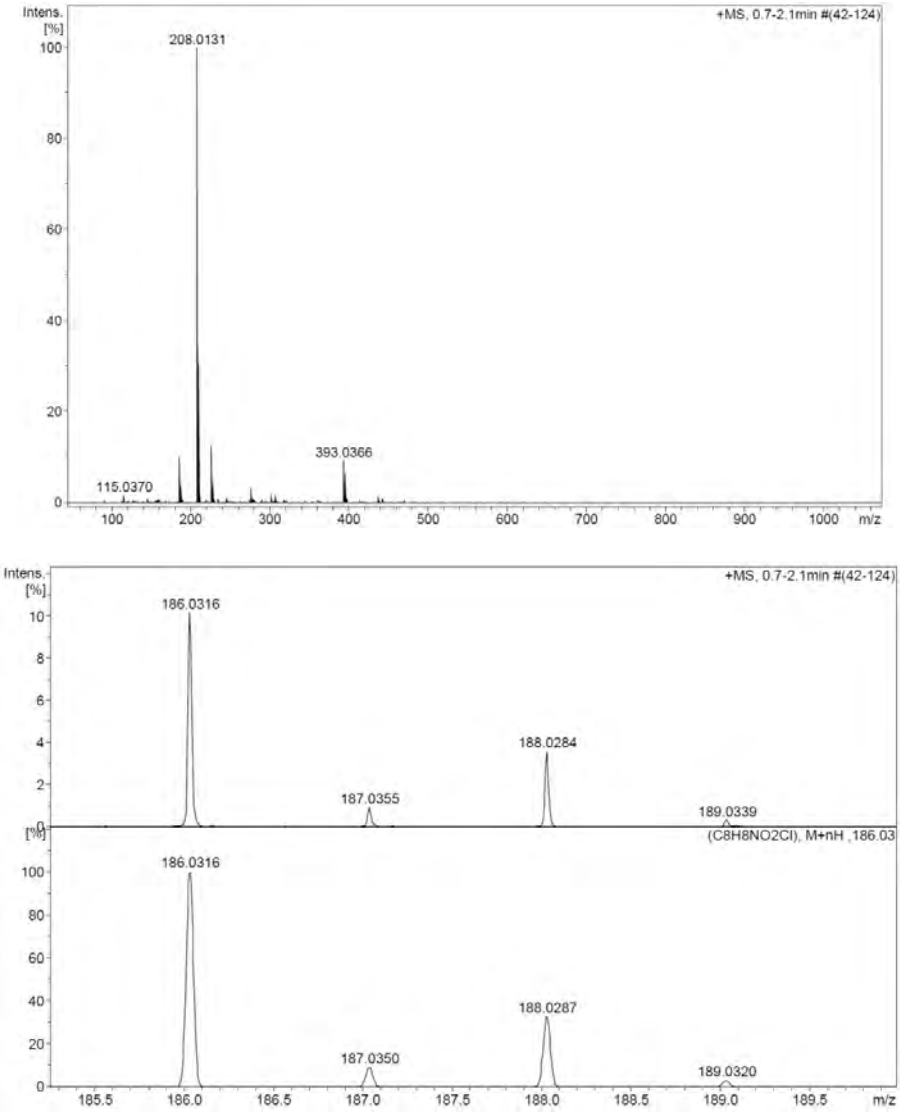

Observed HRMS (top) with the theoretical isotope prediction (bottom).

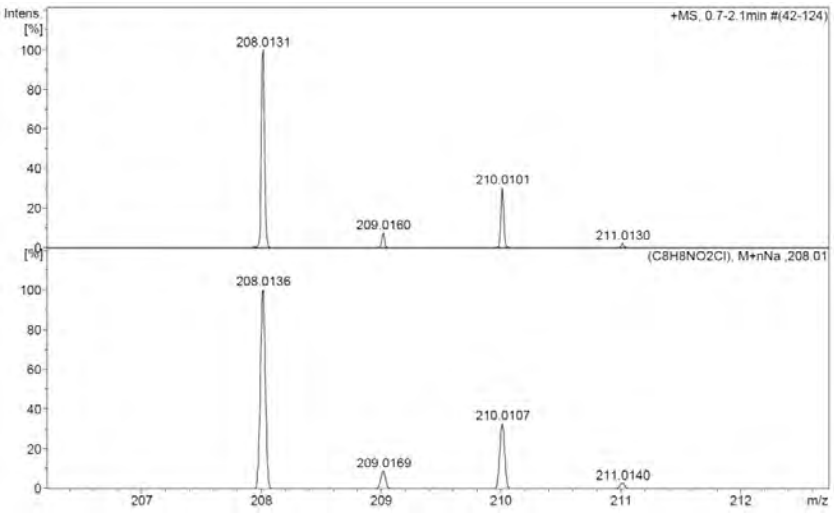

Observed HRMS (top) with the theoretical isotope prediction (bottom).

Figure SV.5: a) ^{1}H NMR spectrum (400 MHz, $CDCl_3$), b) ^{13}C NMR spectrum (100 MHz, $CDCl_3$), c) COSY spectrum (400 MHz, $CDCl_3$), d) HMBC (400 MHz, $CDCl_3$), e) HSQC (400 MHz, $CDCl_3$), f) ESI/MS spectrum (*m/z*), g) HRMS spectrum (*m/z*)

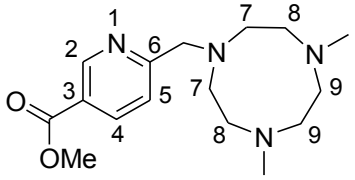

a)

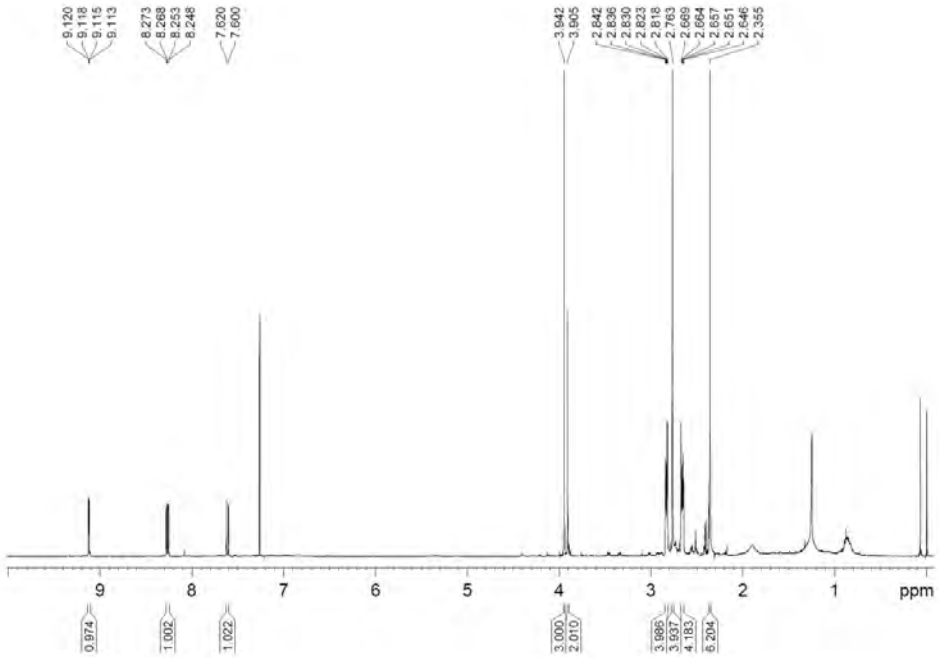

b)

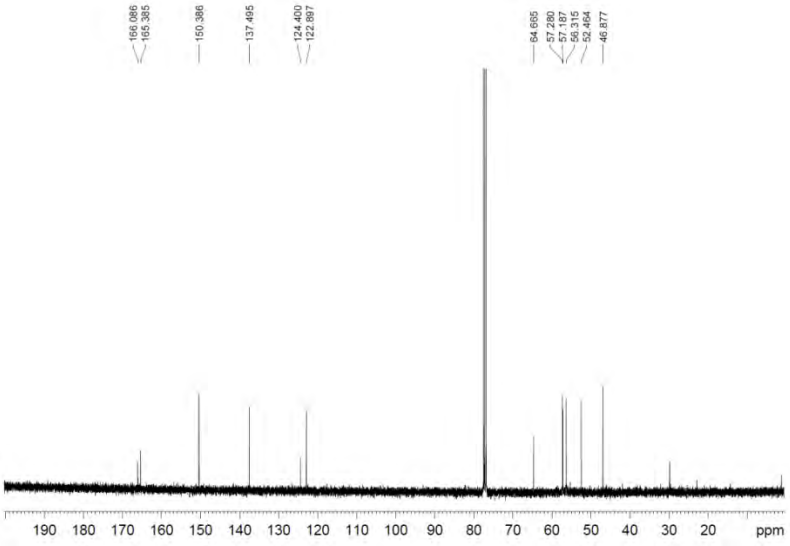

c)

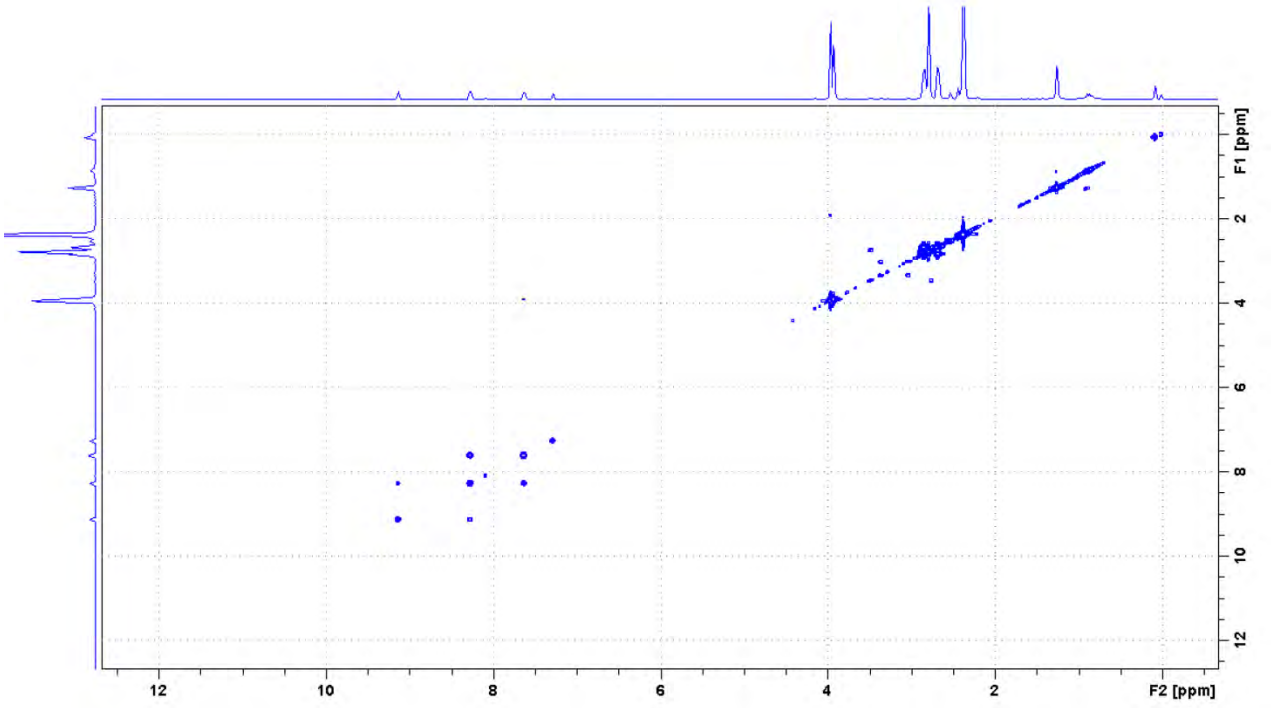
F1 [ppm]
2
4
6
8
10
12
12
10
8
6
4
2
F2 [ppm]

d)

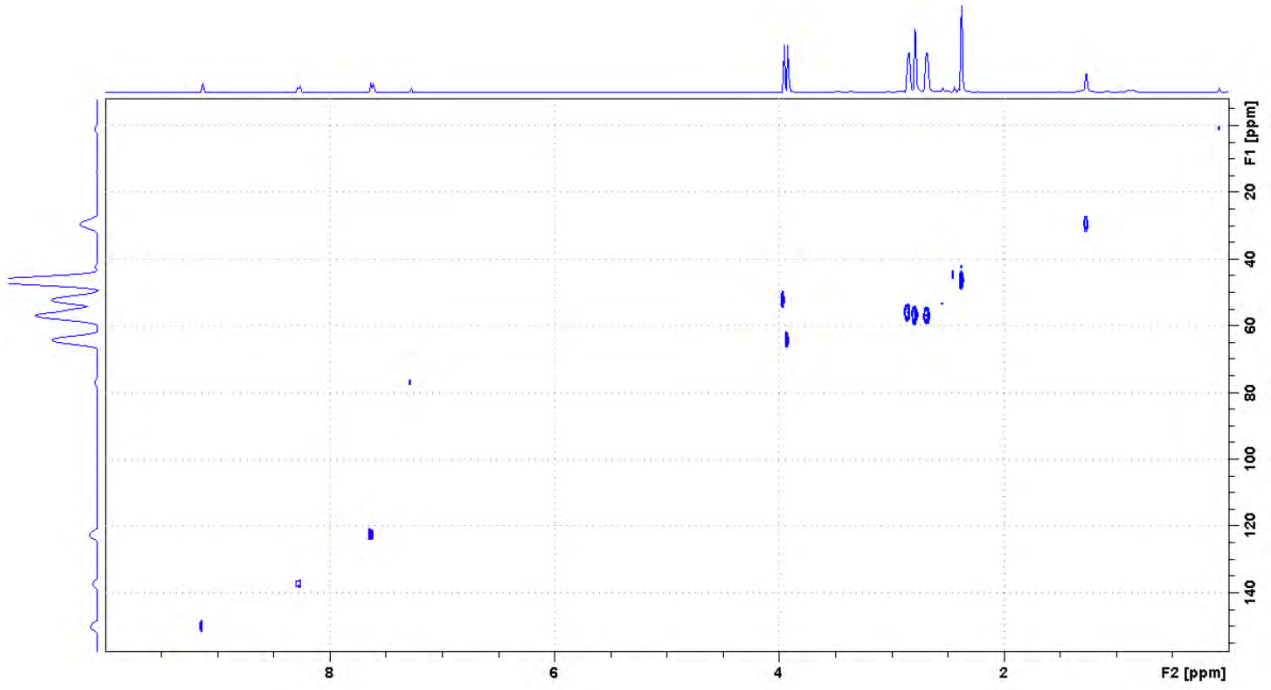
F1 [ppm]
20
40
60
80
100
120
140
8
6
4
2
F2 [ppm]

e)

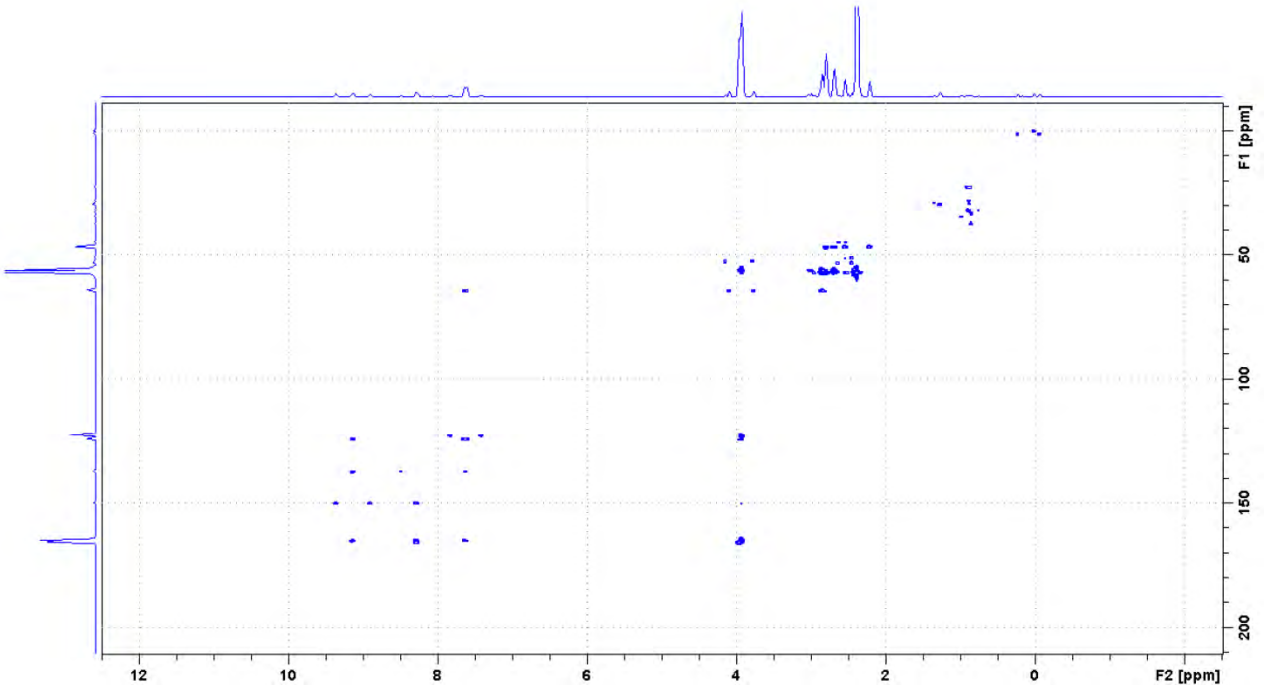
F1 [ppm]
50
100
150
200
12
10
8
6
4
2
0
F2 [ppm]

f)

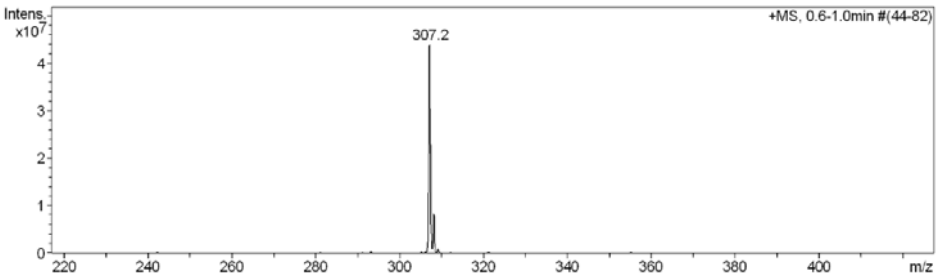
Intens.
x10^7
+MS, 0.6-1.0min #(44-82)
307.2
4
3
2
1
0
220
240
260
280
300
320
340
360
380
400
m/z

g)

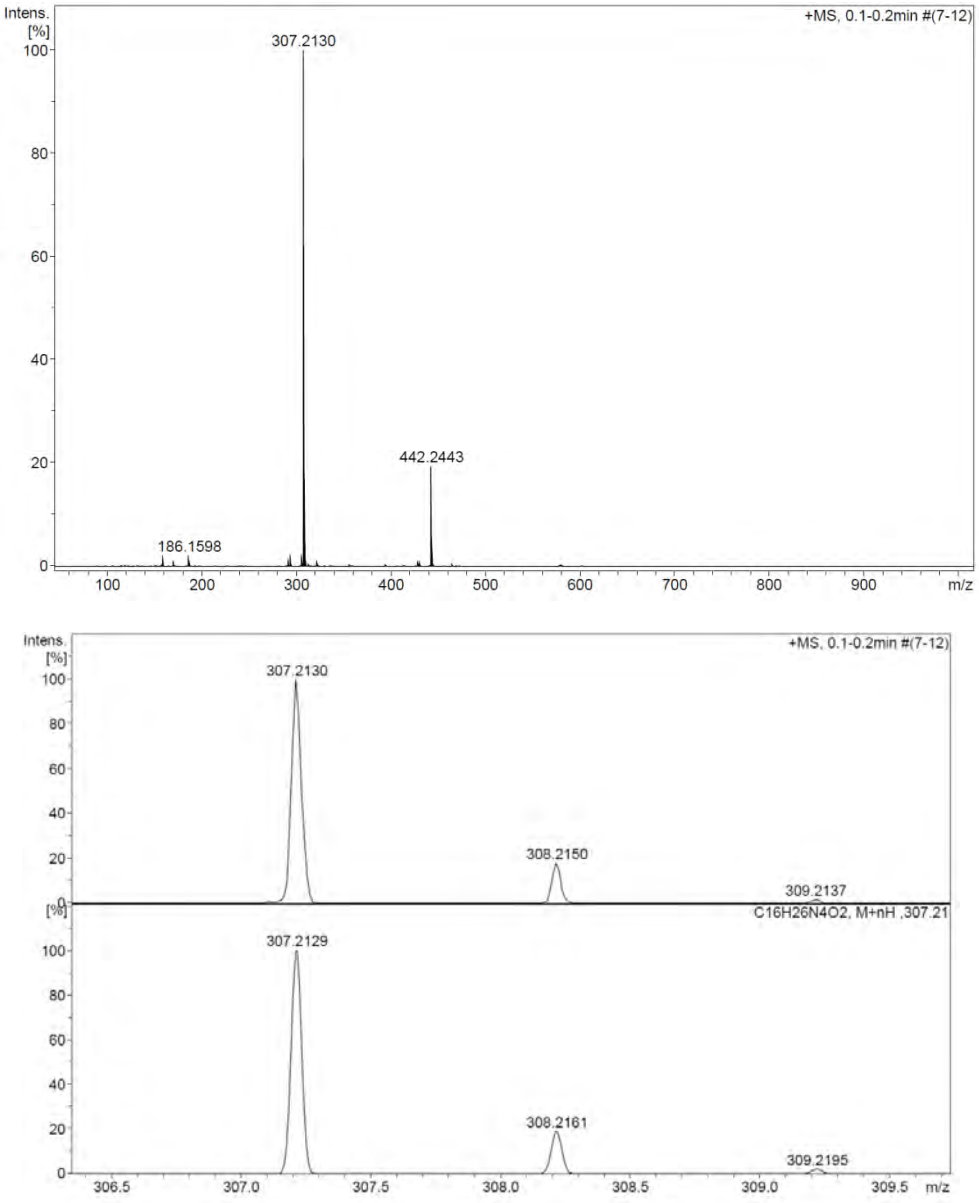

Observed HRMS (top) with the theoretical isotope prediction (bottom).

Figure SV.6: a) ^{1}H NMR spectrum (400 MHz, D_2O) b) ESI/MS spectrum (*m/z*), c) HRMS spectrum (*m/z*)

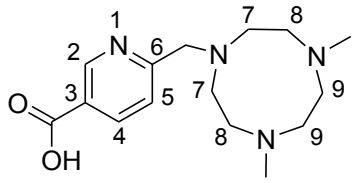

14

a)

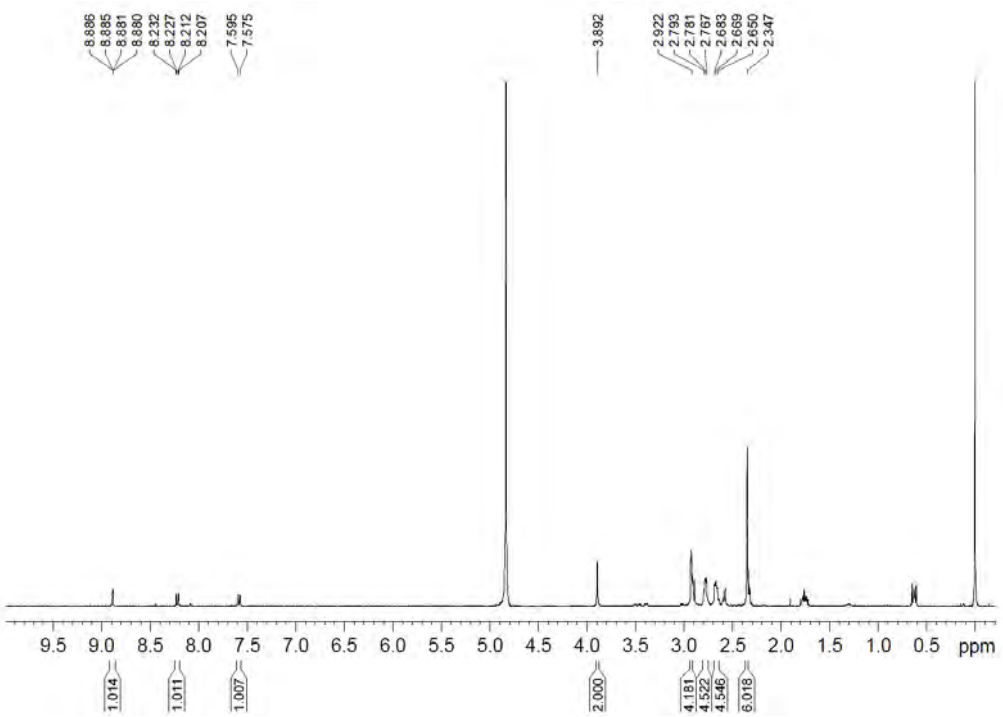

b)

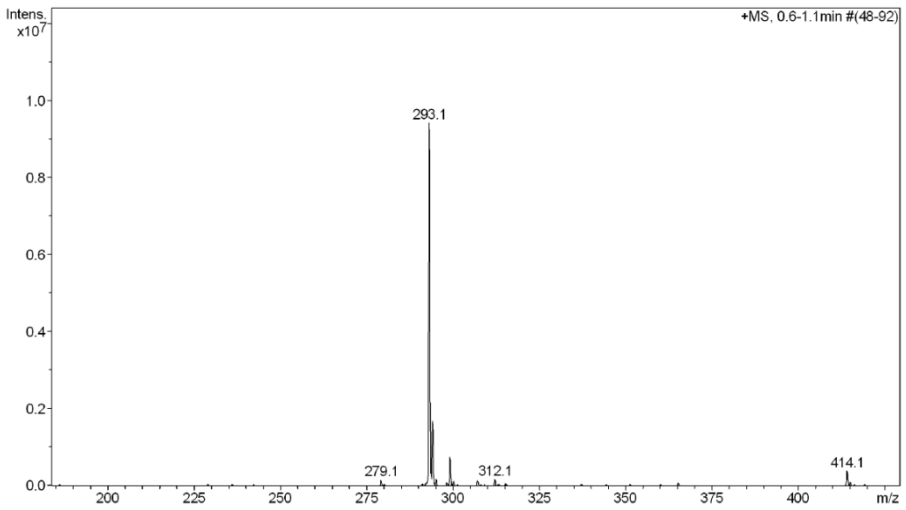

c)

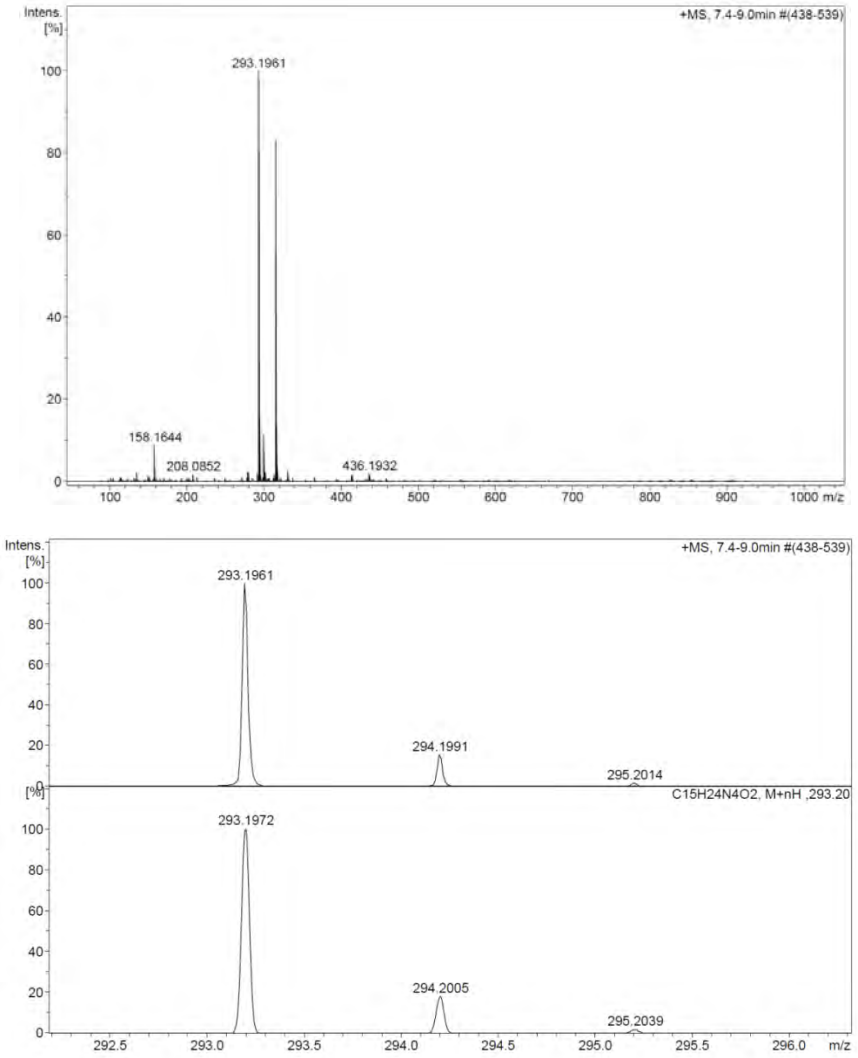

Observed HRMS (top) with the theoretical isotope prediction (bottom).

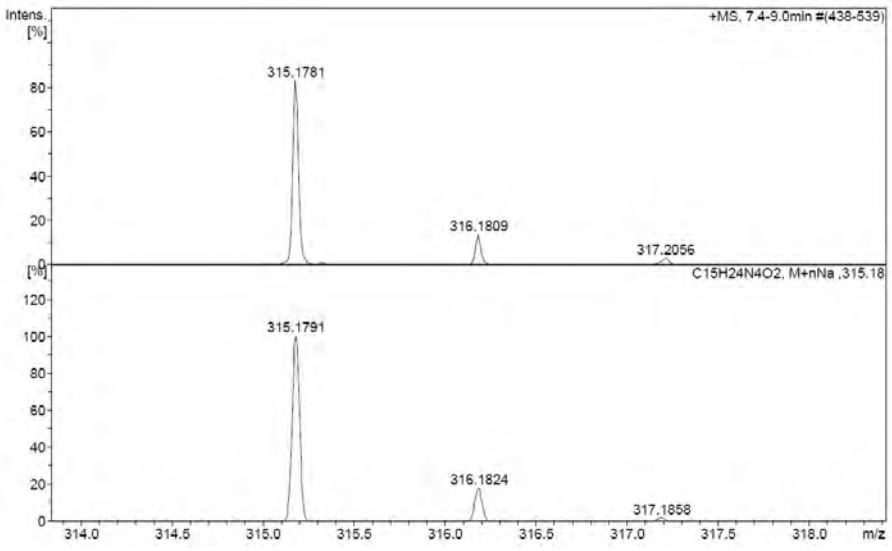

Observed HRMS (top) with the theoretical isotope prediction (bottom).

Figure SV.7: a) ^{1}H NMR spectrum (400 MHz, $CDCl_3$), b) ^{13}C NMR spectrum (100 MHz, $CDCl_3$), c) HSQCed (400 MHz, $CDCl_3$), d) ESI/MS spectrum (*m/z*), e) HRMS spectrum (*m/z*)

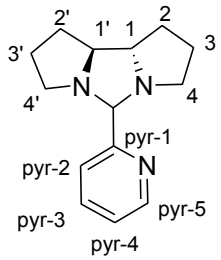

15

a)

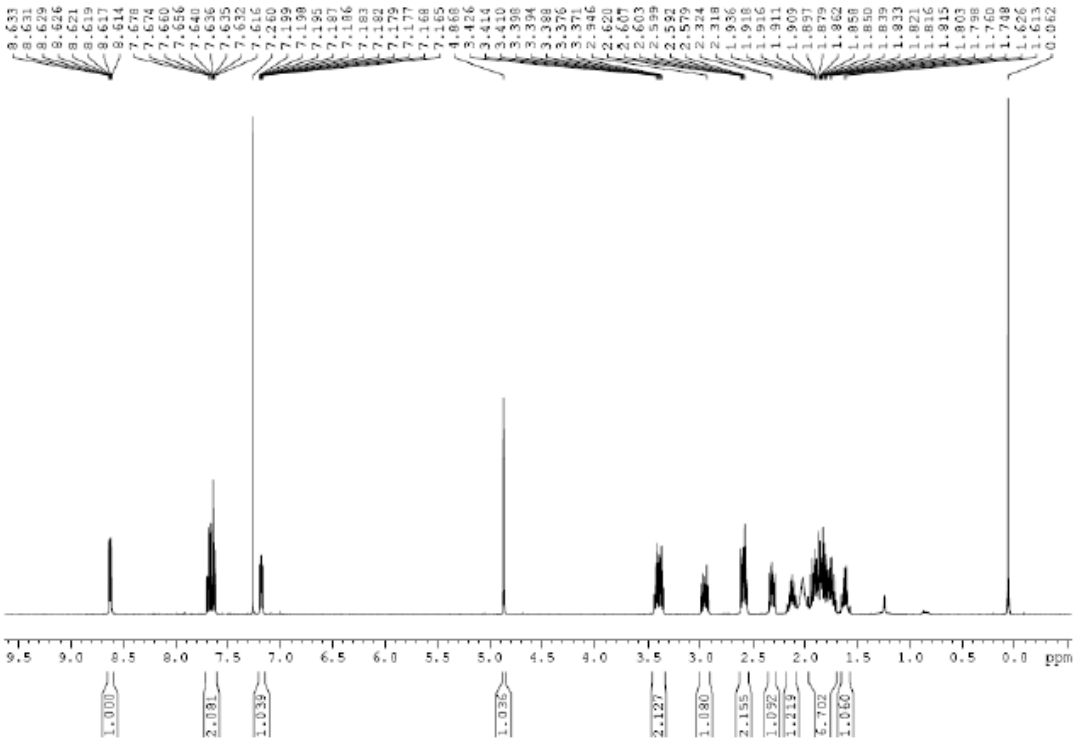

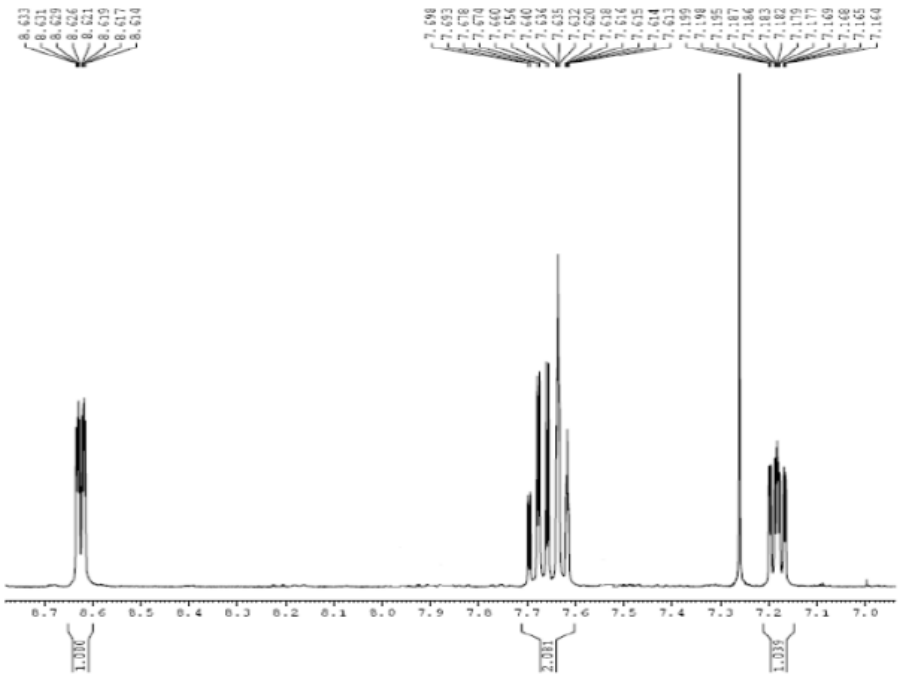

Selected aromatic region.

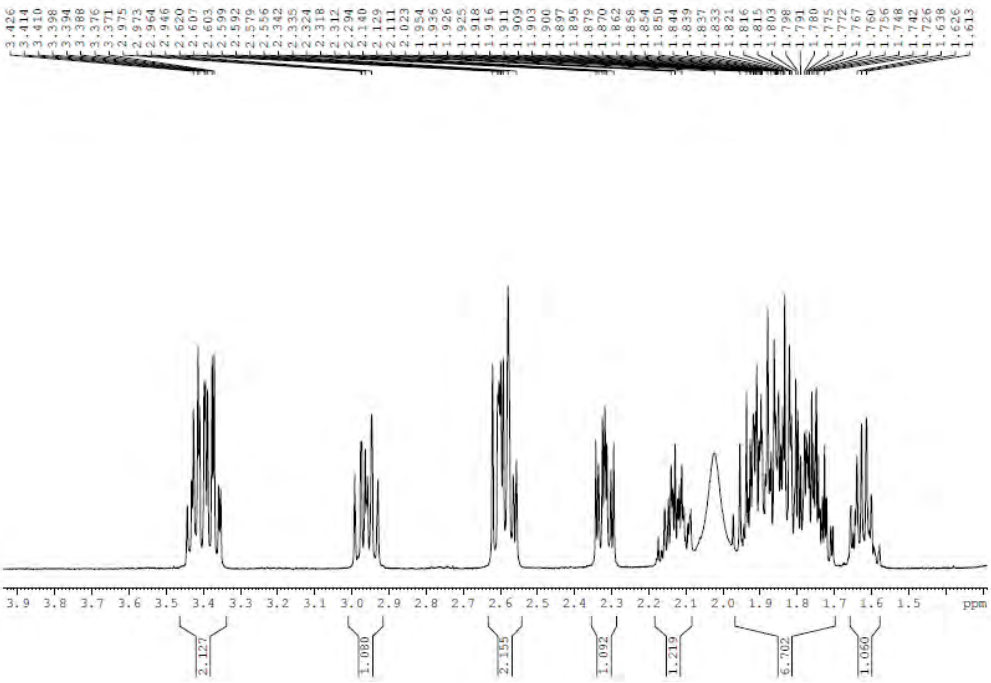

Selected aliphatic region.

b)

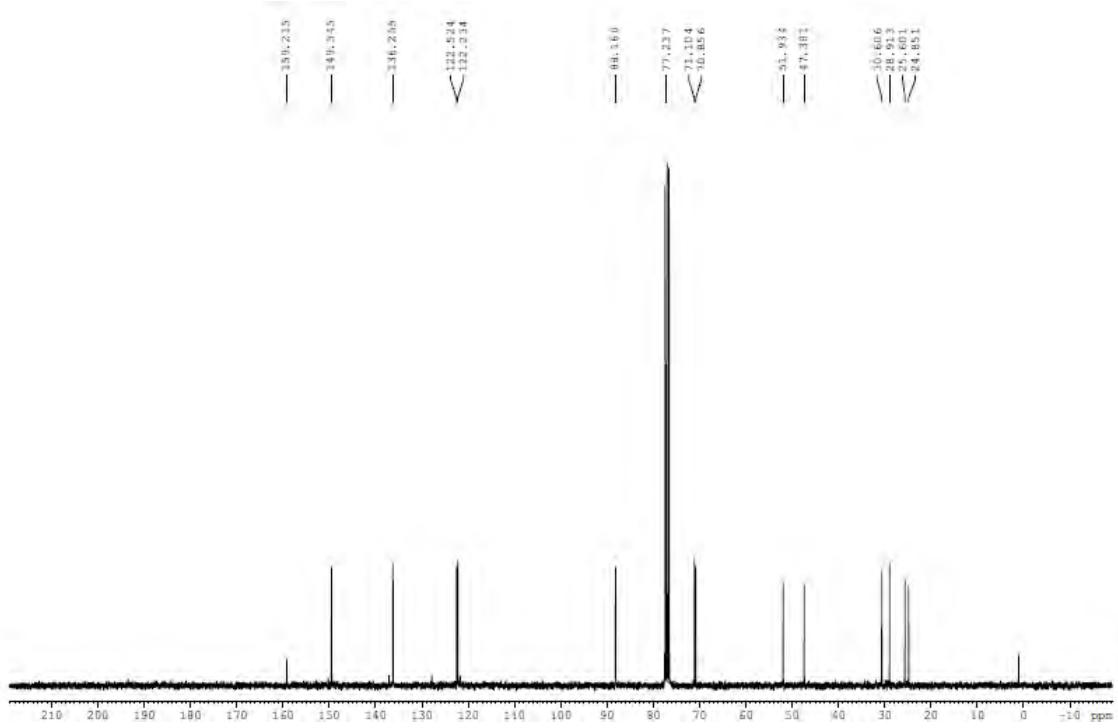
159.235
149.345
136.209
122.524
122.234
84.160
77.237
71.104
70.856
51.938
47.387
30.606
28.913
25.601
24.851
210 200 190 180 170 160 150 140 130 120 110 100 90 80 70 60 50 40 30 20 10 0 -10 ppm

c)

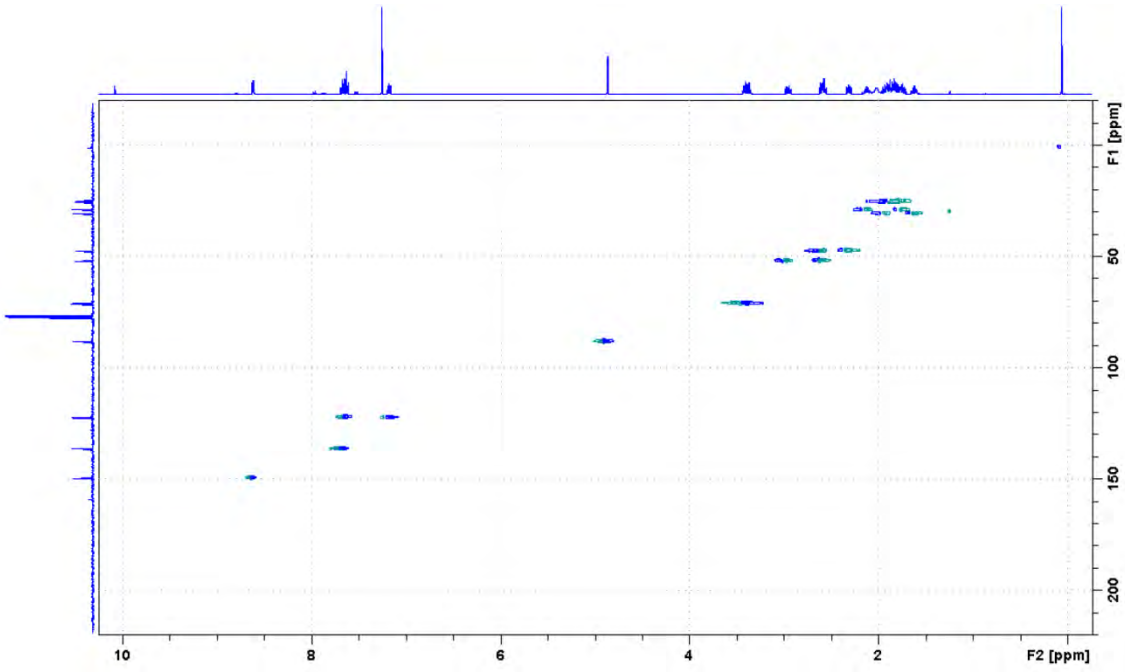
F1 [ppm]
50
100
150
200
10
8
6
4
2
F2 [ppm]

d)

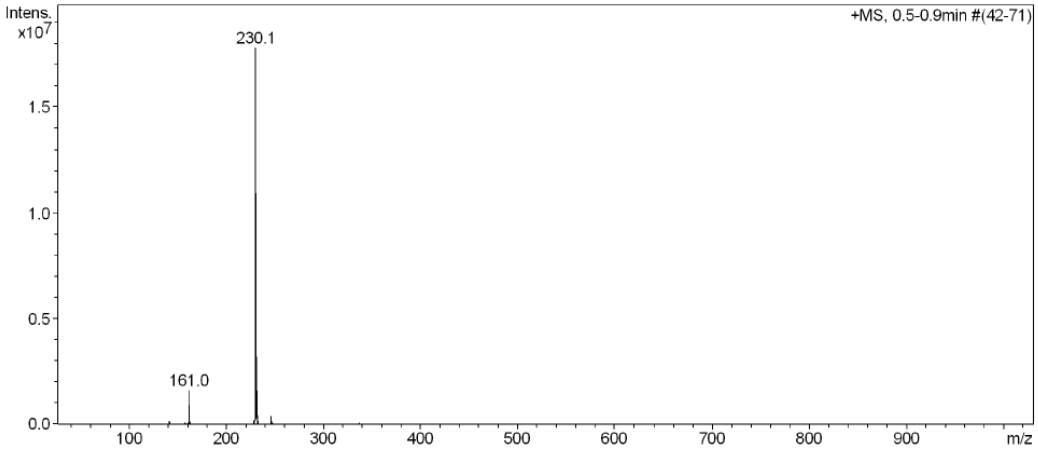
Intens.
x10^7
+MS, 0.5-0.9min #(42-71)
230.1
161.0
m/z

e)

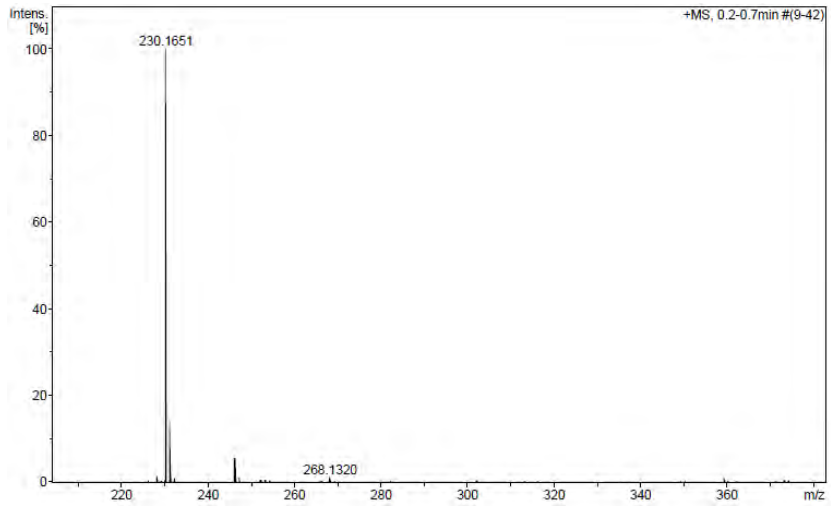
Intens.
[%]
+MS, 0.2-0.7min #(9-42)
230.1651
268.1320
m/z

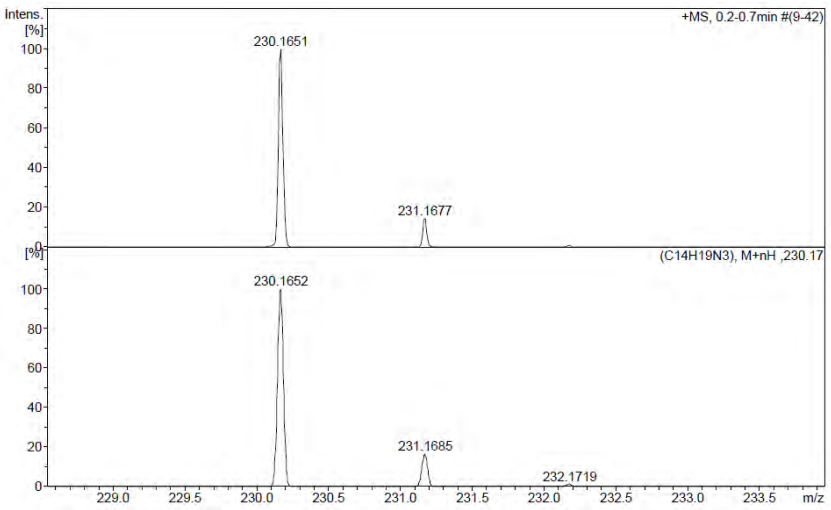
Intens.
[%]
+MS, 0.2-0.7min #(9-42)
230.1651
231.1677
(C14H19N3), M+nH ,230.17
230.1652
231.1685
232.1719
m/z

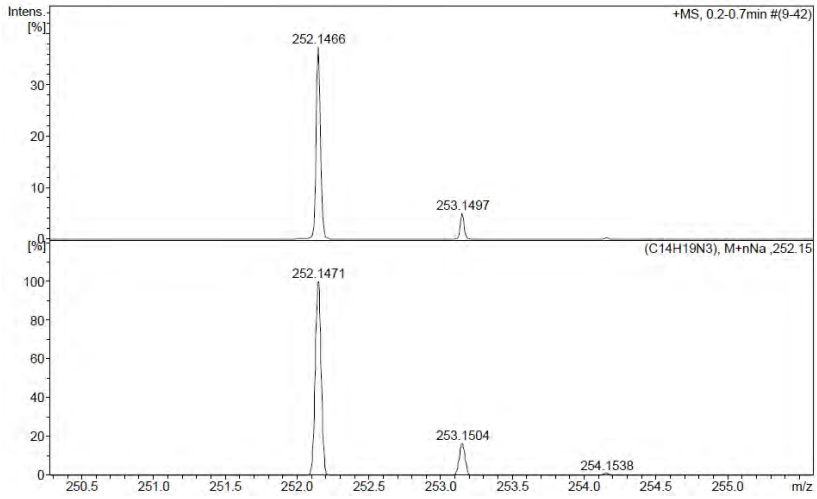

Observed HRMS (top) with the theoretical isotope prediction (bottom).

Figure SV.8: a) ^{1}H NMR spectrum (400 MHz, $CDCl_3$), b) ^{13}C NMR spectrum (100 MHz, $CDCl_3$), c) COSY-NMR spectrum (400 MHz, 298 K, $CDCl_3$), d) HSQCed (400 MHz, $CDCl_3$), e) ESI/MS spectrum (*m/z*), f) HRMS spectrum (*m/z*)

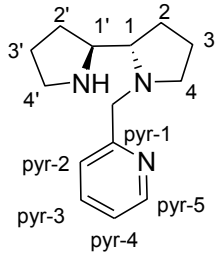

8

a)

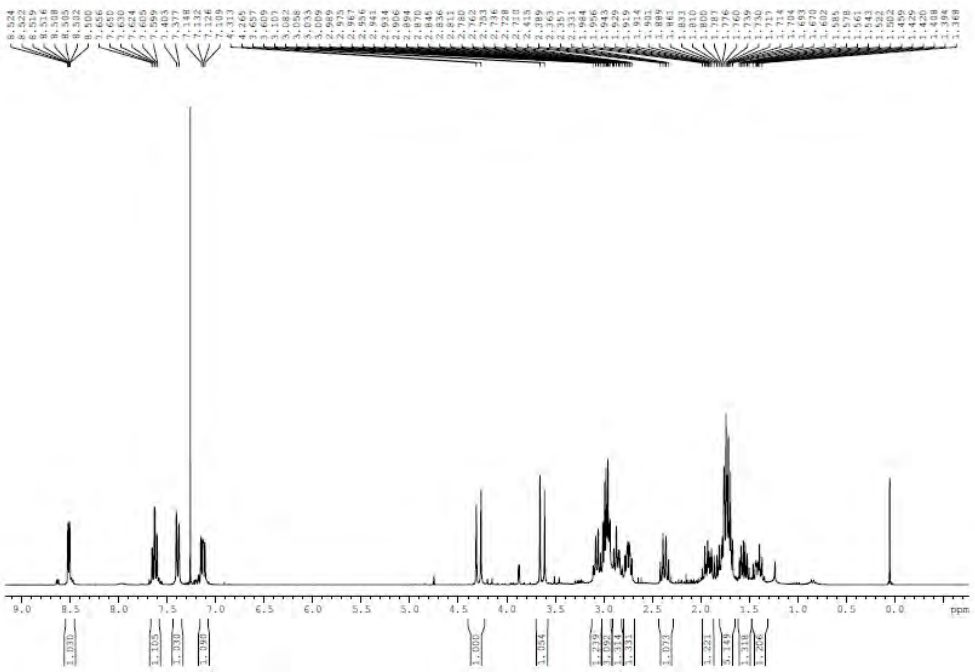

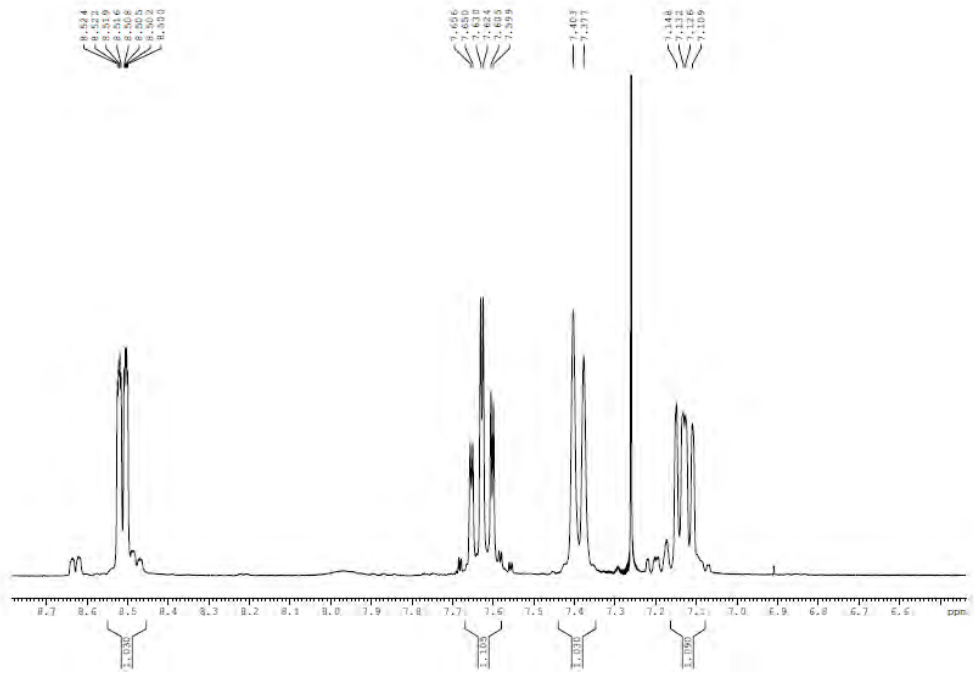

Selected aromatic region.

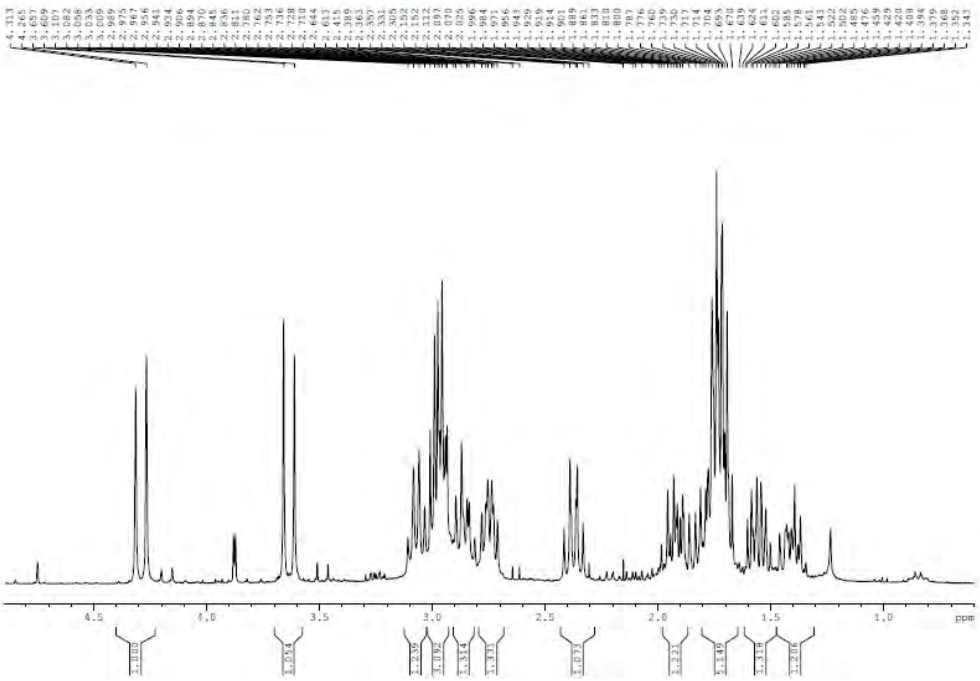

Selected aliphatic region.

b)

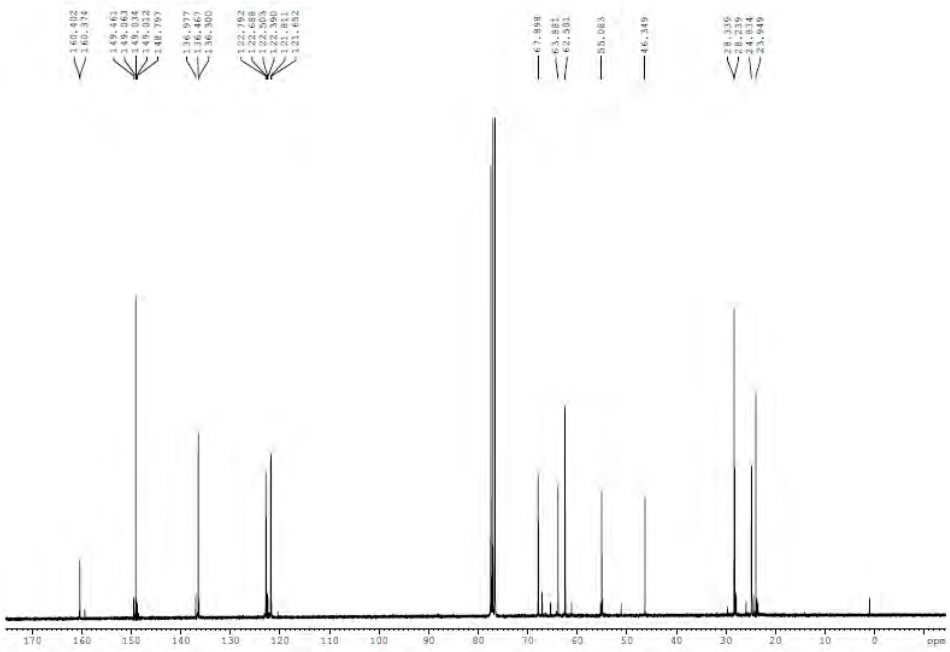

c)

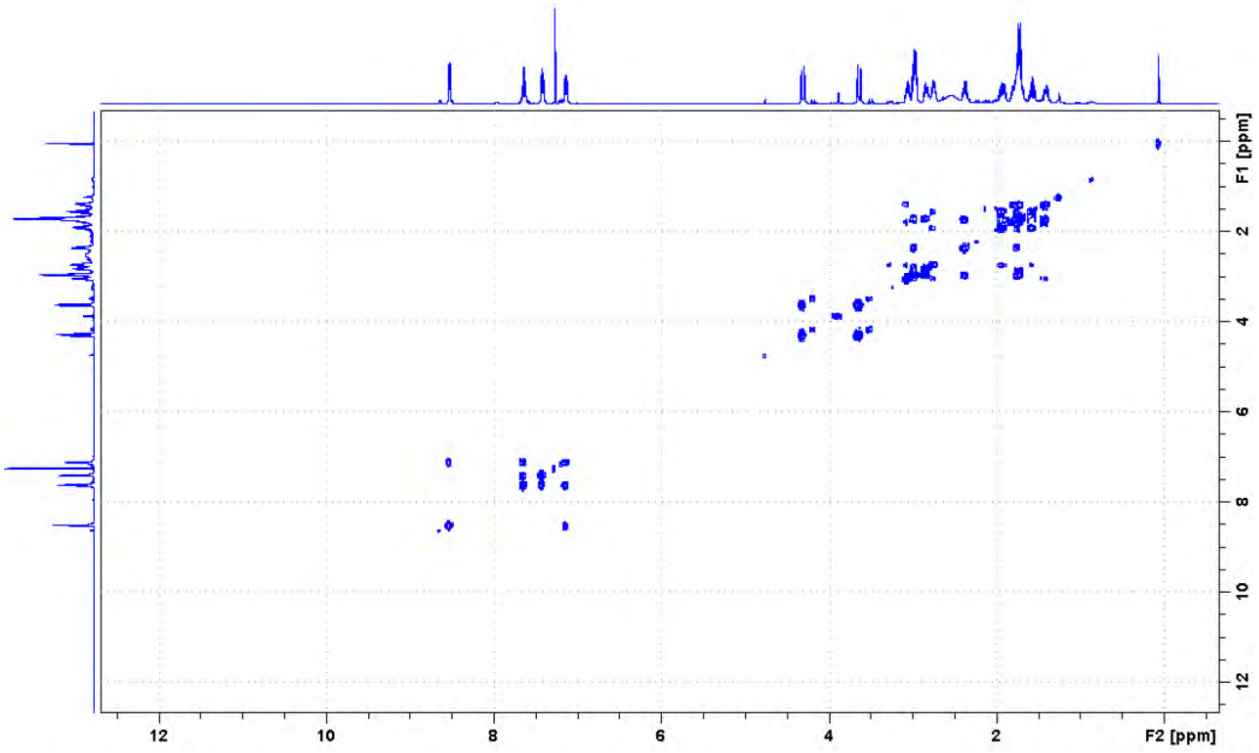

d)

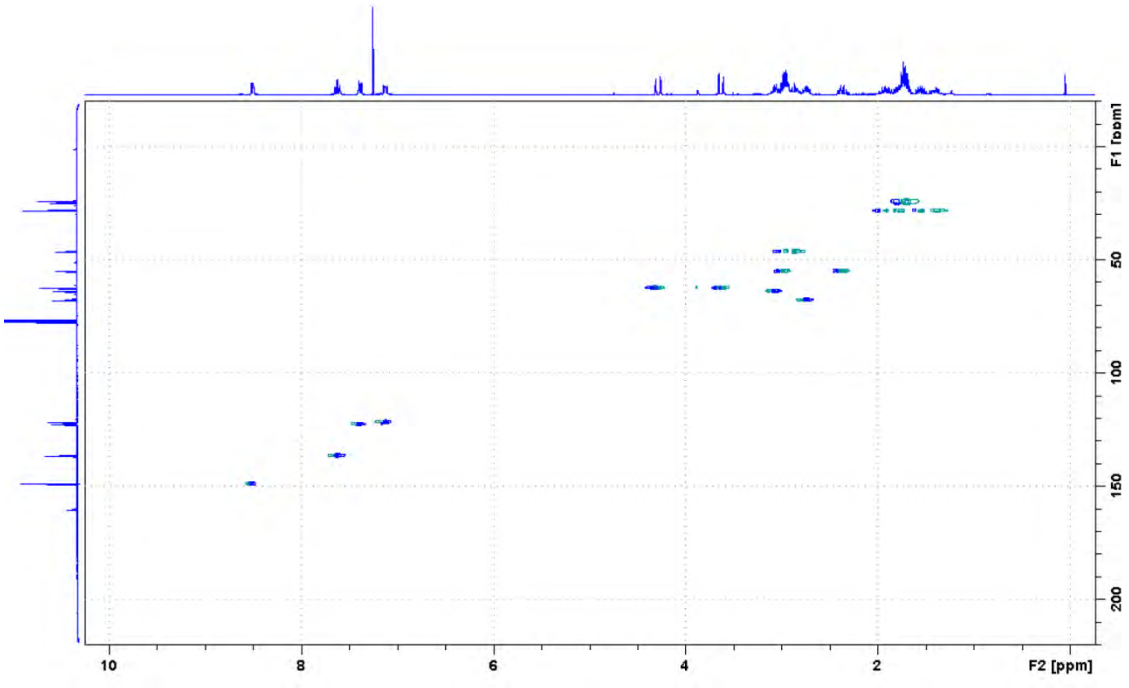
F1 [ppm]
50
100
150
200
10
8
6
4
2
F2 [ppm]

e)

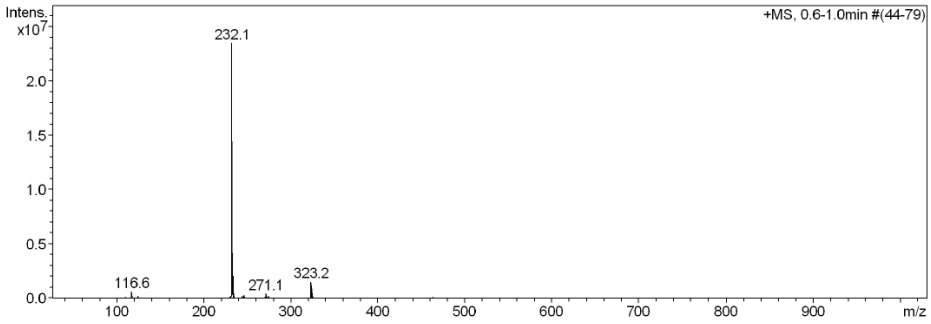
Intens.
x10^7
+MS, 0.6-1.0min #(44-79)
232.1
2.0
1.5
1.0
0.5
0.0
116.6
271.1
323.2
100
200
300
400
500
600
700
800
900
m/z

f)

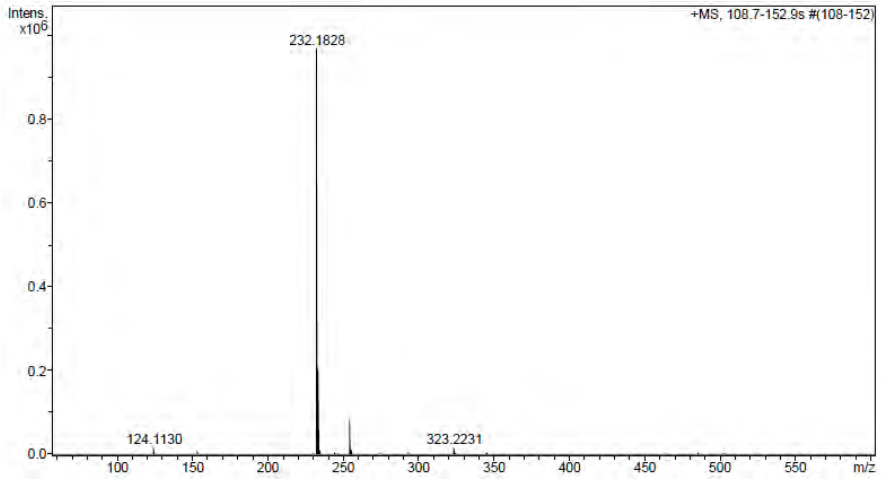
Intens.
x10^6
+MS, 108.7-152.9s #(108-152)
232.1828
0.8
0.6
0.4
0.2
0.0
124.1130
323.2231
100
150
200
250
300
350
400
450
500
550
m/z

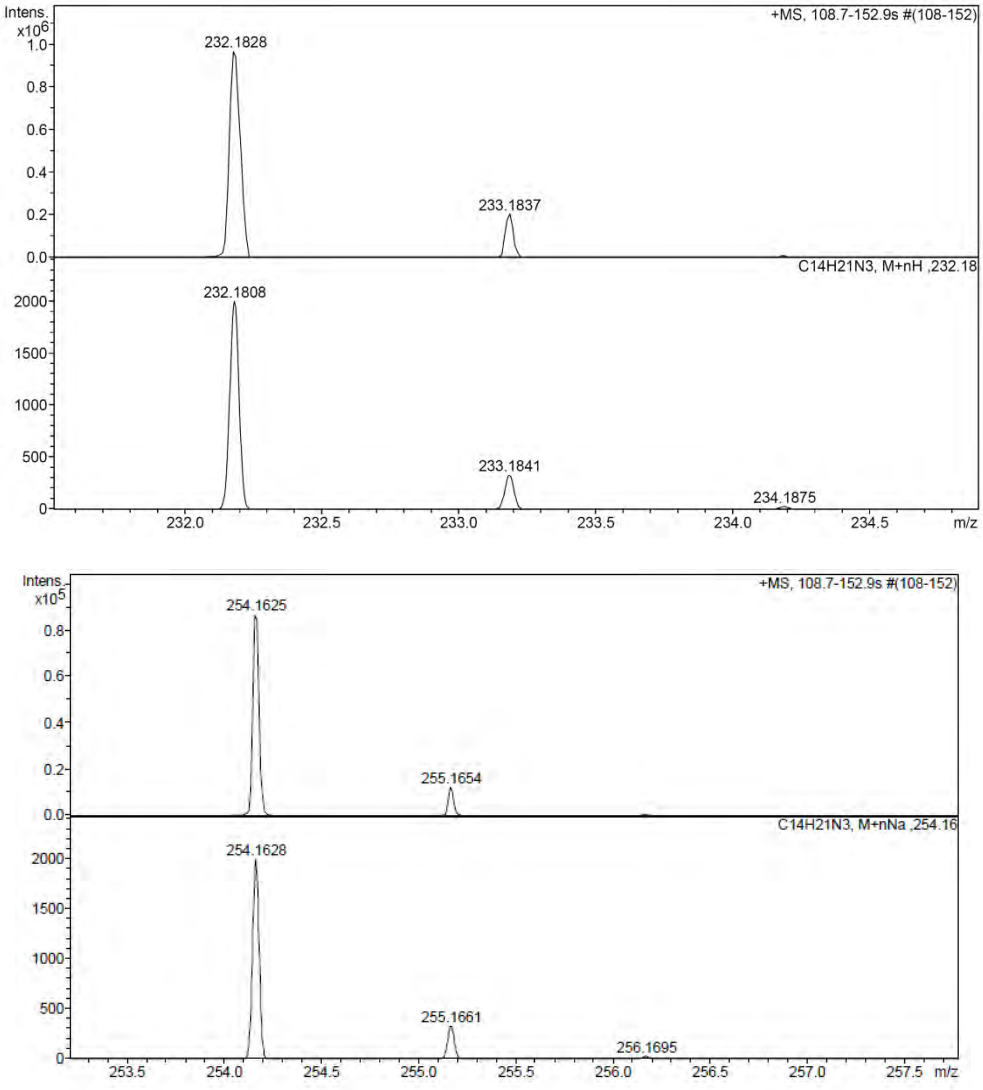

Observed HRMS (top) with the theoretical isotope prediction (bottom).

Figure SV.9: a) HPLC chromatogram (λ= 220 nm), b) ESI/MS spectrum (*m/z*)

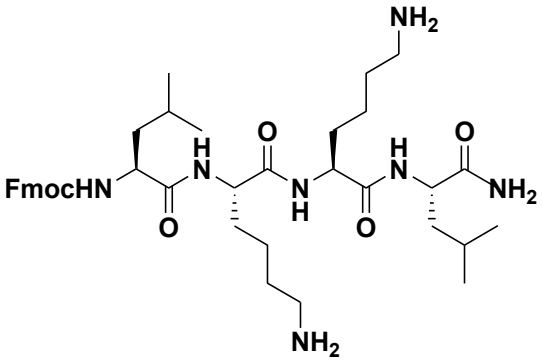

a)

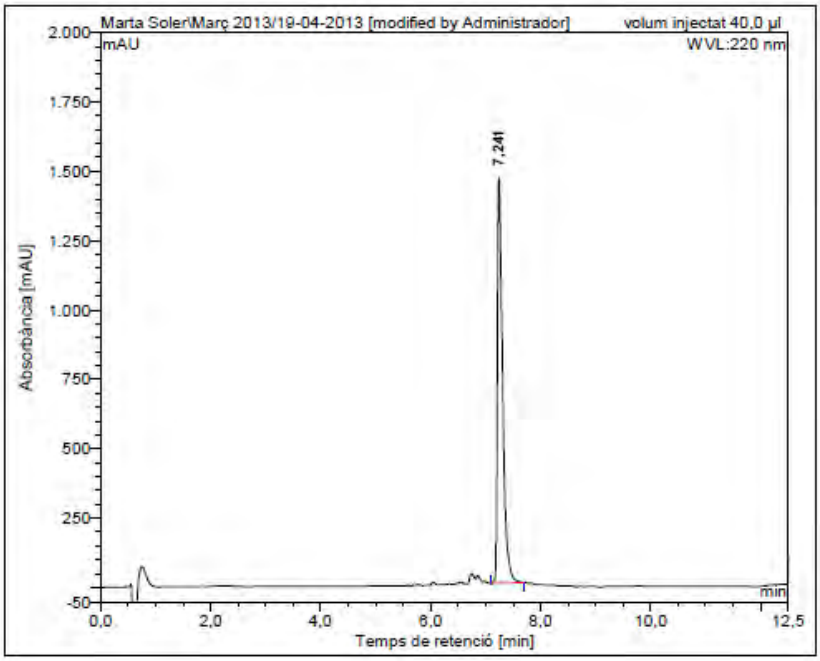

No.	mps retenc min	alçada mAU	Area mAU*min	Area relativa %
1	7,24	1460,388	161,177	100,00
Total:		1460,388	161,177	100,00

b)

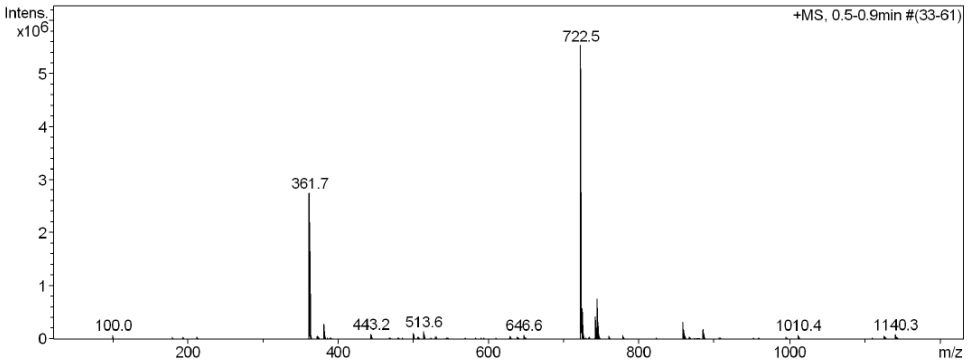

Figure SV.10: a) HPLC chromatogram (λ= 220 nm, conditions a), b) HPLC chromatogram (λ= 220 nm, conditions b), c) ESI/MS spectrum (*m/z*)

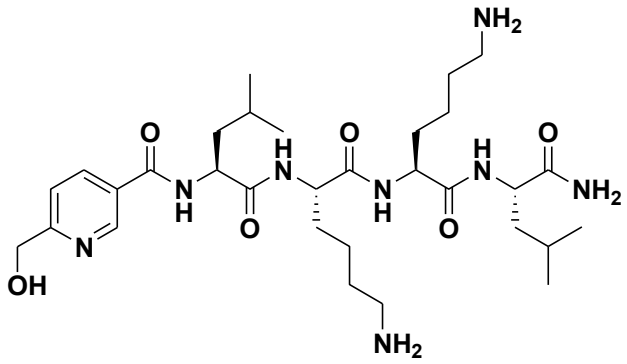

11

a)

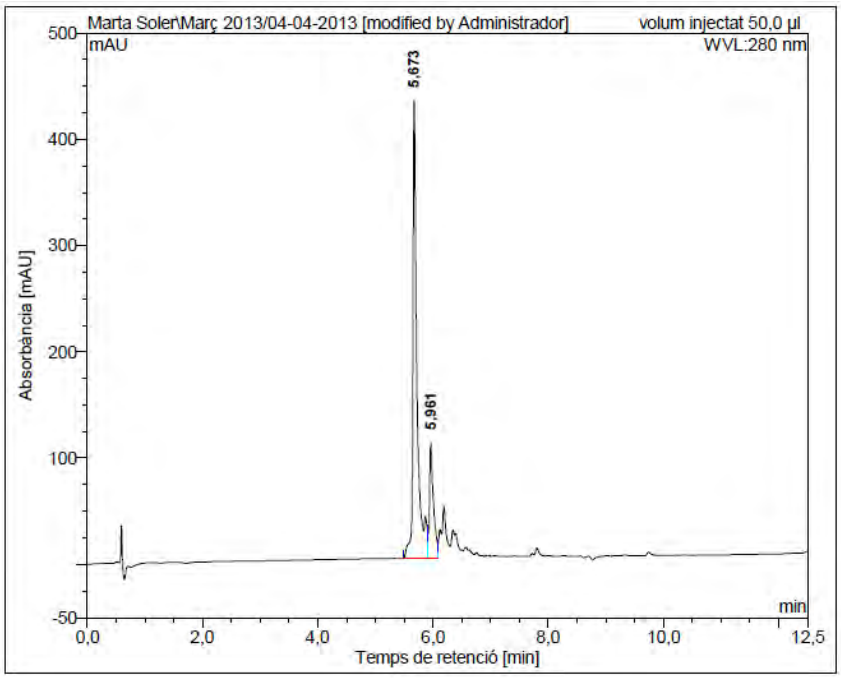

No.	mps retenc min	alçada mAU	Area mAU*min	Area relativa %
1	5,67	431,064	36,098	81,27
2	5,96	109,001	8,319	18,73
Total:		540,065	44,417	100,00

b)

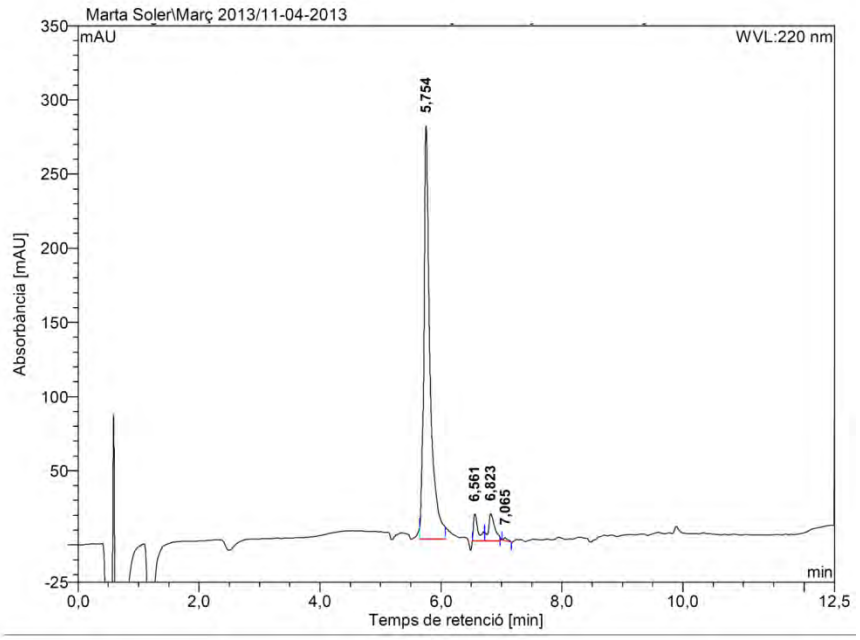

No.	Temps retenció min	alçada mAU	Area mAU*min	Area relativa %
1	5,75	278,477	32,992	89,11
2	6,56	18,134	1,675	4,52
3	6,82	18,215	2,216	5,99
4	7,07	2,053	0,139	0,38
Total:		316,879	37,023	100,00

c)

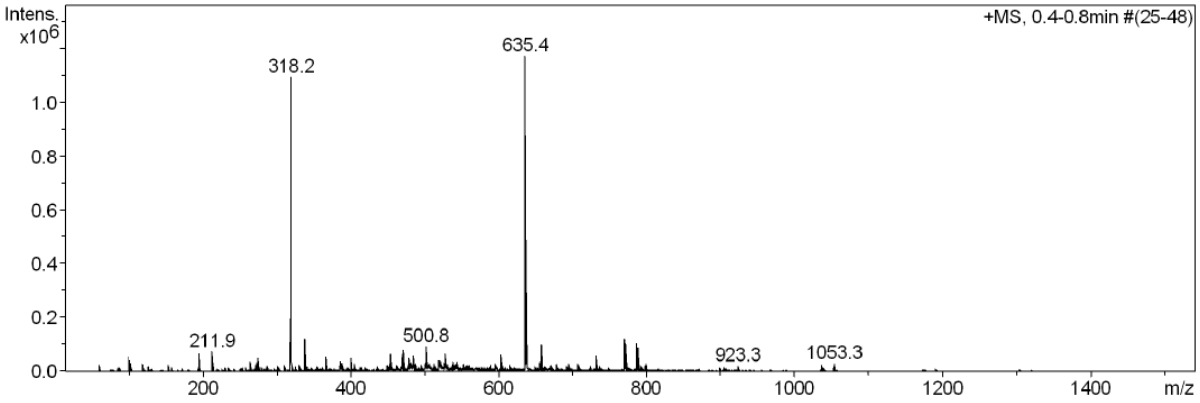

Figure SV.11: a) HPLC chromatogram (λ= 220 nm), b) ESI/MS spectrum (*m/z*)

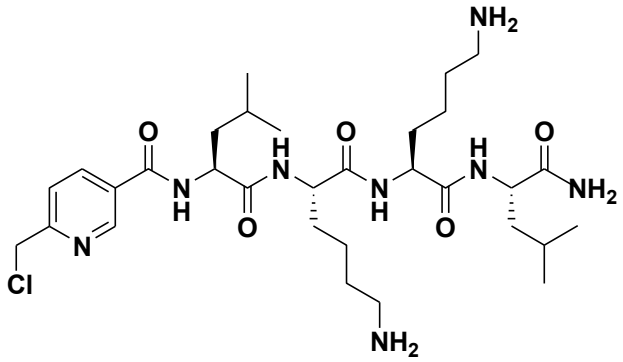

13

a)

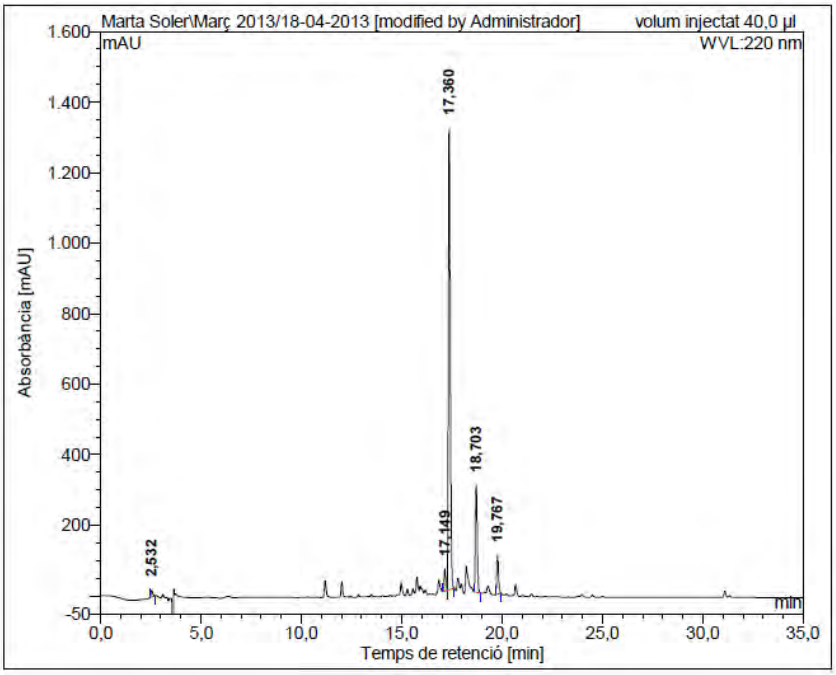

No.	mps retenc min	alçada mAU	Area mAU*min	Area relativa %
1	2,53	17,831	1,761	0,89
2	17,15	60,449	5,460	2,76
3	17,36	1309,544	147,058	74,34
4	18,70	302,499	31,819	16,08
5	19,77	109,640	11,726	5,93
Total:		1799,962	197,825	100,00

b)

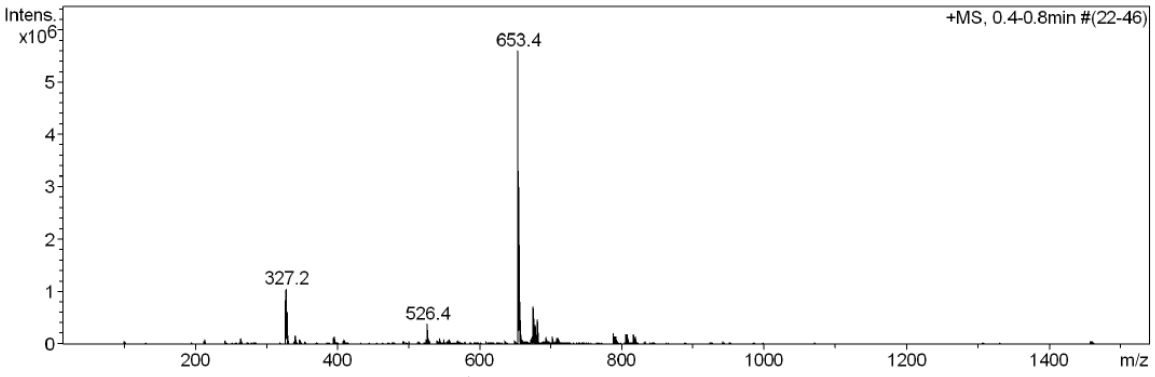
Intens.
x10^6
+MS, 0.4-0.8min #(22-46)
653.4
327.2
526.4
0
1
2
3
4
5
200
400
600
800
1000
1200
1400
m/z

Figure SV.12: a) HPLC chromatogram (λ= 220 nmm), b) ESI/MS spectrum (*m/z*), c) HRMS spectrum (*m/z*), d) ^{1}H NMR spectrum (400 MHz, CD_3OD) through alkylation of peptidyl resin **12a** with **7**, e) ^{1}H NMR spectrum (400 MHz, CD_3OD) through coupling of **14** to peptidyl resin **6a**

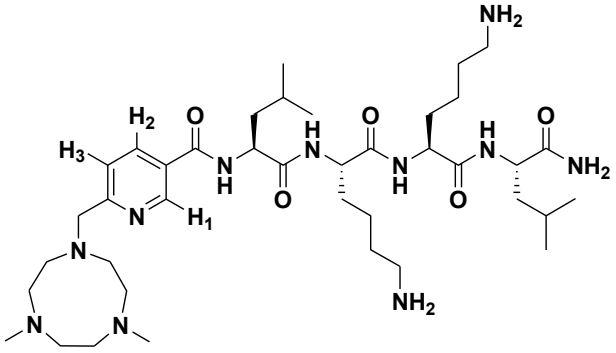

3

a)

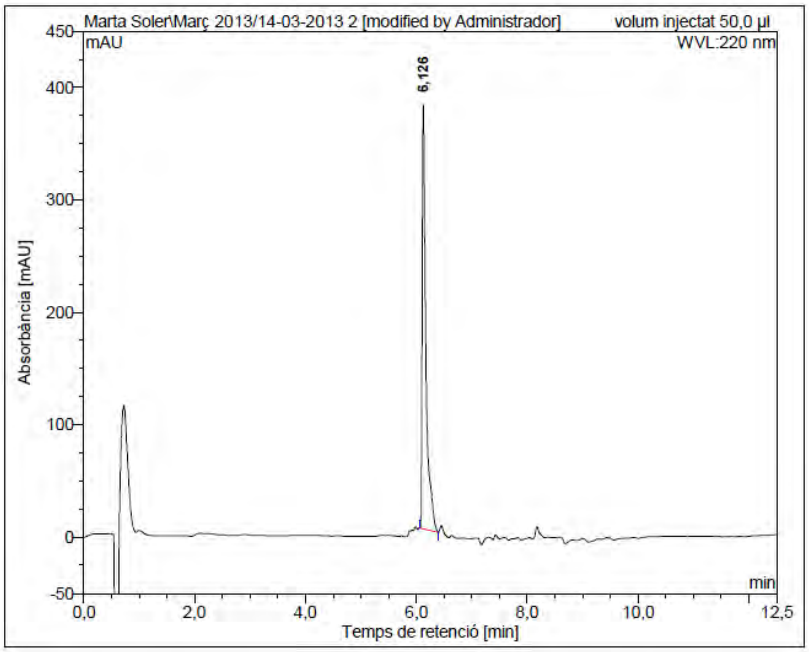

No.	mps retenc min	alçada mAU	Area mAU*min	Area relativa %
1	6,13	376,689	29,322	100,00
Total:		376,689	29,322	100,00

b)

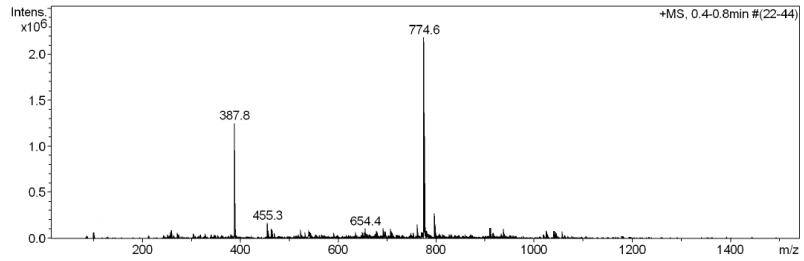

c)

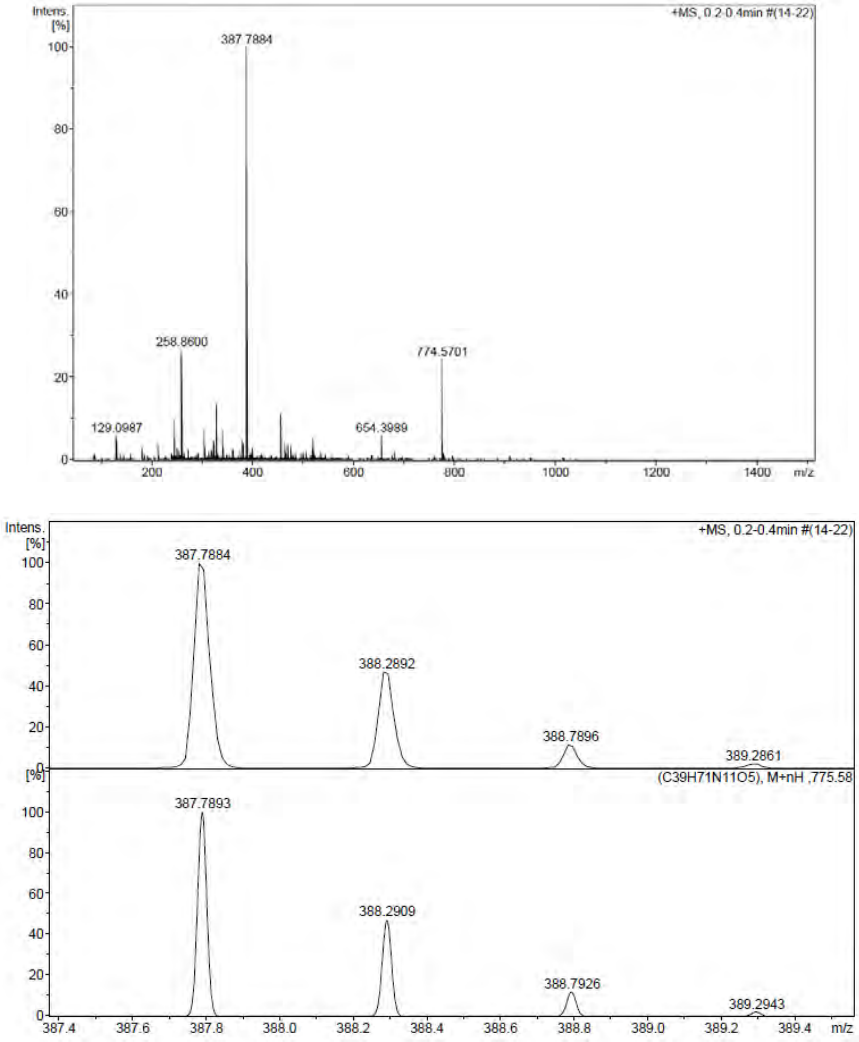

Observed HRMS (top) with the theoretical isotope prediction (bottom).

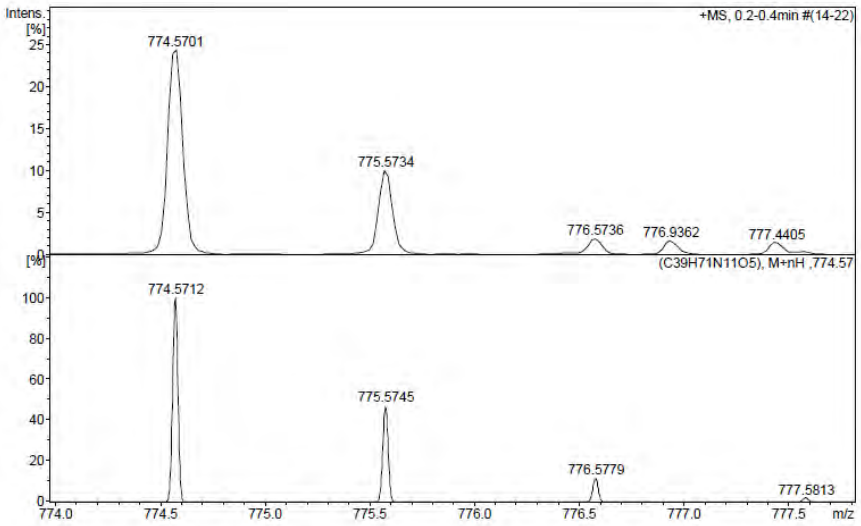

Observed HRMS (top) with the theoretical isotope prediction (bottom).

d)

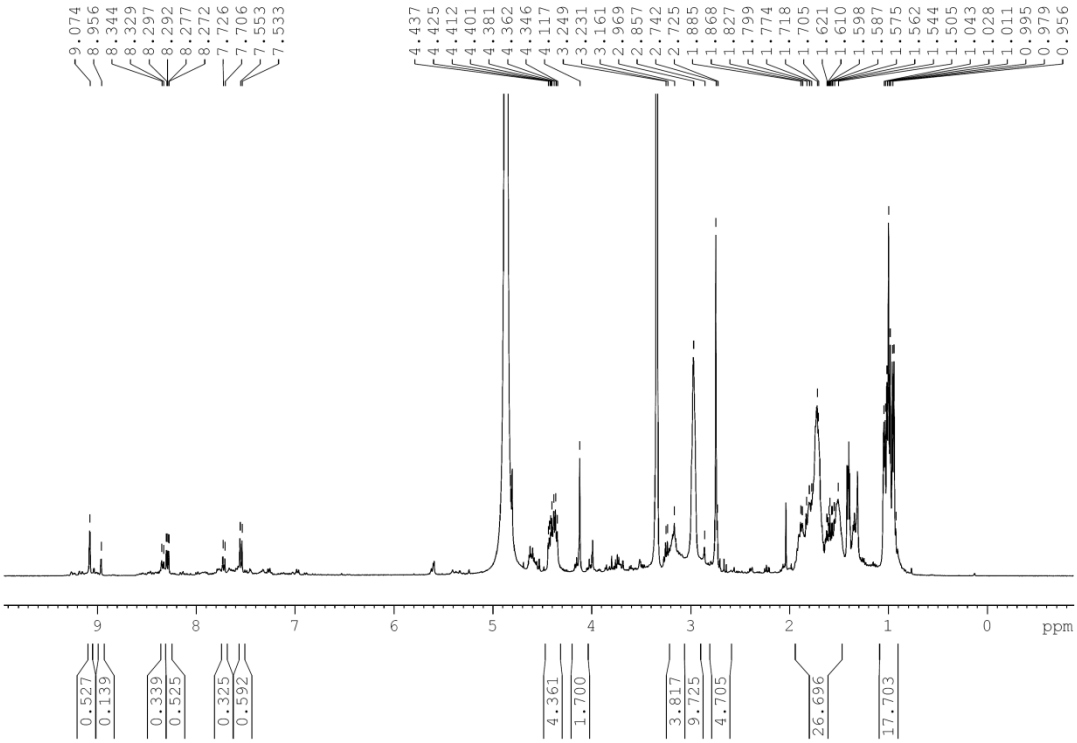

e)

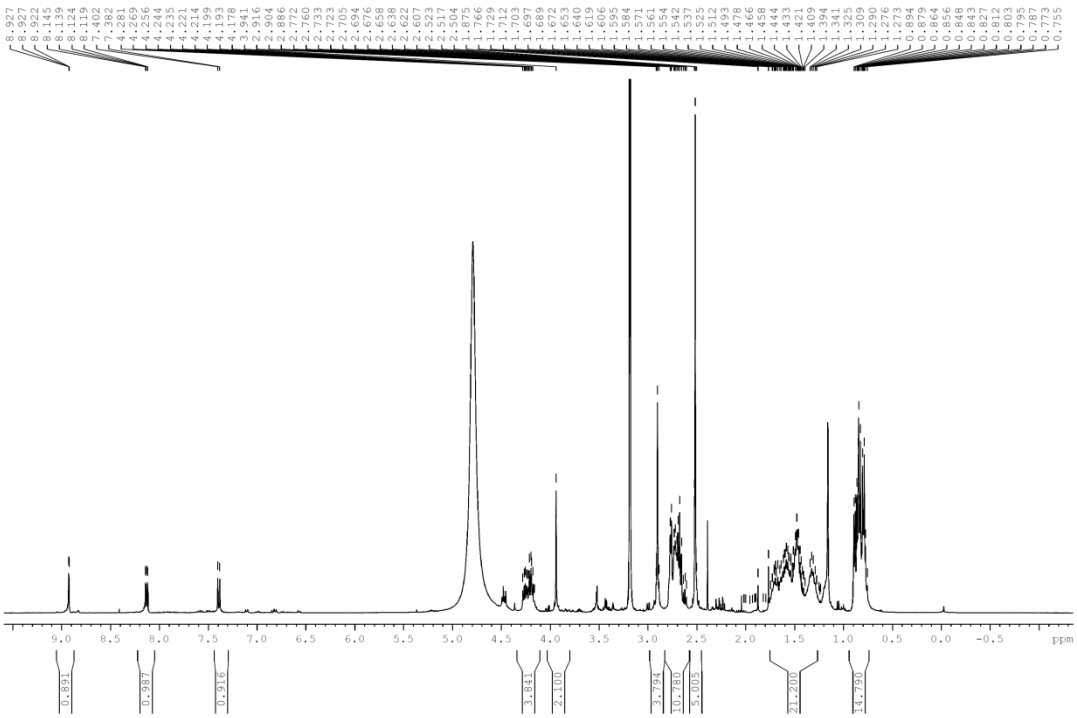
9.0
8.5
8.0
7.5
7.0
6.5
6.0
5.5
5.0
4.5
4.0
3.5
3.0
2.5
2.0
1.5
1.0
0.5
0.0
-0.5
ppm
0.891
0.987
0.916
3.841
2.100
3.794
10.780
5.005
21.200
14.790

Figure SV.13: a) HPLC chromatogram (λ= 220 nm), b) ESI/MS spectrum (*m/z*), c) HRMS spectrum (*m/z*), d) ^{1}H NMR spectrum (400 MHz, CD_3OD)

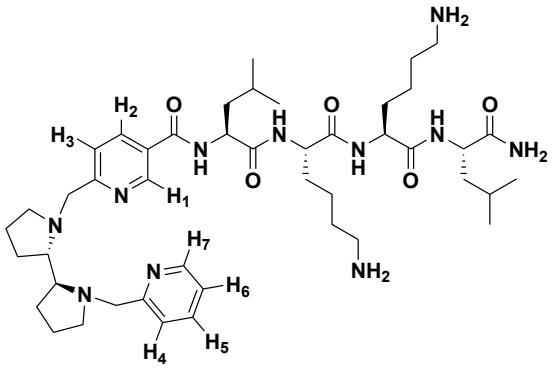

4

a)

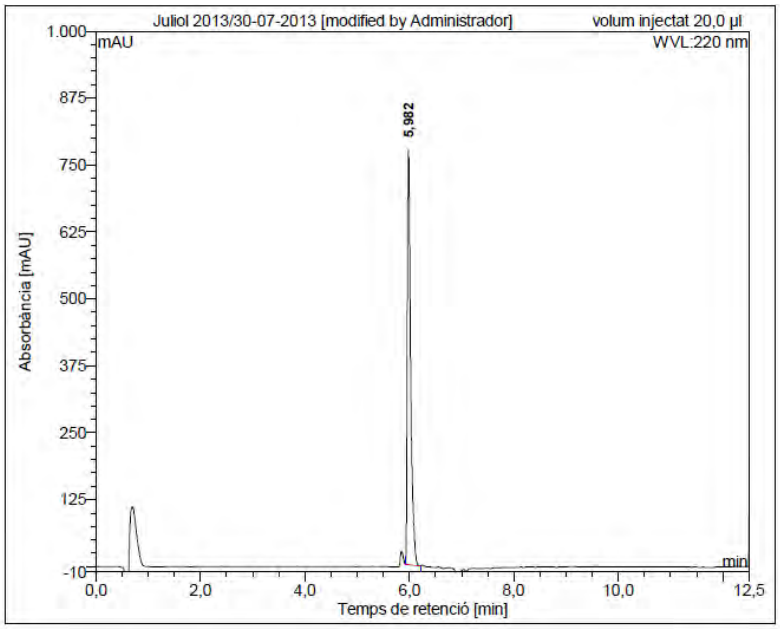

No.	mps retenc min	alçada mAU	Area mAU*min	Area relativa %
1	5,98	774,279	57,048	100,00
Total:		774,279	57,048	100,00

b)

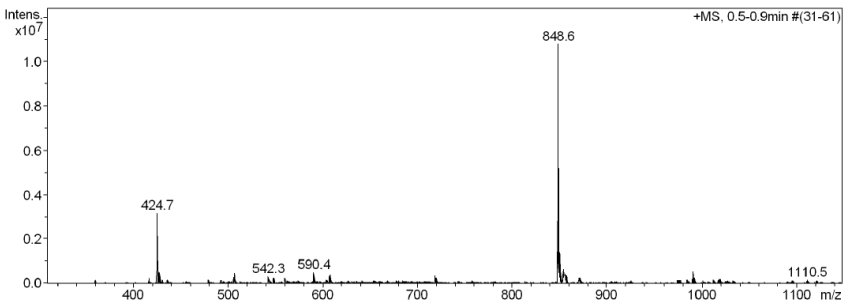

c)

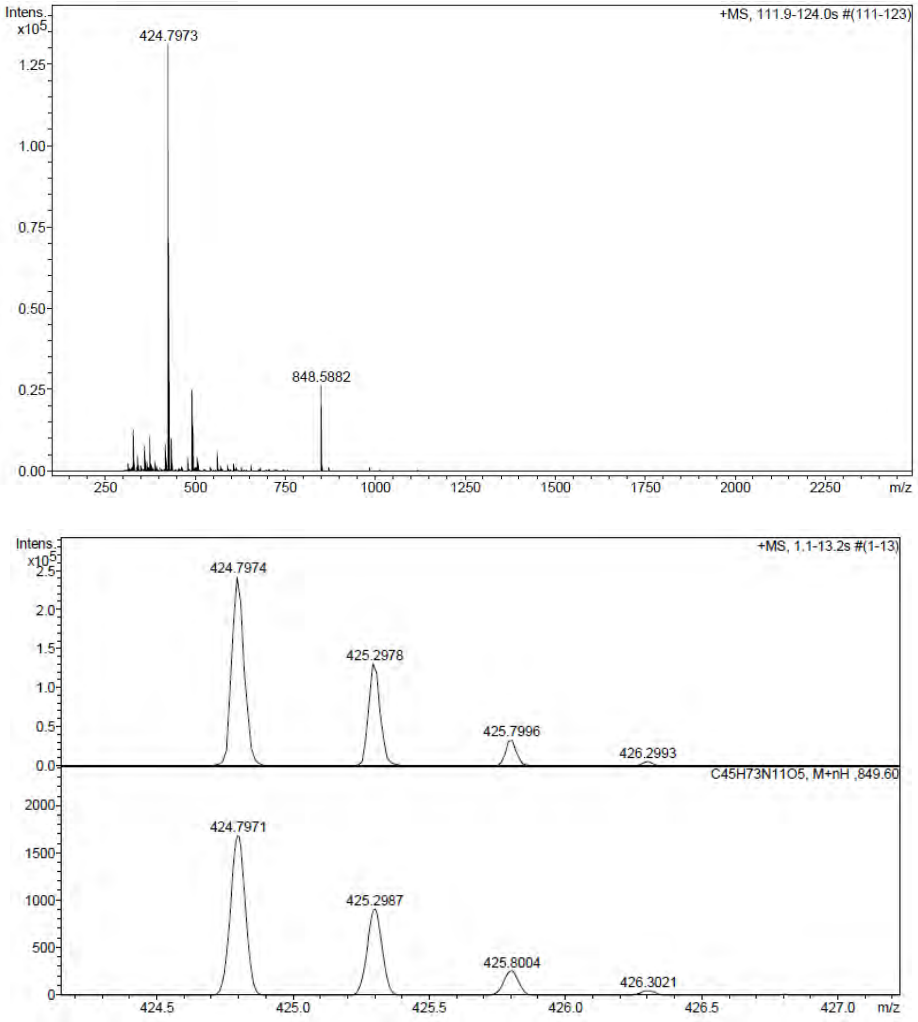

Observed HRMS (top) with the theoretical isotope prediction (bottom).

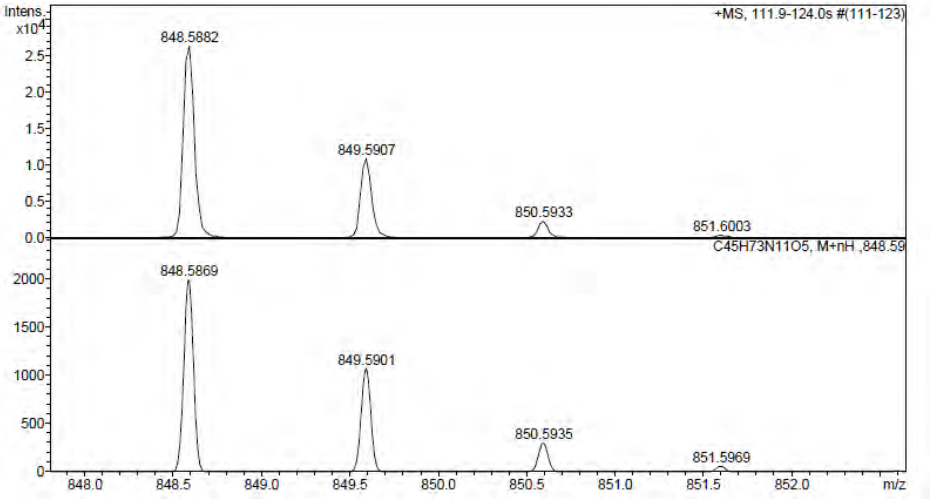

Observed HRMS (top) with the theoretical isotope prediction (bottom).

d)

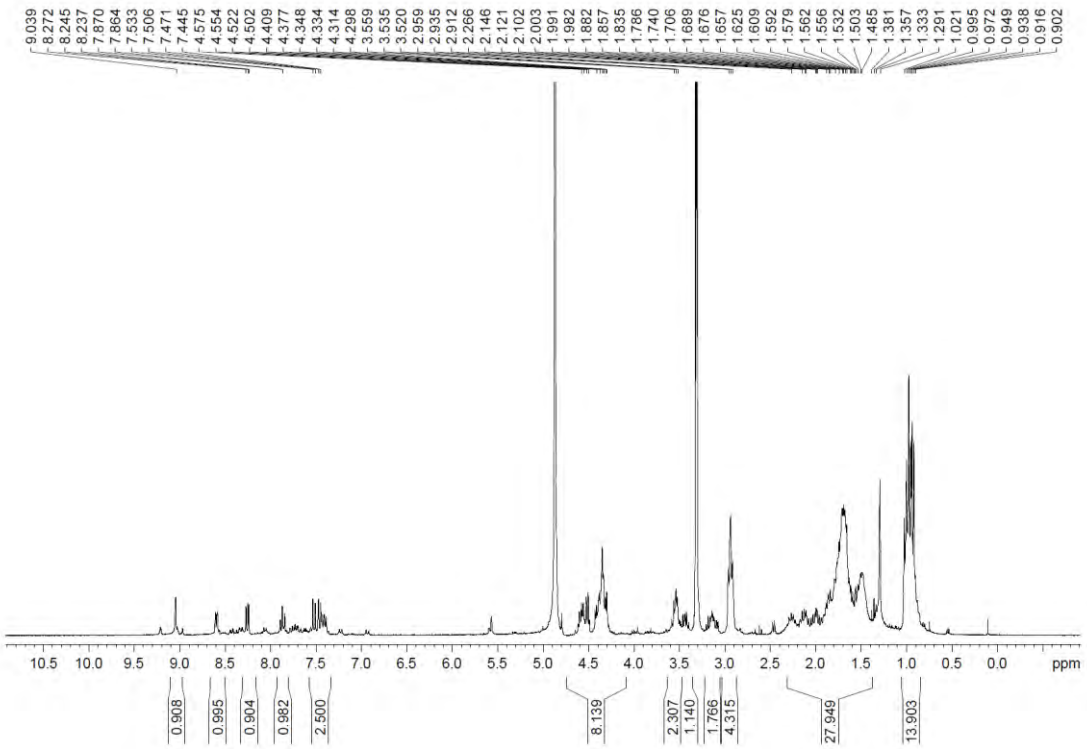
9.039
8.272
8.245
8.237
7.870
7.864
7.533
7.506
7.471
7.445
4.575
4.554
4.522
4.502
4.409
4.377
4.348
4.334
4.314
4.298
3.559
3.535
3.520
2.959
2.935
2.912
2.266
2.146
2.121
2.102
2.003
1.991
1.982
1.882
1.857
1.835
1.786
1.740
1.706
1.689
1.676
1.657
1.625
1.609
1.592
1.579
1.562
1.556
1.532
1.503
1.485
1.381
1.357
1.333
1.291
1.021
0.995
0.972
0.949
0.938
0.916
0.902
10.5 10.0 9.5 9.0 8.5 8.0 7.5 7.0 6.5 6.0 5.5 5.0 4.5 4.0 3.5 3.0 2.5 2.0 1.5 1.0 0.5 0.0 ppm
0.908
0.995
0.904
0.982
2.500
8.139
2.307
1.140
1.766
4.315
27.949
13.903

Figure SV.14: a) HRMS spectrum (*m/z*)

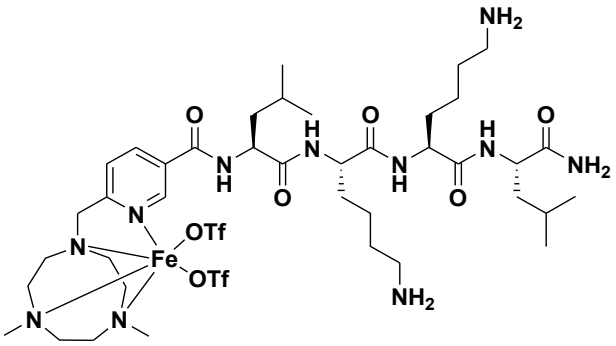

1_{Fe}

a)

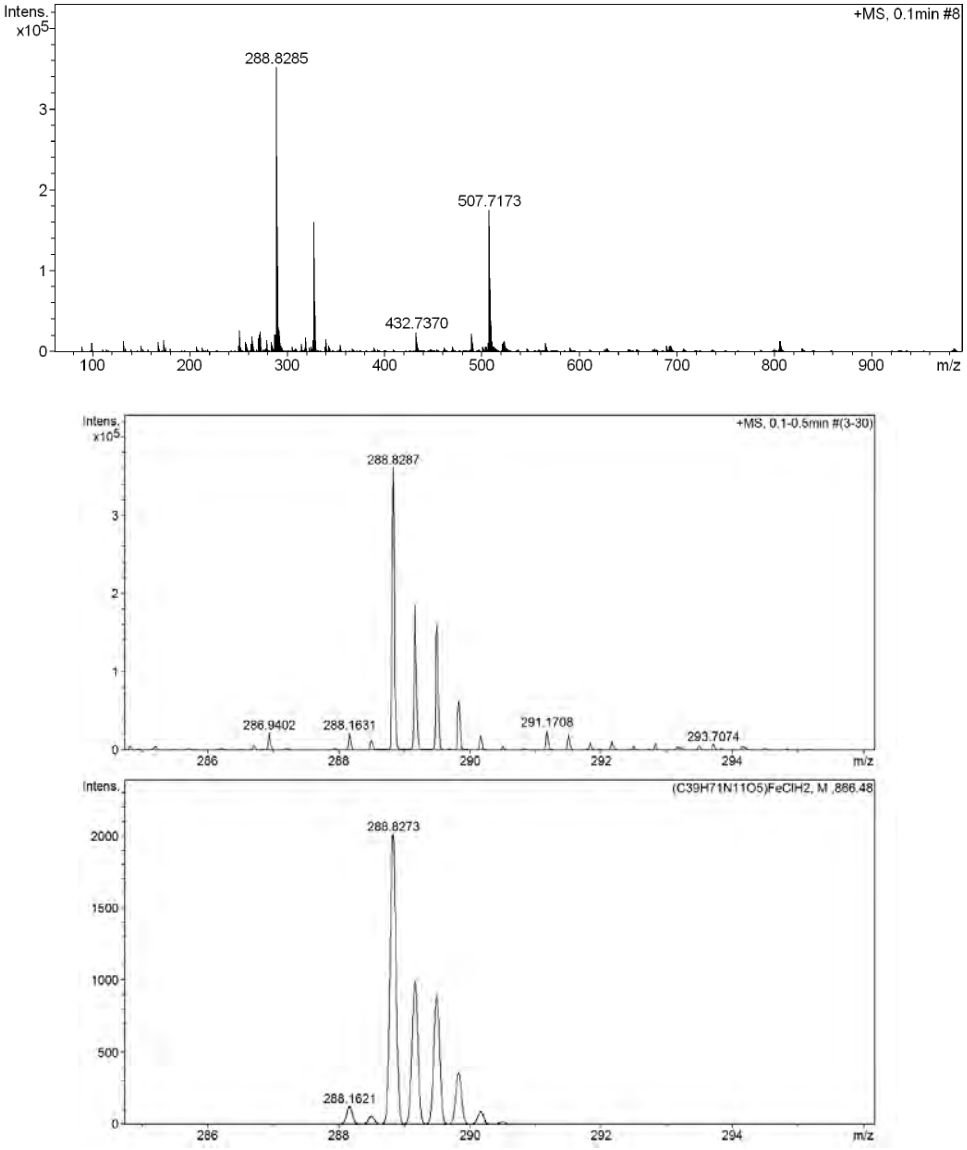

Observed HRMS (top) with the theoretical isotope prediction (bottom).

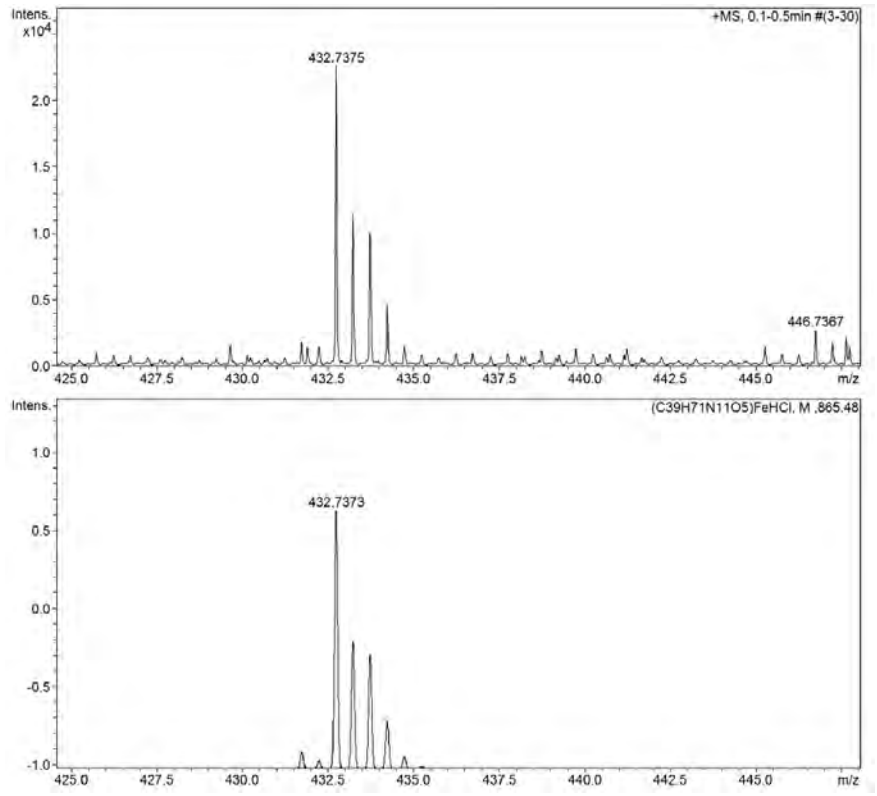

Observed HRMS (top) with the theoretical isotope prediction (bottom).

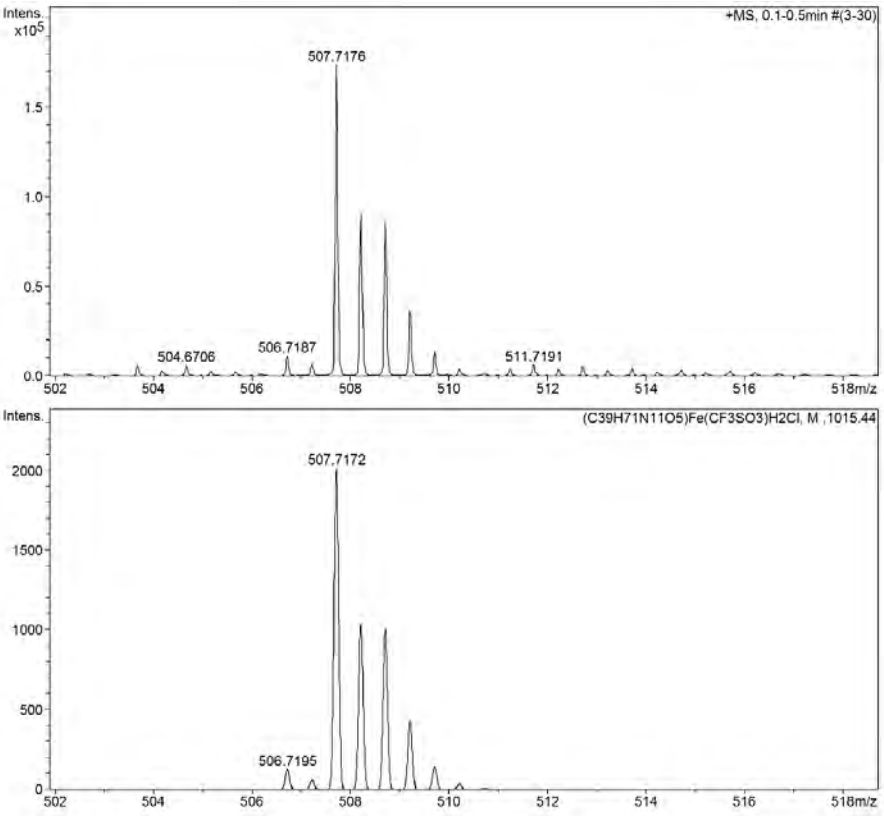

Observed HRMS (top) with the theoretical isotope prediction (bottom).

Figure SV.15: a) HRMS spectrum (*m/z)*

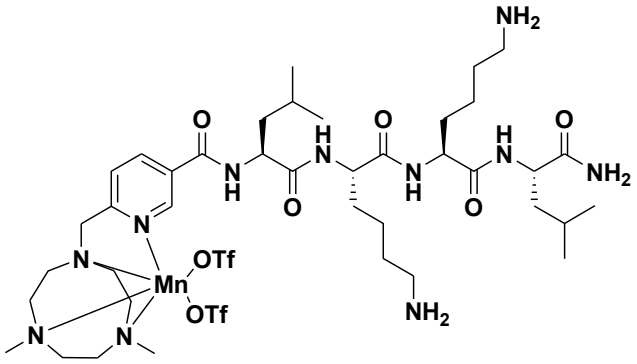

1_{Mn}

a)

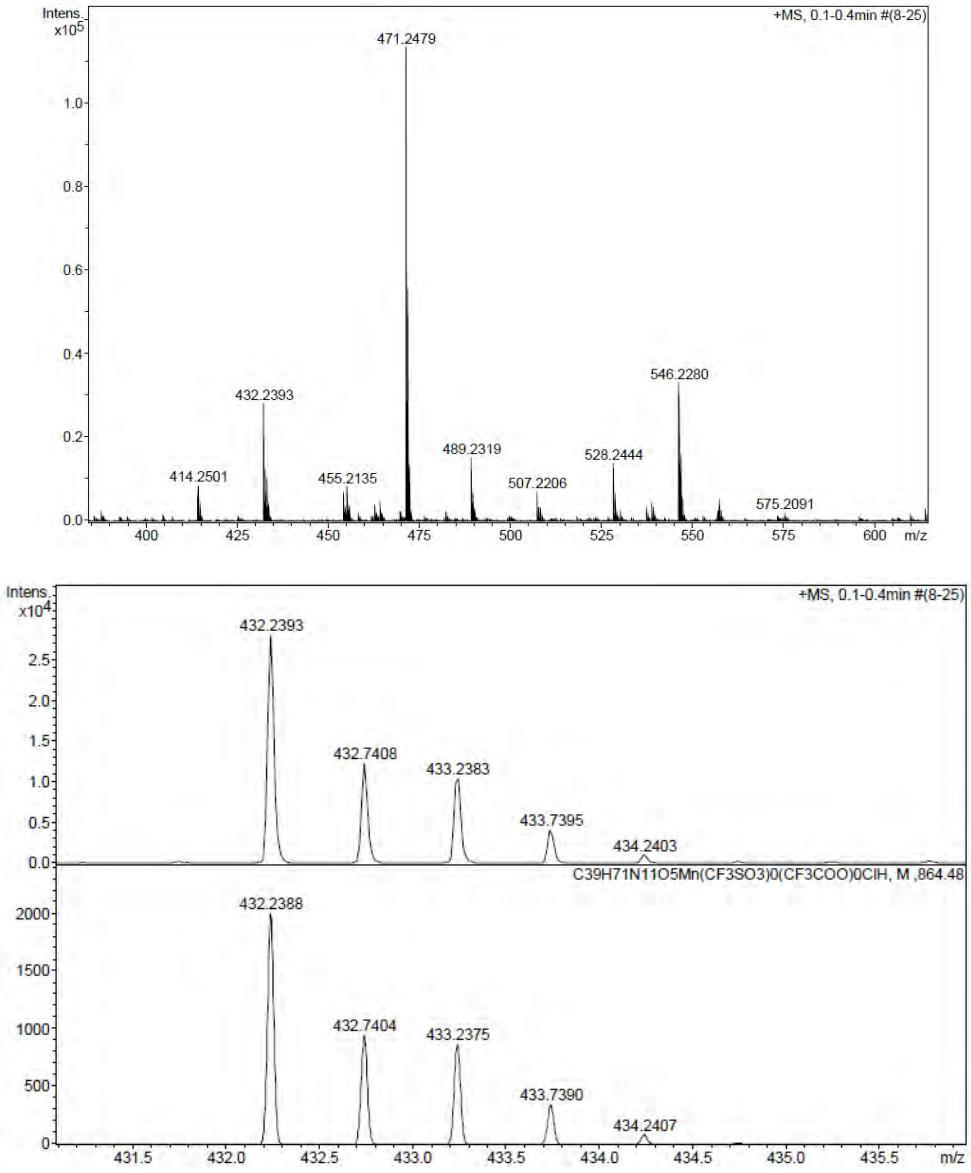

Observed HRMS (top) with the theoretical isotope prediction (bottom).

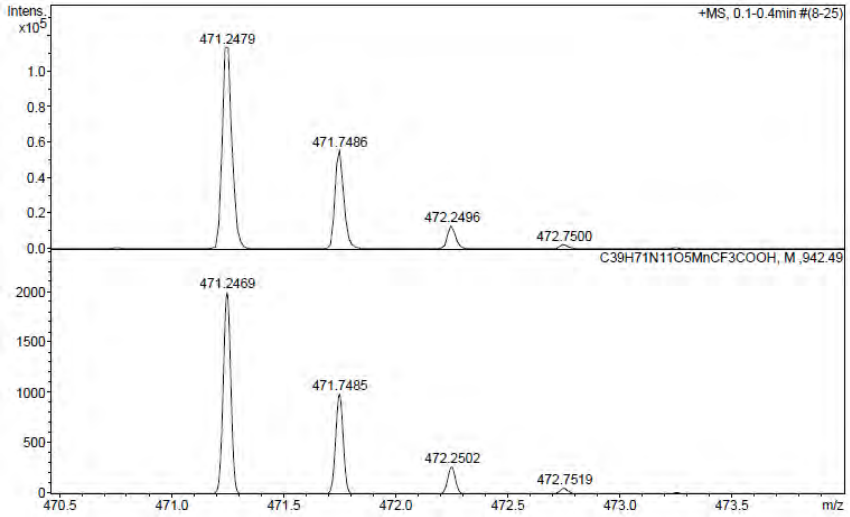

Observed HRMS (top) with the theoretical isotope prediction (bottom).

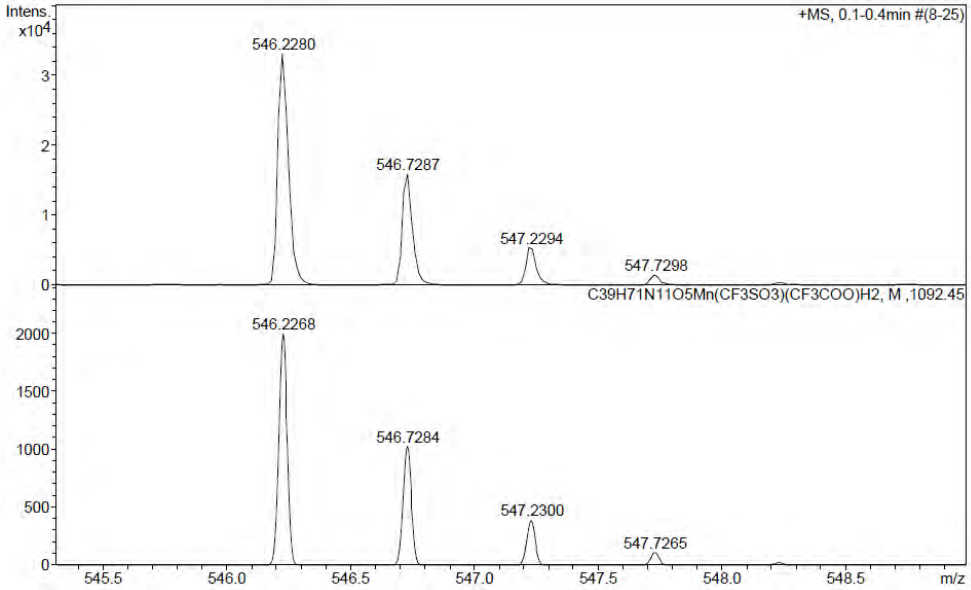

Observed HRMS (top) with the theoretical isotope prediction (bottom).

Figure SV.16: a) HRMS spectrum (*m/z*), b) ^{1}H NMR spectrum (400 MHz, CD_3OD)

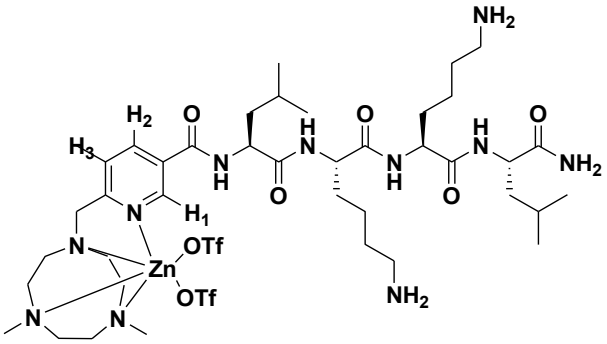

1_{Zn}

a)

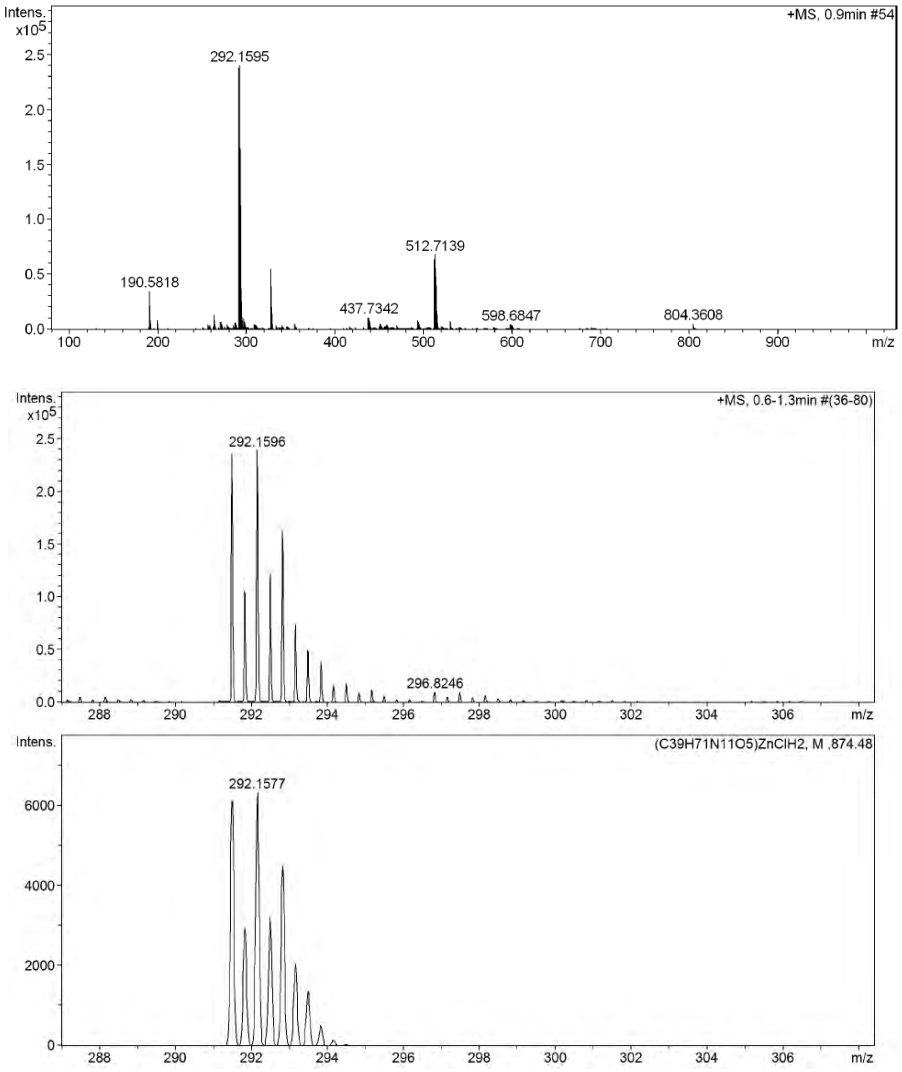

Observed HRMS (top) with the theoretical isotope prediction (bottom).

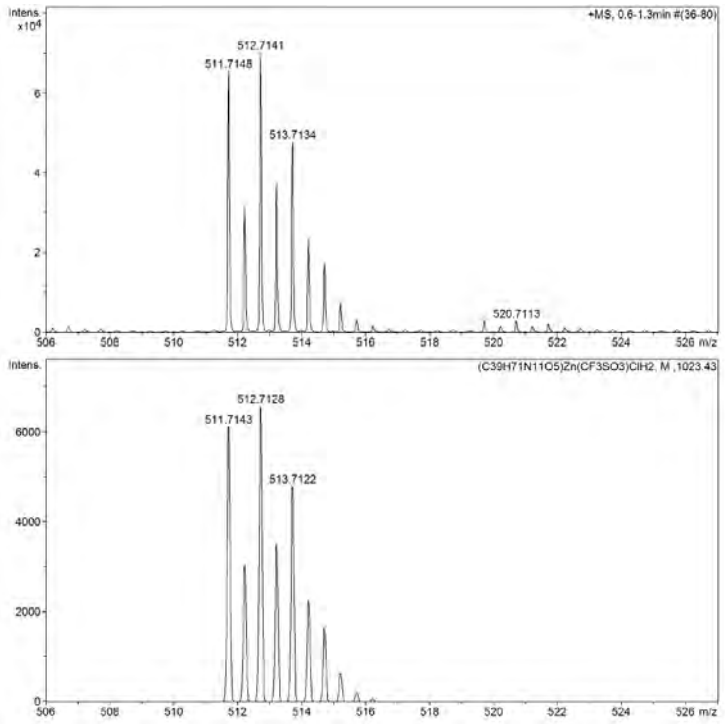

Observed HRMS (top) with the theoretical isotope prediction (bottom).

b)

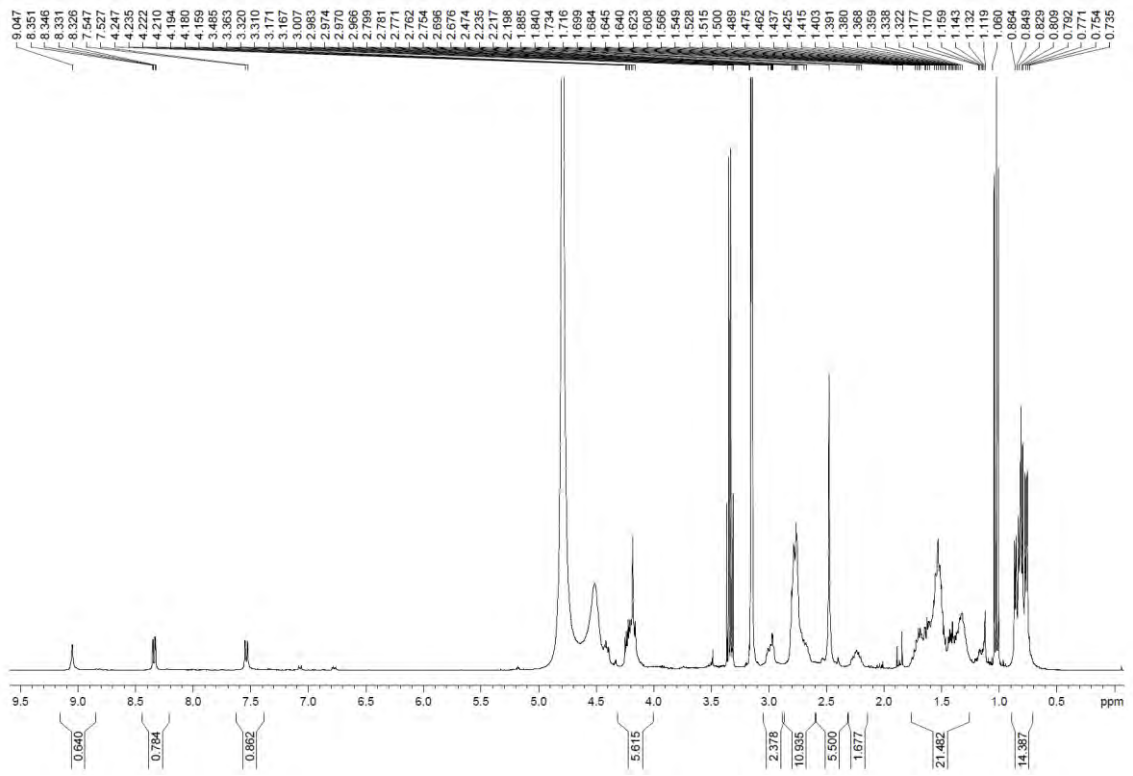

Figure SV.17: a) HRMS spectrum (*m/z*)

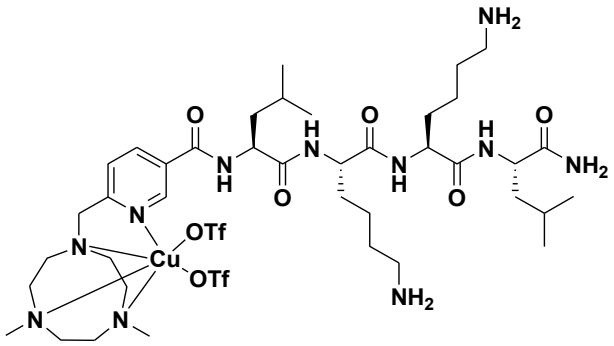

1_{Cu}

a)

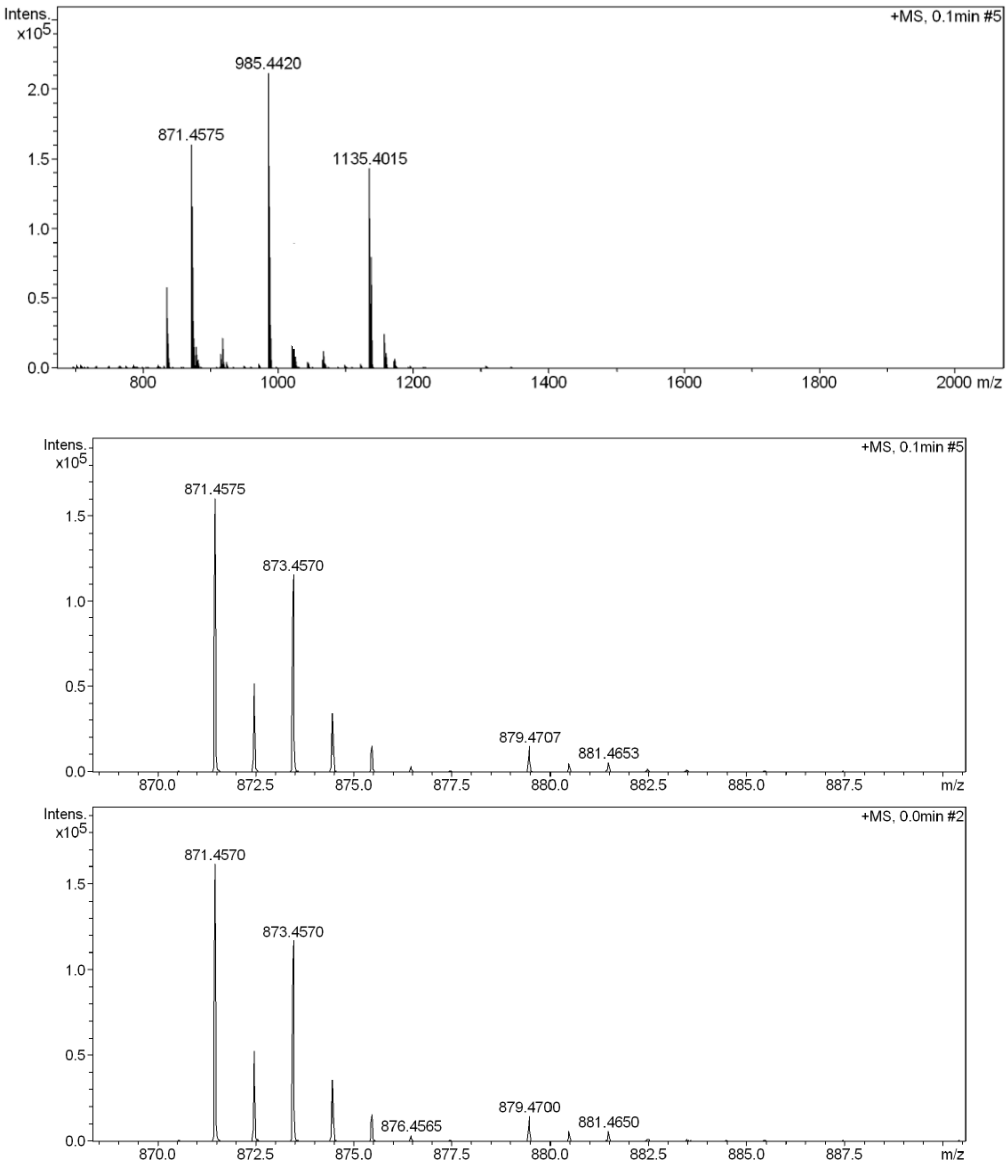

Observed HRMS (top) with the theoretical isotope prediction (bottom).

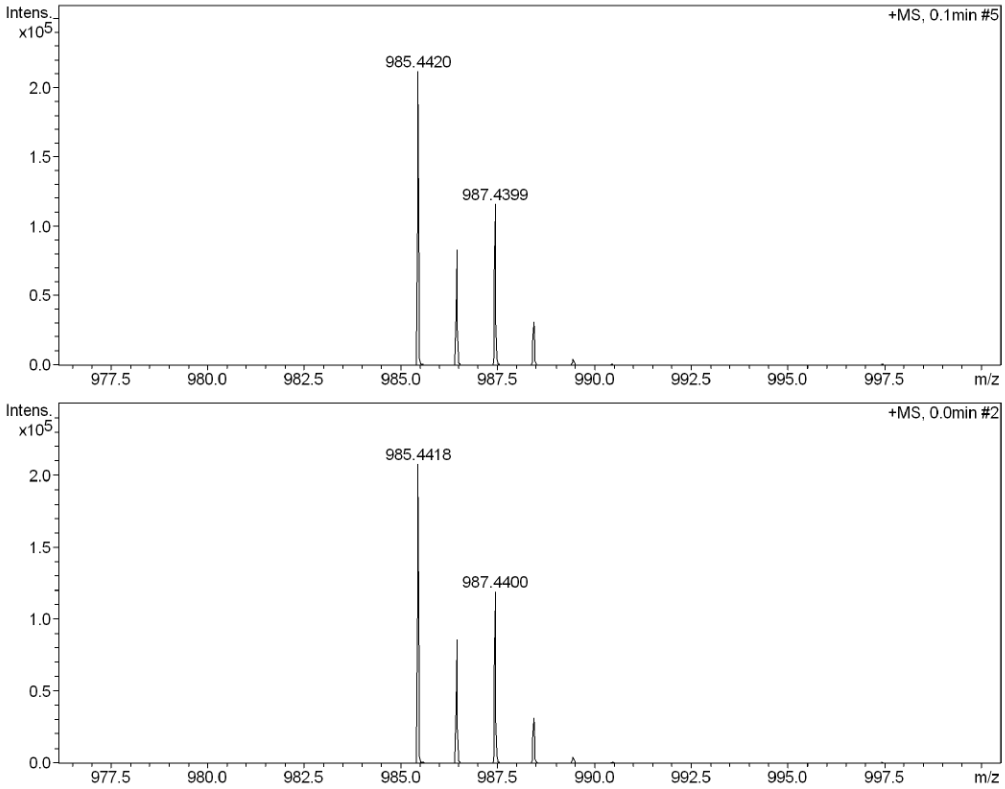

Observed HRMS (top) with the theoretical isotope prediction (bottom).

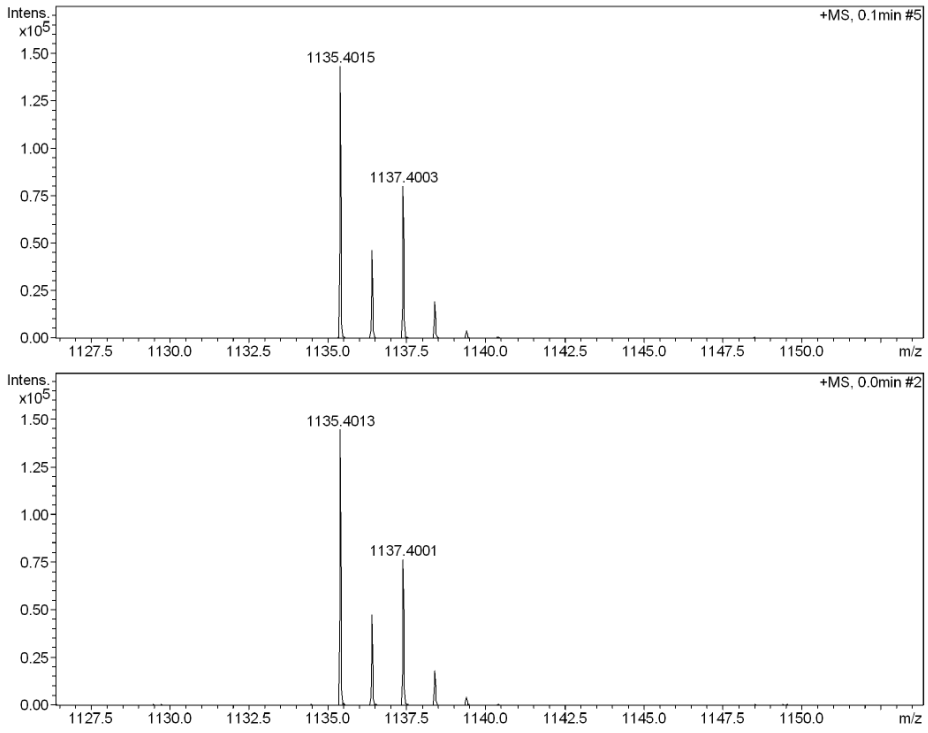

Observed HRMS (top) with the theoretical isotope prediction (bottom).

Figure SV.18: a) HRMS spectrum (*m/z*), b) ^{1}H NMR spectrum (400 MHz, CD_3OD)

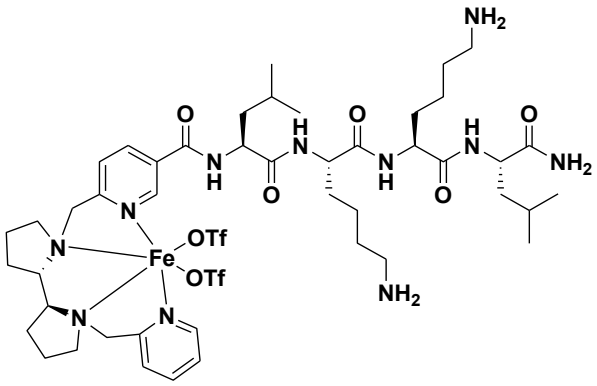

2_{Fe}

a)

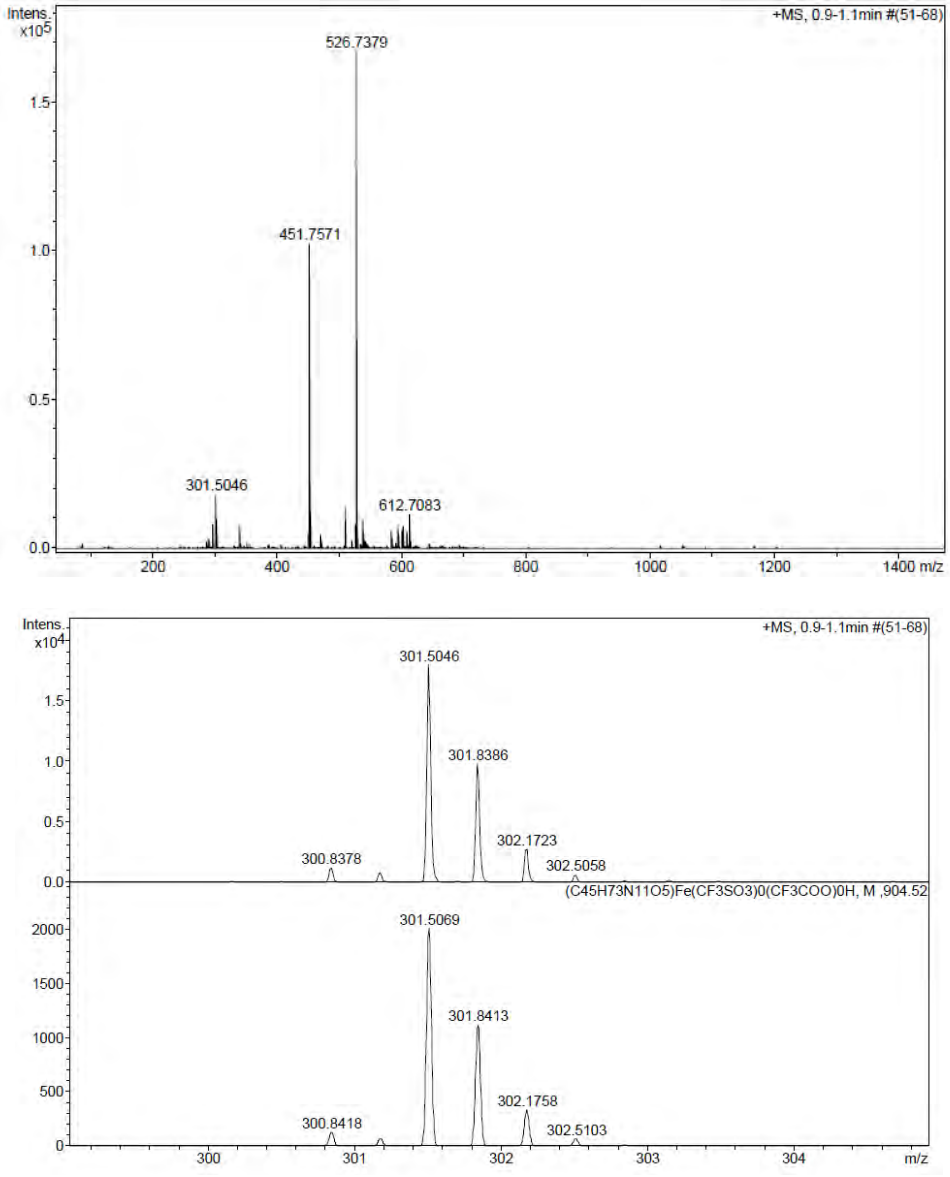

Observed HRMS (top) with the theoretical isotope prediction (bottom).

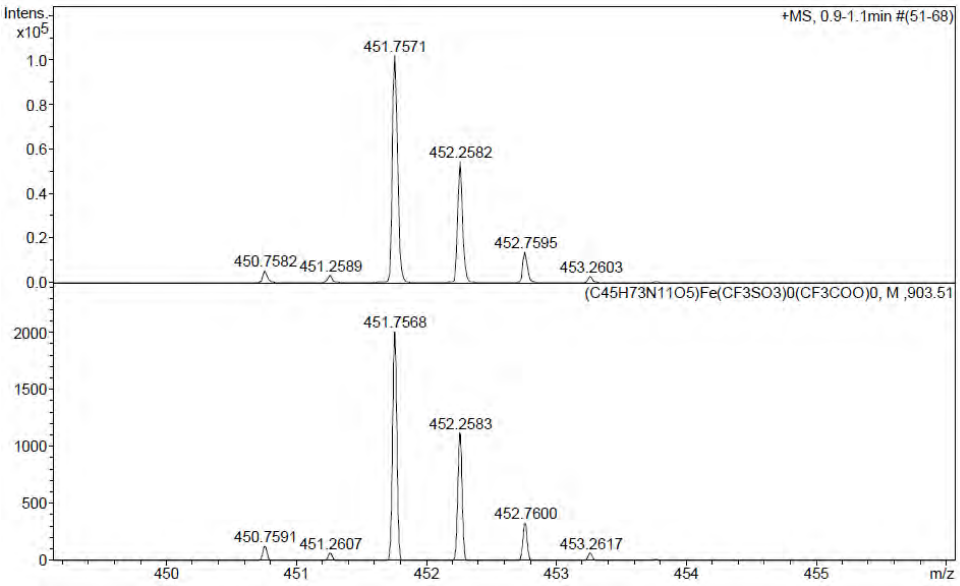

Observed HRMS (top) with the theoretical isotope prediction (bottom).

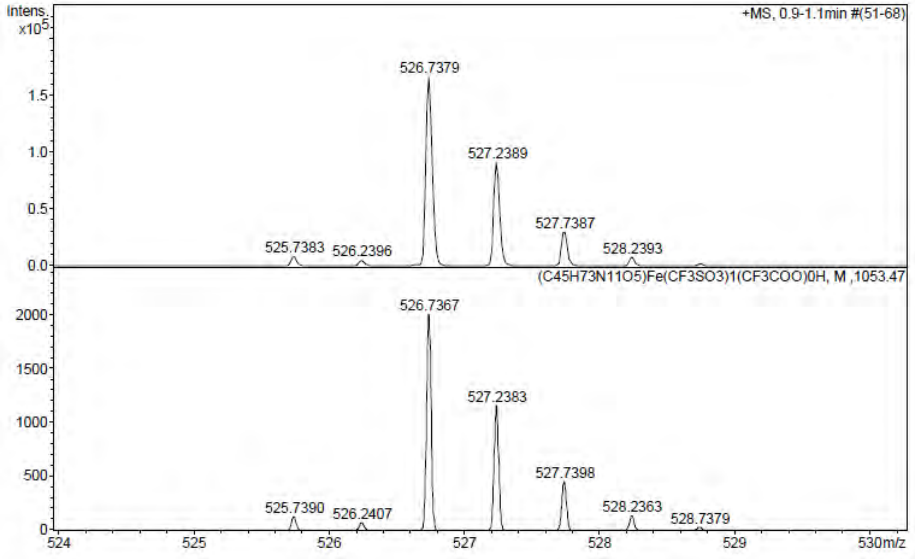

Observed HRMS (top) with the theoretical isotope prediction (bottom).

b)

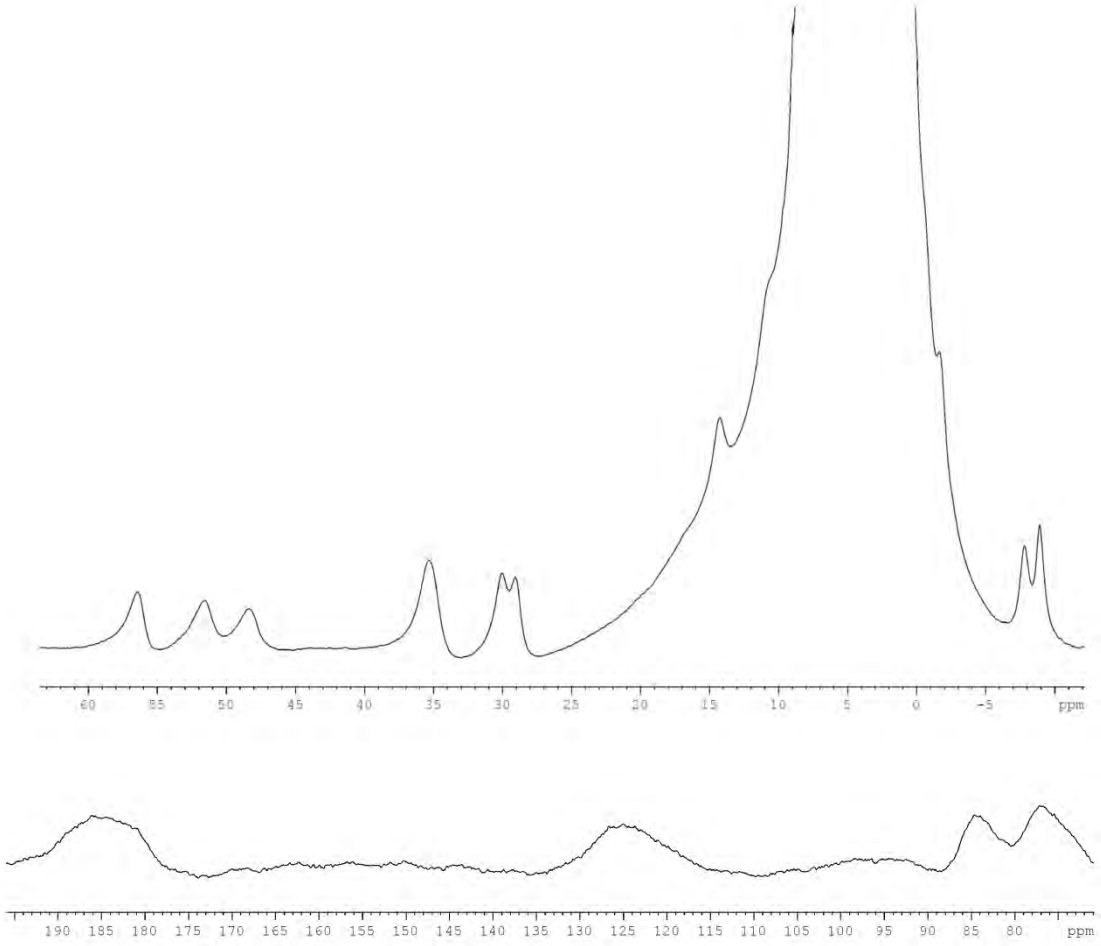
60 55 50 45 40 35 30 25 20 15 10 5 0 -5 ppm
190 185 180 175 170 165 160 155 150 145 140 135 130 125 120 115 110 105 100 95 90 85 80 ppm

Figure SV.19: a) HRMS spectrum (*m/z*)

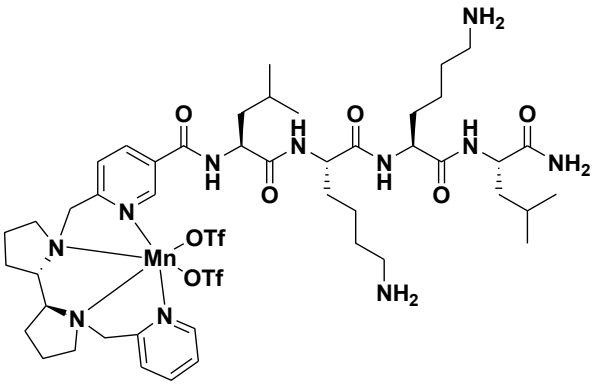

2_{Mn}

a)

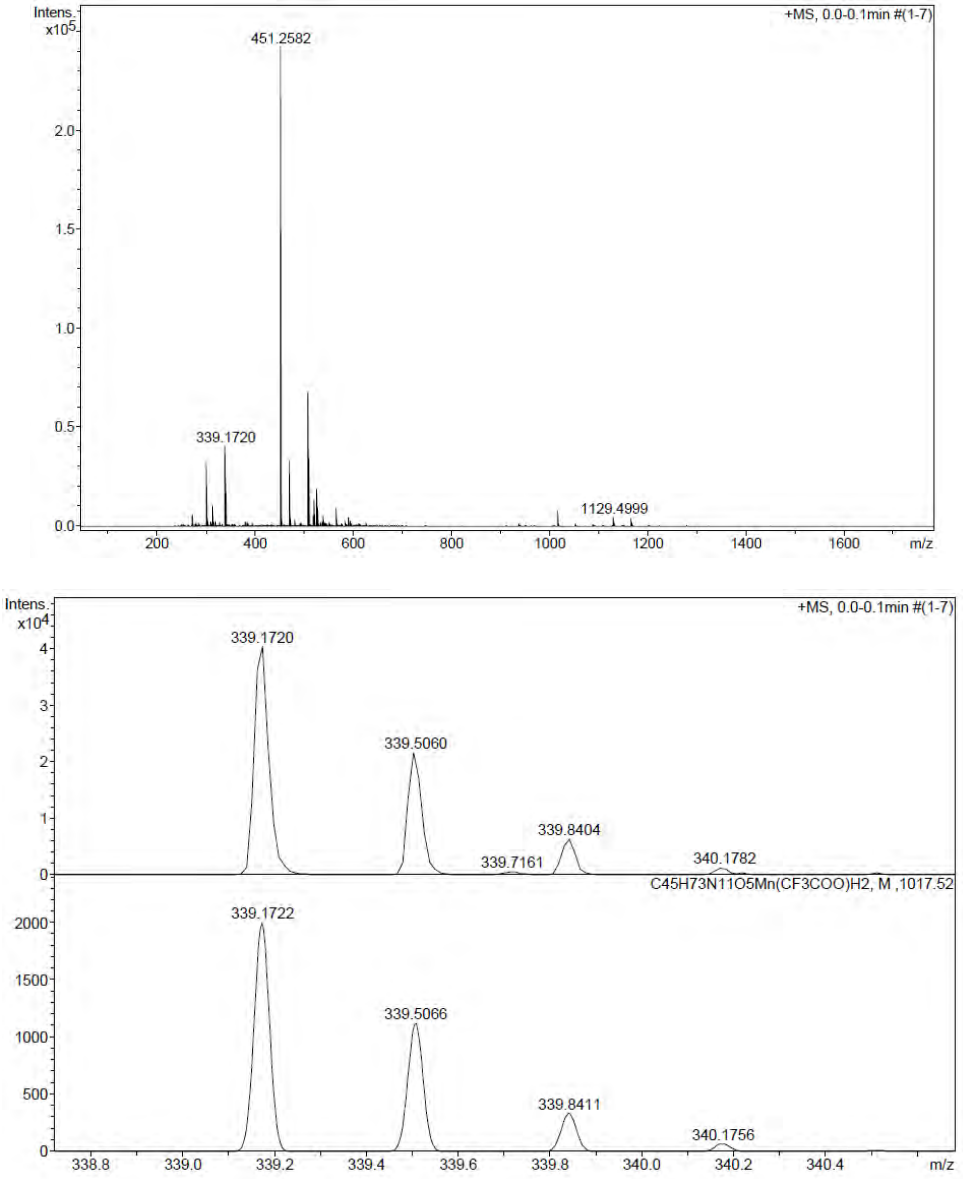

Observed HRMS (top) with the theoretical isotope prediction (bottom).

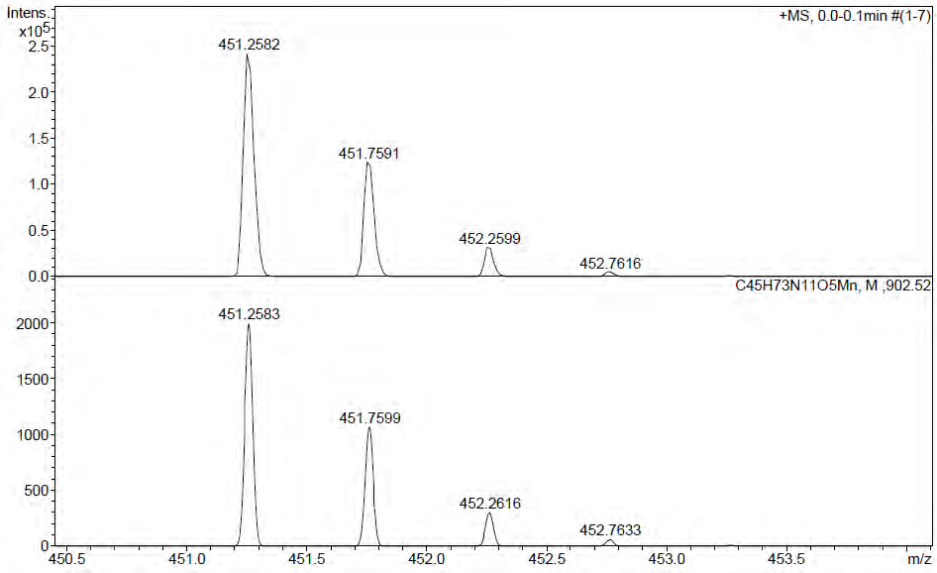

Observed HRMS (top) with the theoretical isotope prediction (bottom).

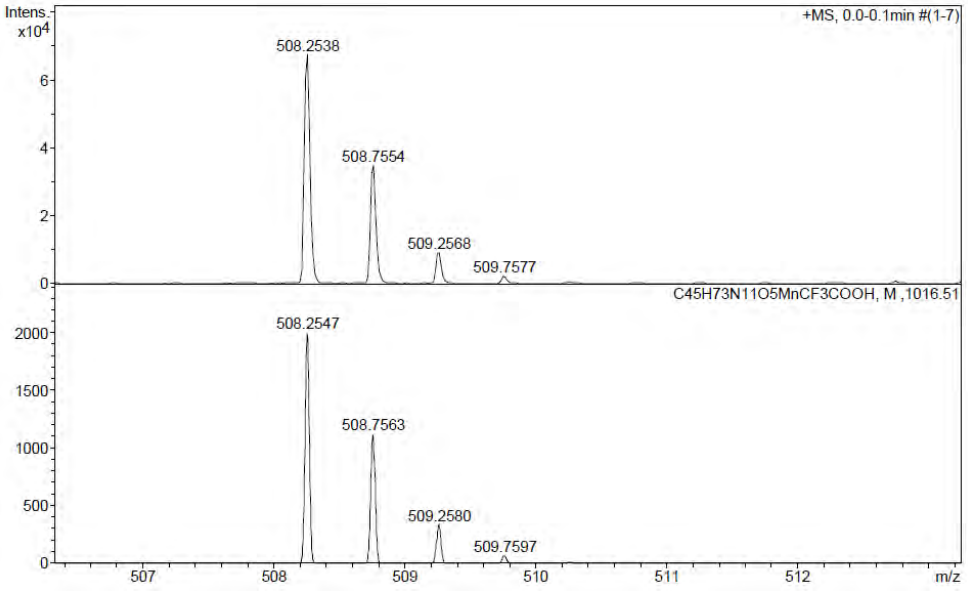

Observed HRMS (top) with the theoretical isotope prediction (bottom).

Figure SV.20: a) HRMS spectrum (*m/z*), b) ^{1}H NMR spectrum (400 MHz, CD_3OD)

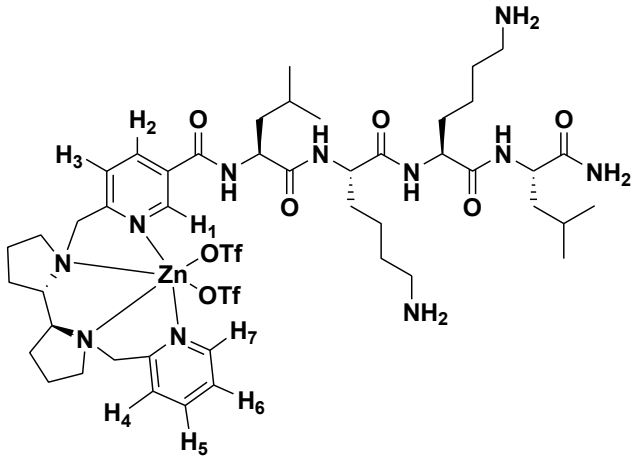

2_{Zn}

a)

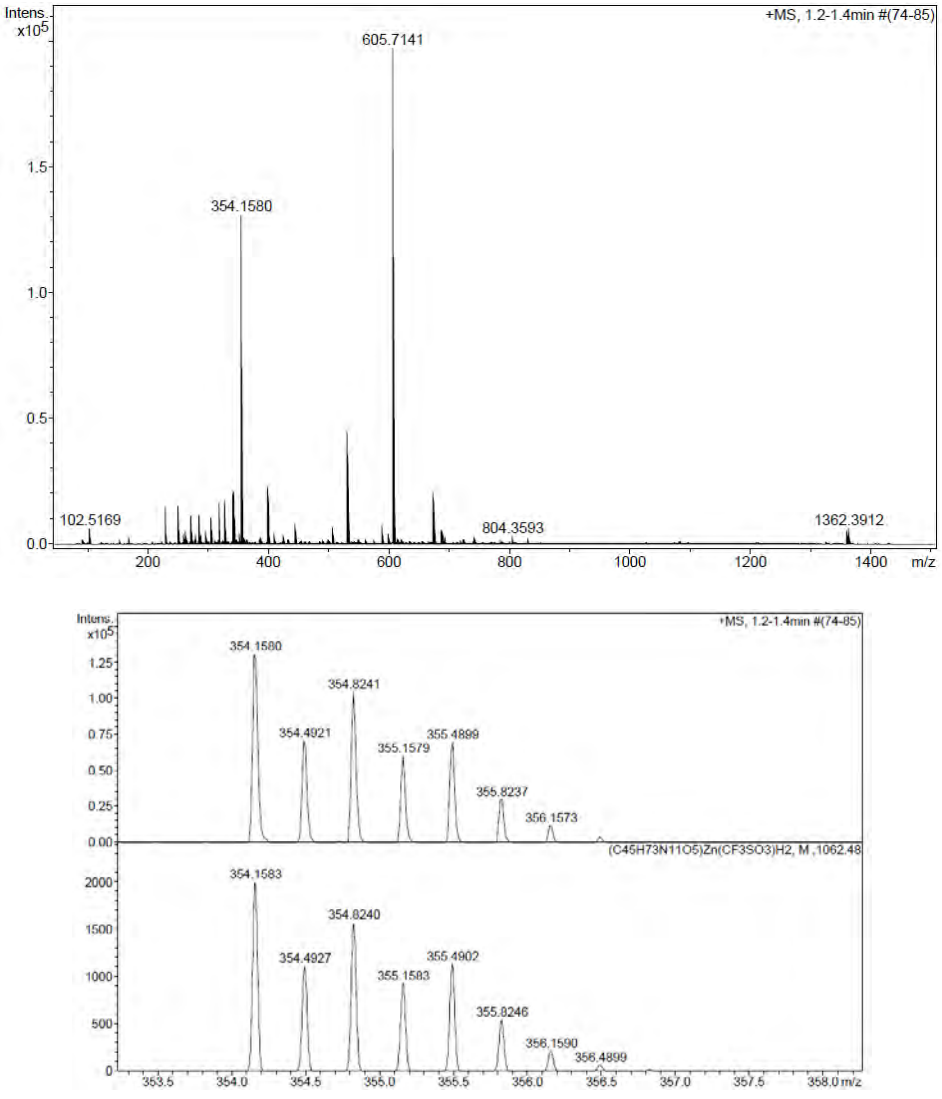

Observed HRMS (top) with the theoretical isotope prediction (bottom).

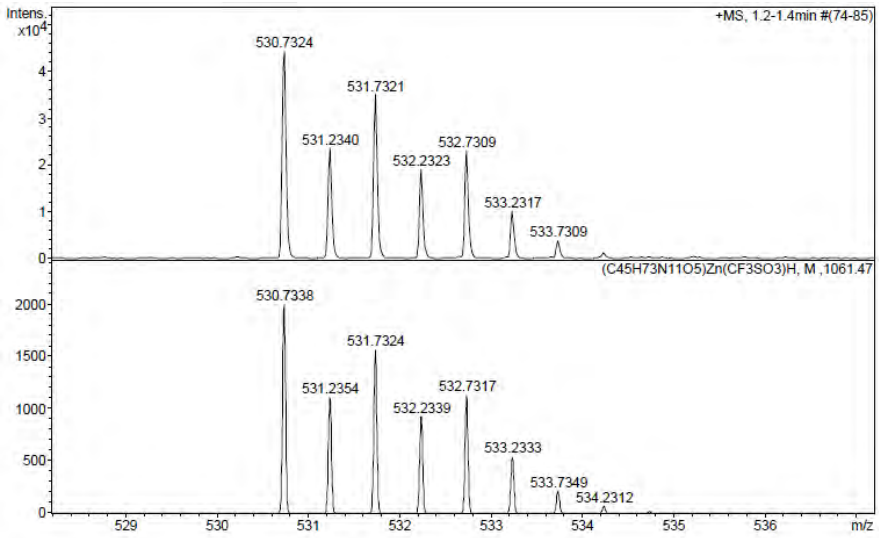

Observed HRMS (top) with the theoretical isotope prediction (bottom).

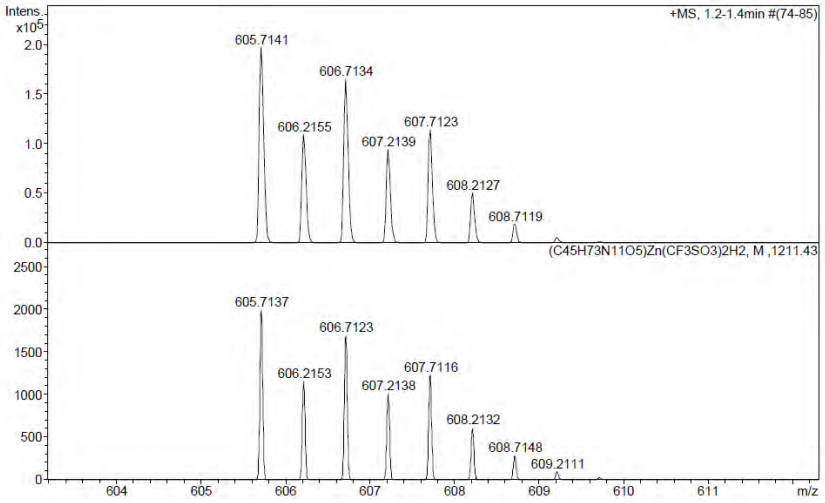

Observed HRMS (top) with the theoretical isotope prediction (bottom).

b)

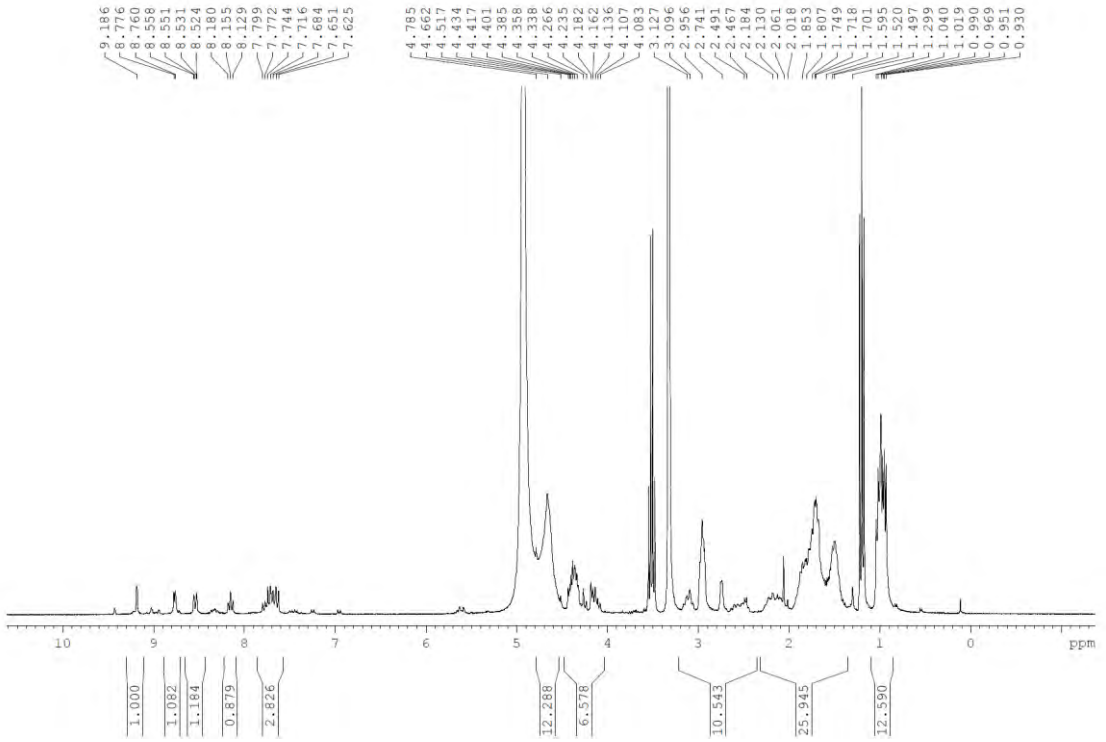
9.186
8.776
8.760
8.558
8.551
8.531
8.524
8.180
8.155
8.129
7.799
7.772
7.744
7.716
7.684
7.651
7.625
4.785
4.662
4.517
4.434
4.417
4.401
4.385
4.358
4.338
4.266
4.235
4.182
4.162
4.136
4.107
4.083
3.127
3.096
2.956
2.741
2.491
2.467
2.184
2.130
2.061
2.018
1.853
1.807
1.749
1.718
1.701
1.595
1.520
1.497
1.299
1.040
1.019
0.990
0.969
0.951
0.930
10
9
8
7
6
5
4
3
2
1
0
ppm
1.000
1.082
1.184
0.879
2.826
12.288
6.578
10.543
25.945
12.590

Figure SV.21: a) HRMS spectrum (*m/z*)

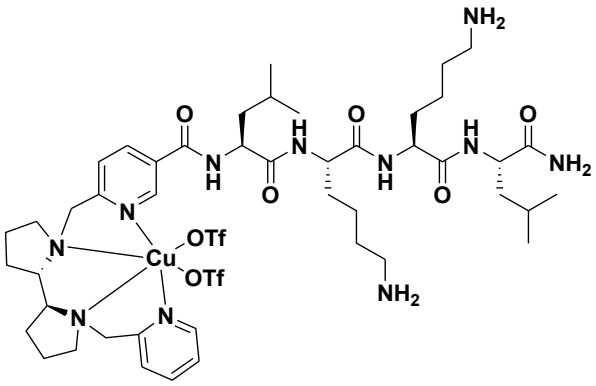

2_{Cu}

a)

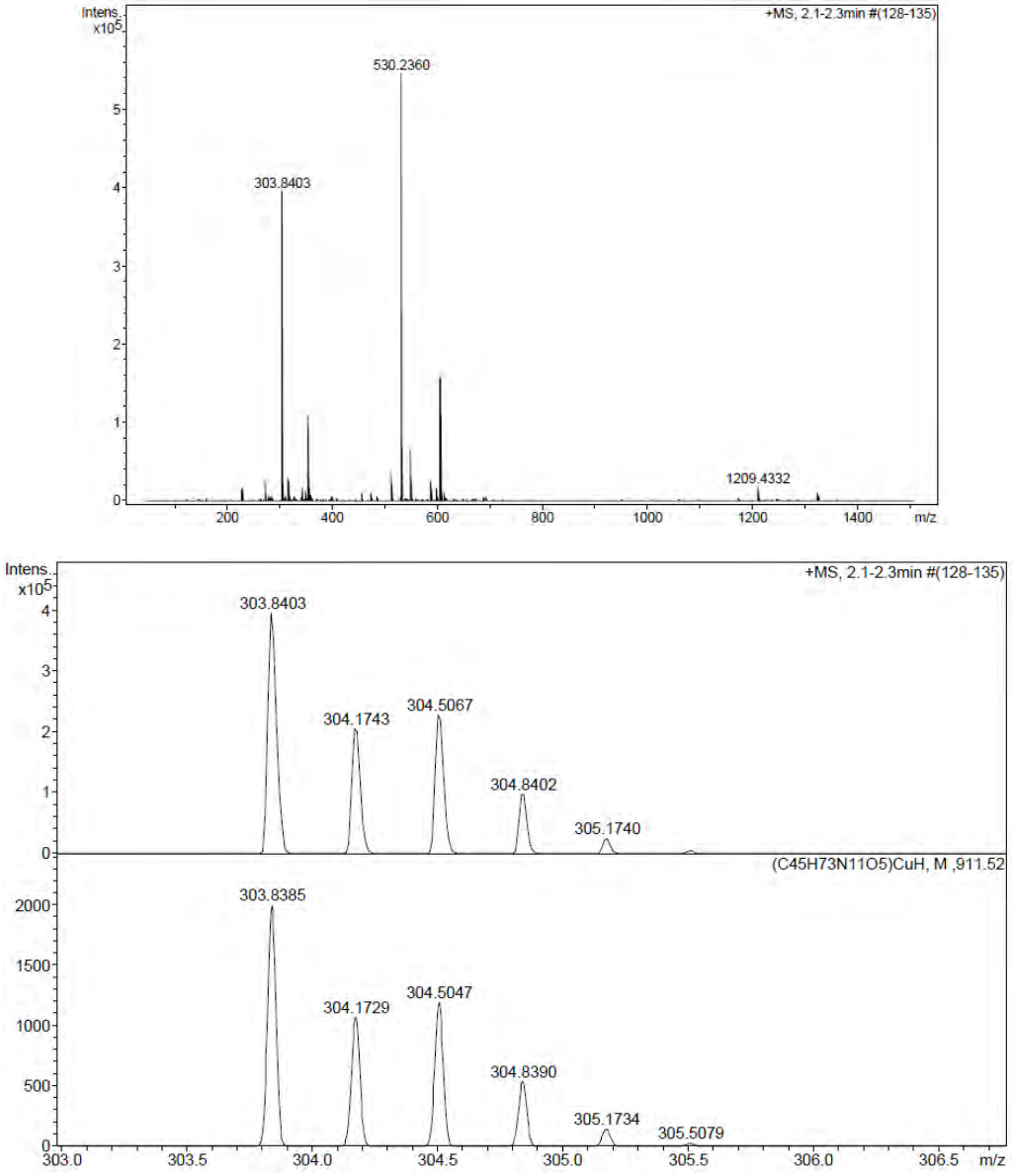

Observed HRMS (top) with the theoretical isotope prediction (bottom).

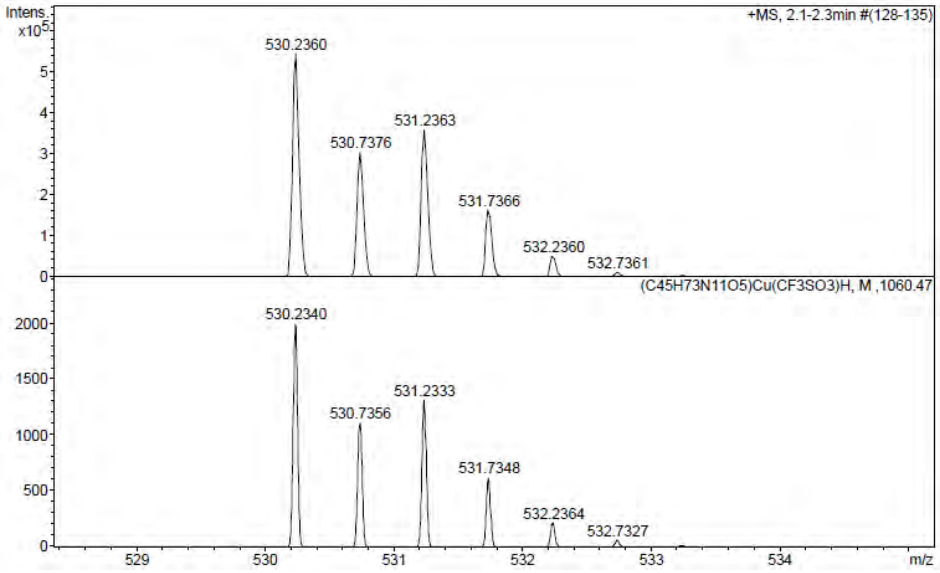

Observed HRMS (top) with the theoretical isotope prediction (bottom).

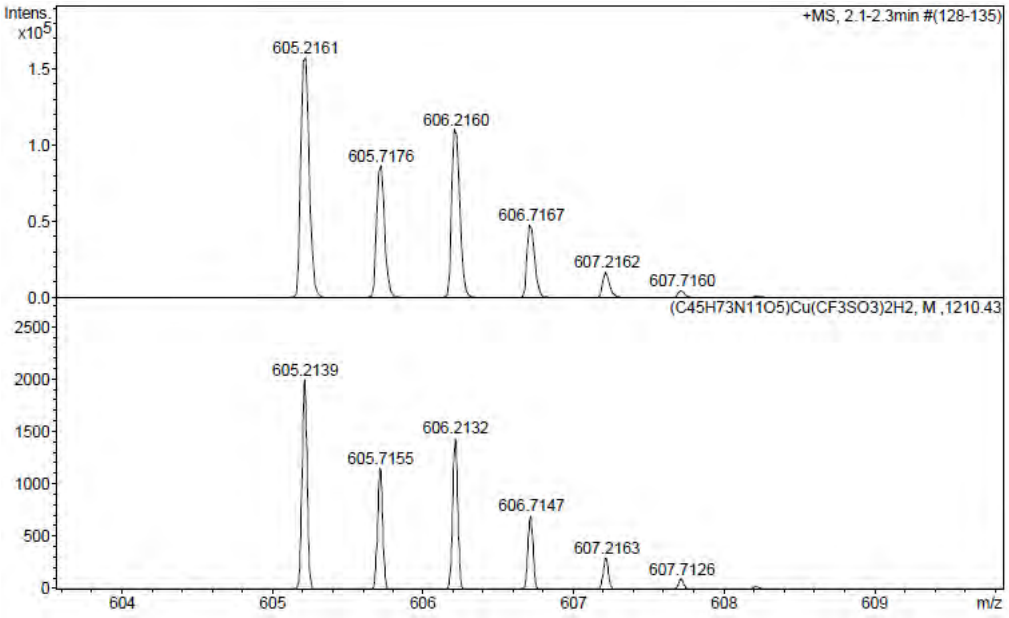

Observed HRMS (top) with the theoretical isotope prediction (bottom).

Figure SV.22: a) ^{19}F-NMR spectrum (400 MHz, CD_3OD) before isolation of free amine

a)

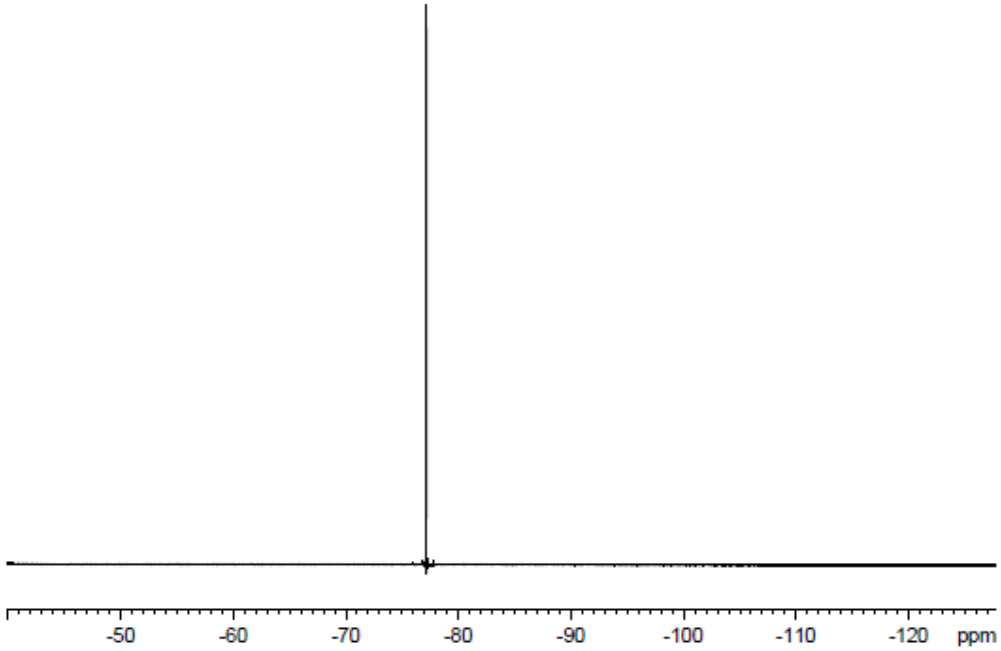

Figure SV.23: a) ^{19}F-NMR spectrum (400 MHz, CD_3OD) after isolation of free amine by column chromatography

a)

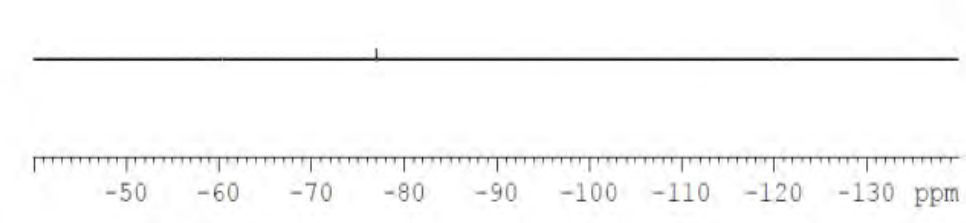

Supporting Information

Chapter VI: Delivering redox-active ligands into cancer cells through conjugation to the cell-penetrating peptide BP16

Table of contents

Figure SVI.1: a) ^{1}H NMR spectrum (400 MHz, $CDCl_3$), b) ^{13}C NMR spectrum (100 MHz, $CDCl_3$), c) ESI/MS spectrum (*m/z*).

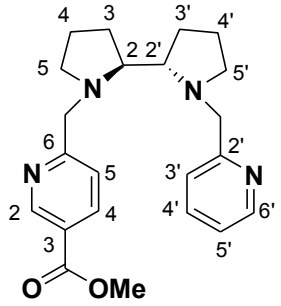

a)

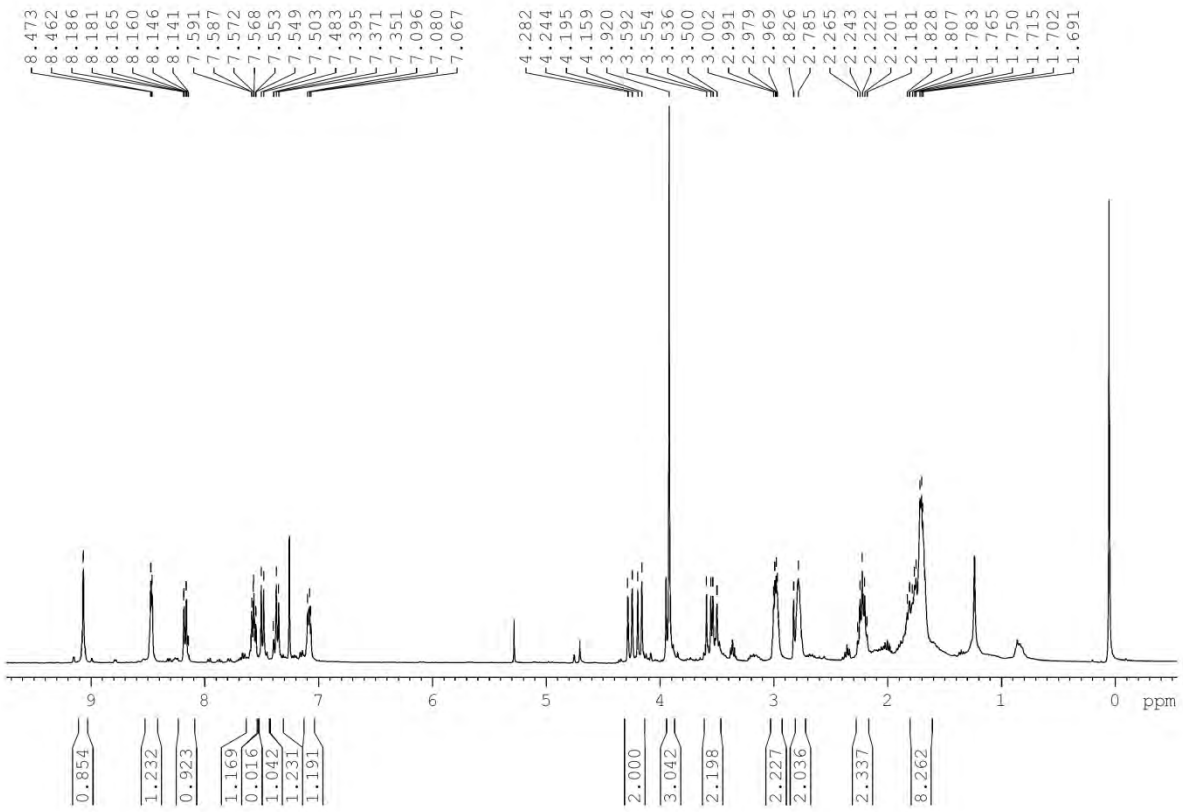

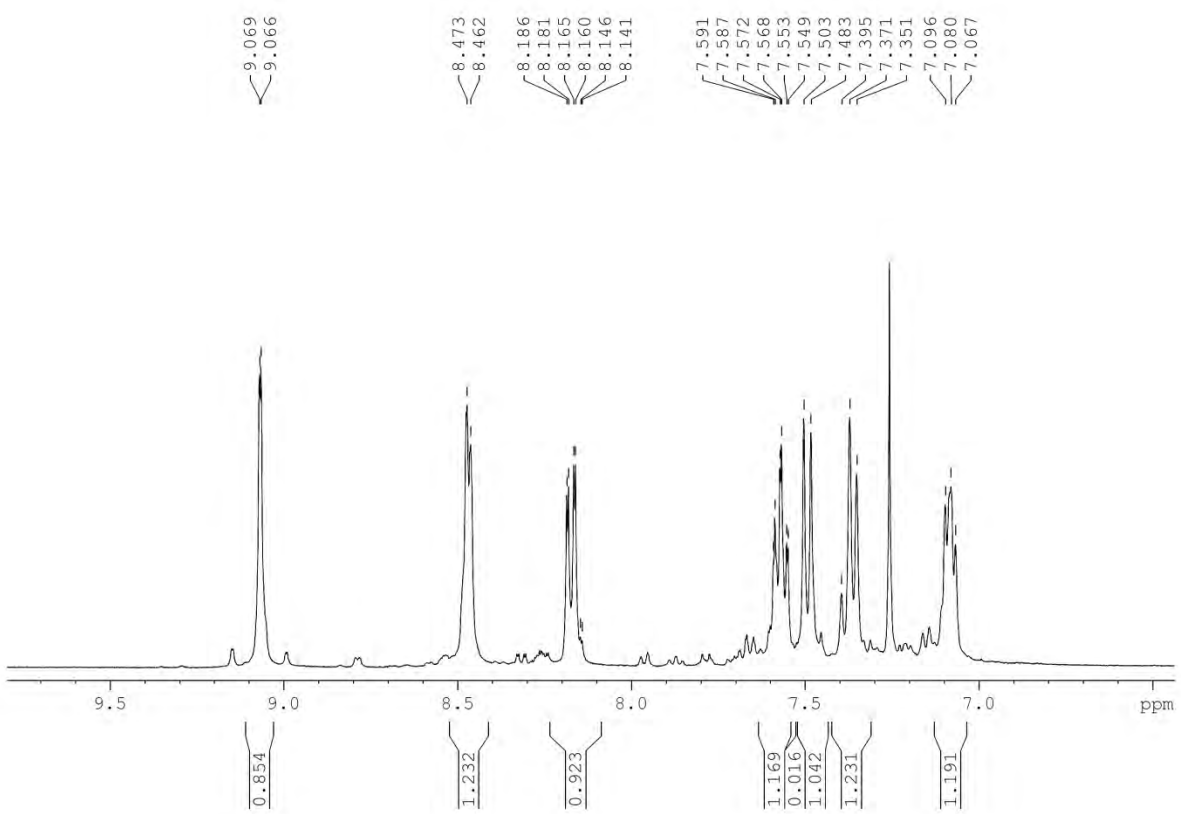

Selected aromatic region.

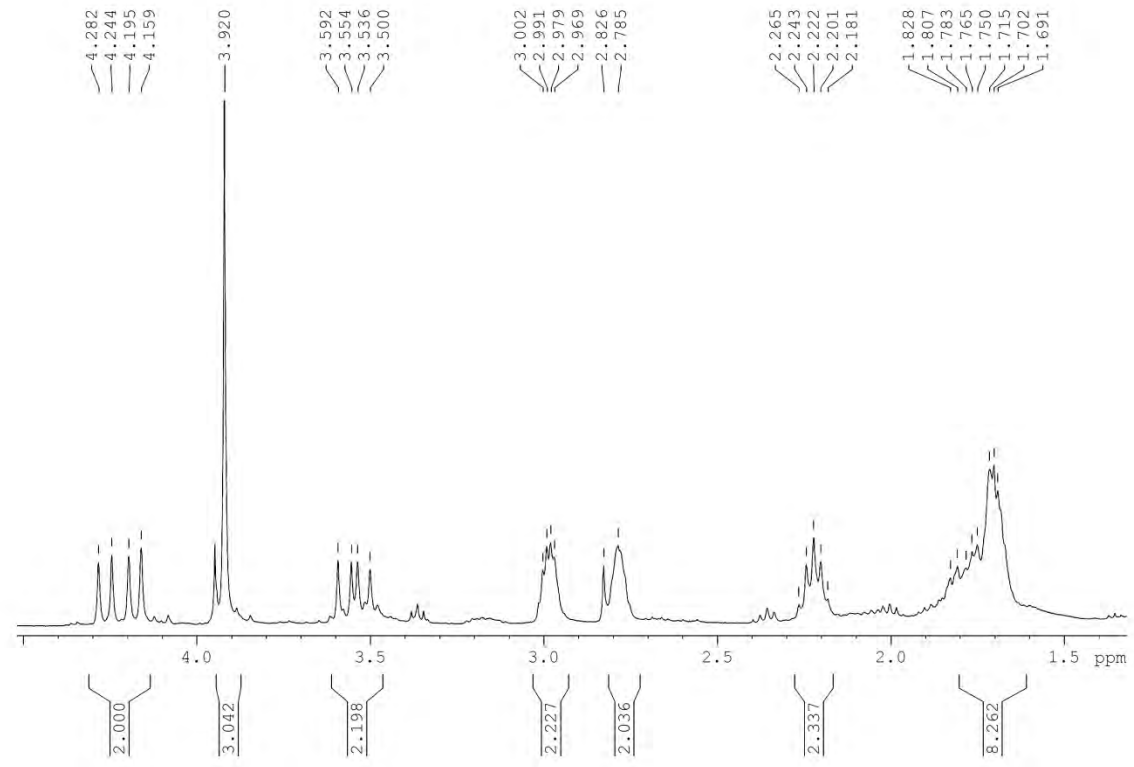

Selected aliphatic region.

b)

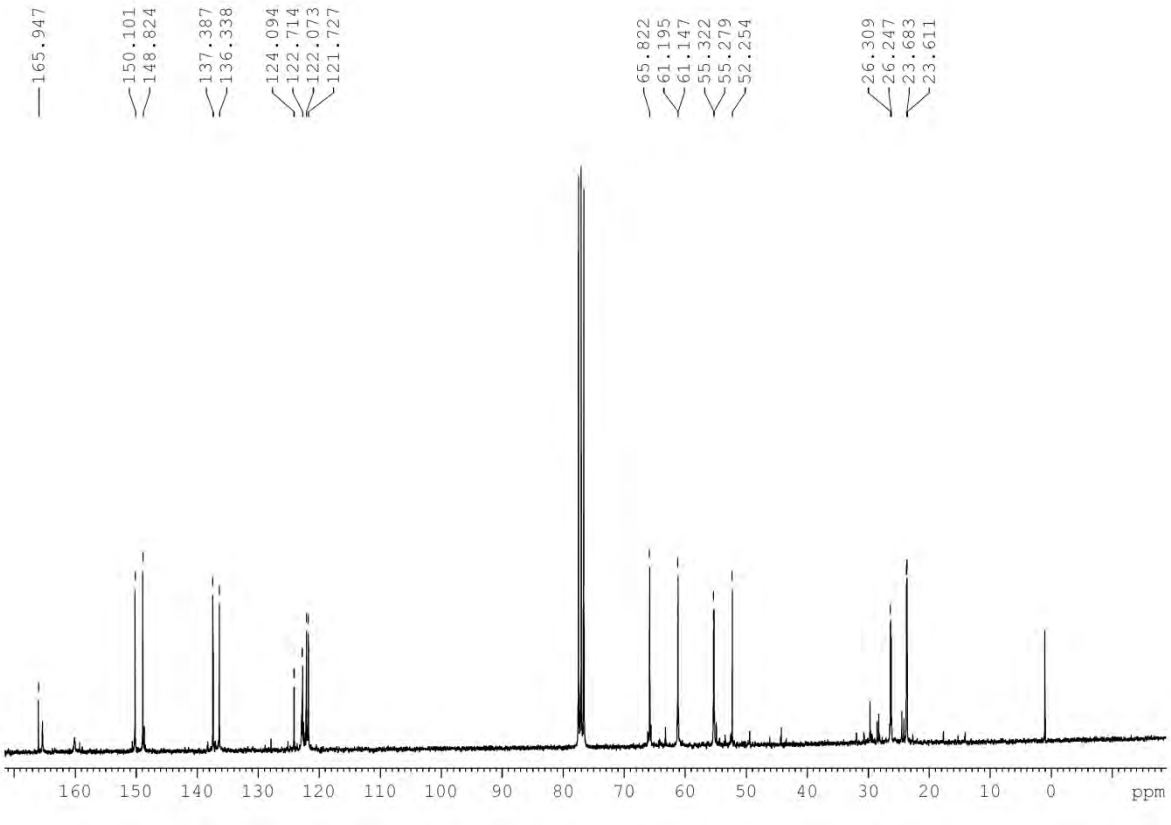
165.947
150.101
148.824
137.387
136.338
124.094
122.714
122.073
121.727
65.822
61.195
61.147
55.322
55.279
52.254
26.309
26.247
23.683
23.611
160 150 140 130 120 110 100 90 80 70 60 50 40 30 20 10 0 ppm

c)

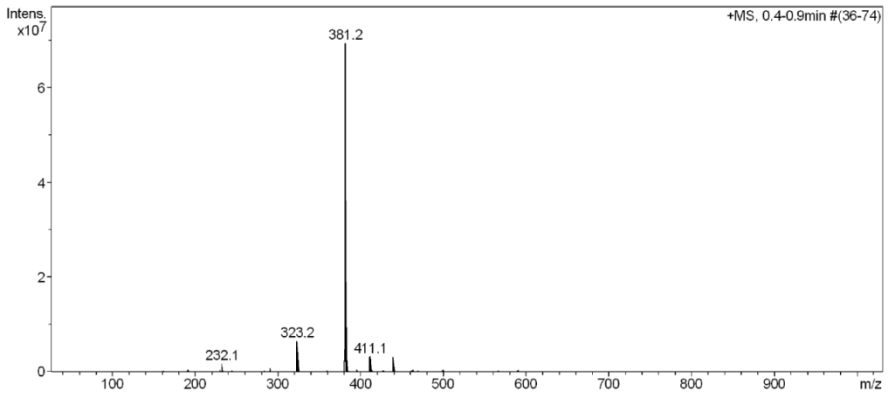
Intens.
x10^7
+MS, 0.4-0.9min #(36-74)
381.2
323.2
232.1
411.1
0 2 4 6
100 200 300 400 500 600 700 800 900 m/z

Figure SVI.2: a) ^{1}H NMR spectrum (400 MHz, $CDCl_3$), b) ESI/MS spectrum (*m/z*), c) HRMS spectrum (*m/z*)

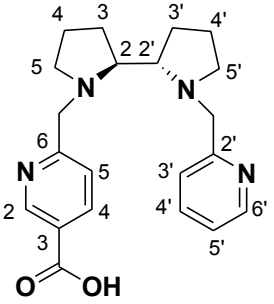

4

a)

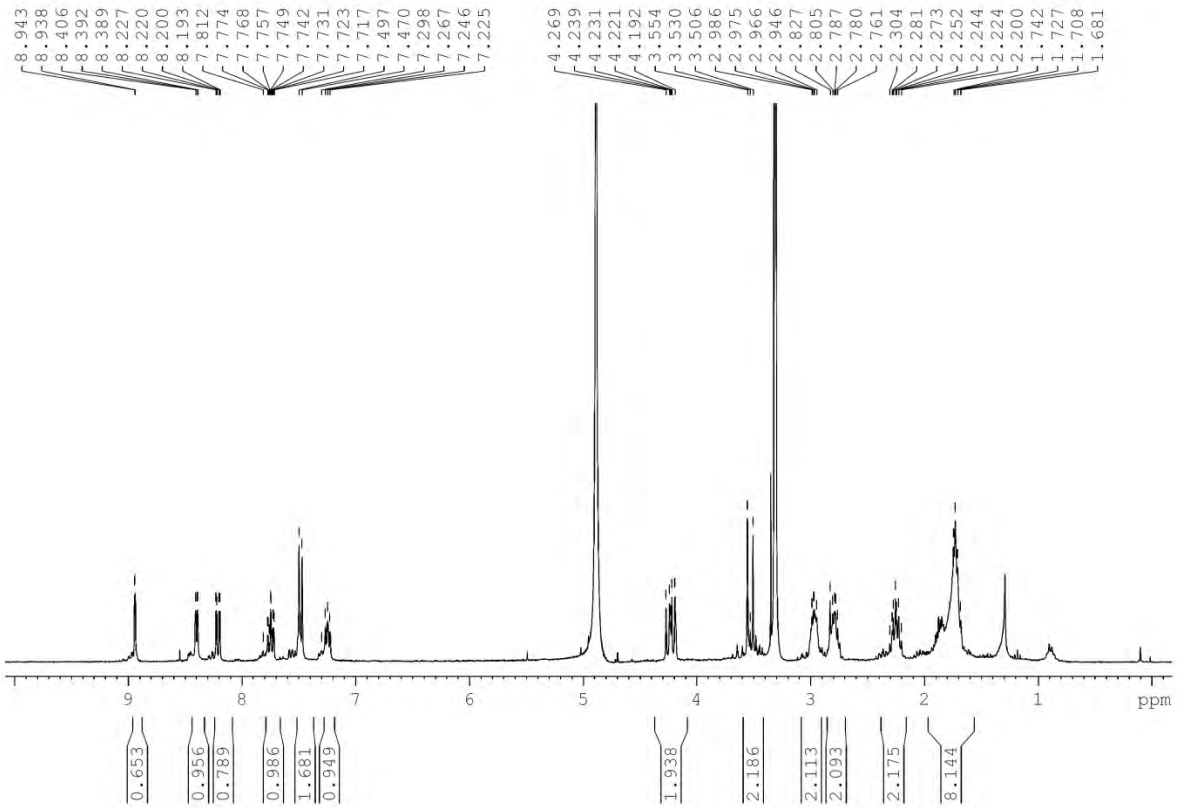

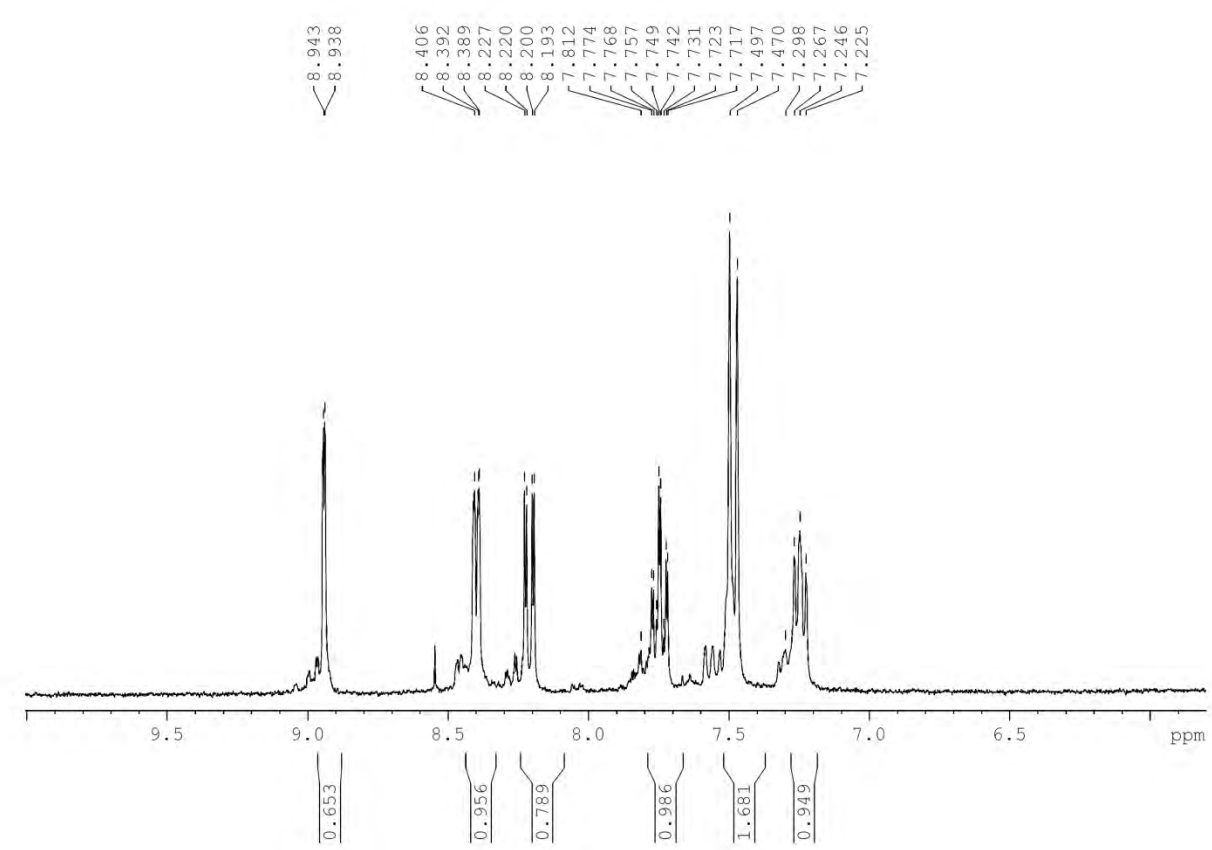

Selected aromatic region.

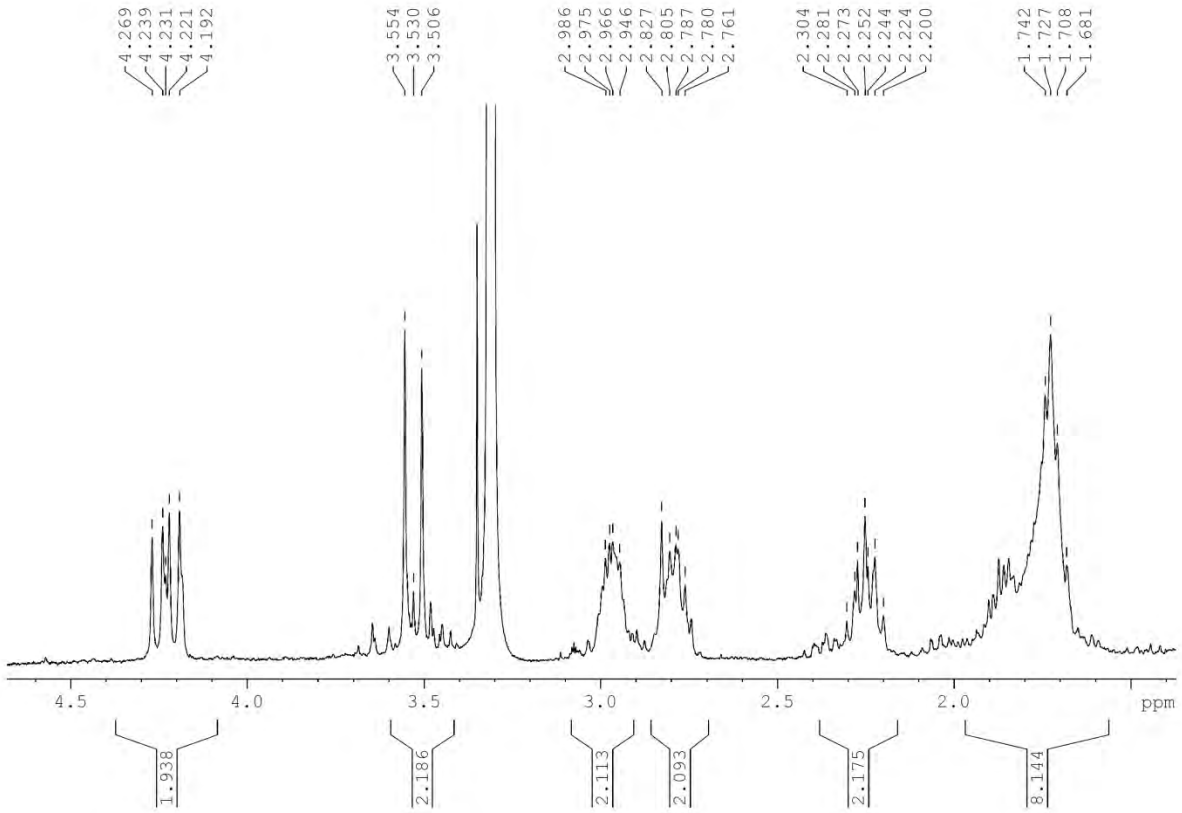

Selected aliphatic region.

b)

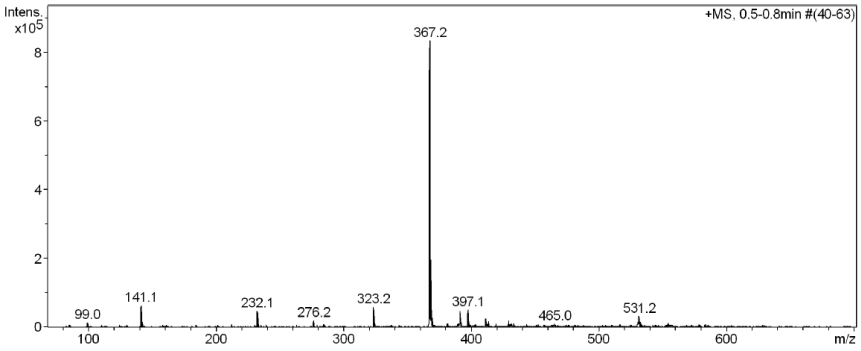

c)

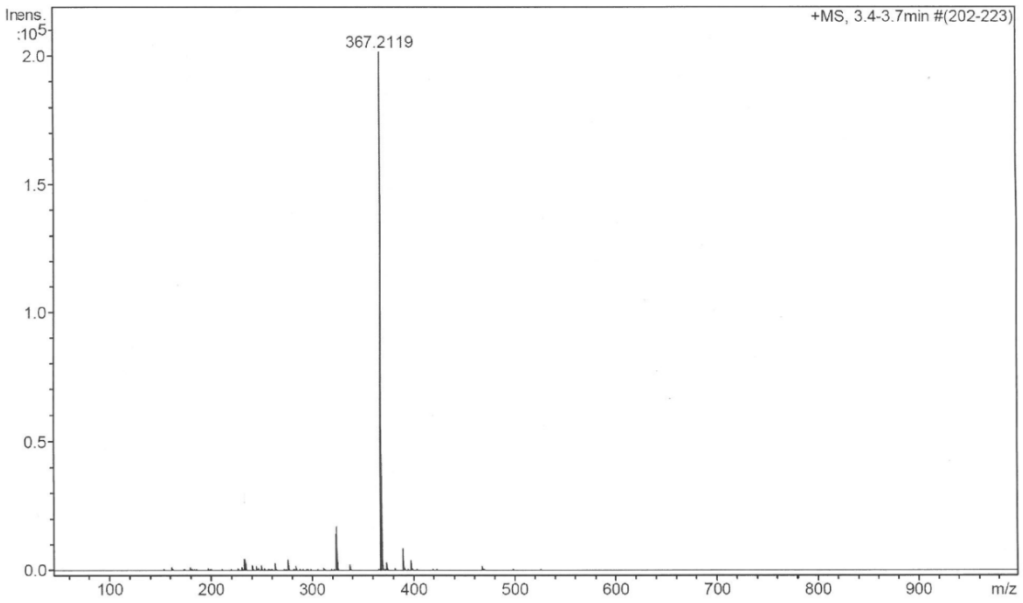

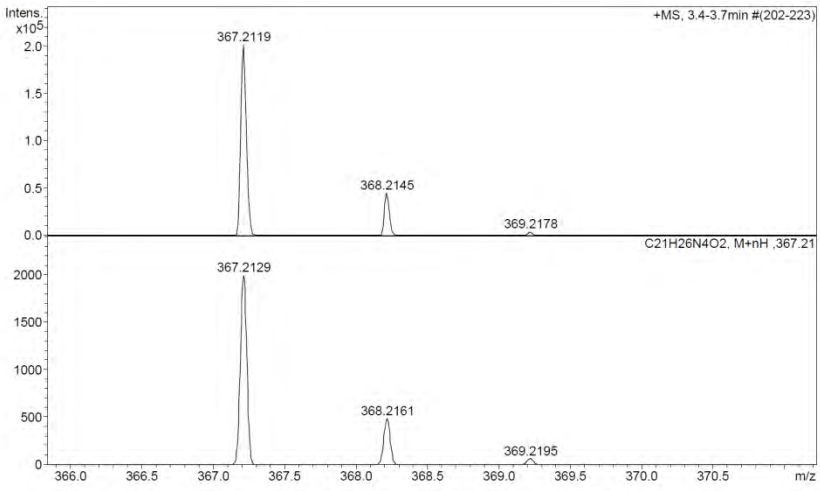

Observed HRMS (top) with the theoretical isotope prediction (bottom).

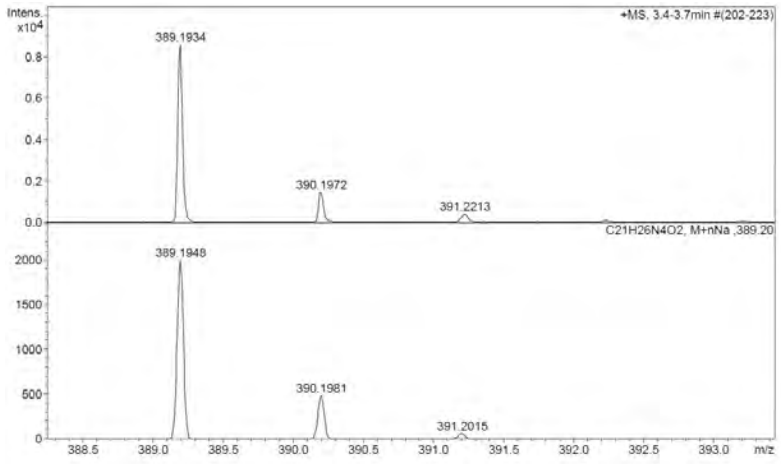

Observed HRMS (top) with the theoretical isotope prediction (bottom).

Figure SVI.3: a) HPLC chromatogram (λ= 220 nm), b) ESI/MS spectrum (*m/z*), c) HRMS spectrum (*m/z*).

PyTACN-BP16 (**BP341**)

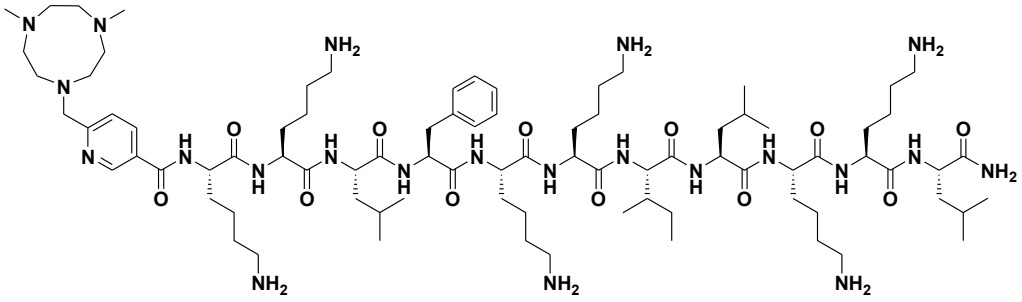

a)

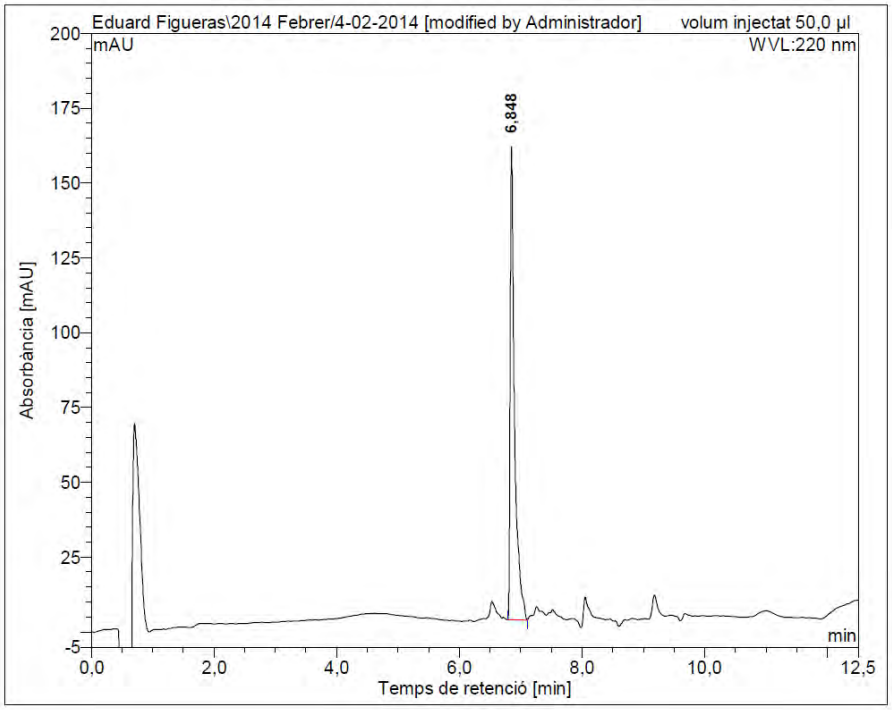

No.	Temps retenció min	alçada mAU	Area mAU*min	Area relativa %
1	6,85	158,135	13,168	100,00
Total:		158,135	13,168	100,00

b)

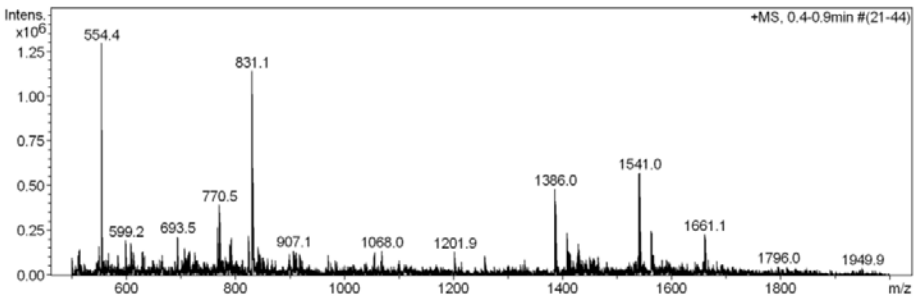

c)

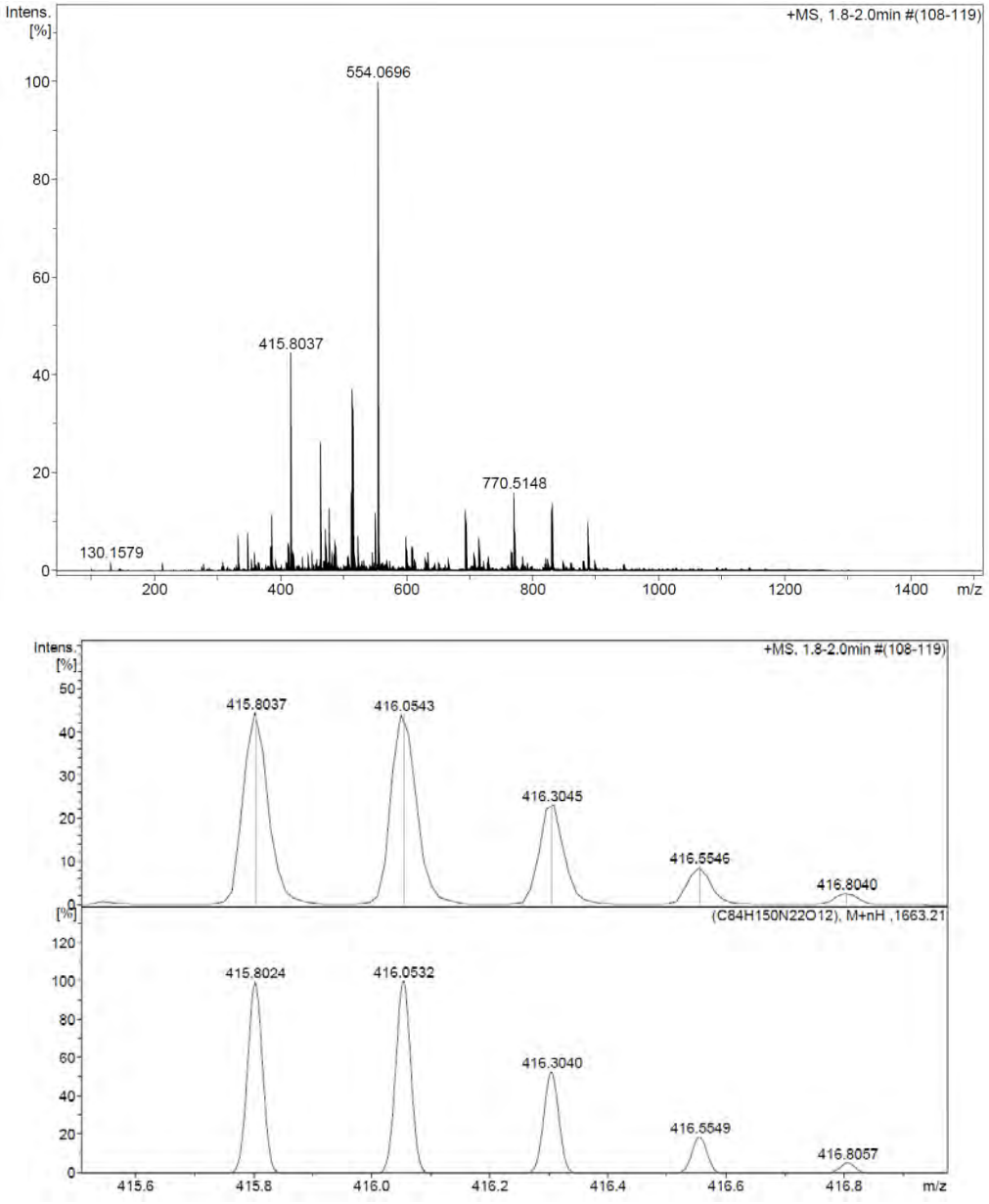

Observed HRMS (top) with the theoretical isotope prediction (bottom).

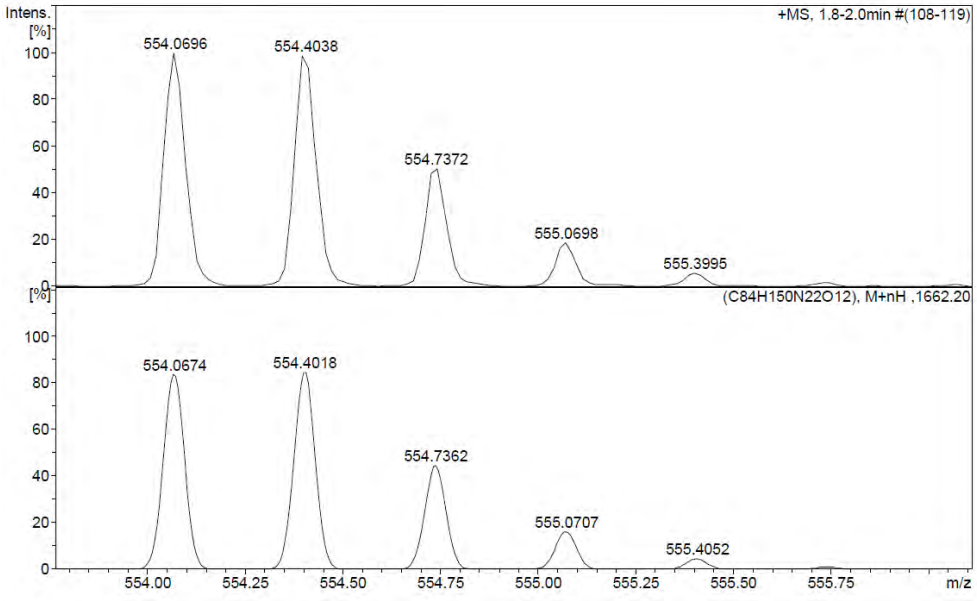

Observed HRMS (top) with the theoretical isotope prediction (bottom).

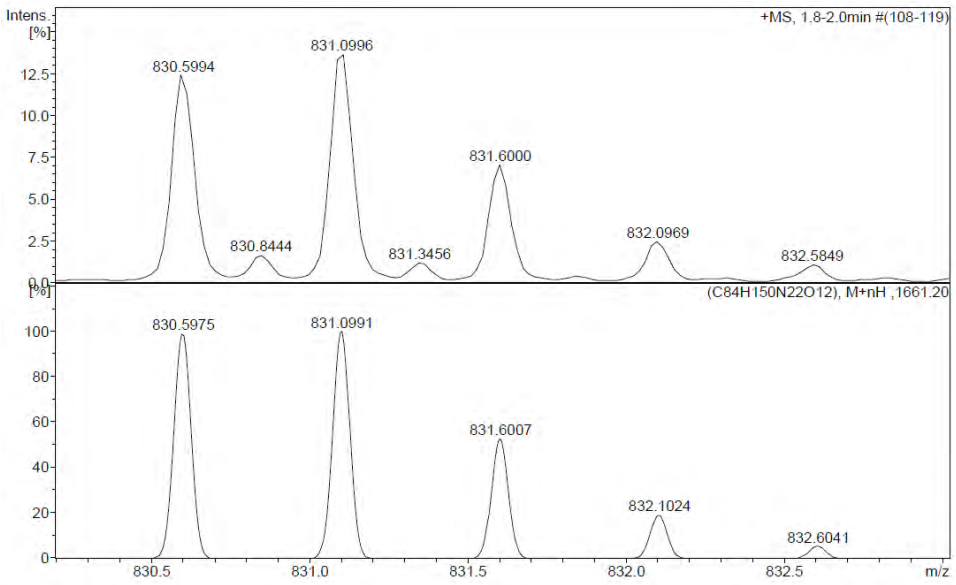

Observed HRMS (top) with the theoretical isotope prediction (bottom).

Figure SVI.4: a) HPLC chromatogram (λ= 220 nm), b) ESI/MS spectrum (*m/z*), c) HRMS spectrum (*m/z*).

BP16-PyTACN (**BP342**)

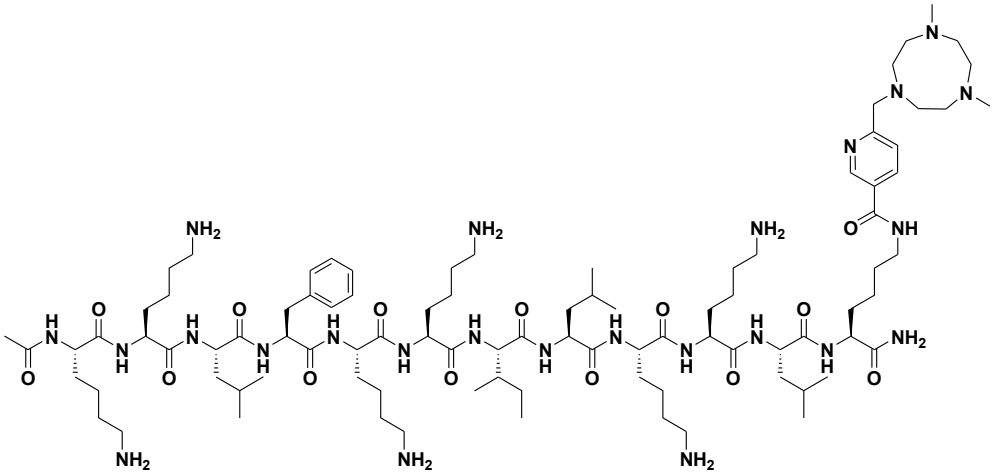

a)

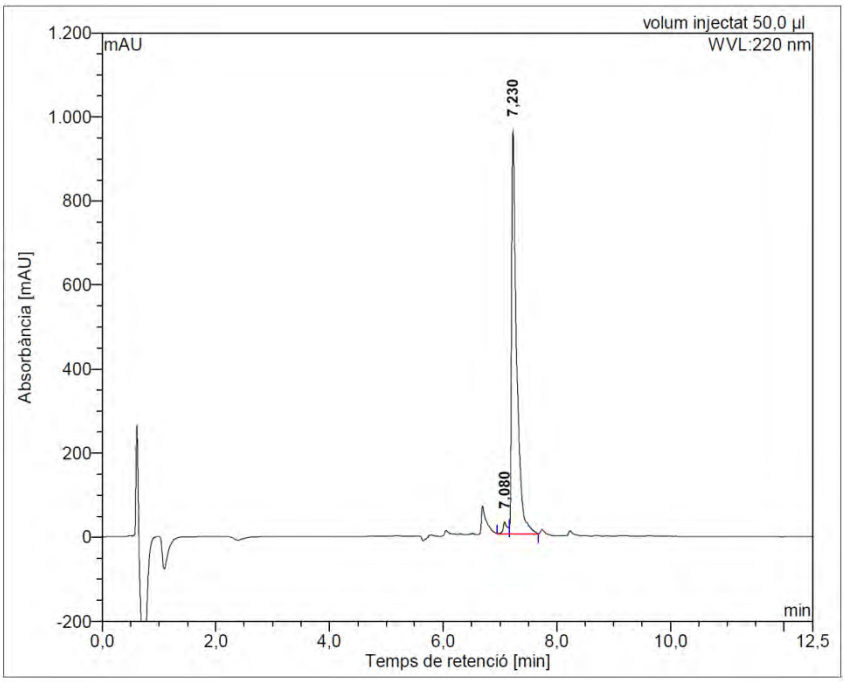

No.	mps retenc min	alçada mAU	Area mAU*min	Area relativa %
1	7,08	27,640	2,269	2,26
2	7,23	960,864	98,165	97,74
Total:		988,504	100,434	100,00

b)

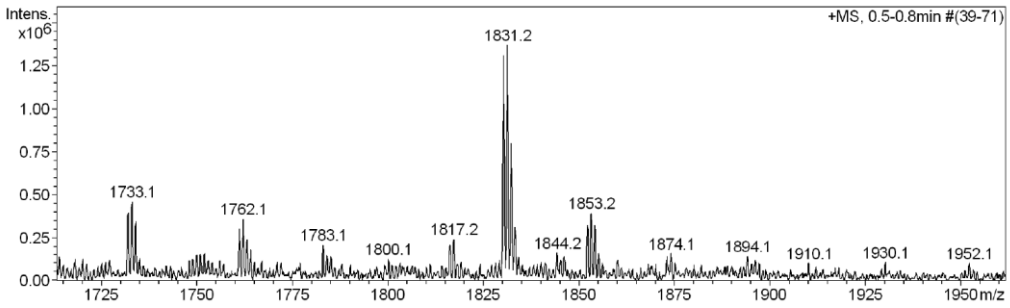

c)

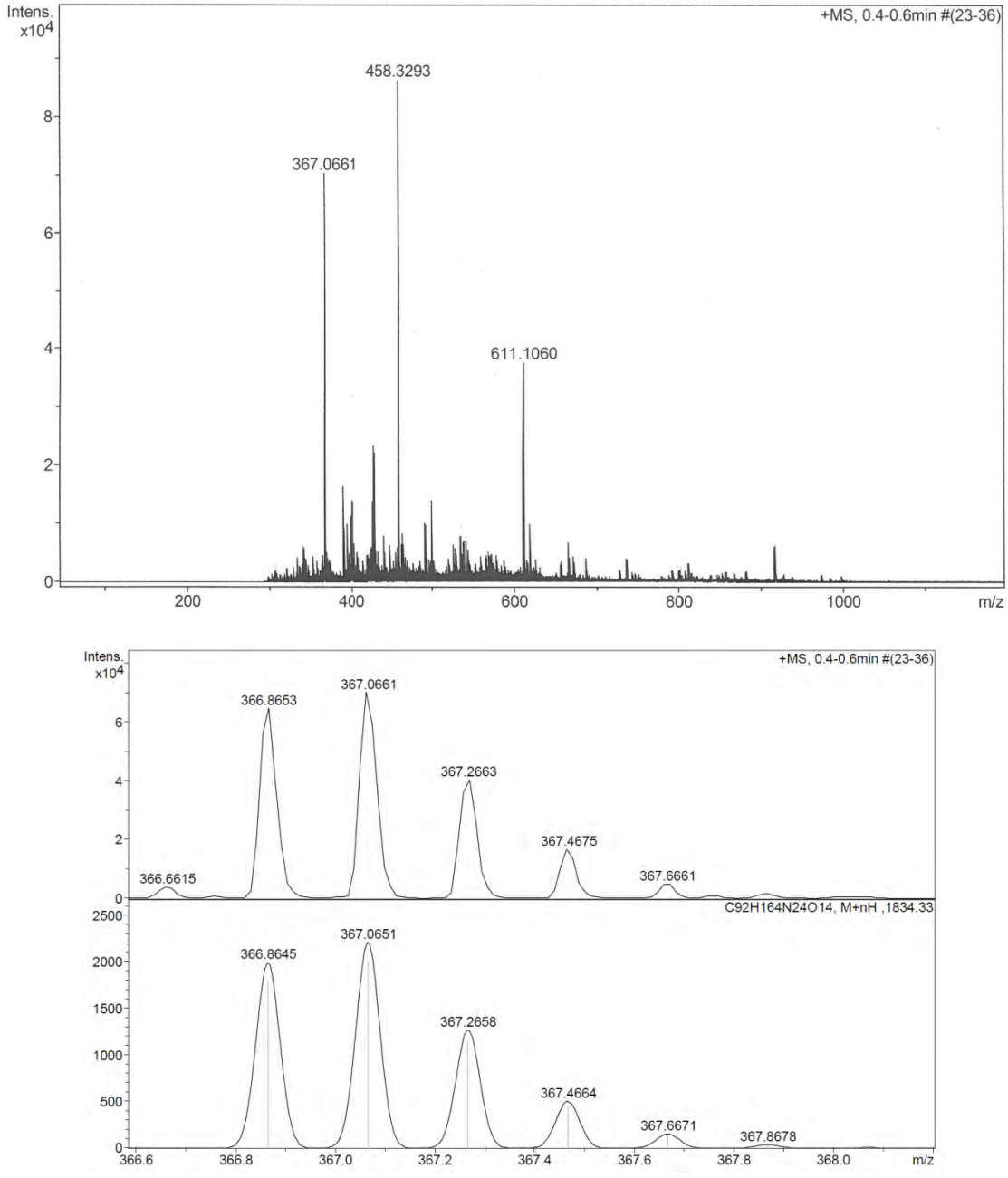

Observed HRMS (top) with the theoretical isotope prediction (bottom).

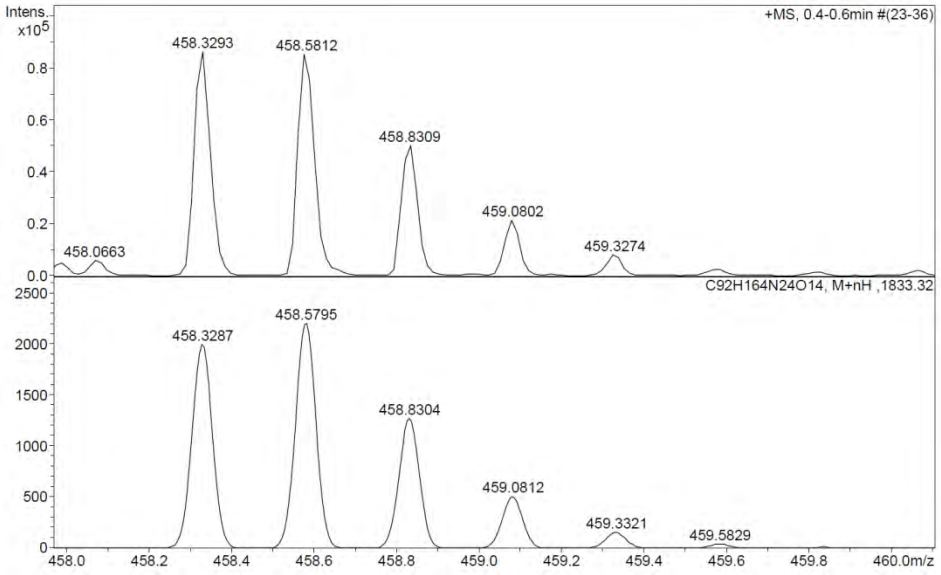

Observed HRMS (top) with the theoretical isotope prediction (bottom).

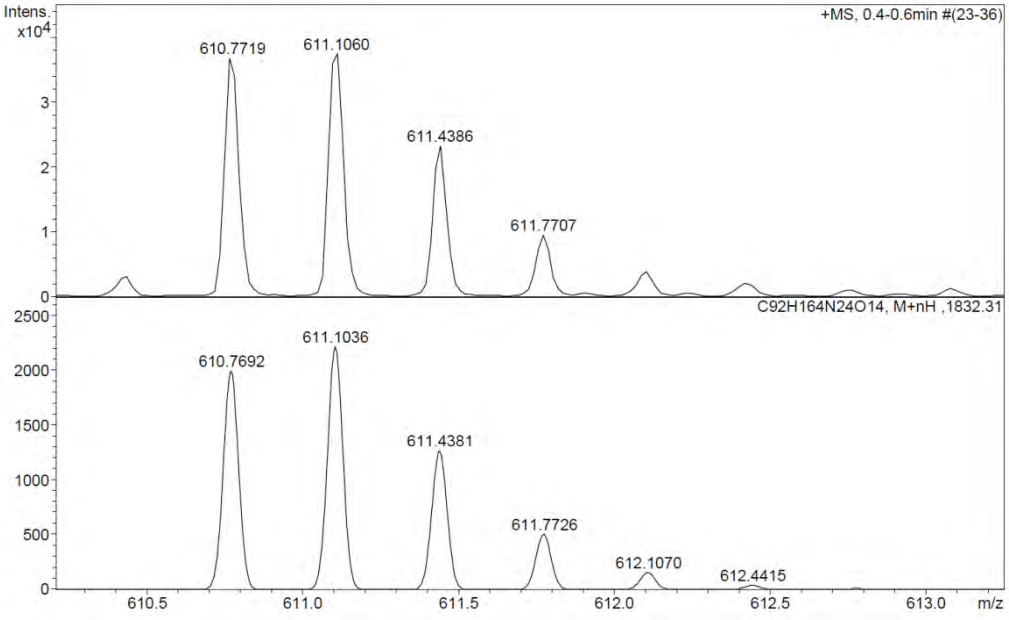

Observed HRMS (top) with the theoretical isotope prediction (bottom).

Figure SVI.5: a) HPLC chromatogram (λ= 220 nm), b) ESI/MS spectrum (*m/z*), c) HRMS spectrum (*m/z*).

BPBP-BP16 (**BP343**)

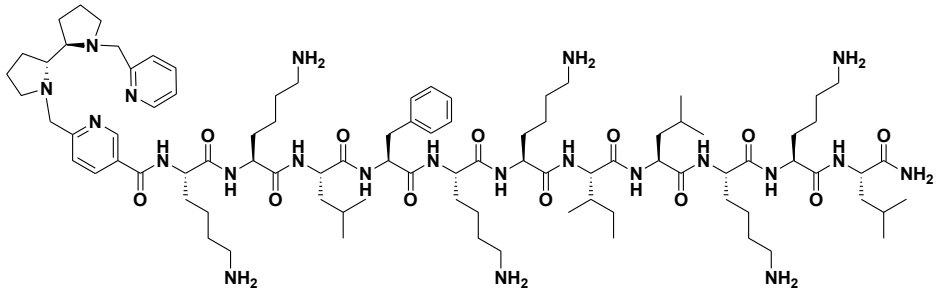

a)

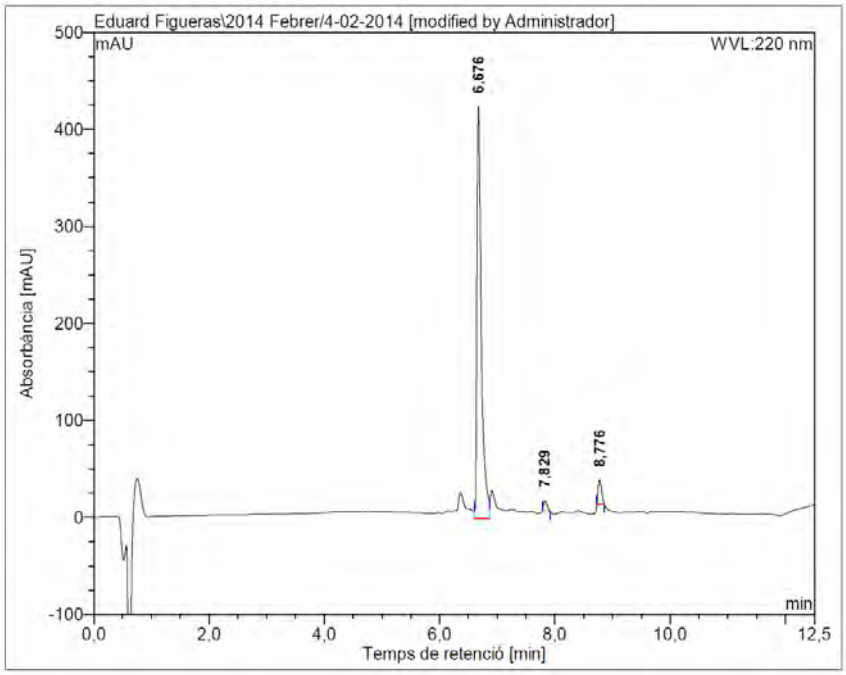

No.	Temps retenció min	alçada mAU	Area mAU*min	Area relativa %
1	6,68	425,084	37,620	93,83
2	7,83	10,533	0,771	1,92
3	8,78	24,513	1,703	4,25
Total:		460,131	40,094	100,00

b)

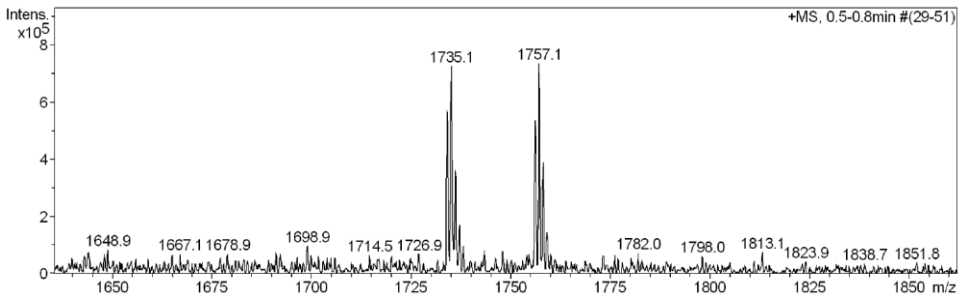

c)

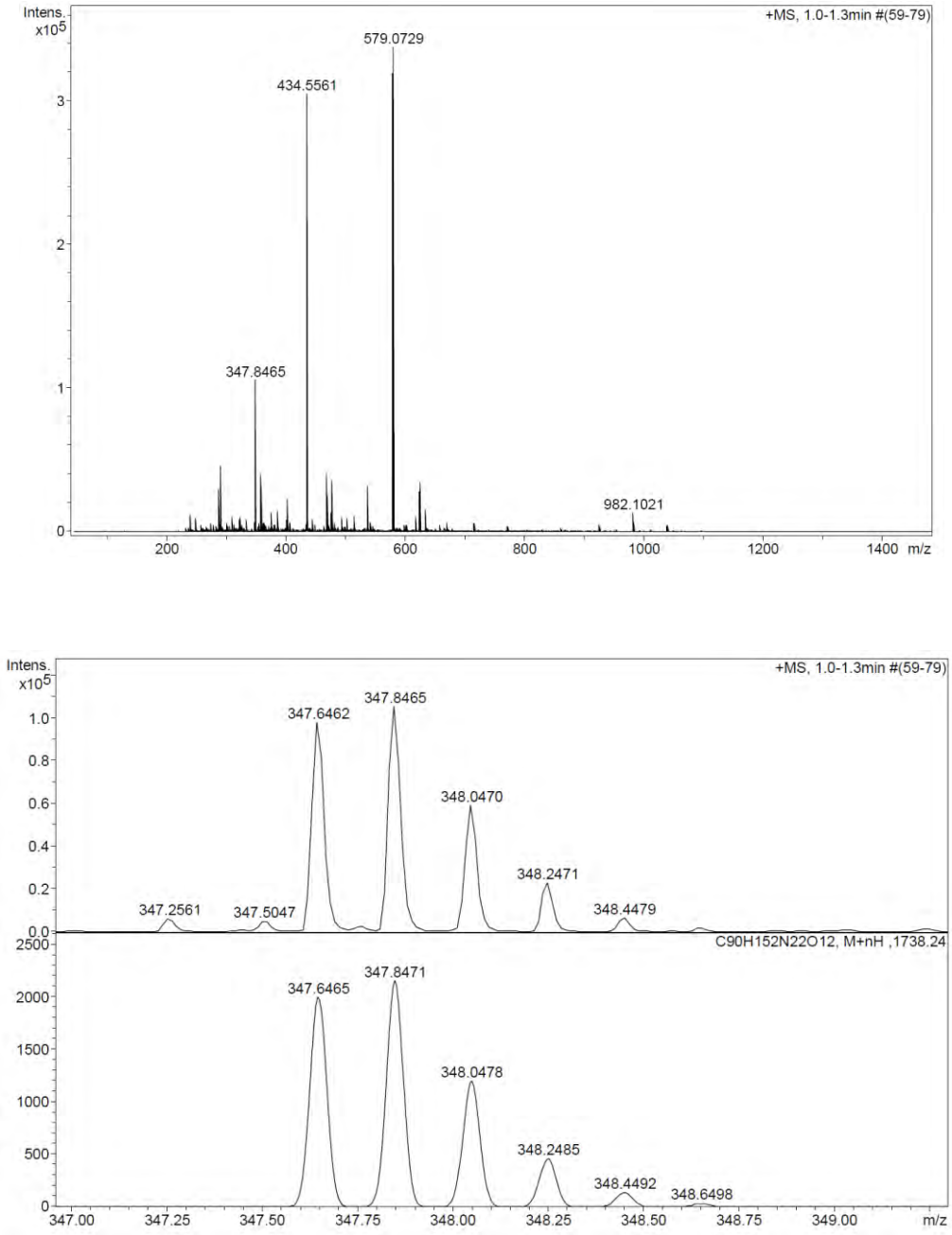

Observed HRMS (top) with the theoretical isotope prediction (bottom).

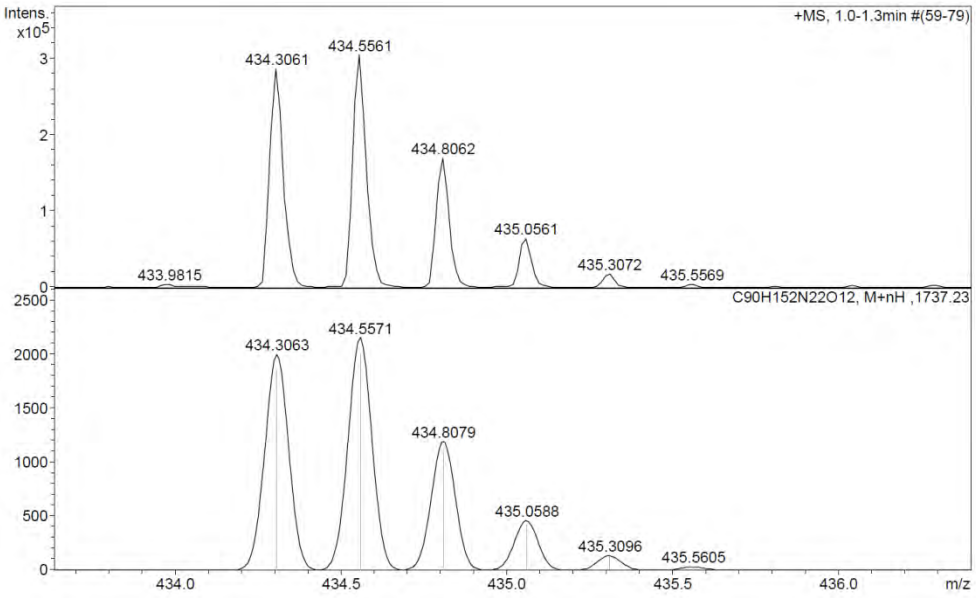

Observed HRMS (top) with the theoretical isotope prediction (bottom).

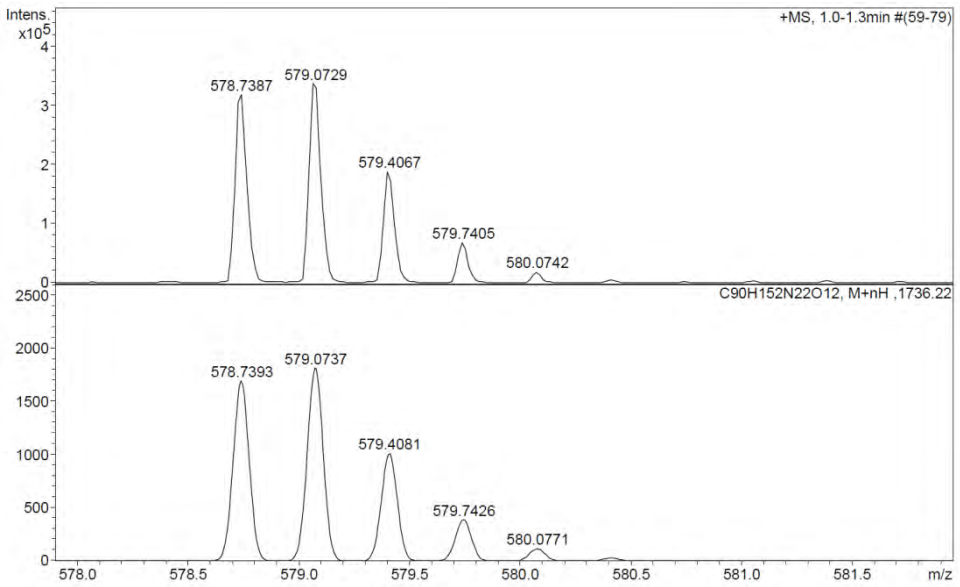

Observed HRMS (top) with the theoretical isotope prediction (bottom).

Figure SVI.6: a) HPLC chromatogram (λ= 220 nm), b) HRMS spectrum (*m/z*).

BP16-BPBP (**BP344**)

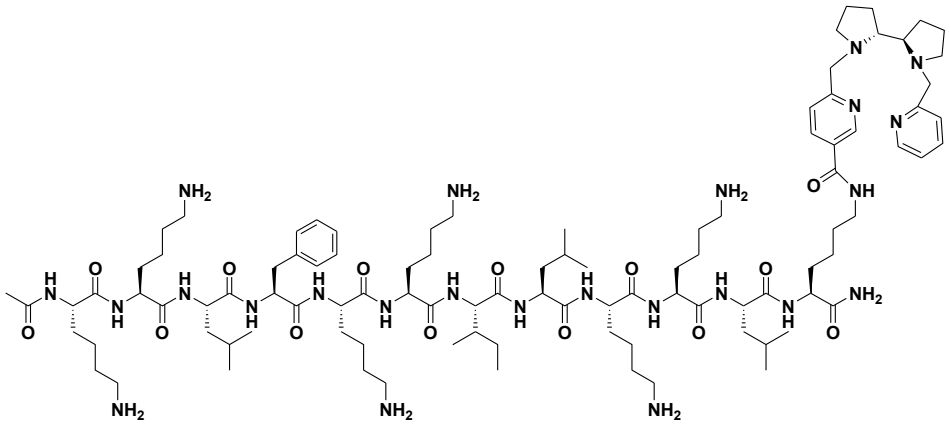

a)

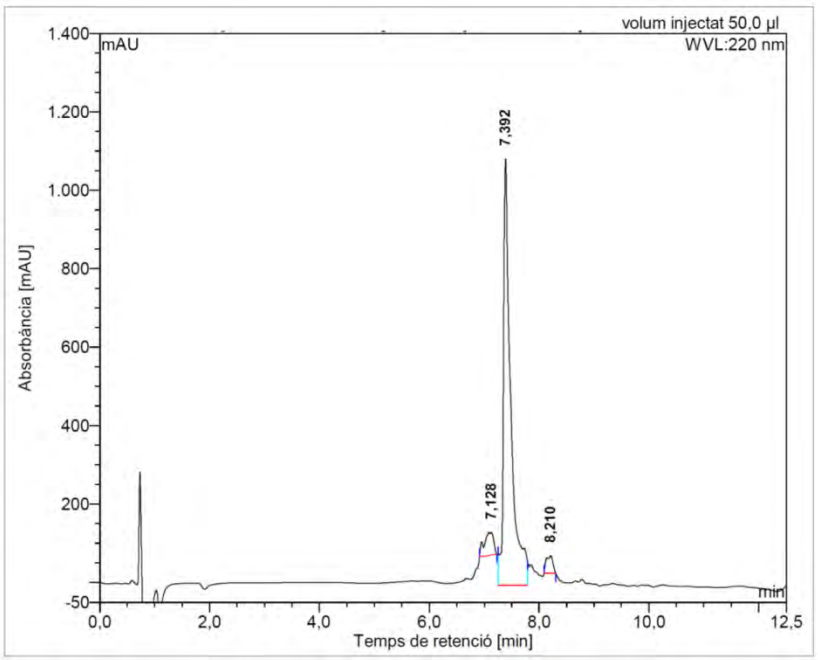

No.	mps retenc min	alçada mAU	Area mAU*min	Area relativa %
1	7,13	58,902	11,867	6,42
2	7,39	1086,835	166,711	90,20
3	8,21	45,621	6,249	3,38
Total:		1191,358	184,827	100,00

b)

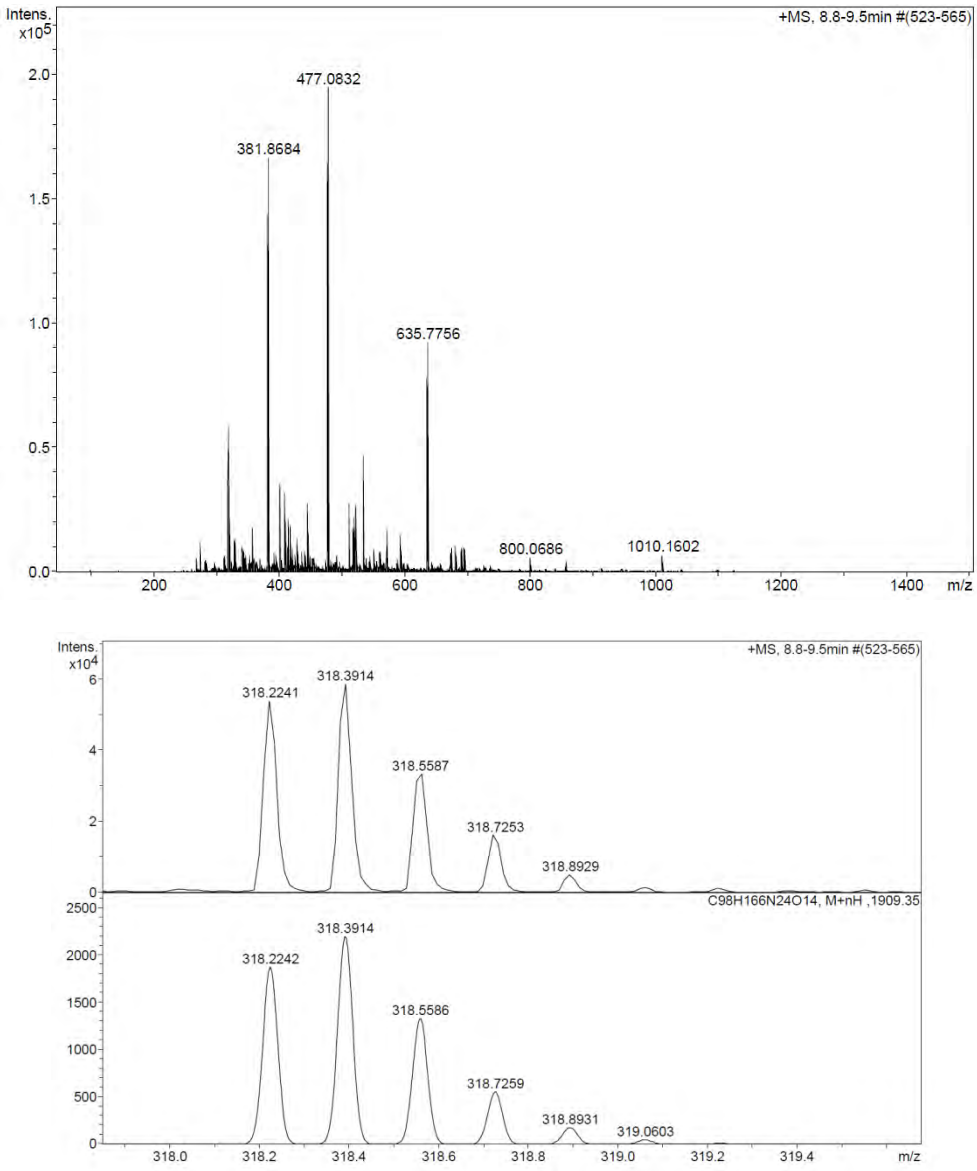

Observed HRMS (top) with the theoretical isotope prediction (bottom).

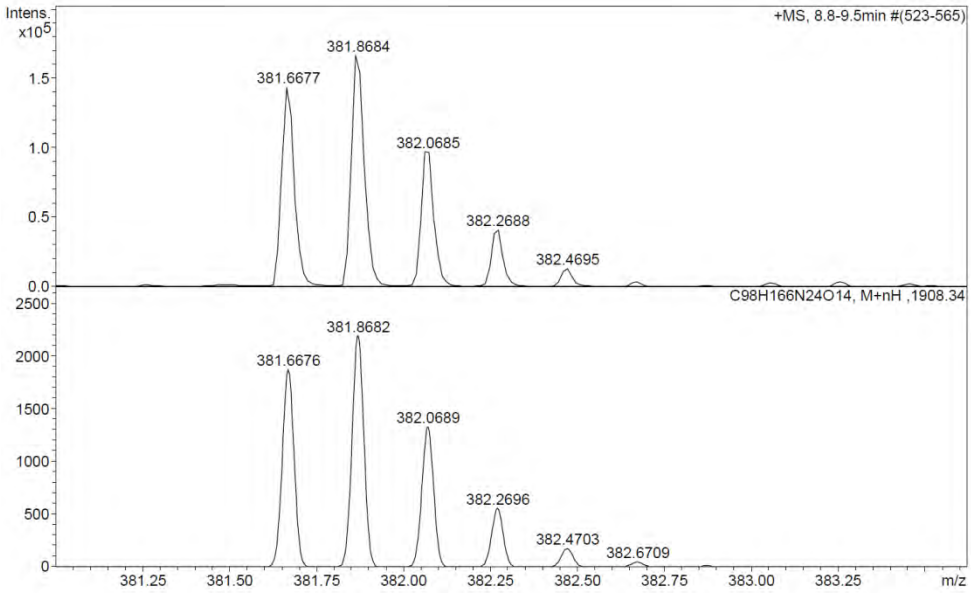

Observed HRMS (top) with the theoretical isotope prediction (bottom).

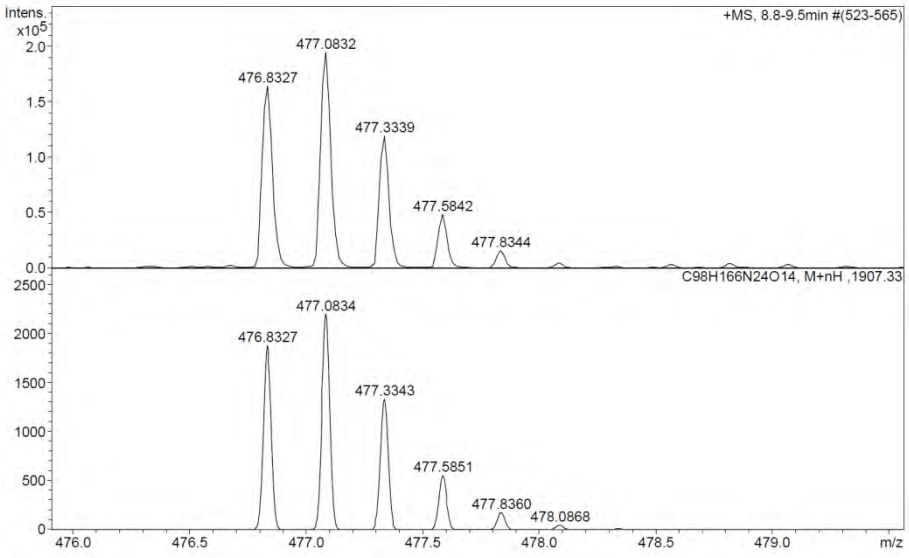

Observed HRMS (top) with the theoretical isotope prediction (bottom).

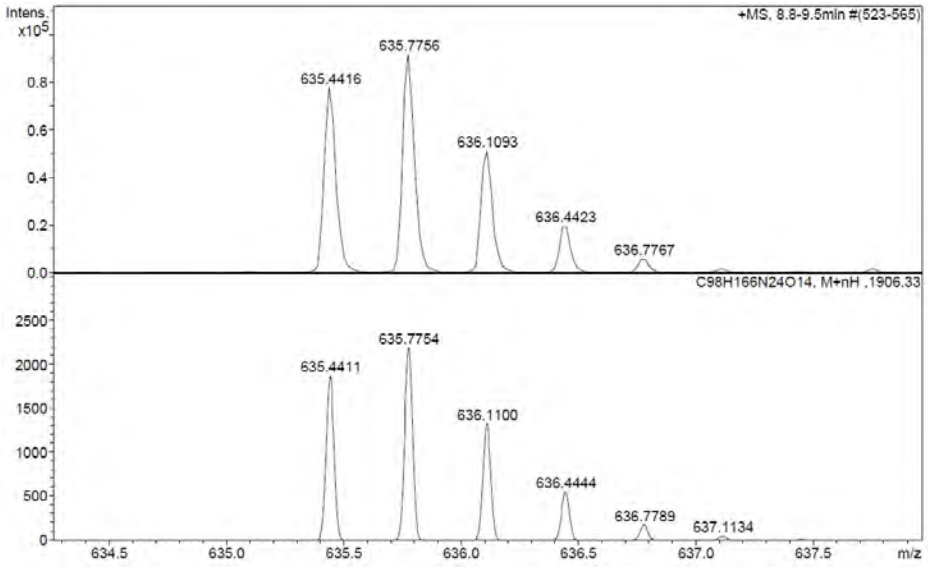

Observed HRMS (top) with the theoretical isotope prediction (bottom).

Figure SVI.7: a) HPLC chromatogram (λ= 220 nm), b) ESI/MS spectrum (*m/z*), c) HRMS spectrum (*m/z*).

PyTACN-βAK-BP16 (**BP345**)

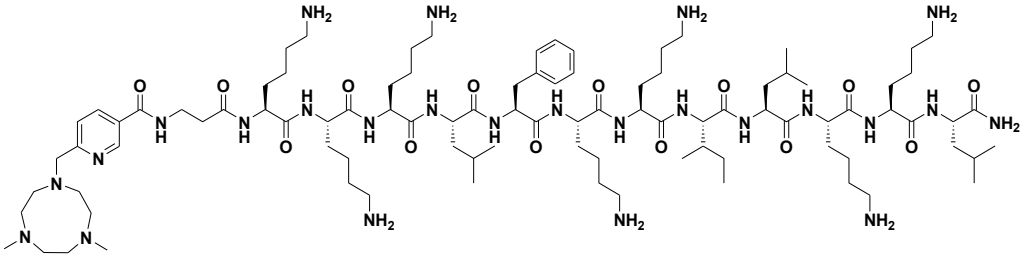

a)

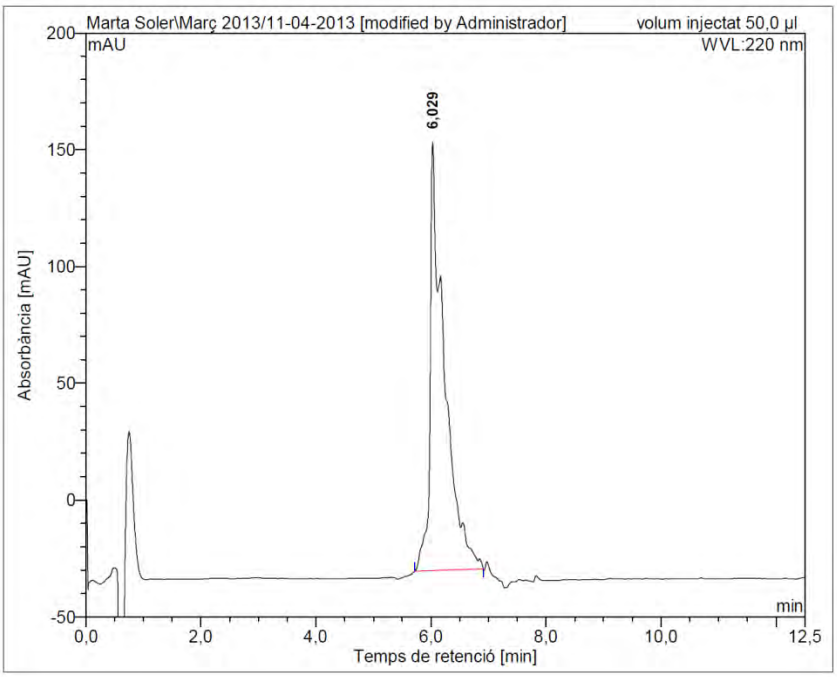

No.	mps retenc min	alçada mAU	Area mAU*min	Area relativa %
1	6,03	183,434	52,770	100,00
Total:		183,434	52,770	100,00

b)

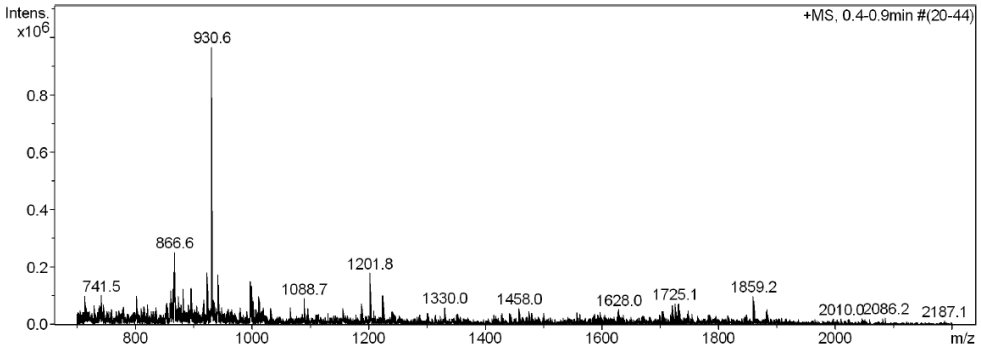

c)

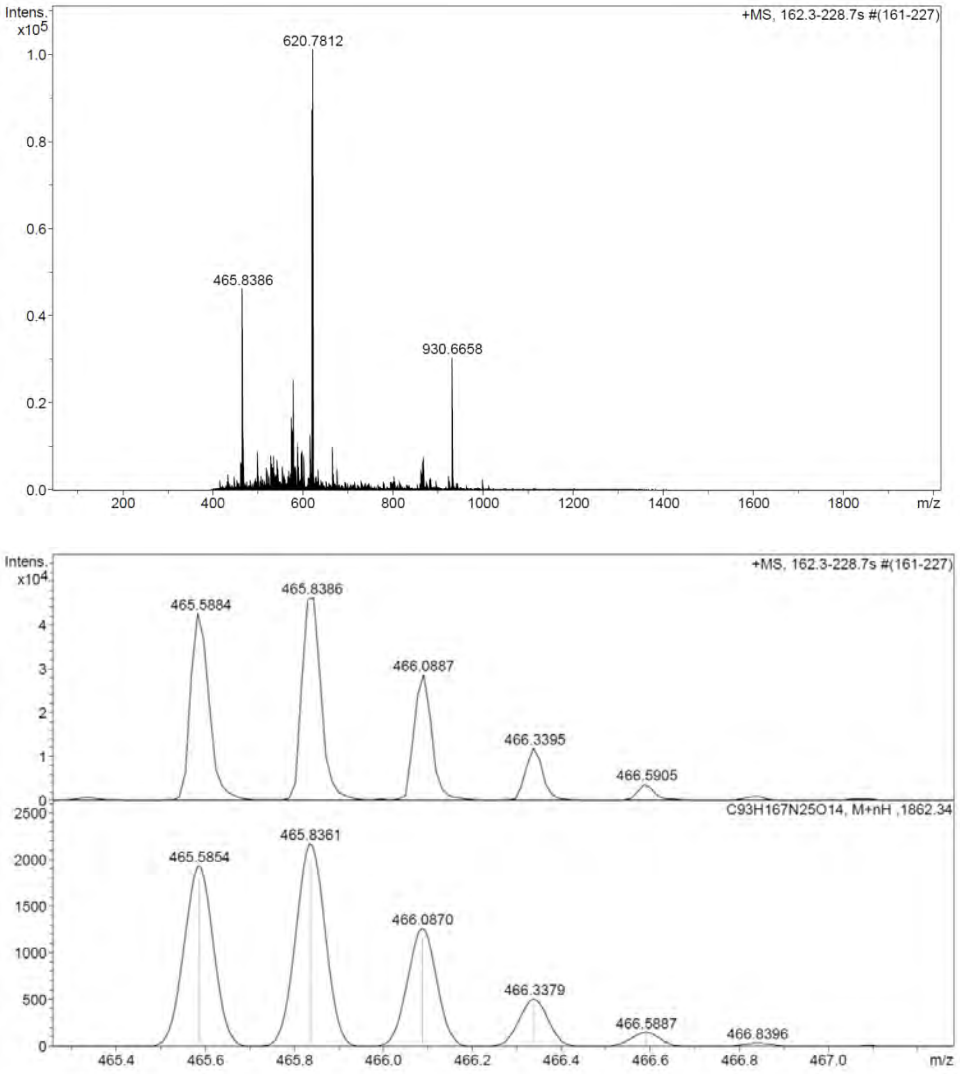

Observed HRMS (top) with the theoretical isotope prediction (bottom).

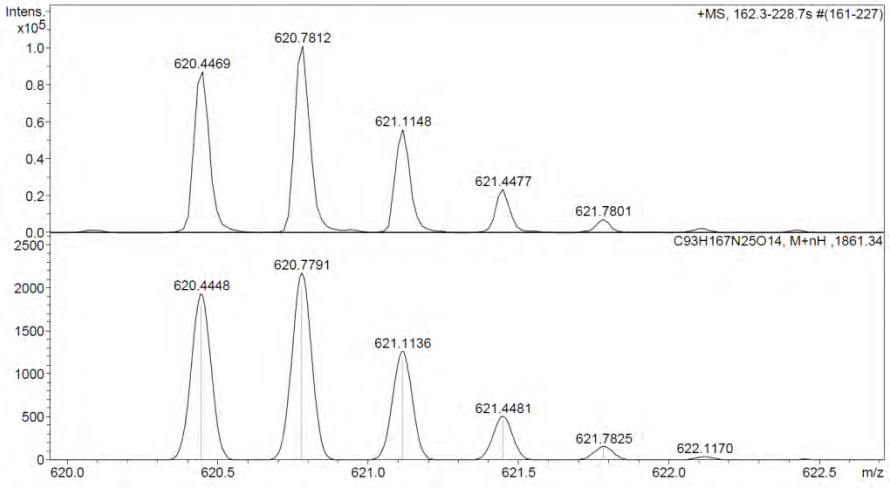

Observed HRMS (top) with the theoretical isotope prediction (bottom).

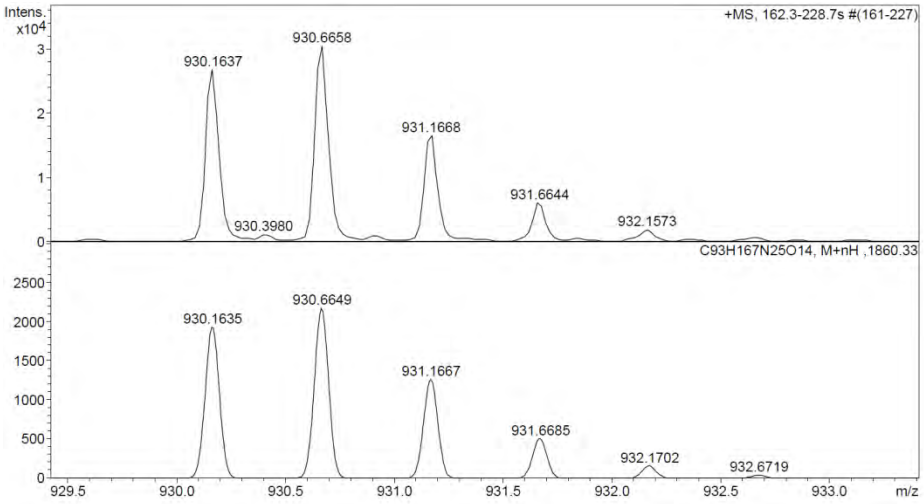

Observed HRMS (top) with the theoretical isotope prediction (bottom).

Figure SVI.8: a) HPLC chromatogram (λ= 220 nm), b) HRMS spectrum (*m/z*).

BPBP-βAK-BP16 (**BP346**)

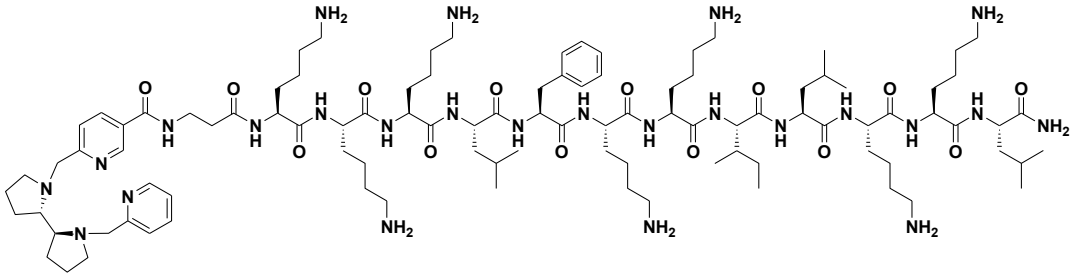

a)

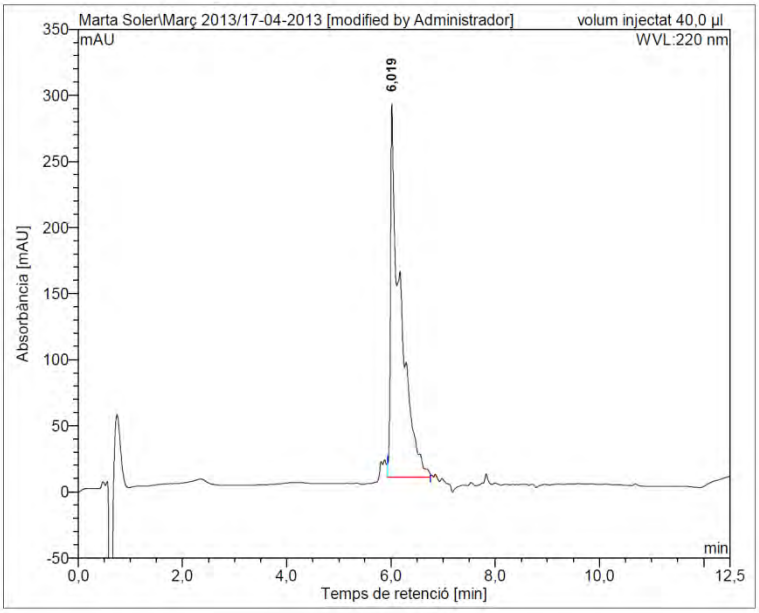

No.	mps retenc min	alçada mAU	Area mAU*min	Area relativa %
1	6,02	282,366	61,202	100,00
Total:		282,366	61,202	100,00

b)

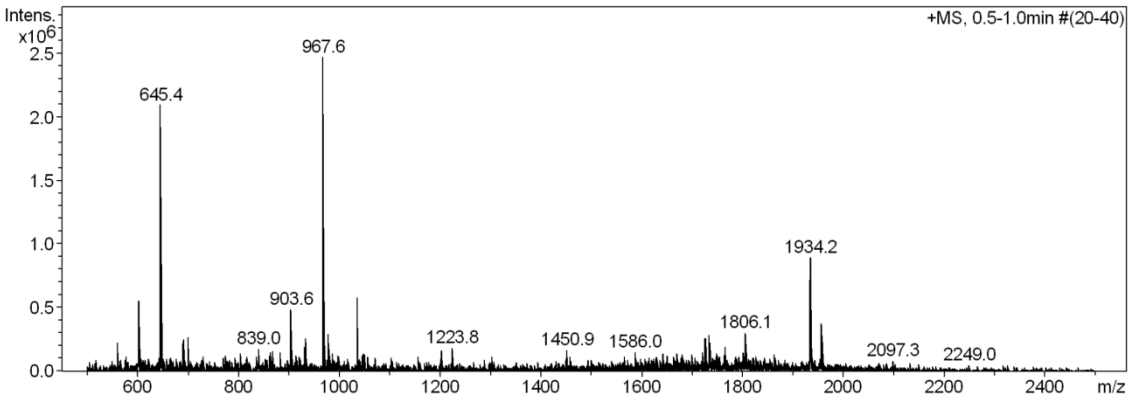

C)

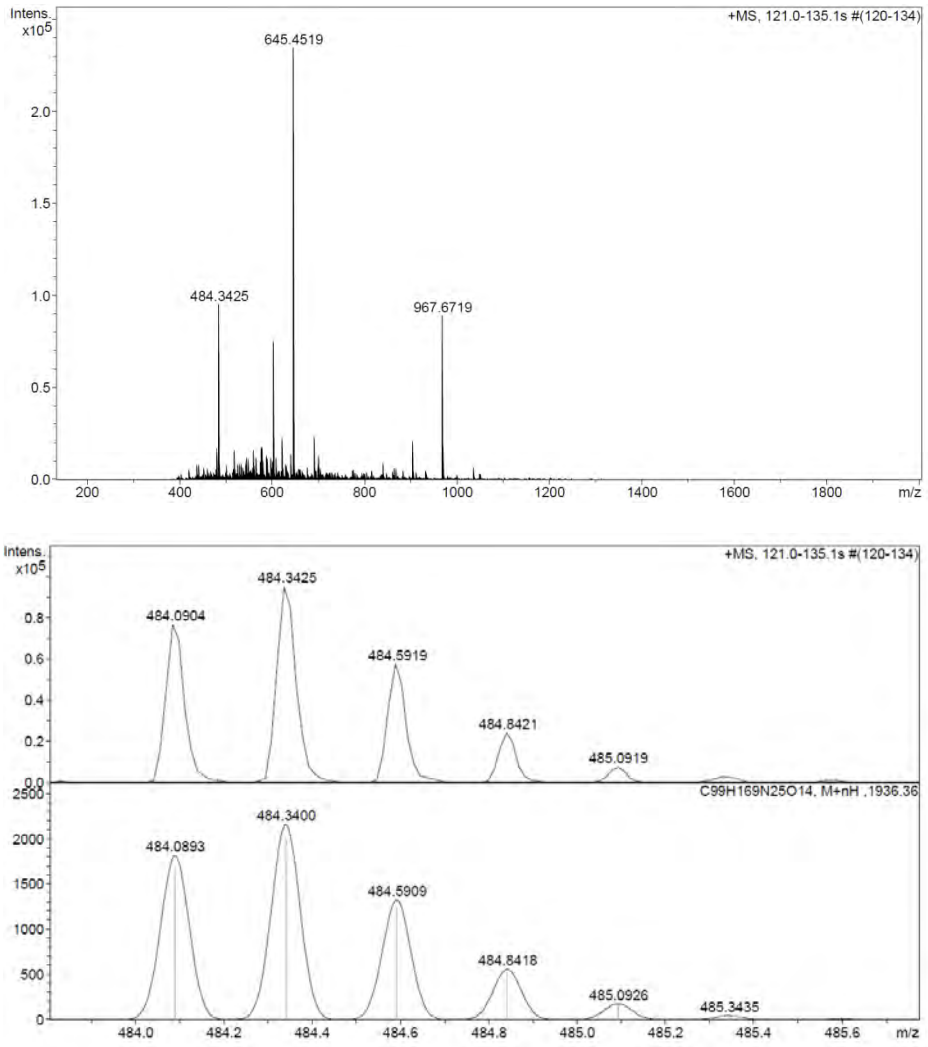

Observed HRMS (top) with the theoretical isotope prediction (bottom).

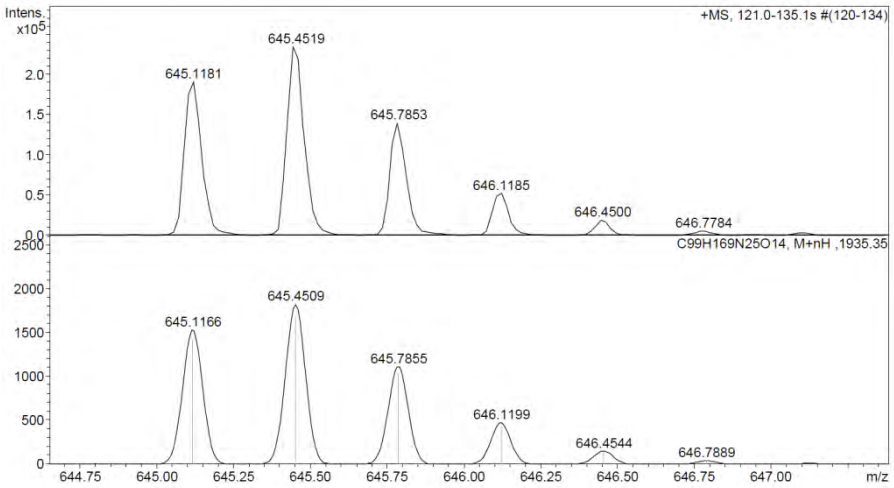

Observed HRMS (top) with the theoretical isotope prediction (bottom).

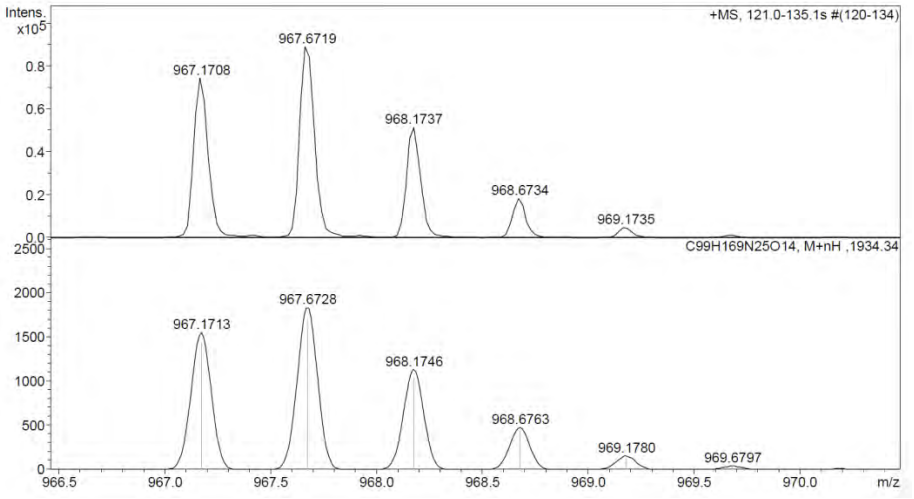

Observed HRMS (top) with the theoretical isotope prediction (bottom).

Figure SVI.9: a) HPLC chromatogram (λ= 220 nm), b) HRMS spectrum (*m/z*).

BPBP-GFLG-BP16 (**BP347**)

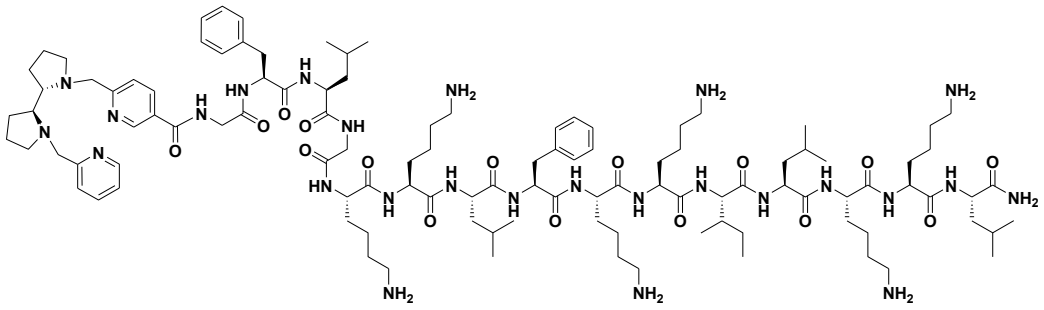

a)

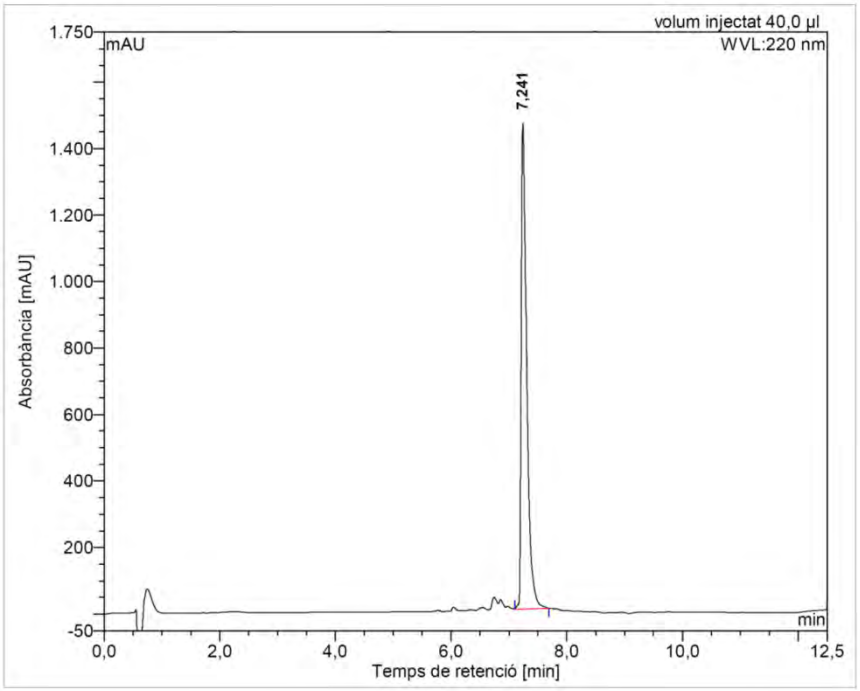

No.	mps retenc min	alçada mAU	Area mAU*min	Area relativa %
1	7,24	1460,388	161,177	100,00
Total:		1460,388	161,177	100,00

b)

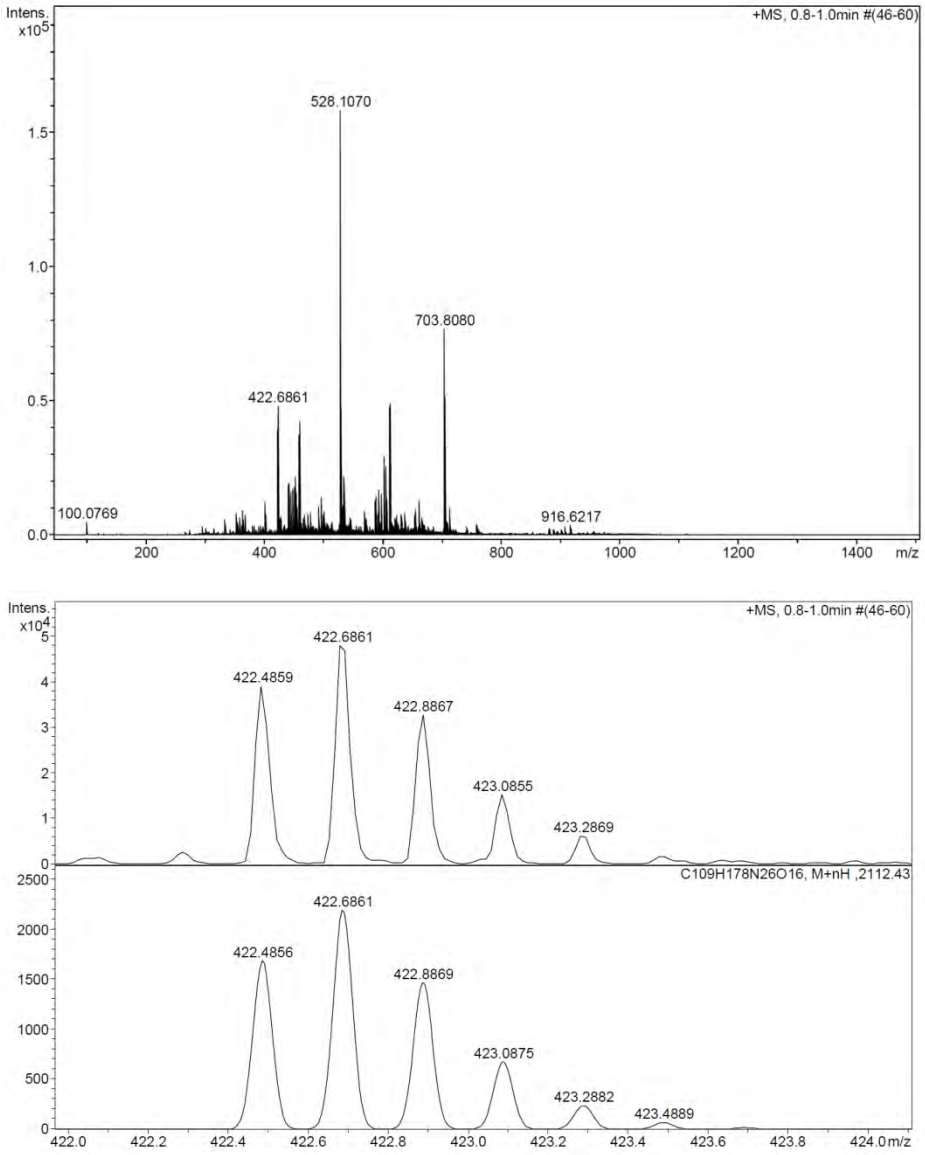

Observed HRMS (top) with the theoretical isotope prediction (bottom).

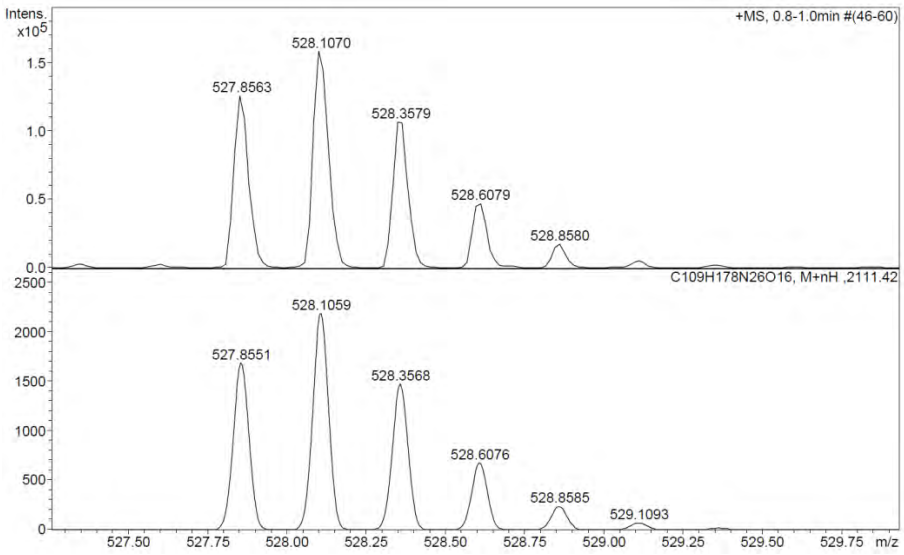

Observed HRMS (top) with the theoretical isotope prediction (bottom).

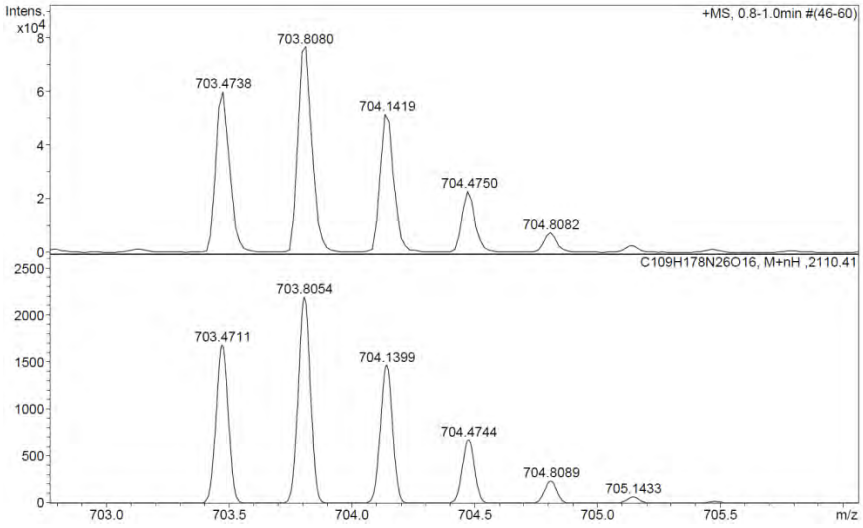

Observed HRMS (top) with the theoretical isotope prediction (bottom).

Figure SVI.10: a) HPLC chromatogram (λ= 220 nm), b) HRMS spectrum (*m/z*).

BP16-GLFG-BPBP (**BP348**)

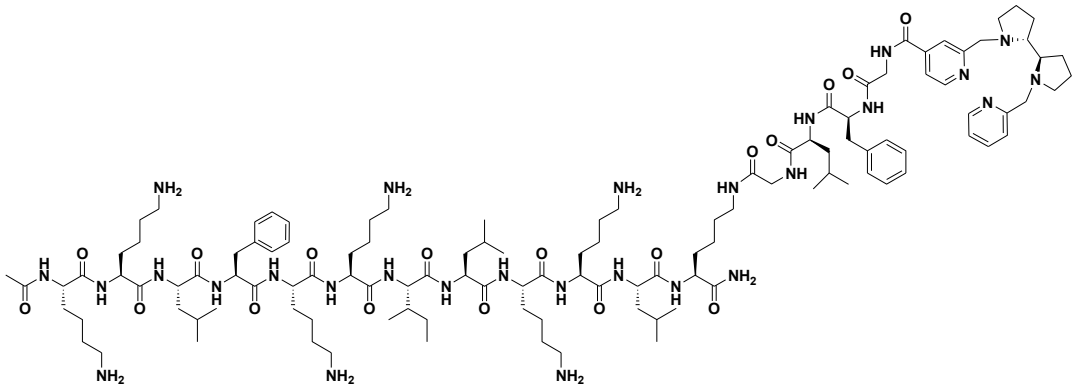

a)

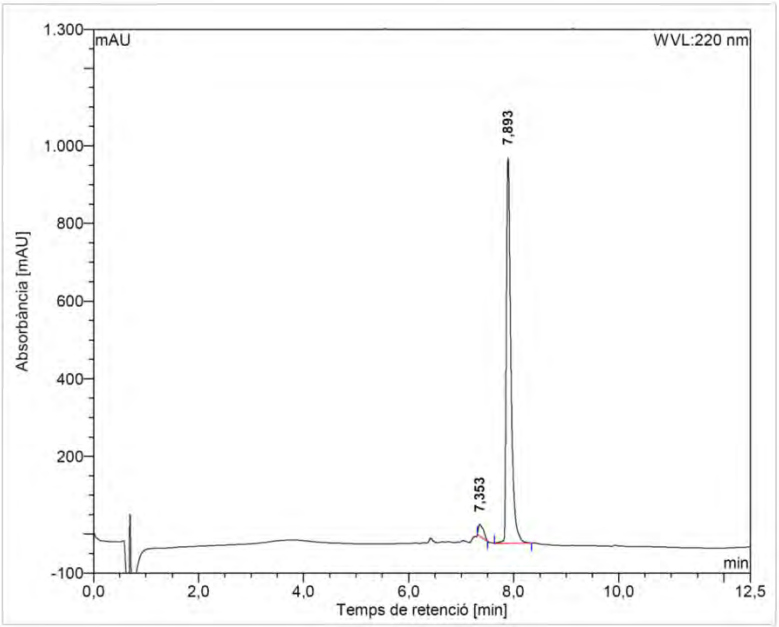

No.	mps retenc min	alçada mAU	Area mAU*min	Area relativa %
1	7,35	30,131	3,543	3,40
2	7,89	993,729	100,753	96,60
Total:		1023,860	104,296	100,00

b)

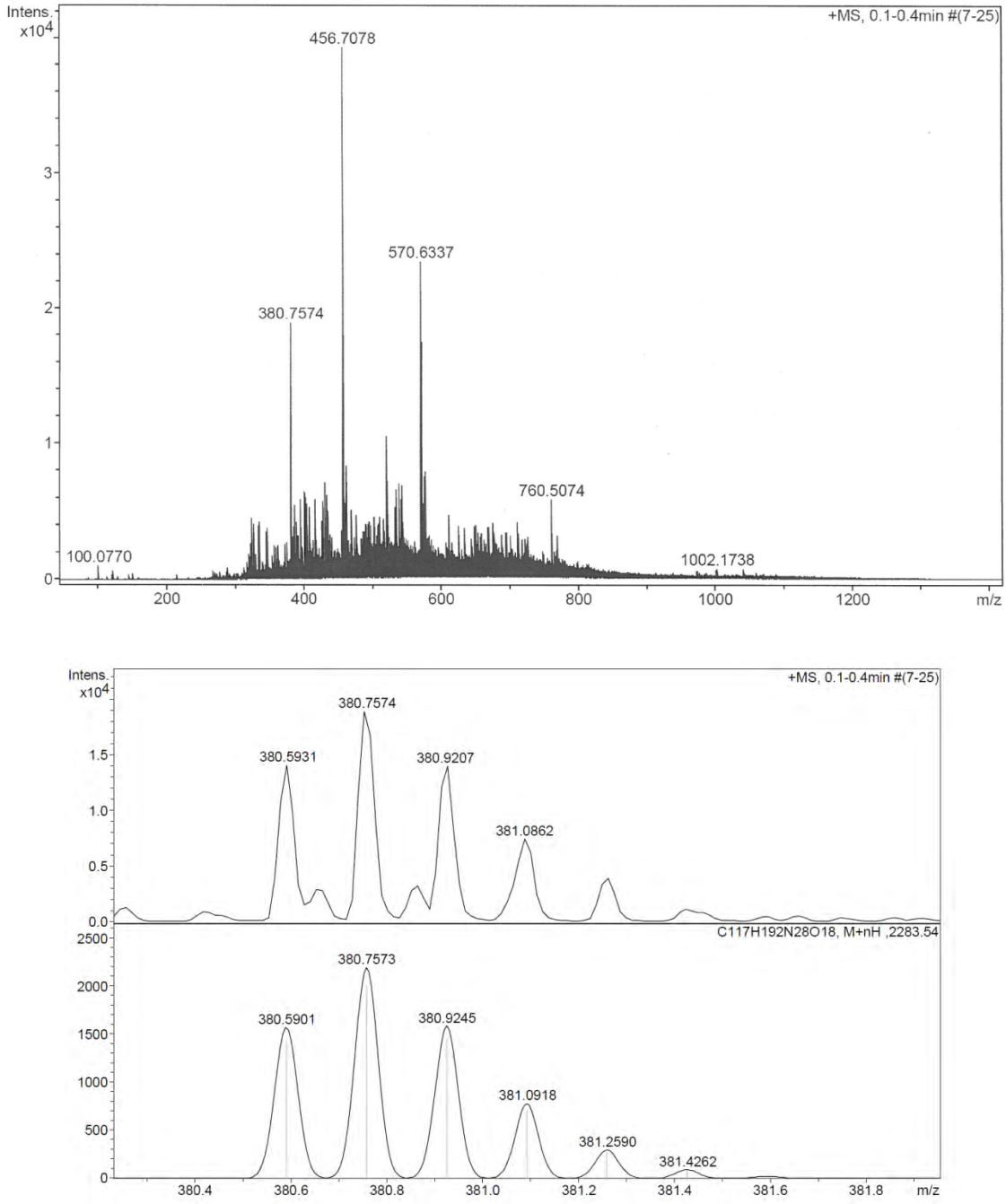

Observed HRMS (top) with the theoretical isotope prediction (bottom).

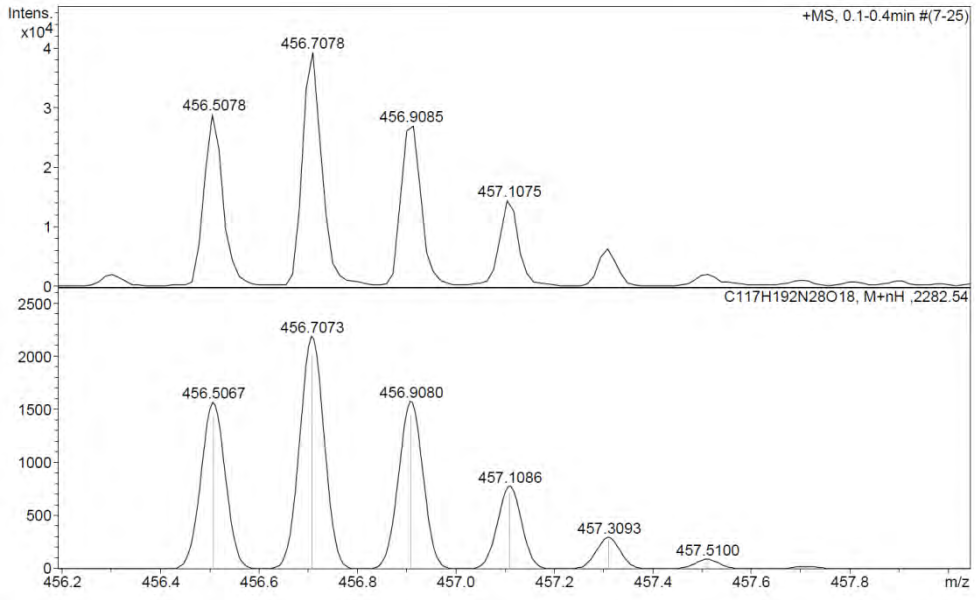

Observed HRMS (top) with the theoretical isotope prediction (bottom).

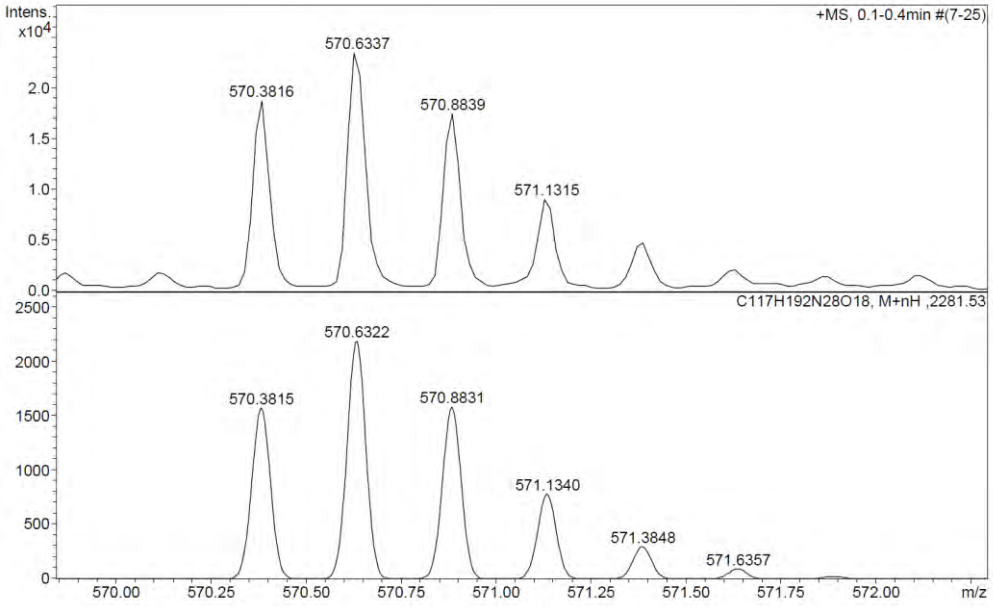

Observed HRMS (top) with the theoretical isotope prediction (bottom).

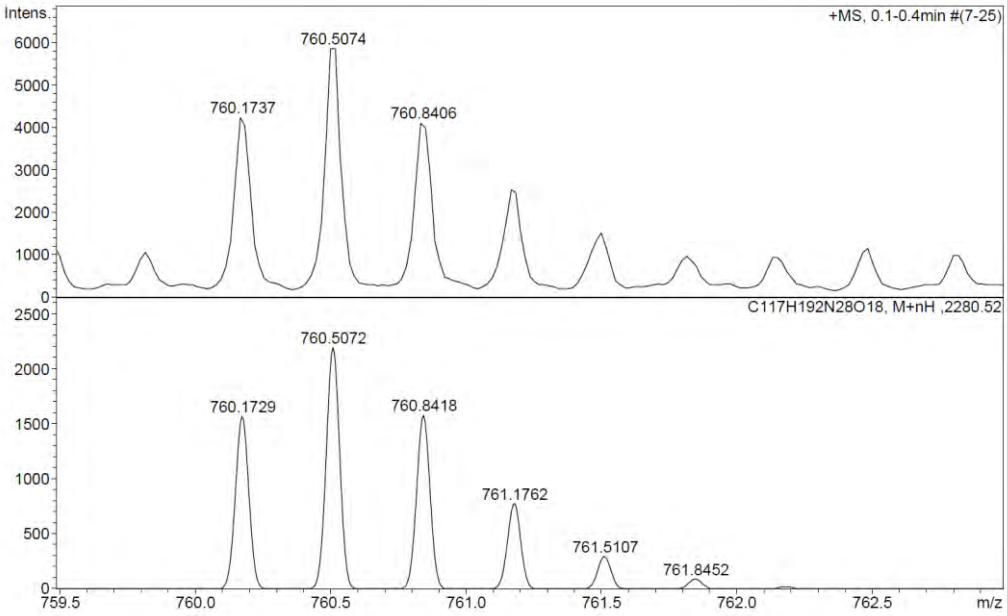

Observed HRMS (top) with the theoretical isotope prediction (bottom).

Figure SVI.11: a) HPLC chromatogram (λ= 220 nm), b) HRMS spectrum (*m/z*).

BPBP-βAK(CF)-BP16 (**BP349)**

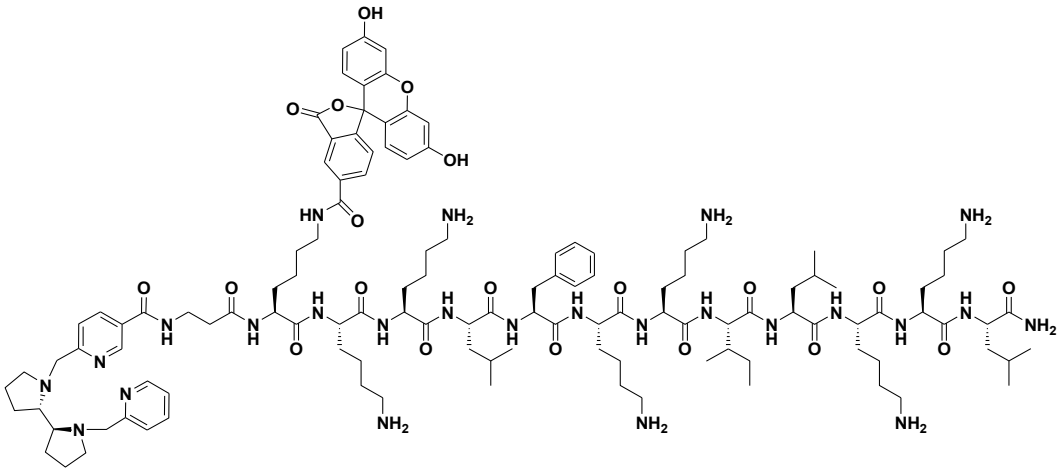

a)

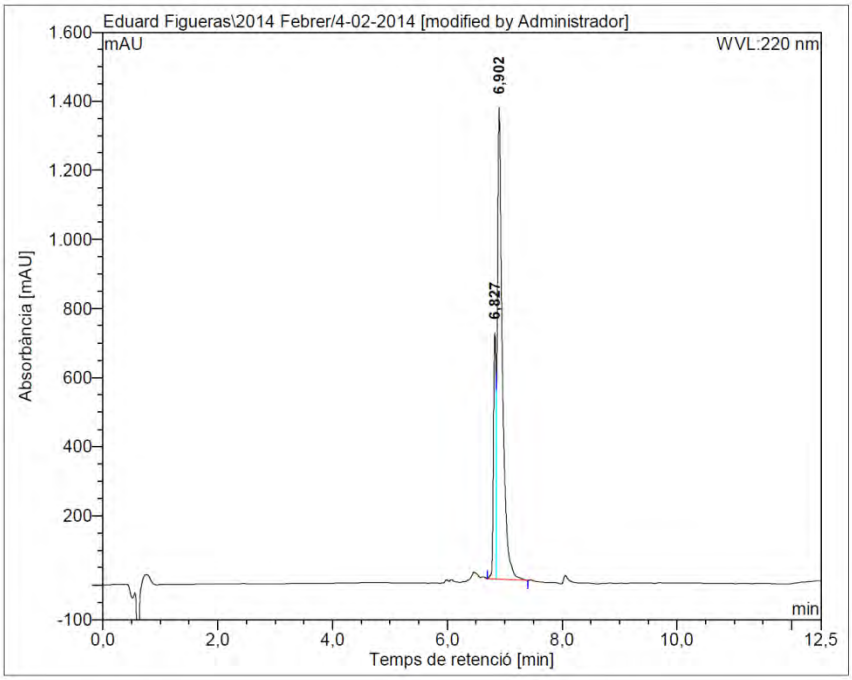

No.	Temps retenció min	alçada mAU	Area mAU*min	Area relativa %
1	6,83	713,518	38,489	21,98
2	6,90	1365,631	136,601	78,02
Total:		2079,149	175,089	100,00

b)

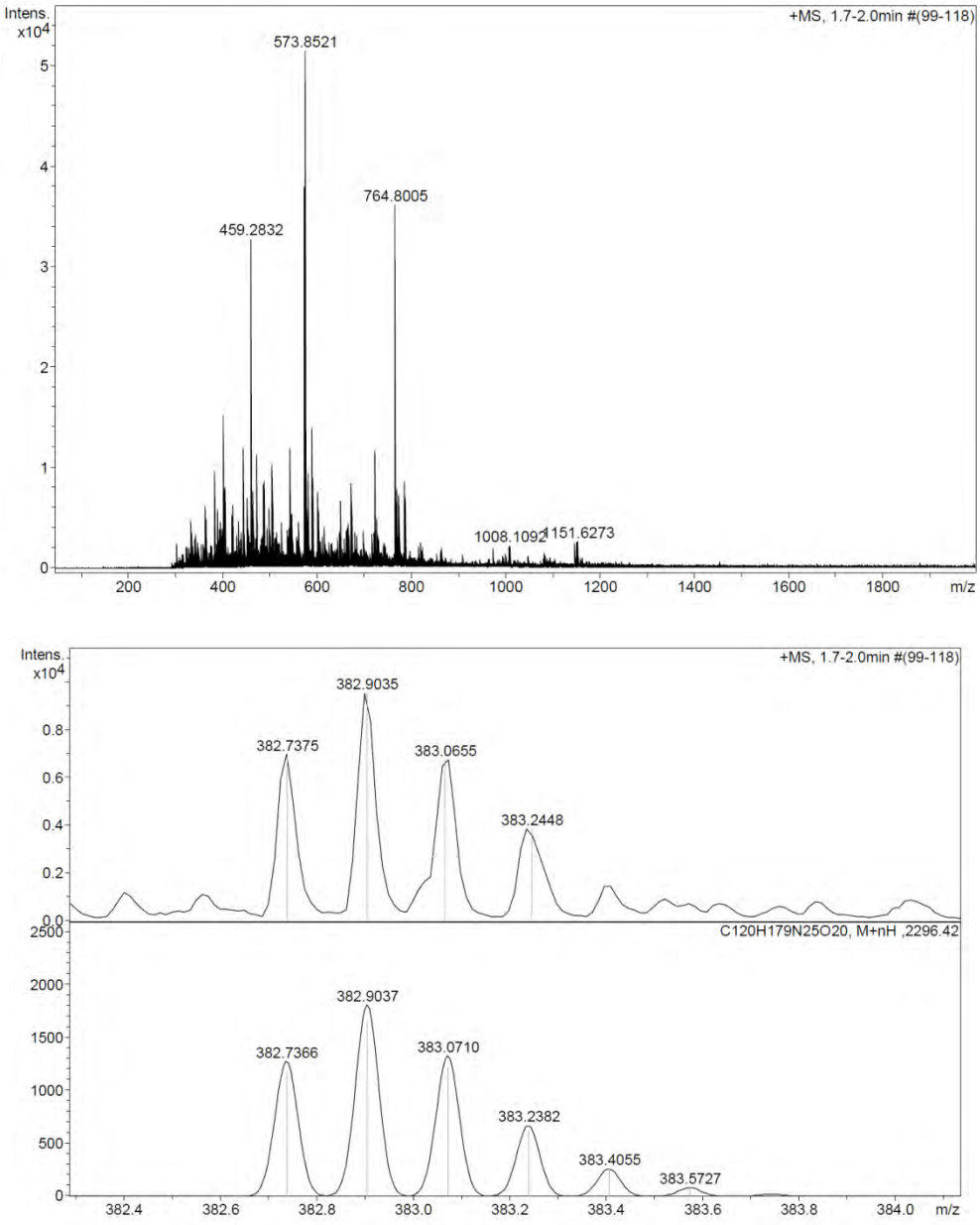

Observed HRMS (top) with the theoretical isotope prediction (bottom).

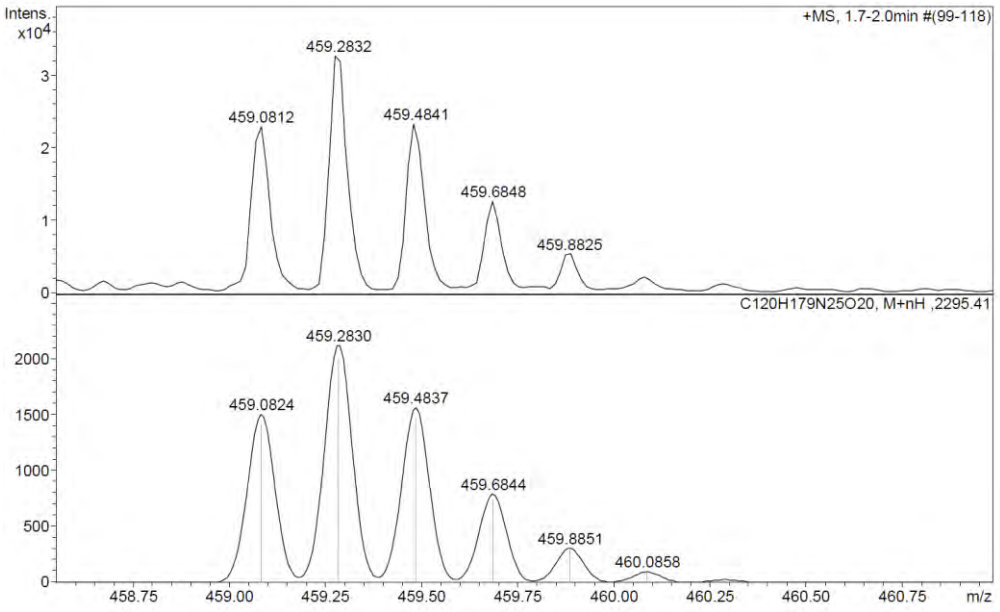

Observed HRMS (top) with the theoretical isotope prediction (bottom).

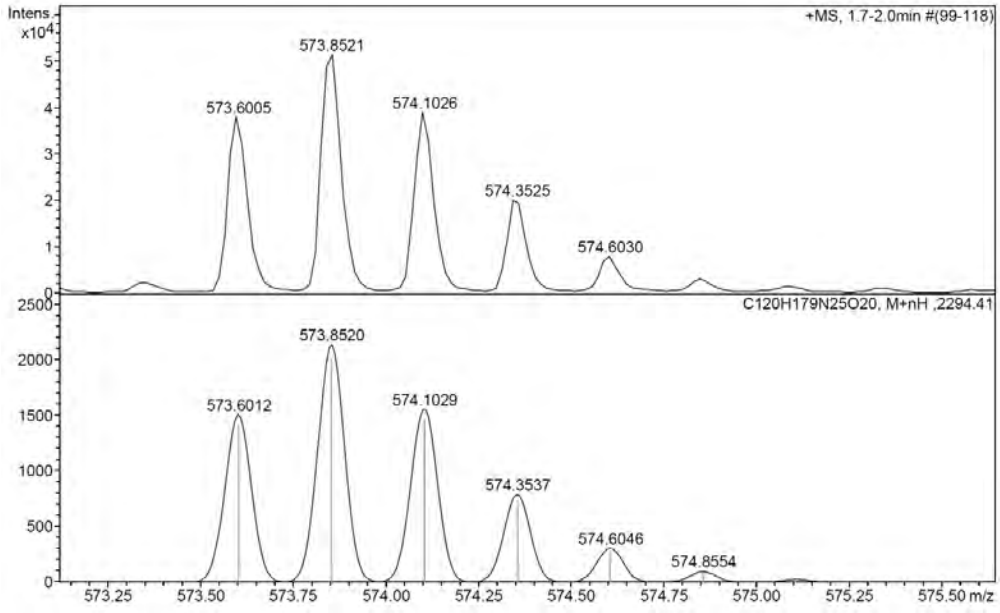

Observed HRMS (top) with the theoretical isotope prediction (bottom).

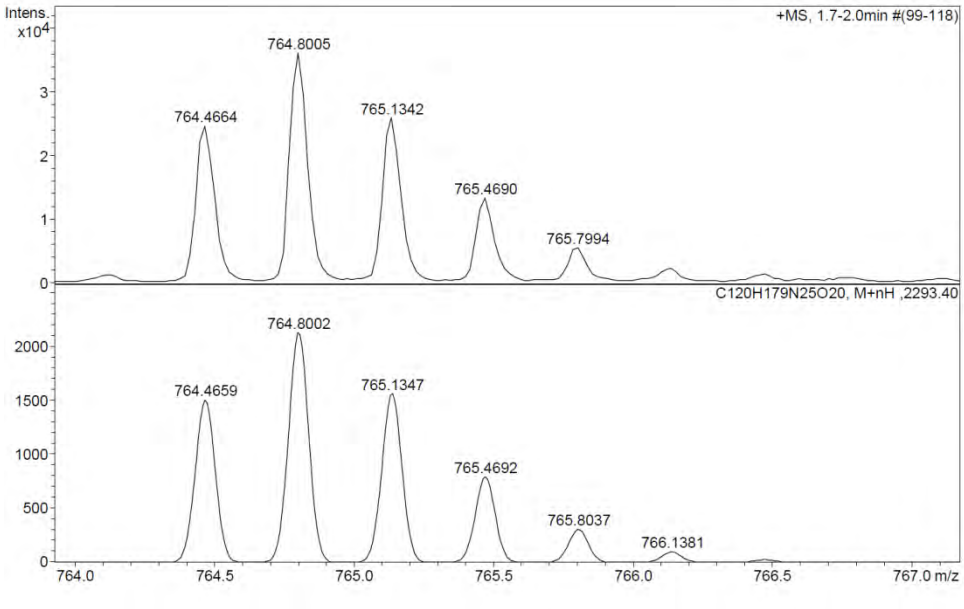

Observed HRMS (top) with the theoretical isotope prediction (bottom).

Figure SVI.12: a) HPLC chromatogram (λ= 220 nm), b) HRMS spectrum (*m/z*).

BPBP-GFLG-BP16-CF (**BP350**)

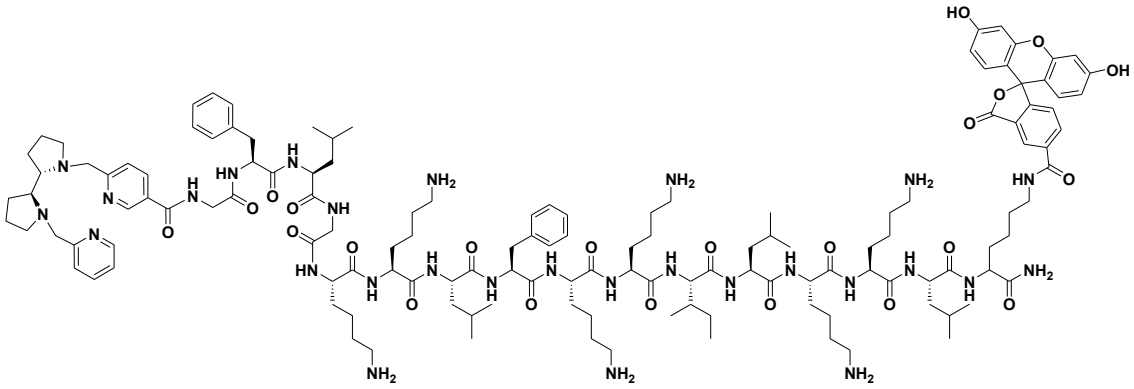

a)

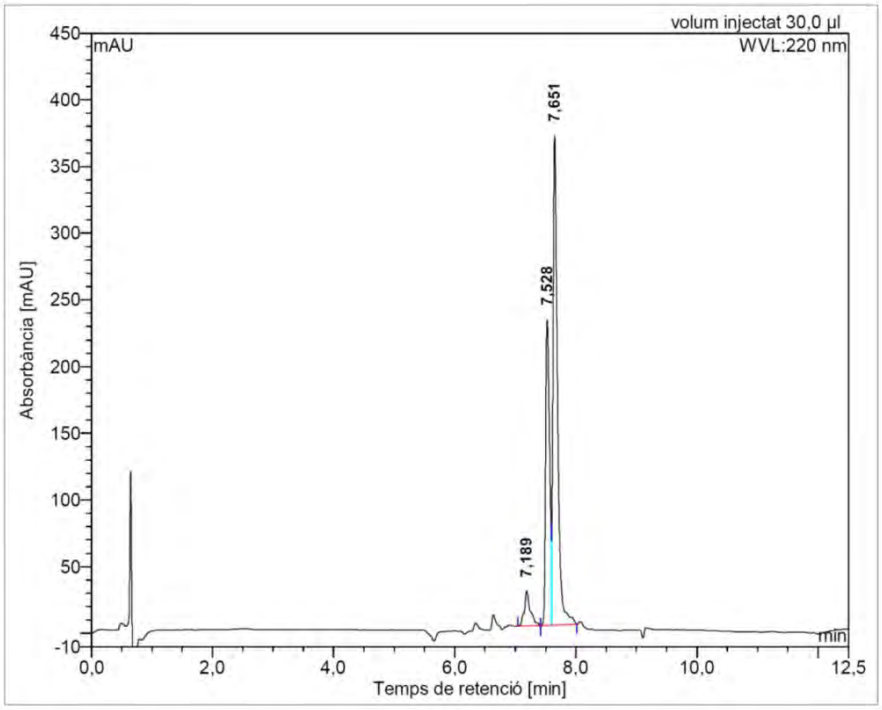

No.	mps retenc min	alçada mAU	Area mAU*min	Area relativa %
1	7,19	26,104	2,979	5,70
2	7,53	229,087	17,335	33,18
3	7,65	366,827	31,932	61,12
Total:		622,017	52,246	100,00

b)

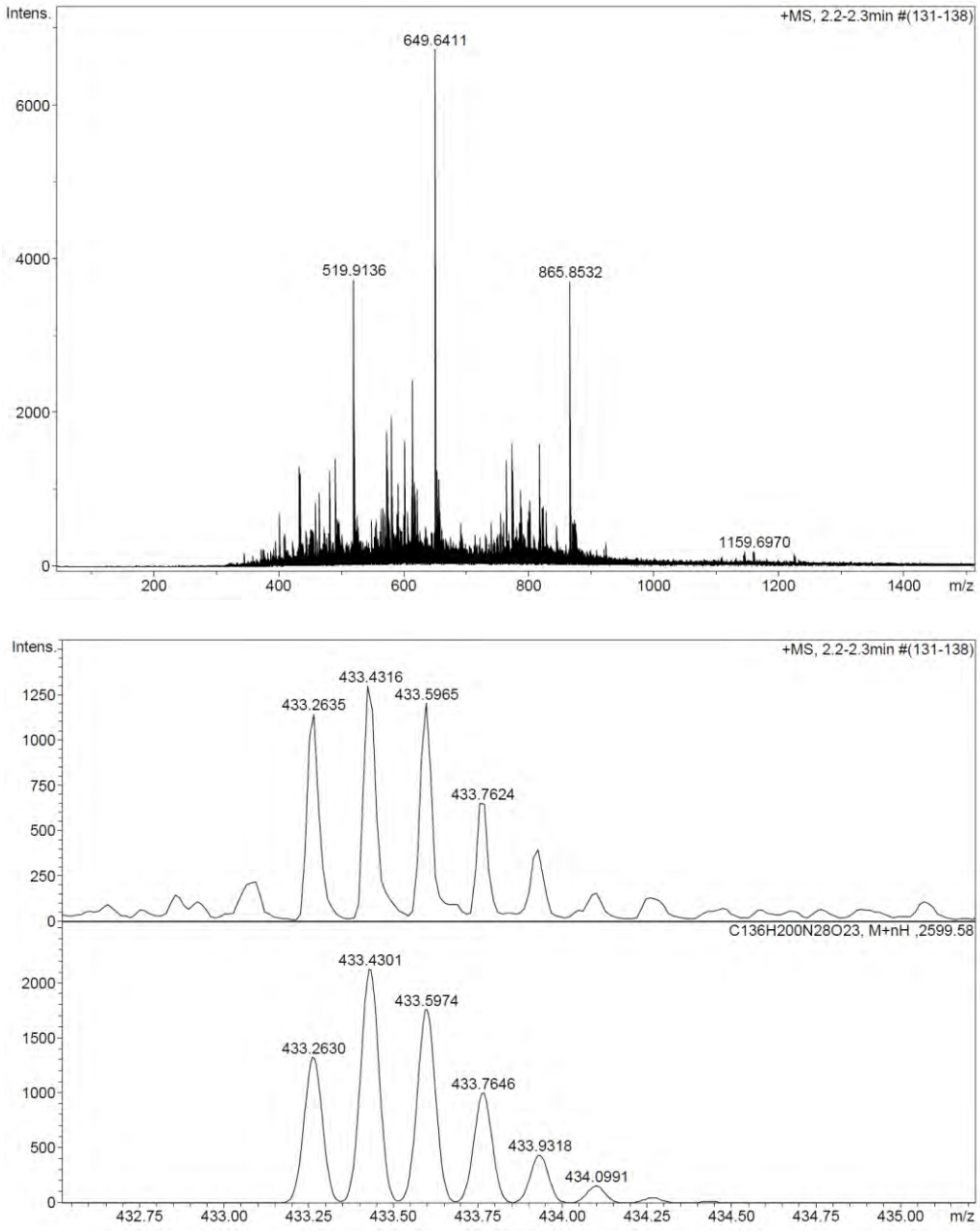

Observed HRMS (top) with the theoretical isotope prediction (bottom).

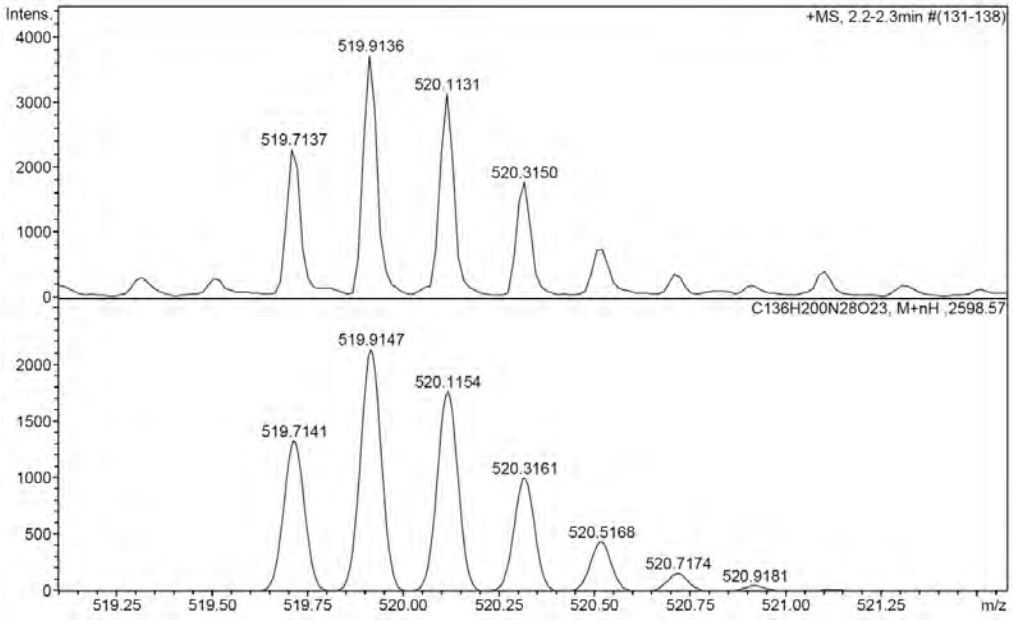

Observed HRMS (top) with the theoretical isotope prediction (bottom).

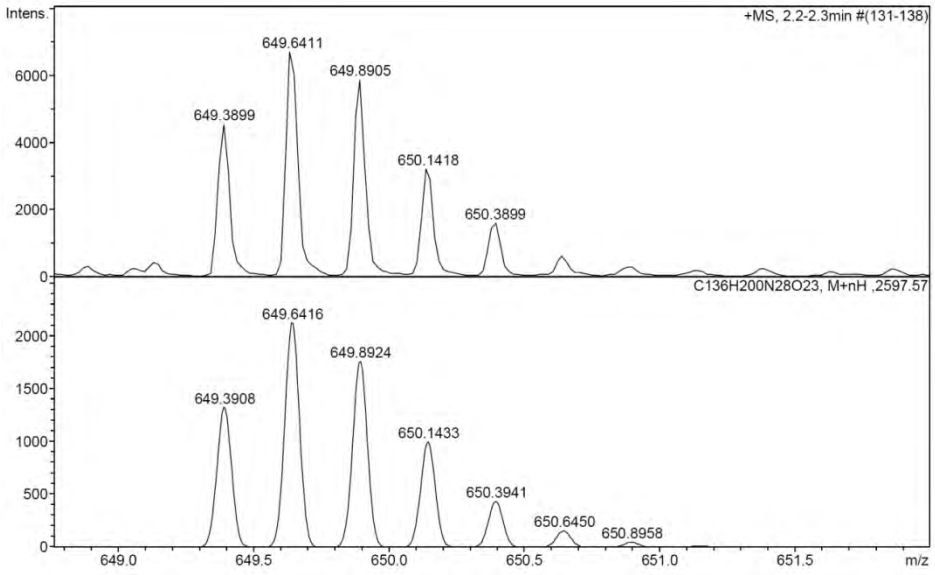

Observed HRMS (top) with the theoretical isotope prediction (bottom).

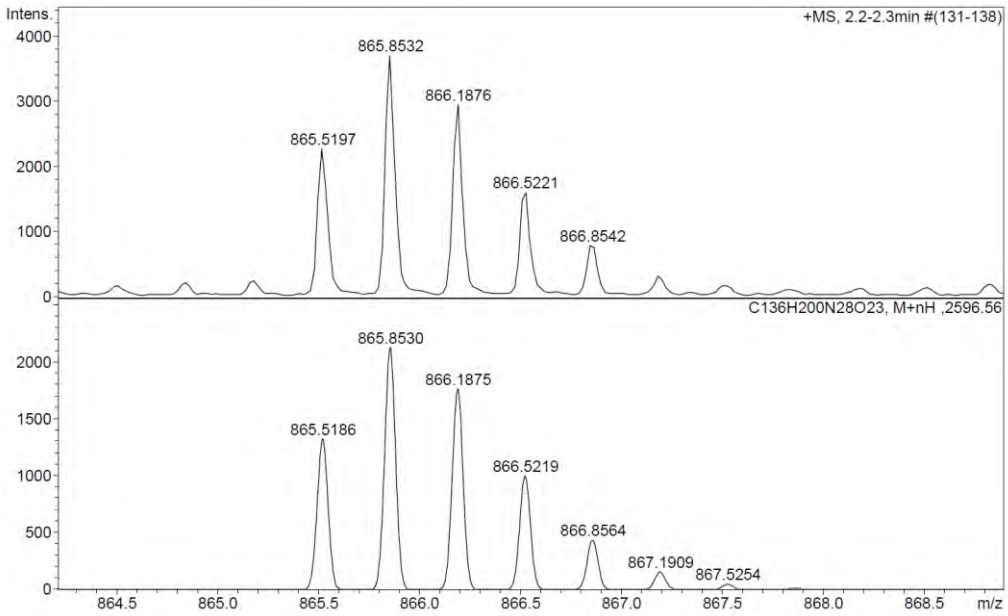

Observed HRMS (top) with the theoretical isotope prediction (bottom).

Supporting Information

Chapter VII: BPBP-PNA conjugate as metal-free artificial nuclease for oncogenic miRNAs targeting

Table of contents

Figure SVII.1: a) HPLC chromatogram (λ= 214 nm), b) ESI/MS spectrum (*m/z*), c) HRMS spectrum (*m/z*).

PNA$_{135}$

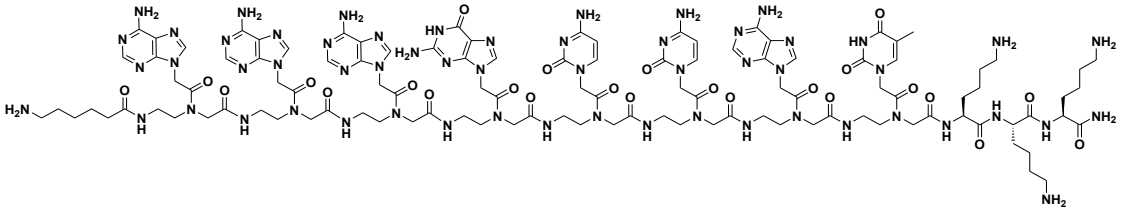

a)

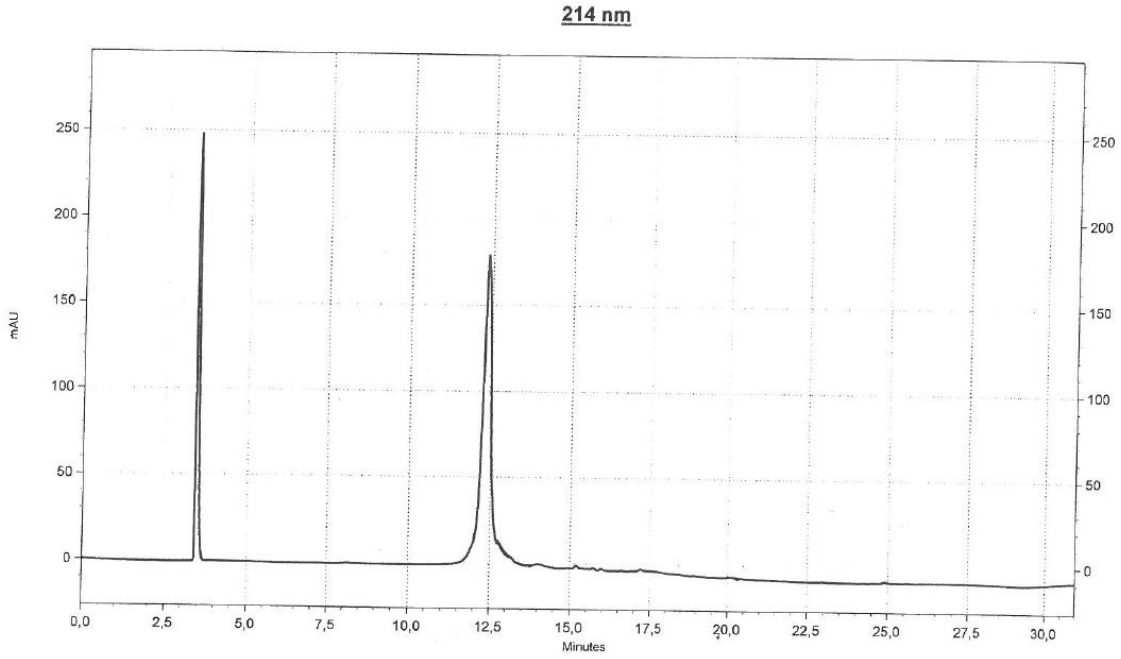

b)

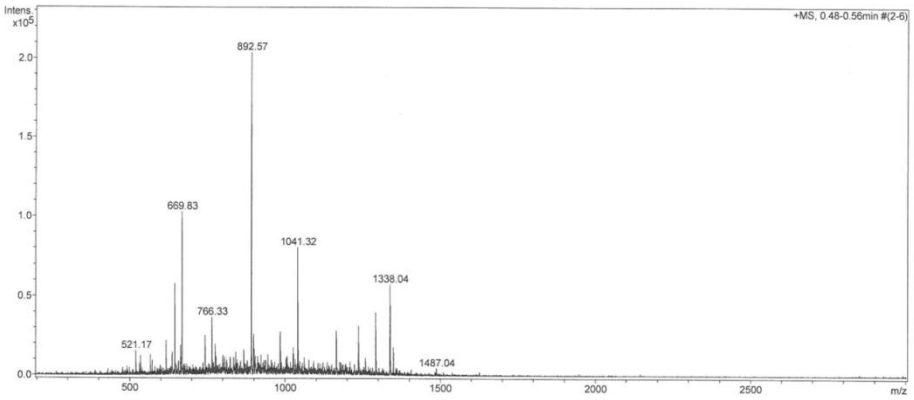

c)

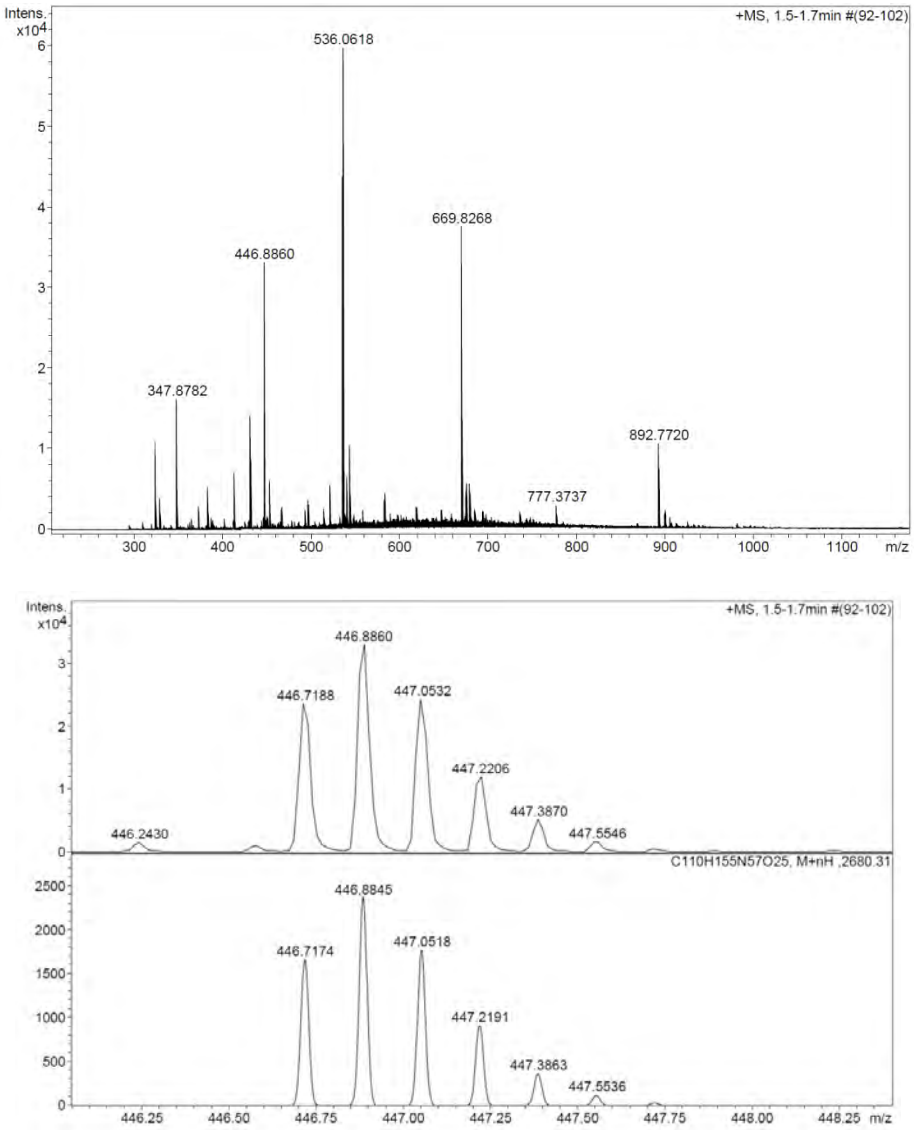

Observed HRMS (top) with the theoretical isotope prediction (bottom).

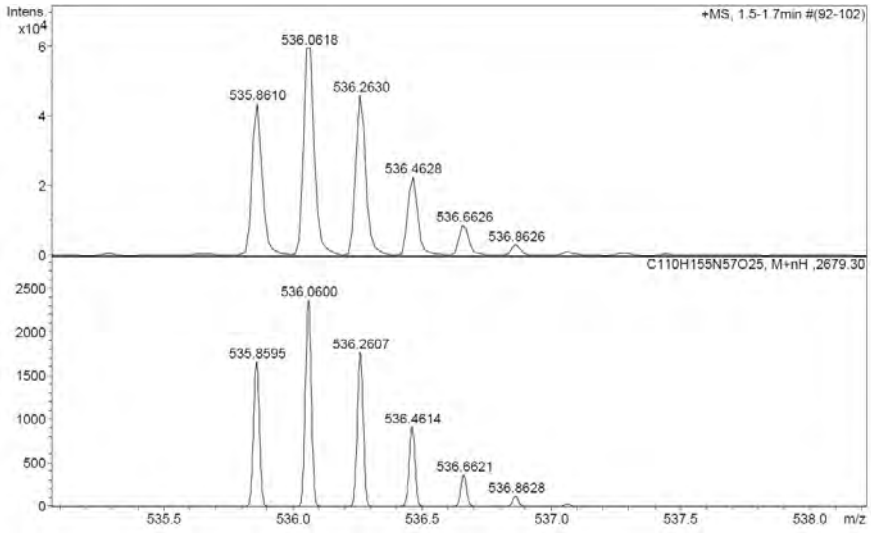

Observed HRMS (top) with the theoretical isotope prediction (bottom).

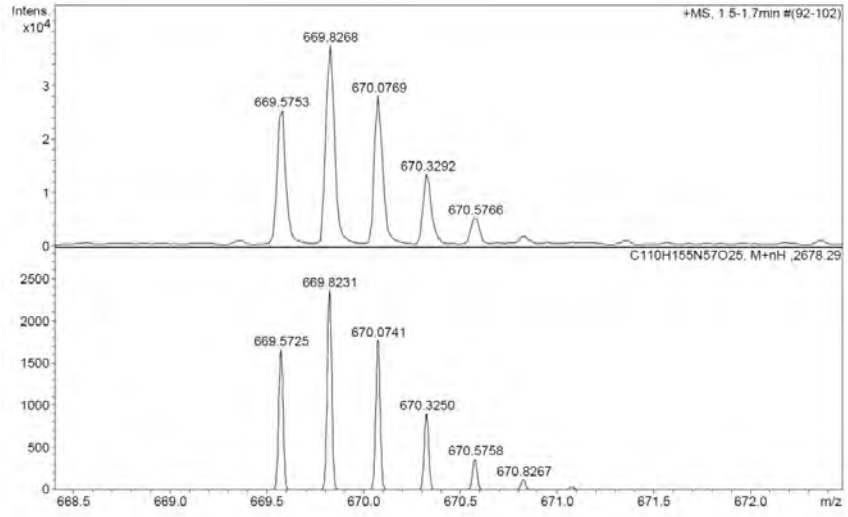

Observed HRMS (top) with the theoretical isotope prediction (bottom).

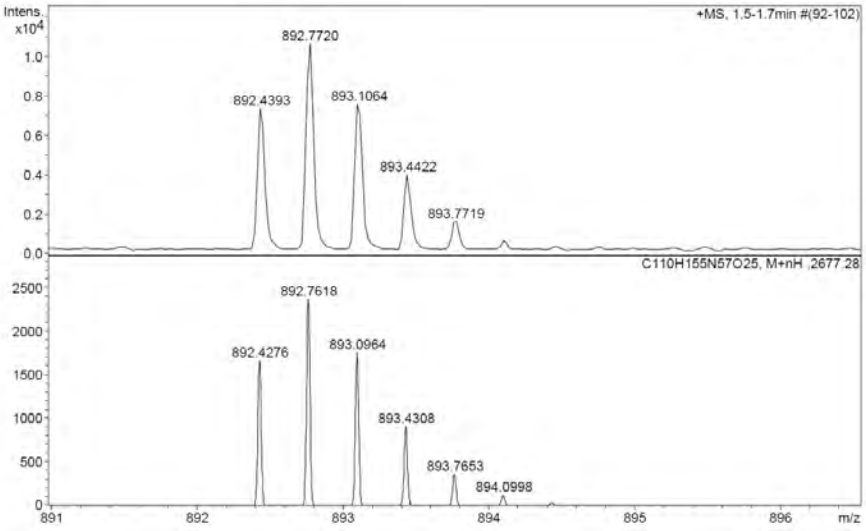

Observed HRMS (top) with the theoretical isotope prediction (bottom).

Figure SVII.2: a) HPLC chromatogram (λ= 214 nm), b) ESI/MS spectrum (*m/z*), c) HRMS spectrum (*m/z*).

PNA_{155}

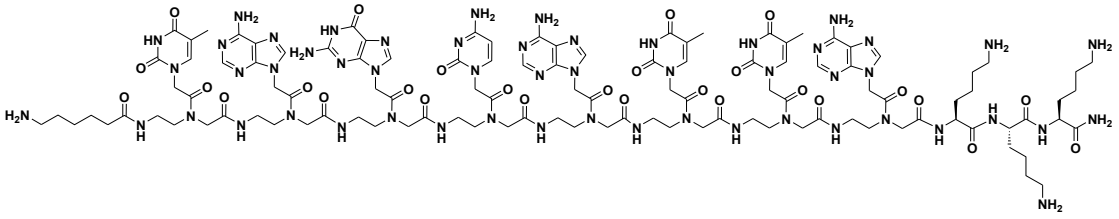

a)

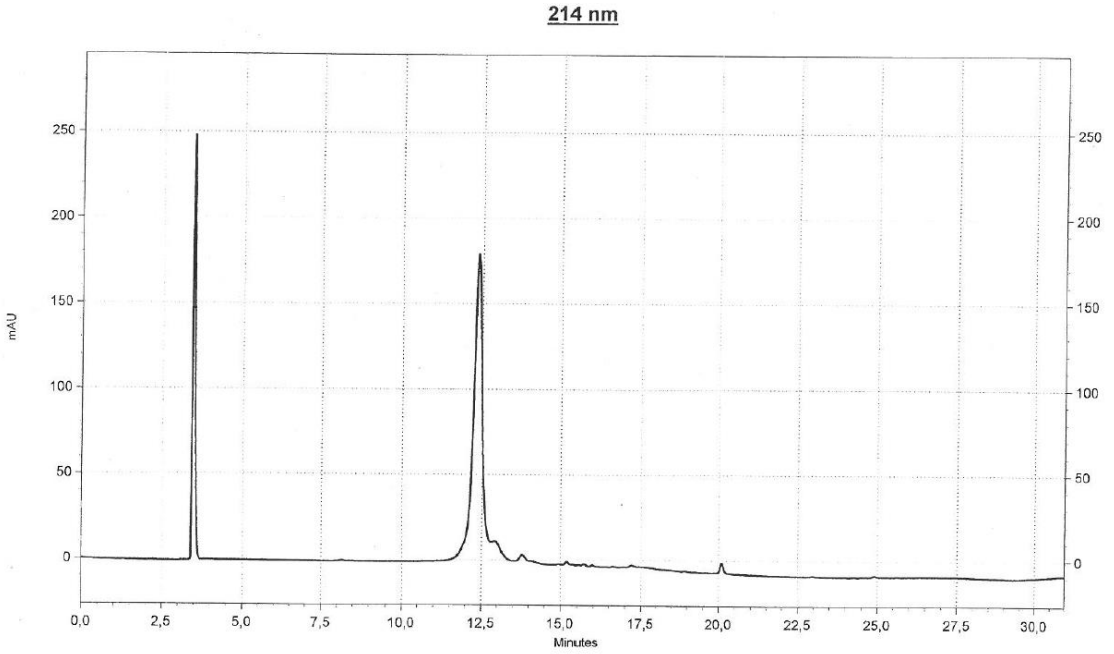

b)

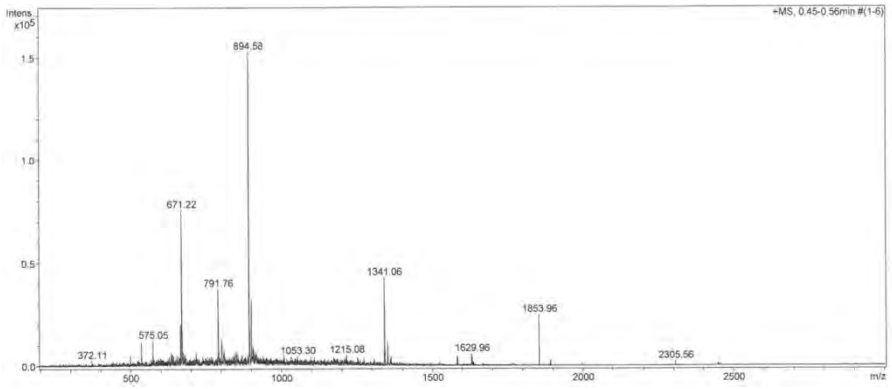

c)

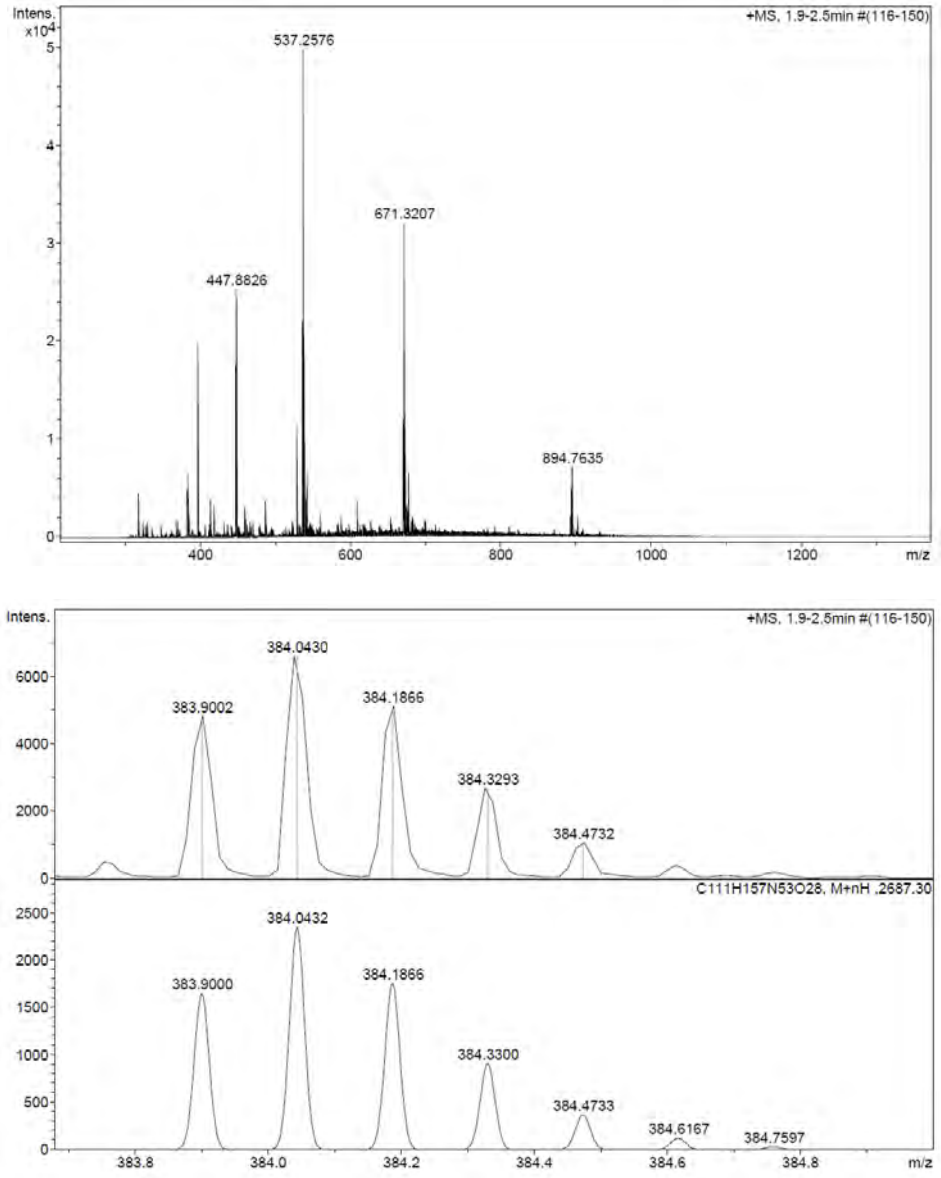

Observed HRMS (top) with the theoretical isotope prediction (bottom).

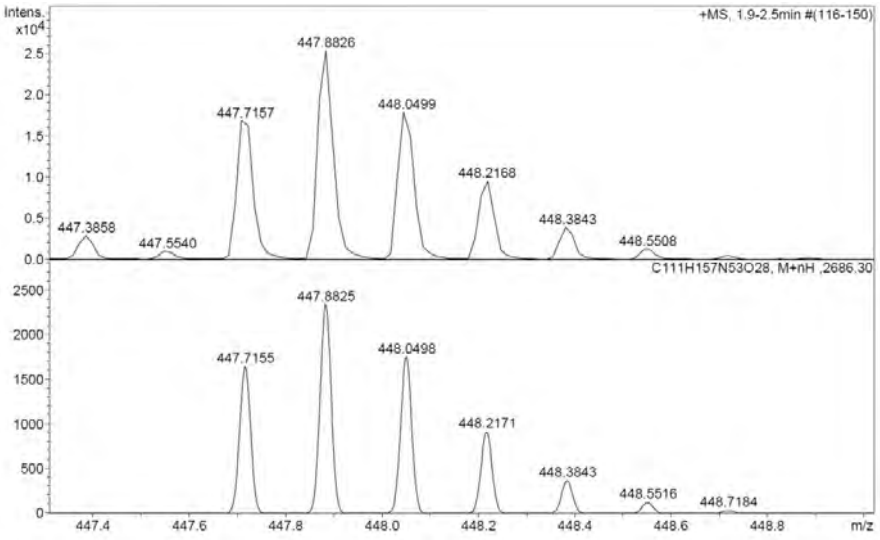

Observed HRMS (top) with the theoretical isotope prediction (bottom).

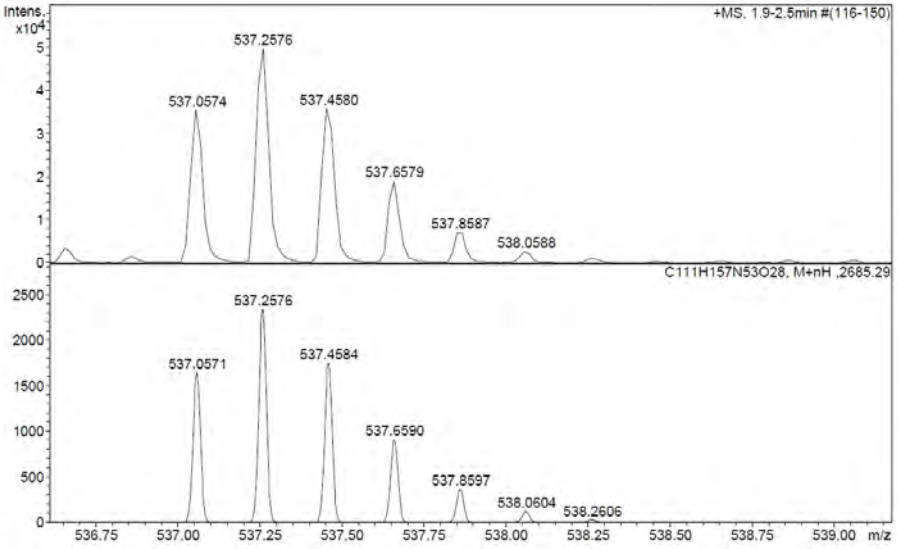

Observed HRMS (top) with the theoretical isotope prediction (bottom).

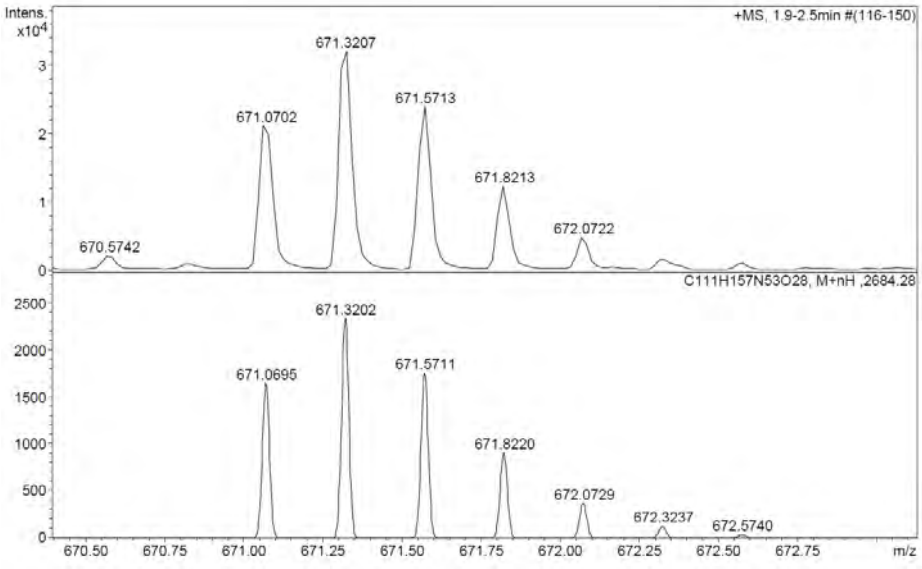

Observed HRMS (top) with the theoretical isotope prediction (bottom).

Figure SVII.3: a) HPLC chromatogram (λ= 220 nm), b) HRMS spectrum (*m/z*).

BPBP-PNA$_{135}$

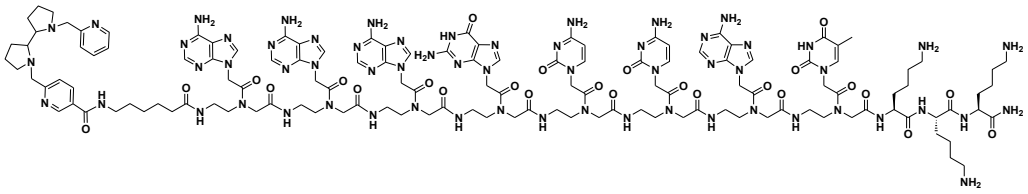

a)

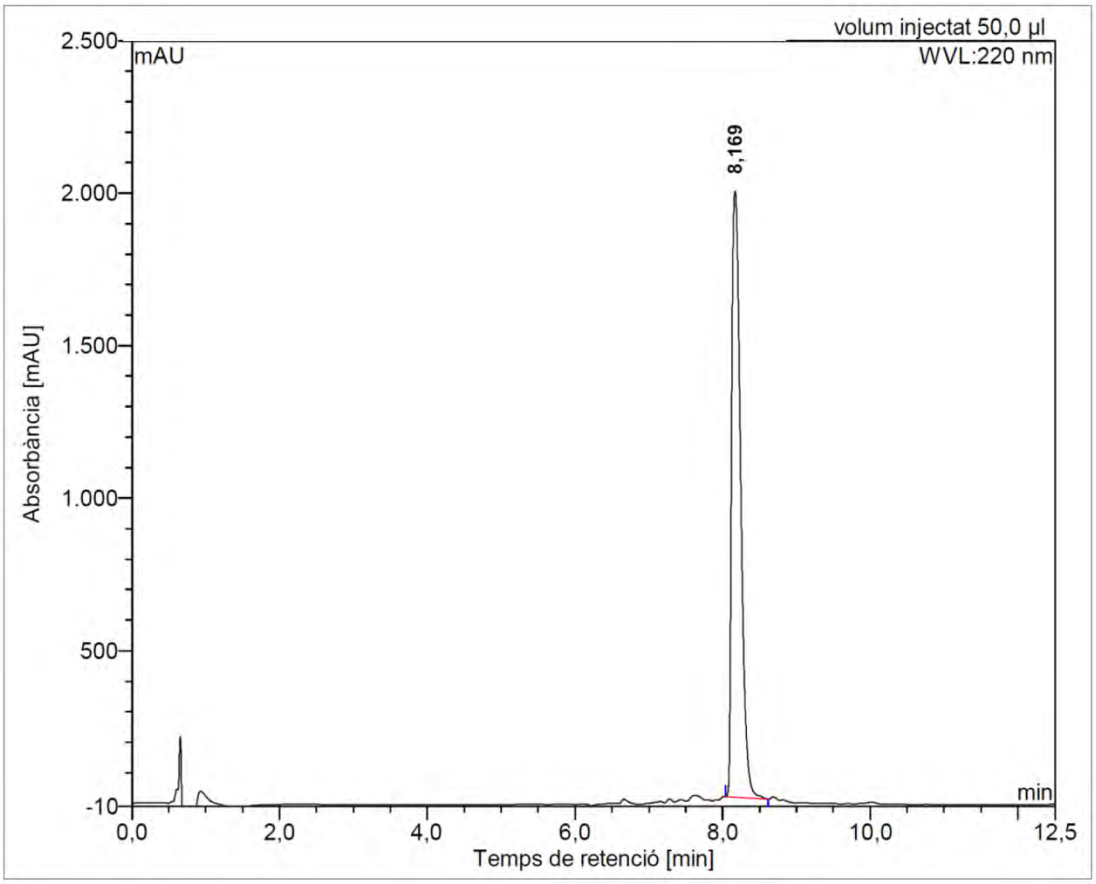

No.	mps retenc min	alçada mAU	Area mAU*min	Area relativa %
1	8,17	1987,128	278,957	100,00
Total:		1987,128	278,957	100,00

b)

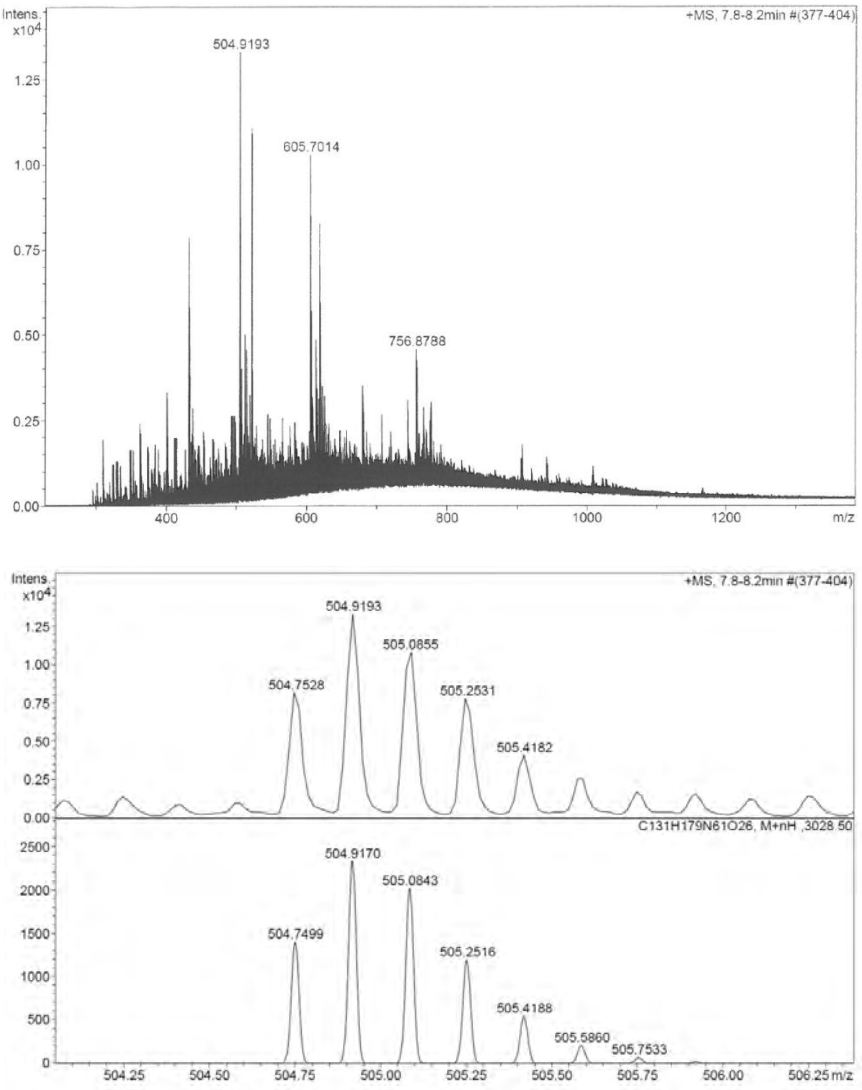

Observed HRMS (top) with the theoretical isotope prediction (bottom).

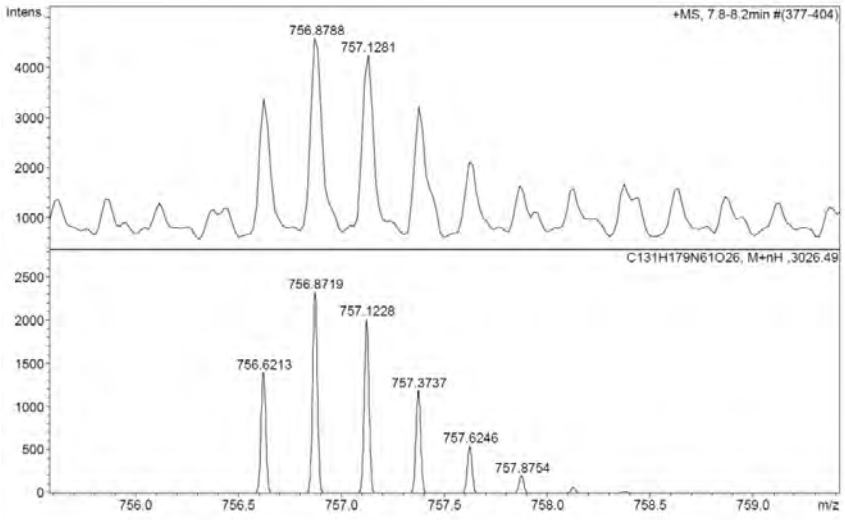

Observed HRMS (top) with the theoretical isotope prediction (bottom).

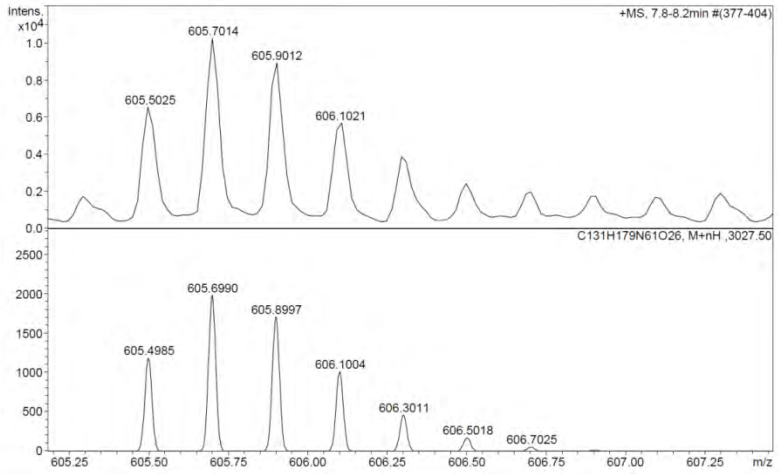

Observed HRMS (top) with the theoretical isotope prediction (bottom).

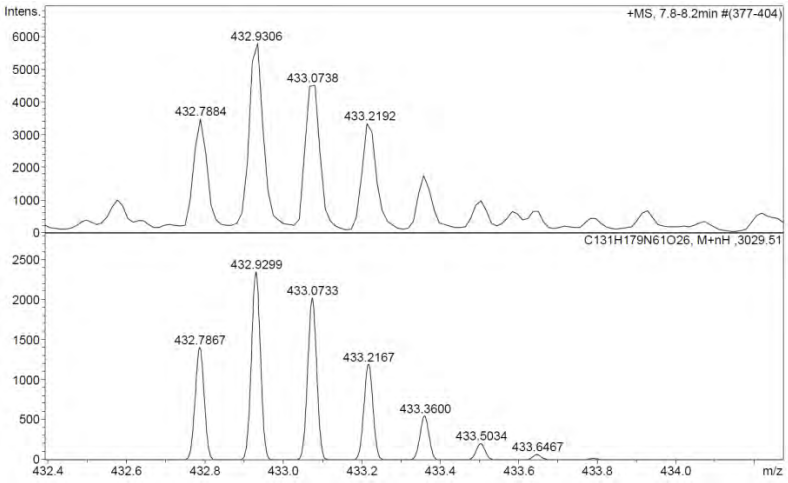

Observed HRMS (top) with the theoretical isotope prediction (bottom).

Figure SVII.4: a) HPLC chromatogram (λ= 214 nm), b) HRMS spectrum (*m/z*).

BPBP-PNA$_{155}$

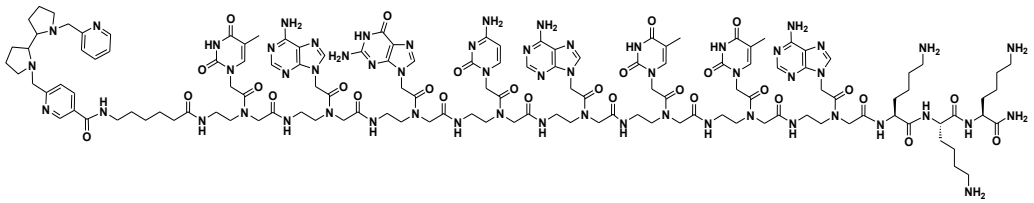

a)

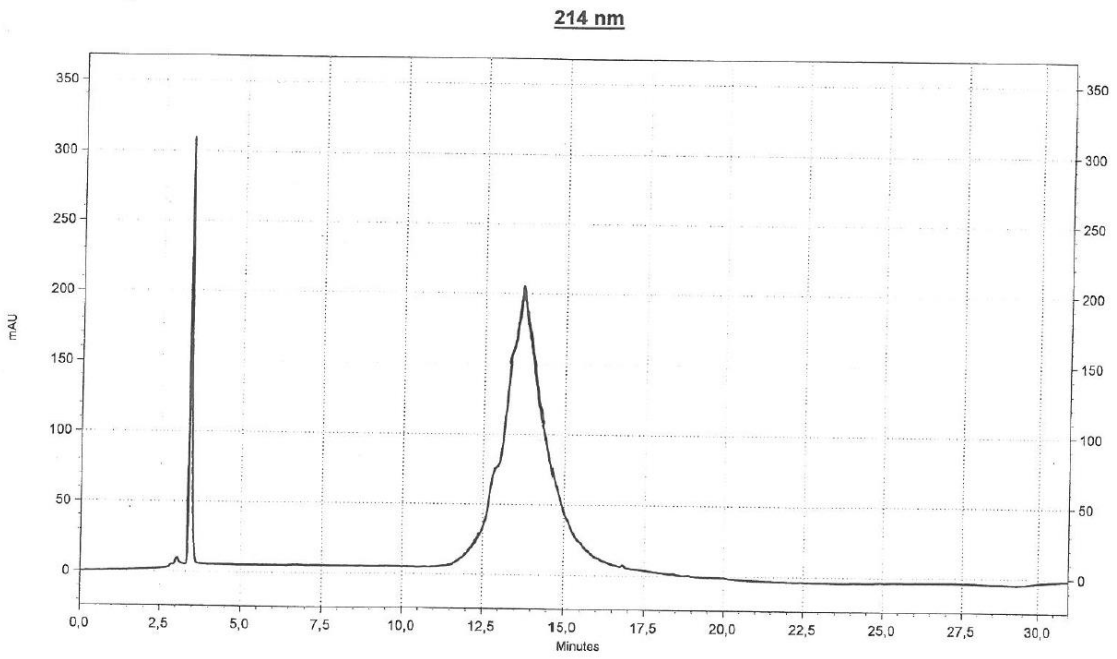

b)

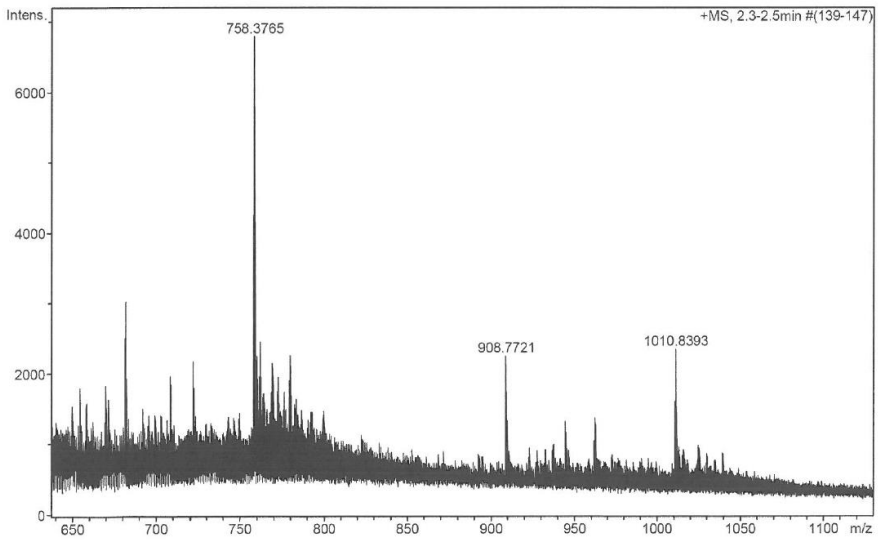

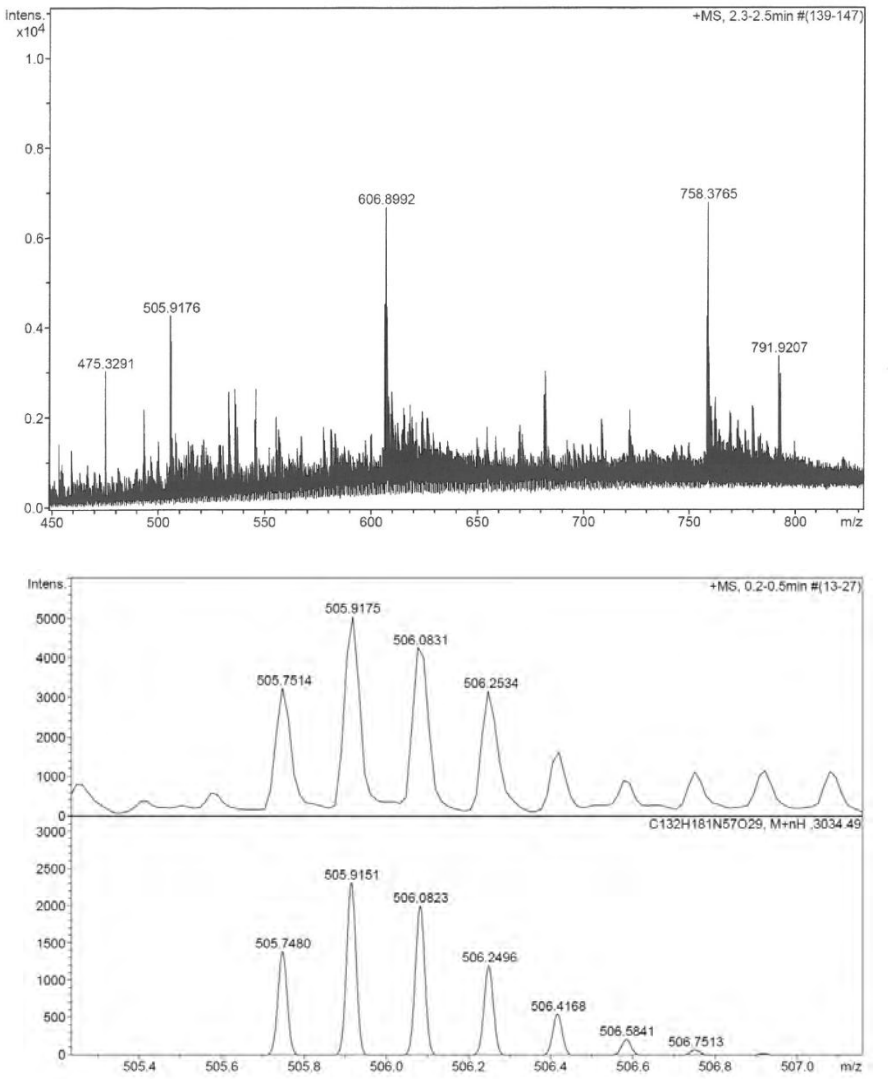

Observed HRMS (top) with the theoretical isotope prediction (bottom).

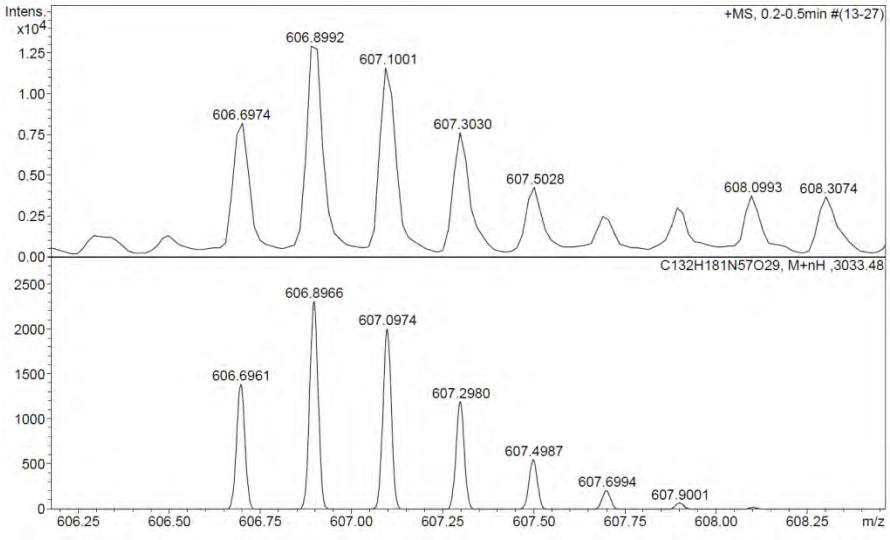

Observed HRMS (top) with the theoretical isotope prediction (bottom).

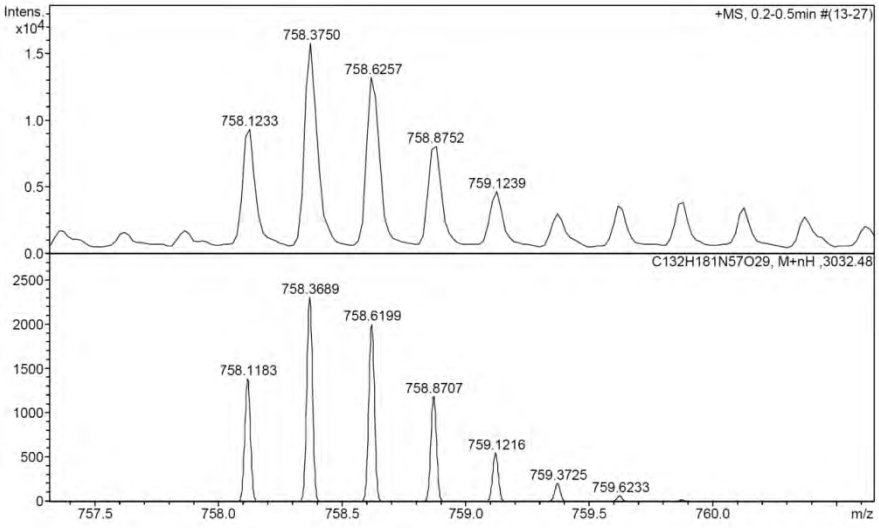

Observed HRMS (top) with the theoretical isotope prediction (bottom).

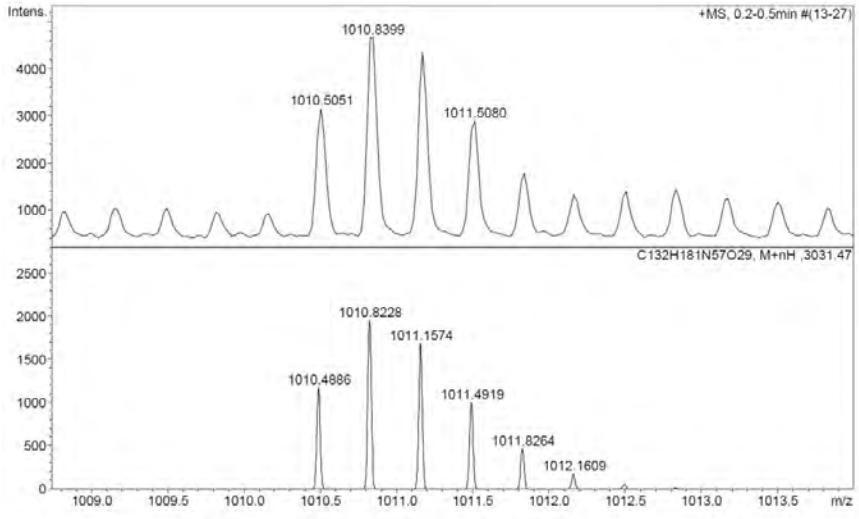

Observed HRMS (top) with the theoretical isotope prediction (bottom).

Figure SVII.5: a) HPLC chromatogram (λ= 220 nm), b) ESI/MS spectrum (*m/z*), c) HRMS spectrum (*m/z*).

CF-PNA$_{135}$

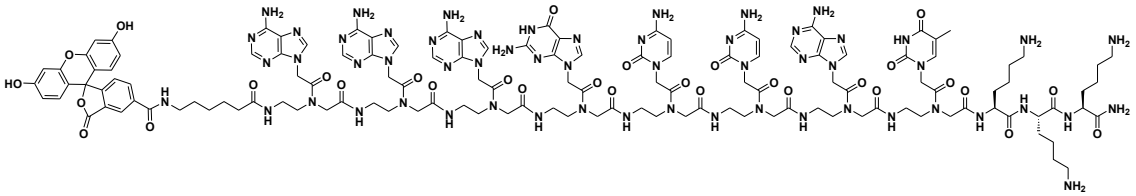

a)

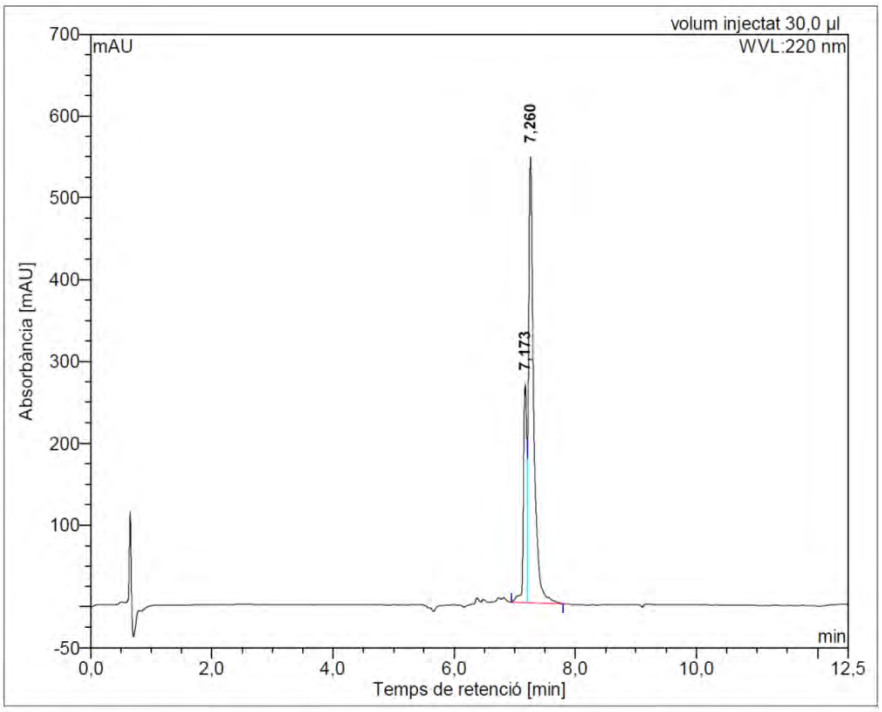

No.	mps retenc min	alçada mAU	Area mAU*min	Area relativa %
1	7,17	266,943	17,277	24,49
2	7,26	544,917	53,282	75,51
Total:		811,861	70,559	100,00

b)

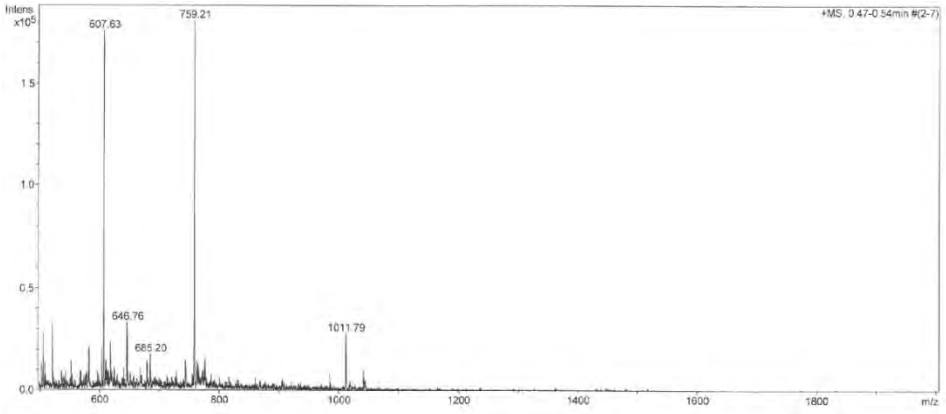

c)

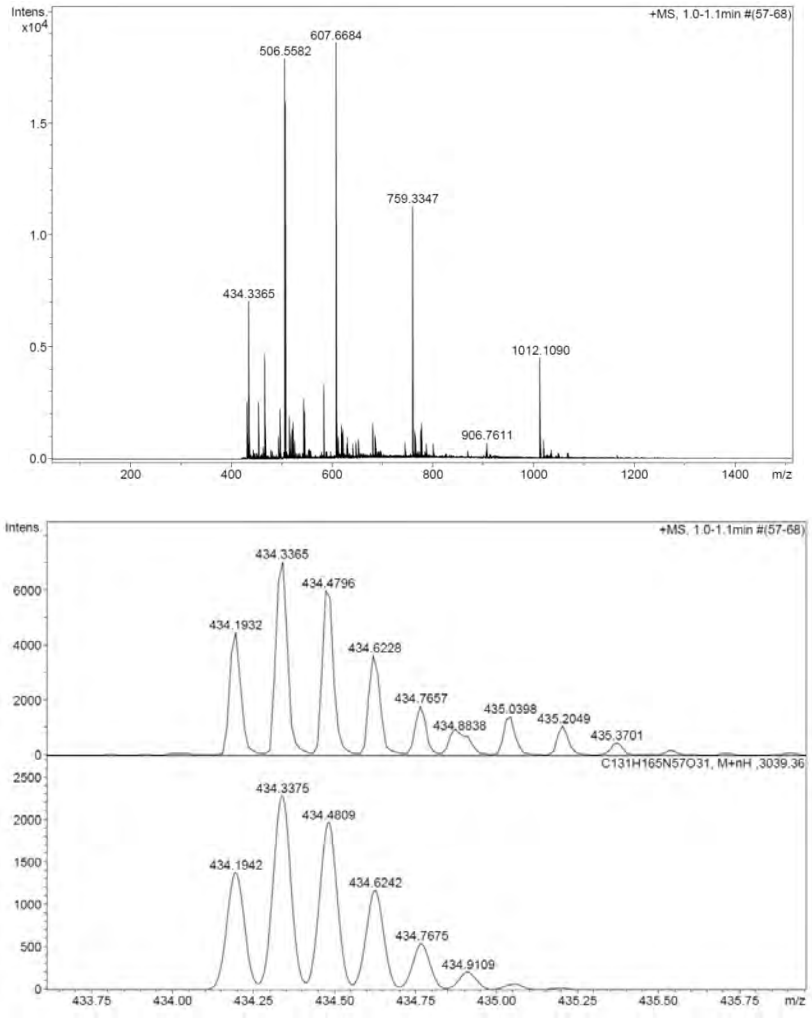

Observed HRMS (top) with the theoretical isotope prediction (bottom).

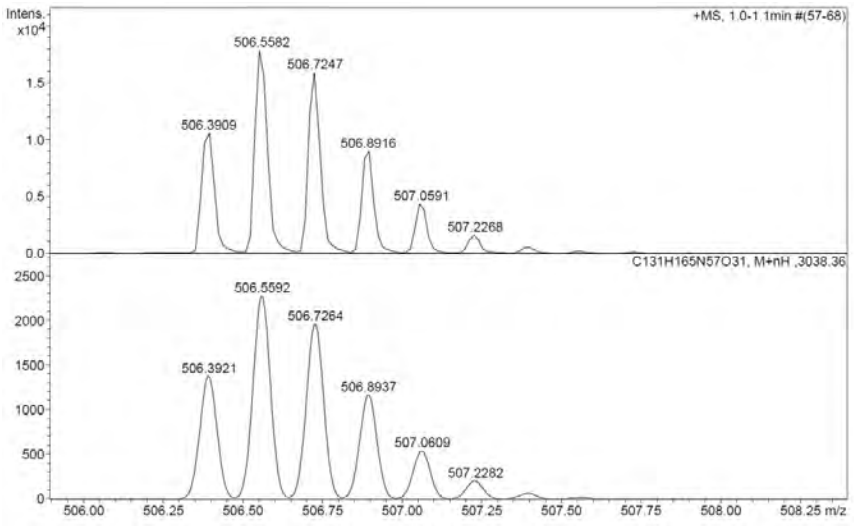

Observed HRMS (top) with the theoretical isotope prediction (bottom).

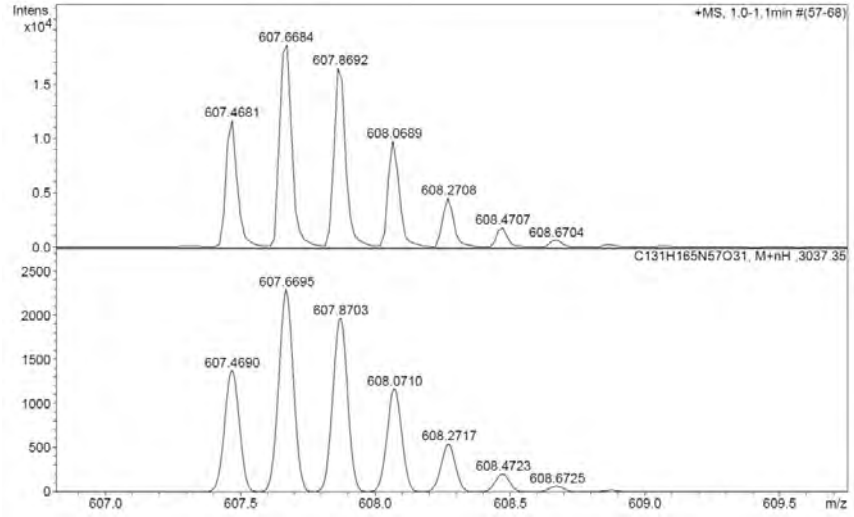

Observed HRMS (top) with the theoretical isotope prediction (bottom).

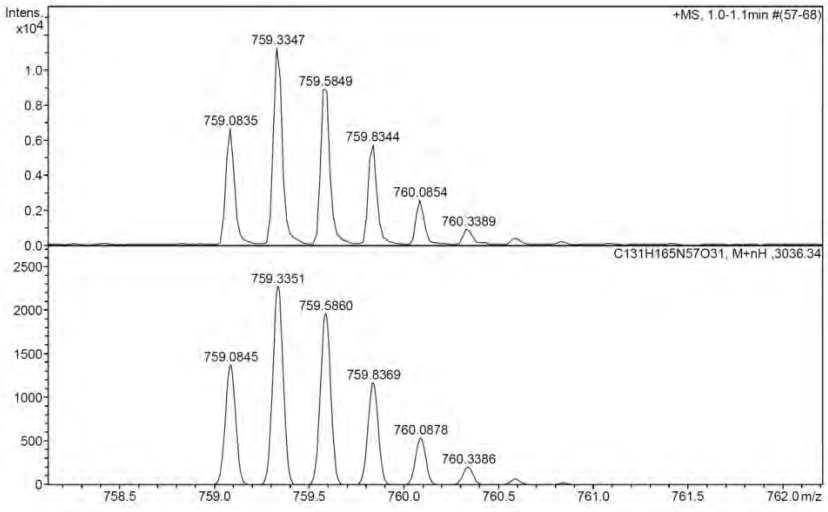

Observed HRMS (top) with the theoretical isotope prediction (bottom).

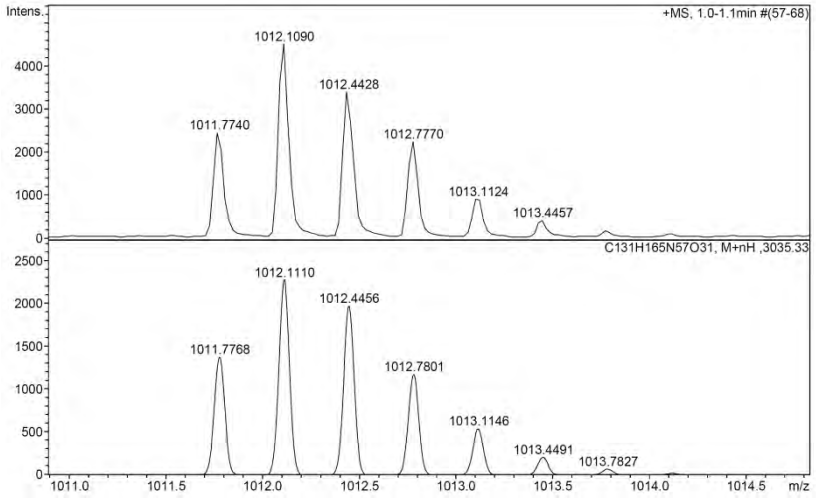

Observed HRMS (top) with the theoretical isotope prediction (bottom).

Figure SVII.6: a) HPLC chromatogram (λ= 220 nm), b) ESI/MS spectrum (*m/z*), c) HRMS spectrum (*m/z*).

CF-PNA$_{155}$

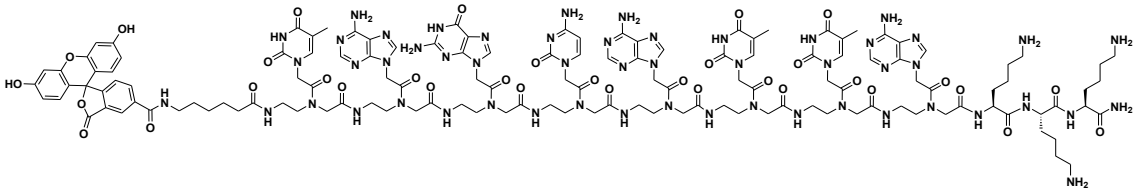

a)

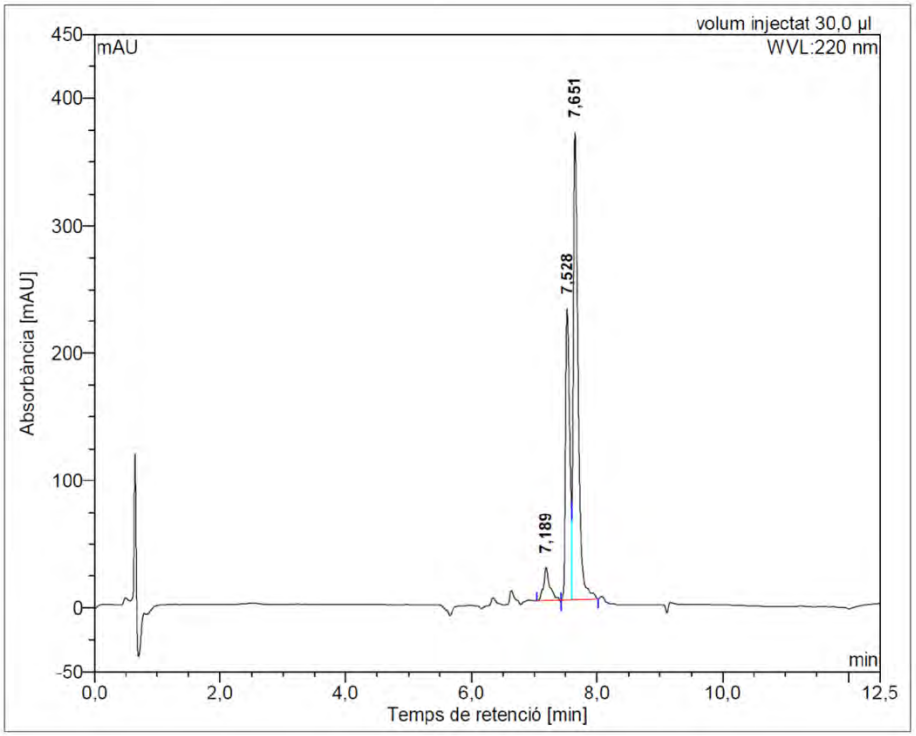

No.	mps retenc min	alçada mAU	Area mAU*min	Area relativa %
1	7,19	26,104	2,979	5,70
2	7,53	229,087	17,335	33,18
3	7,65	366,827	31,932	61,12
Total:		622,017	52,246	100,00

b)

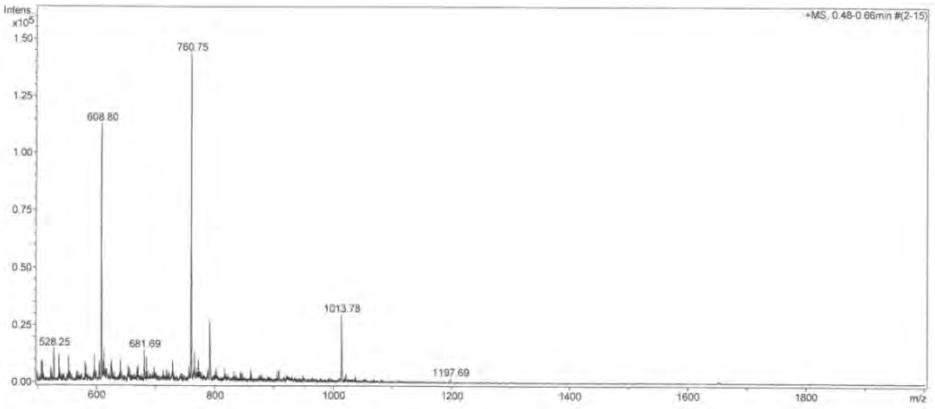

c)

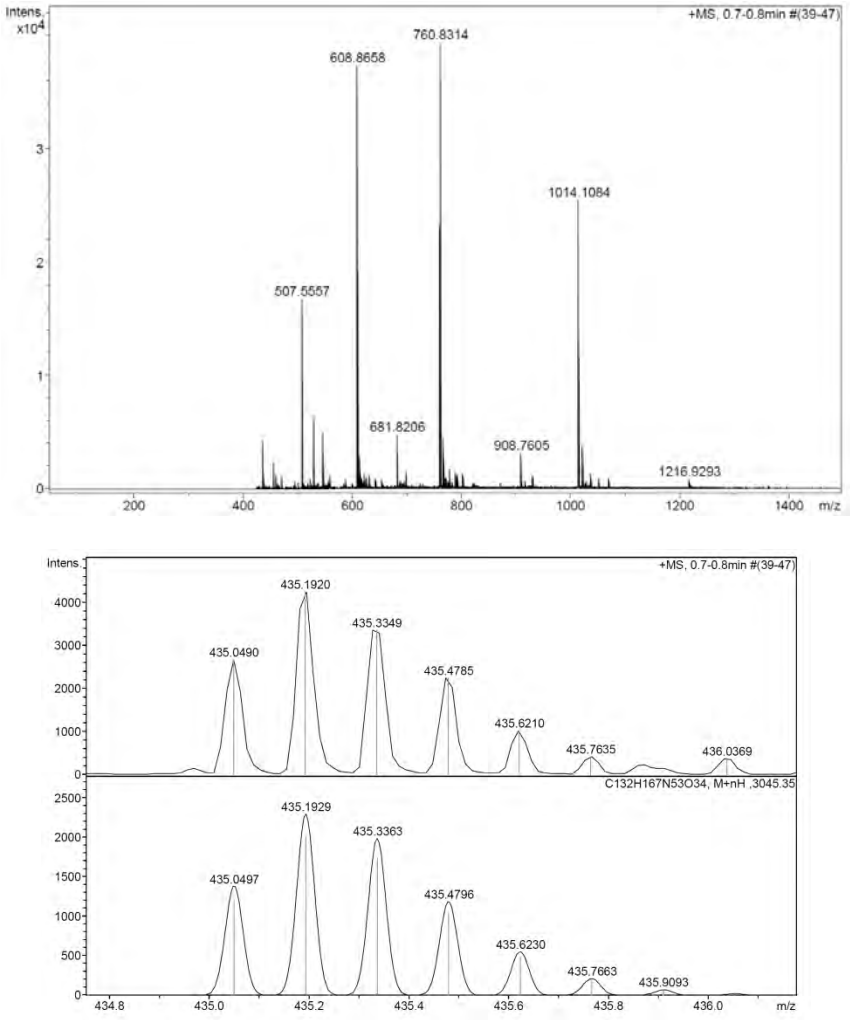

Observed HRMS (top) with the theoretical isotope prediction (bottom).

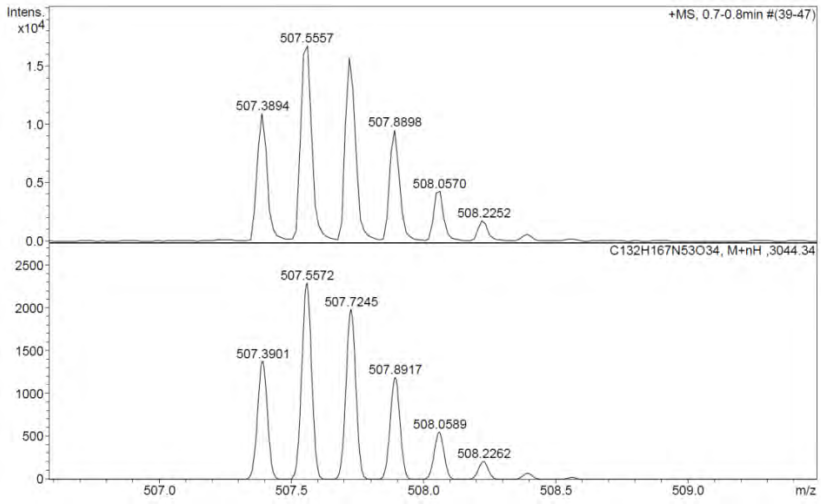

Observed HRMS (top) with the theoretical isotope prediction (bottom).

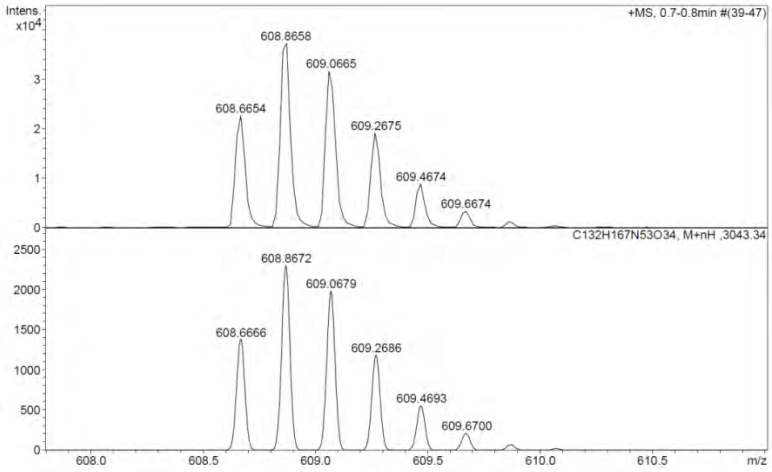

Observed HRMS (top) with the theoretical isotope prediction (bottom).

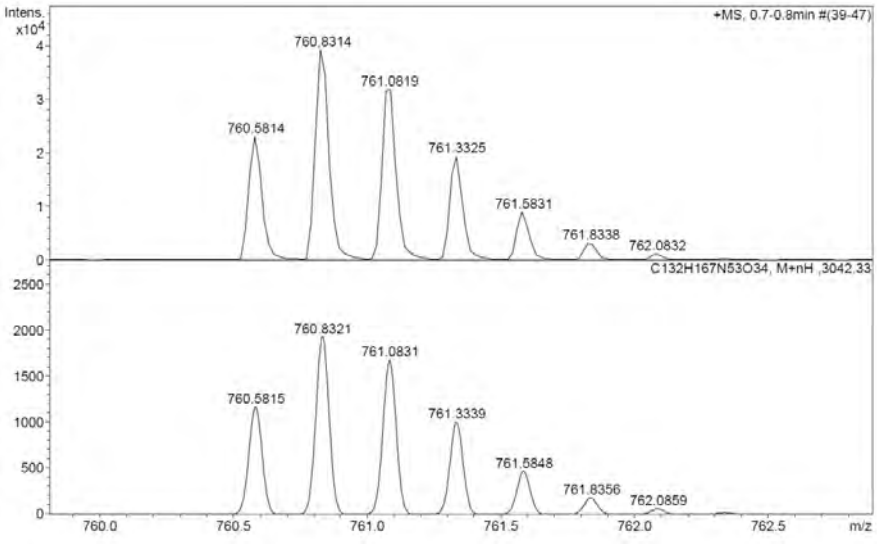

Observed HRMS (top) with the theoretical isotope prediction (bottom).

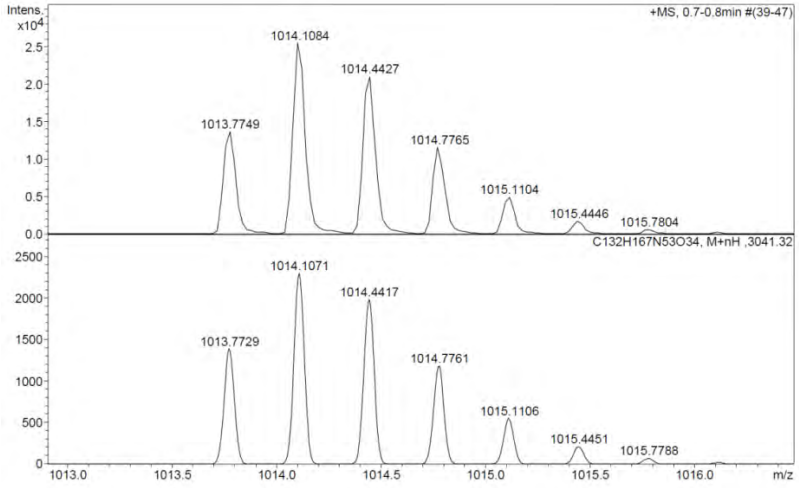

Observed HRMS (top) with the theoretical isotope prediction (bottom).

Hydrolysis experiments

Figure SVII.7: IE-HPLC analysis of the incubation of RNA substrate (miRNA-155 2-18) and free BPBP ligand for 50 h at 37 ºC.

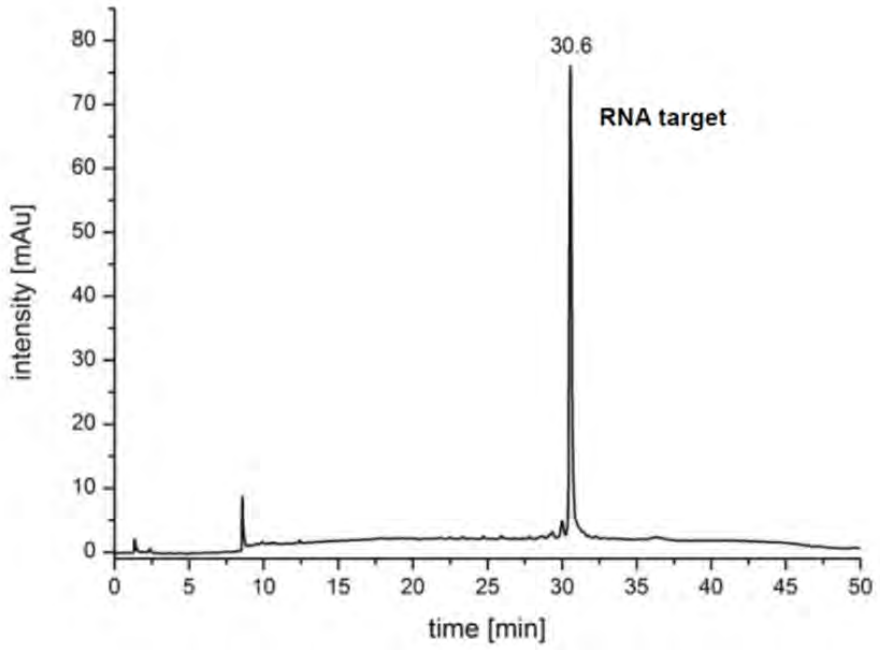

RNA fragments (MALDI-TOF)

Figure SVII.8: **5'-UAAUGCU** (2',3'-cyclic phosphate)

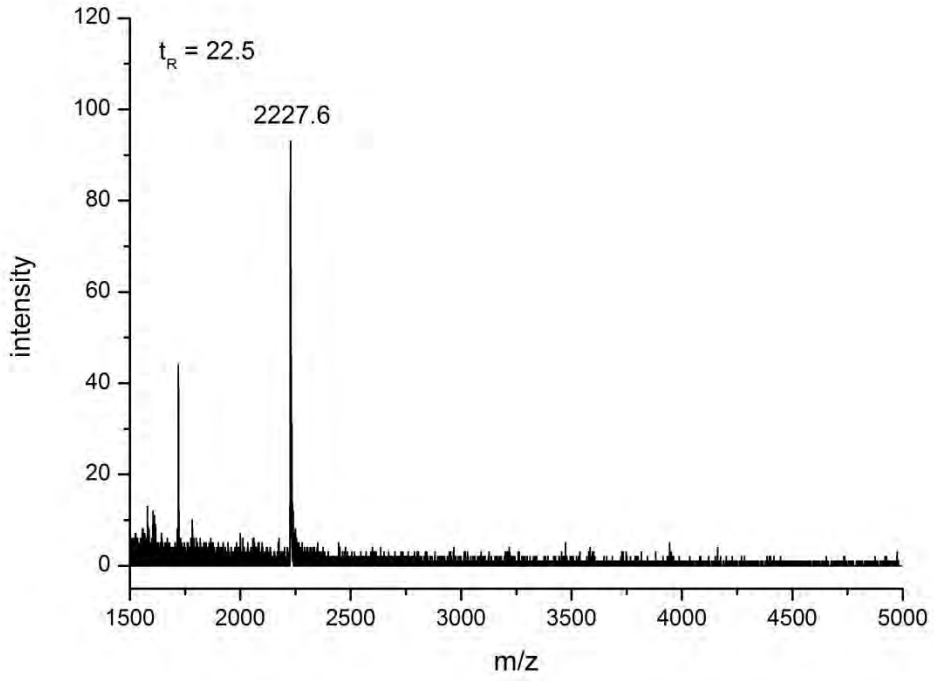

Figure SVII.9: AAUCGUGAUA-3'

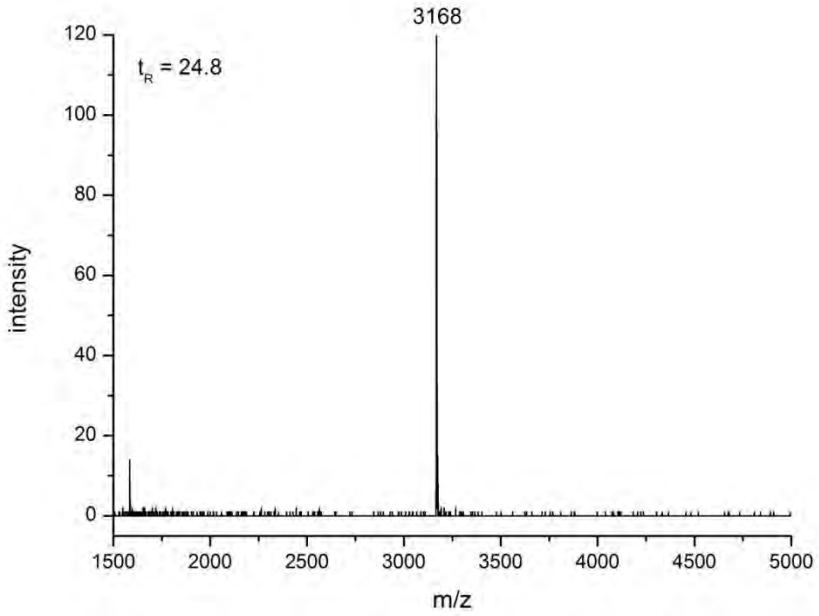

Figure SVII.10: CGUGAUA-3'

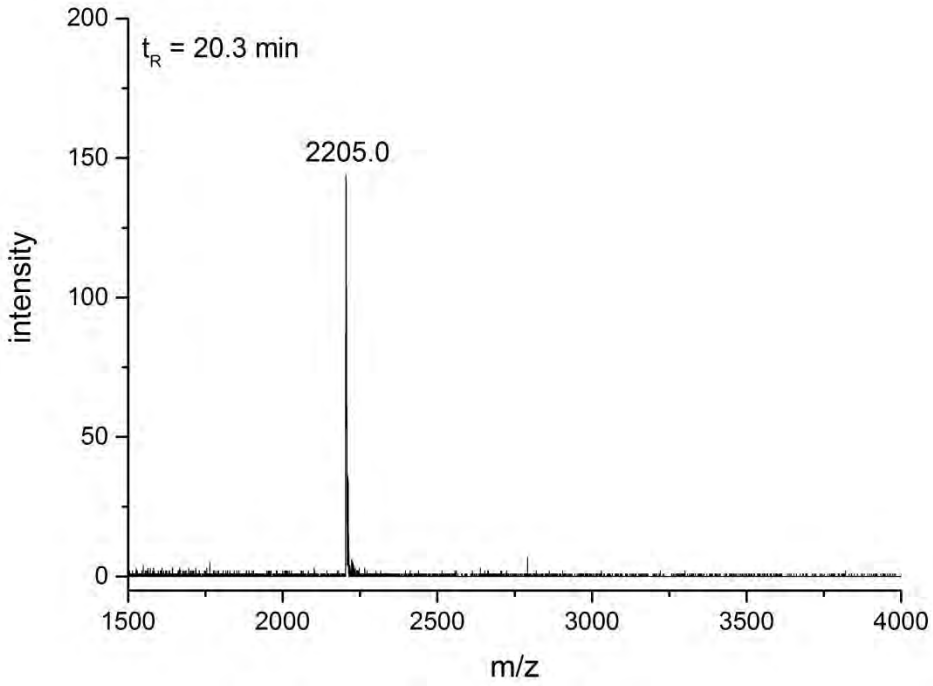

Figure SVII.11: 5'-UAAUGCUAAU (2',3'-cyclic phosphate)

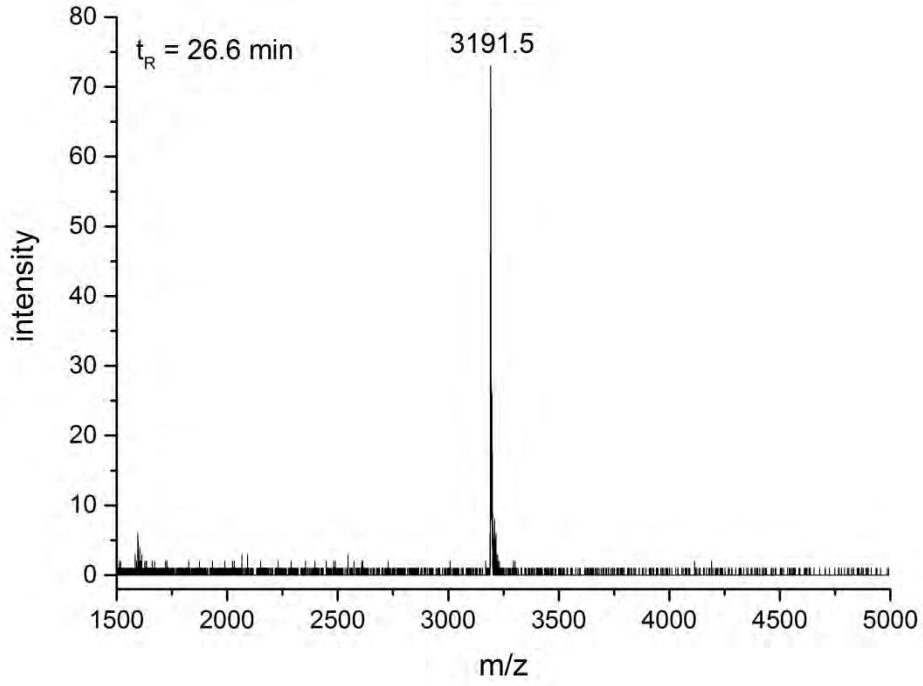

Figure SVII.12: 5'-UAAUGCUAAUC (2',3'-cyclic phosphate)